UAB
Universitat Autònoma de Barcelona

The craniodental morphology of Pliobates cataloniae (Primates: Catarrhini): Phylogenetic implications

FLORIAN BOUCHET

ADVERTIMENT. L'accés als continguts d'aquesta tesi doctoral i la seva utilització ha de respectar els drets de la persona autora. Pot ser utilitzada per a consulta o estudi personal, així com en activitats o materials d'investigació i docència en els termes establerts a l'art. 32 del Text Refós de la Llei de Propietat Intel·lectual (RDL 1/1996). Per altres utilitzacions es requereix l'autorització prèvia i expressa de la persona autora. En qualsevol cas, en la utilització dels seus continguts caldrà indicar de forma clara el nom i cognoms de la persona autora i el títol de la tesi doctoral. No s'autoritza la seva reproducció o altres formes d'explotació efectuades amb finalitats de lucre ni la seva comunicació pública des d'un lloc aliè al servei TDX. Tampoc s'autoritza la presentació del seu contingut en una finestra o marc aliè a TDX (framing). Aquesta reserva de drets afecta tant als continguts de la tesi com als seus resums i índexs.

ADVERTENCIA. El acceso a los contenidos de esta tesis doctoral y su utilización debe respetar los derechos de la persona autora. Puede ser utilizada para consulta o estudio personal, así como en actividades o materiales de investigación y docencia en los términos establecidos en el art. 32 del Texto Refundido de la Ley de Propiedad Intelectual (RDL 1/1996). Para otros usos se requiere la autorización previa y expresa de la persona autora. En cualquier caso, en la utilización de sus contenidos se deberá indicar de forma clara el nombre y apellidos de la persona autora y el título de la tesis doctoral. No se autoriza su reproducción u otras formas de explotación efectuadas con fines lucrativos ni su comunicación pública desde un sitio ajeno al servicio TDR. Tampoco se autoriza la presentación de su contenido en una ventana o marco ajeno a TDR (framing). Esta reserva de derechos afecta tanto al contenido de la tesis como a sus resúmenes e índices.

WARNING. The access to the contents of this doctoral thesis and its use must respect the rights of the author. It can be used for reference or private study, as well as research and learning activities or materials in the terms established by the 32nd article of the Spanish Consolidated Copyright Act (RDL 1/1996). Express and previous authorization of the author is required for any other uses. In any case, when using its content, full name of the author and title of the thesis must be clearly indicated. Reproduction or other forms of for profit use or public communication from outside TDX service is not allowed. Presentation of its content in a window or frame external to TDX (framing) is not authorized either. These rights affect both the content of the thesis and its abstracts and indexes.

Institut Català de Paleontologia
Miquel Crusafont

Universitat Autònoma
de Barcelona

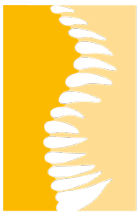
The craniodental morphology of *Pliobates cataloniae* (Primates: Catarrhini): Phylogenetic implications

Florian Bouchet



PhD Dissertation
Universitat Autònoma de Barcelona
PhD Program in Biodiversity
2024

Supervisors
Salvador Moyà-Solà
David M. Alba
Amélie Beaudet



Institut Català de Paleontologia
Miquel Crusafont

UAB
Universitat Autònoma
de Barcelona

The craniodental morphology of *Pliobates cataloniae* (Primates: Catarrhini): Phylogenetic implications

FLORIAN BOUCHET

PhD Dissertation

Universitat Autònoma de Barcelona,
PhD Program in Biodiversity

2024

Supervisors: Salvador Moyà-Solà
David M. Alba
Amélie Beaudet

The craniodental morphology of *Pliobates cataloniae* (Primates: Catarrhini): Phylogenetic implications

Dissertation submitted by **Florian Bouchet** to the PhD Programme in Biodiversity, Department of Animal Biology, Plant Biology and Ecology, in fulfillment of the requirements for obtaining the degree of Doctor by the Universitat Autònoma de Barcelona, and elaborated under the supervision of:

Prof. Salvador Moyà-Solà, ICREA at Institut Català de Paleontologia Miquel Crusafont and Unitat d'Antropologia Biològica (Departament de Biologia Animal, de Biologia Vegetal i d'Ecologia), Universitat Autònoma de Barcelona.

Dr. David Martínez Alba, Institut Català de Paleontologia Miquel Crusafont, Universitat Autònoma de Barcelona.

Dr. Amélie Beaudet, Laboratoire Paléontologie Evolution Paléoécosystèmes Paléoprimatologie, UMR 7262 Université de Poitiers & CNRS.

Signed in Bellaterra on April 18th, 2024:





Prof. Salvador Moyà-Solà	Dr. David M. Alba	Dr. Amélie Beaudet	Florian Bouchet
Supervisor	Supervisor & Tutor	Supervisor	PhD Candidate



La Torre

Drawing made with black stone on cream-colored paper by Ommethée.

"[…] but I think that every myth, every fable must have some roots. Something lies among those roots."

"It does […] Most often a dream, a wish, a desire, a yearning. Faith that there are no limits to possibility. And occasionally chance." [Geralt of Rivia]

Andrzej Sapkowski (Sword of Destiny, 1992)

There will inevitably be resistance, I know this all to well
I have been here before, you shut your eyes and ignore all my words
I am talking to deaf ears, but mark my words
You will never see the light of day
No one can save you now

Vildhjarta (Måsstaden, 2011)

Index

Index 7
Abstract 11
Acknowledgements 13
Chapter 1. Introduction 17
1.1. Miocene stem catarrhines from Africa and Eurasia 19
1.1.1. Pliopithecoids 19
1.1.2. Small-bodied stem catarrhines from the Miocene of East Africa 29
1.1.3. The small-bodied catarrhine *Pliobates cataloniae* 32
1.2. Aims, scope, and structure of this dissertation 34
1.2.1. Scope and specific aims 34
1.2.2. Structure of this work 36
Chapter 2. Materials and methods 39
2.1. Sample composition and acquisition 41
2.1.1. Studied *Pliobates* sample 41
2.1.2. Extant comparative sample 42
2.1.3. Fossil comparative sample 43
2.2. Methods 44
2.2.1. Virtual sample preparation 44
2.2.2. Measurements and anatomical nomenclature 46
2.2.3. Geometric morphometric analyses 48
2.2.4. Statistical techniques 50
2.2.5. Phylogenetic comparative methods 53
2.2.6. Phylogenetic inference 57
Chapter 3. Comparative anatomy of the carotid canal in the Miocene small-bodied catarrhine *Pliobates cataloniae* 63
Abstract 65
Introduction 66
Pliobates and catarrhine evolution 66
The carotid canal in primate phylogenetics 66
Materials and methods 67
Materials 67
Morphometric methods 67
Between-group principal component analyses 70
Statistical analyses 72
Phylogenetically informed methods 72
Results 72
Carotid canal orientation 72
Carotid canal proportions and body size scaling 72
Carotid canal course within the petrosal 75
Discussion 77

Carotid canal orientation 77
Carotid canal proportions 80
Carotid canal course 82
Evolutionary implications 82
Summary and conclusions 83
Acknowledgments 84
References 84
Supplementary Online Material 87
Chapter 4. The Miocene primate *Pliobates* is a pliopithecoid 125
Abstract 127
Introduction 127
Results 128
Systematic paleontology 128
Description of the referred specimens 129
Morphological comparisons and body mass 132
Cladistic analysis 132
Discussion 133
The systematic position of *Pliobates* based on dental morphology 133
Implications for pliopithecoid locomotor diversity 134
Implications for ape evolution 135
Methods 136
Age and geological background 136
MicroCT scan acquisition and segmentation 136
Dental measurements, dental nomenclature, and comparative sample 136
Systematics 136
Body mass estimation 137
Cladistic analysis 137
Data availability 137
References 137
Acknowledgments 139
Supplementary Information 141
Supplementary Data 184
Source Data 211
Chapter 5. Molar enamel-dentine junction shape of *Pliobates cataloniae* and other Iberian pliopithecoids 233
Abstract 236
Introduction 236
Materials and methods 238
Studied and comparative samples 238
Methods 239
Results 241
Description of the enamel-dentine junction shape in *Pliobates* 241
Comparisons 243
Multivariate analyses of the enamel-dentine junction shape 245

Enamel-dentine junction shape variation analyses 246
Discussion....247
Conclusions....249
Acknowledgments 249
References....249
Supplementary Online Material....266
Chapter 6. Discussion 277
6.1. Carotid canal morphology 279
6.1.1. Phylogenetic signal 279
6.1.2. Phylogenetic implications for *Pliobates* 281
6.2. Dental morphology of *Pliobates cataloniae* 282
6.2.1. Tooth external morphology....282
6.2.2. Molar enamel-dentine junction 287
6.3. Cladistic analyses....288
6.3.1. Dental and cranial analyses....288
6.3.2. Postcranial analyses 292
6.3.3. Evolutionary implications 293
Chapter 7. Conclusions 297
References 301

Abstract

The small-bodied catarrhine primate *Pliobates cataloniae* was described in 2015 based on a partial skeleton from the Miocene (11.6 Ma) of Abocador de Can Mata (Vallès-Penedès Basin, NE Iberian Peninsula). This species was originally interpreted as a stem hominoid rather than a stem catarrhine based on a cladistic analysis. However, subsequent cladistic analyses reinterpreted *Pliobates* as a member of the Pliopithecoidea (a clade of stem catarrhines from Eurasia). Alternative plausible phylogenetic hypotheses for *Pliobates* would include being a stem hylobatid or a dendropithecid (a family of putative stem catarrhines from East Africa). This PhD dissertation describes previously unpublished dentognathic material of *P. cataloniae* and focuses on the study of its craniodental morphology, with the ultimate goal of elucidating its systematic status and closest phylogenetic relationships. The specific aims are the following: (i) to evaluate the potential of carotid canal morphology for phylogenetic inference among catarrhines and test whether *Pliobates* is phenetically closer to hylobatids in this regard; (ii) to describe the previously unpublished dentognathic remains of *P. cataloniae* from locality ACM/C5-D1, to clarify its systematic status; (iii) to quantitatively analyze the enamel-dentine junction (EDJ) shape of *Pliobates* molars to test its closest phenetic affinities as compared with pliopithecoids and hominoids; and (iv) to perform cladistic analyses of *Pliobates* including the new craniodental evidence to decipher its phylogenetic relationships with other extinct and extant catarrhines. The methods employed mostly rely on microcomputed tomography scans and landmark-based three-dimensional geometric morphometrics (3DGM). These include an innovative protocol specifically devised for the carotid canal. Phylogenetic comparative methods and bivariate and multivariate statistical analyses were applied to shape data, while cladistic analyses relied on maximum parsimony.

The results are presented in two published articles and an unpublished manuscript. The main conclusions can be summarized as follows: (i) The quantitative analysis of carotid canal 3D morphology among catarrhines, here performed for the first time, indicates that this structure is of limited utility for catarrhine taxonomy and phylogeny and that, in any case, the carotid canal of *Pliobates* is not particularly similar to that of hylobatids, contrary to previous assertions; (ii) The description of previously unpublished teeth from ACM/C5-D1 indicates that *Pliobates* is a pliopithecoid genus that belongs to the family Crouzeliidae; (iii) The EDJ morphology of *Pliobates* most closely resembles that of pliopithecoids instead of hominoids; (iv) A cladistic analysis, performed at the species level based on dental features, recovers the monophyly of the Pliopithecoidea and Crouzeliidae, and supports that *Pliobates* is a derived crouzeliine most closely related to *Crouzelia* and *Plesiopliopithecus*; and (v) Further cladistic analyses performed at the genus level for a wider sample yield similar results when (cranio)dental characters are used but recover

Pliobates and other pliopithecoids as stem hominoids when postcranial features are considered. It is thus concluded that *Pliobates* is a derived pliopithecoid crouzeliid that was previously interpreted as a stem hominoid because of the possession of multiple postcranial convergences with extant apes.

Acknowledgements

This PhD dissertation has been possible thanks to a Formación de Personal Investigador (FPI) predoctoral grant (PRE2018-083299) in the framework of R+D+I project CGL2017-82654-P (led by Salvador Moyà-Solà and Raef Minwer-Barakat as principal investigators), funded by the Agencia Estatal de Investigación of the Ministerio de Ciencia e Innovación (MCIN/AEI/10.13039/501100011033/) from Spain. My research has also been funded by the R+D+I project PID2020-116908GB-100/AEI/10.13039/501100011033 (led by Salvador Moyà-Solà and Júlia Arias-Martorell as principal investigators), the CERCA Programme/Generalitat de Catalunya, and two (Consolidated Research Groups 2022 SGR 01188) funded by the Agència de Gestió d'Ajuts Universitaris i de Recerca of the Generalitat de Catalunya.

Much of the present work is based on μCT scans and 3D models of craniodental structures of *Pliobates* and other Iberian pliopithecoids, for which most were performed at the CENIEH facilities (Burgos, Spain) with the collaboration of the CENIEH staff. With regard to the fossil and extant comparative material, I would like to thank the following people and institutions for granting access to μCT scans: Burkhard Schillinger (Heinz Maier-Leibnitz Zentrum [FRM II], Technische Universität München, Garching, Germany), Claudio Tuniz (Multidisciplinary Laboratory, 'Abdus Salam' International Centre for Theoretical Physics), Clément Zanolli (PACEA, Université de Bordeaux), Deborah Arbulla (Trieste Natural History Museum, Italy), Federico Bernardini (Multidisciplinary Laboratory, 'Abdus Salam' International Centre for Theoretical Physics, Trieste, Italy), Fred Spoor (Natural History Museum of London, UK), Martin Dockner Vienna μCT-Lab (Austria), Matthew M. Skinner (University of Kent, Canterbury, UK), Ursula Göhlich (Naturhistorisches Museum of Wien, Austria), and Sergio Almécija (American Museum of Natural History, New York, USA); The European Synchrotron Radiation Facility (Grenoble, France); the Max Plank Institute for Evolutionary Anthropology (Leipzig, Germany), the Museum für Naturkunde - Leibniz Institute for Evolution and Biodiversity Science, and the National Museums of Kenya (Nairobi, Kenya), ; I further thank Eric Delson (American Museum of Natural History, USA) and the NYCEP Morphometrics Group (the PRImate Morphometrics Online) for granting access to the NYCEP Primate Morphometric database.

I am profoundly grateful to my PhD supervisors: Salvador Moyà-Solà, David M. Alba, and Amélie Beaudet. They all guided me through many aspects of this dissertation and of academic research in general. Amélie first mentored me as a Master student who was, in a way, more of an inexperienced adventurer than a young academic. She gave me the opportunity to publish my first work on paleoprimatology after allowing me to make a special stay in South Africa, as well as to meet other brilliant researchers—including my future PhD supervisors at the ICP. In turn, Salvador

trusted me with the study of the exceptional material of *Pliobates* and gave me the opportunity to develop my PhD dissertation within the framework of his own research project. I am indebted to him for providing me with the technical resources I needed all along this work. I definitely thank him for the various discussions and brainstormings that we had, which allowed me to distance myself from my own scientific thoughts and certainties and showed me that one should sometimes reconsider a hypothesis. I further thank him for his constant support. Finally, I want to express my deepest gratitude to David. He welcomed me at the Institut Català de Paleontologia Miquel Crusafont (ICP) and supervised this PhD from scratch to full completion. His lessons, help, support, and dedication are incommensurable. He managed to make me develop interests for subjects I knew nothing about, made me improve my skills and knowledge in various scientific fields, and opened my mind to many facets of science and research. I was able to produce this work and grow as a scientist thanks to his supervision.

I am also thankful to several other great researchers for their guidance and help over the course of my PhD. First and foremost, to Clément Zanolli, whose expertise on tooth internal morphology was so valuable. He spent countless moments helping me with segmentations and corrections of 3D models as well as teaching me methods and tips on both imaging techniques and biostatistics. I also thank him for his advice and thoughts on life as a researcher. Second, I am grateful to Júlia Arias-Martorell for her support and kindness, as she regularly came to the office to get news. Pickaxing rocks and struggling with some segmentations together were actually memorable moments. I thank her for the time spent discussing about academic research, that was somehow relieving. Last but not least, I want to thank Sergio Almécija for his great contribution to improve the writing of my papers, and his suggestions and help on preparing nice and original figures.

Someone to whom I owe my entrance into academic research is Alexandre Ribéron, perhaps one of the most erudite persons I know. I was a student at Paul Sabatier University and remember his many lectures including evolutionary biology and biogeography—but not only, his anecdotes on field trips abroad, and his reflexions on humanity and history of sciences. He is who introduced me to 3D imaging techniques and the use of morphology in evolutionary studies. Since my time as a bachelor student, he would always get news and support me. Thank you, Alexandre.

I extend my thanks to Assumpció Malgosa (former coordinator of the UAB PhD Program in Biodiversity), Gemma Armengol Rosell (current coordinator of the same program), and the three members of the annual monitoring committee of my PhD (Isaac Casanovas-Vilar, Núria Armentano Oller, and Ferran Estebaranz-Sánchez), for their guidance throughout the process. I further express my gratitude to the following researchers for accepting to be members of my PhD evaluation committee: Ignacio Martínez, Júlia Arias-Martorell, Ghislain Thiery, Isaac Casanovas-Vilar, and Daniel DeMiguel.

Many other people from the ICP assisted me one way or another during my PhD and deserve to be acknowledged here: Josep Fortuny for accompanying me through the bureaucracy when I arrived at the ICP, and, along with Alejandro Serrano-Martínez, for handling the scanning process, providing the CT data, and handling data sharing; Sergio Llácer for his wonderful segmentations; Jordi Galindo for the entertaining time at the Barranc de Can Vila and the help with the access to fossil specimens; Josep M. Robles for facilitating access to the *Pliobates* specimens; Marta Pina, Àngel H. Luján, and J. Manel Mendéz for their field lessons and good time during fieldwork; Josep Torres for his IT assistance at any time; Pere Figuerola for organizing my first internal seminar and handling the dissemination of my results; Enric Menéndez and Mónica Vincent, as well as David Basanta and José Antonio Fuentes for their indefectible help with the many administrative processes; and Pepi for always keeping clean my workspace, and especially, my coffee machine.

Besides research and technical assistance, I am deeply grateful to my current and past ICP colleagues, not only for their mental support but also for the memorable extra moments enjoyed during the development of this PhD, including numerous hilarious discussions, meals and coffee breaks, cinema sessions, and groundbreaking parties: Rafel Matamales-Andreu, Sílvia Jovells-Vaqué, Teresa Calderón Sánchez, Maria Prat-Vericat, Clàudia Tura-Poch, Guillem Pons-Monjo, Carmen Nacarino, David P. Groenewald, Georgina Raventós-Izard, Jordi Pérez-Cano, Kelly A. Vega Pagán, Laia Garcia-Escolà, Raquel Moya-Costa, and Souzanna Siarabi. Special thanks go to my mates Andrea Villa, Chabi(er) de Jaime-Soguero, and Oriol Monclús-Gonzalo: our existential discussions and "cena y peli" nights at the apartment have been historical. Brothers, this is the Way. Another special thank goes to my mate Alessandro Urciuoli. He introduced me to Barcelona life, assisted my settling at the beginning of my PhD, and infinitely supported me both professionally and personally during all this time. Thank you very much, Ale.

Beyond my ICP fellows, there are several people that I would like to genuinely thank. To begin with, my very first flatmates Steven and Xabu, with whom I held the line during pandemic times through regular indoor cross training and sofa meetings. Second, my friends and former flatmates Leonardo and Elpiniki: you have always been warm-hearted to me and very supportive, and I thank you for this. I will remember our life moments in the living-room. "Ciao Belli"! Then, my Catalan brothers and flatmates Guillem and Víctor: Guillem, your presence everyday helped me remain afloat. Your unwavering support and understanding are inestimable, and I thank you for essentially everything. Víctor, your kindness, enthusiasm, and energy have been invigorating and bracing during the last part of this journey. Thank you for having been here. Finally, my best friends and Frankish brothers Thibault, Tristan, Micka, Yohann, and Vincent. I was able to escape with you every time I needed it: Thibault, for our adventures everywhere in France and endless epicurean nights; Tristan, for our leisurely gatherings and spiritual voyages in other worlds; Micka, for our brotherhood diners

in lands and quests at sea; Yohann, for our fantastical assemblies and ethylic councils; Vincent, for our remote storytellings and mountainous expeditions.

Last, I want to thank my family. Above all and from the heart, my parents Anne-Fleur and Patrick and my sisters Alexia and Mélanie. My mother, for teaching me the sense of pragmatism and bequeathing me her philosophical vision of all things; and my father, for teaching me the self-surpassing and bequeathing me his exploration spirit. You both educated me as to have the sense of hard work and perfectionism, giving me what I needed to complete my quests successfully and consistently pushing me to discover the world. My sisters, for their unconditional love and support. You have always been there and attentive, even hundreds or thousands of kilometres away. Then, my grandmothers “Mamies”, Geneviève and Anne-Marie, who always saw in me my liking for biodiversity and encouraged me in my professional choices. Also, my aunt and uncle Julie and Adrien, who, as doctors in specialized medicine would each time show me support and discuss with me about my work and prospects.

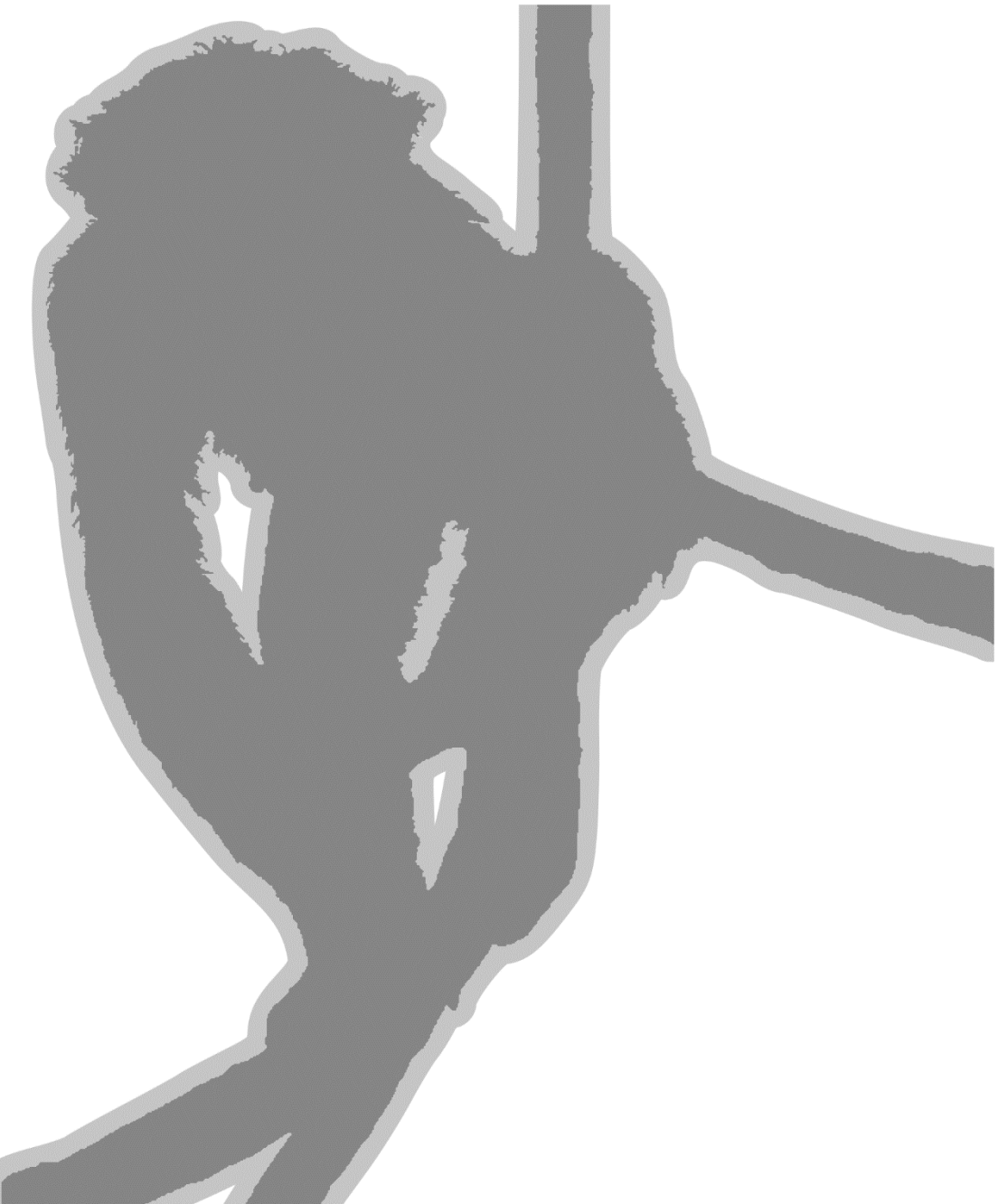
The very last person I want to thank is Lisa, the lady who have walked by my side for more than two years now and inspired me to grow and become a better person. I wish I had known you way before. Thank you for your patience, your words, and your affection. Thank you for your light, because you were here, at dawn, when I looked to the East.

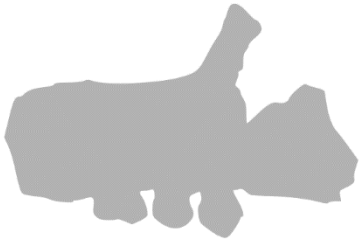




Chapter 1:

Introduction







Chapter 1. Introduction

1.1. Miocene stem catarrhines from Africa and Eurasia

1.1.1. Pliopithecoids

Pliopithecoid origins and systematics. The superfamily Pliopithecoidea is a clade of small to medium-sized (6–15 kg) stem catarrhines distributed across Eurasia from the Iberian Peninsula to eastern China between ~19–18 and 7 Ma (Harrison, 1987, 2005, 2013; Andrews et al., 1996; Harrison and Gu, 1999; Begun, 2002, 2017; Harrison et al., 2020; Figs. 1.1–1.3). Most pliopithecoids have been described on the basis of dentognathic material and their cranial and postcranial morphology is poorly known (Begun, 2002, Harrison, 2013). Partial crania have only been recovered for *Anapithecus hernyaki* from Hungary (Kordos and Begun, 2001), *Epipliopithecus vindobonensis* from Slovakia (Zapfe and Hürzeler, 1957; Zapfe, 1961a), and *Laccopithecus robustus* from China (Wu and Pan, 1985), while mandibular specimens are best preserved for *Pliopithecus canmatensis* from Spain (Alba et al., 2010) and *Pliopithecus. zhangxiangi* from China (Harrison et al., 1991). Three partial skeletons are known for *Epipliopithecus* (Zapfe and Hürzeler, 1957; Zapfe, 1958; Zapfe, 1961a) whereas only a few isolated postcranial elements are available for other pliopithecoid taxa (Begun, 2002; Senut, 2012; Arias-Martorell et al., 2021).

As specified above, most pliopithecoids are known exclusively on the basis of dentognathic remains. They possess the derived dental formula of catarrhines (2.1.2.3), with four cusps on the upper molars and five on their lowers (Begun, 2002, 2017). Compared with other catarrhines, they lack several crown-catarrhine synapomorphies such as the possession of an incompletely ossified tubular ectotympanic, an entepicondylar foramen in the distal humerus (but see Alba and Moyà-Solà, 2014), and a simple hinge-like thumb carpometacarpal joint (Szalay and Delson 1979; Harrison 1987, 2013; Andrews et al., 1996; Begun, 2002, 2017), but share several dental synapomorphies of their own (Andrews et al., 1996; Harrison and Gu, 1999; Harrison, 2013; Harrison et al., 2020; Ji et al., 2022), which justify being considered a clade of stem catarrhines: I1 slightly mesiodistally waisted toward the cervix; M2 and often M3 considerably larger than M1; relatively high-crowned and slender lower incisors (except *Anapithecus*, which has broad and spatulate incisors) that are further waisted toward the cervix (i.e., inverted flask-shaped outline in labial view); p3 mesiodistally short and high-crowned with a relatively short mesiobuccal honing face; and lower molars relatively long and narrow with a pliopithecine triangle. The most distinctive synapomorphy is the pliopithecine triangle of the lower molars—a small triangular fovea on the buccal side of the talonid basin

separated from the rest of the talonid basin by two converging crests, one emerging from the protoconid or the hypoprotocristid/postprotocristid (the mesial arm) and the other from the hypoconid or the prehypocristid (the distal arm; Harrison et al., 1999; Harrison, 2013). The occurrence and development of the pliopithecine triangle generally increase from m1 to m3 but are variable among species. In dionysopithecids, the mesial and distal arms are present—the former being variably-developed—in the m1, and both arms are more well-developed in the m2 and m3 (Harrison and Gu, 1999). In the pliopithecid *Pliopithecus* the triangle is well-developed in m2 and m3 whereas in m1 both arms are generally rudimentary (Begun, 2002; Alba et al., 2010). In contrast, the pliopithecid *Epipliopithecus* shows no triangle in its m1 and only one arm is sometimes distinct in the m2 and m3 (Zapfe, 1961a). In crouzeliids, the development of the triangle is also highly variable from one taxon to another and goes from completely developed in all molars (i.e., *Fanchangia*; Harrison et al., 2020) to poorly developed to absent in almost all molars (i.e., *Laccopithecus*; Ji et al., 2022).

Decades ago, several authors supported the view that pliopithecoids are closely related to extant hylobatids (Hürzeler, 1954; Zapfe, 1958, 1961a; Simons and Fleagle, 1973). It is now widely accepted that pliopithecoids are stem catarrhines more derived than propliopithecoids but less so than crown catarrhines and some other groups of fossil catarrhines, such as dendropithecids (Delson, 1977; Szalay and Delson 1979; Fleagle, 1984; Harrison 1987, 2005, 2013; Andrews et al., 1996; Harrison and Gu 1999; Begun 2002, 2017; Urciuoli et al., 2021a), as further supported by multiple cladistic analyses (Zalmout et al., 2010; Stevens et al., 2013; Nengo et al., 2017; Rossie and Hill, 2018; Gilbert et al., 2020a; Ji et al., 2022; but see Zalmout et al., 2010 and Alba et al., 2015). The more derived status of pliopithecoids compared with propliopithecoids within the catarrhine stem lineage agrees with their more tubular ectotympanic, seemingly more modern brain proportions (smaller olfactory lobes relative to brain size and larger brain relative to body size), and loss of the dorsal epitrochlear fossa of the distal humerus (Szalay and Delson 1979; Harrison 1987, 2013; Andrews et al., 1996; Begun, 2002, 2017).

Catarrhine primates were restricted to Afro-Arabia during their early evolution and pliopithecoids were the first members of this clade to disperse out of Africa (Andrews et al., 1996; Harrison and Gu, 1999; Harrison, 2005), thanks to paleogeographic changes. In particular, during the Early Miocene (Raffi et al., 2020) at ~19 Ma, the Afro-Arabian plate collided with Eurasia and the Tethys seaway closed. Along with fluctuating sea levels, this permitted the establishment of intermittent land bridges between Arabia and Southwest Asia that enabled multiple intercontinental faunal dispersals (Rögl, 1998, 1999; Harzhauser et al. 2007) until about 16 Ma, where such connection was temporarily interrupted again by the Langhian transgression (Steinthorsdottir et al., 2021). There is no evidence of pliopithecoids before 19–18 Ma and their fossil record is restricted to Eurasia. However, on morphological grounds it is likely that they diverged from an African stock of stem

catarrhines that dates back to the Oligocene (Harrison, 1987, 2013; Begun, 2017; Gilbert et al., 2020b). This is supported by the earliest record of crown catarrhines (both cercopithecoids and hominoids) by the Late Oligocene (~25 Ma) in East Africa (Stevens et al., 2013) and molecular estimates indicating that cercopithecoids and hominoids diverged between 32 and 25 Ma (Chatterjee et al., 2009; Perelman et al., 2011; Springer et al., 2012; Finstermeier et al., 2013; Liedigk et al., 2014; Pozzi et al., 2014; Roos and Zinner 2017).

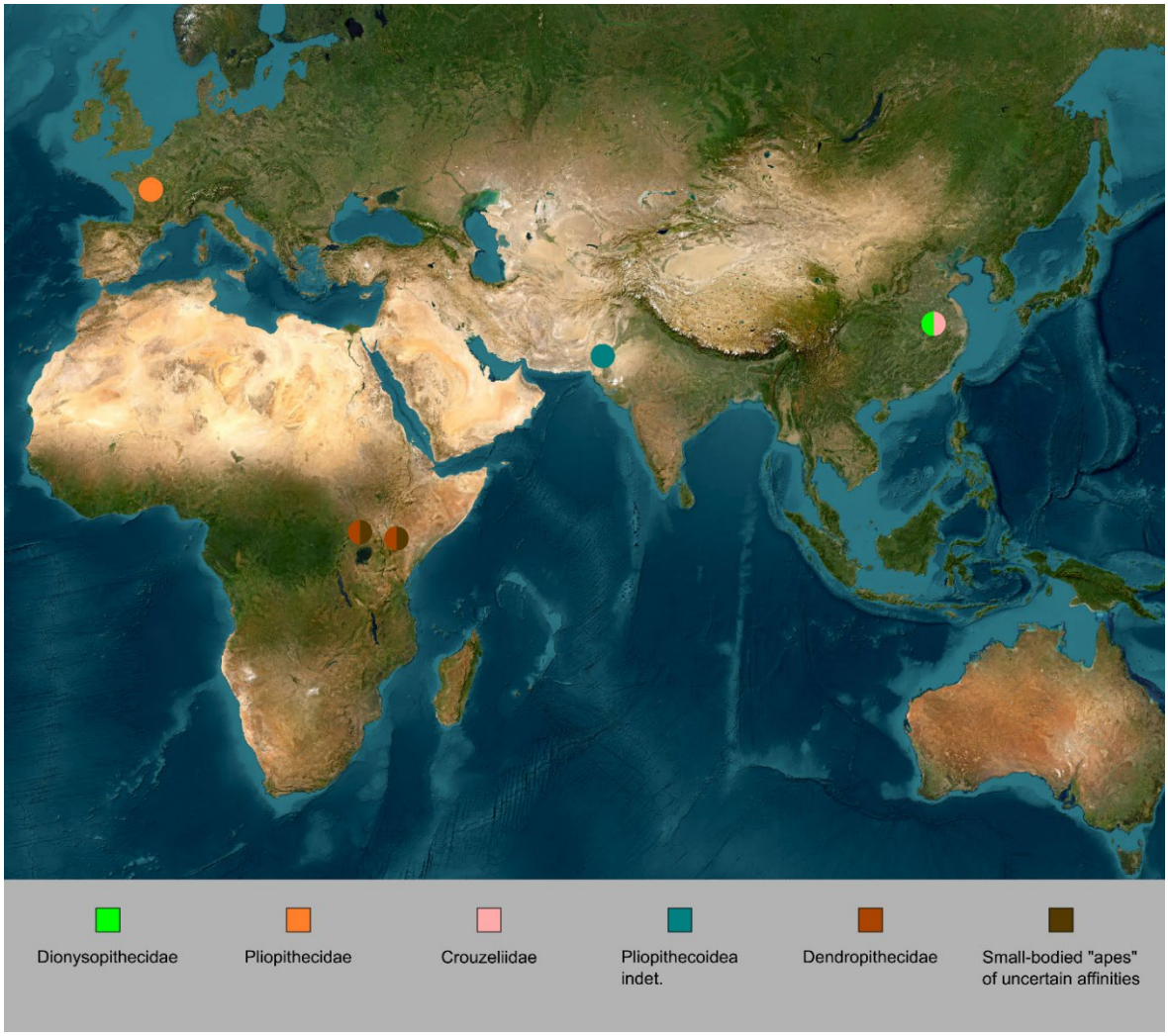


Figure 1.1. Geographic distribution of stem catarrhines in Africa and Eurasia during the Early Miocene (23.0–16.0 Ma), see main text for references and further details. Base map downloaded from ArcGIS Online (https://www.esri.com/it-it/arcgis/products/arcgisonline/); image sources: Esri, Maxar, GeoEye, Earthstar Geographics, CNES/Airbus DS, USDA, USGS, AeroGRID, IGN, and the GIS User Community, Sources: Esri, Airbus DS, USGS, NGA, NASA, CGIAR, N. Robinson, NCEAS, NLS, OS, NMA, Geodatastyrelsen, Rijkswaterstaat, GSA, Geoland, FEMA, Intermap and the GIS user community.

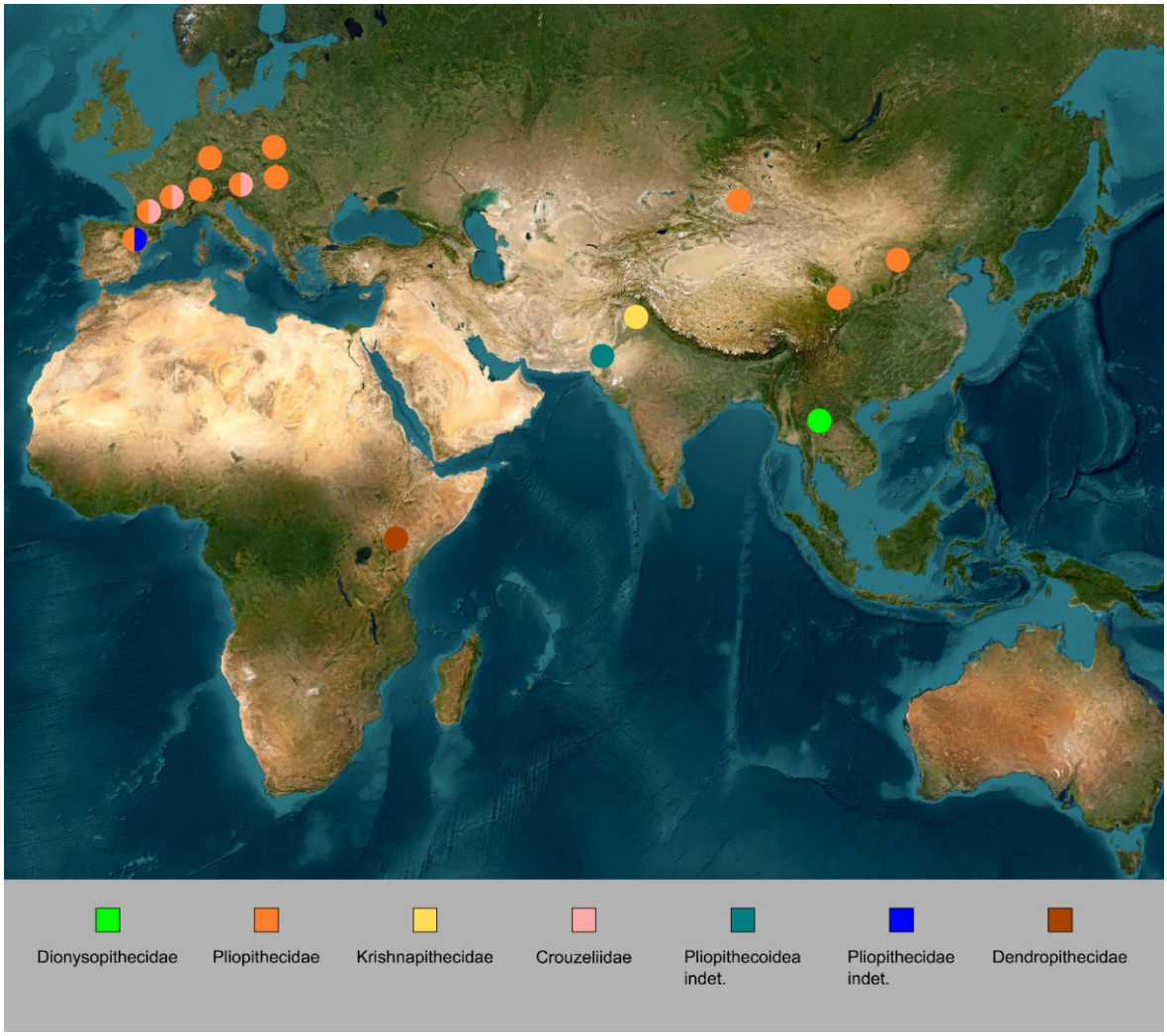


Figure 1.2. Geographic distribution of stem catarrhines in Africa and Eurasia during the Middle Miocene (16.0–11.6 Ma), see main text for references and further details. Base map and image sources are given in the caption of Fig. 1.1.

It is generally considered that pliopithecoids are not recorded outside of Eurasia. At some point, the small-bodied catarrhine *Lomorupithecus* from East Africa was included into the Pliopithecoidea (Rossie and MacLatchy, 2006; see also Stevens et al., 2013; Nengo et al., 2017; Rossie and Hill, 2018; Rasmussen et al., 2019; Gilbert et al., 2020a, 2020b). However, the pliopithecoid synapomorphies inferred by Rossie and MacLatchy (2006) are in contradiction with the ones traditionally used to define the clade (Harrison, 2010) and *Lomorupithecus* is currently still considered by most authors a stem catarrhine not directly related to pliopithecoids (e.g., Alba et al., 2010; Harrison, 2010, 2013, 2017; Pickford et al., 2010, 2017, 2021; Chaimanee et al., 2015; Begun 2017; Sankhyan et al., 2017; Harrison et al., 2020).

Pliopithecoids most probably originated in Afro-Arabia by the end of the Oligocene (Harrison, 1987; Bernor, 1988; Harrison et al., 1991; Andrews, 1996; Harrison and Gu, 1999). The internal phylogeny of pliopithecoids is still unclear and multiple systematic arrangements have been proposed (Harrison and Gu, 1999; Moyà-Solà et al., 2001; Begun, 2002, 2017; Harrison, 2005, 2013; Alba et

al., 2010; Alba and Moyà-Solà, 2012; Sankhyan et al., 2017; Harrison et al., 2020). Even the monophyly of several pliopithecoid taxa is uncertain, especially in the case of pliopithecids, which might be paraphyletic (e.g., Begun, 2002). Three main putative clades were recognized following Harrison and Gu (1999), whereas most recent works distinguished four clades at the family rank (Sankhyan et al., 2017; Harrison et al., 2020; Ji et al., 2022): Dionysopithecidae, Crouzeliidae, Krishnapithecidae, and Pliopithecidae.

Dionysopithecids include the genera *Dionysopithecus* and *Platodontopithecus* from China and Thailand, which represent the earliest recorded members of the clade at ~19–18 Ma (Harrison and Gu, 1999; Figs. 1.1–1.2). The ancestors of pliopithecoids probably dispersed from Africa into Eurasia at ~19 Ma, and, in the subtropical forests of China, locally diversified into the dionysopithecids *Dionysopithecus shuangouensis* and *Platodontopithecus jianghuaiensis* (Li, 1978; Gu and Lin, 1983; Harrison and Gu, 1999). A second species of *Dionysopithecus*, *Dionysopithecus orientalis*, is recorded from the Middle Miocene (~13.5–13 Ma) of northern Thailand (Harrison and Gu, 1999; Chaimanee et al., 2015; Harrison et al., 2020). Dionysopithecids are unlikely to be the direct ancestors of other pliopithecoids given their very specialized molar morphology. However, they probably more closely resemble the pliopithecoid ancestral morphotype than other members of the group (Harrison and Gu, 1999; Harrison et al., 2020).

The more derived pliopithecids (*Pliopithecus* and *Epipliopithecus*) make their first appearance in France during early MN5 (Fig. 1.1), being represented by *Pliopithecus piveteaui* (Ginsburg and Mein, 1980; Ginsburg, 1986), and are further recorded from central Europe, the Iberian Peninsula, and China (Begun, 2002; Alba et al., 2010; Harrison, 2013) between ~16 and 10.6 Ma (Hilgen et al., 2012). The occurrence of the more basal dionysopithecids in China during the Early Miocene suggests that pliopithecids might have originated in Asia and later dispersed westward, during the Mid-Miocene Climatic Optimum (Harrison, 2005; Harrison, 2010; Harrison et al., 2020), which spans between ~16.9 and 14.7 Ma (Steinthorsdottir et al., 2021). From MN5 to MN7+8, three additional species of *Pliopithecus* are recorded in Europe (Figs. 1.2–1.3): *Pliopithecus platyodon* from Elgg, Switzerland (MN5; Ginsburg, 1986) and Göriach, Austria (MN6; Steininger, 1986), *Pliopithecus antiquus* from Sansan (MN6; 14.4 to 14.2 Ma; Hürzeler, 1954; Hilgen et al., 2012; McKenzie et al., 2022) and La Grive-Saint-Alban, France (MN7+8; 12.4 to 11.2 Ma; Hürzeler, 1954; Hilgen et al., 2012; Casanovas-Vilar et al., 2011, 2016a; McKenzie et al., 2022), and *P. canmatensis* from various Abocador de Can Mata (ACM) localities (Spain) restricted to MN7+8 (~11.9–11.7 Ma; Alba et al., 2010, 2017, 2022). Although some isolated teeth from France (MN9), Germany (MN6), Poland (MN7+8), and Switzerland (MN6) were tentatively attributed to *P. antiquus*, they are in some cases more similar to the holotype of *P. platyodon* from Göriach, Austria, or cannot be attributed to species (Begun, 2002).

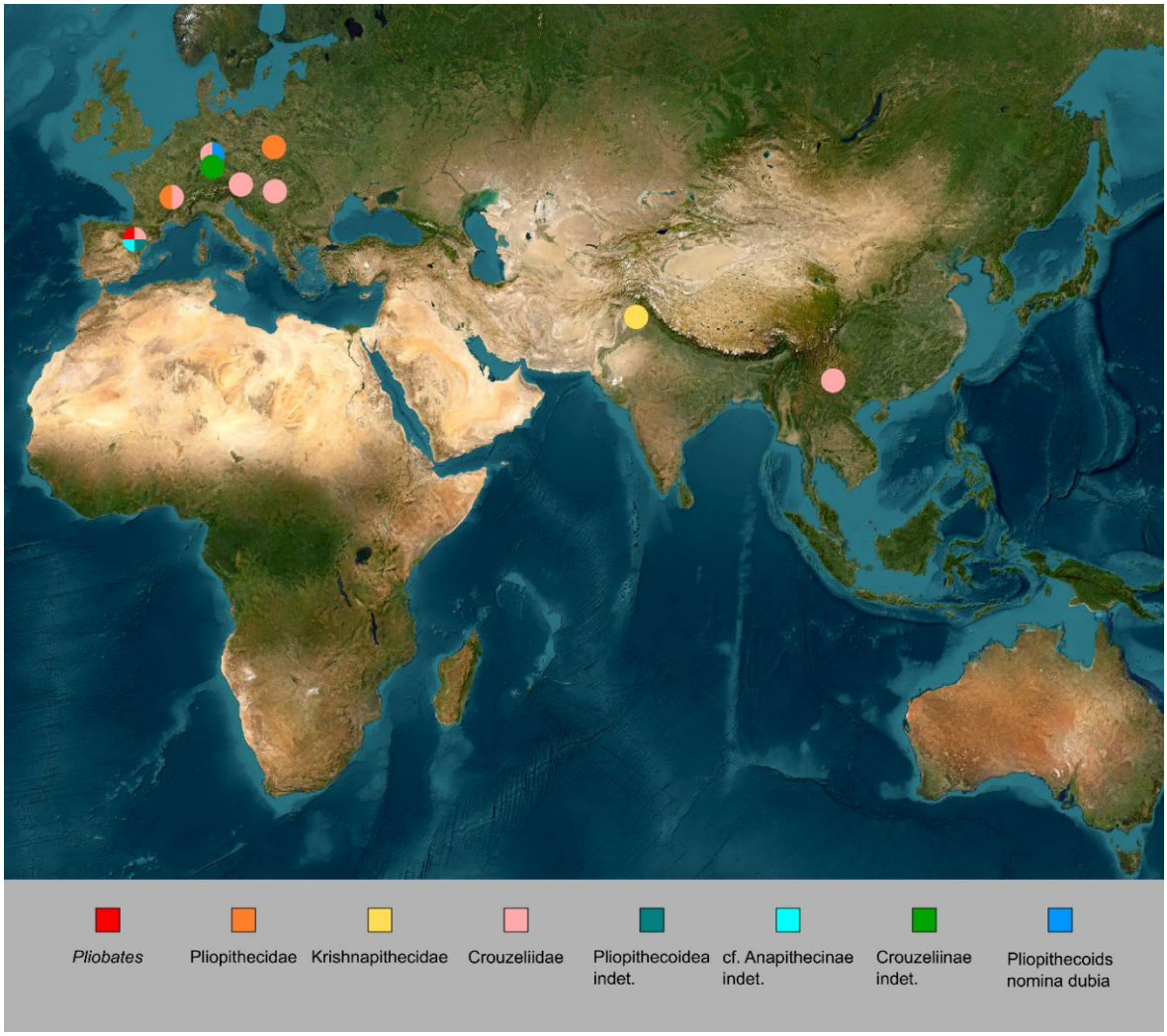


Figure 1.3. Geographic distribution of stem catarrhines in Africa and Eurasia during the Late Miocene (11.6–5.3 Ma), see main text for references and further details. Base map and image sources are given in the caption of Fig. 1.1.

In turn, *Epipliopithecus* is represented by a single species, *Epipliopithecus vindobonensis*, from MN6 of Slovakia (Zapfe and Hürzeler, 1957; Zapfe, 1961a; Fig. 1.2) dated to ~14.7 Ma (Sabol et al., 2021). Originally, *Epipliopithecus* was erected as a subgenus of *Pliopithecus* (Zapfe and Hürzeler, 1957), and while some authors followed this view (Zapfe, 1958, 1961a; Harrison et al., 1991, 2002, 2020; Andrews et al., 1996; Harrison and Gu, 1999; Moyà-Solà and al., 2001; Harrison, 2005, 2013, 2017; Harrison et al., 2020) others preferred instead to consider it a separate genus (Begun, 2002, 2017; Alba et al., 2010, 2015; Alba and Moyà-Solà, 2012; Alba and Berning, 2013; Sankhyan et al., 2017; Ji et al., 2022), which is the view followed here. *Pliopithecus* is also recorded from China (Fig. 1.2), including: *P. zhanxiangi* from Tongxin County, Ningxia Hui Autonomous Region, northcentral China (MN6; Harrison et al., 1991); and *Pliopithecus* sp. (MN6; Qiu and Guan, 1986; Ye et al., 2001) and *Pliopithecus bii* (MN6; Wu et al., 2003) from northern Junggar Basin, northeastern China. The presence of *Pliopithecus* in Asia might represent a back to Asia dispersal event after an origination of this lineage in Europe. However, the MN6 age of *Pliopithecus* in China (Qiu and Guan, 1986;

Harrison et al., 1991; Ye et al., 2001; Wu et al., 2003) does not warrant to conclusively dismiss an Asian origin for pliopithecids. Nevertheless, oldest finds of Asian *Pliopithecus* dating back to at least MN5 would be required to further support such a hypothesis. Pliopithecids are last recorded during MN7+8 (Alba et al., 2010, 2017, 2022).

Krishnapithecids were recently suggested to include the genus *Kapi* (Ji et al., 2022), previously interpreted as a stem hylobatid (Gilbert et al., 2020a), in addition to *Krishnapithecus* (Chopra and Kaul, 1979; Sankhyan et al., 2017). The two genera are restricted to northern India, occurring at ~13.8–12.5 Ma in Ramnagar (Gilbert et al., 2020a) and ~9 Ma in Haritalyangar (Sankhyan et al., 2017), respectively (Figs. 1.2–1.3). Krishnapithecids represent the only known occurrence of pliopithecoids in India. Because krishnapithecids are so distinctive and specialized in their molar morphology, their phylogenetic relationships with other pliopithecoids are uncertain. However, a sister taxon relationship with either dionysopithecids, pliopithecids + crouzeliids, or pliopithecids is plausible (Sankhyan et al., 2017; Ji et al., 2022).

Crouzeliids are more taxonomically diverse at the genus rank than other pliopithecoid families, including *Anapithecus*, *Barberapithecus*, *Crouzelia*, *Egarapithecus*, *Fanchangia*, *Laccopithecus*, and *Plesiopliopithecus*. Both *Barberapithecus* and *Egarapithecus* have been considered pliopithecids instead of crouzeliids by Begun (2002, 2017), but their crouzeliid status is supported by other authors (Moyà-Solà et al., 2001; Alba and Moyà-Solà, 2012; Alba et al., 2010; Harrison, 2013; Harrison et al., 2020). Following Andrews et al. (1996), *Crouzelia* was considered a junior subjective synonym of *Plesiopliopithecus* by most subsequent authors (Harrison and Gu, 1999; Begun, 2002; Harrison, 2005, 2013; Alba et al., 2010; Alba and Moyà-Solà, 2012; Alba and Berning, 2013; Sankhyan et al., 2017), with only few exceptions (Moyà-Solà et al., 2001; Begun, 2017). However, it is here considered distinct following Harrison et al. (2020). *Fanchangia* from China represents the oldest occurrence of crouzeliids at ~18–17 Ma (Harrison et al., 2020; Fig. 1.1). Like pliopithecids, crouzeliids span a wide geographical range, from northeastern Iberian Peninsula to eastern China (Figs. 1.1–1.3), but unlike the former they survived until the Late Miocene in both Europe (*Egarapithecus*, Moyà-Solà et al., 2001; *Anapithecus*, Kretzoi, 1975; Begun, 1989, 2002; Kordos and Begun, 2001) and China (*Laccopithecus*; Wu and Pan, 1984, 1985; Pan, 1988; Pan et al., 1989). It was previously considered that crouzeliids originated in Europe from a pliopithecid-like ancestor (Harrison, 2005), being first recorded there by *Crouzelia auscitanensis* from Sansan, France (MN6; Bergounioux and Crouzel, 1965; Ginsburg and Mein, 1980) and *Plesiopliopithecus lockeri* from Trimmelkam, Austria (MN6; Zapfe, 1960; Zapfe, 1961b; Ginsburg, 1975; Alba and Berning, 2013). However, the recently described *Fanchangia jini* from China (~18–17 Ma), considered the basalmost member of the family, predates the appearance of crouzeliids in Europe at ~14.4–12.4 Ma, and thus supports the view that crouzeliids diverged from pliopithecids in Asia before dispersing into Europe during the late Early Miocene or the Middle Miocene (Harrison, 2013; Harrison et al., 2020). The

plesiomorphic dental features retained by *Fanchangia* contradicts the previous hypothesis of a late divergence of crouzeliids from a pliopithecid ancestor in Europe but favors instead an early divergence between the two groups in Asia (Harrison et al., 2020). Subsequently to the oldest records of crouzeliids in Europe during MN6 (see above), *Crouzelia rhodanica* is recorded at La Grive-Saint-Alban MN7+8 (Lechartier Quarry 7 [L7]; Ginsburg and Mein, 1980; Ginsburg, 1986), France (12.4–11.9 Ma; Casanovas-Vilar et al. 2011, 2016a; McKenzie et al., 2022); *Barberapithecus huerzeleri* at Castell de Barberà, Catalonia, Spain during the earliest Vallesian (~11.2 Ma; Alba and Moyà-Solà, 2012; Alba et al., 2019); cf *Anapithecus priensis* at Priay, France during MN9 (Welcomme et al., 1991); and *Anapithecus hernyaki* at Rudabánya, Hungary (MN9; ~10 Ma; Kretzoi, 1975; Kordos and Begun, 2001) and perhaps also Götzendorf, Austria and Salmendingen, Germany during MN10 (Begun, 1989, 2002). *Egarapithecus narcisoi* from Torrent de Febulines, Spain (Moyà-Solà et al., 2001) represents the last surviving pliopithecoid from Europe, being recorded at ~9.1 Ma (Casanovas-Vilar et al., 2016a). Finally, *Laccopithecus robustus* from Lufeng, China (7 Ma; Wu and Pan, 1984) represents the latest recorded crouzeliid and pliopithecoid (Harrison, 2013; Begun, 2017; Harrison et al., 2020). *Laccopithecus* seems to be closely related to the older *Anapithecus* and *Egarapithecus*, suggesting that anapithecines originated in Europe during (or before) MN9 (Harrison et al., 2020). The lineage leading to *Laccopithecus* would have later dispersed back into China (Harrison et al., 2020). The gradual cooling and increasing isolation between low and middle latitudes since the Middle/Late Miocene led to a greater seasonality, resulting in a shift from laurophyllous subtropical evergreen forests to deciduous broadleaved woodlands in European regions such as France and Spain (Agustí et al., 1997, 2003; Marmi et al., 2012) or to more open and herbaceous lands, with shrubby and bushy vegetation, in central regions of Europe (Merceron et al., 2010). These environmental events were at the origin of the extinction of pliopithecoids and hominoids in Europe during the Late Miocene (Agustí et al., 1997, 2003). In South Asia, the causes of climate change and eventual extinction of pliopithecoids can be explained by the uplift of the Himalayas and Thibetan Plateau, which resulted in decreased rainfall and more open and arid environments (Zhisheng et al., 2001). The subtropical regions of southern China acted as a refuge, where *Laccopithecus* survived until ~7 Ma (Harrison et al., 2020).

Pliopithecoids of uncertain affinities. Several isolated pliopithecoid teeth of uncertain or debatable affinities have been recorded from the Vallès-Penedès Basin in NE Spain (Figs. 1.2–1.3): a dp4 from Can Feliu (Crusafont-Pairó and Golpe-Posse, 1981; Moyà-Solà et al., 1990; Marigó et al., 2014), an M2 from Trinxera del Ferrocarril-Sant Quirze (Harrison et al., 2002), and an M3 from Abocador de Can Mata (ACM/C3-B2; Alba et al., 2012).

The dp4, previously mistaken for an m3 by Crusafont-Pairó and Golpe-Posse (1981), is probably earliest Vallesian in age (Casanovas-Vilar et al., 2016b) and corresponds to a medium-sized

crouzeliid (Moyà-Solà et al., 1990; Andrews et al., 1996; Alba and Moyà-Solà, 2012). Its size does not match with that of *Barberapithecus* and *P. canmatensis*, which appear larger, but might be comparable with that of *Egarapithecus* and the taxon represented by the M2 from Sant Quirze. However, as other tooth positions remain unknown, the dp4 from Can Feliu is tentatively referred to cf. Anapithecinae indet. (Alba and Moyà-Solà, 2012).

The M2 from Sant Quirze (MN7+8; ~11.6–11.2 Ma; Alba et al., 2022) belongs to a medium-sized pliopithecoid, similar in size to *P. platyodon* and, to a lesser extent, *P. zhanxiangi* (see Harrison, 2002). It was originally assigned to *Pliopithecus*' sp. (Harrison et al., 2002) but it might alternatively belong to the same large crouzeliid represented by the Can Feliu dp4, being thus provisionally referred to Pliopithecoidea indet.

In turn, an M3 from ACM/C3-B2 (~12.1 Ma; MN7+8) represents the oldest Iberian pliopithecoid (Alba et al., 2012, 2017, 2022); its morphology does not fit well with that of any known pliopithecoid taxon and it might alternatively represent another stem catarrhine lineage, although on both morphological and paleobiogeographic grounds it was referred to Pliopithecoidea indet. (Alba et al., 2012). Here it is provisionally referred to Pliopithecidae indet., as an attribution to Dionysopithecidae or Crouzeliidae seems unlikely based on the preserved morphology.

A maxillary fragment with P4–M1 from the MN9 locality of Mörgen, Germany (Heißig, 1999; Seehuber, 2008; Fig. 1.3) was described as more closely resembling *Anapithecus* and *Laccopithecus*, maybe representing *Plesiopliopithecus*, for which upper cheek teeth are unknown (Heißig, 1999; Seehuber, 2008). For the reasons that will be exposed in the Discussion, the Mörgen specimen is here left unassigned to genus as Crouzeliinae indet.

An upper molar (M1 rather than M2) from the late Middle Miocene (~12.1 Ma, MN7+8) of Damiao 01, Inner Mongolia (Zhang and Harrison, 2008; Fig. 1.2) differs from other pliopithecoids but displays size and shape resemblances to *Anapithecus* and *Laccopithecus*, being attributed to Anapithecinae indet. (Zhang and Harrison, 2008).

Several isolated teeth of a small catarrhine were reported from the late Early and early Middle Miocene of Kamlial and Manchar Formations in Pakistan (~18–14 Ma; Barry et al., 1986; Bernor et al., 1988; Flynn et al., 2013; Figs. 1.1–1.2) were originally considered to have closest affinities with *Dionysopithecus* or *Micropithecus* (Fleagle, 1984; Barry et al., 1986; Bernor et al., 1988). However, Harrison and Gu (1999) questioned a close relationship with *Dionysopithecus shuangouensis* or other pliopithecoids (see also Harrison, 2005). Most recently, Sankhyan et al. (2017) considered that they might ultimately prove to be plesiomorphic pliopithecoids more closely related to dionysopithecids, but given taxonomic uncertainties they are simply attributed here to Pliopithecoidea indet.

Lastly, two specimens from the Late Miocene (MN9) of Eppelsheim, Germany (Fig. 1.3), a nearly complete femur and male upper canine (Kaup, 1861), were used to erect two taxa. The femur was attributed to *Paidopithex rhenanus* (Pohlig, 1895) and several authors assumed that the taxon was in

fact a junior synonym of *Dryopithecus* (e.g., Simons and Pilbeam, 1965; Szalay and Delson, 1979). It was later showed that the femur was different from any extant or extinct hominoid taxa (Begun, 1992) as well as *Anapithecus* (Kordos and Begun, 1999), generally resembling *Epipliopithecus* while being much larger (Begun, 1992; Köhler et al., 2003). In turn, the male upper canine ("*Pliopithecus eppelsheimensis*"; Hürzeler, 1954) was described as having a morphology comparable to that of the holotype (male) of *P. platyodon* from Göriach, but slightly smaller, and was considered too small in comparison with the Eppelsheim femur to represent the same species (Hürzeler, 1954). Following Begun (2002), the canine closely resembles those of *Epipliopithecus* and *Laccopithecus*, and *Anapithecus* to some extent. Both taxa are still considered nomina dubia, although *Paidopithex* represents in all probability the largest known pliopithecoid (~22 kg; Köhler et al., 2003).

Paleobiology of pliopithecoids. Based on the proportions of the incisors and molars, the occlusal morphology of the premolars and molars, and the development of the molar shearing crests, it was traditionally argued that pliopithecids were primarily fruit eaters, while crouzeliids were specialized folivores (Ginsburg and Mein, 1980; Begun, 1989; Andrews et al., 1996). Conversely, quantitative analyses using shearing crest quotients (Ungar and Kay, 1995; Kay and Ungar, 1997) and dental microwear analyses (Ungar, 1996) rather showed a similar degree of frugivory in *Anapithecus*, *Pliopithecus*, and *Epipliopithecus*, and an extreme degree of folivory in *Barberapithecus* only. Later studies analyzing dental microwear of pliopithecoids supported a frugivorous/mixed feeding diet with a significant sclerocarpic component, including *Barberapithecus* (DeMiguel et al., 2013; Alba et al., 2015). This type of diet was more marked in some pliopithecids than in the crouzeliid *Anapithecus*, suggesting that the crouzeliid dental morphology might has evolved towards increased soft-fruit consumption (i.e., decreased sclerocarpy) rather than folivory (DeMiguel et al., 2013).

Based on *Anapithecus*, the dental development of pliopithecoid would have been fast and precocious, with canines and M1—M2 initiating early, M1—M2 erupting before permanent premolars (especially M2 compared to P4), and M3 also erupting before C1 (Le Cabec et al., 2017). This pattern more closely resembles that of strepsirrhines than that of extant catarrhines, thus likely representing the plesiomorphic condition for stem members of the latter clade (Le Cabec et al., 2017).

Because pliopithecoid postcranial material is scarce and disparate, previous hypotheses on their locomotory repertoire have been limited and largely based on the partial skeletons of the pliopithecid *Epipliopithecus* (Zapfe and Hürzeler, 1957; Zapfe, 1958; Zapfe, 1961a). *Epipliopithecus* may be better interpreted as a generalized quadruped with limited climbing and suspensory abilities (Rose, 1994; Rein et al., 2011, 2015; Arias-Martorell et al., 2015, 2021). Regarding other pliopithecids, *P. antiquus* has been inferred to be a semiterrestrial quadruped with likely slow-climbing abilities (Senut, 2012). In contrast, locomotor inferences for dionysopithecids and crouzeliids have been mainly based on a few isolated specimens available for each genus. The calcaneus of

Platodontopithecus shows resemblances to that of *Epipliopithecus*, suggesting a quadrupedal arboreal locomotor behavior with preference for large supports (Harrison and Gu 1999). Crouzellids have been inferred to include (semi)arboreal quadrupeds with strong climbing abilities and suspensory behaviors to a varying degree (Begun, 1988, 1993; Senut, 2012; Arias-Martorell et al., 2021). In particular *Barberapithecus* was inferred to have restricted forearm pronation/supination capabilities but its morphological similarities in proximal radial shape with the smaller and more agile arboreal monkeys indicate a more rapid arboreal running than in other comparable pliopithecoids (Arias-Martorell et al., 2021). The talus and calcaneus of *Crouzelia* indicate a strong semiterrestrial quadrupedal component including probable rapid running (Senut, 2012). The phalanges and femora of *Anapithecus* (Begun, 1988, 1993; Kordos and Begun, 1999) suggest stronger suspensory abilities in anapithecines as compared to *Epipliopithecus*. The manual proximal phalanx morphology of *Laccopithecus* is more typical of hylobatids, indicating even more marked grasping and manual suspension abilities than in other anapithecines (Meldrum and Pan, 1988).

It is noteworthy that no caudal vertebrae have been recovered for any pliopithecoid, suggesting that they might have been tailless, like extant hominoids, where the external tail has been reduced to an internal vestige (the coccyx). This possibility, which would be at odds with a stem catarrhine status, was supported by Zapfe (1958, 1961a) based on the sacral morphology of *Epipliopithecus*, but it has been disputed by other subsequent authors (Ankel, 1965; Russo, 2016).

1.1.2. Small-bodied stem catarrhines from the Miocene of East Africa

Dendropithecids. The family Dendropithecidae (Harrison, 2002) is a clade of small-bodied (2–10 kg) catarrhines including the genera *Dendropithecus*, *Micropithecus* and *Simiolus*. They are restricted to the Miocene of East Africa (Harrison 2002, 2010, 2013, 2017), spanning a time range from ~21 Ma to 12.8 Ma (Rossie and Hill, 2018; Pickford et al., 2021; Van Couvering and Delson 2020; Urciuoli and Alba, 2023; Figs. 1.1–1.2). It was originally considered that *Dendropithecus*, together with the genera *Limnopithecus* and *Micropithecus*, might constitute a clade just basal to crown catarrhines (Harrison, 1987, 1988). *Simiolus* was subsequently described and found to show most similarities with *Dendropithecus* (Leakey and Leakey, 1987). Considering that *Limnopithecus* was not sufficiently known to be attributed with confidence to any clade, and based on some shared dental and postcranial features of *Micropithecus* and *Simiolus*, Harrison (2002) erected the family Dendropithecidae to accommodate them. Dendropithecids are well known from their dentition, but much less from their cranial morphology (Harrison 2002, 2010, 2013; Rossie and Hill, 2018; Pickford et al. 2017, 2021): some aspect of dendropithecid lower face have been described based only on maxillay specimens of *Dendropithecus* (Le Gros Clark and Thomas, 1951; Le Gros Clark and Leakey, 1951; Andrews, 1978; Harrison, 1981) and of *Micropithecus* (Fleagle and Simons, 1978;

Pickford et al., 2010), although a frontal bone fragment is also likely available for this latter (Pilbeam and Walker, 1968; Fleagle and Simons, 1978; Harrison, 1982, 1988; Pickford et al., 2010). On the other hand, several partial skeletons are known for *Dendropithecus* (Le Gros Clark and Thomas, 1951; Harrison, 1982; Fleagle, 1983; Rose, 1993), whereas a few hindlimb elements but most of the forelimbs were recovered for *Simiolus* (Leakey and Leakey 1987; Rose et al. 1992; Rossie et al., 2012), and even fewer elements are known for *Micropithecus* (Harrison, 1982).

Most authors originally considered that *Dendropithecus* was a fossil hylobatid (e.g., Leakey, 1947; Le Gros Clark, 1949; Le Gros Clark and Leakey, 1951; Le Gros Clark and Thomas, 1951; Andrews, 1978; Andrews and Simons, 1977; Simons and Fleagle, 1973) but it was later recognized that dendropithecids (sensu Harrison, 2002) are stem catarrhines more derived than both propliopithecoids and pliopithecoids (Delson and Andrews, 1975; Fleagle and Simons, 1978; Szalay and Delson 1979; Harrison, 1982, 1987, 2002, 2005, 2010, 2013, 2017; Andrews, 1985; Fleagle, 1986). Dendropithecids would have thus originated somewhere between 32 and 25 Ma in East Africa (Chatterjee et al., 2009; Perelman et al., 2011; Springer et al., 2012; Finstermeier et al., 2013; Stevens et al., 2013; Liedigk et al., 2014; Pozzi et al., 2014; Roos and Zinner, 2017), after the divergence of pliopithecoids but before the split of crown catarrhine clades. Nevertheless, the systematic position of dendropithecids is not settled yet because cladistic analyses have given contradictory results, variously recovering them as stem catarrhines (Nengo et al., 2017; Gilbert et al., 2020a), stem hominoids (Rae, 1999; Zalmout et al., 2010; Alba et al., 2015; Rossie and Hill, 2018; Rasmussen et al., 2019), or stem hylobatids (*Micropithecus* in Ji et al., 2022). The latter results thus highlight the possible paraphyletic status of this group (Rae, 1999; Harrison, 2002).

Dendropithecids are recorded from East Africa during ca. 7 Myr and different species overlap in time or even co-occur at the same locality. The earliest dendropithecids are *Simiolus enjiessi* from Kenyan localities, at ~21–17.5 Ma (Harrison, 2010; Pickford et al., 2017a; Van Couvering and Delson 2020; Urciuoli and Alba, 2023) and *Micropithecus leakeyorum*, that is found in Maboko Island (Kenya) and Uganda at ~21–15.3 Ma (Harrison, 1989; Pickford et al., 2017a,b), whereas the sample from Kipsaraman (Kenya; ~15.8 Ma; Pickford and Kunimatsu, 2005; Van Couvering and Delson 2020) also probably represents this species. The two known *Dendropithecus* species as well as *Micropithecus clarki* and *Micropithecus chamtwaraensis* are recorded almost as early, but have a more restricted timespan: *Dendropithecus ugandensis* and *Micropithecus clarki* in Uganda at ~20.5–19 Ma (Pickford et al., 2021) and *Micropithecus chamtwaraensis* from western Kenya at ~20.3–19 Ma (Pickford et al., 2021; Van Couvering and Delson 2020; Urciuoli and Alba, 2023). Subsequently, *Dendropithecus macinnesi* is recorded from various localities in Kenya, spanning between ca. 20.3 and 17 Ma (Harrison, 2010; Van Couvering and Delson 2020; Urciuoli and Alba, 2023). Given the estimated ages for each locality, both Kenyan occurrences of *M. leakeyorum* represent the last known occurrence of the genus *Micropithecus*. From 15.8–15.3 Ma onward, only *Simiolus* persists in the

fossil record: *Simiolus cheptumoae* in Kipsaraman (~15.8 Ma; Pickford and Kunimatsu, 2005; Van Couvering and Delson 2020) and *Simiolus andrewsi* in Fort Ternan (Kenya) at 13.8 Ma (Harrison, 2010; Van Couvering and Delson 2020). *Simiolus minutus* from Ngorora (Kenya) is by now the youngest and smallest dendropithecid representative, occurring at 12.8 Ma (Rossie and Hill, 2018; Van Couvering and Delson 2020).

Paleobiology of dendropithecids. Between 17 and 14 Ma, environments changed drastically in Africa, with tropical forests and woodlands turning into increasingly drier and more seasonal environments, which must have affected the diversity of the African catarrhine assemblages (Harrison, 1982, 1988, 1989, 1992, 2010; Benefit, 2000). Those changes had an impact on the dietary adaptations of East African Miocene catarrhines (including dendropithecids), causing a shift from mainly soft frugivorous diet in the Early Miocene to the exploitation of more fibrous diets in later Middle Miocene taxa (Harrison, 1982, 1988, 1989, 1992, 2010; Benefit, 2000). Such a shift can be ascertained in *Micropithecus*, with the two Early Miocene species *M. clarki* and *M. chamtwaraensis* inferred to be mostly frugivorous and the Middle Miocene *M. leakeyorum* adapted to the consumption of tougher items (Harrison, 1982, 1989; Shearer et al., 2014). In contrast, *Dendropithecus* is only known from the Early Miocene and its diet has been inferred to be mainly frugivorous (Kay, 1977; Kay and Ungar, 1997; Ungar et al., 2004; Shearer et al., 2014). Thus, dietary selection pressures might have played an important role in dendropithecid evolutionary history.

Based on available postcranial remains, *Dendropithecus* was originally inferred to be a quadruped, although similarities with *Ateles*, suggesting some suspension and/or climbing abilities, were also noted (Le gros Clark and Thomas, 1951; Harrison, 1982; Fleagle, 1983; Harrison, 2002). Other authors described *Dendropithecus* radial morphology as showing the generalized anthropoid morphotype, implying a strict quadrupedal locomotion without extensive suspensory and/or climbing skills as in hominoids and *Ateles* (Rose, 1988, 1993). Most recently, Arias-Martorell et al. (2021) found a high degree of similarity in proximal radial morphology between *Dendropithecus* and *Epipliopithecus*, both derived toward the condition of the semisuspensory *Lagothrix*, thus supporting the initial claim of a generalized quadrupedal locomotor repertoire coupled with some suspensory capabilities for *Dendropithecus* (Le gros Clark and Thomas, 1951; Harrison, 1982; Fleagle, 1983; Harrison, 2002). In turn, *Simiolus* has been primarily interpreted as an agile arboreal quadruped most similar to the large extant platyrrhines, showing good grasping capabilities (Rose et al., 1992; Rose, 1993, 1997; Harrison, 2010), even similar to *Dendropithecus* (Leakey and Leakey, 1987). However, its more elongated forearms compared to *Dendropithecus* and its relatively long metacarpals and phalanges (Rossie et al., 2012) coupled with proximal radial morphology similarities with *Alouatta* (Arias-Martorell et al., 2021) rather suggest that *Simiolus* might have relied on a slow pronograde locomotion with marked climbing abilities.

Other small-bodied stem catarrhines from the Miocene of East Africa. Five additional genera of small-bodied putative stem catarrhines, not included in the Dendropithecidae, have been recorded from the Early and Middle Miocene of Kenya and Uganda (Fig. 1.1): *Kogolepithecus morotoensis* from Uganda at ~21–20 Ma (Pickford et al., 2003, 2017a; Urciuoli and Alba, 2023); *Iriripithecus alekileki* and *Karamojapithecus akisimia* from Uganda at ~20.5–19 Ma (Pickford et al., 2010, 2021); *Lomorupithecus evansi* from Kenya and Uganda at ~20.5–19 Ma (Macinnes, 1943; Andrews, 1978; Harrison, 1982, 1988, 2010; Rossie and MacLatchy, 2006; Pickford et al., 2010, 2021; Van Couvering and Delson, 2020); *Limnopithecus legetet* from Kenya and Uganda at ~20.5–19 Ma (Hopwood, 1933; Andrews, 1978; Harrison, 1981, 2010; Pickford et al., 2010, 2021; Urciuoli and Alba, 2023). The dentognathic morphology of these taxa is well known, but cranial and postcranial remains are very scarce (Harrison, 2010, 2013). These five genera are still best left as incertae sedis at the superfamily rank (Harrison, 2002, 2010). Regarding *Limnopithecus* and *Lomorupithecus*, debates about the status of these taxa are still ongoing: *Limnopithecus* was previously considered to include two species, *Limnopithecus evansi* and *Limnopithecus legetet* (Hopwood, 1933; MacIness, 1943; Andrews and Simons, 1977), distinct from another genus and species, *Lomorupithecus harrisoni*, erected by Rossie and MacLatchy (2006) on the basis of dentognathic material from Napak (Uganda). Cote et al. (2016) recently attributed some specimens from Songhor (Kenya) to *Limnopithecus evansi* and supported its distinctive taxonomic status from the Napak specimens included in *Lomorupithecus harrisoni*. However, other authors rather consider that the holotype snout of *Lomorupithecus harrisoni* belongs to *Limnopithecus evansi* and use the combination *Lomorupithecus evansi* (Pickford et al., 2010, 2021; Harrison, 2010), and even consider that the paratype mandible would belong instead to *Limnopithecus legetet* (Pickford et al., 2010, 2021). Pickford et al. (2021) further asserted that most of the specimens attributed to *Limnopithecus evansi* by Cote et al. (2016) would rather belong to *Kalepithecus songhoerensis* (Harrison, 1988)—currently considered a hominoid (Urciuoli and Alba, 2023)—and *Limnopithecus legetet*, and only a few to *Lomorupithecus evansi*.

1.1.3. The small-bodied catarrhine *Pliobates cataloniae*

In 2011, excavation works conducted at the Abocador de Can Mata landfill (ACM; els Hostalets de Pierola, Catalonia, Spain) led to the recovery of several cranial and postcranial fragments of a single catarrhine primate individual from locality ACM/C8-A4. In 2015, the genus and species *Pliobates cataloniae*, dated to 11.6 Ma (Fig. 1.3), were described on the basis of this adult female partial skeleton with associated cranium (Alba et al., 2015). *Pliobates cataloniae* displays a mosaic of plesiomorphic (stem catarrhine-like) and more derived (hominoid-like) craniodental and postcranial features. Thus, the cranium is overall more derived than the inferred primitive catarrhine

one (Alba et al., 2015; Pugh et al., 2023) and more closely resembles that of hylobatids (e.g., long and rather horizontal nasals, moderately high zygomatic root) and other apes to some extent (Alba et al., 2015; Pugh et al., 2023). However, the short tubular ectotympanic is less derived than that of crown catarrhines and closer to the condition displayed by *Epipliopithecus*. The teeth, represented by upper cheek teeth only, have occlusal morphology and proportions resembling those of other Miocene stem catarrhines, showing similarities to those of *Micropithecus* (i.e., markedly convex lingual profile, moderately developed buccal cingulum, well-developed and lingual hypocone). In turn, the postcranium of *Pliobates* retains some plesiomorphic features for catarrhines (e.g., lack of a spool-shaped trochlea in the distal humerus, narrow trochlear notch without a median keel in the proximal ulna) but further display multiple crown-hominoid synapomorphies (e.g., laterally facing bicipital tuberosity, lack of entepicondylar foramen, slender and hook-like styloid process, and small triquetrum relative to the hamate). A cladistic analysis based on maximum parsimony, conducted by Alba et al. (2015) using both craniodental and postcranial characters, recovered *Pliobates* as a stem hominoid more derived than *Proconsul* s.l. (i.e., *Proconsul* s.s. and *Ekembo*). Alba et al. (2015) erected the hominoid family Pliobatidae to accommodate *Pliobates*, emphasizing that the recovery of *Pliobates* as a hominoid was driven by the remarkable suite of crown hominoid-like humeroradial and wrist joint features it possesses (Alba et al., 2015). However, given the dendropithecid-like dental traits exhibited by *Pliobates*, Alba et al. (2015) noted the possibility that this taxon might be a late descendant of an African lineage.

Benefit and McCrossin (2015), when discussing the implications of Alba et al.'s (2015) results, raised the possibility that *Pliobates* might also be ancestral only to hylobatids or alternatively a pliopithecoid. In the latter case, its numerous extant hominoid-like specializations of the elbow and wrist would have been acquired independently. It is noteworthy than in every scenario, the independent evolution of some characters along different catarrhine lineages is required to explain the mosaic of features displayed by *Pliobates* (Alba et al., 2015; Benefit and McCrossin, 2015). Subsequent cladistic analyses based on a different taxon-character matrix that included *Pliobates* and numerous other catarhines recovered the latter as a basal pliopithecoid most closely related to *Dionysopithecus* (Nengo et al., 2017; Gilbert et al., 2020a). On this basis, Gilbert et al. (2020b) favored the view that *Pliobates* is a pliopithecoid or another type of stem catarrhine that convergently evolved ape-like postcranial characters, as already suggested by Benefit and McCrossin (2015).

Further excavation campaigns conducted at ACM led to the recovery of additional dentognathic remains—including maxillary and mandibular fragments and several isolated teeth—that were reported as cf. *Pliobates catalaniae* (Alba et al. 2017, 2022; DeMiguel et al., 2021) but remained unpublished until recently.

1.2. Aims, scope, and structure of this dissertation

1.2.1. Scope and specific aims

This PhD dissertation is devoted to the small-bodied catarrhine *Pliobates cataloniae*, with the ultimate aim of clarifying its systematic status and closest phylogenetic relationships. Since its original description, different conclusions have been reached regarding the systematic position of this taxon. The best supported hypotheses—based on cladistic results—include being a stem hominoid or a pliopithecoid stem catarrhine; other possibilities include being a dendropithecid or a hylobatid, respectively suggested by previously noted dental and cranial similarities but not supported by most parsimonious cladograms (Fig. 1.4).

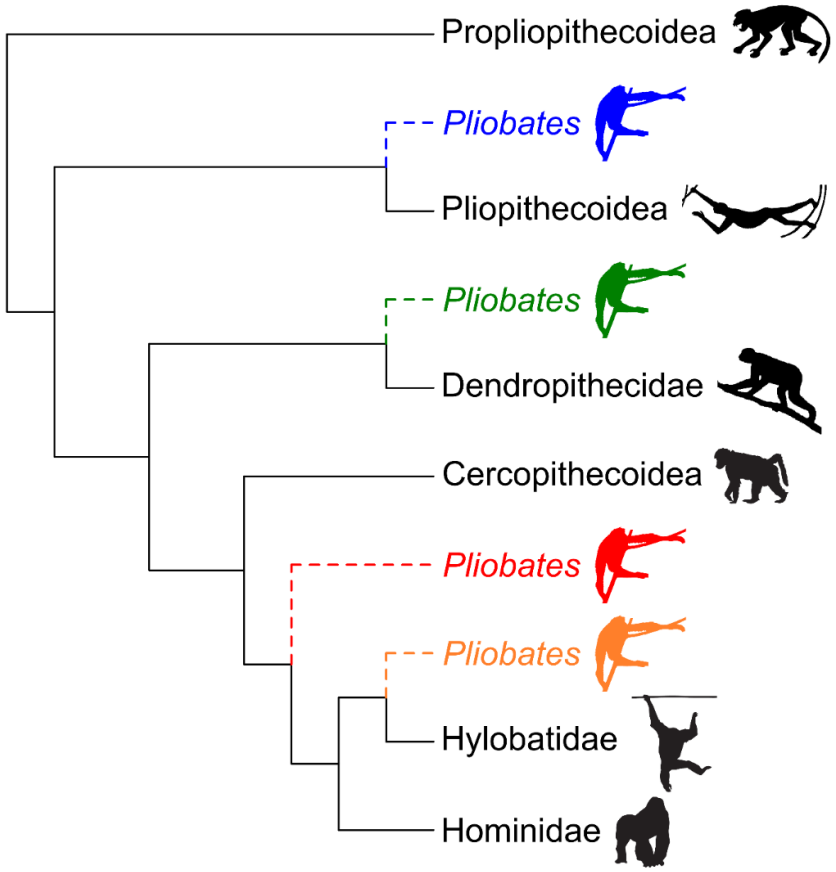


Figure 1.4. Simplified cladogram of extant and extinct catarrhine primates illustrating the four main phylogenetic hypotheses for *Pliobates*. The red dashed lines illustrate the original interpretation of *Pliobates* as a stem hominoid (Alba et al., 2015); the blue dashed lines depict the alternative hypothesis of *Pliobates* being a stem catarrhine more closely related to pliopithecoids (Nengo et al., 2017); finally, the green and orange dashed lines denote the other suggested possibilities by Alba et al. (2015) that *Pliobates* might represent a dendropithecid or a hylobatid, respectively. Black silhouettes (not to scale) of the different lineages were taken or redrawn from different sources described in Chapter 4: Fig. 1 and Chapter 4: Supplementary Fig. 7.

A persisting hindrance in catarrhine phylogenetics focused on fossils, which must be based on morphological evidence, is the pervasive nature of homoplasy. Coupled with the fragmentary and incomplete nature of the fossil record, homoplasy makes it difficult to accurately resolve the phylogenetic relationships of extinct taxa relative to extant ones, ultimately leading to contradictory results that largely depend upon character selection and definition, including the emphasis put on different anatomical areas (see discussion in Urciuoli and Alba, 2023). Postcranial features appear to be particularly prone to evolutionary convergence due to functional reasons related to locomotion, to the extent that strikingly different results can be obtained for particular extinct taxa depending on whether postcranial features are included in cladistic analyses (e.g., *Oreopithecus*; see Pugh, 2022; Urciuoli and Alba, 2023). This dissertation builds on the working hypothesis that craniodental features yield more reliable phylogenetic signal and hence focuses on the study of the craniodental morphology of *Pliobates*. Emphasis is put on the study of the carotid canal morphology as well as both external and internal tooth morphology of *Pliobates*, and their comparison with those of other catarrhines (especially hominoids and pliopithecoids).

With the ultimate goal of determining the closest phylogenetic relationships of *Pliobates*, the following four specific aims were devised for this dissertation:

(i) To quantitatively measure and compare the carotid canal morphology of *Pliobates* with that of other extinct and extant catarrhines to determine if this structure is a reliable source of phylogenetic information and, more specifically, to test whether *Pliobates* is phenetically closer to hylobatids in this regard. Alba et al. (2015) reported similarities in carotid canal orientation between *Pliobates* and hylobatids, so this structure deserved particular attention as potentially denoting a close phylogenetic link between these taxa.

(ii) To describe the previously unpublished dental remains of *Pliobates cataloniae* reported (but not described or figured) as cf. *Pliobates cataloniae* (Alba et al. 2017, 2022; DeMiguel et al., 2021) to provide a more comprehensive and detailed diagnosis of this taxon and clarify its systematic status based on qualitative and metrical comparisons with pliopithecoids, dendropithecids, and hominoids. Given that dental features are the main basis of fossil primate taxonomy and highly diagnostic in pliopithecoids, the new material (including lower molars) offers the prospect of better evaluating the systematic affinities of *Pliobates*.

(iii) To quantitatively analyze the enamel-dentine junction (EDJ) shape of *Pliobates* molars as compared with that of both hominoids and pliopithecoids (no EDJ data are yet available for dendropithecids) to determine the closest phenetic affinities of this genus. Due to the strong phylogenetic signal embedded in EDJ shape (Zanolli et al., 2022a) and its usefulness for distinguishing extinct and extant catarrhine groups (Olejniczak et al., 2004, 2007; Zanolli et al., 2022a, 2023), this structure has the potential to give strong insights on the closest affinities of *Pliobates*.

(iv) To construct a novel taxon-character matrix for *Pliobates* and other extinct and extant catarrhines, with emphasis on dental features, to perform new cladistic analyses of this taxon to accurately infer its most likely phylogenetic relationships as well as to critically evaluate the contrasting phylogenetic signal yielded by dental, cranial, and postcranial characters.

1.2.2. Structure of this work

This PhD dissertation is conceived as a compendium of scientific articles and structured into various chapters: the Introduction (Chapter 1), the Materials and methods (Chapter 2), the Results (Chapters 3–5), the Discussion (Chapter 6), and the Conclusions (Chapter 7), plus the references of Chapters 1, 2, and 6, as Chapters 3–5 have the cited references therein.

Chapter 1 reviews the evolutionary history of African and Eurasian Miocene stem catarrhines, including previous research on *Pliobates*. It is divided into two main sections: the first focuses on pliopithecoids, dendropithecids, and small-bodied stem catarrhines of uncertain affinities from the Miocene of Africa; the second, in turns, is specifically devoted to *Pliobates* and its controversial phylogenetic relationships.

Chapter 2 expands the materials and methods used in any of the three chapters of results, with emphasis on the studied material (i.e., the *Pliobates* sample), the extinct and extant comparative samples, visualization techniques and methods of shape analysis in 3D, and the various analytical and statistical techniques applied.

The chapters of results include two papers published in first quartile journals indexed by the Journal Citation Reports (Chapters 3 and 4), as well as an unpublished manuscript under review (Chapter 5). They are the following:

- Bouchet, F., Urciuoli, A., Beaudet, A., Pina, M., Moyà-Solà, S., Alba, D.M., 2021. Comparative anatomy of the carotid canal in the Miocene small-bodied catarrhine *Pliobates cataloniae.* J. Hum. Evol. 161, 103073. https://doi.org/10.1016/j.jhevol.2021.103073
- Bouchet, F., Zanolli, C., Urciuoli, A., Almécija, S., Fortuny, J., Robles, J.M., Beaudet, A., Moyà-Solà, S., Alba, D.M., 2024. The Miocene primate *Pliobates* is a pliopithecoid. Nat. Commun. 15, 2822. https://doi.org/10.1038/s41467-024-47034-9
- Bouchet, F., Zanolli, C., Skinner, M.M., Urciuoli, A., Fortuny, J., Almécija, S., Bernardini, F., Tuniz, C., Schillinger, B., Moyà-Solà, S., Alba, D.M. (under review). Molar enamel-dentine junction shape of *Pliobates cataloniae* and other Iberian pliopithecoids. J. Hum. Evol.

Chapter 3 fulfills the specific aim (i) of this dissertation by clarifying previous carotid canal similarities noted between *Pliobates* and hylobatids and re-evaluating the phylogenetic potential of this structure in extinct and extant catarrhines. In turn, Chapter 4 fulfills the specific aims (ii) and (iv), by expanding the hypodigm of *Pliobates cataloniae*, providing an emended diagnosis, and

performing new cladistic analyses including (cranio)dental and postcranial characters, both jointly and separately. Finally, Chapter 5 fulfills the specific aim (iii) of this dissertation, by analyzing the molar EDJ shape of *Pliobates* and testing among three competing hypotheses on its closest phylogenetic affinities.

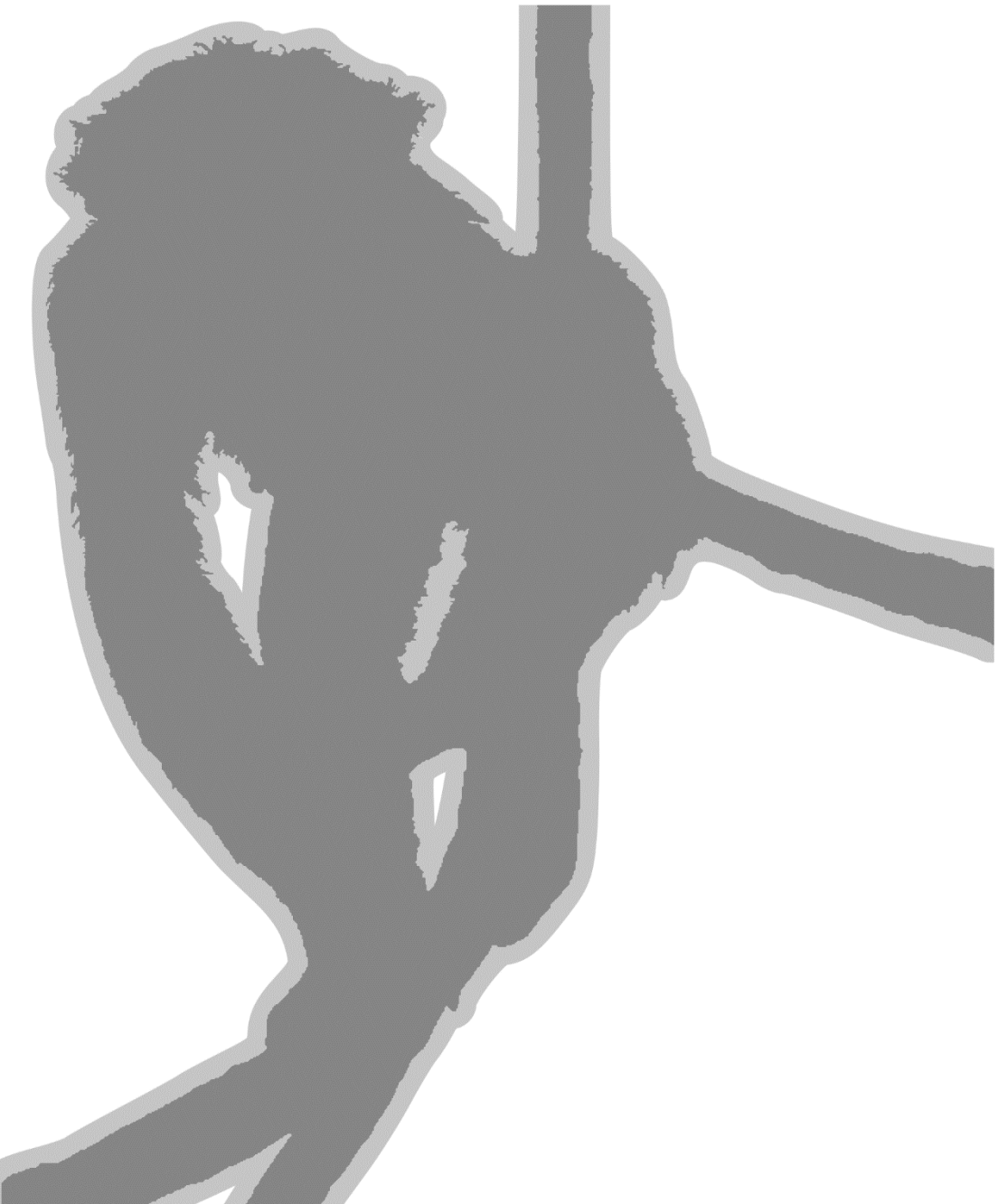
The discussion provided in Chapter 6 contextualizes the results of the three papers and relates them to one another as well as to the aforementioned specific aims, whereas Chapter 7 briefly recapitulates the main conclusions of this dissertation.

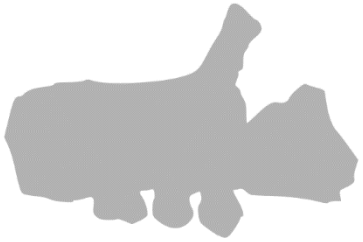


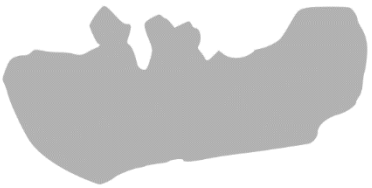


Chapter 2:

Materials and methods







Chapter 2. Materials and methods

2.1. Sample composition and acquisition

2.1.1. Studied *Pliobates* sample

The studied sample of *Pliobates cataloniae* includes the holotype partial cranium IPS58443 from Abocador de Can Mata (ACM) locality ACM/C8-A4 (Alba et al., 2015) as well as previously unpublished dental remains from the adjacent and roughly coeval (11.6 Ma) locality ACM/C5-D1 attributed to the same species (Alba et al., 2017, 2022; DeMiguel et al., 2021). The cranium of *P. cataloniae* is composed of 13 separate specimens that include two dentognathic fragments: IPS58443.1 preserves the basicranium as well as the right maxilla with P^3–M^3, while IPS58443.2 is a left maxillary fragment with P^2–M^3; the teeth are moderately to very worn in both specimens (Alba et al., 2015). Additional dentognathic remains from ACM/C5-D1, attributable to the same taxon, remained unpublished until this dissertation; they include three maxillary fragments, a mandibular fragment, and 12 isolated teeth.

To explore the external and/or internal morphology of specific *Pliobates* anatomical structures (i.e., carotid canal and teeth), the two dentognathic fragments and basicranium of the holotype as well as most other dentognathic specimens from ACM/C5-D1 were scanned using X-ray microtomography. IPS58443 was scanned at the Centro Nacional de Investigación sobre la Evolución Humana (CENIEH; Burgos, Spain) using a Phoenix V|Tome|X s240 mCT scanner with the following parameters: 0.35 mA current, 170 kV voltage, 0.2 mm Cu filter, a magnification of 9.52, and final reconstructed volume isometric voxel sizes of 21 µm (basicranium of IPS58443.1) and 33 µm (maxilla of IPS58443.1 and IPS58443.2). In turn, nine specimens from ACM/C5-D1 (Table 2.1) were also scanned at the CENIEH with the following parameters: 120 mA current and 115 kV voltage, 0.2 mm Cu filter, and a magnification of 16.67. The final reconstructed volumes have an isometric voxel size of 12 µm. Given that the carotid canal is only entirely preserved in the right temporal fragment of IPS58443.1, the carotid canal three-dimensional (3D) model of this single fragment was used in Chapter 3. The dental 3D models derived from the microcomputed tomographic (µCT) scans of IPS58443.1 and IPS58443.2 were used in Chapter 4, and only the 3D models of the complete molars were employed in Chapter 5. Then, a total of 24 tooth models from ACM/C5-D1 were used in Chapter 4, whereas the models of nine molars (Table 2.1) were specifically selected and studied in Chapter 5.

Table 2.1. List of the *P. cataloniae* dentognathic specimens scanned by X-ray µCT and virtually extracted teeth. Non-molar tooth positions were not included in Chapter 5 and are thus marked as not applicable (N/A) in the third column.

Catalogue No.	Virtually extracted teeth	Molars included in Chapter 5	Voxel size (µm)
IPS42977	All (left DP4 and P4)	N/A	12
IPS43936	All (left dp3–dp4, left i1–m2 and right i1)	Left m1–m2	12
IPS44014	Left P3–M1	Left M1	12
IPS58443.1	Right M2–M3	Right M2–M3	33
IPS58443.2	Left M3	Left M3	33
IPS93524	Right p4	N/A	12
IPS94886	Right m2	Not included	12
IPS94888	Left M2	Left M2	12
IPS100379	Right M1	Right M1	12
IPS100384	Left M2	Left M2	12
IPS106878	Left dp4	N/A	12

2.1.2. Extant comparative sample

The extant comparative sample comprises 36 anthropoid genera, including all extant ape genera and representatives of all cercopithecoid subtribes and platyrrhine (sub)families. The carotid canal 3D models derived from the µCT scans of 127 crania of fully adult individuals (i.e., exhibiting the M3 in occlusion, or the M2 in callitrichines) belonging to 41 species from 36 genera were used in Chapter 3. In Chapter 4, visual inspections of teeth and dental measurements at the genus rank for the extant cercopithecoid *Macaca*, the extant hylobatid *Hylobates*, and the three extant great ape genera were conducted based on or taken from the published literature, the PRImate Morphometrics Online (PRIMO) database, and casts housed at the American Museum of Natural History (AMNH; New York). In Chapter 5, the extant comparative sample includes 90 molar 3D models from µCT scans of hominids (five species from the three genera) and 40 molar 3D models from µCT scans of hylobatids (six species from two genera).

Most of the µCT scans used in Chapter 3 were downloaded from MorphoSource (https://www.morphosource.org). Three hominoid µCT scans from the AMNH were provided by Sergio Almécija, while seven others are housed in the Institut Català de Paleontologia Miquel Crusafont (ICP; Sabadell, Spain). The voxel size for the extant specimens ranges from 27 to131 mm. In turn, all hominid specimens studied in Chapter 5 had been previously used in Zanolli et al. (2023), while among the 40 hylobatid molars 24 were kindly provided by Clément Zanolli: one of these hylobatid specimens is from the Trieste Natural History Museum and was provided by Deborah Arbulla, whereas the remaining 23 were downloaded from MorphoSource or the European Synchrotron Radiation Facility (ESRF heritage database for palaeontology, evolutionary biology and archaeology; http://paleo.esrf.eu). Among the 16 remaining hylobatid molars, eight were taken from

μCT scans downloaded from MorphoSource and eight from μCT scans kindly provided by Matthew M. Skinner.

2.1.3. Fossil comparative sample

The fossil comparative sample used in this dissertation includes the Oligocene stem catarrhines *Aegyptopithecus zeuxis* and *Saadanius hijazensis*, the dendropithecids *Dendropithecus macinnesi*, *Micropithecus clarki*, and *Simiolus enjiessi*, most pliopithecoid species (all but *Dionysopithecus orientalis*), the stem cercopithecoid (victoriapithecid) *Victoriapithecus macinnesi*, the stem hominoid (proconsulid) *Ekembo heseloni*, and Iberian dryopithecines (stem hominids). In Chapter 3, the 3D carotid canal models derived from the μCT scans of the left temporal of the holotype (individual III; NHMW 1970/1397/0003) of the pliopithecoid *Epipliopithecus vindobonensis* (Zapfe, 1961a), the left temporal of the KNM-MB 29100 cranium of *Victoriapithecus macinnesi* (Benefit and McCrossin, 1997), and of the right temporal of the holotype (KNM-RU 2036al) of *Ekembo heseloni* (Davis and Napier, 1963; Walker et al., 1993; McNulty et al., 2015) were used. In Chapter 4, visual inspections of teeth and dental measurements of *Aegyptopithecus zeuxis*, *Saadanius hijazensis*, *Victoriapithecus macinessi*, *Ekembo heseloni*, the aforementioned three dendropithecids, and pliopithecoids were conducted based on or taken from the published literature and casts housed in the ICP. Further visual inspections and dental measurement at the genus rank, including the Iberian dryopithecines *Hispanopithecus* and *Pierolapithecus*, were conducted based on or taken from the published literature. In Chapter 5, 10 specimens (16 molars in total) from the four following pliopithecoid taxa from the Vallès-Penedès Basin were investigated: the crouzeliids *Barberapithecus huerzeleri* and *Egarapithecus narcisoi*; the pliopithecid *Pliopithecus canmatensis*; and the indeterminate pliopithecoid from Sant Quirze (Harrison et al., 2002). In addition, 27 dryopithecine molars of *Anoiapithecus brevirostris*, *Dryopithecus fontani*, *Hispanopithecus crusafonti*, *Hispanopithecus laietanus*, *Pierolapithecus catalaunicus*, and '*Sivapithecus*' *occidentalis* species inquirenda were also included.

Regarding μCT scan provenance, the *Epipliopithecus vindobonensis* specimen included in Chapter 3 was scanned at the Vienna μCT lab (Vμ-CTL) and has a final reconstructed isometric voxel size of 22 μm. In turn, the μCT scans of both *Victoriapithecus macinnesi* and *Ekembo heseloni*, with isometric voxel sizes of 64 μm and 44 μm, respectively, were made available by the Department of Earth Sciences, National Museums of Kenya (which holds the copyright) and the Department of Human Evolution, Max Plank Institute for Evolutionary Anthropology (Leipzig, Germany). In Chapter 5, eight pliopithecoid specimens were scanned by X-ray microtomography, either at the CENIEH or at the Multidisciplinary Laboratory of the 'Abdus Salam' International Centre for Theoretical Physics (ICTP, Trieste, Italy), while two were scanned by neutron-based computed

microtomography at the cold neutron radiography and tomography station (ANTARES) of the Heinz Maier-Leibnitz Zentrum (Garching bei München, Germany). The EDJ of all dryopithecine molars included had been previously analyzed (Alba et al., 2020; Fortuny et al., 2021; Zanolli et al., 2023) and the corresponding 3D models are openly available from MorphoSource.

2.2. Methods

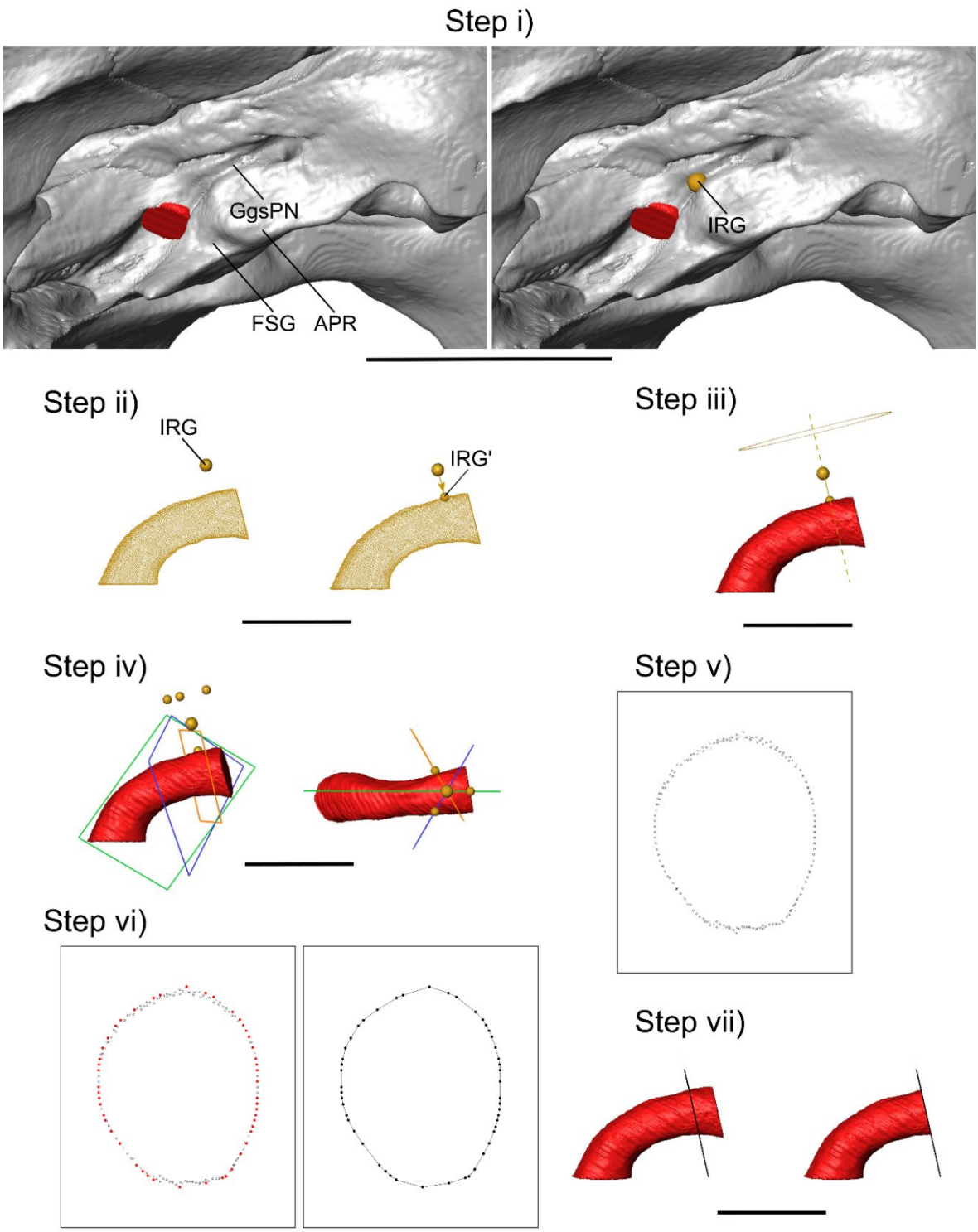
2.2.1. Virtual sample preparation

Carotid canal. In Chapter 3, the carotid canal of each specimen was virtually extracted in Avizo v. 7.0 (Visualization Sciences Group, Hillsboro). Because the bony material of the canal becomes very thin in some parts and is pierced with alveoli that regularly disrupt its internal contour, coupled with the fact that the canal is a hollow structure and is sometimes filled with matrix, semiautomatic threshold-based segmentations or mostly manual segmentations were conducted. When possible, the right carotid canal was preferentially extracted, but otherwise the left canal was segmented and mirrored. The 3D models were generated in Avizo using a 'Constrained smoothing' of 3. As specified above, the carotid canal is a hollow and open structure; since the segmentation process alone does not allow to obtain 3D models with homologous ends, a specifically devised plane was computed for each canal end and used to cut the 3D model (in Avizo) in a homologous manner among all specimens in the sample. Moreover, the internal (anterior) opening of the carotid canal on the petrosal part of the temporal bone is very irregular in shape and varies intraspecifically. For the posterior end, the best-fit plane of a series of 10 landmarks placed on the (external) carotid foramen was used and further translated to the centroid of this landmark series. To obtain the cutting plane of the canal anterior end a semiautomatic iterative protocol coded in R v.4.0.2 (R Core Team, 2020) specifically

---

Figure 2.1. (*Next page*) Schematic illustration of the protocol devised for cutting the anterior canal end: i) virtual rendering of the petrous part of the temporal bone in superomedial view with anterior part of the carotid canal 3D model (in red) and IRG landmark; ii) medial view of the carotid canal 3D model converted as a point cloud with IRG and IRG'; iii) medial view of the carotid canal 3D model (instead of the canal point cloud for easier visualisation) with IRG, IRG', the axis passing by the two points, and 360 points rotating around the latter; iv) medial and superior views of the carotid canal 3D model (instead of the canal point cloud for easier visualization) with IRG, IRG', and an example of 3 possibilities of rotating points among the 360 ones, with the 3 associated possibilities of cutting planes; v–vi) example of a slice derived from one possibility of cutting plane (here the final selected plane, i.e., the orthogonal plane to the anterior part of the canal) showing the points of the canal point clouds sliced by the cutting plane (i.e., canal cross-section; step v) and those that are most external (red points) further permitting obtaining the canal contour shape sliced by the plane (step vi); vii) medial views of the carotid canal 3D model with the selected cutting plane and the anterior end cut. Abbreviations: APR = anterior pyramidal ridge; FSG = fossa for the semilunar ganglion; GgsPn = groove of the greater superficial petrosal nerve; IRG = intersection ridge–groove; IRG' = projection of IRG onto the canal surface. Scales = 10 mm.

devised for this purpose was applied. This protocol consists in computing the orthogonal plane to the anterior part of the 3D canal model passing through a particular landmark and includes the following steps (Fig. 2.1): (i) A landmark is placed at the intersection between the anterior pyramidal ridge and the groove for the greater superficial petrosal nerve (called IRG), (ii) the canal surface is imported in R as a point cloud and the projection of IRG onto the canal (IRG') is found, (iii) 360 points rotating



around the IRG-IRG' axis are created, (iv) 360 different planes, each one based on the coordinates of IRG, IRG' and one possibility of point among the 360 rotating ones, are computed, (v) for each plane the points of the canal point cloud that are the closest to the plane (i.e., those points that have an orthogonal distance to the plane equal or shorter to the most common distance between two adjacent points of the canal point cloud) are selected and projected onto the plane so that a cross-section of the canal cloud cut by the actual plane is obtained, (vi) the most external points on the cross-section are kept to have an actual representation of the canal contour sliced by the plane, and the surface area is calculated, and (vii) after reiterating the calculus for the 360 planes, the plane for which the surface area of the slice is the smallest is kept. Such plane is considered the (most) orthogonal plane to the anterior part of the canal, among the 360 possible ones. The coordinates of such plane are then used to cut the anterior end of the carotid canal 3D model, in Avizo. The centroid of the cross-section derived from this plane is also recorded.

Prior to morphometric analyses, and for each specimen, the cut 3D model of the carotid canal was reimported in R as a point cloud and eight equidistant streampoints located between the two centroids of the two canal ends (canal endpoints) were computed as follows: nine slices with the same plane coordinates as the orthogonal plane used to cut the anterior canal end were generated equidistantly between the two canal endpoints, and their respective centroid was calculated based on the cross section of the canal cloud obtained, similarly to the procedure described above. From those nine centroids the 'digit.curve' function of 'Geomorph' v. 3.3.1 (Adams et al., 2019) was applied to slide the points and get a final number of 8 points. Together, the 10 streampoints represent the carotid canal shape.

Teeth. In Chapter 5, the virtual models of 16 extant hylobatid molars were obtained using the watershed segmentation tool in Avizo, whereas watershed or semiautomatic threshold-based segmentations were applied to the *Pliobates* and the Iberian pliopithecoid sample, also in Avizo. To have as many specimens as possible for the 3DGM analyses, dentine horns were reconstructed for eight extant hylobatid, five *Pliobates*, and nine Iberian pliopithecoid molars. Reconstructions of the dentine horn tips were made for sections showing light to moderate wear (e.g., Smith et al., 2012; Fortuny et al., 2021; Alba et al., 2024b) based on the natural curvature and orientation of the EDJ preserved portion and/or, when possible, based on the profile of the antimere, or other teeth, if less worn.

2.2.2. Measurements and anatomical nomenclature

Carotid canal. The volume of the carotid canal was computed using the 'Surface Area Volume' module in Avizo, after generating again the 3D canal model without smoothing—given that, to

measure areas and volumes from 3D models, it is recommended to use non-smoothed models to avoid any calculation bias related to a potential loss of voxels due to the effect of smoothing. In turn, the length was calculated by the sum of the length of the nine canal segments resulting from the 10 canal streampoints. A robusticity index was measured as canal length divided by the cubic root of canal volume.

Teeth. The dental measurements of *P. cataloniae* reported in Chapter 4 were taken with a digital caliper to the nearest 0.1 mm, except for the P4 of IPS42977 and the m1 and m2 of IPS43936; these teeth had to be digitally extracted from µCT scans and therefore they were measured using the 2D Length tool in Avizo. The measurements include mesiodistal length (MD) and buccolingual (for the cheek teeth) or labiolingual (for incisors and canines) breadth (BL); BL was measured separately at the mesial and distal lobes in the case of molars and dp4. For cheek teeth, the breadth/length index (BLI, in %) was computed as BLI = maximum BL / MD × 100. Dental nomenclature (Fig. 2.2) follows Harrison and Gu (1999).

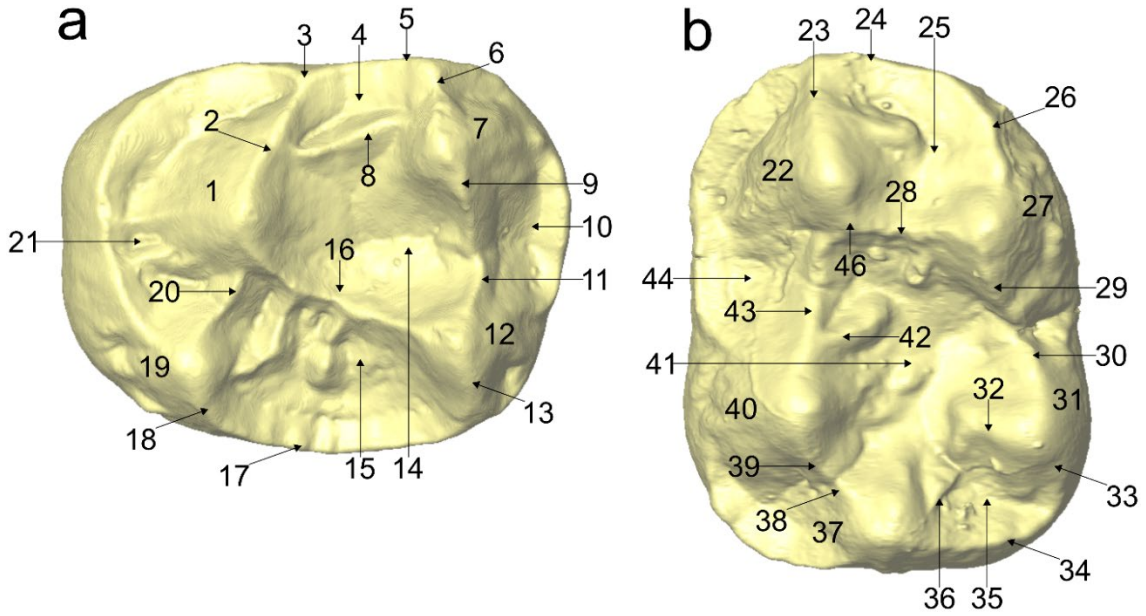


Figure 2.2. Molar terminology used in this dissertation as exemplified in two 3D outer enamel surface molar models of *P. cataloniae* in occlusal view: a) Left M2 IPS94888; b) Left m1 IPS43936. Legend: 1 = protocone; 2 = preprotocrista; 3 = paraconule (= protoconule); 4 = mesial fovea; 5 = mesial marginal ridge; 6 = preparacrista; 7 = paracone; 8 = hypoparacrista; 9 = postparacrista; 10 = buccal cingulum; 11 = premetacrista; 12 = metacone; 13 = postmetacrista; 14 = trigon basin; 15 = distal fovea; 16 = cristid obliqua (=hypometacrista + postprotocrista); 17 = distal marginal ridge; 18 = posthypocrista; 19 = hypocone; 20 = prehypocrista; 21 = lingual cingulum; 22 = protoconid; 23 = preprotocristid ; 24 = mesial marginal ridge; 25 = mesial fovea; 26 = premetacristid; 27 = metaconid; 28 = hypoprotocristid + hypometacristid; 29 = postmetacristid; 30 = postentocristid; 31 = entoconid; 32 = hypoentocristid; 33 = postentocristid; 34 = distal marginal ridge; 35 = distal fovea; 36 = postcristid; 37 = hypoconulid; 38 = prehypoconulid cristid; 39 = posthypocristid; 40 = hypoconid; 41 = talonid basin; 42 = distal arm of the pliopithecine triangle; 43 = cristid obliqua (= prehypocristid + postprotocristid); 44 = buccal cingulid.

2.2.3. Geometric morphometric analyses

Geometric morphometrics (GM) is the quantitative analysis of the form (size and shape) of biological structures based on geometrical (spatial) data. In standard GM, spatial data are collected by means of landmarks, assumed to be biologically homologous among the investigated specimens (Bookstein, 1991; Rohlf and Marcus, 1993). Other approaches in GM include landmark-free and homology-free methods–called surface matching methods (e.g., Glaunès and Joshi, 2006; Boyer et al., 2011). Among them, the most powerful thus far is the diffeomorphic surface matching, which warps the complete surface meshes from one to another and map the deformations (Durrleman et al., 2012a, b), and that has gained popularity over the last decade in palaeoanthropology (e.g., Beaudet et al., 2016a, 2016b; Urciuoli et al., 2020, 2021a, 2021b, 2022; Zanolli et al., 2023). In traditional GM, landmarks are defined as anatomical loci that have coordinates in a Cartesian coordinate system and that are biologically homologous among forms (Bookstein, 1991; Mitteroecker and Gunz, 2009). Three categories of landmarks were characterized by Bookstein (1991), later supplemented by three other categories, for semilandmarks (Weber and Bookstein, 2011): Type 1 landmarks are discrete points corresponding to juxtaposition of tissues, or, more clearly, points only defined locally by adjacent surrounding structures (Zelditch et al., 2012), such as the confluence of three cranial sutures, foramina, or ligament attachment points. Type II landmarks are similarly locally defined but rather refer to geometric constructs, corresponding to extremes of curvature (e.g., tips of incisors; Bookstein, 1991; Weber and Bookstein, 2011; Zelditch et al., 2012). Type III landmarks, considered the least reliable landmarks, are extrema characterized by information from multiple curves and by symmetry, and are constructed geometrically (Bookstein, 1991; Weber and Bookstein, 2011; Zelditch et al., 2012). These include farthest points from other points, centroids, etc. (Bookstein, 1991). Types 4, 5, and 6 landmarks actually refer to points that are not strictly landmarks, i.e., semilandmarks (Weber and Bookstein, 2011; Gunz and Mitteroecker, 2013), used to describe curves, surfaces, and constructed points, respectively. Therefore, semilandmarks are points used to define anatomical aspects that are not strictly homologous among forms because, unlike landmarks, they do not correspond to potentially homologous points in anatomical terms, but rather to comparable points in terms of geometric properties.

Once the landmark and semilandmark coordinates are recorded for all specimens in the selected sample, the configurations are aligned via a generalized Procrustes superimposition, also known as generalized Procrustes analysis (GPA; Rohlf and Slice, 1990; Bookstein, 1991; Klingenberg, 2020). This final step consists in scaling, translating, and orienting the landmark configurations to have them in a standardized coordinate system in which only the shape information remains. This coordinate system is termed the shape space and for the simplest forms—i.e., triangles—corresponds to Kendall's shape space, in which all the shapes of the specimens in a sample lie on a sphere or a

hemisphere around the mean shape (Kendall, 1984; Klingenberg, 2020). For more complex shapes in 3D, the shape space is a generalization to higher dimensions of a curved surface in 3D (Mitteroecker and Gunz, 2009). In those spaces of k dimensions (e.g., for k landmarks in 3D the number of dimensions is originally $3k$ to which are subtracted seven degrees of freedom, lost due to the Procrustes standardization, including one for the size, three for the translation, and three for the orientation), each shape (i.e., specimen) is represented by a point and the distances among points represent the magnitude of shape differences among them (Klingenberg, 2020). Because such spaces are non-linear (non-Euclidean)—i.e., the points cannot be represented on a single line or a plane—calculations involving the specimen shapes are inconvenient and a flat space (a plane) approximation is generally used: the shape tangent space. This space is simply a plane tangent to the mean shape point into which the specimen shapes are orthogonally projected (Klingenberg, 2020).

In this dissertation, landmark-based 3DGM approaches are applied in both Chapters 3 and 5, but in Chapter 3 an indirect Procrustes alignment is performed on the carotid canal landmark configurations, as detailed below.

Carotid canal. The main aim of Chapter 3 is to study the carotid canal not as an isolated element but as a structure spatially integrated within the cranium. The objective is to retain the information on canal form, position, and orientation within the cranium, and within the petrosal in particular. The carotid canal runs through the petrous part of the temporal bone so, to establish a common standardized coordinate system for all specimens, a GPA was performed on nine petrosal/tympanic landmarks using the 'gpagen' function of the R package 'Geomorph' v. 3.3.1. Having the petrosal/tympanic area(s) aligned among all specimens in the sample is a substitute for the use of cranial planes of reference (e.g., Frankfurt Horizontal, sella-nasion, etc.) for subsequent morphometric analyses of the carotid canal. This is necessary because most specimens, including *Pliobates*, either do not preserve enough of the cranium to determine the standard anatomical planes of reference, or else μCT scans of the whole cranium were not available.

The orientation of the carotid canal was quantified by computing the vector representing the canal direction and decomposing it into two two-dimensional (2D) angles, relative to a reference vector. First, following the GPA of the petrosal/tympanic landmarks, the resulting transformation matrices of all the rounds of fitting were simply applied to the streampoints of the carotid canal, more exactly to the two canal endpoints. This was achieved by exploring the source code of the 'gpagen' function of 'Geomorph' and extracting the transformation matrix after each round of fitting while running the function on the petrosal/tympanic landmark dataframe. After this indirect Procrustes alignment of the canal endpoints, the 3D vector representing the canal direction was computed (from posterior to anterior). In the post-alignment common Cartesian coordinate system, the X-axis corresponds to the anteromedial-posterolateral direction of the canal, the Y-axis to its inferomedial-superolateral

direction, and the Z-axis to its anterolateral-posteromedial direction. The superior and medial orientations were calculated as the angle between the YZ and XY coordinates of the canal and the coordinates of the anteroposterior axis of the cranium—the latter defined based on the average configuration of the petrosal landmarks, respectively (see Chapter 3).

As for canal orientation, the transformation matrices of all the rounds of fitting resulting from the GPA of the petrosal/tympanic landmarks were applied to the 10 canal streampoints to obtain the shape of the carotid canal while retaining the information on canal form, position, and orientation within the petrosal, i.e., the carotid canal course. The canal landmark configurations obtained after this indirect Procrustes alignment therefore represent the scaled, translated, and oriented carotid canal courses.

Teeth. Two different sets of landmarks and semilandmarks were designed for the M2 and m1–m2. The M2 set is composed of four landmarks placed at the dentine horn apices of the four main cusps (protocone, paracone, metacone, and hypocone), a fifth landmark placed at the mesiobuccal end of the cervix, and 104 semilandmarks; the latter include 75 semilandmarks positioned along the occlusal crests and the mesial and distal marginal ridges, and 29 distributed along the cervical contour of the crown. In turn, the m1–m2 set consists of five landmarks placed at the dentine horn apices of the main cusps (metaconid, protoconid, entoconid, hypoconid, and hypoconulid) and 70 semilandmarks positioned along most of the occlusal crests and the mesial and distal marginal ridges.

2.2.4. Statistical techniques

Multivariate analyses. In Chapter 3, box-and-whisker plots performed with R were used to evaluate the variation in carotid canal orientation, canal robusticity index, and carotid canal course (using the between-group principal component scores for the latter, see below). To test for significant differences among means of the extant groups, Kruskal-Wallis tests followed by Bonferroni-corrected Mann-Whitney post hoc pairwise comparisons were performed in R. The Kruskal-Wallis test is a nonparametric analysis of variance aimed to determine if multiple samples significantly differ in average, used instead of the traditional analysis of variance when data are not normally distributed. Indeed, it is the extension for three or more samples of the Mann-Whitney test, which is a nonparametric pairwise test used for not normally distributed samples. In this case, Bonferroni correction is required to compensate for the likelihood of incorrectly rejecting a null hypothesis—which increases as the number of groups involved in the comparisons increases—by simply dividing the *p*-value of each pairwise comparison by the total number of groups, so that the *p*-value significant threshold is lower than 5%. When significant differences among extant groups were found, *Pliobates* and other fossil specimens were compared with the distributions of extant groups using z-scores.

The canal landmark configurations (Chapter 3) were further investigated by means of a between-group principal component analysis (bgPCA). The rationale behind a PCA is to perform a dimensional reduction of the original number of investigated variables by finding linear combinations of variables—the principal components (PCs)–passing through the scatter of points of the (multidimensional) data that best describe the variance of the data. The PCs are defined by their respective direction of maximum variance (eigenvector) and amount of variance explained by the eigenvector (eigenvalue). The first PC incorporates the maximum percentage of the variance and the others are orthogonal to the first one and to one another, incorporating a progressively lesser amount of variance until none is left. More specifically, the covariance matrix of the original data (with *p* original variables) is decomposed into *p* eigenvectors and *p* eigenvalues. The mean adjusted original data matrix is then multiplied by the eigenvector matrix to obtain the new data. The PCA data therefore represent the projection of all original data into each PC. While a standard PCA maximizes the variance among individuals, a bgPCA is a PCA that seeks to maximize the variance between pre-existing (a priori defined) groups and is computed as a PCA run on the covariance matrix of the group means (on the covariance elements), i.e., as a PCA for which the PCs maximize the distance between the group means (Mitteroecker and Bookstein, 2011). The bgPCA was performed using the 'groupPCA' function of the R package 'Morpho' v. 2.8 (Schlager, 2017).

A potential issue regarding the application of bgPCA with 3DGM data is that when there are fewer groups than variables, it may result in marked differences among groups when in reality the differences do not exist or are at least minimal (Cardini et al., 2019). This problem is more worrisome in 3DGM than in traditional morphometrics because the use of landmarks exponentially increases the number of variables. In light of this potential issue, it was ensured that the grouping structure obtained from the bgPCAs was not spurious by first comparing the original bgPCA results with those of a cross-validated bgPCA, for which the potential distortion is highly reduced (Cardini et al., 2019). A cross-validated bgPCA is based on a leave-one-out approach, which iteratively resamples the data set by excluding one individual at a time and uses the remaining individuals to compute the model that is then used to classify the omitted individual. Following the recommendation of Cardini and Polly (2020), a permutational analysis of variance (PERMANOVA, consisting of randomly resampling *n* times the data set and each time recomputing the distance between the centroids of all pairs of newly formed groups) was further conducted to estimate the variance (R^2) between group means and their significance (*p*). Both *p* and R^2 were computed from the Euclidean distances between group means within the full space of canal course configurations (raw coordinates) as well as within the bgPCA spaces (both standard and cross-validated bgPCAs). Comparing the *p* and R^2 values of the bgPCA (before and after cross-validation) with those of the raw canal course configuration coordinates permits verifying if the bgPCA exaggerates the differences among groups. This is the case if *p* is significant in the standard bgPCA space but is not in the full space or, in the case *p* is

significant in all spaces, if R^2 is higher in the standard bgPCA space than in the cross-validated bgPCA space and much higher than in the full space–R^2 in the cross-validated bgPCA space being always higher than in the full space due to the principle of between-group variance maximization in the bgPCA. The 'lm.rrpp' function of the R package 'RRPP' v. 0.6.1 (Collyer and Adams, 2018) was used for that purpose.

In Chapter 5, the EDJ shape data obtained after performing GPAs on the molar landmark configurations were analyzed by means of PCAs as well as canonical variate analyses (CVAs). Like PCA, CVA is a dimensional reduction method. It is conceived as a multivariate extension of (bivariate) linear discriminant analysis (e.g., Campbell and Atchley, 1981) and seeks to maximize the variance among more than two a priori defined groups. It differs from the bgPCA in finding new linear combinations of variables—the canonical variates (CVs)—which not only maximize the variance between group means but also minimize the variance within each group (run on both the variance and covariance elements of the covariance matrix). Additionally, unlike the PCs and bgPCs, the CVs must not be orthogonal to each other. However, in Chapter 5, the CVAs were not performed on the original data matrix (i.e., the landmark configurations after GPA) but from the PC scores, based on the minimum number of PCs incorporating the highest percentage of correct classification after cross-validation (following Zanolli et al., 2023). Because the CVA statistical reliability requires the number of variables to be smaller than the sample size (Mitteroecker and Bookstein, 2011), computing the CVA from a limited number of PCs instead from the whole original variables (k landmarks in 3D correspond to $3k$ variables) compensates for this issue and is a also a compromise between including a sufficient proportion of overall shape variation and avoiding unrealistic and unstable levels of discrimination (Skinner et al., 2009; Zanolli et al., 2023). The PCAs and CVAs were computed using the R packages 'ade4' v. 1.7-18 (Dray and Dufour, 2007) and 'Morpho,', respectively.

In Chapter 3 and 5, morphological similarities between fossil specimens and extant groups were further assessed by computing typicality probabilities, which correspond to the probability for a fossil specimen to fit within the multivariate normal distribution of the a priori defined groups (e.g., Albrecht, 1992). Typicality probabilities are defined as the probabilities for a fossil specimen to have the given bgPC or CV score if it indeed belongs to a particular a priori defined group (separately for each of them). Therefore, these probabilities do not assume that a fossil specimen necessarily belong to one of the groups defined a priori. This approach relies on the squared Mahalanobis distances (i.e., based on both the variance and covariance of the groups) between the fossil specimens and the centroids of each group, which were calculated using the 'typprobClass' function of 'Morpho.' A probability lower than 0.05 indicates that the specimen does not fit within the distribution of the group. In Chapter 5, posterior probabilities of group membership were computed as well. A posterior probability is the likelihood of a given specimen not included in the analysis a priori (as in the case

of fossil specimens) to be classified as a member of one of the a priori defined groups. They are computed using the Mahalanobis distances between the CV scores estimated for the fossil specimens and the group centroids, the prior probabilities for the groups (here assumed to be equal among groups, i.e., equal to one divided by the number of groups, for each group), and assuming a normal distribution for the CV scores (to calculate the probability density for the specimens if they come from the groups, for each specimen, for each group), by applying the Bayes theorem. Posterior probabilities assume that the fossil specimens necessarily belong to one of the groups and sum to 1 across the groups.

Finally, in Chapter 3, to ascertain the phenetic similarities between taxa in the morphospace resulting from the bgPCA, a neighbor-joining (NJ) cluster analysis (Saitou and Nei, 1987) was performed on the Euclidean distances (EDs) among species mean raw coordinates of the canal course configurations using the 'nj' function of the R package 'phangorn' v. 2.5.5 (Schliep, 2011).

Permutation tests. In Chapter 5, the degree of EDJ shape variation in the molars of *Pliobates* as compared to that of extant genera was evaluated through permutation tests coded in R, and previously applied to the EDJ shape of dryopithecine molars in Zanolli et al. (2023). These permutation tests enabled testing the null hypothesis that the molars—in particular, the M2s—included in the hypodigm of *P. cataloniae* (see Chapter 4) belong to a single taxon. This was done by comparing the variation of *Pliobates* with that of extant hominoid genera. The variation was measured as the average of the EDs between pairs of specimens of the same taxon based on all the PC scores. For *Pliobates*, EDs were computed between each possible pair of M2 specimens. For each extant hominoid genus, all possible combinations (i.e., permutations) of M2 specimens for subsamples of the same size as the *Pliobates* M2 sample were generated, and the average ED for each permutation was calculated. The average ED of *Pliobates* was then compared with the distribution of the average EDs for the permutations of each extant hominoid genus. The probability (interpreted as a *p*-value) that *Pliobates* displays a lower variation than a given extant hominoid genus was computed by dividing the number of permutations with a higher or equal average ED than that of *Pliobates* by the total number of permutations. The null hypothesis that the *Pliobates* sample is not more variable than a given extant hominoid genus was rejected when $p < 0.05$.

2.2.5. Phylogenetic comparative methods

Phylogenetic signal. In morphometric studies, phylogenetic signal measures the tendency of closely related species to be more similar to each other than are species drawn at random (e.g., Felsenstein, 1985; Blomberg et al., 2003). To assess the phylogenetic signal embedded in carotid canal course (Chapter 3), two univariate quantitative metrics were computed: Pagel's λ (Pagel, 1999)

and Blomberg's K (Blomberg et al., 2003). They were computed using the R package 'phytools' v. 0.7e70 (Revell, 2012). These statistics rely on the Brownian motion evolutionary model in which the value of traits changes randomly in both direction and distance and over any time interval (i.e., "random walk")—the value of a trait at time *t* corresponds to its value at time 0 plus the sum of all the random changes of the trait from time 0 to time *t*, and is always drawn from a normal distribution with mean 0 and variance proportional to branch length (Pagel, 1999; Freckleton et al., 2002; Blomberg et al., 2003). These metrics consist in comparing the observed values with those expected under a Brownian motion model through randomization.

Pagel's λ is a parameter transformation of the given phylogeny that ensures the best fit of trait values to a Brownian motion model. The covariance matrix among related species in the given tree (i.e., the expected covariance under Brownian motion) is computed from branch lengths and scaled by λ down to the observed covariation matrix (computed from the observed species trait values). λ is thus a scaling parameter for the expected phylogenetic correlation applied to the covariance elements of the expected covariance matrix and ranges from 0 (i.e., maximum of covariance adjustment needed to explain the observed trait values, implying that the traits have not evolved according to Brownian motion on the given phylogeny and thus there is no phylogenetic correlation) to 1 (i.e., no need for adjustment, so that the covariance matrix computed from the given phylogeny explains the observed species trait values, implying that the effect of phylogeny is total, as in a Brownian motion model). In terms of tree topology, the closer is λ to zero, the more the observed species trait values are explained by a species tree having its branching structure removed—i.e., the internal branches shorten until the nodes collapse in the extreme case of $\lambda = 0$—meaning that the species data are less and less phylogenetically correlated until they are completely independent from phylogeny.

Blomberg's K reflects to what extent the investigated phylogeny matches the variance-covariance in the data. It compares the (observed) ratio between the mean squared error of the species trait values measured from the phylogenetic corrected mean and the mean squared error of the covariance matrix computed from the given phylogeny (Brownian motion) with the (expected) analytically derived ratio under Brownian motion: $K \approx 1$ means that trait evolution approximates the expectations under a Brownian motion model; $K < 1$ means that distantly related taxa resemble each other more than expected under a Brownian motion model (i.e., variance is mostly found within clades); and $K > 1$ means that closely related taxa resemble each other more than expected under a Brownian motion model (i.e., variance is mostly found among clades). Values of $K < 1$ are generally interpreted as indicating that distantly related taxa have independently evolved similarities unrelated to phylogeny (i.e., homoplasy). In contrast, $K > 1$ is indicative of evolutionary constraints or stabilizing selection.

To compute the phylogenetic signal metrics, a time-calibrated molecular phylogenetic tree of the investigated extant species was primarily derived from the 10kTrees v.3 website

(https://10ktrees.nunn-lab.org/; Arnold et al., 2010) and supplemented with results for the lacking species (not included in 10ktrees) after Meyer et al. (2011) and Springer et al. (2012).

Allometric analyses. In Chapter 3, the correlations among canal size variables (i.e., length, cubic root of the volume, centroid size), between canal shape (i.e., robusticity index, bgPCs) and size variables, and between canal size or shape variables and body-mass (BM), were assessed through bivariate regressions computed for the whole anthropoid sample. To minimize the effects of body size dimorphism, average female BM data were taken from the literature (Smith and Jungers, 1997; Delson et al., 2000; Turner et al., 2018). The size variables were log-transformed using natural logarithms (ln) in all instances. For all allometric regressions, a phylogenetic generalized least-squares (PGLS) method was used. The PGLS is a modified GLS used when one of the assumptions of the ordinary least squares (OLS) method, namely the non-independence of the regression residuals, is thought to be violated (i.e., the residuals are thought to covary) because of the phylogenetic relationships among taxa (Rohlf, 2001). No correlation among residuals—which is the assumption of the OLS method—implies that, in the covariation matrix of the residuals, the covariation values equal zero. Using a PGLS therefore allows correcting the phylogenetic effect on the residuals by adjusting their covariance matrix. The phylogenetic signal (Pagel's λ, see above) is estimated and multiplied to the covariance elements (i.e., the off-diagonal elements) in the residual covariance matrix (e.g., Symonds and Blomberg, 2014). The resulting phylogenetically corrected matrix is then used to compute the regression (e.g., Symonds and Blomberg, 2014). The phylogenetic tree employed for the computation of PGLS regressions is the molecular one described above for phylogenetic signal.

The BM of *P. cataloniae* was estimated in Chapter 4 based on the dental measurements of all available molars using anthropoid allometric equations based on occlusal tooth square area (A, computed as A = MD × BL) following Egi et al. (2004). These authors calculated the equations via the least squared regression model, from regressions between ln BM (dependent variable) and ln A (independent variable) of anthropoid samples, these equations being negatively allometric as the body mass does not increase in a linear fashion relative to A and the former variable increases less than the latter. In Chapter 4, average A was used to estimate BM for tooth loci that comprised several specimens. Logarithmic detransformation bias, i.e., the error due to the fact of predicting a BM value based on a regression equation that primarily used log-transform BM data (Smith, 1993), was corrected using the ratio estimator (Egi et al., 2004): the predicted BM value is simply multiplied by the ratio estimator, which is the ratio between the arithmetic mean of the original (untransformed to logarithmic units) BM data used in the regression over the mean of the predicted body masses (from the regression) for all the original independent variable values (Smith, 1993). The 50% confidence interval (CI) was computed for each tooth locus using the standard error of estimate (the standard

deviation of the residuals) and an inverse Student's t distribution–better for calculating CIs than using a standard normal distribution as for small samples it allows reducing the difference between the estimated standard deviation from the sample and the true standard deviation (from the population)–with the degrees of freedom determined by the effective sample size (Egi et al., 2004). The effective sample size, compared to sample size, allows correcting for the phylogenetic component in explaining the variance among trait values, and is computed as the sum of the variance nested multiplied by the group size at each taxonomic rank (Smith, 1994). The degrees of freedom are thus reduced (nested degree of freedom) which widens the CIs calculated (Smith, 1994). An average BM estimate was computed as the arithmetic mean of estimates for the various tooth loci, with the confidence interval (CI) taken as the maximum and minimum ends of the 50% CIs of the included tooth loci. Compared to the commonly used equations of Gingerich et al. (1982), the equations of Egi et al. (2023) have the advantage of being computed using effective sample sizes, therefore controlling for phylogenetic effect; they are also the most appropriate for small catarrhines such as *P. cataloniae* because their computations exclude large primates. Moreover, the species included in the sample include a lower percentage of cercopithecoids and are more evenly distributed among the higher taxonomic ranks than in Gingerich et al. (1982). However, the regressions of Egi et al. (2004) are based on species mean BM and are therefore most appropriate for deriving estimated species BM; for that reason, an average estimate of *P. cataloniae* BM was computed from the different tooth locus averages rather than from specimens/individuals.

Phylomorphospace and ancestral morphotype reconstruction. In Chapter 3, patterns of carotid canal course variation among the branches of the phylogeny were identified by mean of a phylomorphospace, in which the phylogenetic tree was projected onto the two first bgPCs (Sidlauskas, 2008). The phylomorphospace allows visualizing the magnitude and direction of the carotid canal course change. The investigated extinct taxa were added to the molecular tree of extant species employed for the computation of PGLS regressions and phylogenetic signal. Two different phylogenetic hypotheses were considered for *Ekembo*, *Epipliopithecus*, and *Pliobates*: one following Alba et al. (2015), in which *Epipliopithecus*, *Ekembo*, and *Pliobates* are successive stem hominoid taxa; and a second following Nengo et al. (2017), in which *Ekembo* is a stem hominoid while *Epipliopithecus* and *Pliobates* together form a clade of stem catarrhines (i.e., are both considered pliopithecoids). Given the two competing phylogenetic hypotheses for these extinct taxa, two distinct phylomorphospaces were generated.

The position (i.e., bg PC scores) of the internal nodes—the last common ancestors (LCAs) of the various clades—were estimated based on a maximum likelihood (ML) method for continuous characters (Schluter et al., 1997) using the ‘fastAnc’ function of 'phytools.' This method relies on the Brownian motion model, governed by a rate parameter. The assumption is that the expected variance

between any two species equals rate parameter multiplied by the time since their LCA. The ML ancestor states are thus those minimizing the sum of squared changes along the branches (Schluter et al., 1997). The bgPC scores estimated for the LCAs were then rotated and translated back into the Kendall's shape space (i.e., raw landmark configuration space after GPA) to obtain and visualize the estimated ancestral carotid canal course conformations.

2.2.6. Phylogenetic inference

In Chapter 4, cladistic analyses were conducted to infer the phylogenetic relationships of *P. cataloniae*. Cladistics, originally developed by Hennig (1966) and subsequently developed by other researchers from the 1970s onward, refers to both a systematics school (also known as phylogenetic systematics) and a method of phylogenetic inference. In phylogenetic systematics, only clades (i.e., monophyletic groups–those including all the descendants from a common ancestor) are considered natural and can be hence erected as taxa. As a method, the main innovation of cladistics was the explicit recognition that only synapomorphies (i.e., shared derived features) are phylogenetically informative (Hennig, 1966; Farris, 1983)—whereas symplesiomorphies (shared primitive features), constant characters, and autapomorphies (derived features present in a single taxon) cannot be used to determine phylogenetic closeness—and the proposal that the most likely phylogenetic hypothesis is that requiring the least possible amount of change (Cartmill, 2018). The latter epistemological assumption is known as the principle of maximum parsimony.

Cladistics has been for many years the mainstream method in morphology-based phylogenetic inference, particularly since the spread of personal computers and the implementation of computer-based algorithms to compute the most parsimonious trees given a certain group of taxa and a particular distribution of character states. Of course, the primitive or derived nature of a character state is relative to clades of interest, so that a synapomorphy of a group can also represent a symplesiomorphy for a clade at a lower taxonomical rank within this group. Confounding effects include homoplasies, that are character states that evolved independently in closely related or more distant clades, and thus do not the result from shared ancestry—i.e., false homologies. The homoplastic nature of a character also depends on the studied clades and a non-homologous character state shared by two different lineages can still represent a synapomorphy of one of these two, or both, lineages. From an epistemological viewpoint however, homoplasies cannot be identified a priori but only a posteriori based on the most parsimonious cladogram(s). The principle of maximum parsimony assumes that the most likely cladogram topology is that including the minimum possible number of steps (character state changes) to explain character state distribution for a given taxon-character matrix. In other words, this principle minimizes homology to determine the topology of the most parsimonious cladogram(s).

Cladistic analysis does not take chronostratigraphic data (i.e., age of the fossils included) into account. For some authors, this is positive because it allows the topology of most parsimonious cladograms to be compared with that expected from the fossil record (Smith, 2000). For others, this is a problem because it misses one of the most important data that the fossil record provides. Decades ago, an alternative approach of phylogenetic inference, termed stratocladistics, was developed to simultaneously consider morphological data and stratigraphic data using a modified parsimony criterion (Fisher, 2008). Despite some successful applications of this method (e.g., Finarelli and Clyde, 2004), this approach never became mainstream, according to Urciuoli and Alba (2003) probably because of the development of Bayesian methods a couple of decades ago. The latter rely on probabilistic assumptions and require the assumption of an evolutionary model, being generally used to analyze molecular data but being also applicable to morphological data (Nylander et al., 2004). What is most interesting of Bayesian approaches is that they can not only combine morphological with molecular data to produce time-calibrated phylogenies (i.e., node dating) but also incorporate the chronostratigraphic data to derive the most likely topology (i.e., tip dating or total-evidence Bayesian analysis; Ronquist et al., 2016; Pozzi and Penna, 2022). This approach is receiving increasing attention in primate phylogenetics (Pozzi and Penna, 2022) and some attempts have been made in the case of hominoids (Pugh, 2020), but their application has yet to become generalized (see Urciuoli and Alba, 2023, for further discussion). Simulation studies have shown that tip-dating may provide more accurate phylogenies than parsimony-based cladistic analyses (Mongiardino et al., 2021) but, at the same time, Bayesian analysis generally result in less resolved trees (O'Reilly et al., 2016; Goloboff et al., 2018; Pugh, 2022). For this reason, in Chapter 4 parsimony-based cladistic analysis was employed to investigate the phylogenetic relationships of *P. cataloniae* based on the new dental data provided in this dissertation and compare these results with those previously obtained using similar methods for this taxon in previous studies (Alba et al., 2015; Nengo et al., 2017; Gilbert et al., 2020; Ji et al., 2022).

To investigate the phylogenetic relationships of *P. cataloniae*, a newly compiled dental character-taxon matrix was used, including most pliopithecoid species (see above), three dendropithecid species (see above), the stem cercopithecoid *Victoriapithecus macinnesi*, the stem hominoid *Ekembo heseloni*, and the stem catarrhines *Aegyptopithecus zeuxis* (used as outgroup) and *Saadanius hijazensis*. The dental features used in this analysis are discrete characters that include qualitative as well as discretized quantitative ones, and were taken or modified from Alba et al. (2015), Harrison et al. (2020), and Ji et al. (2022), or else, newly defined. Quantitative characters were discretized using the gap-weighted coding method (Thiele, 1993), which range-standardizes the value for each taxon using the following formula: (taxon value – minimum value) / (maximum value – minimum value) × (number of desired states – 1); here, 2 states were desired. A maximum parsimony cladistic analysis was run on PAUP* v. 4.0a169 (Swofford, 2003) using a heuristic instead of an exact search

method. The former do not guarantee to recover all the optimal (shortest) trees but require less computational effort, and in this case the dataset was too large to use exact methods such as branch-and-bound or exhaustive searches. Using heuristic search therefore implies that one may find only a subset of the optimal trees or may not find the "true" minimum length trees (i.e., local optimum vs. global optimum). The heuristic search uses a stepwise addition process followed by branch swapping (Swofford and Bell, 2017). Potential local-optimum issues affect the stepwise addition process but can be corrected to some extent by means of branch swapping. Nevertheless, the results of a heuristic search for a given dataset will depend on the parameters chosen (e.g., type of addition sequence and associated reference taxon, swapping algorithm, etc.). In any case, heuristic methods used by PAUP* appear so far very effective (Swofford and Bell, 2017). Stepwise addition starts with an initial three-taxon tree and then connects taxa one at a time until all are placed; here, a simple addition sequence was chosen, which consists in choosing an initial taxon that is the closest to a hypothetical ancestor possessing the assumed ancestral state for each character (i.e., determined by the outgroup) as well as the two closest taxa to it, and then adds the remaining taxa by order of increasing differences from the initial one (Swofford and Bell, 2017). The simple addition sequence is generally a very effective option (Swofford and Bell, 2017) and was used it here, being considered the most logical option because it is based on the outgroup. Given that the placement of a taxon may be best relative to the taxa already making up the tree but may become suboptimal upon the addition of subsequent taxa, a branch swapping is performed; the algorithm used here is the tree bisection-reconnection, which is considered the most effective in PAUP* (Swofford and Bell, 2017). It cuts the tree along a branch to yield two subtrees that are then reconnected by a different pair of branches, formed by one from each subtree (Swofford and Bell, 2017); all possible bisections and reconnections are evaluated and rounds of swapping are performed until the global optimal tree, i.e., the tree for which the least number of character state changes are required (shortest tree length = best score), is found. Such tree is the most parsimonious. Multiple topologies may yield the best score, in which case a consensus tree is computed; here, a strict consensus was computed, so that the clades recovered in all the most parsimonious trees are kept, whereas clades not recovered in all the most parsimonious trees are collapsed into polytomies (Swofford and Bell, 2017).

The length of the most parsimonious consensus tree as well as three commonly used metrics to evaluate the congruence of the tree were computed (Kluge and Farris, 1969; Farris, 1989a, 1989b): the consistency index (CI) excluding uninformative characters; the retention index (RI); and the rescaled consistency index (RCI). CI is a measure of homoplasy computed as the minimum number of steps needed to explain the data divided by the number of steps in the most parsimonious tree(s) (Kluge and Farris, 1969). CI varies between a low value that tends towards 0–its exact value depends on how character states are distributed among taxa–and 1. The higher the CI, the lower is the level of homoplasy. In turn, RI is an improvement of CI (Farris, 1989a), so that besides being a metric of

homoplasy it also measures how well synapomorphies explain the tree; it is calculated as the difference between the maximum number of steps and the number of steps in the most parsimonious tree(s) divided by the difference between the maximum number of steps and the minimum number of steps needed to explain the data; contrary to CI, RI strictly varies between 0 and 1. Finally, Farris (1989b) further defined RCI as the product of CI and RI, to rescale the low value of CI to 0 (the maximum remaining at 1).

Clade support was assessed by means of bootstrap analysis (Felsenstein, 1985) and Bremer's index (Bremer, 1988). Bootstrap analysis is a statistical procedure of resampling with replacement (here, 1000 replicates were used) that creates subsamples of the character list–in which a number of characters are replaced by other characters, randomly. The analysis is then rerun on each subsample, implying that for each of them a list of one or more most parsimonious trees is produced. Based on all most parsimonious trees resulting from all replicate analyses, the percentage of occurrence of any clade recovered is computed; when a replicate results in more than a single most parsimonious tree, each clade recovered on each of these *n* most parsimonious trees contributes 1/*n* % to the total clade count (Swofford and Bell, 2017). Finally, a 50% majority-rule consensus tree is computed—so that only the clades recovered in 50% or more of the cases are considered supported, whereas the remaining ones are collapsed into polytomies. Therefore, this procedure assesses if each particular clade would still be recovered when some characters are omitted while others are given more weight, i.e., if the correlation among characters were modified. In turn, Bremer's index (also known as decay index) is a measure of clade support and is calculated for each of them; it corresponds to the number of additional steps required for a clade to collapse in the consensus tree of nearly most parsimonious trees. If a clade is not recovered in the consensus of the most parsimonious trees, its Bremer's index is 0; in contrast, all clades recovered in the strict consensus will have a Bremer index of 1 or more, equaling the number of additional steps required to make the clade collapse. Together, these two metrics allow evaluating the node support of the consensus of the most parsimonious tree(s)—the higher they are, the better supported.

A second cladistic analysis was performed at the genus level, considering the same dental features as in the first analysis but further including cranial and postcranial characters. A more reduced representation of pliopithecoids was included (the analysis mainly included those genera that preserve cranial and/or postcranial remains), whereas a wider sample of both extant and extinct hominoids was included (as in Alba et al., 2015; see above). A modified version of the cranial and postcranial characters analyzed in Alba et al. (2015) was used, relying on results from Chapter 3 and recently published papers dealing with *Pliobates* or other pliopithecoids (Urciuoli et al., 2021a, 2022; Arias-Martorell et al., 2021). Given the suspicion that postcranial homoplasy might be distorting the most parsimonious topology recovered for hominoids by parsimony analyses (Pugh, 2022; Urciuoli

et al., 2023), dental, craniodental, and postcranial characters were analyzed both jointly and separately, to evaluate the influence of these anatomical regions on the results.

Chapter 3:

Comparative anatomy of the carotid canal in the Miocene small-bodied catarrhine *Pliobates cataloniae*

Reproduced from:
Bouchet, F., Urciuoli, A., Beaudet, A., Pina, M., Moyà-Solà, S., Alba, D.M., 2021. Comparative anatomy of the carotid canal in the Miocene small-bodied catarrhine *Pliobates cataloniae*. J. Hum. Evol. 161, 103073. https://doi.org/10.1016/j.jhevol.2021.103073

Journal of Human Evolution 161 (2021) 103073

Contents lists available at ScienceDirect

Journal of Human Evolution

journal homepage: www.elsevier.com/locate/jhevol

Comparative anatomy of the carotid canal in the Miocene small-bodied catarrhine *Pliobates cataloniae*

Florian Bouchet [a, *], Alessandro Urciuoli [a], Amélie Beaudet [a, b, c, d], Marta Pina [a, e], Salvador Moyà-Solà [a, f, g], David M. Alba [a, *]

[a] *Institut Català de Paleontologia Miquel Crusafont, Universitat Autònoma de Barcelona, Edifici ICTA-ICP, c/ Columnes s/n, Campus de la UAB, 08193 Cerdanyola del Vallès, Barcelona, Spain*
[b] *Department of Archaeology, University of Cambridge, The Old Schools, Trinity Lane, Cambridge CB2 1TN, UK*
[c] *School of Geography, Archaeology and Environmental Studies, University of the Witwatersrand, 1 Jan Smuts Avenue, Braamfontein 2000, Johannesburg, South Africa*
[d] *Department of Anatomy, University of Pretoria, Lynnwood Road, Hatfield 0002, Pretoria, South Africa*
[e] *Department of Earth and Environmental Sciences, University of Manchester, Williamson Building, Oxford Road, Manchester M13 9PL, UK*
[f] *Institució Catalana de Recerca i Estudis Avançats (ICREA), Passeig de Lluís Companys 23, 08010 Barcelona, Spain*
[g] *Unitat d'Antropologia (Dept. BABVE), Universitat Autònoma de Barcelona, Edifici C, Facultat de Biociències, Campus de la UAB, 08193 Cerdanyola del Vallès, Barcelona, Spain*

ARTICLE INFO

Article history:
Received 15 February 2021
Accepted 25 August 2021
Available online xxx

Keywords:
Internal carotid artery
Petrosal
Geometric morphometrics
Fossil primates
Phylogeny
Evolution

ABSTRACT

The small-bodied Miocene catarrhine *Pliobates cataloniae* (11.6 Ma, Spain) displays a mosaic of catarrhine symplesiomorphies and hominoid synapomorphies that hinders deciphering its phylogenetic relationships. Based on cladistic analyses, it has been interpreted as a stem hominoid or as a pliopithecoid. Intriguingly, the carotid canal orientation of *Pliobates* was originally described as hylobatid-like. The variation in carotid canal morphology among anthropoid clades shown in previous studies suggests that this structure might be phylogenetically informative. However, its potential for phylogenetic reconstruction among extinct catarrhines remains largely unexplored. Here we quantify the orientation, proportions, and course of the carotid canal in *Pliobates*, extant anthropoids and other Miocene catarrhines (*Epipliopithecus*, *Victoriapithecus*, and *Ekembo*) using three-dimensional morphometric techniques. We also compute phylogenetic signal and reconstruct the ancestral carotid canal course for main anthropoid clades. Our results reveal that carotid canal morphology embeds strong phylogenetic signal but mostly discriminates between platyrrhines and catarrhines, with an extensive overlap among extant catarrhine families. The analyzed extinct taxa display a quite similar carotid canal morphology more closely resembling that of extant catarrhines. Nevertheless, our results for *Pliobates* highlight some differences compared with the pliopithecid *Epipliopithecus*, which displays a somewhat more platyrrhine-like morphology. In contrast, *Pliobates* appears as derived toward the modern catarrhine condition as the stem cercopithecid *Victoriapithecus* and the stem hominoid *Ekembo*, which more closely resemble one another. Moreover, *Pliobates* appears somewhat derived toward the reconstructed ancestral hominoid morphotype, being more similar than other Miocene catarrhines to the condition of great apes and the hylobatid *Symphalangus*. Overall, our results rule out previously noted similarities in carotid canal morphology between *Pliobates* and hylobatids, but do not show particular similarities with pliopithecoids either—as opposed to extant and other extinct catarrhines. Additional analyses will be required to clarify the phylogenetic relationships of *Pliobates*, particularly given its dental similarities with dendropithecids.

© 2021 Elsevier Ltd. All rights reserved.

* Corresponding authors.
E-mail addresses: florian.bouchet@icp.cat (F. Bouchet), david.alba@icp.cat (D.M. Alba).

https://doi.org/10.1016/j.jhevol.2021.103073
0047-2484/© 2021 Elsevier Ltd. All rights reserved.

1. Introduction

1.1. Pliobates and catarrhine evolution

Crown catarrhines include two main extant clades distinguished at the superfamily rank: Old World monkeys (Cercopithecoidea) and apes and humans (Hominoidea). Earliest stem catarrhines have been reported from the latest Eocene (34.5–29.5 Ma) of Afro-Arabia (Seiffert, 2006, 2012; Seiffert et al., 2010). In turn, earliest crown catarrhines (both cercopithecoids and hominoids) date back to the late Oligocene (~25 Ma) of East Africa (Stevens et al., 2013)—in accordance with molecular estimates indicating that the cercopithecoid-hominoid divergence occurred during the Oligocene (Chatterjee et al., 2009; Perelman et al., 2011; Springer et al., 2012; Finstermeier et al., 2013; Pozzi et al., 2014). Catarrhines did not disperse into Eurasia until later in the early Miocene, after the closure of the Tethys Seaway and the establishment of intermittent land bridges at ~19 Ma (Harzhauser et al., 2007; Harrison, 2013). Several catarrhine lineages eventually dispersed from Afro-Arabia into Eurasia (Roos et al., 2019; Gilbert et al., 2020a), including pliopithecoids (considered an Eurasian clade of stem catarrhines, first recorded ~18–17 Ma; Harrison and Gu, 1999; Begun, 2002, 2017; Harrison, 2013); hylobatids (first recorded ~13.8–12.5 Ma; Gilbert et al., 2020b); large-bodied hominoids (presumably hominids, first recorded ~16.5–14 Ma; Casanovas-Vilar et al., 2011; Harrison, 2017); and various lineages of cercopithecoid primates, successively recorded at different times in Eurasia, namely colobines (~8.5 Ma; Alba et al., 2015a), cercopithecins (~8–6.5 Ma; Gilbert et al., 2014), macaques (~5.9–5.3 Ma; Alba et al., 2014a), and geladas (1.6–1.2 Ma; Alba et al., 2014b).

A panoply of small-bodied, putative stem catarrhine genera (including, but not restricted to, dendropithecids) are recorded in the early to middle Miocene of Africa (Harrison, 2010, 2013). Some Miocene Eurasian taxa have previously been linked to some of these African stem catarrhines—implying yet another catarrhine dispersal event from Africa—but such claims have been mostly rejected by reinterpreting them as pliopithecoids or hylobatids (Harrison, 2016 and references therein). The most likely exception is some isolated dental remains from Pakistan (~17–16 Ma; Barry et al., 1987; Bernor et al., 1988), which are most similar to African dendropithecids (Harrison, 2016) but might ultimately prove to be stem pliopithecoids (Sankhyan et al., 2017). In turn, as remarked by Roos et al. (2019), the small-bodied catarrhine *Pliobates* (middle/late Miocene of Spain, 11.6 Ma; Alba et al., 2015b) might denote an additional out-of-Africa dispersal event of catarrhines unless it is interpreted as a pliopithecoid. This taxon was originally recovered by Alba et al.'s (2015b) cladistic analysis as a stem hominoid morphologically more derived than *Proconsul* s.l. (currently split into *Proconsul* s.s. and *Ekembo*; McNulty et al., 2015) and subsequently reinterpreted as a pliopithecoid by different cladistic analyses (Nengo et al., 2017; Gilbert et al., 2020b), as first suggested by Benefit and McCrossin (2015). However, given the mosaic nature of its cranial and postcranial skeleton—combining plesiomorphic, stem catarrhine-like features (including dental resemblances with dendropithecids) with crown hominoid synapomorphies (Alba et al., 2015b)—the possibility remains that *Pliobates* is a late descendant of an African stem catarrhine lineage.

Deciphering the phylogenetic position of *Pliobates* would have important implications for our current understanding of catarrhine evolution and paleobiogeography during the Miocene. If ultimately shown to be a pliopithecoid or a member of a different stem catarrhine lineage, it would imply remarkable cranial and postcranial convergences with crown hominoids; in turn, if interpreted as a non-pliopithecoid stem catarrhine or as a stem hominoid, it would indicate that pliopithecoids were not the only small catarrhines to disperse from Africa into Europe. Unfortunately, determining the evolutionary history and phylogenetic relationships of small-bodied catarrhines is still hindered by the fragmentary nature of their fossil remains and the incompleteness of their fossil record—with long ghost lineages for both pliopithecoids and hylobatids. Deciphering the phylogenetic position of extinct taxa ultimately requires performing cladistic analyses with all available evidence from multiple anatomical regions. However, as mentioned earlier, previous attempts in this regard have yielded contradictory results for *Pliobates* (compare Alba et al., 2015b with Nengo et al., 2017 and Gilbert et al., 2020b). Therefore, additional research on the various characters included in these analyses is required to refine their definition and scoring for both extant and extinct taxa. With this aim in mind, here we focus on one of the most intriguing features included in the original diagnosis of *Pliobates*: the orientation of the carotid canal, which was originally described as more closely resembling hylobatids than either pliopithecoids or other hominoids (Alba et al., 2015b). Given the potential implications of such similarities—if interpreted as a hylobatid synapomorphy or hominoid symplesiomorphy—we decided to analyze them quantitatively by means of a novel morphometric approach devised to measure the size and shape of the carotid canal. To the best of our knowledge, this is the first study to quantitatively assess the orientation, proportions, and course of this anatomical structure in extant and extinct anthropoids.

1.2. The carotid canal in primate phylogenetics

All haplorhines and non-cheirogaleid lemuriforms have an internal carotid artery enclosed by a bony canal (termed 'carotid canal') that derives from the anterior lamina of the petrosal plate (Bugge, 1974, 1980; Cartmill et al., 1981; MacPhee and Cartmill, 1986; Kay et al., 2008; Boyer et al., 2016). The carotid canal runs from the posterolaterally located external carotid foramen to the endocranial space (Bugge, 1980; MacPhee and Cartmill, 1986; Kay et al., 2008; Boyer et al., 2016). In haplorhines, the carotid canal displays a 'perbullar pathway': it is located in the primary medial wall of the auditory bulla and runs through the middle ear cavity, passing through the transverse septum that separates the tympanic cavity from the anterior accessory cavity (Cartmill et al., 1981; MacPhee and Cartmill 1986; Kay et al., 2008). The canal then opens more anteromedially into the endocranial surface, with an opening located either on the basisphenoid or between the basisphenoid and petrosal (Boyer et al., 2016). In adult anthropoids, one of the two branches of the internal carotid artery (the stapedial artery) is missing and only the promontory artery remains patent (Bugge 1974, 1980; Rosenberger and Szalay, 1980; MacPhee and Cartmill, 1986; Kay et al., 2008; Boyer et al., 2016). Therefore, the carotid canal of anthropoid primates corresponds to a unique and well-developed bony enclosure.

Low homoplasy is one of the most important criteria for choosing phylogenetically informative morphological characters (Lieberman, 1999). Among characters least affected by homoplasy (convergence, parallelism, reversal, and homoiology), soft-tissue traits have previously been proven more efficient in producing accurate primate phylogenies than hard-tissue traits (Gibbs et al., 2000, 2002; Diogo and Wood, 2011). Given that vessel- and nerve-related characters are soft-tissue traits, this rationale might potentially apply to the carotid canal as well. A few previous studies have included carotid canal features in character-taxon matrices devised for cladistic analysis, focusing on the position of the carotid foramen in the bulla as well as on the overall direction and orientation of the canal itself (Beard and MacPhee, 1994; Ross, 1994; Shoshani et al., 1996; Ross et al., 1998; Kay et al., 2008; Alba et al., 2015b). These studies aimed at resolving phylogenetic

relationships among higher-rank primate clades (Beard and MacPhee, 1994; Ross, 1994; Shoshani et al., 1996; Ross et al., 1998; Kay et al., 2008) and/or deciphering the phylogenetic relationships of particular fossil taxa (Ross et al., 1998; Kay et al., 2008; Alba et al., 2015b). Nonetheless, some of them found differences between platyrrhines and catarrhines, as well as among some catarrhine groups. Based on these studies, the morphology of the carotid canal seems promising for phylogenetic reconstruction in catarrhine primates. However, the exact phylogenetic potential of this structure for distinguishing among catarrhine subclades and, hence, clarifying the relationships of extinct taxa remains unexplored.

In the light of all the aforementioned considerations, the aim of this study is threefold: (1) to investigate the orientation, proportions, and course of the carotid canal in a wide sample of extant anthropoid primates, to test its potential for phylogenetic inference in extinct catarrhines; (2) to re-evaluate previously noted differences and similarities among several catarrhine clades; and (3) to describe the carotid canal morphology of *Pliobates* and compare it with that of extant and fossil catarrhines, so as to gain additional insights into the controversial phylogenetic relationships of this genus. To do so, we collected μCT scans of both fossil taxa and an extant comparative sample and developed a newly devised semi-automatic iterative protocol to obtain comparable three-dimensional (3D) carotid canal surfaces (i.e., 3D models). These are analyzed by means of traditional morphometrics and three-dimensional geometric morphometric (3DGM) and imaging techniques, to quantify the orientation, proportions, and course of the carotid canal within the petrosal in a standardized manner.

2. Materials and methods

2.1. Materials

Studied sample This study focuses on the cranium of the holotype (IPS58443) of *Pliobates cataloniae*, which consists of a partial skeleton (Alba et al., 2015b). The carotid canal is entirely preserved in the right temporal fragment (IPS58443.1; Alba et al., 2015b: Fig. 1A). In contrast, in the left temporal fragment (same specimen), the inferiormost part of the canal is broken, with most of its lateral and anterior walls missing along a length of >1.5 mm. IPS58443.1 was originally scanned at a resolution of 95 μm (Alba et al., 2015b). To explore fine bony structures, the specimen was scanned again by X-ray microtomography at the Centro Nacional de Investigación sobre la Evolución Humana (Burgos, Spain) using a Phoenix V|Tome|X s240 μCT scanner with the following parameters: 0.35 mA current, 170 kV voltage, 0.2 mm Cu filter, and a magnification of 9.52. The final reconstructed volume has an isometric voxel size of 21 μm.

Fossil comparative sample Three Miocene catarrhines are included in the comparative sample: the Miocene pliopithecoid *Epipliopithecus vindobonensis* (see Zapfe, 1961), the stem cercopithecoid (victoriapithecid) *Victoriapithecus macinnesi* (see review in Benefit and McCrossin, 1997), and the stem hominoid (proconsulid) *Ekembo heseloni* (see review in McNulty et al., 2015). There are four available fragmentary temporal bones of *Epipliopithecus* (Zapfe, 1961): NMB OE 303 (right and left temporals, individual II), NHMW 1970/1397/0002 (right temporal, individual III; holotype), and NHMW 1970/1397/0003 (left temporal, individual III; holotype). The carotid canal is only sufficiently preserved in the latter specimen, which includes a portion of the bulla, the external acoustic meatus, and most of the petrosal (Zapfe, 1961: Fig. 28). In contrast, the anterior end of the canal is missing from the remaining specimens. The petrosal of the holotype was scanned at the Vienna μCT lab (Vμ-CTL) using a Viscom X8060 μCT scanner with the following parameters: 0.24 mA current, 120 kV voltage, 0.5 mm Cu filter, and a magnification of 7.50. The final reconstructed volume has an isometric voxel size of 22 μm. *Ekembo heseloni* is represented by the right temporal specimen KNM-RU 2036al (Davis and Napier, 1963: Fig. 1; Alba et al., 2015b: Fig. 4C), which is part of the holotype (Walker et al., 1993), while *V. macinnesi* is represented by the left temporal of the cranium KNM-MB 29100 (Benefit and McCrossin, 1997: Fig. 1; Benefit, 1999: Fig. 3; Jablonski and Frost, 2010: Fig. 23.1). The μCT scans of KNM-RU 2036al and KNM-MB 29100 have isometric voxel sizes of 64 μm and 44 μm, respectively. They were both kindly made available for this study by the Department of Earth Sciences, National Museums of Kenya (which holds the copyright) and the Department of Human Evolution, Max Plank Institute for Evolutionary Anthropology, Leipzig, Germany.

Extant comparative sample Our extant comparative sample consists of μCT scans of 127 crania belonging to 41 anthropoid species (13 platyrrhines and 28 catarrhines) from 36 genera, representing all extant hominoid genera as well as all cercopithecoid subtribes and platyrrhine (sub)families (Table 1; Supplementary Online Material [SOM] Table S1). A minimum of three individuals per genus are included. Ontogenetic changes in basicranial angulation and elongation—somewhat related to each other and potentially affecting petrosal morphology—continue up to adulthood as measured by M^3 eruption (Lieberman and McCarthy, 1999; Lieberman et al., 2000). Therefore, all individuals included in the comparative sample are fully adult (exhibiting the M^3 in occlusion or the M^2 in callitrichines). Most of the μCT scans included in our extant comparative sample were downloaded from MorphoSource (https://www.morphosource.org; Table 1; SOM Table S1). Three μCT scans of specimens from the American Museum of Natural History were kindly provided by Sergio Almécija, while seven additional μCT scans of specimens housed in the Institut Català de Paleontologia Miquel Crusafont (Sabadell, Spain) were scanned at the Centro Nacional de Investigación sobre la Evolución Humana. The μCT resolution for the specimens included in the extant comparative sample ranges from 27 to 131 μm (Table 1; SOM Table S1).

2.2. Morphometric methods

Segmentation For each specimen, the carotid canal was virtually extracted through semiautomatic threshold-based segmentation in Avizo v. 7.0 (Visualization Sciences Group, Mérignac). The right carotid canal was segmented for most specimens; when this was not possible, the left canal was segmented and mirrored. Both extremities of the resulting 3D canal surfaces (i.e., 3D models) were cut along homologous planes to allow their comparison among different individuals. First, to cut the posterior end of the canal, we used a best-fit plane based on landmarks placed on its external aperture (Fig. 1a, l; SOM Fig. S1a, b). Then, the anterior limit of the carotid canal was identified by determining a landmark on the anterior part of the petrosal (the 'intersection ridge-groove' [IRG]; Fig. 1b–l; SOM Fig. S1c, d; see SOM S1) and cut through such a homologous point using a script coded in R v. 4.0.2 (R Core Team, 2020; see SOM File S1).

Alignment and canal orientation The orientation of the carotid canal within the petrosal was quantified by means of two two-dimensional (2D) angles representing the canal superior orientation along the (para)sagittal plane (2DYZA) and its medial orientation along a transverse plane (2DXYA)—which can be related to canal 'orientation' and 'direction' sensu Alba et al. (2015b: Tables S5 and S6), respectively. Each was computed as the angle between the vector connecting the canal endpoints

Table 1
Extant comparative sample used in this study based on μCT scans. Sample size and sex composition, institutional repository for the specimens, digital repository source, and voxel size range are indicated for each species. See SOM Table S1 for further details on the specimens included.

Taxon	Species	*n*	M	F	?	Repository	Source	Voxel size (μm)
Platyrrhini	*Alouatta palliata*	5	2	3	0	DUEA	MS	52–67
Platyrrhini	*Aotus griseimembra*	5	2	3	0	USNM	MS	34–38
Platyrrhini	*Ateles geoffroyi*	3	0	3	0	AMNH, MCZ	MS	62–63
Platyrrhini	*Cebus imitator*	3	0	3	0	MCZ	MS	80
Platyrrhini	*Chiropotes chiropotes*	3	1	2	0	USNM	MS	47–49
Platyrrhini	*Lagothrix lagotricha*	3	1	2	0	USNM	MS	58–60
Platyrrhini	*Mico argentatus*	3	2	1	0	MCZ	MS	40
Platyrrhini	*Pithecia monachus*	1	0	0	1	MCZ	MS	50
Platyrrhini	*Pithecia pithecia*	2	1	1	0	MCZ	MS	50
Platyrrhini	*Plecturocebus cupreus*	5	3	2	0	AMNH, MCZ	MS	47–51
Platyrrhini	*Saguinus fuscicollis*	1	0	1	0	AMNH	MS	27
Platyrrhini	*Saguinus midas*	2	2	0	0	MCZ	MS	40
Platyrrhini	*Saimiri sciureus*	3	1	1	1	MCZ	MS	47
Cercopithecidae	*Cercocebus torquatus*	2	2	0	0	AMNH	MS	90–120
Cercopithecidae	*Cercocebus galeritus*	1	1	0	0	AMNH, MCZ	MS	70
Cercopithecidae	*Cercopithecus mitis*	3	0	3	0	MCZ	MS	80
Cercopithecidae	*Chlorocebus pygerythrus*	3	1	2	0	SIU	MS	46–54
Cercopithecidae	*Colobus guereza*	3	1	2	0	AMNH	MS	66–73
Cercopithecidae	*Erythrocebus patas*	3	2	1	0	MCZ	MS	80
Cercopithecidae	*Lophocebus albigena*	3	1	2	0	MCZ	MS	90
Cercopithecidae	*Macaca fascicularis*	5	2	3	0	MCZ	MS	60–91
Cercopithecidae	*Mandrillus sphinx*	3	2	1	0	AMNH, MCZ	MS	75–126
Cercopithecidae	*Miopithecus talapoin*	3	3	0	0	MCZ	MS	50
Cercopithecidae	*Nasalis larvatus*	3	0	3	0	MCZ	MS	71
Cercopithecidae	*Papio anubis*	3	3	0	0	MCZ	MS	108–118
Cercopithecidae	*Piliocolobus badius*	3	2	1	0	MCZ	MS	80–90
Cercopithecidae	*Presbytis rubicunda*	3	1	2	0	MCZ	MS	80
Cercopithecidae	*Procolobus verus*	2	1	1	0	AMNH	MS	76–80
Cercopithecidae	*Semnopithecus entellus*	3	2	1	0	AMNH	MS	52–108
Cercopithecidae	*Simias concolor*	2	1	1	0	AMNH	MS	56
Cercopithecidae	*Theropithecus gelada*	3	2	1	0	AMNH	MS	84–120
Cercopithecidae	*Trachypithecus cristatus*	3	0	3	0	MCZ	MS	50
Hominidae	*Gorilla gorilla*	6	1	5	0	AMNH, MCZ	MS	106–131
Hominidae	*Pan paniscus*	5	1	3	1	AMNH, ICP, MCZ	MS, own data	66–116
Hominidae	*Pan troglodytes*	6	3	3	0	AMNH, ICP, MCZ	MS, own data	77–111
Hominidae	*Pongo* sp.	6	0	6	0	ICP, MCZ	MS, own data	77–125
Hylobatidae	*Hoolock hoolock*	3	1	2	0	AMNH	MS	52–84
Hylobatidae	*Hylobates agilis*	1	0	0	1	ICP	MS, own data	52
Hylobatidae	*Hylobates lar*	4	0	4	0	MCZ	MS	67
Hylobatidae	*Nomascus leucogenys*	1	1	0	0	AMNH	MS	105
Hylobatidae	*Symphalangus syndactylus*	2	0	2	0	AMNH	MS	62–79

Abbreviations: M = male; F = female; ? = unknown sex; AMNH = American Museum of Natural History, New York, USA; DUEA = Duke University, Evolutionary Anthropology, Durham, USA; ICP = acronym of the collections of the Institut Català de Paleontologia Miquel Crusafont, Sabadell, Spain; MCZ = Museum of Comparative Zoology, Harvard University, Cambridge, USA; MS = MorphoSource (https://www.morphosource.org); SIU = Southern Illinois University, Carbondale, USA; USNM = Smithsonian National Museum of Natural History, Washington, D.C., USA.

(from posterior to anterior) and a standard reference vector. Both the canal vector and the reference vector were computed after performing a Procrustes alignment based on petrosal/tympanic landmarks (Fig. 2; Table 2) and applying the translation-scaling-rotation parameters resulting from this alignment to the two canal endpoints (SOM S1). This procedure allowed us to retain the information on the position, orientation, and shape variation of the canal inside the petrosal. For both angles, the standard reference vector corresponds to a 2D vector parallel to the anteroposterior cranial axis (from posterior to anterior), in lateral view for 2DYZA and in superior view for 2DXYA (Fig. 3). Aligning the carotid canal on the basis of petrosal/tympanic landmarks instead of the cranium as a whole enables the analysis of fragmentary fossils and has several advantages (see SOM S1 for further details), while being consistent with previous studies (Beard and MacPhee, 1994; Ross, 1994; Shoshani et al., 1996; Ross et al., 1998; Kay et al., 2008; Alba et al., 2015b) that assessed carotid foramen locations relative to the bulla instead of general cranial axes or planes.

Volume and length The volume (V, in mm^3) of the 3D canal surfaces was computed using the module 'Surface Area Volume' in Avizo. To calculate canal length (L, in mm), we used equidistant slices between the two canal endpoints (which correspond to type III landmarks; Bookstein, 1991). These slices were used to generate 8 additional equidistant semilandmarks that follow the canal streamline using the 'digit.curve' function of 'Geomorph' v. 3.3.1 (Adams et al., 2019), summing a total of 10 canal landmarks, which define the canal streamline. This canal landmark configuration thus corresponds to a total of 10 canal streampoints. Canal length was taken as the sum of the length of the resulting nine canal segments (see SOM S1 for further details).

Robusticity index Carotid canal proportions were measured by a dimensionless index of canal robusticity as $L/V^{1/3}$. Even though the carotid canal is a hollow structure, we refer to this index as 'robusticity' because it measures how thick the canal is on average relative to its length. Low values of the index denote robust canals, whereas high values denote slender canals. The same terms have been applied to other hollow cranial structures, such as the semicircular canals of the bony labyrinth (Urciuoli et al., 2020, 2021a, 2021b). The diameter (and hence the cross-sectional area) of the carotid canal varies along its length, so that using the cube root of the volume as the denominator is equivalent to relying on the

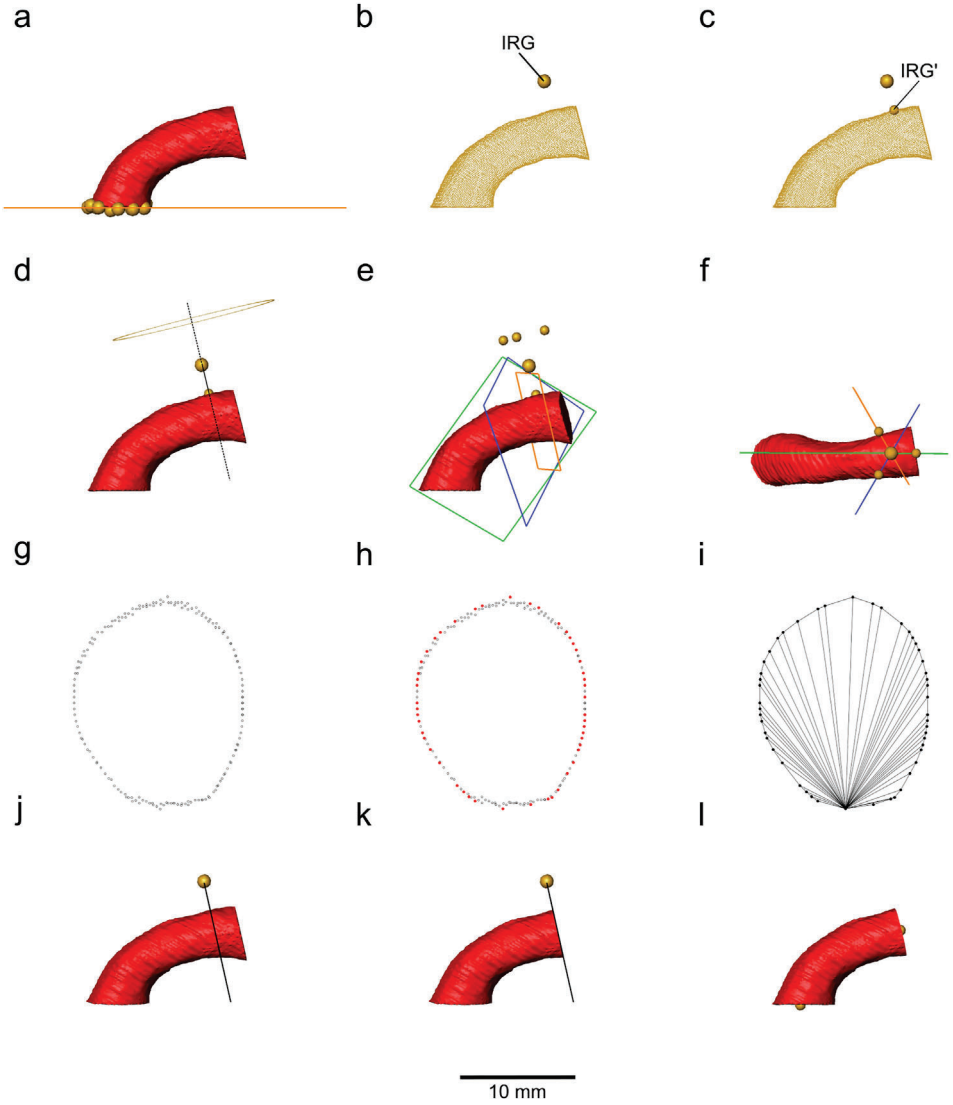


Figure 1. Schematic illustration of the protocol used in this study for cutting the extremities of the carotid canal as exemplified in a *Macaca fascicularis* individual. a) To cut the posterior end, a best-fit plane defined by the landmarks placed at the carotid foramen is computed. b) To cut the anterior end, the 3D canal surface is first imported as a cloud of points in R. c) The projection of IRG on the cloud of points (IRG') is computed. d) 360 points are created around the axis IRG–IRG'. e, f) 360 possible cutting planes passing through IRG are created (each being based on IRG, IRG' and one of the points rotating around the axis), here depicted in anterior (e) and superior (f) views. The cross-sectional area obtained by cutting the canal using each possible plane is calculated as follows: g–i) the points of the cloud belonging to the plane are recorded (g), the most external points (in red) are kept to create a convex hull that approximates the shape of the canal contour (h), and a set of triangles is drawn, each of them having the same point of the contour as the most acute vertex, and the two subsequent points on the contour as the other vertices (i); the total area is the obtained by summing those of each individual triangle. j, k) The plane with the smallest cross-sectional area (that is, orthogonal to the 3D canal surface and therefore to the canal streamline) (j) is used as a reference for cutting the canal at its anterior end (k). l) The centroids of the (posterior) carotid foramen landmark set and of the anterior cross-section (i.e., obtained by cutting with the orthogonal plane), representing the posterior and anterior endpoints of the carotid canal, respectively, are calculated. Abbreviations: IRG = intersection ridge-groove; IRG' = orthogonal projection on the 3D carotid canal surface of IRG. (For interpretation of the references to color in this figure legend, the reader is referred to the Web version of this article.)

hypothetical average cross-sectional area. We used the cube root of the volume to make the index dimensionless (i.e., a shape variable) and verified that the robusticity index was free from allometric (size-scaling) effects by computing a phylogenetic generalized least-squares (PGLS) regression of ln L against ln $V^{1/3}$ on the species means of the whole sample. We further computed a major axis regression of the same parameters, using the function 'lmodel2' of the R package 'lmodel2' v. 1.7–3 (Legendre, 2018). The objective was to test whether length and volume of the carotid canal covary in a linear (i.e., isometric) or nonlinear (i.e., allometric) fashion and to do so under the assumptions that the independent variable is measured with error (major axis) or without error (PGLS). Note that, under geometric similarity, linear dimensions and volumes are expected to be correlated with an allometric slope of 1/3 (Gould, 1966). However, this does not apply here because we used the cube root of the canal volume, so that allometry would imply an allometric slope significantly different from 1.

Canal course configuration To assess carotid canal course within the petrosal, we applied the translation-scaling-rotation parameters resulting from the alignment of the petrosal/tympanic landmarks described earlier to the 10 canal landmark configuration. As for canal orientation, we were able to retain the position, orientation, and shape variation of the canal inside the petrosal. Therefore, the postalignment 10 canal landmark configuration represents the course of the carotid canal within

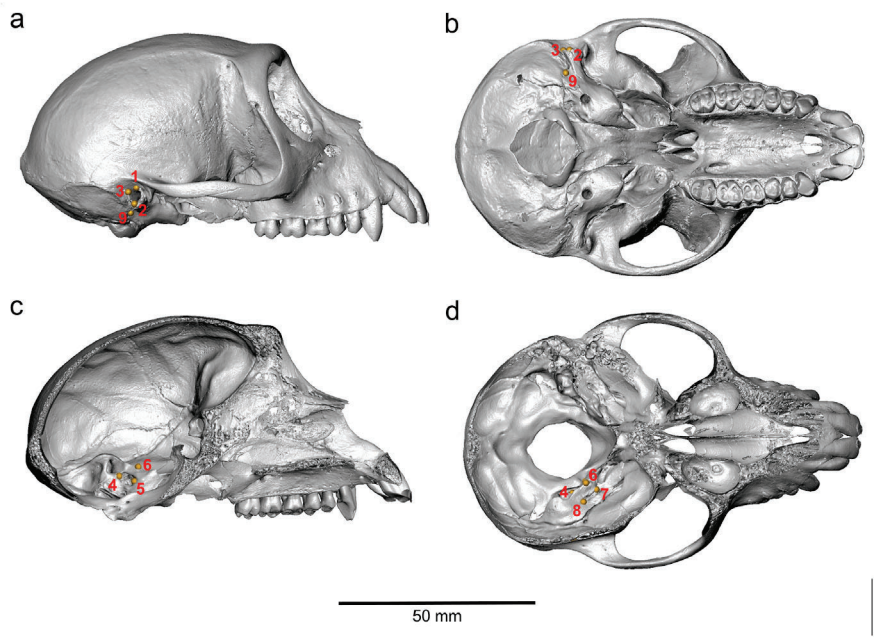


Figure 2. Petrosal landmarks used for aligning the specimens as exemplified in a *Macaca fascicularis* individual in different views: a) right lateral; b) inferior; c) sagittal cross section (right-mirrored for visualization purpose); d) superior transverse cross section. Landmarks: 1 = porion; 2 = inferior external auditory meatus; 3 = posterior external auditory meatus; 4 = posterior internal auditory meatus; 5 = anterior internal auditory meatus; 6 = medial anterior pyramidal ridge; 7 = intersection ridge-groove; 8 = greater superficial petrosal nerve hiatus; 9 = stylomastoid foramen.

Table 2
Definition of the petrosal/tympanic landmarks used in this article for aligning the specimens.

No.	Landmark	Definition
1	Porion	Most superior point on the margin of the external auditory meatus
2	Inferior external auditory meatus	Most inferior point on the margin of the external auditory meatus
3	Posterior external auditory meatus	Most posterior point on the margin of the external auditory meatus
4	Posterior internal auditory meatus	Most posterior point on the margin of the internal auditory meatus
5	Anterior internal auditory meatus	Most anterior point on the margin of the internal auditory meatus
6	Medial anterior pyramidal ridge	Most medial point where anterior pyramidal ridge starts running laterally above the fossa for the semilunar ganglion
7	Intersection ridge-groove	Point of intersection between the laterally running anterior pyramidal ridge and the groove of the greater petrosal nerve
8	Greater petrosal nerve hiatus	Most superior, anterior point on the margin of the hiatus for the greater petrosal nerve
9	Stylomastoid foramen	Center of the stylomastoid foramen

the petrosal (SOM S1) and will be thereafter referred to as 'carotid canal course configuration.'

Size scaling To better understand the influence of size-scaling (allometric) effects on carotid canal shape, we computed multiple bivariate regressions using PGLS. On the one hand, we relied on allometric regressions of canal measurements (as measured by L and $V^{1/3}$) against overall canal size (as measured by centroid size [CS]; see Section 2.3) and body size (as measured by body mass [BM]); the allometric regression between CS and BM was also computed. On the other hand, we computed regressions between carotid canal shape—including not only the aforementioned index of canal robusticity but also the multivariate shape variables derived by means of between-group principal component analysis (bgPCA; see Section 2.3)—against log-transformed carotid canal size (as measured by $V^{1/3}$ and CS) and BM. To minimize the effects of body size dimorphism, for each taxon we relied exclusively on average female BM taken from the literature (Smith and Jungers, 1997; Delson et al., 2000; Turner et al., 2018). Natural logarithms (ln) were used in all instances. For allometric regressions between metrical linear variables, the null hypothesis of isometry was rejected when unity was excluded from the 95% confidence interval (CI) of the allometric slope. In contrast, for bivariate regressions of shape vs. size, isometry was rejected when the regression was significant (i.e., when the slope was significantly different from zero).

2.3. Between-group principal component analyses

Carotid canal course variation among clades was examined using a bgPCA of the carotid canal course configurations using the 'groupPCA' function of the R package 'Morpho' v. 2.8 (Schlager, 2017). We used the following four main crown anthropoid clades as a grouping factor: platyrrhines, cercopithecids, hylobatids, and hominids, with fossils projected onto the morphospace a posteriori. The bgPCA was repeated based on a catarrhine-only subsample to see if it provided a better discrimination among extant catarrhine families once the variance introduced by platyrrhines was removed.

As explained in the preceding section, allometric effects on canal course configuration were assessed by means of PGLS regressions of between-group principal component (bgPCs) against log-transformed canal size (ln CS and ln $V^{1/3}$) or log-transformed body size (ln BM)—see Section 2.2 for further details.

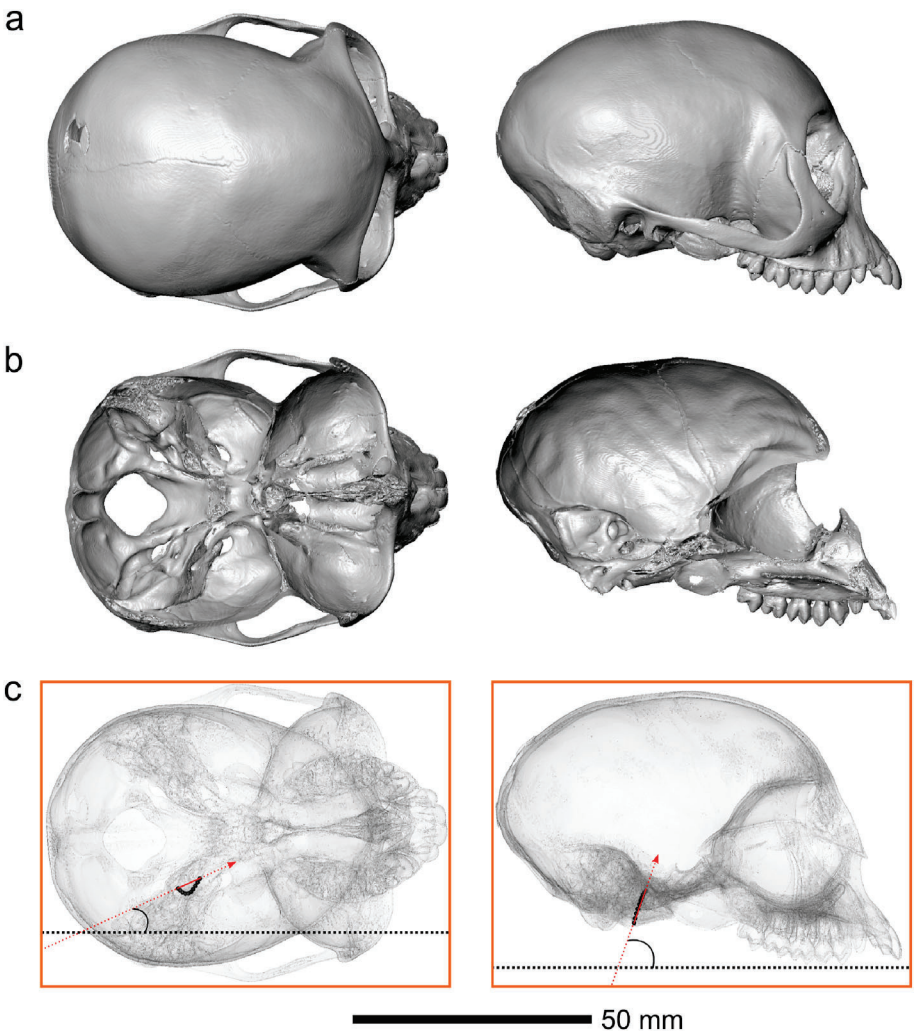


Figure 3. Graphic representation of the 2D angles defining the carotid canal orientation relative to the cranium. a) Virtual external reconstructions of the cranium, in superior (left) and lateral (right) views. b) Virtual cross sections of the cranium to visualize the petrosal bone, in transverse (left) and sagittal (right) views. c) Representations of the carotid canal medial orientation (2DXYA; left) and superior orientation (2DYZA; right) within the cranium, rendered in semitransparency; red lines represent the 2D canal vector and its direction, orange squares represent the plane along which the angle can vary, and dotted black lines represent the standard reference vector. For 2DXYA, the plane of angle variation is a transverse plane, whereas for 2DYZA, the plane of angle variation is a (para)sagittal plane. For both angles, the standard reference vector is a 2D vector parallel to the anteroposterior cranial axis (from posterior to anterior). Both angles are calculated between the 2D canal vector and the 2D standard reference vector. Because the anthropoid mean configuration is extremely similar to the canal course configuration of *Presbytis* (i.e., before alignment), the cranium of this taxon is used as a reference for orienting the canal following the cranial axes of reference. (For interpretation of the references to color in this figure legend, the reader is referred to the Web version of this article.)

We verified that the bgPCA grouping structure was not spurious by comparing our bgPCA results with those of a cross-validated bgPCA (Cardini et al., 2019). This procedure iteratively resamples the data set by excluding one individual at a time and using the remaining (n−1) individuals to compute the model that is then used to classify the omitted individual. A cross-validated bgPCA significantly reduces the distortion of mean group differences, so that its comparison with the non-cross-validated bgPCA allows one to ascertain whether (or to what extent) the latter is affected by spurious grouping effects. As further recommended by Cardini and Polly (2020), we also relied on a permutational analysis of variance (PERMANOVA) to (1) explore the significance (p) of group mean differences and (2) compute the variance (R^2) explained by them. The permutations consist in randomly resampling n times the data set (thus modifying group composition, as the individuals are permuted), each time recomputing the distance between the centroids of all pairs of newly formed groups. Based on this set of permutations, here consisting of between-group Euclidean distances, both p and R^2 were computed within the full space of canal course configurations as well as within the bgPCA spaces (both standard and cross-validated bgPCs). As in the case of the cross-validated bgPCA scatterplot, comparing the p and R^2 values of the bgPCA (before and after cross-validation) with those of the raw canal course configuration coordinates permits verifying if the former inflates the differences among groups. These computations were done using the 'lm.rrpp' function of the R package 'RRPP' v. 0.6.1 (Collyer and Adams, 2018).

The discrimination among a priori defined groups was evaluated on the basis of correctly classified individuals after cross-validation. Posterior probabilities of group membership were computed for fossil specimens based on the squared Mahalanobis distances between their bgPC scores (bgPC1 and bgPC2) and those of extant group centroids using the 'typprobClass' function of 'Morpho.'

Finally, a neighbor-joining (NJ) cluster was computed using a matrix of Euclidean distances based on the raw coordinates of the canal course configurations with the 'nj' function of the R package 'phangorn' v. 2.5.5 (Schliep, 2011).

2.4. Statistical analyses

Box-and-whisker plots were used to assess the variation in carotid canal orientation (2DYZA and 2DXYA), proportions (index $L/V^{1/3}$), and course (bgPC1 and bgPC2). To test for significant differences among extant groups, we used Kruskal–Wallis nonparametric tests and Bonferroni-corrected Mann–Whitney post hoc pairwise comparisons performed in R. When significant differences were found, *Pliobates* and other extinct genera were compared with the distributions of extant groups using z-scores—computed as z = (individual value−group mean)/SD—to assess if the fossil specimens fall within the variation of the latter ($|z| \leq 1.96$).

2.5. Phylogenetically informed methods

Phylogenetic tree To compute PGLS regressions and the phylomorphospaces, as well as to quantify phylogenetic signal, we used a time-calibrated phylogenetic tree among the investigated taxa. The tree for the extant taxa was primarily derived from the 10kTrees v.3 website (Arnold et al., 2010), although some species that were not included there were added a posteriori following Meyer et al. (2011) and Springer et al. (2012)—see SOM S1 for further details. Two different hypotheses for the extinct genera were considered, except for *Victoriapithecus*, which was invariably considered a stem cercopithecoid. Under hypothesis 1 (SOM Fig. S2a), *Epipliopithecus, Ekembo*, and *Pliobates* were considered successive stem hominoids, following the results of the cladistic analysis of Alba et al. (2015b). In contrast, under hypothesis 2 (SOM Fig. S2b), only *Ekembo* was considered a stem hominoid, while both *Pliobates* and *Epipliopithecus* were considered stem catarrhines (pliopithecoids), following the results of other cladistic analyses (Nengo et al., 2017; Gilbert et al., 2020b). The tip and divergence dates for the extinct taxa are detailed in SOM S1.
Phylogenetic signal To assess the phylogenetic signal embedded in carotid canal course, we computed Pagel's λ (Pagel, 1999) and Blomberg's K (Blomberg et al., 2003) statistics using the R package 'phytools' v. 0.7–70 (Revell, 2012). These metrics compare the variance in the phylogenetic tree tips relative to that expected under a Brownian motion evolutionary model. Pagel's λ measures the covariance among related species and ranges from 0 (no phylogenetic signal) to 1 (high phylogenetic signal). In turn, Blomberg's K reflects to what extent the phylogenetic tree matches the variance in the data (and where variance is concentrated): $K \approx 1$ means that trait evolution approximates the expectations under a Brownian motion model; $K \ll 1$ means that closely related taxa resemble each other less than expected under a Brownian motion model (such that variance is mostly found within clades); finally, $K \gg 1$ means that closely related units resemble each other more than expected under a Brownian motion model (such that variance is mostly found among clades).
Phylomorphospace and reconstruction of ancestral morphotypes To quantify and visualize patterns of carotid canal course variation along the branches of the phylogeny, we produced a phylomorphospace by projecting the phylogenetic tree onto the two first bgPCs (Sidlauskas, 2008). In a phylomorphospace, the taxon centroids are connected to one another in the morphospace following the phylogenetic relationships given by the chosen phylogeny. In the case of fossil taxa, because there are competitive hypotheses regarding their phylogenetic relationships, various time-calibrated cladograms were devised a priori—resulting in a different phylomorphospace for each phylogenetic hypothesis. Scores of the internal nodes—last common ancestors (LCAs)—were estimated based on a maximum likelihood method for continuous characters using the 'fastAnc' function of 'phytools.' To explore the extent to which extant and extinct taxa differ from the various LCAs, we rotated and translated the bgPC scores estimated for the LCAs back into the Kendall's shape space (i.e., configuration space) to obtain their landmark coordinates and thus visualize the estimated ancestral carotid canal course conformations.

3. Results

The 3D carotid canal surface of *Pliobates* (SOM File S2) is compared with those of *Ekembo*, *Epipliopithecus*, and *Victoriapithecus*, as well as selected taxa from the extant comparative sample in Figure 4. Individual data for the variables describing the orientation, proportions, and course of the carotid canal in the extant comparative sample are reported in SOM Table S2.

3.1. Carotid canal orientation

For 2DYZA, the angle values range from ca. 30° to 90° (Fig. 5a; Tables 3 and 4). On this basis, and taking into account the mean extant clade differences (SOM Tables S3 and S4), we defined three different states (potentially usable in future cladistic analyses): oblique (<55°); subvertical (55–65°); and vertical (>65°). Hominoids have smaller angles than platyrrhines and cercopithecids, i.e., a less vertically oriented canal, whereas cercopithecids have the highest angles, corresponding to vertical canals (Fig. 5a; Table 3; SOM Tables S3 and S4). *Pliobates* has the lowest value among Miocene catarrhines and does not significantly differ from the hylobatid range of variation (Fig. 5a; Tables 4 and 5). *Epipliopithecus* and *Ekembo* display very similar values to one another and most closely fit with the hominoid variation, although they only significantly differ from cercopithecids (Fig. 5a; Tables 4 and 5). In contrast, *Victoriapithecus* has a higher angle, more similar to the monkey condition (i.e., a more vertical canal; Fig. 5a; Table 4), although it does not significantly differ from any extant group (Table 5).

In the case of 2DXYA, the values range from ca. −4° to 45° (Fig. 5a; Tables 3 and 4; see SOM S1 regarding the interpretation of negative angles). On this basis, and taking into account the mean differences among extant clades (SOM Tables S3 and S4), we defined two discrete states: anteriorly oriented (≤30°) and medially oriented (>30°). Despite some overlap, platyrrhines display a significantly higher 2DXYA—i.e., a more medially (less anteriorly) directed canal—than the three catarrhine families, which do not differ significantly from one another (Fig. 5b; Table 3; SOM Tables S3 and S4). Among the fossil specimens, *Ekembo* shows the highest 2DXYA whereas *Victoriapithecus* shows the lowest (Fig. 5b; Table 4). Based on the z-scores (Table 5), *Ekembo* displays a higher angle than extant hominoids, *Victoriapithecus* and *Pliobates* show a lower angle than extant platyrrhines, and *Epipliopithecus* displays a higher angle than hylobatids.

3.2. Carotid canal proportions and body size scaling

Robusticity index The two allometric regressions between L and $V^{1/3}$ are significant ($p < 0.001$; Table 6), but the PGLS regression indicates slight negative allometry, whereas the major axis regression does not allow us to exclude isometry. This suggests that the canal robusticity index $L/V^{1/3}$ is only slightly affected by intrinsic size-scaling effects, i.e., that carotid canal length and volume covary in an almost linear

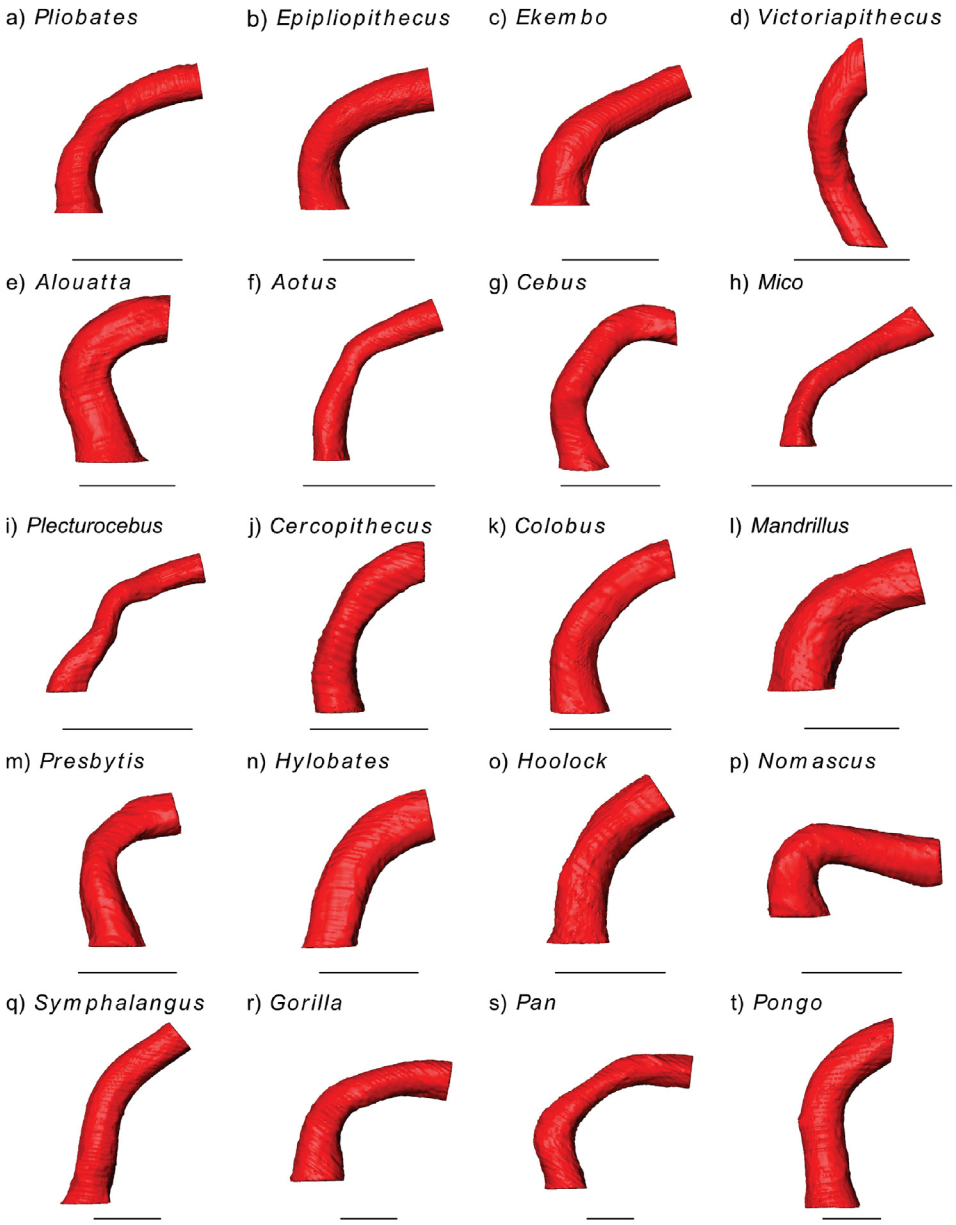


Figure 4. Virtual reconstructions of carotid canal comparing *Pliobates* with extant anthropoids and some Miocene catarrhines: a) *Pliobates* (IPS58443.1); b) *Epipliopithecus* (NHMW 1970/1397/0003); c) *Ekembo* (KNM-RU 2036al); d) *Victoriapithecus* (KNM-MB 29100); e) *Alouatta*; f) *Aotus*; g) *Cebus*; h) *Mico*; i) *Plecturocebus*; j) *Cercopithecus*; k) *Colobus*; l) *Mandrillus*; m) *Presbytis*; n) *Hylobates*; o) *Hoolock*; p) *Nomascus*; q) *Symphalangus*; r) *Gorilla*; s) *Pan*; t) *Pongo*. The canals are shown in lateral view with their posterior ends horizontally aligned. Scale bars = 5 mm.

fashion when geometric similarity is considered. This is further confirmed by the lack of significant correlation between $L/V^{1/3}$ against CS (Table 6). When separate allometric regressions of L and $V^{1/3}$ against CS are computed, it emerges that $V^{1/3}$ and CS display an isometric relationship, whereas L and CS display a minimally positive allometric relationship (with a slope very close to 1). Overall, this suggests that these three variables are suitable proxies for the size of the carotid canal and that the robusticity index is only very slightly affected, if at all, by intrinsic size-scaling effects related to the overall size of the canal.

Based on the robusticity index, and despite some overlap, platyrrhines display significantly slenderer canals than catarrhine families, while hominids also display slenderer canals than both cercopithecids and hylobatids, with the latter showing the stoutest canals (Fig. 5c; Table 3; SOM Tables S3 and S4). *Ekembo* and *Epipliopithecus* exhibit similar indices, while *Victoriapithecus* shows a somewhat higher value but similarly overlaps with all catarrhine families (Fig. 5c; Table 4), and *Pliobates* shows an even higher value and falls outside the hylobatid range (Fig. 5c; Table 4). However, none of the fossil specimens significantly differ from any extant clade (Table 5).

Body-size allometry The fact that the robusticity index is not markedly affected by the size of the canal itself notwithstanding, either carotid canal size and/or proportions could still be affected by body size-scaling effects as measured by regressions against BM (Table 6). Both L and CS display a negative allometric relationship relative to BM—slightly below the theoretical isometric slope of 1/3 predicted by geometric similarity—whereas, in contrast, $V^{1/3}$ fits well with the prediction of geometric isometry. This suggests that the volume of the carotid canal is a better proxy for BM than

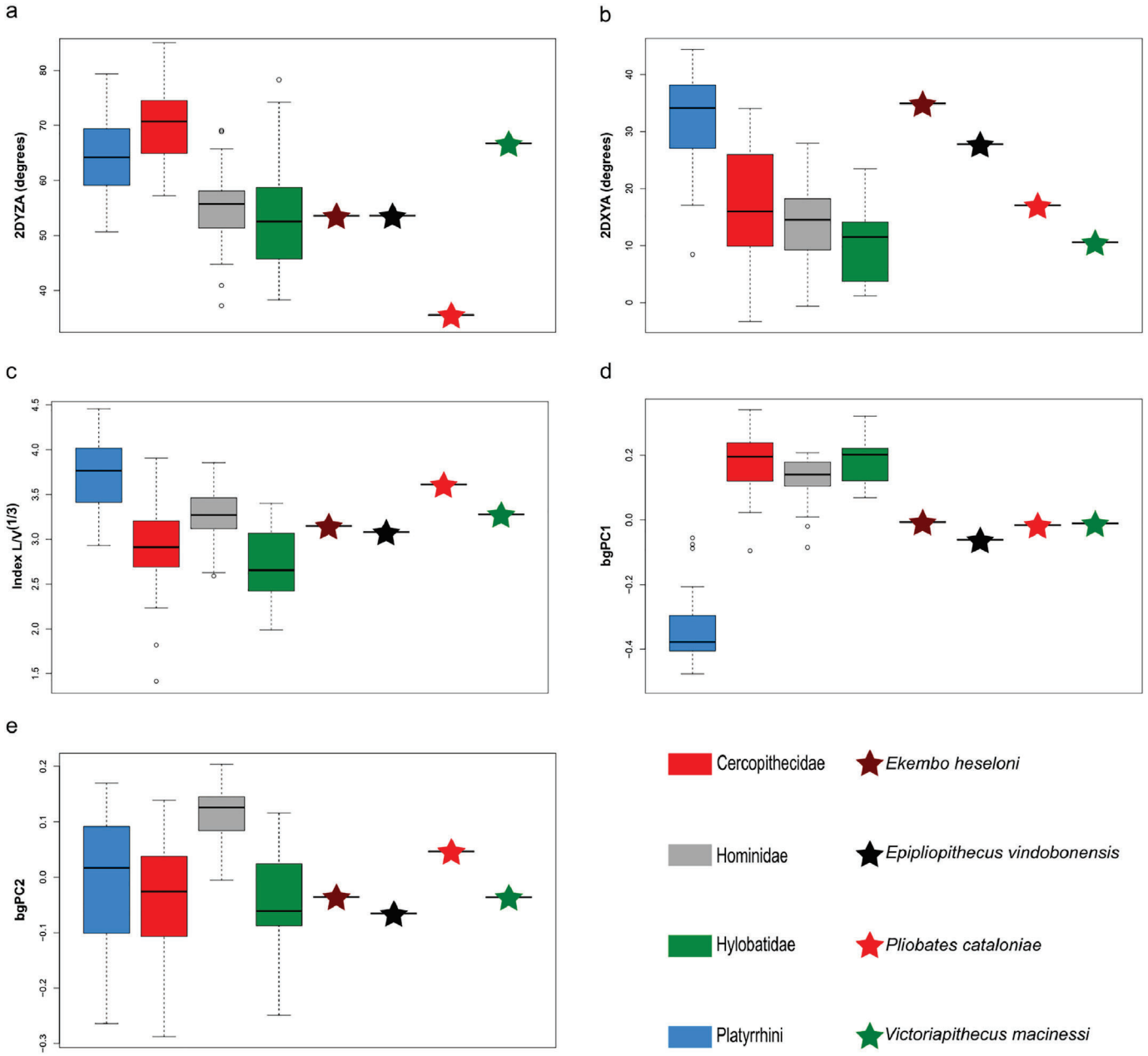


Figure 5. Box-and-whisker plots of the variables describing the orientation, proportions, and course of the carotid canal in the fossil specimens and main extant clades analyzed in this study: a) 2D YZ angle; b) 2D XY angle; c) index $L/V^{(1/3)}$; d) bgPC1; e) bgPC2. Horizontal lines denote medians, boxes depict the interquartile range, whiskers the minimum-maximum values excluding outliers, and dots denote outliers (beyond 1.5 times above or below the interquartile range). Abbreviations: L = length (in mm); V = volume (in mm^3); bgPC = between-group principal component; 2DYZA = 2D angle in the YZ plane (canal superior orientation; in degrees); 2DXYA = 2D angle in the XY plane (canal medial orientation; in degrees).

Table 3
Descriptive statistics of the variables describing the orientation, proportions, and course of the carotid canal in the main extant anthropoid clades. See SOM Table S2 for the individual values of extant anthropoid specimens.

Clade	*n*	2DYZA			2DXYA			$L/V^{(1/3)}$			bgPC1			bgPC2		
		Mean	SD	Range	Mean	SD	Range	Mean	SD	Range	Mean	SD	Range	Mean	SD	Range
Platyrrhini	39	64.06	7.33	50.66–79.36	31.92	7.57	8.25–44.26	3.68	0.39	2.90–4.42	−0.36	0.11	0.50–0.07	−0.01	0.11	−0.26–0.17
Cercopithecidae	54	69.71	7.42	57.2–85	16.69	10	−3.54–33.87	2.86	0.42	1.40–3.87	0.17	0.08	−0.11–0.34	−0.04	0.09	−0.29–0.14
Hominidae	23	54.90	7.83	37.27–69.11	13.74	7.38	−0.82–27.78	3.23	0.31	2.57–3.82	0.12	0.08	−0.10–0.20	0.12	0.05	−0.01–0.20
Hylobatidae	11	54.51	12.39	38.27–78.27	10.27	7.44	1.00–23.27	2.68	0.47	1.97–3.37	0.18	0.08	0.06–0.32	−0.04	0.10	−0.25–0.12

Abbreviations: 2DYZA = 2D angle in the YZ plane (canal superior orientation; in degrees); 2DXYA = 2D angle in the XY plane (canal medial orientation; in degrees); L = length (in mm); V = volume (in mm^3); bgPC = between-group principal component.

Table 4
Variables describing the orientation, proportions, and course of the carotid canal in the fossil specimens.

Species	Catalog No.	2DYZA	2DXYA	$L/V^{(1/3)}$	bgPC1	bgPC2
Ekembo heseloni	KNM-RU 2036al	53.58	34.73	3.12	−0.02	−0.03
Epipliopithecus vindobonensis	NHMW 1970/1397/0003	53.59	27.62	3.05	−0.08	−0.06
Pliobates cataloniae	IPS58443.1	35.58	16.86	3.58	−0.03	0.05
Victoriapithecus macinessi	KNM-MB 29100	66.73	10.36	3.25	−0.02	−0.04

Abbreviations: 2DYZA = 2D angle in the YZ plane (canal superior orientation; in degrees); 2DXYA = 2D angle in the XY plane (canal medial orientation; in degrees); L = length (in mm); V = volume (in mm^3); bgPC = between-group principal component.

Table 5
Z-score analysis of the three variables describing the orientation, proportions, and course of the carotid canal in the fossil specimens and compared with the variation expressed by the main extant anthropoid clades.[a]

Variable and species	Catalog No.	Platyrrhini	Cercopithecidae	Hominidae	Hylobatidae
2DYZA					
Ekembo heseloni	KNM-RU 2036al	−1.43	**−2.17**	−0.17	−0.08
Epipliopithecus vindobonensis	NHMW 1970/1397/0003	−1.43	**−2.17**	−0.17	−0.07
Pliobates cataloniae	IPS58443.1	**−3.88**	**−4.60**	**−2.46**	−1.52
Victoriapithecus macinnesi	KNM-MB 29100	0.36	−0.40	1.51	0.98
2DXYA					
Ekembo heseloni	KNM-RU 2036al	0.37	1.80	**2.84**	**3.29**
Epipliopithecus vindobonensis	NHMW 1970/1397/0003	−0.56	1.09	1.88	**2.33**
Pliobates cataloniae	IPS58443.1	**−1.99**	0.02	0.42	0.89
Victoriapithecus macinnesi	KNM-MB 29100	**−2.85**	−0.63	−0.46	−0.02
$L/V^{(1/3)}$					
Ekembo heseloni	KNM-RU 2036al	−1.46	0.61	−0.36	0.93
Epipliopithecus vindobonensis	NHMW 1970/1397/0003	−1.64	0.44	−0.58	0.78
Pliobates cataloniae	IPS58443.1	−0.27	1.69	1.09	1.89
Victoriapithecus macinnesi	KNM-MB 29100	−1.13	0.91	0.04	1.20
bgPC1					
Ekembo heseloni	KNM-RU 2036al	**3.23**	**−2.30**	−1.78	**−2.39**
Epipliopithecus vindobonensis	NHMW 1970/1397/0003	**2.70**	**−2.97**	**−2.50**	**−3.08**
Pliobates cataloniae	IPS58443.1	**3.14**	**−2.41**	−1.90	**−2.51**
Victoriapithecus macinnesi	KNM-MB 29100	**3.19**	**−2.35**	−1.83	**−2.45**
bgPC2					
Ekembo heseloni	KNM-RU 2036al	−0.25	0.02	**−3.16**	0.04
Epipliopithecus vindobonensis	NHMW 1970/1397/0003	−0.51	−0.31	**−3.78**	−0.27
Pliobates cataloniae	IPS58443.1	0.48	0.93	−1.47	0.87
Victoriapithecus macinnesi	KNM-MB 29100	−0.25	0.02	**−3.17**	0.03

Abbreviations: 2DYZA = 2D angle in the YZ plane (canal superior orientation; in degrees); 2DXYA = 2D angle in the XY plane (canal medial orientation; in degrees); L = length (in mm); V = volume (in mm^3); bgPC = between-group principal component.
[a] Significant z-scores at $p < 0.05$ are bolded.

either L or CS, if size-scaling effects are not corrected for, because the former variable is directly proportional to BM in a linear fashion, whereas both L and CS display negative allometry relative to BM. The similar allometric pattern of L and CS is not surprising because the latter was computed from the carotid canal configurations—which are sets of canal streampoints—and, hence, it only contains information about carotid canal length (but not volume).

Differences in size scaling between L and V are reflected in the existence of a mild negatively allometric relationship when L is considered the dependent variable, although such a relationship is not significant when both variables are considered to display error (i.e., isometry cannot be excluded in the major axis regression; Table 6). Differences in scaling between L and V relative to BM, in any case, are reflected in the regression between the robusticity index and BM (Table 6), which is of inverse proportionality (i.e., a negative slope): given that the numerator (L) of the index increases slightly slower than the denominator ($V^{1/3}$) relative to BM, the index tends to decrease as the body size increases. However, it is noteworthy that despite being significant, the correlation between the robusticity index and body size only explains 14% of the variance (Table 6).

3.3. Carotid canal course within the petrosal

Principal components analysis The bgPCA discriminates between platyrrhines and catarrhines but not among catarrhine families (Fig. 6). The cross-validated bgPCA (SOM Fig. S3) is virtually identical to the standard bgPCA, and the permutational ANOVA results (SOM Table S5) show that mean group differences are significant in all instances. The percentage of variance explained by bgPCAs only increases slightly as compared with the raw data—indicating that grouping structure is not spurious. The percentage of correctly classified individuals by the bgPCA (Table 7) is moderately high (79%), even after cross-validation (77%), although much higher in the case of platyrrhines (92%) and hominids (91%) than for cercopithecoids (63%) and hylobatids (64%).

bgPC1 (Fig. 6a) explains most of the variance (94%), is not significantly correlated with CS ($p = 0.21$; Table 6), and shows a strong phylogenetic signal at $p < 0.001$ ($\lambda = 0.95$; $K = 3.28$). Although bgPC1 is not significantly correlated to ln CS, it displays significant allometry relative to both $V^{1/3}$ and BM, which nevertheless only explain 19% and 25% of the shape variance, respectively (Table 6). This axis discriminates platyrrhines (negative scores) from catarrhines (positive scores) at $p < 0.001$ (Fig. 5d; Table 3;

Table 6
Phylogenetic generalized least-squares (PGLS) allometric regressions between carotid canal size variables (L, $V^{1/3}$, or CS) or between carotid canal size and BM, together with PGLS bivariate regressions between carotid canal shape (as represented by the canal robusticity index or bgPCs) vs. log-transformed carotid canal size or BM.

Regression	p[a]	R^2	Slope	Slope 95% CI
ln L vs. ln $V^{1/3}$	<0.001	0.81	0.86	0.73, 0.99
ln L vs. ln $V^{1/3}$[b]	<0.001	0.81	0.95	0.81, 1.10
$L/V^{1/3}$ vs. ln CS	>0.05	−0.02	0.11	−0.34, 0.57
ln L vs. ln CS	<0.001	0.99	1.04	1.02, 1.06
ln $V^{1/3}$ vs. ln CS	<0.001	0.81	0.99	0.84, 1.13
ln L vs. ln BM	<0.001	0.68	0.25	0.20, 0.31
ln $V^{1/3}$ vs. ln BM	<0.001	0.90	0.30	0.27, 0.34
ln CS vs. ln BM	<0.001	0.69	0.25	0.19, 0.30
$L/V^{1/3}$ vs. ln BM	<0.01	0.14	−0.17	−0.29, −0.05
bgPC1 vs. ln CS	>0.05	0.01	0.12	−0.07, 0.31
bgPC1 vs. ln $V^{1/3}$	<0.01	0.19	0.26	0.10, 0.41
bgPC1 vs. ln BM	<0.001	0.25	0.10	0.05, 0.15
bgPC2 vs. ln CS	<0.001	0.58	0.21	0.16, 0.27
bgPC2 vs. ln $V^{1/3}$	<0.001	0.46	0.17	0.11, 0.23
bgPC2 vs. ln BM	<0.001	0.35	0.05	0.04, 0.08

Abbreviations: L = carotid canal length (mm); $V^{1/3}$ = carotid canal volume cube root (mm); $L/V^{1/3}$ = shape index of canal robusticity; CS = carotid canal centroid size (mm); BM = body mass (g); bgPC = between-group principal component (representing carotid canal course).
[a] Regressions are significant when $p < 0.05$.
[b] For ln L vs. ln $V^{1/3}$, a major axis regression was also computed to test whether the two variables are isometric when deviation from the best-fit line is minimized simultaneously for both variables (instead of only the dependent variable, in this case ln L). Our results show that, unlike for the PGLS regression (which displays slight negative allometry), isometry cannot be discounted for the major axis regression.

SOM Tables S3 and S4) because of longer canals that originate more inferolaterally in the petrosal of the former (Figs. 6b, 7; SOM Figs. S4–S6). In contrast, catarrhines display shorter canals that originate more superiorly and are overall located more medially in the petrosal (Figs. 6b and 7; SOM Figs. S4–S6). Extant catarrhine families extensively overlap along bgPC1 and do not significantly differ in terms of canal length and foramen/canal superoinferior and mediolateral position (Fig. 5d; Table 3; SOM Tables S3 and S4). *Pliobates* and the remaining fossil taxa display similar (moderately negative) bgPC1 scores that are intermediate between those of extant catarrhines and extant platyrrhines (Figs. 5d and 6a; Table 4) and only slightly overlap with cercopithecids and hominids or, in the case of *Epipliopithecus*, also marginally with platyrrhines. Their canal configuration (SOM Figs. S4–S6) is thus somewhat shorter and more medially located than in platyrrhines, although *Epipliopithecus* more closely resembles the platyrrhine condition than *Pliobates*, *Victoriapithecus*, and *Ekembo* do.

bgPC2 (Fig. 6a) explains only 5% of variance, is significantly correlated with CS, $V^{1/3}$, and BM (explaining, respectively, 58%, 46%, and 35% of the shape variance; Table 6), and shows significant phylogenetic signal at $p < 0.001$ ($\lambda = 0.99$; $K = 0.62$). Variation along bgPC2 (Figs. 6b, 7) reflects the canal position on the petrosal (more anterior toward negative values and more posterior toward positive scores). Platyrrhines and catarrhines extensively overlap along this axis, but hominids display significantly more positive values than other groups despite considerable overlap (Fig. 5e; SOM Figs. S4–S6; SOM Tables S3 and S4). Along bgPC2, *Epipliopithecus*, *Victoriapithecus*, and *Ekembo* are found on slightly negative scores and overlap with platyrrhines, cercopithecids, and hylobatids, whereas *Pliobates* has a slightly positive score that further overlaps with hominids (Figs. 5e and 6a; Table 4). The canal configuration of *Pliobates* is thus somewhat more posteriorly located than in the other extinct taxa (SOM Figs. S4–S6), particularly *Epipliopithecus*.

Z-scores (Table 5) indicate that, for bgPC1, *Epipliopithecus* significantly differs from all extant groups, while other extinct taxa match the hominid distribution only. In contrast, for bgPC2, *Epipliopithecus*, *Victoriapithecus*, and *Ekembo* only significantly differ from hominids, whereas *Pliobates* matches the variation of the four extant groups. When both bgPCs are considered simultaneously, the analyzed extinct taxa differ from the four extant anthropoid groups except for *Pliobates*, which matches the hominid variation. This is confirmed by posterior probabilities of group membership (Table 8), according to which *Epipliopithecus*, *Victoriapithecus*, and *Ekembo* are classified as cercopithecoids—although *Epipliopithecus* falls outside their range of variation ($p = 0.018$)—whereas *Pliobates* is classified as a hominid and only significantly differs from platyrrhines. According to these results, the canal course of both *Ekembo* and *Victoriapithecus* fit better the cercopithecoid variation, whereas *Pliobates* fits better with hominids, and *Epipliopithecus* does not fit well with any of the extant groups analyzed. This notwithstanding, the results of the NJ cluster analysis (Fig. 8) indicate that *Pliobates* and *Epipliopithecus* are most similar to one another. Indeed, the four analyzed extinct taxa are grouped together in a cluster of their own, distinct from the subcluster of great apes and that of platyrrhines.

The discrimination among the catarrhine families in the catarrhine-only bgPCA is slightly better than in the analysis based on the whole sample, but the three groups still overlap to an important extent (SOM Fig. S7). The first axis explains most of the variance (85.33%) and is the only one that discriminates between hominids and the remaining groups—as in the whole sample analysis, in which only one axis (bgPC2) discriminates between them. The results for the fossils in the catarrhine-only analysis are not more conclusive than for the analysis including platyrrhines, with only minor differences. In particular, *Epipliopithecus* falls closer to the hylobatid centroid and is classified as a hylobatid ($p = 0.54$), although it displays no significant differences with either cercopithecids ($p = 0.30$) or hominids ($p = 0.29$); *Victoriapithecus* still matches better the cercopithecid range of variation ($p = 0.22$), as it is the case for *Ekembo* ($p = 0.73$), while *Pliobates* is classified first as a hominid ($p = 0.39$) but also falls within the range of hylobatids ($p = 0.14$)—apparently owing to the more hominid-like condition of *Symphalangus* compared with other hylobatids.

Phylomorphospace The results of the phylomorphospace (Fig. 9; SOM Fig. S8) and the reconstructed ancestral morphotypes (Fig. 10; SOM Fig. S9) are virtually identical irrespective of the hypothesis considered. The crown platyrrhine LCA displays a very long canal that originates inferiorly and is located very laterally in the petrosal (Fig. 10e; SOM Fig. S9e), whereas the crown catarrhine LCA displays a condition almost indistinguishable from the mean anthropoid configuration (Fig. 10f; SOM Fig. S9f). The inferred crown cercopithecoid (Fig. 10g; SOM Fig. S9g) and crown hominoid (Fig. 10h; SOM Fig. S9h) ancestral morphotypes are not very divergent from one another or from the catarrhine LCA, but both are more derived than the latter by displaying a somewhat shorter and more medially and posteriorly located canal. The crown hylobatid (Fig. 10i; SOM Fig. S9i) and crown hominid (Fig. 10j; SOM Fig. S9j) LCAs more clearly diverge from the crown hominoid LCA in different directions. Thus, the hylobatid LCA displays a higher bgPC1 score overlapping with extant hylobatids and cercopithecoids, due to a shorter and more medially located canal. In contrast, the hominid LCA displays a higher bgPC2 than the crown hominoid LCA (like the extant hylobatid *Symphalangus*) due to a more posteriorly located canal.

The four analyzed extinct taxa are broadly similar to the crown catarrhine LCA's condition (Fig. 9). Indeed, both *Victoriapithecus* (Fig. 10d) and *Ekembo* (Fig. 10c) most closely resemble the crown catarrhine LCA rather than the crown cercopithecoid (Fig. 10g) or

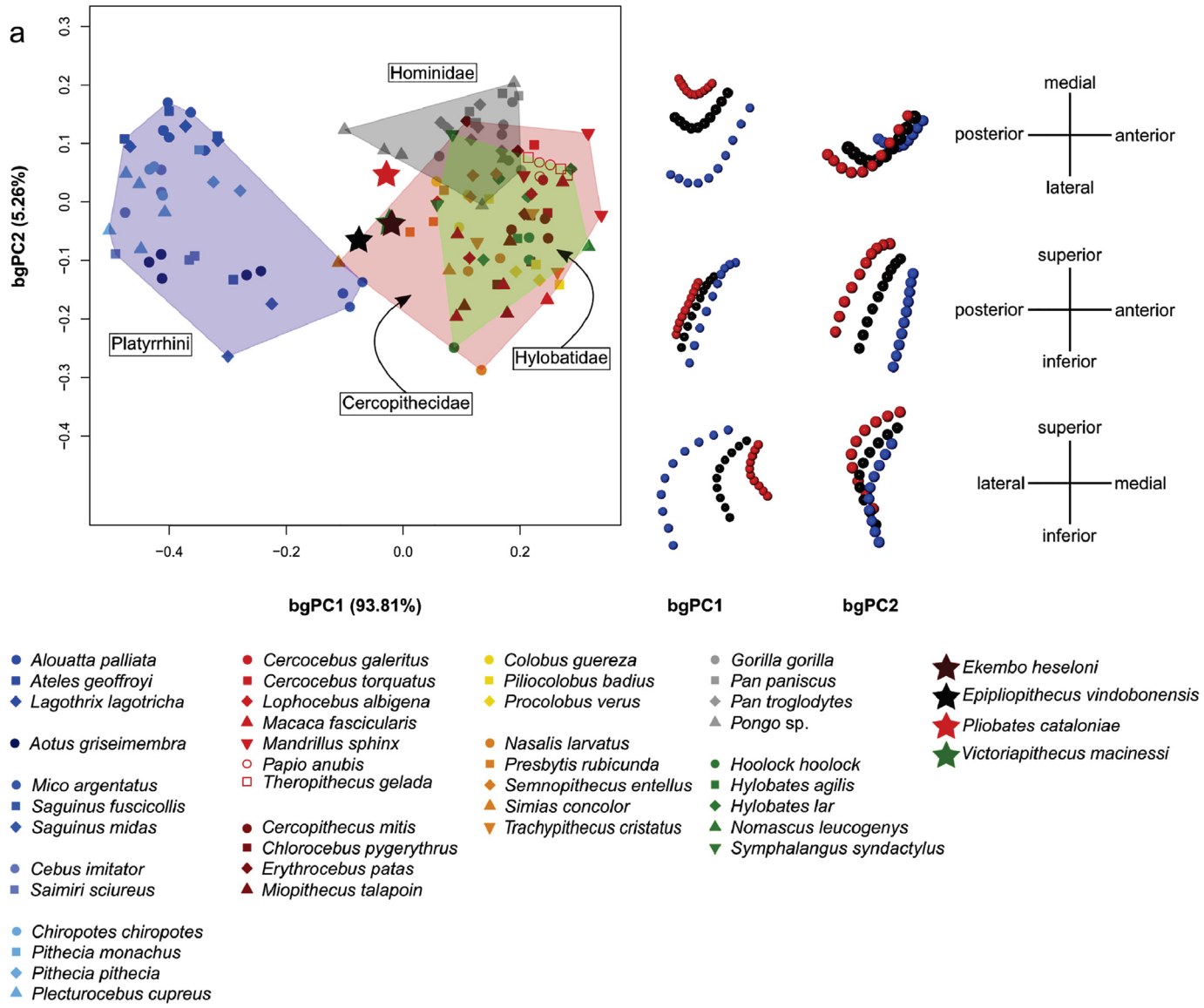


Figure 6. Results of the between-group principal component analysis (bgPCA) based on carotid canal course variation among main extant anthropoid clades. a) Bivariate plot of bgPC2 vs. bgPC1 (the variance explained by each bgPC is denoted in parentheses). b) Minimum (blue) and maximum (red) landmark conformations compared with the anthropoid mean configuration (black) for bgPC1 and bgPC2, in superior (top), lateral (middle), and anterior (bottom) views (anatomical axes of reference are specified next to each view; see Fig. 7 for a representation of the carotid canal within the cranium). Convex hulls correspond to platyrrhines (blue), cercopithecids (red), hylobatids (green), and hominids (gray). Abbreviation: bgPC = between-group principal component. (For interpretation of the references to color in this figure legend, the reader is referred to the Web version of this article.)

Table 7
Number (*n*) and percentages (%) of correctly and incorrectly classified individuals obtained by the between-group principal components analysis after cross-validation. In total, 98 of 127 (77.2%) individuals were correctly classified (in bold).

Taxon	Platyrrhini	Cercopithecidae	Hominidae	Hylobatidae
Platyrrhini	**36 (92.3%)**	0 (0%)	0 (0%)	3 (7.7%)
Cercopithecidae	1 (1.9%)	**34 (63.0%)**	9 (16.7%)	10 (18.5%)
Hominidae	0 (0%)	2 (8.7%)	**21 (91.3%)**	0 (0.0%)
Hylobatidae	0 (0%)	3 (27.3%)	1 (9.1%)	**7 (63.6%)**

hominoid (Fig. 10h) LCAs. *Epipliopithecus* (Fig. 8b) displays a slightly more platyrrhine-like condition in bgPC1 but is nevertheless very distinct from the crown platyrrhine LCA (Fig. 10e) and closer to the inferred crown catarrhine ancestral condition. *Pliobates* (Fig. 10a) closely resembles the crown catarrhine LCA in canal length and carotid foramen/canal superoinferior and mediolateral position (as reflected in bgPC1), but unlike *Victoriapithecus* and *Ekembo*, it appears derived along bgPC2 toward the reconstructed ancestral hominid condition—albeit being more similar along this axis to *Symphalangus* than to extant great apes—owing to its more posteriorly located canal.

4. Discussion

4.1. Carotid canal orientation

Two different characters were defined by Alba et al. (2015b: Tables S5 and S6) to code the carotid canal morphology, one describing the canal 'orientation' (more or less horizontal) and another (following Shoshani et al., 1996) describing the canal 'direction' (more or less anterior). In Alba et al. (2015b), canal

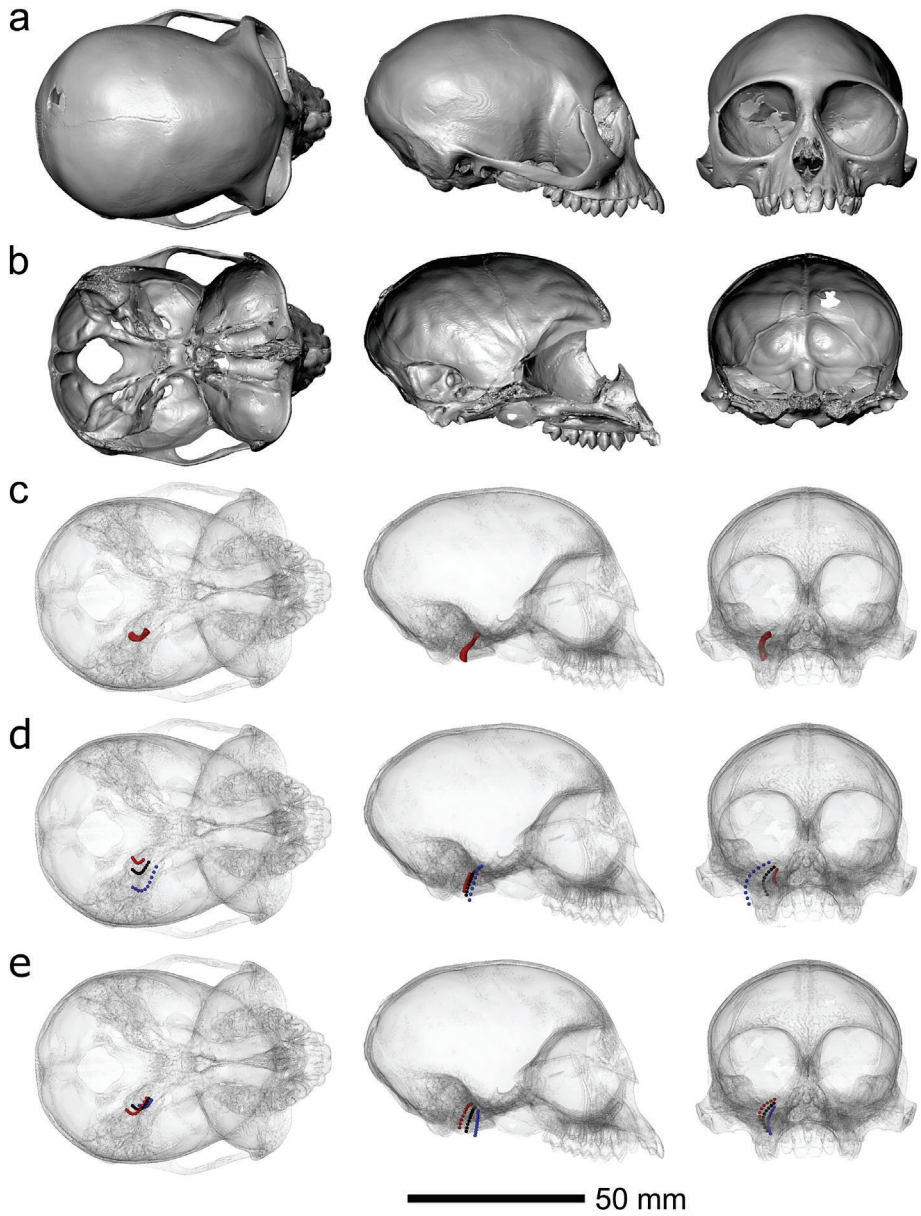


Figure 7. Representations of the carotid canal relative to the cranium in superior (left), lateral (middle), and anterior (right) views. a) Virtual external reconstruction of the cranium. b) Virtual cross sections of the cranium to visualize the petrosal bone (from left to right, transverse, sagittal, and coronal sections are depicted). c) Virtual reconstructions of the carotid canal within the cranium rendered in semitransparency. d, e) Minimum (blue) and maximum (red) landmark conformations compared with the anthropoid mean configuration (black) for bgPC1 (d) and bgPC2 (e) within the cranium rendered in semitransparency. Because the anthropoid mean configuration is extremely similar to the canal course configuration of *Presbytis* (i.e., before alignment), the cranium of this taxon is used as a reference for orienting the canal following the cranial axes of reference. (For interpretation of the references to color in this figure legend, the reader is referred to the Web version of this article.)

Table 8
Posterior probabilities of group membership based on the between-group principal component scores of fossil specimens[a].

Species	Catalog No.	Platyrrhini	Cercopithecidae	Hominidae	Hylobatidae
Ekembo heseloni	KNM-RU 2036al	<0.001	**0.098**	0.059	0.087
Epipliopithecus vindobonensis	NHMW 1970/1397/0003	<0.001	**0.018**	0.009	0.016
Pliobates cataloniae	IPS58443.1	<0.001	0.064	**0.169**	0.056
Victoriapithecus macinessi	KNM-MB 29100	<0.001	**0.089**	0.054	0.079

[a] Each value corresponds to the probability of having the given score if the specimen was a member of the group considered, not the likelihood of group membership in each of the a priori defined groups given a particular score (the greater the number, the higher the probability). For each specimen the highest probability is bolded.

'orientation' was defined as the inclination between the canal and the basioccipital, whereas canal 'direction' was coded based on the spatial relationship between the imaginary line emerging from the canal and the foramen magnum. Canal 'direction' sensu Alba et al. (2015b) could be anterior or posterior relative to the foramen magnum, i.e., more laterally or more anteriorly directed,

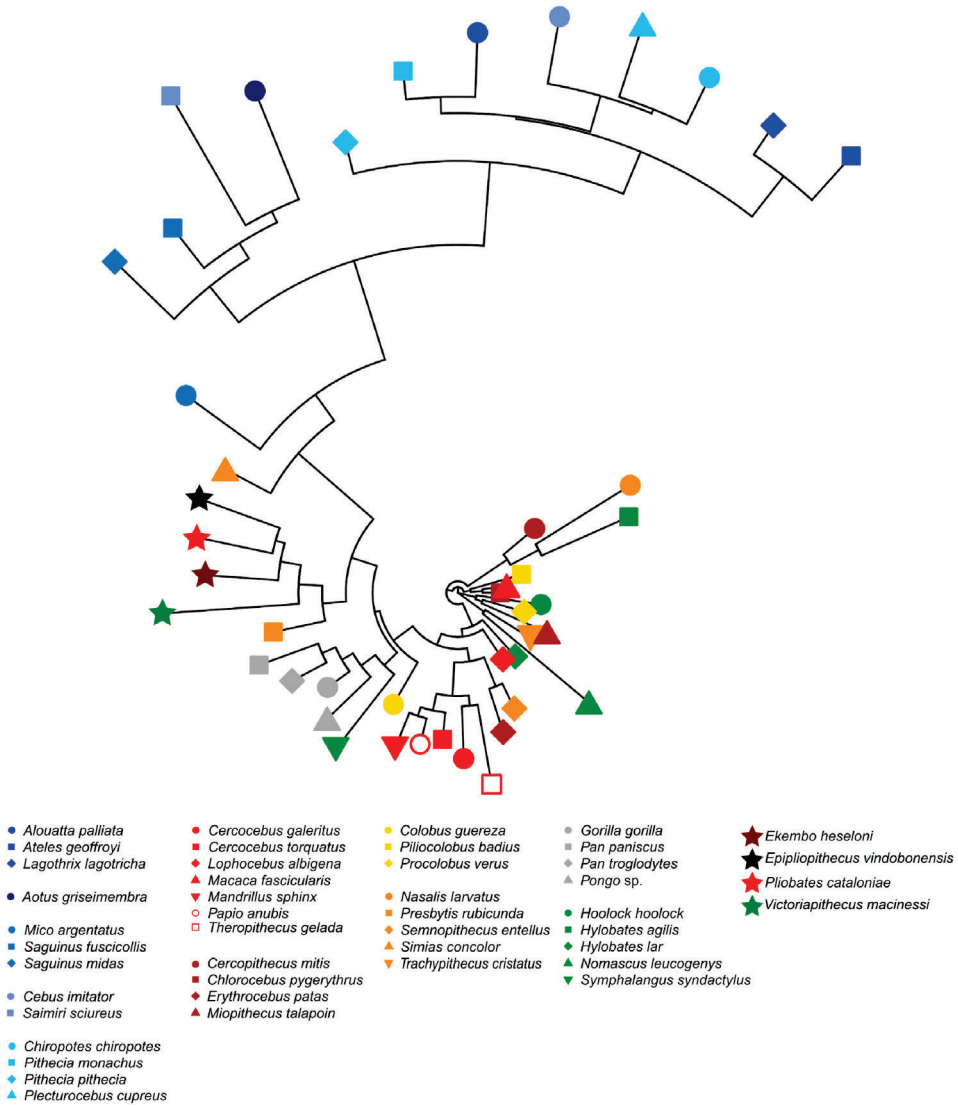


Figure 8. Neighbor-joining cluster (unrooted) based on the Euclidean distances calculated from raw coordinates of the canal course configurations in *Pliobates*, extant anthropoids and other Miocene catarrhines. Cophenetic = 0.94.

respectively. To evaluate this character, previous authors (Shoshani et al., 1996) placed a straight wire inside the carotid canal and noted the point of intersection between the imaginary line along the wire and the foramen magnum. In Alba et al. (2015b) on the other hand, this character was evaluated conducting visual inspections on μCT scans, drawing the course of the canal in basicranial inferior view and noting the point of intersection between the imaginary line in continuation of the canal course and the foramen magnum. 2DYZA (canal superior orientation in the present study) is comparable with the canal 'orientation' of Alba et al. (2015b) because this angle is measured along the parasagittal plane, although based on values obtained, we prefer to categorize them as oblique/subvertical/vertical (as opposed to horizontal/oblique/subvertical as in Alba et al., 2015b). In contrast, 2DXYA (canal medial orientation in the present study) is not directly comparable with the canal 'direction' of Alba et al. (2015b) because, while both studies rely primarily on the line passing through the two canal endpoints (i.e., whole carotid canal), in the present study the alignment process and the quantitative assessment of this character (i.e., possibility of having more than two states vs. two qualitative states only in Alba et al., (2015b)) make that this measure of canal orientation, for the same canal specimen, might differ between the two studies.

Pliobates was coded by Alba et al. (2015b) as displaying a horizontal orientation parallel to the basioccipital, like hylobatids, whereas the stem catarrhine *Saadanius*, cercopithecoids (including *Victoriapithecus*) and hominids were coded with a subvertical orientation, and *Epipliopithecus* and *Ekembo* with an intermediate (oblique) condition. Our results for superior canal orientation (2DYZA) indicate that, in this regard, *Pliobates* does not differ from hylobatids and displays a lower value than *Ekembo* and *Epipliopithecus*. However, our results further show that both hylobatids and hominids display a rather oblique orientation (i.e., a horizontal orientation parallel to the basioccipital using the terminology of Alba et al., 2015b), with *Ekembo* and *Epipliopithecus* resembling hominoids as a whole. Nonetheless, all these taxa possess a less vertical orientation than platyrrhines (i.e., a subvertical canal) and, especially, cercopithecoids (including *Victoriapithecus*), in which the canal is vertical. To sum up, according to Alba et al. (2015b), hylobatids and *Pliobates* had a horizontal canal, *Ekembo* and *Epipliopithecus* an oblique canal, and

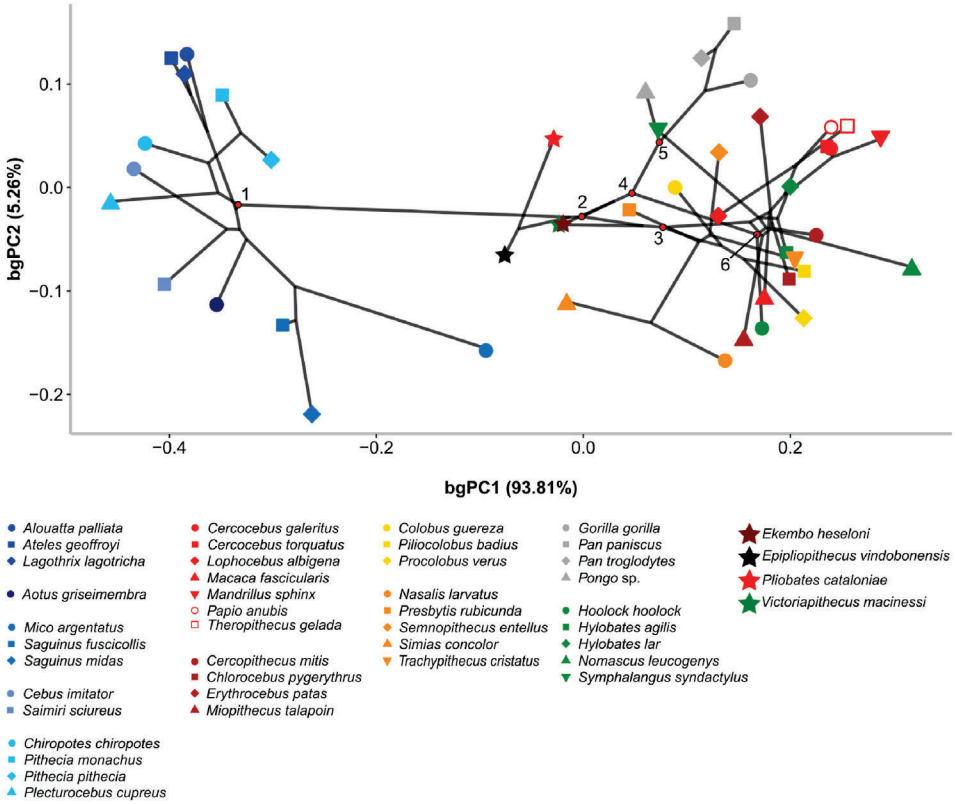


Figure 9. Phylomorphospace of carotid canal course variation in extant anthropoids and extinct Miocene catarrhines including *Pliobates*. *Epipliopithecus* and *Pliobates* are considered sister taxa within a stem catarrhine pliopithecoid clade and *Ekembo* is considered a stem hominoid, while *Victoriapithecus* is considered a stem cercopithecoid (see SOM Fig. S2b for a representation of this phylogenetic hypothesis). Ancestral nodes: 1 = crown platyrrhines; 2 = crown catarrhines; 3 = crown cercopithecoids; 4 = crown hominoids; 5 = crown hominids; 6 = crown hylobatids. See SOM Figure S8 for a phylomorphospace derived from the alternative phylogenetic hypothesis (SOM Fig. S2a).

cercopithecoids (including *Victoriapithecus*) and hominids a subvertical canal, whereas according to our results, all hominoids (including *Ekembo*), *Epipliopithecus*, and *Pliobates* have an oblique canal, platyrrhines a subvertical canal, and cercopithecoids (including *Victoriapithecus*) an even more vertical canal. Therefore, the superior orientation of the carotid canal is consistent with the cercopithecoid status of *Victoriapithecus*, but it is not informative regarding the stem catarrhine vs. stem hominoid status of *Pliobates*.

In turn, *Pliobates* was coded by Alba et al. (2015b) as resembling *Epipliopithecus* and hylobatids in the 'direction' of the canal. The condition of all these taxa was coded as anteriorly directed, the imaginary line emerging from the carotid canal crossing the foramen magnum more posteriorly than in *Saadanius*, cercopithecids, and hominids, whose canal would be more laterally directed, as in platyrrhines (see also Shoshani et al., 1996). In contrast, our results indicate that hylobatids extensively overlap in canal medial orientation with other extant catarrhines, which only significantly differ from platyrrhines. Furthermore, *Pliobates* does not specifically resemble hylobatids or *Epipliopithecus*, but rather crown catarrhines as a whole, including *Victoriapithecus*. On the other hand, *Epipliopithecus* and, especially, *Ekembo,* exhibit a more platyrrhine-like condition, i.e., a medially directed canal. To sum up, our results indicate that cercopithecoids (including *Victoriapithecus*), crown hominoids, and *Pliobates* have an anteriorly oriented canal, whereas platyrrhines, *Ekembo*, and *Epipliopithecus* have a medially oriented canal.

4.2. Carotid canal proportions

Volumetric proportions—which were not considered by Alba et al. (2015b)—as measured by the robusticity index of the carotid canal, further confirm the differences in carotid canal morphology between platyrrhines and catarrhines. Our allometric analyses indicate that these differences cannot be explained by body size-scaling effects alone. In particular, the volume of the carotid canal displays an isometric relationship with body size, whereas length displays a slight negative allometric relationship with the latter. As a result, larger-bodied taxa tend to display lower values of the robusticity index (i.e., slightly stouter carotid canals). However, correlation with body mass only explains 14% of the variance in carotid canal robusticity.

Based on our results, platyrrhines display on average slenderer canals (i.e., lesser volume relative to length) than catarrhines. However, as for medial canal orientation, catarrhine families largely overlap in canal proportions, although great apes display less robust canals than cercopithecids and hylobatids, and are somewhat intermediate between them and platyrrhines. The analyzed fossil catarrhines more closely resemble each other in canal proportions than in canal orientation—being catarrhine-like but further overlapping with the platyrrhine range of variation. *Pliobates* displays a somewhat slenderer canal than the other extinct taxa, and, unlike them, it does not overlap with hylobatids, even more clearly than in the case of medial canal orientation, thus

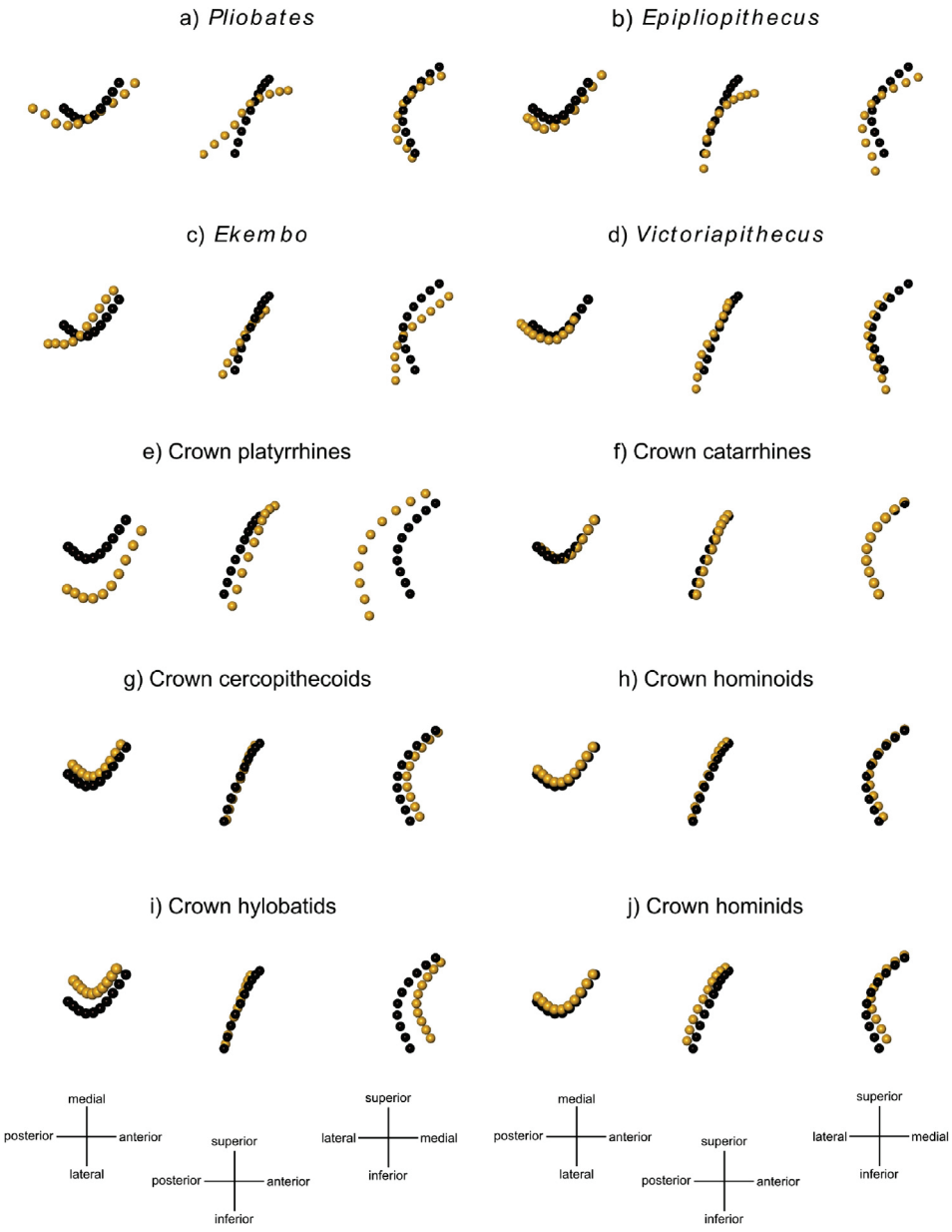


Figure 10. Configurations of the carotid canal course in *Pliobates* compared with other Miocene catarrhines and the reconstructed carotid canal course for the last common ancestors (LCAs) of various anthropoid clades: a) *Pliobates* (IPS58443.1); b) *Epipliopithecus* (NHMW 1970/1397/0003); c) *Ekembo* (KNM-RU 2036al); d) *Victoriapithecus* (KNM-MB 29100); e) crown platyrrhines; f) crown catarrhines; g) crown cercopithecoids; h) crown hominoids; i) crown hylobatids; j) crown hominids. The canal courses of the LCAs have been inferred based on the phylomorphospace displayed in Figure 9 (see SOM Fig. S9 for the inferred LCA configurations derived from the alternative phylogenetic hypothesis). For each specimen/LCA, the configurations are displayed in superior (left), lateral (middle), and anterior (right) views. The mean configuration computed for the whole anthropoid sample is represented by black dots, while configurations for Miocene catarrhines and LCAs are represented in beige. The anthropoid mean configuration was used as a reference for visualizing all the configurations at the same relative scale.

further reinforcing the rejection of possible closer similarities with the latter family.

Our results for the extant taxa are in broad agreement with those previously obtained by Boyer et al. (2016) on relative internal carotid artery area. Boyer et al. (2016) found internal carotid area to scale isometrically with cranial area (measured as the square root of the product between prosthion-inion length and bizygomatic breadth). Among catarrhines, these authors found a pattern of decreasing robusticity in the relative carotid artery area from hylobatids to hominids, and to cercopithecids, which is the same as we found for the carotid canal as a whole. The main difference between our results and those of Boyer et al. (2016) is that, in the latter study, the carotid artery robusticity of platyrrhines was found to be intermediate between hylobatids and hominids, whereas our results show that platyrrhines have slenderer canals than catarrhines. This discrepancy is easily explained by the fact that Boyer et al. (2016) considered internal carotid artery area relative to cranial area, whereas we relied on the ratio between the length and the volume of the canal. Our results (see below for further discussion) indicate that platyrrhines display relatively longer carotid canals than catarrhines, thereby resulting in less robust volumetric proportions for the canal as a whole. Given that Boyer et al. (2016) did not take canal length into account, this explained the aforementioned

discrepancy for platyrrhines (but not the other groups) as compared with our results.

4.3. Carotid canal course

Our bgPCA results indicate that the morphology of the canal embeds strong phylogenetic signal, although most of the variance merely discriminates between platyrrhines and catarrhines, due to differences in canal length and location reflected in bgPC1. In particular, extant catarrhines display shorter canals that originate more superiorly and medially than in platyrrhines. It is noteworthy to stress beforehand that *Pliobates* and hylobatids do not show particular similarities in bgPC1 scores.

Previous studies suggested that the carotid foramen is located ventrally (Ross, 1994; Ross et al., 1998) and posteriorly (Ross, 1994; Ross et al., 1998; Kay et al., 2008) in both platyrrhines and catarrhines, whereas Alba et al. (2015b) noted some differences in the anteroposterior carotid foramen location between hylobatids and other catarrhines (with the former displaying a more anteriorly located carotid foramen). Previous studies also noted that platyrrhines display a more medially located foramen than catarrhines (Ross et al., 1998; Kay et al., 2008). Our bgPC1 results indicate that extant platyrrhines and catarrhines differ regarding not only the length of the canal but also the location of the (external) carotid foramen, such that in catarrhines the entire carotid canal (i.e., not only the foramen but the whole structure) is more superiorly and medially located within the petrosal. Our results therefore point to differences between platyrrhines and catarrhines in terms of dorsoventral location of the carotid foramen, contrary to previous studies (Ross, 1994; Ross et al., 1998). This might be attributable to the different methodologies used (i.e., because of having performed an alignment on the specimens in the present study). Similarly, because of the alignment, our conclusions for the location along the mediolateral axis might be the opposite as those noted by previous authors (Ross et al., 1998; Kay et al., 2008), who simply recorded foramen position relative to the bulla. As catarrhines possess a tubular ectotympanic, catarrhine landmark configurations are shifted more medially. This is the consequence of alignment optimization of their tympanic landmarks with those of platyrrhines, whose annular ectotympanic causes their tympanic landmarks to be more medially positioned. Regardless, we observe an extensive overlap among extant catarrhine families in the position of the carotid foramen, at least based on bgPC1.

Our results for bgPC2 lend some support that hylobatids display on average a more anteriorly located foramen in the petrosal than hominids. However, rather than indicating a particular condition for hylobatids, our bgPC2 results suggest that only hominids differ in this regard from other catarrhines by displaying a more posteriorly located foramen. This conclusion should be taken with caution, given that bgPC2 shows an extensive overlap between hominids and the upper range of other crown catarrhines. Furthermore, bgPC2 reflects a smaller amount of variance, embeds lesser phylogenetic signal than bgPC1, and is more strongly correlated with size—although the percentage of variance explained by allometry varies depending on whether canal size or body size is considered, our results clearly indicate that this axis is more strongly influenced by size-scaling than bgPC1. Therefore, one should be cautious when interpreting similarities among taxa based on bgPC2 scores.

Our 3DGM results for the analyzed fossil taxa do not support particular similarities between *Pliobates* and hylobatids in terms of overall carotid canal course (contra Alba et al., 2015b) and indicate instead that *Pliobates* is most similar in this regard to *Epipliopithecus*, *Victoriapithecus*, and *Ekembo*. All these fossil catarrhines appear overall closer to extant catarrhines in terms of canal length and location in the petrosal, albeit being somewhat intermediate between platyrrhines and catarrhines. *Epipliopithecus* appears slightly more platyrrhine-like, whereas the other extinct genera only overlap with the lowest range of cercopithecids and hominids (but not hylobatids). *Pliobates* only differs slightly from the remaining fossil catarrhines by more closely resembling hominids and *Symphalangus* along bgPC2 (reflecting a more posteriorly located foramen/canal). As noted earlier, bgPC2 is quite strongly correlated with CS, suggesting that the differences between hominids and the rest of the sample could merely result from the larger body size of the former. However, this cannot explain the differences along this axis between *Pliobates* and *Epipliopithecus*, as the former more closely resembles the large-bodied hominids and the largest-bodied hylobatid (*Symphalangus*) despite a much lower estimated body size than *Epipliopithecus* (4–5 kg vs. 11–12 kg, respectively; Alba et al., 2015b).

4.4. Evolutionary implications

Alba et al. (2015b) concluded that *Pliobates* displays a mosaic of plesiomorphic (stem catarrhine-like) cranial and postcranial features and more derived (crown hominoid) cranial and postcranial synapomorphies, coupled with a dendropithecid-like dentition and some cranial similarities with hylobatids. A stem hominoid status more derived than that of *Ekembo* was supported for *Pliobates* by Alba et al. (2015b) based on the results of their cladistic analysis. Such a phylogenetic placement would support the view that some purported synapomorphies of crown catarrhines, best exemplified by the completely ossified tubular ectotympanic, would have been acquired independently in cercopithecoids and hominoids—a possibility taken into account by some previous authors (Begun, 2002). A stem hominoid status for *Pliobates* would further support that the last common ancestor of crown hominoids would have been more hylobatid-like than previously assumed (Alba et al., 2015b). Interestingly, one of the resemblances between *Pliobates* and hylobatids found by Alba et al. (2015b) was the carotid canal morphology, which is at odds with the results of our more elaborate analyses of this anatomical structure, which denote a generalized catarrhine morphology with some closer similarities with extant hominids and uniquely *Symphalangus* among hylobatids.

Contrary to Alba et al. (2015b), subsequent cladistic analyses—based on different taxon-character matrix—have recovered *Pliobates* as a stem catarrhine more closely related to pliopithecoids (Nengo et al., 2017; Gilbert et al., 2020b). Based on these results, Gilbert et al. (2020a: 399) concluded that "*Pliobates* is most likely a derived, late-occurring pliopithecoid or other stem catarrhine taxon that has converged on some interesting but minor details of extant hominoid elbows and wrists". In fact, the similarities in elbow and wrist morphology between *Pliobates* and hominoids are not minor but quite extensive, more so than those displayed by *Ekembo* and certainly than those convergently acquired by atelids (Alba et al., 2015b). However, it is not unconceivable that these similarities—being functionally related to enhanced forearm rotation and ulnar deviation capabilities—might have independently evolved between *Pliobates* and crown hominoids. Under such a scenario, in which postcranial similarities between *Pliobates* and crown hominoids would be dismissed as convergences, it should be taken into account that the dental morphology of *Pliobates* suggests much closer affinities to dendropithecids (particularly *Micropithecus*) than to pliopithecoids (Alba et al., 2015b). A dendropithecid status for *Pliobates* would not imply an independent acquisition of a fully ossified ectotympanic, but would not automatically resolve the phylogenetic placement of the former, given the controversies surrounding the phylogenetic relationships of

dendropithecids—considered either stem catarrhines more derived than pliopithecoids (Harrison, 2010, 2013, 2017; Nengo et al., 2017; Gilbert et al., 2020b) or stem hominoids more basal than proconsulids (Rae, 1999; Zalmout et al., 2010; Begun, 2015; Alba et al., 2015b; Rossie and Hill, 2018).

Unfortunately, the carotid canal morphology of dendropithecids is currently unknown, thereby precluding a direct comparison with *Pliobates*. Furthermore, despite substantial differences between platyrrhines and catarrhines in terms of carotid canal orientation and proportions as well as carotid canal length and (foramen) location in the petrosal, our results indicate a considerable overlap among extant catarrhines. As a result, carotid canal morphology is of limited utility for investigating the phylogenetic position of fossil catarrhines, although some insights can be drawn for the investigated taxa. Before discussing the evolutionary implications of our results, however, it should be noted that the small sample sizes available for extinct taxa make it necessary to interpret the differences among the analyzed fossil specimens by assuming that they are more or less representative of their respective taxa. Although this caveat is not restricted to the carotid canal morphology, it should not be forgotten that we cannot know a priori how similar in carotid canal morphology a particular fossil specimen is to the (unknown) average condition of the taxon to which it belongs. For example, given the considerable variation that can be observed in some extant taxa for carotid canal course (e.g., *Aotus*, *Macaca*, *Mandrillus*), the possibility remains that some of the differences inferred among extinct taxa, or between them and extant catarrhine clades, might vanish (or become more accentuated) if additional specimens became available. In the meantime, caution is required by bearing in mind that the reliability of inferences for fossil taxa is limited by the number of specimens available to them, which often preclude an adequate assessment of intraspecific variability.

Based on the currently available specimens, our results indicate that the stem hominoid *Ekembo* and the stem cercopithecoid *Victoriapithecus* are virtually identical in carotid canal volumetric proportions and course morphology, although *Ekembo* displays a more platyrrhine-like medial orientation (similar to *Epipliopithecus*) and a more hominoid-like superior orientation (similar to *Epipliopithecus* and *Pliobates* to some extent). The less medially/more anteriorly oriented carotid canal in *Pliobates* than in *Ekembo* would be consistent with a more derived stem hominoid status, but given the modern cercopithecoid-like carotid canal orientation of *Victoriapithecus*, the condition of extant cercopithecoids and hominoids might have evolved independently to some extent. In turn, based on the condition of *Epipliopithecus*, the possession of an obliquely oriented canal in hominoids might represent a catarrhine symplesiomorphy; in that case, the condition of extant cercopithecoids would have independently evolved from that of extant platyrrhines. Alternatively, the oblique orientation of the canal might be synapomorphic for hominoids, in which case the similar condition of *Epipliopithecus* would be a convergence. Either way, this feature is not informative regarding the phylogenetic position of *Pliobates*.

In terms of carotid canal course, as reflected by our 3DGM analysis, *Pliobates* does not show particular affinities with hylobatids and rather resembles the other analyzed extinct taxa, which are overall more similar to catarrhines but somewhat intermediate between platyrrhines and both cercopithecids and hominids. The phylomorphospace shows that both *Victoriapithecus* and *Ekembo* apparently reflect well the inferred ancestral crown catarrhine morphotype, despite their generally accepted crown catarrhine (respectively, stem cercopithecoid and stem hominoid) status (e.g., Benefit and McCrossin, 1997; Benefit, 1999; Alba et al., 2015b; Nengo et al., 2017; Gilbert et al., 2020b). In contrast, *Epipliopithecus* appears somewhat more plesiomorphic, whereas *Pliobates* appears slightly derived (in the anteroposterior position of the carotid foramen/canal) toward the great ape condition, being closer to the inferred ancestral hominid morphotype as well as the hylobatid *Symphalangus*.

In the case of *Epipliopithecus*, our results are in agreement with the widely held opinion that pliopithecoids are a clade of stem catarrhines, predating the divergence of cercopithecoids and hominoids (Harrison, 2013; Begun, 2002, 2017; Nengo et al., 2017; Gilbert et al., 2020a, b; Sankhyan et al., 2017; Harrison et al., 2020; Urciuoli et al., 2021; contra Alba et al., 2015b). For *Pliobates*, our results are more ambiguous and subject to interpretation, although it is noteworthy that they do not support a closer relationship with pliopithecoids—at least, based on the information provided by *Epipliopithecus*. They suggest instead that, in carotid canal morphology, *Pliobates* is more derived than *Epipliopithecus* toward the inferred ancestral crown catarrhine morphotype, similar to *Ekembo* and *Victoriapithecus*. Furthermore, our results discount very close similarities in carotid canal morphology between *Pliobates* and hylobatids as a whole but indicate some resemblances with the hylobatid *Symphalangus* and great apes. In the latter regard, *Pliobates* is approximately equidistant from the crown catarrhine and crown hominoid reconstructed morphotypes. It is uncertain whether this reflects a more derived status of *Pliobates* or an independent development, although the latter is plausible in light of the *Symphalangus* condition—if the hylobatid LCA reconstructed in the phylomorphospace is broadly correct, *Symphalangus* must have independently acquired a more great ape-like condition; alternatively, the condition shared by the hominid LCA and *Symphalangus* might be plesiomorphic for crown hominoids and the reconstructed hylobatid LCA would reflect a secondary reversal of the remaining hylobatids. Of course, the morphology of a single anatomical region cannot provide much insight into the phylogenetic position of a given taxon among catarrhines, particularly if—as it is the case of the carotid canal—it does not adequately discriminate among catarrhine clades. However, our results for this structure do not show any particular resemblances between pliopithecoids and *Pliobates* (beyond those displayed by all the extinct taxa analyzed) and further fail to contradict the alternative phylogenetic status of *Pliobates* as a stem hominoid. The phylogenetic status of *Pliobates* thus seems far from being settled.

5. Summary and conclusions

Previous research on the primate carotid canal within a phylogenetic context has been limited to the inclusion of qualitative features related to carotid foramen position in the bulla and overall direction and orientation of the canal itself in character-taxon matrices devised for cladistic analysis (Beard and MacPhee, 1994; Ross, 1994; Shoshani et al., 1996; Ross et al., 1998; Kay et al., 2008; Alba et al., 2015b). From a quantitative viewpoint, only Boyer et al. (2016) investigated the allometric relationship between carotid canal area and BM (Boyer et al., 2016), whereas some authors relied on the carotid canal area for inferring encephalic blood flow rates and blood flow metabolism by further taking vertebral canal size into account (Boyer and Harrington, 2018, 2019; Beaudet et al., 2020). Thus, our study is the first to rigorously quantify the orientation, direction, overall course, and volumetric proportions of the carotid canal in 3D among a large sample of anthropoids. The allometric regressions performed also represent some advancement in the understanding of body size-scaling effects on carotid canal

morphology. The methodological protocols devised here enable repeatability among different researchers and thus will enable a refinement of our conclusions by including additional extant and/or fossil specimens in the future. The analyzed variables are no panacea for clarifying the phylogeny of extinct catarrhines because various extant groups overlap to a large extent and also because intraspecific variation will be difficult to evaluate due to small samples sizes. However, the analyzed variables offer the prospect to provide taxonomically and phylogenetically relevant information for extinct taxa, particularly if they are added to character-taxon matrices devised for cladistic analysis including information from other anatomical areas. Other future directions of work on the carotid canal should deepen our current understanding about the influence of function, as well as allometric and phylogenetic constraints, on the evolution of this anatomical structure. This would be required not only to better interpret carotid canal morphology from an adaptive viewpoint but also to derive from it paleobiological inferences for extinct taxa.

In this study, we rely on 3D morphometric techniques to quantify the orientation, proportions, and course of the carotid canal in the small-bodied catarrhine *Pliobates* and compare it with extant anthropoids and other Miocene catarrhines (*Epipliopithecus*, *Victoriapithecus,* and *Ekembo*). Our results reveal that *Pliobates* and the other analyzed Miocene catarrhines are broadly similar to one another in carotid canal morphology and more closely resemble extant catarrhines than platyrrhines. Unfortunately, carotid canal morphology does not adequately discriminate among catarrhine clades, thereby hindering a more detailed phylogenetic assessment of *Pliobates* on this basis. The difficulty of assessing intraspecific variation in carotid canal morphology in the extinct taxa, coupled with the lack of marked differences among extant catarrhine families, makes it impossible to reach definitive conclusions about the systematic position of *Pliobates* on this basis alone. However, our results rule out the previously noted similarities in carotid canal morphology between *Pliobates* and hylobatids and indicate instead that this extinct catarrhine is broadly similar to catarrhines as a whole and, in particular, to other Miocene catarrhines (both stem and crown).

It is however noteworthy that the carotid canal of *Pliobates* is not particularly similar to that of pliopithecoids (as represented by *Epiplioithecus*, which appears somewhat more platyrrhine-like), thereby not supporting (or contradicting) the hypothesis that *Pliobates* is a pliopithecoid. Similar to the stem hominoid *Ekembo* and the stem cercopithecoid *Victoriapithecus*, *Pliobates* appears somewhat more derived than *Epipliopithecus* toward the modern catarrhine condition, and indeed, in some respects, *Pliobates* appears even more derived toward the ancestral hominoid morphotype than the remaining Miocene catarrhines analyzed, more closely resembling extant hominids and the hylobatid *Symphalangus*. Therefore, our results do not enable us to discount the hypothesis that *Pliobates* is a stem hominoid rather than a stem catarrhine. Given the dental similarities between *Pliobates* and African dendropithecids, the former might be a late offshot of the latter clade that dispersed into Eurasia independently from pliopithecoids. Unfortunately, this possibility could not be directly assessed in this study because the carotid canal morphology of dendropithecids is unknown. Additional analyses focused on other anatomical (both cranial and postcranial) areas will be required to further clarify the phylogenetic relationships of *Pliobates*, as well as to clarify whether its postcranial similarities with crown hominoids might have been independently acquired.

Conflict of interest

The authors declare no conflict of interest.

Acknowledgments

This work has been funded by the Agencia Estatal de Investigación (CGL2016-76431-P and CGL2017-82654-P, AEI/FEDER, EU), the Generalitat de Catalunya (CERCA Programme and Consolidated Research Groups 2017 SGR 086 and 2017 SGR 116), the Ministerio de Ciencia, Innovación y Universidades (PRE2018-083299 to F.B. and BES-2015−071318 to A.U.), and the European Commission under the Marie Skłodowska-Curie Individual Fellowship Programme (H2020-MSCA−IF−2018-837966 to M.P.). A.B. was funded by the Centre of Excellence in Palaeosciences (CoE-Pal), Institut français d'Afrique du Sud (IFAS), National Research Foundation (NRF), Palaeontological Scientific Trust (PAST), and Wits. Regarding the CT scanning of *Epipliopithecus*, this research also received support from the Synthesys Project (http://synthesys3.myspecies.info/), which is financed by the European Community Research Infrastructure Action under the FP7 (ref. AT-TAF-4689). We thank Fred Spoor, the Department of Earth Sciences of the National Museums of Kenya, and the Department of Human Evolution of the Max Planck Institute for Evolutionary Anthropology in Lepzig for granting access to the CT scans of *Ekembo* and *Victoriapithecus*, as well as Ursula Göhlich for access to the *Epipliopithecus* material housed in the Naturhistorisches Museum Wien and Martin Dockner for assistance during the CT scanning process of this material at the μCT lab of Universität Wien. We also thank the following people and institutions for providing access to scans used in this study: Eric Delson and the American Museum of Natural History (AMNH), funded by the AMNH and the New York Consortium in Evolutionary Primatology (NYCEP); Lauren A. Gonzales, the Museum of Comparative Zoology (MCZ), the Southern Illinois University (SIU), and the Smithsonian National Museum of Natural History (USNM), funded by NSF grants BCS 1440742 & 1552848; Kari L. Allen and the Duke University, Department of Evolutionary Anthropology (DUEA), regarding scans that originally appeared in Allen's PhD dissertation, funded by an NSF DDIG and the Leakey Foundation; Lynn Copes, Lynn Lucas, and the MCZ, funded by an NSF DDIG #0925793 and the Wenner-Gren Foundation; and Sergio Almécija, funded by NSF grant BCS 1316947 and Stony Brook University. These scans were downloaded from MorphoSource.org, a web-accessible archive for 3D digital data housed by Duke University. We further thank the Editor (Clément Zanolli), the Associate Editor (Eric Delson), and three anonymous reviewers for helpful comments that helped us to improve a previous version of this article.

Supplementary Online Material

Supplementary Online Material to this article can be found online at https://doi.org/10.1016/j.jhevol.2021.103073.

References

Adams, D.C., Collyer, M.L., Kaliontzopoulou, A., 2019. Geomorph: Software for geometric morphometric analyses. R Package Version 3.3.1. https://cran.r-project.org/web/packages/geomorph/index.html.

Alba, D.M., Delson, E., Carnevale, G., Colombero, S., Delfino, M., Giuntelli, P., Pavia, M., Pavia, G., 2014a. First joint record of *Mesopithecus* and cf. *Macaca* in the Miocene of Europe. J. Hum. Evol. 67, 1−18.

Alba, D.M., Colombero, S., Delfino, M., Martínez-Navarro, B., Pavia, M., Rook, L., 2014b. A thorny question: The taxonomic identity of the Pirro Nord cervical vertebrae revisited. J. Hum. Evol. 76, 92−106.

Alba, D.M., Montoya, P., Pina, M., Rook, L., Abella, J., Morales, J., Delson, E., 2015a. First record of *Mesopithecus* (Cercopithecidae, Colobinae) from the Miocene of the Iberian Peninsula. J. Hum. Evol. 88, 1−14.

Alba, D.M., Almécija, S., DeMiguel, D., Fortuny, J., Pérez de los Ríos, M., Pina, M., Robles, J.M., Moyà-Solà, S., 2015b. Miocene small-bodied ape from Eurasia sheds light on hominoid evolution. Science 350, aab2625.

Arnold, C., Matthews, L.J., Nunn, C.L., 2010. The 10kTrees website: A new online resource for primate phylogeny. Evol. Anthropol. 19, 114−118.

Barry, J.C., Jacobs, L.L., Kelley, J., 1987. An early middle Miocene catarrhine from Pakistan with comments on the dispersal of catarrhines into Eurasia. J. Hum. Evol. 15, 501–508.
Beard, K.C., MacPhee, R.D.E., 1994. Cranial anatomy of *Shoshonius* and the antiquity of Anthropoidea. In: Fleagle, J.G., Kay, R.F. (Eds.), Anthropoid Origins. Plenum Press, New York, pp. 55–97.
Beaudet, A., Clarke, R.J., Heaton, J.L., Pickering, T.R., Carlson, K.J., Crompton, R.H., Jashashvili, T., Bruxelles, L., Jakata, K., Bam, L., Van Hoorebeke, L., Kuman, K., Stratford, D., 2020. The atlas of StW 573 and the late emergence of human-like head mobility and brain metabolism. Sci. Rep. 10, 4285.
Begun, D.R., 2002. The Pliopithecoidea. In: Hartwig, W.C. (Ed.), The Primate Fossil Record. Cambridge University Press, Cambridge, pp. 221–240.
Begun, D.R., 2015. Fossil record of Miocene hominoids. In: Henke, W., Tattersall, I. (Eds.), Handbook of Paleoanthropology, 2nd ed. Springer, Heidelberg, pp. 1261–1332.
Begun, D.R., 2017. Evolution of the Pliopithecoidea. In: Fuentes, A. (Ed.), The International Encyclopedia of Primatology. John Wiley & Sons, Hoboken. https://doi.org/10.1002/9781119179313.wbprim0165.
Benefit, B.R., 1999. *Victoriapithecus*: The key to Old World monkey and catarrhine origins. Evol. Anthropol. 7, 155–174.
Benefit, B.R., McCrossin, M.L., 1997. Earliest known Old World monkey skull. Nature 388, 368–371.
Benefit, B.R., McCrossin, M.L., 2015. A window into ape evolution. Science 350, 515–516.
Bernor, R.L., Flynn, L.J., Harrison, T., Hussain, S.T., Kelley, J., 1988. *Dionysopithecus* from southern Pakistan and the biochronology and biogeography of early Eurasian catarrhines. J. Hum. Evol. 17, 339–358.
Blomberg, S.P., Garland, T., Ives, A.R., 2003. Testing for phylogenetic signal in comparative data: Behavioral traits are more labile. Evolution 57, 717–745.
Bookstein, F.L., 1991. Morphometric Tools for Landmark Data: Geometry and Biology. Cambridge University Press, Cambridge.
Boyer, D.M., Kirk, E.C., Silcox, M.T., Gunnell, G.F., Gilbert, C.C., Yapuncich, G.S., Allen, K.L., Welch, E., Bloch, J.I., Gonzales, L.A., Kay, R.F., Seiffert, E.R., 2016. Internal carotid arterial canal size and scaling in Euarchonta: Re-assessing implications for arterial patency and phylogenetic relationships in early fossil primates. J. Hum. Evol. 97, 123–144.
Boyer, D.M., Harrington, A.R., 2018. Scaling of bony canals for encephalic vessels in euarchontans: Implications for the role of the vertebral artery and brain metabolism. J. Hum. Evol. 114, 85–101.
Boyer, D.M., Harrington, A.R., 2019. New estimates of blood flow rates in the vertebral artery of euarchontans and their implications for encephalic blood flow scaling: A response to Seymour and Snelling (2018). J. Hum. Evol. 128, 93–98.
Bugge, J., 1974. The cephalic arterial system in insectivores, primates, rodents, and lagomorphs, with special reference to the systematic classification. Acta Anat. 87, 1–160.
Bugge, J., 1980. Comparative anatomical study of the carotid circulation in new and Old World primates. In: Ciochon, R.L., Chiarelli, A.B. (Eds.), Evolutionary Biology of the New World Monkeys and Continental Drift. Plenum Press, New York, pp. 293–316.
Cardini, A., O'Higgins, P., Rohlf, F.J., 2019. Seeing distinct groups where there are none: Spurious patterns from between-group PCA. Evol. Biol. 46, 303–316.
Cardini, A., Polly, P.D., 2020. Cross-validated between group PCA scatterplots: A solution to spurious group separation? Evol. Biol. 47, 85–95.
Cartmill, M., MacPhee, R.D.E., Simons, E.L., 1981. Anatomy of the temporal bone in early anthropoids, with remarks on the problem of anthropoid origins. Am. J. Phys. Anthropol. 56, 1–21.
Casanovas-Vilar, I., Alba, D.M., Garcés, M., Robles, J.M., Moyà-Solà, S., 2011. Updated chronology for the Miocene hominoid radiation in Western Eurasia. Proc. Natl. Acad. Sci. USA 108, 5554–5559.
Chatterjee, H.J., Ho, S.Y.W., Barnes, I., Groves, C., 2009. Estimating the phylogeny and divergence times of primates using a supermatrix approach. BMC Evol. Biol. 13, 259.
Collyer, M.L., Adams, D.C., 2018. RRPP: An R package for fitting linear models to high-dimensional data using residual randomization. Methods Ecol. Evol. 9, 1772–1779.
Davis, P.R., Napier, J.R., 1963. A reconstruction of the skull of *Proconsul africanus* (R.S.51). Folia Primatol. 1, 20–28.
Delson, E., Terranova, C.J., Sargis, E.J., Jungers, W.L., Jablonski, N.G.C., Dechow, P., 2000. Body mass in Cercopithecidae (Primates, Mammalia): Estimation and scaling in extinct and extant taxa. Anthropol. Pap. Am. Mus. Nat. Hist. 83, 1–159.
Diogo, R., Wood, B., 2011. Soft-tissue anatomy of the primates: Phylogenetic analyses based on the muscles of the head, neck, pectoral region and upper limb, with notes on the evolution of these muscles. J. Anat. 219, 272–359.
Finstermeier, K., Zinner, D., Brameier, M., Meyer, M., Kreuz, E., Hofreiter, M., Roos, C., 2013. A mitogenomic phylogeny of living primates. PLoS One 8, e69504.
Gibbs, S., Collard, M., Wood, B., 2000. Soft-tissue characters in higher primate phylogenetics. Proc. Natl. Acad. Sci. USA 97, 11130–11132.
Gibbs, S., Collard, M., Wood, B., 2002. Soft-tissue anatomy of the extant hominoids: A review and phylogenetic analysis. J. Anat. 200, 3–49.
Gilbert, C.C., Bibi, F., Hill, A., Beech, M.J., 2014. Early guenon from the late Miocene Baynunah Formation, Abu Dhabi, with implications for cercopithecoid biogeography and evolution. Proc. Natl. Acad. Sci. USA 111, 10119–10124.
Gilbert, C.C., Pugh, K.D., Fleagle, J.G., 2020a. Dispersal of Miocene hominoids (and pliopithecoids) from Africa to Eurasia in light of changing tectonics and climate. In: Prasad, G.V., Patnaik, R. (Eds.), Biological Consequences of Plate Tectonics. New Perspectives on Post-gondwana Break-Up—A Tribute to Ashok Sahni. Springer, Cham, pp. 393–412.
Gilbert, C.C., Ortiz, A., Pugh, K.D., Campisano, C.J., Patel, B.A., Premjit, N., Fleagle, J.G., Patnaik, R., 2020b. New Middle Miocene ape (Primates: Hylobatidae) from Ramnagar, India fills major gaps in the hominoid fossil record. Proc. R. Soc. B 287, 20201655.
Gould, S.J., 1966. Allometry and size in ontogeny and phylogeny. Biol. Rev. 41, 587–640.
Harrison, T., 2010. Dendropithecoidea, Proconsuloidea and Hominoidea (Catarrhini, primates). In: Werdelin, L., Sanders, W.J. (Eds.), Cenozoic Mammals of Africa. University of California Press, Berkeley, pp. 429–469.
Harrison, T., 2013. Catarrhine origins. In: Begun, D.R. (Ed.), A Companion to Paleoanthropology. Blackwell Publishing, Oxford, pp. 376–396.
Harrison, T., 2016. The fossil record and evolutionary history of hylobatids. In: Reichard, U.H., Hirai, H., Barelli, C. (Eds.), Evolution of Gibbons and Siamang. Phylogeny, Morphology, and Cognition. Springer, New York, pp. 90–110.
Harrison, T., 2017. Miocene primates. In: Fuentes, A. (Ed.), The International Encyclopedia of Primatology. John Wiley & Sons, Hoboken. https://doi.org/10.1002/9781119179313.wbprim0227.
Harrison, T., Gu, Y., 1999. Taxonomy and phylogenetic relationships of early Miocene catarrhines from Sihong, China. J. Hum. Evol. 37, 225–277.
Harrison, T., Zhang, Y., Wei, G., Sun, C., Wang, Y., Liu, J., Tong, H., Huang, B., Xu, F., 2020. A new genus of pliopithecoid from the late Early Miocene of China and its implications for understanding the paleozoogeography of the Pliopithecoidea. J. Hum. Evol. 145, 102838.
Harzhauser, M., Kroh, A., Mandic, O., Piller, W.E., Göhlich, U., Reuter, M., Berning, B., 2007. Biogeographic responses to geodynamics: A key study all around the Oligo–Miocene Tethyan Seaway. Zool. Anz. 246, 241–256.
Jablonski, N., Frost, S., 2010. Cercopithecoidea. In: Cenozoic Mammals of Africa. University of California Press, Berkeley, pp. 393–428.
Kay, R.F., Simons, E., Ross, J.L., 2008. The basicranial anatomy of African Eocene/Oligocene anthropoids. Are there any clues for platyrrhine origins? In: Fleagle, J.G., Gilbert, C.C. (Eds.), Elwyn Simons: A Search for Origins. Springer, New York, pp. 125–158.
Legendre, P., 2018. lmodel2: Model II regression. https://cran.r-project.org/web/packages/lmodel2/index.html.
Lieberman, D.E., 1999. Homology and hominid phylogeny: Problems and potential solutions. Evol. Anthropol. 7, 142–151.
Lieberman, D.E., McCarthy, R.C., 1999. The ontogeny of cranial base angulation in humans and chimpanzees and its implications for reconstructing pharyngeal dimensions. J. Hum. Evol. 36, 487–517.
Lieberman, D.E., Ross, C.F., Ravosa, M.J., 2000. The primate cranial base: Ontogeny, function, and integration. Yearbk. Phys. Anthropol. 43, 117–169.
MacPhee, R.D.E., Cartmill, M., 1986. Basicranial structures and primate systematics. In: Swisher, D.R., Erwin, J. (Eds.), Comparative Primate Biology: Systematics, Evolution, and Anatomy. Alan R. Liss, New York, pp. 219–275.
McNulty, K.P., Begun, D.R., Kelley, J., Manthi, F.K., Mbua, E.N., 2015. A systematic revision of *Proconsul* with the description of a new genus of early Miocene hominoid. J. Hum. Evol. 84, 42–61.
Meyer, D., Rinaldi, IrD., Ramlee, H., Perwitasari-Farajallah, D., Hodges, J.K., Roos, C., 2011. Mitochondrial phylogeny of leaf monkeys (genus *Presbytis*, Eschscholtz, 1821) with implications for taxonomy and conservation. Mol. Phylogenet. Evol. 59, 311–319.
Nengo, I., Tafforeau, P., Gilbert, C.C., Fleagle, J.G., Miller, E.R., Feibel, C., Fox, D.L., Feinberg, J., Pugh, K.D., Berruyer, C., Mana, S., Engle, Z., Spoor, F., 2017. New infant cranium from the African Miocene sheds light on ape evolution. Nature 548, 169–174.
Pagel, M., 1999. Inferring the historical patterns of biological evolution. Nature 401, 877–884.
Perelman, P., Johnson, W.E., Roos, C., Seuánez, H.N., Horvath, J.E., Moreira, M.A.M., Kessing, B., Pontius, J., Roelke, M., Rumpler, Y., Schneider, M.P.C., Silva, A., O'Brien, S.J., Pecon-Slattery, J., 2011. A molecular phylogeny of living primates. PLoS Genet. 7, e1001342.
Pozzi, L., Hodgson, J.A., Burrell, A.S., Sterner, K.N., Raaum, R.L., Disotell, T.R., 2014. Primate phylogenetic relationships and divergence dates inferred from complete mitochondrial genomes. Mol. Phylogenet. Evol. 75, 165–183.
R Core Team, 2020. R: A Language and Environment for Statistical Computing. R Foundation for Statistical Computing, Vienna.
Rae, T.C., 1999. Mosaic evolution in the origin of the Hominoidea. Folia Primatol. 70, 125–135.
Revell, L.J., 2012. *Phytools*: An R package for phylogenetic comparative biology (and other things). Methods Ecol. Evol. 3, 217–223.
Roos, C., Kothe, M., Alba, D.M., Delson, E., Zinner, D., 2019. The radiation of macaques out of Africa: Evidence from mitogenome divergence times and the fossil record. J. Hum. Evol. 133, 114–132.
Rosenberger, A.L., Szalay, F., 1980. On the tarsiiform origins of the Anthropoidea. In: Ciochon, R.L., Chiarelli, A.B. (Eds.), Evolutionary Biology of the New World Monkeys and Contnental Drift. Plenum Press, New York, pp. 139–157.
Ross, C., 1994. Evidence for anthropoid and tarsier relationships. In: Fleagle, J.G., Kay, R.F. (Eds.), Anthropoid Origins. Plenum Press, New York, pp. 469–547.
Ross, C., Williams, B., Kay, R.F., 1998. Phylogenetic analysis of anthropoid relationships. J. Hum. Evol. 35, 221–307.
Rossie, J.B., Hill, A., 2018. A new species of *Simiolus* from the middle Miocene of the Tugen hills, Kenya. J. Hum. Evol. 125, 50–58.

Sankhyan, A.R., Kelley, J., Harrison, T., 2017. A highly derived pliopithecoid from the Late Miocene of Haritalyangar, India. J. Hum. Evol. 105, 1–12.
Schlager, S., 2017. Morpho and Rvcg e shape analysis in R: R-packages for geometric morphometrics, shape analysis and surface manipulations. In: Zheng, G., Li, S., Székely, G. (Eds.), Statistical Shape and Deformation Analysis. Methods, Implementation and Applications. Academic Press, London, pp. 217–256. https://cran.r-project.org/web/packages/Morpho/index.html.
Schliep, K.P., 2011. phangorn: Phylogenetic analysis in R. Bioinformatics 27, 592–593.
Seiffert, E.R., 2006. Revised age estimates for the later Paleogene mammal faunas of Egypt and Oman. Proc. Natl. Acad. Sci. USA 103, 5000–5005.
Seiffert, E.R., 2012. Early primate evolution in Afro-Arabia. Evol. Anthropol. 21, 239–253.
Seiffert, E.R., Simons, E.L., Fleagle, J.G., Godinot, M., 2010. Paleogene anthropoids. In: Werdelin, L., Sanders, W.J. (Eds.), Cenozoic Mammals of Africa. University of California Press, Berkeley, pp. 369–391.
Shoshani, J., Groves, C.P., Simons, E.L., Gunnell, G.F., 1996. Primate phylogeny: Morphological vs molecular results. Mol. Phylogenet. Evol. 5, 102–154.
Sidlauskas, B., 2008. Continuous and arrested morphological diversification in sister clades of characiform fishes: A phylomorphospace approach. Evolution 62, 3135–3156.
Smith, R.J., Jungers, W.L., 1997. Body mass in comparative primatology. J. Hum. Evol. 32, 523–559.
Springer, M.S., Meredith, R.W., Gatesy, J., Emerling, C.A., Park, J., Rabosky, D.L., Stadler, T., Steiner, C., Ryder, O.A., Janečka, J.E., Fisher, C.A., Murphy, W.J., 2012. Macroevolutionary dynamics and historical biogeography of primate diversification inferred from a species supermatrix. PLoS One 7, e49521.
Stevens, N.J., Seiffert, E.R., O'Connor, P.M., Roberts, E.M., Schmitz, M.D., Krause, C., Gorscak, E., Ngasala, S., Hieronymus, T.L., Temu, J., 2013. Palaeontological evidence for an Oligocene divergence between Old World monkeys and apes. Nature 497, 611–614.
Turner, T.R., Schmitt, C.A., Cramer, J.D., Lorenz, J., Grobler, J.P., Jolly, C.J., Freimer, N.B., 2018. Morphological variation in the genus *Chlorocebus*: Ecogeographic and anthropogenically mediated variation in body mass, postcranial morphology, and growth. Am. J. Phys. Anthropol. 166 (S3), 682–707.
Urciuoli, A., Zanolli, C., Beaudet, A., Dumoncel, J., Santos, F., Moyà-Solà, S., Alba, D.M., 2020. The evolution of the vestibular apparatus in apes and humans. eLife 9, e51261.
Urciuoli, A., Zanolli, C., Beaudet, A., Pina, M., Almécija, S., Moyà-Solà, S., Alba, D.M., 2021a. A comparative analysis of the vestibular apparatus in *Epipliopithecus vindobonensis*: Phylogenetic implications. J. Hum. Evol. 151, 102930.
Urciuoli, A., Zanolli, C., Almécija, S., Beaudet, A., Dumoncel, J., Morimoto, N., Nakatsukasa, M., Moyà-Solà, S., Begun, D.R., Alba, D.M., 2021b. Reassessment of the phylogenetic relationships of the late Miocene apes *Hispanopithecus* and *Rudapithecus* based on vestibular morphology. Proc. Natl. Acad. Sci. USA 118, e2015215118.
Walker, A., Teaford, M.F., Martin, L., Andrews, P., 1993. A new species of *Proconsul* from the early Miocene of Rusinga/Mfangano Islands, Kenya. J. Hum. Evol. 25, 43–53.
Zalmout, I.S., Sanders, W.J., MacLatchy, L., Gunnell, G., Al-Mufarreh, Y.A., Ali, M.A., Nasser, A.-A.H., Al-Masary, A.M., Al-Sobhi, S.A., Nadhra, A.O., Matari, A.H., Wilson, J.A., Gingerich, P.D., 2010. New Oligocene primate from Saudi Arabia and the divergence of apes and Old World monkeys. Nature 466, 360–365.
Zapfe, H., 1961. Die Primatenfunde aus der miozänen Spaltenfüllung von Neudorf an der March (Děvínská Nová Ves), Tschechoslowakei. Schweiz. Palaeontol. Abh. 78, 1–293.

Supplementary Online Material (SOM):

Comparative anatomy of the carotid canal in the Miocene small-bodied catarrhine *Pliobates cataloniae*

Florian Bouchet [a, *], Alessandro Urciuoli [a], Amélie Beaudet [b, c, d, a], Marta Pina [e, a], Salvador Moyà-Solà [a, f, g], David M. Alba [a, *]

[a] *Institut Català de Paleontologia Miquel Crusafont, Universitat Autònoma de Barcelona, Edifici ICTA-ICP, c/ Columnes s/n, Campus de la UAB, 08193 Cerdanyola del Vallès, Barcelona, Spain*

[b] *Department of Archaeology, University of Cambridge, The Old Schools, Trinity Lane, Cambridge CB2 1TN, UK*

[c] *School of Geography, Archaeology and Environmental Studies, University of the Witwatersrand, 1 Jan Smuts Avenue, Braamfontein 2000, Johannesburg, South Africa*

[d] *Department of Anatomy, University of Pretoria, Lynnwood Road, Hatfield 0002, Pretoria, South Africa*

[e] *Department of Earth and Environmental Sciences, University of Manchester, Williamson Building, Oxford Road, Manchester M13 9PL, UK*

[f] *Institució Catalana de Recerca i Estudis Avançats (ICREA), Passeig de Lluís Companys 23, 08010 Barcelona, Spain*

[g] *Unitat d'Antropologia (Dept. BABVE), Universitat Autònoma de Barcelona, Edifici C, Facultat de Biociències, Campus de la UAB, 08193 Cerdanyola del Vallès, Barcelona, Spain*

[*] Corresponding authors.

E-mail addresses: florian.bouchet@icp.cat (F. Bouchet); david.alba@icp.cat (D.M. Alba).

SOM S1

Extended methodology

3D carotid canal surfaces

For each specimen, the carotid canal was virtually extracted through semiautomatic threshold-based segmentation in Avizo v. 7.0 (Visualization Sciences Group, Bordeaux). The right carotid canal was segmented for most specimens; when this was not possible, the left canal was segmented and mirrored. We devised a protocol to identify the two ends (anterior and posterior) of the carotid canal and cut them at homologous points (Fig. 1; SOM Fig. S1), to obtain 3D canal surfaces comparable among specimens. For the posterior end of the canal, we placed landmarks on its external aperture (carotid foramen; SOM Fig. S1a, b), computed the best-fit plane to these landmarks, translated it to be located at the centroid of the landmark set, and finally cut the canal (Fig. 1a). The centroid of the landmarks on the carotid foramen was taken as the posterior endpoint of the canal (Fig. 1l).

The methodology employed to cut the anterior part of the carotid canal was more complex, because its opening on the endocranial surface of the petrosal is irregular and displays a variable outline among individuals. Furthermore, it was not completely preserved in fossil specimens we included here. We started by defining a landmark located posteriorly to the canal opening, and used it to determine the anterior limit at which we could later cut the anterior part of the canal. We defined a landmark termed 'intersection ridge–groove' (IRG) that corresponds to the intersection between the anterior pyramidal ridge and the groove of the greater superficial petrosal nerve (SOM Fig. S1c, d; Table 2). Based on IRG, we applied a semiautomatic protocol coded on R v. 3.6.3 (R Core Team, 2020; see script in SOM File S1) to find the plane orthogonal to the 3D carotid canal surface passing through IRG. In particular, the 3D canal surface is first generated and smoothed in Avizo (using a constrained smoothing and a smoothing extent of 3) and then imported as a cloud of points in R (Fig. 1b); the orthogonal projection of IRG onto the canal (IRG') is calculated (Fig. 1c). These two points (IRG and IRG') define a main axis, around which infinity of points can be generated, further enabling the creation of infinity of planes. Indeed, a plane can be defined by three points expressed as two vectors, and the axis defined by IRG and IRG' corresponds to one of the two vectors necessary to compute the orthogonal plane to the canal (passing through IRG), because IRG' is the orthogonal projection of IRG onto the canal. However, to obtain the second vector, a third point is required, which cannot be defined a priori. We decided to

define the cutting plane as the one that is orthogonal to the 3D canal surface (and therefore to the canal streamline) and thus that minimizes the cross-sectional area resulting from the cut. The protocol generates multiple cutting planes—defined on IRG, IRG', and multiple possible third points—and calculates the cut area for each of them. In particular, we created 360 equally distributed points (differing in 1° of orientation) around the IRG–IRG' axis (Fig. 1d) and computed the cutting cross-sectional area for all the 360 possible cutting planes (Fig. 1e, f). For each plane possibility, among the cloud of points representing the canal, the points that are closest to the plane (i.e., those having an orthogonal distance to the plane equal or shorter than the distance between two adjacent points of the cloud) are identified (Fig. 1g). Among them, only the most external ones are kept and used to form a convex hull approximating the contour of the canal cross-section (Fig. 1h). The area subtended by the convex hull is then subdivided in *n*-2 triangles, where *n* is the number of points that form the hull, using one of the points as the shared vertex (the most acute one) for all the triangles; the area of the triangles is computed and their sum is used as an approximation of the total area of the cross-section (Fig. 1i). The plane for which the resulting cross-sectional area is the smallest is kept and used as reference for cutting the canal at its anterior end (Fig. 1i, j). The centroid of the cross-section obtained by cutting with this orthogonal plane (Fig. 2h–i) is calculated and used as the anterior endpoint of the canal (Fig. 1l).

Carotid canal orientation

We quantified the orientation of the carotid canal within the petrosal by computing a 3D vector representing the canal direction and decomposing it into two 2D angles relative to standard anatomical planes: one angle represents the canal superior orientation (2DYZA) along the (para)sagittal plane, and the other represents its medial orientation (2DXYA) along a transverse plane—respectively corresponding to canal 'orientation' and 'direction' sensu Alba et al. (2015: Tables S5 and S6). The 3D vector representing the canal was computed as a single direction, from the posterior to the anterior endpoints of the canal. All the specimens were first put in the same coordinate system by performing a generalized Procrustes analysis (GPA; Rohlf and Slice, 1990; Bookstein, 1991) using the R package 'Geomorph' v. 3.3.1 (Adams et al., 2019) based on nine petrosal/tympanic landmarks (Fig. 2; Table 2). This allowed us to scale, orient, and locate the petrosals in a standardized way within a common Cartesian coordinate system. The translation-scaling-rotation parameters resulting from this

alignment were then extracted and applied to the two endpoints of the canal vector. Performing the alignment on the petrosal, instead of the canal endpoints or both structures simultaneously, enables the retention of the canal position, orientation and shape inside the petrosal, for each specimen. The coordinates of the posterior and anterior endpoints after the petrosal/tympanic-based alignment were used to compute the 3D vector representing the 3D canal direction.

As the specimens were prealigned, we were able to use a single reference vector to calculate the two 2D angles. Despite some variation among the sample, there is an overall correspondence (with no extreme deviations) between spatial axes of the common Cartesian coordinate system and canal directions after alignment: the X-axis corresponds to the anteromedial–posterolateral direction of the canal, the Y-axis corresponds to its inferomedial–superolateral direction, and the Z-axis corresponds to its anterolateral–posteromedial direction. Considering these correspondences, 2DYZA was calculated as the 2D angle between the YZ coordinates of the canal vector and a reference vector with coordinates (1, -1) corresponding to the cranial anteroposterior axis (from posterior to anterior). In turn, 2DXYA was calculated as the 2D angle between the XY coordinates of the canal vector and a reference vector with coordinates (-0.2, 1) also corresponding to the cranial anteroposterior axis (from posterior to anterior). While in anthropoids the canal runs from a posterolateral location to an anteromedial location, after alignment some specimens display a canal running almost anteroposteriorly or slightly (postero)medio(antero)laterally. To take into account those exceptions the 2DXYA angle was calculated so that positive values correspond to medially oriented canals and negative values identify canals (only a few) slightly laterally oriented.

Because the alignment is based on petrosal/tympanic landmarks, one should consider the possibility that two specimens possessing similar angles relative to the petrosal may display different angles if computed relative to the whole cranium, depending on the orientation and position of the petrosal inside the cranium. However, based on Spoor's (1993) data, differences of superior petrosal surface orientations in the sagittal plane and superior and inferior petrosal surface orientations in the transverse plane are not significant among the main crown anthropoid clades. Furthermore, relying on petrosal/tympanic landmarks for scaling-translating-orienting carotid canal specimens, instead of landmarks from the cranium as a whole, has several advantages besides enabling the analysis of fragmentary fossil

remains. In particular, this procedure may prevent alignment problems related to striking shape differences between extant lineages (such as the elongated muzzle of some papionins, the much more globulous neurocranium of some hominoids, the longer parietal of platyrrhines, etc.), because the variation in petrosal shape seems less marked.

Carotid canal proportions

After cutting the two ends of the carotid canal, the 3D canal surfaces were generated again without smoothing in Avizo, and the volume (V, in mm^3) of the closed 3D surfaces was computed using the module 'Surface Area Volume'. The 3D surfaces were then reimported in R and, for each specimen, we calculated canal length (L, in mm). To do so, we computed nine semilandmarks corresponding to the centroids of the canal cross-sections obtained by means of nine equidistant slices generated along the two canal endpoints (i.e., type III landmarks; Bookstein, 1991). The resulting 11 streampoints (2 endpoints + 9 centroids in between) were used to generate 8 equidistant streampoints between the 2 endpoints using the 'digit.curve' function of 'Geomorph' v. 3.3.1—the sliding process embedded in this function requiring to set a number of final points smaller than the original number of points. Based on these 10 equidistant streampoints representing the canal streamline we computed nine segments (distances), whose sum was taken as canal length.

Carotid canal course within the petrosal

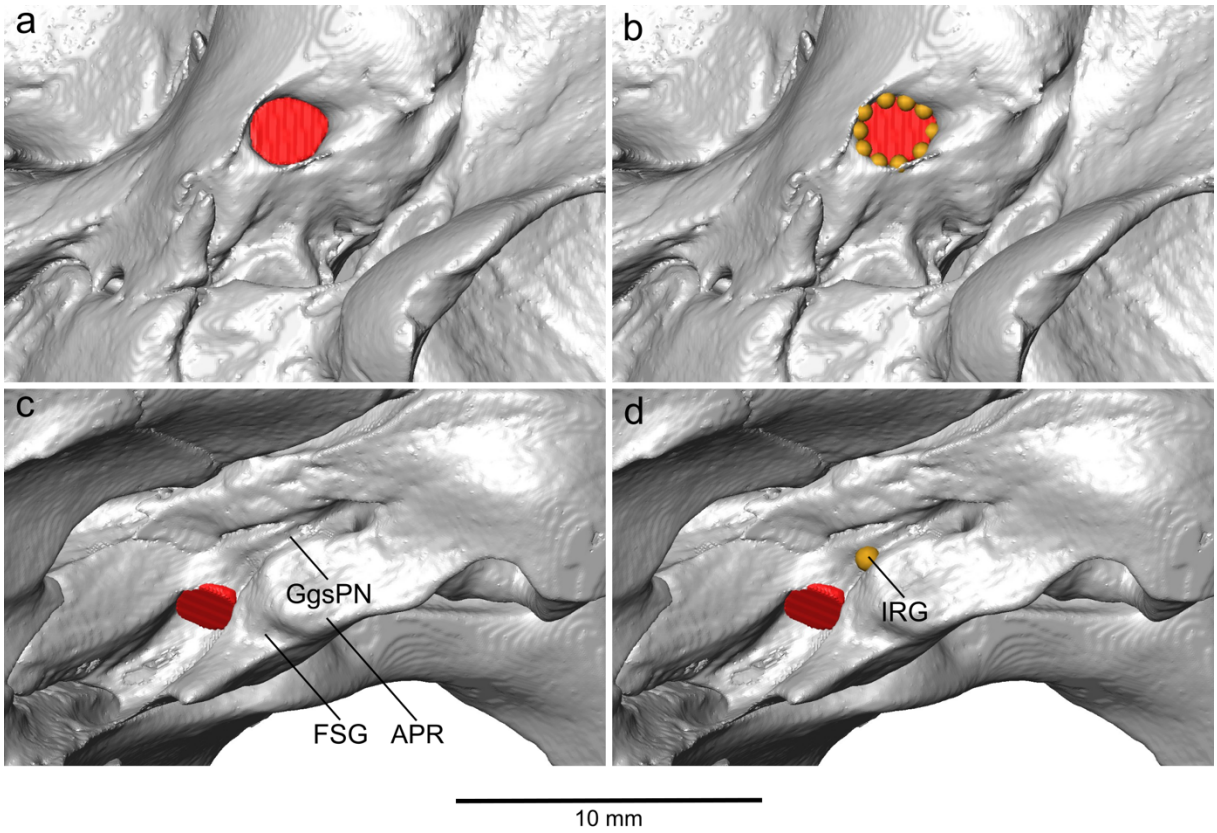
To assess the course of the carotid canal within the petrosal we used a similar approach to that employed for computing L. We took the 10 equidistant streampoints previously computed during the calculation of L. As mentioned above, these 10 streampoints follow the streamline of the canal, i.e., de facto they represent the canal course. Then we applied the translation-scaling-rotation parameters resulting from the alignment of the petrosals described above to the 10 streampoints. As for the canal orientation, this procedure allowed us retaining the information on the variation of position, orientation and shape of the canal inside the petrosal. The configuration of the 10 canal streampoints obtained after alignment therefore represents the course of the carotid canal within the petrosal.

Phylogenetic tree

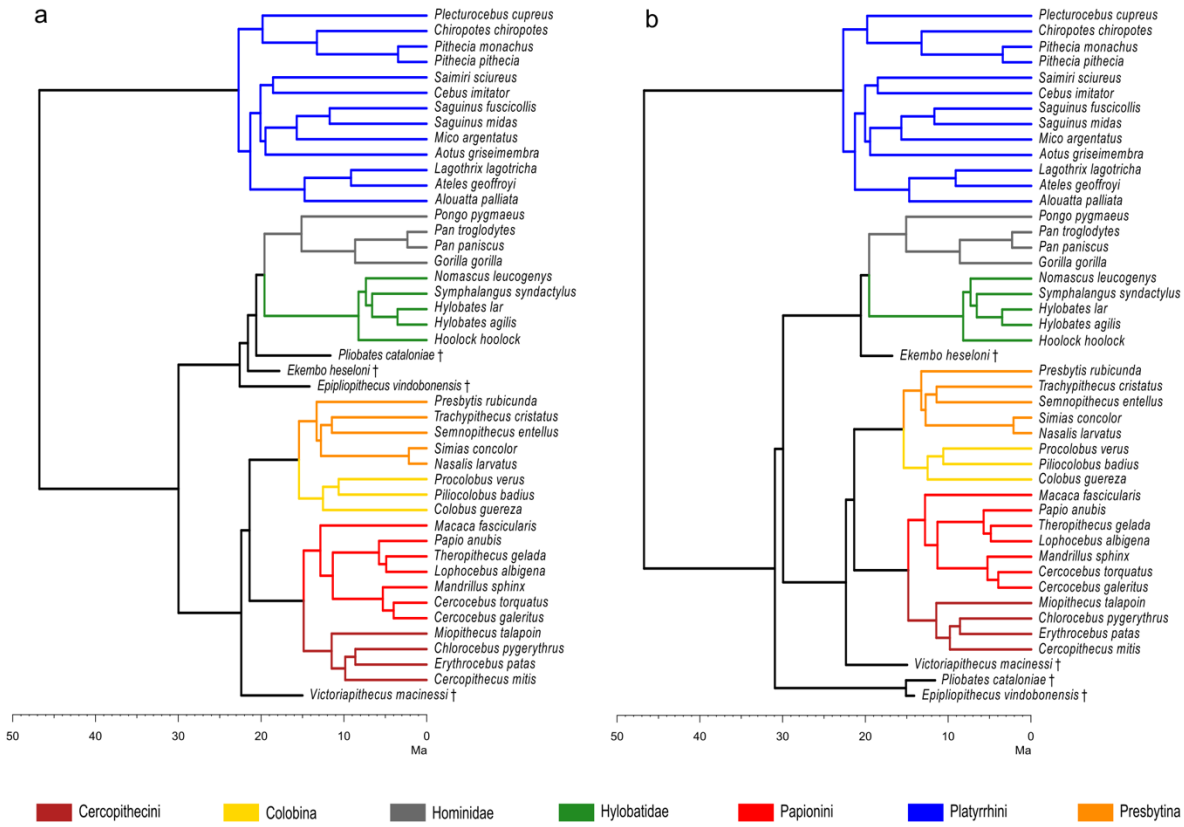
To compute PGLS regressions and quantify phylogenetic signal we used a time-calibrated tree representing the phylogenetic relationships among the extant taxa included in the comparative sample. The tree was derived from the 10kTrees website (Arnold et al., 2010), with some modifications to account for not included species in the 10kTrees website: (1) *Simias concolor* was added as the sister taxon of *Nasalis larvatus* with a divergence time at 2.16 Ma (Springer et al., 2012); (2) *Presbytis rubicunda* was replaced by data on *Presbytis melalophos*, which is its closest species (Meyer et al., 2011; Springer et al., 2012); (3) *Pithecia monachus* was added as the sister taxon of *Pithecia pithecia*, with a divergence time between both taxa set at 3.46 Ma (Springer et al., 2012); (4) *Chiropotes chiropotes* was added as the sister taxon of *Pithecia* spp., with a divergence time set at 13.27 Ma (Springer et al., 2012); (5) *Plecturocebus cupreus* was added as the sister taxon of the *Chiropotes-Pithecia* clade, with a divergence time set at 19.84 Ma (Springer et al., 2012).

We further used two different hypotheses for the phylogenetic relationships among the investigated fossil genera and extant catarrhines, with the exception of *Victoriapithecus*, considered a stem cercopithecoid in both instances. The tips of the fossil taxa were set based on their geological age: *Victoriapithecus* at 15 Ma (Benefit, 1999); *Epipliopithecus* at 14.15 Ma (as estimated from the midpoint of MN6 in Europe based on van der Meulen et al., 2011); *Pliobates* at 11.62 Ma (Alba et al. 2017); and *Ekembo* at 17.8 Ma (as the midpoint of the maximum-minimum range of the Kulu Formation in Rusinga Island, where *E. heseloni* has been found; Drake et al., 1988; Peppe et al., 2009; Harrison, 2010). The divergence between *Victoriapithecus* and crown cercopithecoids was set 1 Myr older than the cercopithecine-colobine divergence (21.41 Ma). Under hypothesis 1 (SOM Fig. S2a), *Epipliopithecus, Ekembo*, and *Pliobates* are considered successive stem hominoids, following the results of Alba et al.'s (2015) cladistic analysis. Their divergence from crown hominoids was set 3, 2 and 1 Myr before the hominid-hylobatid divergence date (19.61 Ma), respectively. In contrast, under hypothesis 2 (SOM Fig. S2b) only *Ekembo* is considered a stem hominoid, while both *Pliobates* and *Epipliopithecus* are considered stem catarrhines within a pliopithecoid clade, following the results of other cladistic analyses (Nengo et al., 2017; Gilbert et al., 2020). The divergence between *Epipliopithecus* and *Pliobates* was set 1 Myr older than the oldest occurrence of either of them (1 Myr older than *Epipliopithecus*, i.e., 15.15 Ma), while the divergence between pliopithecoids and crown catarrhines was set 1 Myr older than the divergence between cercopithecoids and hominoids (30 Ma), as this is

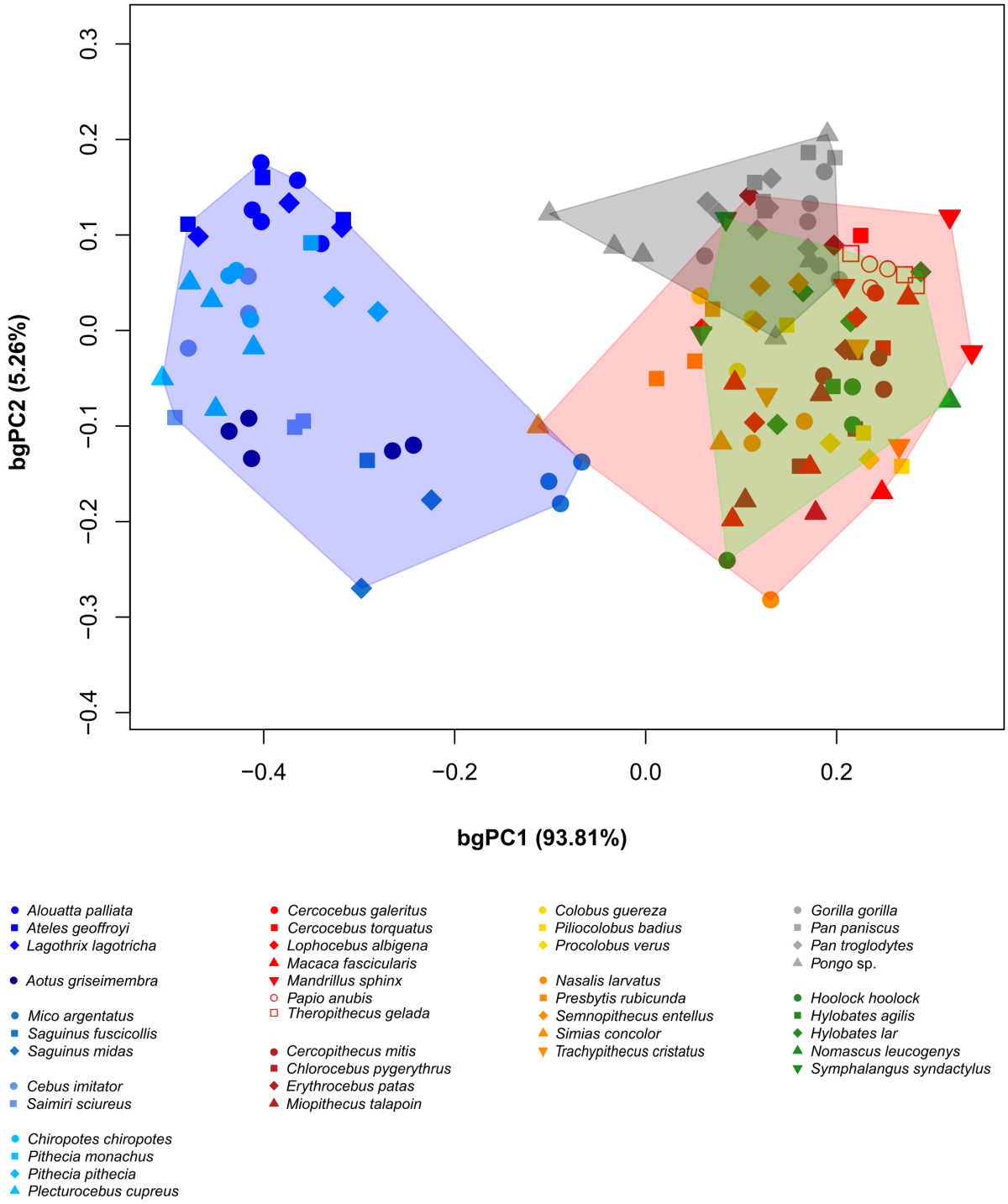
older than the oldest documented occurrence of pliopithecoids in the fossil record (18–17 Ma; Harrison, 2013, 2017; Begun, 2017).



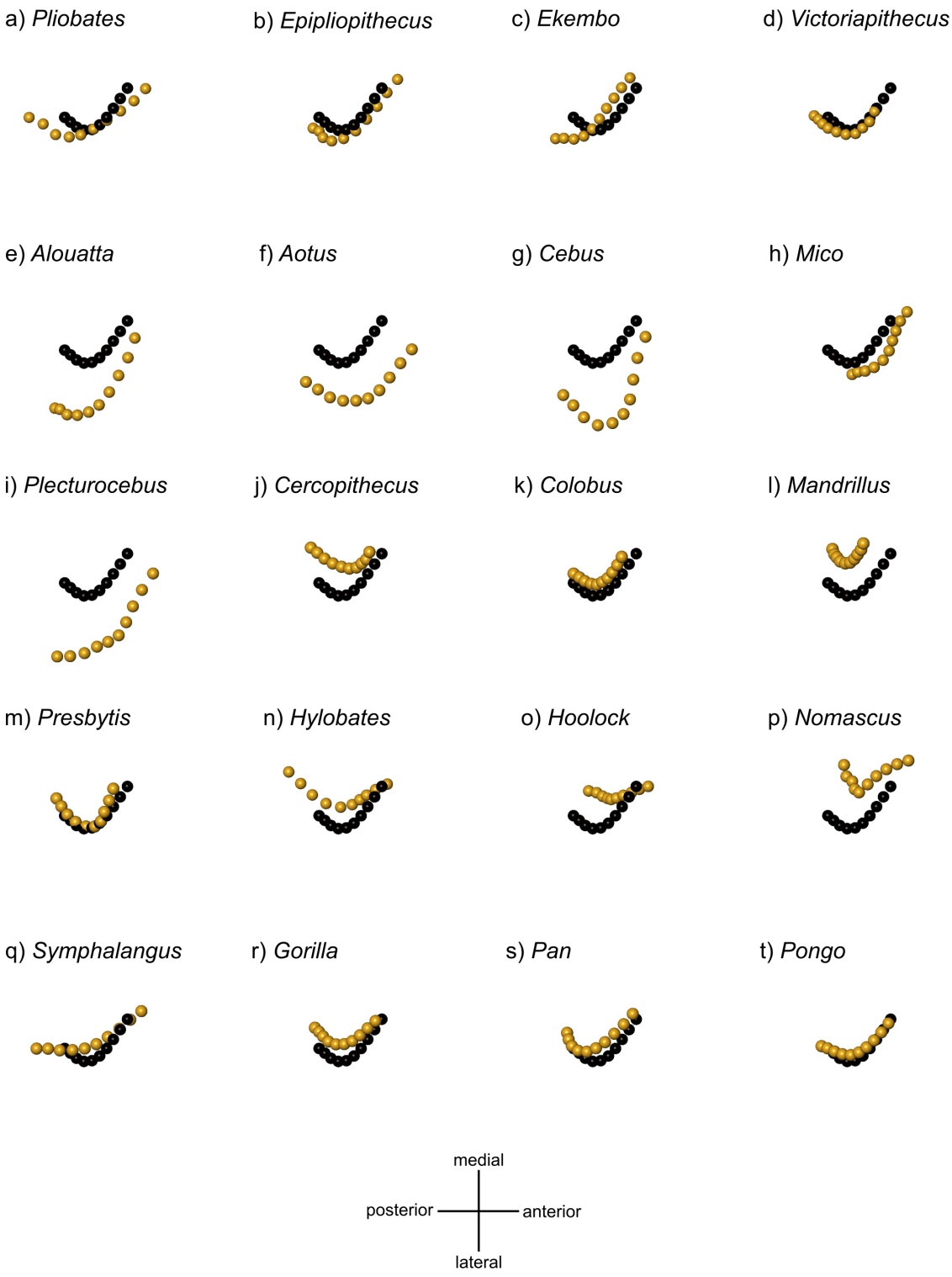
SOM Figure S1. Landmarks used for delimiting the extremities of the carotid canal as exemplified in a *Macaca fascicularis* individual. The 3D canal surface (in red; a) is posteriorly defined by putting landmarks on the rim of the carotid foramen (b). The anterior limit of the canal (in red; c) is identified by placing a landmark (IRG) at the intersection between the anterior pyramidal ridge and the groove for the greater superficial petrosal nerve (d). Abbreviations: APR = anterior pyramidal ridge; FSG = fossa for the semilunar ganglion; GgsPn = groove of the greater superficial petrosal nerve; IRG = intersection ridge–groove.



SOM Figure S2. Time-calibrated phylogenetic trees of extant anthropoids and selected extinct catarrhines (denoted by a dagger) used in this paper to compute phylogenetic generalized least-squares regressions (excluding fossils), phylogenetic signal (excluding fossils), and phylomorphospaces. The trees are based on molecular data and derived from the 10kTrees website v. 3 (Arnold et al., 2010) with some modifications based on Meyer et al. (2011) and Springer et al. (2012). Extinct taxa were added a posteriori according to the two phylogenetic hypotheses considered in this paper: a) *Epipliopithecus*, *Ekembo* and *Pliobates* are considered successive stem hominoids following Alba et al. (2015: Fig. 8); b) *Epipliopithecus* and *Pliobates* are considered sister taxa within a stem catarrhine pliopithecoid clade and *Ekembo* is considered a stem hominoid, following Nengo et al. (2017: Fig. 5) and Gilbert et al. (2020: Fig. 4). *Victoriapithecus* is considered a stem cercopithecoid under both hypotheses. The point estimates for extinct taxa correspond to their occurrence in the fossil record (Drake et al., 1988; Benefit, 1999; Peppe et al., 2009; van der Meulen et al., 2011; Alba et al., 2017). See SOM S1 for further details.

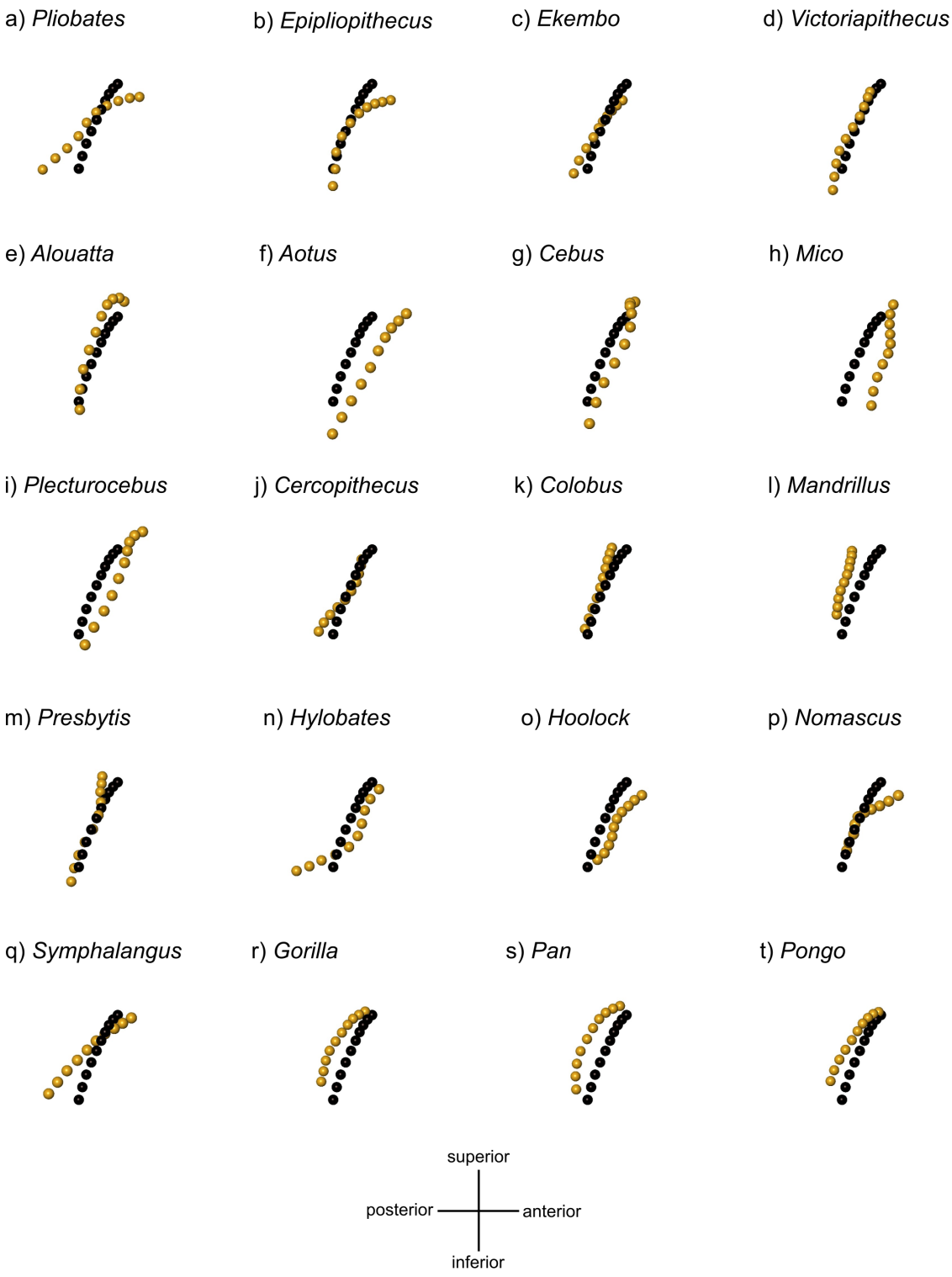


SOM Figure S3. Results of the cross-validated between-group principal component analysis (CV-bgPCA) using main extant anthropoid clades as the grouping factor, as depicted by a bivariate plot of bgPC2 vs. bgPC1. Convex hulls correspond to: platyrrhines (blue), cercopithecids (red), hylobatids (green), and hominids (gray). Abbreviation: CV-bgPC = cross-validated between-group principal component.



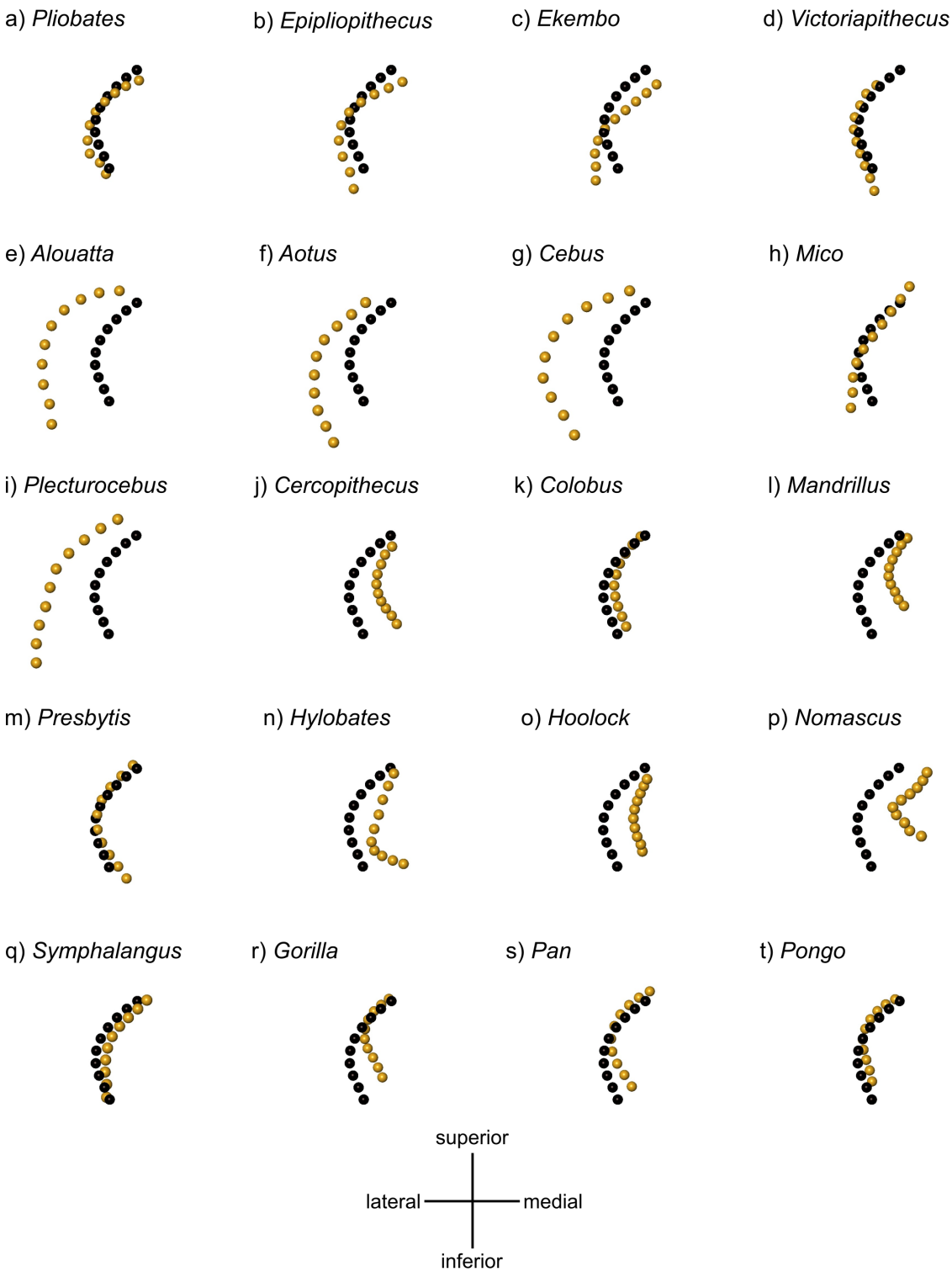
SOM Figure S4. Configurations of the carotid canal course in *Pliobates* compared with fossil and extant anthropoids in superior view: a) *Pliobates* (IPS58443.1); b) *Epipliopithecus* (NHMW 1970/1397/0003); c) *Ekembo* (KNM-RU 2036al); d) *Victoriapithecus* (KNM-MB 29100); e) *Alouatta*; f) *Aotus*; g) *Cebus*; h) *Mico*; i) *Plecturocebus*; j) *Cercopithecus*; k) *Colobus*; l) *Mandrillus*; m) *Presbytis*; n) *Hylobates*; o) *Hoolock*; p) *Nomascus*; q)

Symphalangus; r) *Gorilla*; s) *Pan*; t) *Pongo*. The mean configuration computed for the whole anthropoid sample is represented by black dots while configurations for specimens are represented in beige. For a better understanding of the canal course variation in space the anthropoid mean configuration was used as a reference for visualizing all the configurations at the same relative scale.



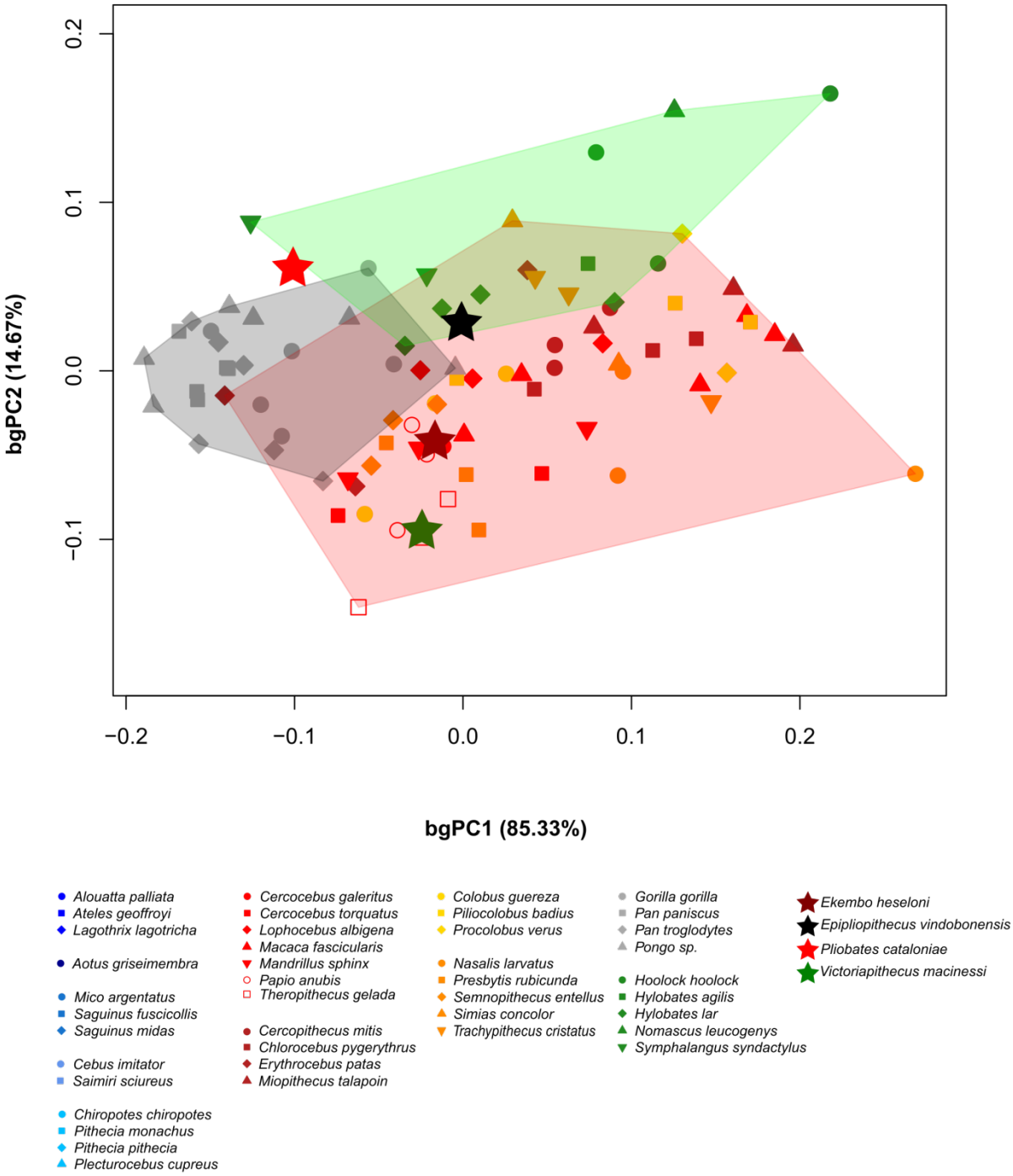
SOM Figure S5. Configurations of the carotid canal course in *Pliobates* compared with fossil and extant anthropoids in lateral view: a) *Pliobates* (IPS58443.1); b) *Epipliopithecus* (NHMW 1970/1397/0003); c) *Ekembo* (KNM-RU 2036al); d) *Victoriapithecus* (KNM-MB 29100); e) *Alouatta*; f) *Aotus*; g) *Cebus*; h) *Mico*; i) *Plecturocebus*; j) *Cercopithecus*; k) *Colobus*; l) *Mandrillus*; m) *Presbytis*; n) *Hylobates*; o) *Hoolock*; p) *Nomascus*; q) *Symphalangus*; r) *Gorilla*;

s) *Pan*; t) *Pongo*. The mean configuration computed for the whole anthropoid sample is represented by black dots while configurations for specimens are represented in beige. For a better understanding of the canal course variation in space the anthropoid mean configuration was used as a reference for visualizing all the configurations at the same relative scale.

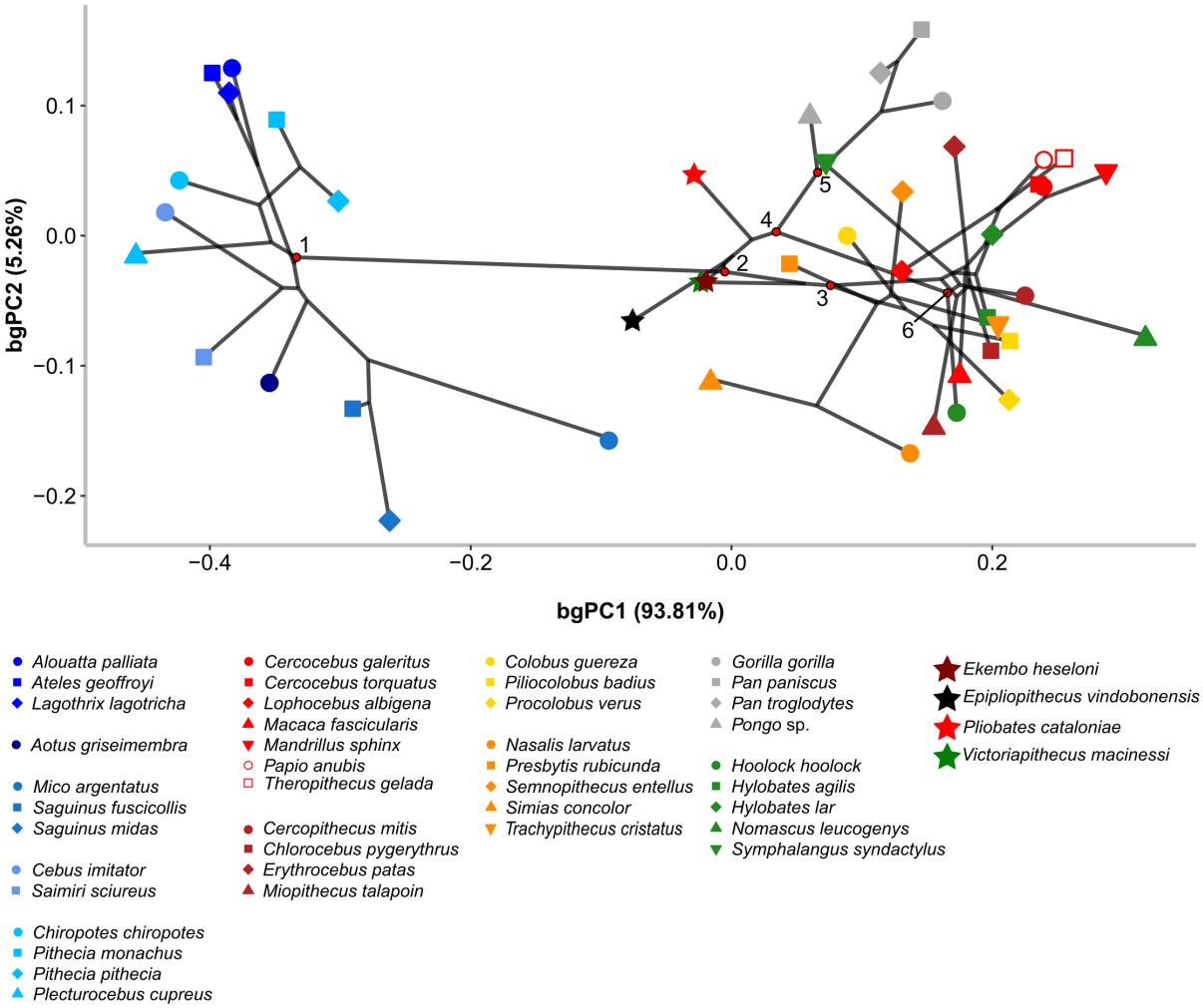


SOM Figure S6. Configurations of the carotid canal course in *Pliobates* compared with fossil and extant anthropoids in anterior view: a) *Pliobates* (IPS58443.1); b) *Epipliopithecus* (NHMW 1970/1397/0003); c) *Ekembo* (KNM-RU 2036al); d) *Victoriapithecus* (KNM-MB 29100); e) *Alouatta*; f) *Aotus*; g) *Cebus*; h) *Mico*; i) *Plecturocebus*; j) *Cercopithecus*; k) *Colobus*; l) *Mandrillus*; m) *Presbytis*; n) *Hylobates*; o) *Hoolock*; p) *Nomascus*; q)

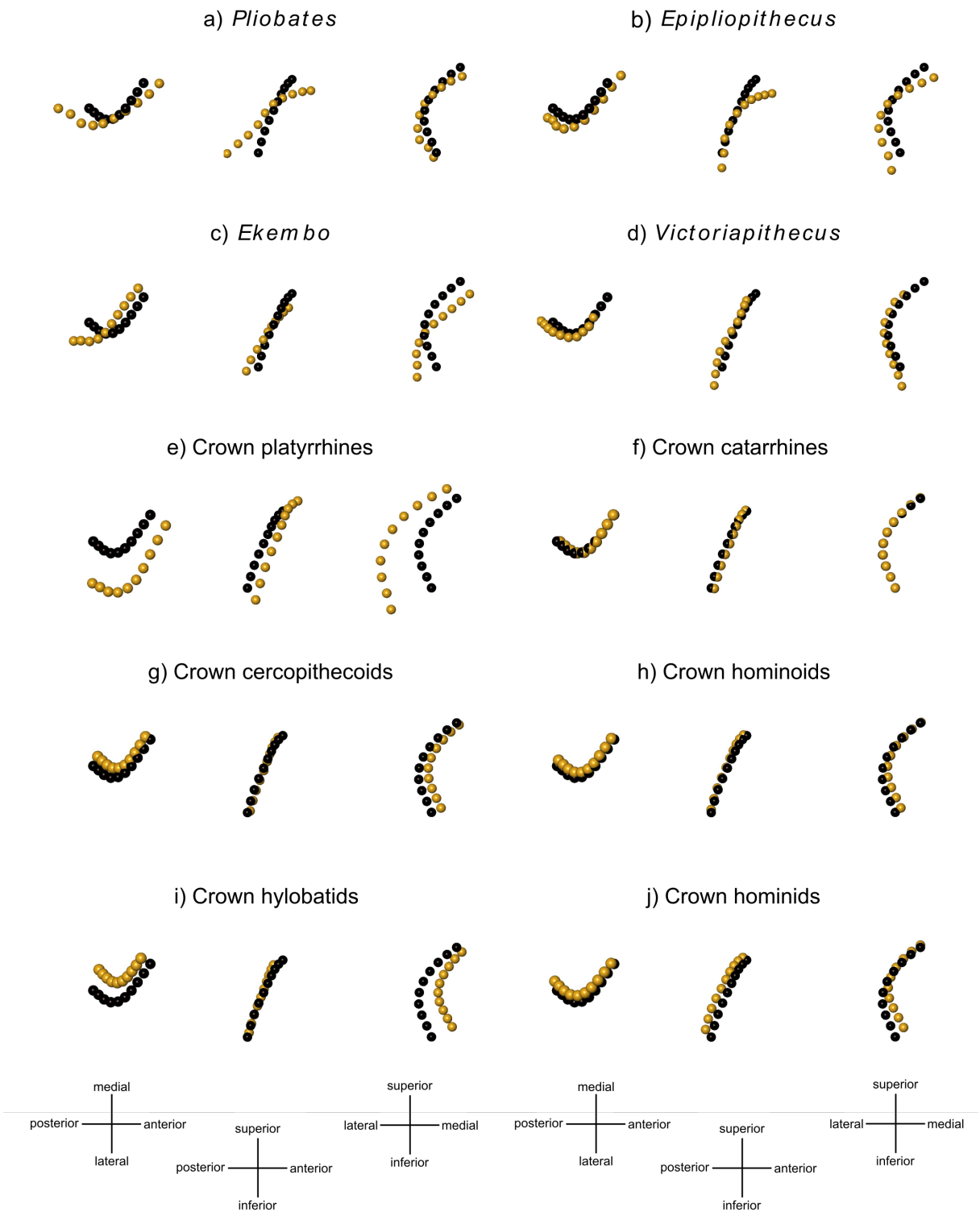
Symphalangus; r) *Gorilla*; s) *Pan*; t) *Pongo*. The mean configuration computed for the whole anthropoid sample is represented by black dots while configurations for specimens are represented in beige. For a better understanding of the canal course variation in space the anthropoid mean configuration was used as a reference for visualizing all the configurations at the same relative scale.



SOM Figure S7. Results of the between-group principal component analysis (bgPCA) based on carotid canal course variation among the catarrhine subsample, as depicted by a bivariate plot of bgPC2 vs. bgPC1. Convex hulls correspond to: cercopithecids (red), hylobatids (green), and hominids (gray). Abbreviation: bgPC = between-group principal component.



SOM Figure S8. Phylomorphospace of carotid canal course variation in extant anthropoids and extinct Miocene catarrhines including *Pliobates*. *Epipliopithecus*, *Ekembo* and *Pliobates* are considered successive stem hominoids following Alba et al. (2015: Fig. 8), while *Victoriapithecus* is considered a stem cercopithecoid. See SOM Figure S2a for a representation of this phylogenetic hypothesis. Ancestral nodes: 1 = crown platyrrhines; 2 = crown catarrhines; 3 = crown cercopithecoids; 4 = crown hominoids; 5 = crown hominids; 6, crown hylobatids.



SOM Figure S9. Configurations of the carotid canal course in *Pliobates* compared with other Miocene catarrhines and with the reconstructed carotid canal course for the last common ancestors (LCAs) of various anthropoid clades: a) *Pliobates* (IPS58443.1); b) *Epipliopithecus* (NHMW 1970/1397/0003); c) *Ekembo* (KNM-RU 2036al); d) *Victoriapithecus* (KNM-MB 29100); e) crown platyrrhines; f) crown catarrhines; g) crown cercopithecoids; h) crown

hominoids; i) crown hylobatids; j) crown hominids. The canal courses of the LCAs have been inferred based on the phylomorphospace displayed in SOM Figure S8. For each specimen/LCA, the configurations are displayed in superior (left), lateral (middle), and anterior (right) views. The mean configuration computed for the whole anthropoid sample is represented by black dots, while configurations for Miocene catarrhines and LCAs are represented in beige. The anthropoid mean configuration was used as a reference for visualizing all the configurations at the same relative scale.

SOM Table S1

List of extant anthropoid specimens included in this work. µCT scans were mainly downloaded from MorphoSource (https://www.morphosource.org, Duke University) or provided by Sergio Almécija (used in Urciuoli et al., 2020; µCT scans stored at the AMNH, New York, USA) and the Institut Català de Paleontologia Miquel Crusafont (ICP; Sabadell, Spain).

Species	ID	Source	Voxel size (mm)	Sex	DOI/Ark identifier/Occurrence ID	MorphoSource ID
Alouatta palliata	DUEALP 04	Morphosource	0.061	M	—	S1924
Alouatta palliata	DUEALP 06	Morphosource	0.067	M	—	S78
Alouatta palliata	DUEALP 13	Morphosource	0.052	F	—	S1108
Alouatta palliata	DUEALP 14	Morphosource	0.055	F	—	S1925
Alouatta palliata	DUEALP 16	Morphosource	0.058	F	—	S80
Aotus griseimembra	USNM 281551	Morphosource	0.036	M	http://n2t.net/ark:/65665/31db1d5a6-9879-459b-b08e-89e55015542e	S3994
Aotus griseimembra	USNM 281552	Morphosource	0.034	F	http://n2t.net/ark:/65665/3b29a3a53-e84f-4f04-9e48-bc203f45765c	S3980
Aotus griseimembra	USNM 284776	Morphosource	0.035	F	http://n2t.net/ark:/65665/34fb1e7f4-ed5d-4d36-9f36-e7741dcd02bd	S3996
Aotus griseimembra	USNM 284777	Morphosource	0.035	M	http://n2t.net/ark:/65665/30fe89705-6148-4207-9b9c-f5435c669587	S3997
Aotus griseimembra	USNM 284779	Morphosource	0.038	F	http://n2t.net/ark:/65665/354427a46-c645-4785-90d2-b08310d3110d	S3979
Ateles geoffroyi	AMNH-M 26593	Morphosource	0.062	F	urn:catalog:AMNH:Mammals:M-26593	S5312
Ateles geoffroyi	MCZ 10138	Morphosource	0.063	F	http://dx.doi.org/10.17602/M2/M2917	S971
Ateles geoffroyi	MCZ 29628	Morphosource	0.063	F	http://dx.doi.org/10.17602/M2/M2919	S973
Cebus imitator	MCZ 10135	Morphosource	0.080	F	http://dx.doi.org/10.17602/M2/M5151	S1676
Cebus imitator	MCZ 34326	Morphosource	0.080	F	http://dx.doi.org/10.17602/M2/M5148	S1673
Cebus imitator	MCZ 34353	Morphosource	0.080	F	http://dx.doi.org/10.17602/M2/M5147	S1672
Cercocebus galeritus	AMNH-M 52641	Morphosource	0.068	M	urn:catalog:AMNH:Mammals:M-52641	S1513
Cercocebus torquatus	AMNH-M 70063	Morphosource	0.118	M	urn:catalog:AMNH:Mammals:M-70063	S4046
Cercocebus torquatus	MCZ 32625	Morphosource	0.091	M	http://dx.doi.org/10.17602/M2/M2589	S777
Cercopithecus mitis	MCZ 25022	Morphosource	0.080	F	http://dx.doi.org/10.17602/M2/M2929	S983
Cercopithecus mitis	MCZ 26832	Morphosource	0.080	F	http://dx.doi.org/10.17602/M2/M2930	S984

Cercopithecus mitis	MCZ 7088	Morphosource	0.080	F	http://dx.doi.org/10.17602/M2/M2927	S981
Chiropotes chiropotes	USNM 388161	Morphosource	0.047	F	http://n2t.net/ark:/65665/3bd51f984-2926-4bd6-a368-1c2be2fb4a87	S3926
Chiropotes chiropotes	USNM 388163	Morphosource	0.047	F	http://n2t.net/ark:/65665/3007743ab-5f8c-4542-a384-bc68d16bd910	S3928
Chiropotes chiropotes	USNM 388165	Morphosource	0.049	M	http://n2t.net/ark:/65665/3b5260e90-e411-4638-9257-f4e65440a1ea	S3935
Chlorocebus pygerythrus	SIU 4799	Morphosource	0.050	F	—	S4045
Chlorocebus pygerythrus	SIU 4800	Morphosource	0.046	F	—	S4047
Chlorocebus pygerythrus	SIU 4801	Morphosource	0.055	M	—	S4048
Colobus guereza	AMNH-M 52211	Morphosource	0.073	M	urn:catalog:AMNH:Mammals:M-52211	S1143
Colobus guereza	AMNH-M 52213	Morphosource	0.066	F	urn:catalog:AMNH:Mammals:M-52213	S3768
Colobus guereza	AMNH-M 52238	Morphosource	0.068	F	urn:catalog:AMNH:Mammals:M-52238	S1215
Erythrocebus patas	MCZ 47015	Morphosource	0.083	M	http://dx.doi.org/10.17602/M2/M2923	S977
Erythrocebus patas	MCZ 47016	Morphosource	0.083	M	http://dx.doi.org/10.17602/M2/M2924	S978
Erythrocebus patas	MCZ 47018	Morphosource	0.083	F	http://dx.doi.org/10.17602/M2/M2926	S980
Gorilla gorilla	AMNH-A 999686	Morphosource	0.131	M	—	S5189
Gorilla gorilla	AMNH-M 54356	Morphosource	0.106	F	urn:catalog:AMNH:Mammals:M-54356	S5125
Gorilla gorilla	MCZ 17684	Morphosource	0.126	F	http://dx.doi.org/10.17602/M2/M2943	S644
Gorilla gorilla	MCZ 26850	Morphosource	0.123	F	http://dx.doi.org/10.17602/M2/M2947	S995
Gorilla gorilla	MCZ 37264	Morphosource	0.126	F	http://dx.doi.org/10.17602/M2/M2949	S997
Gorilla gorilla	MCZ 46325	Morphosource	0.126	F	http://dx.doi.org/10.17602/M2/M2955	S1001
Hoolock hoolock	AMNH-M 112720	Morphosource	0.052	M	urn:catalog:AMNH:Mammals:M-112720	S1206
Hoolock hoolock	AMNH-M 201743	Morphosource	0.064	F	urn:catalog:AMNH:Mammals:M-201743	S12604
Hoolock hoolock	AMNH-M 83425	AMNH	0.084	F	urn:catalog:AMNH:Mammals:M-83425	S1209
Hylobates agilis	IPS3773	CENIEH	0.052	?	—	
Hylobates lar	MCZ 41412	Morphosource	0.067	F	http://dx.doi.org/10.17602/M2/M2961	S1005
Hylobates lar	MCZ 41418	Morphosource	0.067	F	http://dx.doi.org/10.17602/M2/M2967	S1008
Hylobates lar	MCZ 41421	Morphosource	0.067	F	http://dx.doi.org/10.17602/M2/M2969	S1009
Hylobates lar	MCZ 41424	Morphosource	0.067	F	http://dx.doi.org/10.17602/M2/M3007	S1017

Lagothrix lagotricha	USNM 269839	Morphosource	0.058	F	http://n2t.net/ark:/65665/3d05a410d-2384-4415-a7cb-9d53b2d58726	S3004
Lagothrix lagotricha	USNM 461930	Morphosource	0.060	F	http://n2t.net/ark:/65665/35d3a334f-9bc6-48e9-864d-6fe2cf11beba	S3006
Lagothrix lagotricha	USNM 545879	Morphosource	0.058	M	http://n2t.net/ark:/65665/30f0814b2-a584-4c20-96c2-fbcb4e5778e2	S283
Lophocebus albigena	MCZ 14725	Morphosource	0.090	F	http://dx.doi.org/10.17602/M2/M2626	S794
Lophocebus albigena	MCZ 18614	Morphosource	0.090	M	http://dx.doi.org/10.17602/M2/M2622	S790
Lophocebus albigena	MCZ 22737	Morphosource	0.090	F	http://dx.doi.org/10.17602/M2/M2621	S789
Macaca fascicularis	MCZ 12758	Morphosource	0.062	F	http://dx.doi.org/10.17602/M2/M3028	S1032
Macaca fascicularis	MCZ 22277	Morphosource	0.062	F	http://dx.doi.org/10.17602/M2/M3029	S1033
Macaca fascicularis	MCZ 23812	Morphosource	0.062	M	http://dx.doi.org/10.17602/M2/M3030	S1034
Macaca fascicularis	MCZ 35765	Morphosource	0.062	F	http://dx.doi.org/10.17602/M2/M3033	S1037
Macaca fascicularis	MCZ 41167	Morphosource	0.091	M	http://dx.doi.org/10.17602/M2/M3038	S1042
Mandrillus sphinx	AMNH-A 9912049	Morphosource	0.075	M	—	S5815
Mandrillus sphinx	AMNH-M 89367	Morphosource	0.080	F	urn:catalog:AMNH:Mammals:M-89367	S4599
Mandrillus sphinx	MCZ 34089	Morphosource	0.126	M	http://dx.doi.org/10.17602/M2/M5096	S1571
Mico argentatus	MCZ 30579	Morphosource	0.041	M	http://dx.doi.org/10.17602/M2/M5192	S1708
Mico argentatus	MCZ 30580	Morphosource	0.041	M	http://dx.doi.org/10.17602/M2/M5193	S1709
Mico argentatus	MCZ 32164	Morphosource	0.041	F	http://dx.doi.org/10.17602/M2/M5196	S1712
Miopithecus talapoin	MCZ 23196	Morphosource	0.050	M	http://dx.doi.org/10.17602/M2/M5094	S1665
Miopithecus talapoin	MCZ 23197	Morphosource	0.050	M	http://dx.doi.org/10.17602/M2/M5093	S1664
Miopithecus talapoin	MCZ 5547	Morphosource	0.050	M	http://dx.doi.org/10.17602/M2/M5087	S1659
Nasalis larvatus	MCZ 37341	Morphosource	0.071	F	http://dx.doi.org/10.17602/M2/M5082	S1655
Nasalis larvatus	MCZ 41560	Morphosource	0.071	F	http://dx.doi.org/10.17602/M2/M5056	S1642
Nasalis larvatus	MCZ 41562	Morphosource	0.071	F	http://dx.doi.org/10.17602/M2/M5055	S1641
Nomascus leucogenys	AMNH-M 87251	Morphosource	0.105	M	urn:catalog:AMNH:Mammals:M-87251	S5127
Pan paniscus	AMNH-M 86857	AMNH	0.116	F	urn:catalog:AMNH:Mammals:M-86857	S1590
Pan paniscus	IPS9033	CENIEH	0.066	F	—	
Pan paniscus	MCZ 38018	Morphosource	0.094	M	http://dx.doi.org/10.17602/M2/M4399	S1333

Pan paniscus	MCZ 38019	Morphosource	0.092	F	http://dx.doi.org/10.17602/M2/M4398	S1332
Pan paniscus	MCZ 38020	Morphosource	0.099	?	http://dx.doi.org/10.17602/M2/M4397	S1331
Pan troglodytes	AMNH-M 167342	Morphosource	0.089	M	urn:catalog:AMNH:Mammals:M-167342	S5129
Pan troglodytes	AMNH-M 167344	Morphosource	0.111	M	urn:catalog:AMNH:Mammals:M-167344	S5313
Pan troglodytes	IPS5698	CENIEH	0.077	M	—	
Pan troglodytes	MCZ 17702	Morphosource	0.102	F	http://dx.doi.org/10.17602/M2/M4395	S1330
Pan troglodytes	MCZ 23167	Morphosource	0.106	F	http://dx.doi.org/10.17602/M2/M4390	S1326
Pan troglodytes	MCZ 26849	Morphosource	0.106	F	http://dx.doi.org/10.17602/M2/M4388	S1324
Papio anubis	MCZ 17342	Morphosource	0.108	M	http://dx.doi.org/10.17602/M2/M4885	S1615
Papio anubis	MCZ 21160	Morphosource	0.118	M	http://dx.doi.org/10.17602/M2/M4881	S1613
Papio anubis	MCZ BOM 8304	Morphosource	0.118	M	http://dx.doi.org/10.17602/M2/M4887	S1616
Piliocolobus badius	MCZ 24080	Morphosource	0.080	M	http://dx.doi.org/10.17602/M2/M2892	S947
Piliocolobus badius	MCZ 24775	Morphosource	0.090	M	http://dx.doi.org/10.17602/M2/M2893	S948
Piliocolobus badius	MCZ 24793	Morphosource	0.080	F	http://dx.doi.org/10.17602/M2/M2894	S949
Pithecia monachus	MCZ 27124	Morphosource	0.050	?	http://dx.doi.org/10.17602/M2/M4708	S1496
Pithecia pithecia	MCZ 30718	Morphosource	0.050	M	http://dx.doi.org/10.17602/M2/M4707	S1495
Pithecia pithecia	MCZ 30719	Morphosource	0.0501	F	http://dx.doi.org/10.17602/M2/M4706	S1494
Plecturocebus cupreus	AMNH-M 72141	Morphosource	0.049	F	urn:catalog:AMNH:Mammals:M-72141	S5132
Plecturocebus cupreus	AMNH-M 72143	Morphosource	0.049	M	urn:catalog:AMNH:Mammals:M-72143	S5133
Plecturocebus cupreus	AMNH-M 75987	Morphosource	0.051	M	urn:catalog:AMNH:Mammals:M-75987	S5134
Plecturocebus cupreus	AMNH-M 75988	Morphosource	0.049	F	urn:catalog:AMNH:Mammals:M-75988	S5135
Plecturocebus cupreus	MCZ 37828	Morphosource	0.047	M	http://dx.doi.org/10.17602/M2/M5171	S1692
Pongo sp.	IPS10647	CENIEH	0.077	F	—	
Pongo sp.	IPS10651	CENIEH	0.077	F	—	
Pongo sp.	IPS9031	CENIEH	0.077	F	—	
Pongo sp.	IPSSN	CENIEH	0.077	F	—	
Pongo sp.	MCZ 37518	Morphosource	0.126	F	http://dx.doi.org/10.17602/M2/M4613	S1458

Pongo sp.	MCZ 35719	Morphosource	0.103	F	http://dx.doi.org/10.17602/M2/M4615	S1459
Presbytis rubicunda	MCZ 35704	Morphosource	0.080	F	http://dx.doi.org/10.17602/M2/M4552	S1419
Presbytis rubicunda	MCZ 35705	Morphosource	0.080	F	http://dx.doi.org/10.17602/M2/M4551	S1418
Presbytis rubicunda	MCZ 36820	Morphosource	0.080	M	http://dx.doi.org/10.17602/M2/M4554	S1420
Procolobus verus	AMNH-M 89438	Morphosource	0.076	F	urn:catalog:AMNH:Mammals:M-89438	S4627
Procolobus verus	AMNH-M 89439	Morphosource	0.080	M	urn:catalog:AMNH:Mammals:M-89439	S4628
Saguinus fuscicollis	AMNH-M 74051	Morphosource	0.027	F	urn:catalog:AMNH:Mammals:M-74051	S4404
Saguinus midas	MCZ 30597	Morphosource	0.041	M	http://dx.doi.org/10.17602/M2/M4498	S1385
Saguinus midas	MCZ 30601	Morphosource	0.041	M	http://dx.doi.org/10.17602/M2/M4497	S1384
Saimiri sciureus	MCZ 20187	Morphosource	0.047	?	http://dx.doi.org/10.17602/M2/M4486	S1373
Saimiri sciureus	MCZ 30568	Morphosource	0.047	F	http://dx.doi.org/10.17602/M2/M4483	S1370
Saimiri sciureus	MCZ 30569	Morphosource	0.047	M	http://dx.doi.org/10.17602/M2/M4447	S1362
Semnopithecus entellus	AMNH-A 9912285	Morphosource	0.060	M	—	S4396
Semnopithecus entellus	AMNH-A 9912286	Morphosource	0.108	M	—	S3764
Semnopithecus entellus	AMNH-M 90328	Morphosource	0.052	F	urn:catalog:AMNH:Mammals:M-90328	S4193
Simias concolor	AMNH-M 103369	Morphosource	0.056	M	urn:catalog:AMNH:Mammals:M-103369	S3558
Simias concolor	AMNH-M 103371	Morphosource	0.056	F	urn:catalog:AMNH:Mammals:M-103371	S3965
Symphalangus syndactylus	AMNH-M 102724	Morphosource	0.062	F	—	S5810
Symphalangus syndactylus	AMNH-M 106583	AMNH	0.079	F	urn:catalog:AMNH:Mammals:M-106583	S533
Theropithecus gelada	AMNH-M 238034	Morphosource	0.120	F	urn:catalog:AMNH:Mammals:M-238034	S4889
Theropithecus gelada	AMNH-M 60568	Morphosource	0.085	M	urn:catalog:AMNH:Mammals:M-60568	S4042
Theropithecus gelada	AMNH-M 80126	Morphosource	0.087	M	urn:catalog:AMNH:Mammals:M-80126	S4065
Trachypithecus cristatus	MCZ 35567	Morphosource	0.050	F	http://dx.doi.org/10.17602/M2/M4439	S1355
Trachypithecus cristatus	MCZ 35584	Morphosource	0.051	F	http://dx.doi.org/10.17602/M2/M4436	S1353
Trachypithecus cristatus	MCZ 35586	Morphosource	0.050	F	http://dx.doi.org/10.17602/M2/M4435	S1352

Abbreviations: F = female; M = male; ? = unknown sex; AMNH = American Museum of Natural History, New York, USA; AMNH-A = American Museum of Natural History, Anthropology Collection, New York, USA; AMNH-M = American Museum of Natural History, Mammal collection,

New York, USA; DUEA = Duke University, Evolutionary Anthropology, Durham, USA; ICP = acronym of the collections of the Institut Català de Paleontologia Miquel Crusafont, Sabadell, Spain; MCZ = Museum of Comparative Zoology, Harvard University, Cambridge, USA; MCZ-BOM = Museum of Comparative Zoology, Bones of Mammals collection, Harvard University, Cambridge, USA; SIU = Southern Illinois University, Carbondale, USA; USNM = Smithsonian National Museum of Natural History, Washington, D.C., USA.

SOM Table S2

Raw data of the variables describing the orientation, proportions and course of the carotid canal in extant anthropoid specimens.

Species	ID	2DYZA	2DXYA	$L/V^{(1/3)}$	bgPC1	bgPC2
Alouatta palliata	DUEALP 04	66.73	30.17	3.06	-0.36	0.15
Alouatta palliata	DUEALP 06	61.00	44.25	3.56	-0.40	0.17
Alouatta palliata	DUEALP 13	70.71	29.86	3.17	-0.40	0.11
Alouatta palliata	DUEALP 14	68.50	26.13	2.90	-0.34	0.09
Alouatta palliata	DUEALP 16	64.95	38.50	3.50	-0.41	0.12
Aotus griseimembra	USNM 281551	60.21	20.69	4.29	-0.41	-0.09
Aotus griseimembra	USNM 281552	57.58	16.89	3.60	-0.41	-0.13
Aotus griseimembra	USNM 284776	55.28	19.84	3.37	-0.24	-0.12
Aotus griseimembra	USNM 284777	55.09	23.71	3.90	-0.43	-0.10
Aotus griseimembra	USNM 284779	52.21	8.25	3.39	-0.27	-0.12
Ateles geoffroyi	AMNH-M 26593	59.21	32.81	3.53	-0.48	0.11
Ateles geoffroyi	MCZ 10138	50.66	38.21	3.69	-0.40	0.16
Ateles geoffroyi	MCZ 29628	57.38	39.33	4.05	-0.32	0.11
Cebus imitator	MCZ 10135	64.39	23.90	3.38	-0.41	0.02
Cebus imitator	MCZ 34326	72.30	37.16	4.01	-0.48	-0.02
Cebus imitator	MCZ 34353	64.19	26.39	4.14	-0.41	0.05
Cercocebus galeritus	AMNH-M 52641	57.39	11.66	2.40	0.24	0.04
Cercocebus torquatus	AMNH-M 70063	79.78	14.60	2.28	0.25	-0.02
Cercocebus torquatus	MCZ 32625	73.83	19.02	2.91	0.22	0.10
Cercopithecus mitis	MCZ 25022	57.20	-0.89	2.77	0.25	-0.06
Cercopithecus mitis	MCZ 26832	58.20	1.59	2.78	0.24	-0.03
Cercopithecus mitis	MCZ 7088	57.59	14.39	3.19	0.19	-0.05
Chiropotes chiropotes	USNM 388161	71.59	26.41	3.23	-0.41	0.01
Chiropotes chiropotes	USNM 388163	67.98	39.14	3.73	-0.43	0.06
Chiropotes chiropotes	USNM 388165	63.98	34.79	3.33	-0.43	0.06
Chlorocebus pygerythrus	SIU 4799	66.70	12.29	2.74	0.22	-0.10
Chlorocebus pygerythrus	SIU 4800	80.13	19.28	2.84	0.16	-0.14
Chlorocebus pygerythrus	SIU 4801	65.77	26.59	2.79	0.22	-0.02
Colobus guereza	AMNH-M 52211	71.43	26.52	2.88	0.06	0.03
Colobus guereza	AMNH-M 52213	58.93	10.06	3.13	0.10	-0.04
Colobus guereza	AMNH-M 52238	76.34	18.85	2.44	0.11	0.01
Erythrocebus patas	MCZ 47015	72.58	28.49	2.65	0.20	0.09
Erythrocebus patas	MCZ 47016	58.13	31.28	2.86	0.11	0.14

Erythrocebus patas	MCZ 47018	57.22	20.98	2.70	0.21	-0.02
Gorilla gorilla	AMNH-A 999686	56.92	10.14	3.10	0.17	0.13
Gorilla gorilla	AMNH-M 54356	50.82	6.84	2.99	0.20	0.05
Gorilla gorilla	MCZ 17684	61.71	18.12	2.85	0.19	0.17
Gorilla gorilla	MCZ 26850	55.54	3.89	3.28	0.17	0.12
Gorilla gorilla	MCZ 37264	55.97	16.40	3.24	0.18	0.07
Gorilla gorilla	MCZ 46325	56.37	12.71	3.51	0.06	0.08
Hoolock hoolock	AMNH-M 112720	52.89	4.59	2.26	0.09	-0.25
Hoolock hoolock	AMNH-M 201743	57.65	15.22	2.53	0.22	-0.10
Hoolock hoolock	AMNH-M 83425	52.54	11.33	2.57	0.22	-0.06
Hylobates agilis	IPS3773	44.51	1.00	3.19	0.20	-0.06
Hylobates lar	MCZ 41412	59.84	11.48	2.63	0.16	0.04
Hylobates lar	MCZ 41418	50.05	1.19	2.65	0.21	0.01
Hylobates lar	MCZ 41421	78.27	2.48	1.97	0.29	0.06
Hylobates lar	MCZ 41424	74.17	12.69	2.08	0.14	-0.10
Lagothrix lagotricha	USNM 269839	52.40	38.35	3.78	-0.47	0.09
Lagothrix lagotricha	USNM 461930	61.55	31.61	3.36	-0.32	0.11
Lagothrix lagotricha	USNM 545879	59.62	34.10	4.18	-0.37	0.13
Lophocebus albigena	MCZ 14725	76.19	30.79	2.53	0.06	0.00
Lophocebus albigena	MCZ 18614	69.57	7.34	3.03	0.11	-0.10
Lophocebus albigena	MCZ 22737	61.40	18.58	2.40	0.22	0.01
Macaca fascicularis	MCZ 12758	73.31	31.62	3.84	0.09	-0.06
Macaca fascicularis	MCZ 22277	70.90	13.51	2.73	0.17	-0.14
Macaca fascicularis	MCZ 23812	74.49	22.03	3.07	0.09	-0.20
Macaca fascicularis	MCZ 35765	73.79	26.47	2.21	0.25	-0.17
Macaca fascicularis	MCZ 41167	70.90	5.01	2.77	0.27	0.03
Mandrillus sphinx	AMNH-A 9912049	78.47	24.83	3.87	0.21	0.05
Mandrillus sphinx	AMNH-M 89367	69.43	13.60	2.44	0.34	-0.02
Mandrillus sphinx	MCZ 34089	70.52	2.25	2.37	0.32	0.12
Mico argentatus	MCZ 30579	79.36	33.38	4.16	-0.07	-0.14
Mico argentatus	MCZ 30580	70.89	37.76	3.40	-0.09	-0.18
Mico argentatus	MCZ 32164	71.40	36.16	3.86	-0.10	-0.16
Miopithecus talapoin	MCZ 23196	75.86	-3.12	3.74	0.10	-0.18
Miopithecus talapoin	MCZ 23197	84.14	-3.55	3.18	0.18	-0.19
Miopithecus talapoin	MCZ 5547	76.48	6.76	3.41	0.18	-0.07
Nasalis larvatus	MCZ 37341	68.96	8.49	2.94	0.17	-0.10
Nasalis larvatus	MCZ 41560	68.07	8.32	3.28	0.11	-0.12
Nasalis larvatus	MCZ 41562	69.62	2.58	2.90	0.13	-0.29

Nomascus leucogenys	AMNH-M 87251	46.95	10.01	2.88	0.32	-0.08
Pan paniscus	AMNH-M 86857	51.61	10.73	3.15	0.11	0.15
Pan paniscus	IPS9033	58.88	7.58	3.31	0.12	0.13
Pan paniscus	MCZ 38018	52.37	2.45	3.53	0.20	0.18
Pan paniscus	MCZ 38019	37.27	-0.82	3.35	0.12	0.14
Pan paniscus	MCZ 38020	44.76	10.08	3.12	0.17	0.19
Pan troglodytes	AMNH-M 167342	57.40	27.78	3.52	0.13	0.17
Pan troglodytes	AMNH-M 167344	40.91	17.19	3.42	0.08	0.13
Pan troglodytes	IPS5698	68.86	14.32	3.15	0.17	0.09
Pan troglodytes	MCZ 17702	58.80	8.02	3.44	0.13	0.13
Pan troglodytes	MCZ 23167	69.11	15.22	2.55	0.12	0.11
Pan troglodytes	MCZ 26849	65.72	19.18	3.82	0.06	0.14
Papio anubis	MCZ 17342	71.02	12.95	3.00	0.25	0.06
Papio anubis	MCZ 21160	77.92	12.01	3.06	0.23	0.04
Papio anubis	MCZ BOM 8304	84.99	13.10	2.89	0.23	0.07
Piliocolobus badius	MCZ 24080	72.37	13.36	1.80	0.23	-0.11
Piliocolobus badius	MCZ 24775	63.44	25.62	2.73	0.15	0.01
Piliocolobus badius	MCZ 24793	70.48	26.93	1.40	0.27	-0.14
Pithecia monachus	MCZ 27124	61.35	31.85	3.95	-0.35	0.09
Pithecia pithecia	MCZ 30718	65.29	33.95	4.17	-0.32	0.03
Pithecia pithecia	MCZ 30719	64.58	24.78	3.91	-0.28	0.02
Plecturocebus cupreus	AMNH-M 72141	60.37	36.47	3.82	-0.50	-0.05
Plecturocebus cupreus	AMNH-M 72143	58.98	35.27	4.03	-0.41	-0.02
Plecturocebus cupreus	AMNH-M 75987	54.55	29.05	3.95	-0.47	0.05
Plecturocebus cupreus	AMNH-M 75988	67.10	39.93	3.84	-0.45	-0.08
Plecturocebus cupreus	MCZ 37828	59.76	34.57	4.42	-0.45	0.03
Pongo sp.	IPS10647	35.58	26.47	3.08	-0.10	0.12
Pongo sp.	IPS10651	57.41	14.44	3.41	0.00	0.08
Pongo sp.	IPS9031	45.95	23.54	2.81	-0.03	0.09
Pongo sp.	IPSSN	51.04	12.11	3.22	0.19	0.20
Pongo sp.	MCZ 35719	55.71	21.61	2.61	0.14	-0.01
Pongo sp.	MCZ 37518	55.44	18.00	2.57	0.17	0.07
Presbytis rubicunda	MCZ 35704	73.37	9.72	3.28	0.05	-0.03
Presbytis rubicunda	MCZ 35705	59.19	10.94	3.26	0.07	0.02
Presbytis rubicunda	MCZ 36820	79.70	20.06	3.31	0.01	-0.05
Procolobus verus	AMNH-M 89438	72.35	13.25	3.05	0.19	-0.12
Procolobus verus	AMNH-M 89439	76.59	3.64	2.67	0.23	-0.13
Saguinus fuscicollis	AMNH-M 74051	74.69	29.71	4.08	-0.29	-0.13

Saguinus midas	MCZ 30597	79.05	43.03	3.18	-0.30	-0.26
Saguinus midas	MCZ 30601	75.43	34.46	3.27	-0.22	-0.17
Saimiri sciureus	MCZ 20187	68.68	38.36	2.91	-0.49	-0.09
Saimiri sciureus	MCZ 30568	67.23	27.31	3.44	-0.36	-0.09
Saimiri sciureus	MCZ 30569	70.14	38.60	3.48	-0.37	-0.10
Semnopithecus entellus	AMNH-A 9912285	66.06	28.37	2.52	0.12	0.05
Semnopithecus entellus	AMNH-A 9912286	64.95	33.39	3.01	0.16	0.05
Semnopithecus entellus	AMNH-M 90328	62.09	25.82	3.17	0.12	0.01
Simias concolor	AMNH-M 103369	73.52	29.07	3.13	0.08	-0.12
Simias concolor	AMNH-M 103371	71.86	33.87	3.40	-0.11	-0.10
Symphalangus syndactylus	AMNH-M 102724	38.27	19.77	3.37	0.08	0.12
Symphalangus syndactylus	AMNH-M 106583	44.54	23.27	3.32	0.06	0.00
Theropithecus gelada	AMNH-M 238034	66.58	7.26	2.87	0.28	0.05
Theropithecus gelada	AMNH-M 60568	68.61	20.77	3.02	0.27	0.06
Theropithecus gelada	AMNH-M 80126	65.87	24.69	3.11	0.21	0.08
Trachypithecus cristatus	MCZ 35567	58.10	27.71	3.38	0.13	-0.07
Trachypithecus cristatus	MCZ 35584	80.20	17.07	3.23	0.26	-0.12
Trachypithecus cristatus	MCZ 35586	61.67	21.44	3.35	0.22	-0.02

Abbreviations: 2DYZA = 2D angle in the YZ plane (canal superior orientation; in degrees); 2DXYA = 2D angle in the XY plane (canal medial orientation; in degrees); L = length (in mm); V = volume (in mm^3); bgPC = between-group principal component; AMNH = American Museum of Natural History, New York, USA; AMNH-A = American Museum of Natural History, Anthropology Collection, New York, USA; AMNH-M = American Museum of Natural History, Mammal collection, New York, USA; DUEA = Duke University, Evolutionary Anthropology, Durham, USA; ICP = acronym of the collections of the Institut Català de Paleontologia Miquel Crusafont, Sabadell, Spain; MCZ = Museum of Comparative Zoology, Harvard University, Cambridge, USA; MCZ-BOM = Museum of Comparative Zoology, Bones of Mammals collection, Harvard University, Cambridge, USA; SIU = Southern Illinois University, Carbondale, USA; USNM = Smithsonian National Museum of Natural History, Washington, D.C., USA.

SOM Table S3

Results of the Kruskal-Wallis comparisons for the indices and bgPCs describing the orientation, proportions and course of the carotid canal in the main extant anthropoid clades.

	H	*p*
2DYZA	45.74	<0.001
2DXYA	58.57	<0.001
$L/V^{(1/3)}$	63.73	<0.001
bgPC1	83.36	<0.001
bgPC2	39.31	<0.001

Abbreviations: 2DYZA = 2D angle in the YZ plane (canal superior orientation; in degrees); 2DXYA = 2D angle in the XY plane (canal medial orientation; in degrees); L = length (in mm); V = volume (in mm^3); bgPC = between-group principal component; H = Kruskal-Wallis statistic.

SOM Table S4

Results of the Bonferroni-corrected Mann-Whitney post hoc pairwise comparisons for the indices and bgPCs describing the orientation, proportions and course of the carotid canal in the main extant anthropoid clades.

	Platyrrhini	Cercopithecidae	Hominidae	Hylobatidae
2DYZA				
Platyrrhini	—	<0.01	<0.001	0.035
Cercopithecidae	<0.01	—	<0.001	<0.01
Hominidae	<0.001	<0.001	—	1
Hylobatidae	0.035	<0.01	1	—
2DXYA				
Platyrrhini	—	<0.001	<0.001	<0.001
Cercopithecidae	<0.001	—	1	0.240
Hominidae	<0.001	1	—	1
Hylobatidae	<0.001	0.240	1	—
$L/V^{(1/3)}$				
Platyrrhini	—	<0.001	<0.001	<0.001
Cercopithecidae	<0.001	—	<0.01	1
Hominidae	<0.001	<0.01	—	0.016
Hylobatidae	<0.001	1	0.016	—
bgPC1				
Platyrrhini	—	<0.001	<0.001	<0.001
Cercopithecidae	<0.001	—	0.068	1
Hominidae	<0.001	0.068	—	0.390
Hylobatidae	<0.001	1	0.390	—
bgPC2				
Platyrrhini	—	0.760	<0.001	1
Cercopithecidae	0.760	—	<0.001	1
Hominidae	<0.001	<0.001	—	<0.001
Hylobatidae	1	1	<0.001	—

Abbreviations: 2DYZA = 2D angle in the YZ plane (canal superior orientation; in degrees); 2DXYA = 2D angle in the XY plane (canal medial orientation; in degrees); L = length (in mm); V = volume (in mm^3); bgPC = between-group principal component.

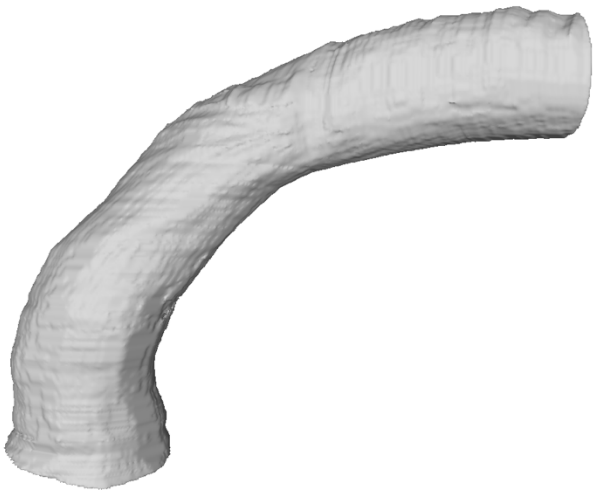
SOM Table S5

Results of the permutational analysis of variance based on the Euclidean distances between group means. Groups correspond to the main extant anthropoid clades (i.e., platyrrhines, cercopithecids, hylobatids, and hominids) used in the bgPCA and further analyses (see the main text). The tests have been computed with the streampoint configurations (i.e., full space) and with the bgPC scores with and without cross-validation (i.e., bgPCA spaces). While *p* is the significance of group mean differences, the coefficient of determination (R^2) denotes the variance explained by the grouping structure.

	p	R^2
Full space	0.001	0.67
bgPCA space without CV	0.001	0.77
bgPCA space with CV	0.001	0.77

Abbreviations: bgPCA = between-group principal component analysis; CV = cross-validation.

SOM File S1. R script used to import the 3D carotid canal surface and iteratively find the orthogonal plane to the canal passing through IRG (intersection ridge–groove) among several cutting plane possibilities. (Provided as a separate R file.)



SOM File S2. 3D model of the carotid canal surface of *Pliobates cataloniae*, available from MorphoSource.org (http://dx.doi.org/10.17602/M2/M344218).

SOM References

Adams, D.C., Collyer, M.L., Kaliontzopoulou, A., 2019. Geomorph: Software for geometric morphometric analyses. R Package Version 3.3.1. https://cran.r-project.org/web/packages/geomorph/index.html.

Alba, D.M., Almécija, S., DeMiguel, D., Fortuny, J., Pérez de los Ríos, M., Pina, M., Robles, J.M., Moyà-Solà, S., 2015. Miocene small-bodied ape from Eurasia sheds light on hominoid evolution. Science 350, aab2625.

Alba, D.M., Casanovas-Vilar, I., Garcés, M., Robles, J.M., 2017. Ten years in the dump: An updated review of the Miocene primate-bearing localities from Abocador de Can Mata (NE Iberian Peninsula). J. Hum. Evol. 102, 12–20.

Arnold, C., Matthews, L.J., Nunn, C.L., 2010. The 10kTrees website: A new online resource for primate phylogeny. Evol. Anthropol. 19, 114–118.

Begun, D.R., 2017. Evolution of the Pliopithecoidea. In: Fuentes, A. (Ed.), The International Encyclopedia of Primatology. John Wiley & Sons, Hoboken. https://doi.org/10.1002/9781119179313.wbprim0165.

Benefit, B.R., 1999. *Victoriapithecus*: The key to Old World monkey and catarrhine origins. Evol. Anthropol. 7, 155–174.

Bookstein, F.L., 1991. Morphometric Tools for Landmark Data: Geometry and Biology. Cambridge University Press, Cambridge.

Drake, R.E., Van Couvering, J.A., Pickford, M.H., Curtis, G.H., Harris, J.A., 1988. New chronology for the Early Miocene mammalian faunas of Kisingiri, Western Kenya. J. Geol. Soc. 145, 479–491.

Gilbert, C.C., Ortiz, A., Pugh, K.D., Campisano, C.J., Patel, B.A., Premjit, N., Fleagle, J.G., Patnaik, R., 2020. New Middle Miocene ape (Primates: Hylobatidae) from Ramnagar, India fills major gaps in the hominoid fossil record. Proc. R. Soc. B. 287, 20201655.

Harrison, T., 2010. Dendropithecoidea, Proconsuloidea and Hominoidea (Catarrhini, Primates). In: Werdelin, L., Sanders, W.J. (Eds.), Cenozoic Mammals of Africa. University of California Press, Berkeley, pp. 429–469.

Harrison, T., 2013. Catarrhine origins. In: Begun, D.R. (Ed.), A Companion to Paleoanthropology. Blackwell Publishing, Oxford, pp. 376–396.

Harrison, T., 2017. Miocene primates. In: Fuentes, A. (Ed.), The International Encyclopedia of Primatology. John Wiley & Sons, Hoboken. https://doi.org/10.1002/9781119179313.wbprim0227.

Meyer, D., Rinaldi, Ir.D., Ramlee, H., Perwitasari-Farajallah, D., Hodges, J.K., Roos, C., 2011. Mitochondrial phylogeny of leaf monkeys (genus *Presbytis*, Eschscholtz, 1821) with implications for taxonomy and conservation. Mol. Phylogenet. Evol. 59, 311–319.

Nengo, I., Tafforeau, P., Gilbert, C.C., Fleagle, J.G., Miller, E.R., Feibel, C., Fox, D.L., Feinberg, J., Pugh, K.D., Berruyer, C., Mana, S., Engle, Z., Spoor, F., 2017. New infant cranium from the African Miocene sheds light on ape evolution. Nature 548, 169–174.

R Core Team, 2020. R: A language and environment for statistical computing. R Foundation for Statistical Computing, Vienna.

Peppe, D.J., McNulty, K.P., Cote, S.M., Harcourt-Smith, W.E.H., Dunsworth, H.M., VanCouvering, J.A., 2009. Stratigraphic interpretation of the Kulu Formation (Early Miocene, Rusinga Island, Kenya) and its implications for primate evolution. J. Hum. Evol. 56, 447–461.

Rohlf, F.J., Slice, D.E., 1990. Extensions of the Procrustes method for the optimal superimposition of landmarks. Syst. Zool. 39, 40–59.

Spoor, F. 1993. The comparative morphology and phylogeny of the human bony labyrinth. Ph.D. Dissertation, Utrecht University.

Springer, M.S., Meredith, R.W., Gatesy, J., Emerling, C.A., Park, J., Rabosky, D.L., Stadler, T., Steiner, C., Ryder, O.A., Janečka, J.E., Fisher, C.A., Murphy, W.J., 2012. Macroevolutionary dynamics and historical biogeography of primate diversification inferred from a species supermatrix. PLoS One 7, e49521.

Urciuoli, A., Zanolli, C., Beaudet, A., Dumoncel, J., Santos, F., Moyà-Solà, S., Alba, D.M., 2020. The evolution of the vestibular apparatus in apes and humans. eLife 9, e51261.

van der Meulen, A.J., García-Paredes, I., Álvarez-Sierra, M.Á., van den Hoek Ostende, L.W., Hordijk, K., Oliver, A., López-Guerrero, P., Hernández-Ballarín, V., Peláez-Campomanes, P., 2011. Biostratigraphy or biochronology? Lessons from the Early and Middle Miocene small Mammal Events in Europe. Geobios 44, 309–321.

Chapter 4:

The Miocene primate *Pliobates* is a pliopithecoid

Reproduced from:
Bouchet, F., Zanolli, C., Urciuoli, A., Almécija, S., Fortuny, J., Robles, J.M., Beaudet, A., Moyà-Solà, S., Alba, D.M., 2024. The Miocene primate *Pliobates* is a pliopithecoid. Nat. Commun. 15, 2822. https://doi.org/10.1038/s41467-024-47034-9

nature communications

Article

https://doi.org/10.1038/s41467-024-47034-9

The Miocene primate *Pliobates* is a pliopithecoid

Received: 24 May 2023

Accepted: 29 February 2024

Published online: 01 April 2024

Check for updates

Florian Bouchet[1] ✉, Clément Zanolli[2], Alessandro Urciuoli[1,3,4,5], Sergio Almécija[1,6,7], Josep Fortuny[1], Josep M. Robles[1], Amélie Beaudet[8,9,10], Salvador Moyà-Solà[1,11,12] & David M. Alba[1] ✉

The systematic status of the small-bodied catarrhine primate *Pliobates cataloniae*, from the Miocene (11.6 Ma) of Spain, is controversial because it displays a mosaic of primitive and derived features compared with extant hominoids (apes and humans). Cladistic analyses have recovered *Pliobates* as either a stem hominoid or as a pliopithecoid stem catarrhine (i.e., preceding the cercopithecoid–hominoid divergence). Here, we describe additional dental remains of *P. cataloniae* from another locality that display unambiguous synapomorphies of crouzeliid pliopithecoids. Our cladistic analyses support a close phylogenetic link with poorly-known small crouzeliids from Europe based on (cranio)dental characters but recover pliopithecoids as stem hominoids when postcranial characters are included. We conclude that *Pliobates* is a derived stem catarrhine that shows postcranial convergences with modern apes in the elbow and wrist joints—thus clarifying pliopithecoid evolution and illustrating the plausibility of independent acquisition of postcranial similarities between hylobatids and hominids.

The small-bodied catarrhine primate *Pliobates cataloniae*, from the Miocene (11.6 Ma) of northeast Spain, was originally described on the basis of a partial skeleton and associated cranium[1]. The systematic position of *Pliobates* among catarrhine primates (i.e., Old World monkeys, apes, and humans) remains unsettled. Dental similarities with dendropithecids from the Miocene of East Africa, interpreted as stem catarrhines[2,3]—i.e., preceding the divergence between cercopithecoids (Old World Monkeys) and hominoids (apes and humans)—or as basal hominoids[1,4,5], were noted[1]. However, *Pliobates* was originally interpreted as a stem hominoid more derived than proconsulids based on the results of a cladistic analysis (Fig. 1)[1]. Given the mosaic of both cranial and postcranial primitive (stem catarrhine-like) and derived (crown catarrhine and, especially, hominoid-like) features displayed by *Pliobates*, other authors proposed that this taxon might be alternatively interpreted as a pliopithecoid (i.e., a stem catarrhine) postcranially convergent with hominoids[6,7]. The latter view has been supported by subsequent cladistic analyses[2,3,8] (Fig. 1). A recent analysis of *Pliobates* carotid canal anatomy showed no particular similarities with either the pliopithecoid *Epipliopithecus* or hylobatids[9] and preliminary morphometric analyses of the inner ear semicircular

[1]Institut Català de Paleontologia Miquel Crusafont (ICP-CERCA), Universitat Autònoma de Barcelona, 08193 Cerdanyola del Vallès, Barcelona, Spain. [2]Univ. Bordeaux, CNRS, MCC, PACEA, UMR 5199, F-33600 Pessac, France. [3]Universitat Autònoma de Barcelona, Campus de la UAB, 08193 Cerdanyola del Vallès, Barcelona, Spain. [4]Division of Palaeoanthropology, Senckenberg Research Institute and Natural History Museum Frankfurt, Frankfurt am Main, Germany. [5]Universidad de Alcalá, Cátedra de Otoacústica Evolutiva y Paleoantropología (HM Hospitales-UAH), Departamento de Ciencias de la Vida, 28871 Alcalá de Henares, Madrid, Spain. [6]Division of Anthropology, American Museum of Natural History, New York, NY 10024, USA. [7]New York Consortium in Evolutionary Primatology, New York, NY 10016, USA. [8]Laboratoire de Paléontologie, Évolution, Paléoécosystèmes et Paléoprimatologie (PALEVOPRIM), UMR 7262 CNRS, Univ. Poitiers, Poitiers, France. [9]Department of Archaeology, University of Cambridge, Cambridge CB2 1QH, United Kingdom. [10]School of Geography, Archaeology, and Environmental Studies, University of the Witwatersrand, Johannesburg, WITS 2050, South Africa. [11]Institució Catalana de Recerca i Estudis Avançats, 08010 Barcelona, Spain. [12]Unitat d'Antropologia Biològica (Departament de Biologia Animal, de Biologia Vegetal i d'Ecologia), Universitat Autònoma de Barcelona, 08193 Cerdanyola del Vallès, Barcelona, Spain. ✉e-mail: florian.bouchet@icp.cat; david.alba@icp.cat

https://doi.org/10.1038/s41467-024-47034-9

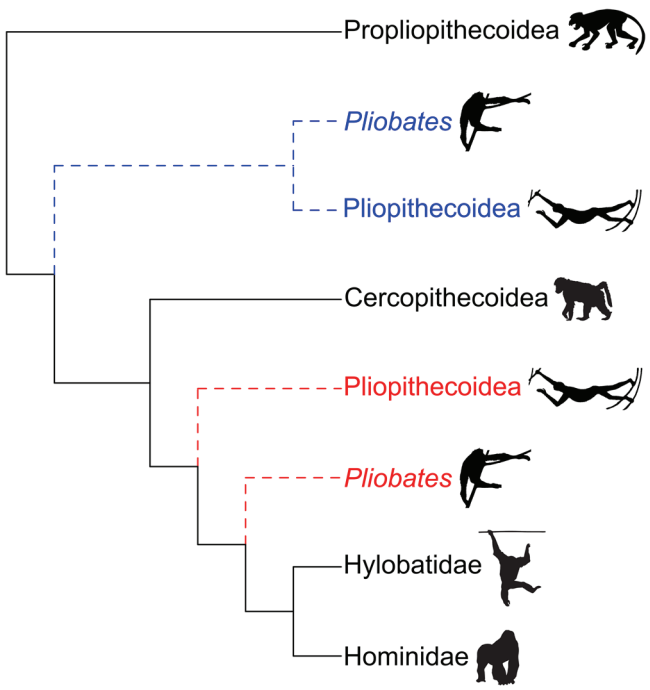


Fig. 1 | Simplified cladogram of extant and extinct catarrhine primates depicting the two main phylogenetic hypotheses previously supported for *Pliobates*. The red dashed lines depict the original interpretation of pliopithecoids and *Pliobates* as successive stem hominoids[1], whereas the blue dashed lines denote the alternative hypothesis of *Pliobates* being a stem catarrhine more closely related to pliopithecoids[2]. Black silhouettes (not to scale) of Propliopithecoidea, Cercopithecoidea, Hylobatidae, and Hominidae were taken from the following sources: Propliopithecoidea from Fig. 3 in ref. 71; Cercopithecoidea, Hylobatidae, and Hominidae from Summary Figure in ref. 13, reprinted with permission from AAAS; black silhouette (not to scale) of Pliopithecoidea was redrawn from Fig. 15.12 in ref. 72, reprinted with permission from Elsevier.

canals supported a stem catarrhine status more derived than propliopithecoids and *Epipliopithecus*, despite some similarities with the latter[10].

The contradictory results yielded by previous cladistic analysis for *Pliobates*—i.e., stem hominoid[1] vs. pliopithecoid[2,3] largely stem from the different emphasis put by the respective authors on postcranial features. The original topology recovering *Pliobates* as a hominoid was largely driven by the possession of numerous purported crown hominoid postcranial synapomorphies, which many authors consider homoplastic (i.e., independently evolved) to a large extent among various extant ape lineages[11–15]. Given the impossibility of disentangling homologous from homoplastic features a priori, an alternative approach to test whether *Pliobates* is a pliopithecoid would be to focus on dental morphology—as it is on this basis that pliopithecoids are distinguished from other catarrhines and considered to constitute a clade[8,16–20]. The holotype of *P. cataloniae* only preserves rather worn upper cheek teeth that did not enable ascertaining the most diagnostic features of pliopithecoids in the original description[1]. In contrast, here we describe unpublished, more diagnostic dentognathic material of *P. cataloniae* that includes the lower molars and is key to settling the debate about its systematic position, allowing us to confirm its pliopithecoid status. This material comes from Abocador de Can Mata (ACM) locality ACM/C5-D1, which is spatially close to and roughly coeval with ACM/C8-A4[21,22], the type locality of *P. cataloniae*. Based on the new material, we provide an emended diagnosis of this species and further evaluate its phylogenetic relationships among pliopithecoids by means of a cladistic analysis at the species level based on a taxon-character data matrix that includes qualitative and quantitative dental characters. To further evaluate the phylogenetic relationships of *P. cataloniae* among catarrhines and the phylogenetic signal provided by other anatomical areas, we also conducted additional cladistic analyses at the genus level, including a wider representation of extinct and extant hominoids and considering (cranio)dental and postcranial characters both jointly and separately. Our results indicate that *Pliobates* is most closely related to crouzeliids, a diverse and widely distributed pliopithecoid family that was thus far mostly known from dental remains. They further support that *Pliobates* is not closely related to crown hominoids despite the possession of remarkable postcranial similarities, which has deep implications for our current understanding of ape and human evolution that are explored in this paper.

Results

Systematic paleontology

Order Primates Linnaeus, 1758
Suborder Anthropoidea Mivart, 1864
Infraorder Catarrhini É. Geoffroy Saint-Hilaire, 1812
Superfamily Pliopithecoidea Zapfe, 1961
Family Crouzeliidae Ginsburg and Mein, 1980
Subfamily Crouzeliinae Ginsburg and Mein, 1980
Genus *Pliobates* Alba et al. 2015
Pliobates cataloniae Alba et al. 2015

Holotype. IPS58443, a partial skeleton with associated skull of an adult female individual (see Table 1 in ref. 1 for details). It includes two dentognathic specimens: IPS58443.1, a right maxillary fragment with the I1–C1 alveoli, partial P3, and P4–M3 series; and IPS58443.2, a left maxillary fragment with M2 (partial) and M3. See Table 1 for dental measurements.

Referred specimens. Four maxillary and mandibular fragments and 12 isolated teeth from locality ACM/C5-D1 (see Supplementary Table 1 for a list of specimens). See Table 1 for dental measurements.

Type locality. ACM/C8-A4 (ACM composite stratigraphic sequence, els Hostalets de Pierola, Vallès-Penedès Basin, NE Iberian Peninsula).

Distribution and age. Only known from two localities of the ACM sequence dated to 11.6 Ma, thus roughly coinciding with the Middle/Late Miocene boundary[21,22]; see Materials & Methods for further details.

Emended diagnosis. (Diagnosis based on dental features emended from the original description; for cranial and postcranial features, see ref. 1; see Supplementary Text 1 for a differential diagnosis; see Supplementary Figs. 1–3 for comparison plates). Small-bodied catarrhine (~5 kg) with adult dental formula 2.1.2.3. Molars with buccolingually compressed cusps and sharp crests. Upper dental arcade somewhat divergent, with slightly heteromorphic upper incisors. I1 spatulate, mesiodistally waisted at the cervix, and very tilted mesialward. C1 moderately compressed and larger in males. Upper cheek teeth with extensive distal basin (premolars) or trigon basin (molars). Upper premolars ovoid with heteromorphic cusps, protocone more mesial and peripheral than paracone, distinct lingual cingulum (in the P4 only), and postparacrista forming an abrupt angle with the distal marginal ridge. Upper molars moderately (M1–M2) to very (M3) broad relative to length, with M2 larger than M1 and M3; small paraconule; small metacone and reduced hypocone (even more so in M3); protocone more distal than paracone; C-shaped lingual cingulum that does not surround the hypocone; and discontinuous buccal cingulum. M1–M2 with well-developed lingual cingulum and peripheral hypocone with prehypocrista directed toward the protocone but also a

secondary crest linking it to the crista obliqua. M3 markedly trapezoidal with rudimentary distal cusps. Lower incisors waisted toward cervix, i2 with a distinct distal prong. Female c1 with a marked cuspule-like thickening where the mesiolingual cristid meets the marked lingual cingulid. p3 with a single main cuspid. p4 suboval, with heteromorphic and mesially located metaconid and protoconid, rudimentary distal cuspids, poorly-developed buccal cingulid, and extensive talonid basin. Lower molars (m1–m2) with five main cuspids; protoconid more mesial than metaconid; hypoconulid centrally located; hypoprotocristid emerging distally from the protoconid; moderately inclined cristid obliqua (more so in the m1); extensive mesial fovea and larger talonid basin with incomplete pliopithecine triangle (well-developed distal arm) and not completely isolated from the distal fovea; broad and continuous buccal cingulid. DI1 similar to I1, with a moderately ledge-like lingual cingulum. DP3 trapezoidal with indistinct metacone and no crista obliqua. DP4 larger than DP3 and similar to M1–M2 but more triangular and with a comparatively smaller hypocone. dp3 mesially very tapering, with protoconid much more mesially located than metaconid and a lingually open mesial fovea (no distinct premetacristid). dp4 similar to m1 but more mesially tapering, with a longer mesial fovea, a more obliquely oriented cristid obliqua (directed toward the hypoprotocristid and hypometacristid junction, so that the postprotocristid originates from the latter junction), no pliopithecine triangle, and a discontinuous buccal cingulid.

Description of the referred specimens

The previously unpublished specimens of *P. cataloniae* from ACM/C5-D1 include four dentognathic fragments and 12 isolated teeth (Supplementary Table 1). Descriptions of specimen preservation and occlusal shape are provided in Supplementary Texts 2 and 3, respectively. Although upper cheek tooth morphology was described based on the holotype[1], some of the new specimens display a lesser degree of wear and thus can be used to refine the assessment of the occlusal morphology of *P. cataloniae*. These remains from ACM/C5-D1 provide the unique opportunity to describe several tooth loci previously unknown for this taxon: I1, i2, female c1, p4, m1–m2, DI1, and both upper and lower deciduous premolars (Figs. 2–4). Most informative is the female infant mandible IPS43936 (Figs. 2g–i and 3), which enables to ascertain the morphology of the deciduous lower premolars (dp3–dp4) and digitally extract the germs of the permanent teeth, including the lower molars (m1–m2) (Figs. 2x, 4k, l and o, p). 3D models of the OES and EDJ of the 11 scanned specimens are presented in Fig. 4.

The occlusal morphology in the best preserved maxillary fragment from ACM/C5-D1 is comparable to that of the holotype (Fig. 1 in ref. 1; Fig. 2a–c). The difference in size between I1 and I2 alveoli confirms some degree of incisor heteromorphy. The isolated I1 shows that the crown is moderately low and labiolingually broader than mesiodistally long, spatulate, mesiodistally waisted at the cervix, and tilted mesially with an inclined apical margin (Fig. 2z). The C1 alveolus in the maxillary fragment is much larger than that of the holotype and most likely belongs to a male individual, further suggesting a marked degree of canine sexual dimorphism. The P3 provides further evidence of the morphology of this tooth (Figs. 2n and 4c), which was damaged in the holotype. The P4s (including a germ; Figs. 2n and 4d, e) display in turn an entirely comparable morphology to that of the holotype. Both upper premolars are broader than long and rather ovoid, with the two main cusps that are somewhat buccolingually compressed and heteromorphic, with the protocone being more peripheral than the paracone. The single hypoparacrista separates the restricted mesial fovea from the extensive and deep distal basin, while the postparacrista and the distal marginal ridge constitute an abrupt angle. The buccal cingulum is variably developed but always discontinuous whereas the lingual cingulum, only well-developed in the P4 (remnant in the P3), is short but wide. The six additional M1s and M2s from ACM/C5-D1 (Figs. 2n–r and 4f–i) are similar in occlusal morphology to one another and to the corresponding teeth in the holotype, but additional details can be ascertained due to the less advanced degree of wear. They display a moderately broad subsquare occlusal contour that is somewhat buccolingually waisted at crown midlength with four main cusps, which are buccolingually compressed and connected by sharp crests. The protocone is more extensive than the paracone and metacone, which are similar in size in M1 but not in M2 (due to the smaller metacone), and slightly more distally situated than the paracone. The hypocone is smaller than the trigon cusps and more peripheral than the protocone. A small paraconule is present at the end of the preprotocrista. The crista obliqua is distinct and continuous. The mesial fovea is restricted and buccally located, while the trigon basin is much more extensive and deeper and the distal fovea is intermediate in size. Next to the prehypocrista, which is directed toward the protocone, there is a secondary crest that links the hypocone with the crista obliqua (this cannot be ascertained in 4 out of 9 molars due to wear). The buccal cingulum is discontinuous, whereas the lingual cingulum is broad (shelf-like) and C-shaped but does not surround the hypocone. When the whole sample is considered, the M1s and M2s display some variability in the degree of cusp compression, crest sharpness, lingual cingulum development, and hypocone size. However, the two first features largely depend on the degree of wear, with unworn or slightly worn specimens evincing more compressed cusps and sharper crests than those with a more advanced degree of wear.

Table 1 | Dental measurements of *Pliobates cataloniae*

Catalog No.	Tooth	Sex	MD	BLm	BLd	BLI
IPS42977	L DP4	?	5.5	5.7	5.4	103.6
IPS42977	L P4	?	(5.0)	(6.4)		(128.0)
IPS43013	L DP3	?	3.9	4.8		123.1
IPS43433	L c1	F	4.6	3.5		76.1
IPS43488	L I1	?	>3.9	(3.6)		–
IPS43758	R M1	?	5.0	6.1	6.0	122.0
IPS43758	L M2	?	(5.8)	6.8	6.4	(117.2)
IPS43820	R p4	?	>3.9	>4.7		–
IPS43936	L dp3	?	>3.9	3.1		–
IPS43936	L dp4	?	5.0	3.5	3.8	76.0
IPS43936	L m1	?	(6.1)	(4.4)	(4.7)	(77.0)
IPS43936	L m2	?	(6.6)	(4.9)	(5.0)	(75.8)
IPS44014	L P3	M	4.2	6.1		145.2
IPS44014	L P4	M	4.1	5.9		143.9
IPS44014	L M1	M	5.3	6.4	6.1	120.8
IPS44273	L i2	?	3.0	3.8		126.7
IPS44393	R dI1	?	3.3	2.5		75.8
IPS58443.1	R P3	F	>2.8	>4.5		–
IPS58443.1	R P4	F	3.2	5.3		165.6
IPS58443.1	R M1	F	5.0	5.9	5.8	118.0
IPS58443.1	R M2	F	5.3	6.5	6.4	122.6
IPS58443.1	R M3	F	4.6	6.4	5	139.1
IPS58443.2	L M2	F	>5.0	–	–	–
IPS58443.2	L M3	F	4.5	6.7	5.1	148.9
IPS93524	R p4	?	>3.9	>4.1		–
IPS94888	L M2	?	5.5	7.0	6.6	127.3
IPS100379	R M1	?	(5.2)	(6.1)	(5.7)	(117.3)
IPS100384	L M2	?	6.1	7.5	7.0	123.0
IPS106878	L dp4	?	4.7	3.2	3.4	72.3

Values within parentheses are estimated measurements whereas the 'greater than' symbol (>) denotes incomplete measurements due to damage.
BLI breadth/length index, *BLd* buccolingual breadth at distal lobe, *BLm* buccolingual breadth at mesial lobe, *F* female, *M* male, *MD* mesiodistal length, *?* unknown sex.

https://doi.org/10.1038/s41467-024-47034-9

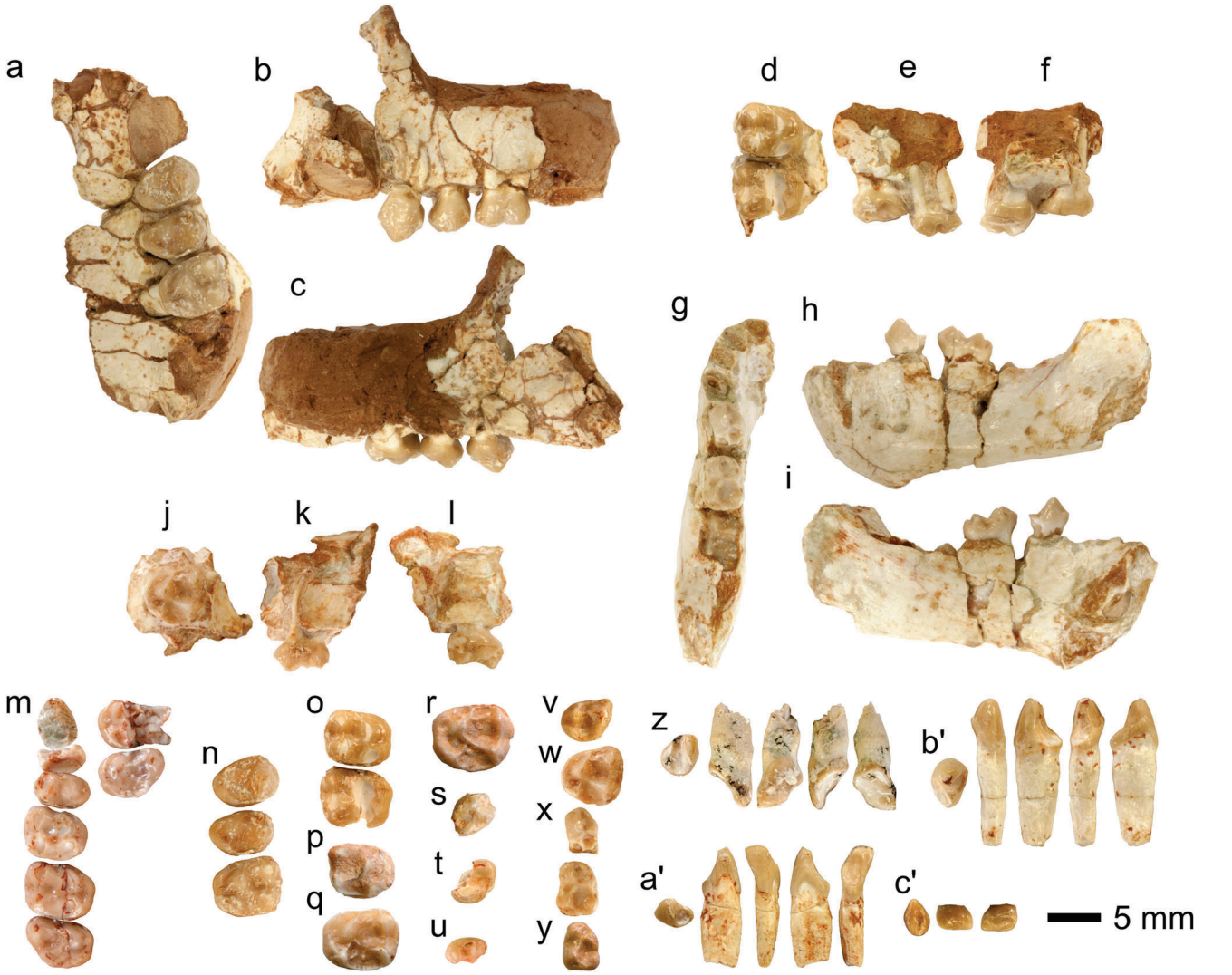


Fig. 2 | Dentognathic fragments and teeth of *Pliobates cataloniae*. Cheek teeth are depicted in occlusal view; for other specimens, views are indicated. **a**–**c** left male maxillary fragment with P3–M1 (IPS44014), in occlusal (**a**), buccal (**b**), and lingual (**c**) views; **d**–**f** right maxillary fragment with M1–M2 (IPS43758), in occlusal (**d**), buccal (**e**), and lingual (**f**) views; **g**–**i** left female mandibular fragment with dp3–dp4 and m1 inside crypt (IPS43936), in occlusal (**g**), buccal (**h**), and lingual (**i**) views; **j**–**l** left maxillary fragment with dP4 (IPS42977), in occlusal (**j**), buccal (**k**), and lingual (**l**) views; **m** right C1 alveolus and P3–M3 series (P3 broken) and left M2–M3 series (M2 broken) (IPS58443.1, holotype, female); **n** left P3–M1 series (IPS44014, male); **o** right M1–M2 series (IPS403758); **p** right M1 (IPS100379); **q** left M2 germ (IPS94888); **r** left M2 germ (IPS100384); **s** damaged right p4 (IPS93524); **t** partial right p4 (IPS43820); **u** right m2 germ mesial fragment (IPS94886); **v** left dP3 (IPS43013); **w** left dP4 (IPS42977); **x** left dp3–dp4 series (dp3 damaged) (IPS43936, female); **y** left dp4 (IPS106878); **z** left I1 (IPS43488), in occlusal, mesial, labial, distal, and lingual views; **a′** left i2 (IPS44273), in occlusal, mesial, labial, distal, and lingual views; **b′** left female c1 (IPS43433), in occlusal, mesial, labial, distal, and lingual views; **c′** right dI1 germ (IPS44393), in occlusal, labial, and lingual views. In occlusal view, mesial is on top. All the remains are from ACM/C5-D1 except the holotype, which is from ACM/C8-A4.

The lower incisor germs from the mandible (Fig. 3c, d) include the almost complete i1 crown and the still unfinished i2 crown. Coupled with the isolated i2 (Fig. 2a′), they show that both incisors are moderately high-crowned but that the i2 crown is much more asymmetrical, being mesially tilted and displaying a distinct distal prong at about crown midheight. The female c1 (Fig. 2b′ and 3e) is low-crowned and displays three cristids that originate from the apex of the single cuspid, the distobuccal cristid being longer than the mesiolingual and distolingual cristids; the mesiolingual cristid forms a marked cuspule-like thickening at about crown midheight when it merges with the narrow lingual cingulid. The incompletely formed p3 germ of IPS43936 (Fig. 3f) shows that there is a single main cuspid (the protoconid) from which three cristids originate. The p4s, including an incompletely formed germ (Figs. 2s, t, 3g, and 4j), denote a suboval occlusal contour with well-developed albeit heteromorphic mesial cuspids (the metaconid being more peripheral than the protoconid) and rudimentary distal cuspids; the mesial fovea displays a secondary cristid and is moderately large, although smaller and shallower than the talonid basin; the buccal cingulid is poorly developed. The three lower molar germs (Figs. 3h, i and 4k–m) indicate that the m1 and m2 display a subrectangular and elongated contour and five buccolingually compressed cuspids connected by sharp cristids. The protoconid is more mesial than the metaconid, whereas the hypoconid and entoconid are less peripheral than the mesial cuspids, and the hypoconulid is smaller than the other cuspids and centrally located close to the distal marginal ridge. The mesial fovea is very extensive but slightly wider than long, and displays a secondary transverse cristid that extends from the preprotocristid to the center of the fovea (IPS43936) or to the premetacristid (IPS94886), thus completely dividing the fovea in the latter specimen. The hypoprotocristid emerges distally from the protoconid and angles before meeting the hypometacristid, completely separating the mesial fovea from the more extensive and deeper talonid basin.

https://doi.org/10.1038/s41467-024-47034-9

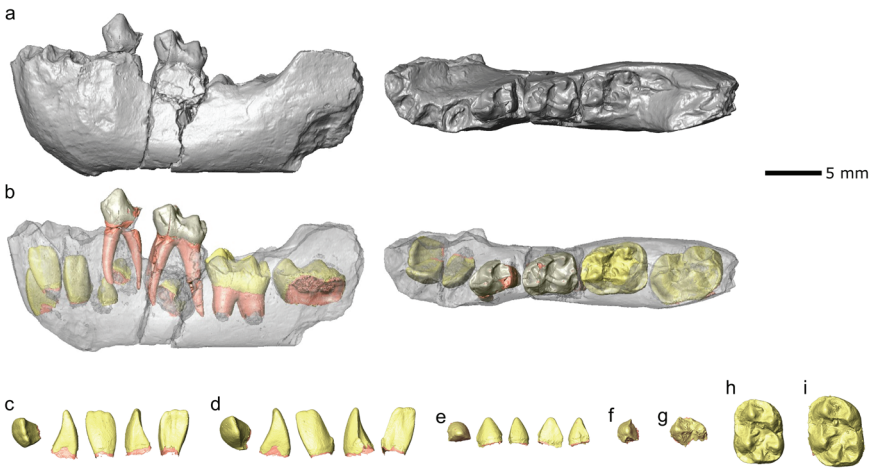


Fig. 3 | Virtual rendering of the *Pliobates cataloniae* female infant mandible (IPS43936) from ACM/C5-D1 with extracted permanent tooth germs. Mandible in lateral and occlusal view (**a**), with the bone in semitransparency (**b**) showing the deciduous (light gray) and permanent (yellow) teeth; **c** left i1 in occlusal, mesial, labial, distal, and lingual views; **d** left i2 in occlusal, mesial, labial, distal, and lingual views; **e** left c1 in occlusal, mesial, labial, distal, and lingual views; **f** left p3 in occlusal view; **g** left p4 in occlusal view; **h** left m1 in occlusal view; **i** left m2 in occlusal view. Completed or forming roots are showed in pink.

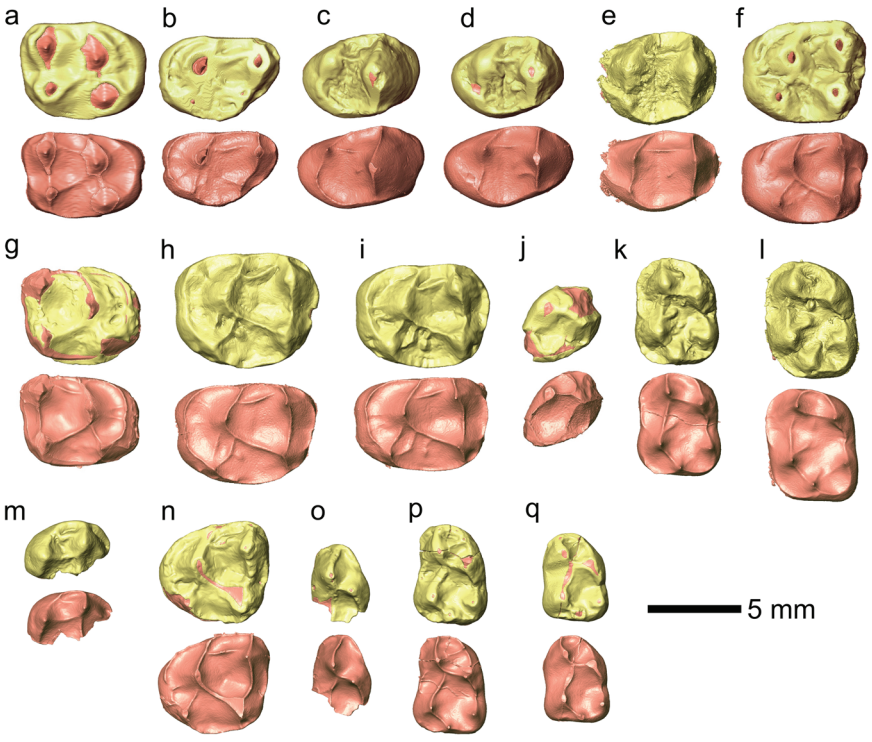


Fig. 4 | Three-dimensional virtual renderings of the OES and EDJ of *Pliobates cataloniae* cheek teeth from ACM/C5-D1 in occlusal view. a right M2 (IPS58443.1; holotype); **b** left M3 (IPS58443.2; holotype); **c** left P3 (IPS44014); **d** left P4 (IPS44014); **e** left P4 incompletely formed germ (IPS42977); **f** left M1 (IPS44014); **g** right M1 (IPS100379); **h** left M2 germ (IPS100384); **i** left M2 germ (IPS94888); **j** partial right p4 (IPS93524); **k** left m1 (IPS43936); **l** left m2 (IPS43936); **m** right m2 germ mesial fragment (IPS94886); **n** left dP4 (IPS42977); **o** partial left dp3 (IPS43936); **p** left dp4 (IPS43936); **q** left dp4 (IPS106878). Dentine horns were reconstructed by C.Z. for **a**, **b**, **f**, and **g**. OES and EDJ models are shown in yellow and rose, respectively. Mesial is on top.

The cristid obliqua, constituted by a short postprotocristid and a much longer prehypocristid, is slightly obliquely oriented and directed toward the distal aspect of the protoconid. A well-defined distal arm of the pliopithecine triangle runs mesiolingually into the talonid basin, originating from midway along the prehypocristid (m1) or the mesial aspect of the hypoconid (m2). There is no mesial arm of the pliopithecine triangle originating from the protoconid, but a short and mesiodistally aligned secondary cristid runs from the hypometacristid (m1) or the center of the transverse cristid (m2) toward the center of the trigonid basin. The distal fovea is located on the distolingual corner of the crown, continuous with the talonid basin (m1) or only partially separated from it (m2). The buccal cingulid is broad and continuous.

The DI1 crown (Fig. 2c') is somewhat mesially tilted, spatulate, and waisted at the cervix, and displays a moderately ledge-like lingual cingulum. The DP3 (Fig. 2v) has a trapezoidal occlusal contour slightly broader than long and displays three main cusps, with the extensive paracone being transversely aligned with the slightly smaller protocone, and the hypocone being much smaller, while there is no distinct metacone. The mesial fovea is restricted whereas the distal basin is very extensive and lacks a crista obliqua; the prehypocrista is directed

to the protocone. The cingula are not well developed. The DP4 (Figs. 2w and 4n) resembles in occlusal morphology the M1–M2 (including the presence of four main cusps, the shape and size of the trigon basin and distal fovea, the presence of a continuous crista obliqua and a C-shaped lingual cingulum, and the peripheral position of the hypocone) but differs in several other respects (more triangular in occlusal contour, more restricted mesial fovea, more rudimentary hypocone, and lack of secondary crest between hypocone and crista obliqua). The dp3 (Figs. 2x and 4o) is mesially very tapering, with a very mesially located protoconid and without a distinct premetacristid, so that the mesial fovea is lingually open. The cristid obliqua, composed of the prehypocristid, is very obliquely inclined. The dp4 (Figs. 2x, y and 4p, q) is more similar to the m1 but displays multiple differences, including a more mesially tapering contour and a longer mesial fovea (albeit similarly divided by a secondary cristid), a more inclined cristid obliqua (directed toward the junction of the hypoprotocristid and hypometacristid; Y-shaped configuration), lack of pliopithecine triangle, and less developed buccal cingulid.

Morphological comparisons and body mass

The occlusal morphology of *Pliobates* most closely resembles that of crouzeliine pliopithecoids, particularly the indeterminate species from Mörgen as well as *Plesiopliopithecus* and *Crouzelia*. The I1 resembles that of *Barberapithecus*, although the crown is even more asymmetrical in *Pliobates* (unknown in other crouzeliines). The P4 is comparable in shape to that from Mörgen, while the upper molars resemble those of *Barberapithecus* and the Mörgen crouzeliine in the degree of cusp compression and crest sharpness, together with other occlusal details (more distal location of the protocone, i.e., more so than in other taxa, relatively small metacone, and M1 and M2 occlusal contour, small hypocone more peripheral than the protocone, narrow trigon basin, short distal fovea, and lingual cingulum not surrounding the hypocone). Nevertheless, the M1 of *Pliobates* more closely resembles that from Mörgen in the moderate buccolingual wasting and narrow buccal cingulum, resulting in more peripheral buccal cusps. In contrast, the lingual cingulum of *Pliobates* M1 and M2 is broader than in *Barberapithecus* and the Mörgen crouzeliine (unknown in *Plesiopliopithecus* and *Crouzelia*). The M3 hypocone is mesiodistally aligned with the protocone, as in *Barberapithecus* (unknown in other crouzeliines), but the crown is much more trapezoidal and displays a smaller hypocone, narrower cingula, more peripheral buccal cusps, and a more lingually located metacone. As for the lower dentition, the i2 is comparable to that of *Plesiopliopithecus*, while the female c1 is very similar to that of *Barberapithecus*, although relatively broader and with a more marked mesiolingual cuspulid-like enamel thickening. The p4, in contrast, differs from those of other crouzeliines, although the occlusal contour and non-peripheral protoconid approximate the condition of *Plesiopliopithecus* and *Crouzelia*, while the buccal cingulid is as developed as in *Barberapithecus*. The lower molars display the typical crouzeliine pattern, characterized by quite compressed cusps, large foveae, a mesially located protocone relative to the metacone, and a continuous lingual cingulid, except that the mesial arm of the pliopithecine triangle is missing in both the m1 and m2 of *Pliobates*. Among crouzeliines, the lower molars of *Pliobates* more closely resemble *Barberapithecus* (and differ from both *Plesiopliopithecus* and *Crouzelia*) in the well-developed hypoconulid and distal arm of the pliopithecine triangle, and the alignment of the entoconid with the hypoconid. In contrast, the occlusal contour and the distal origin of the hypoprotocristid from the protoconid most closely resemble the condition in *Plesiopliopithecus* and *Crouzelia*, while the distinct hypoentocristid and postcristid can also be found in *Barberapithecus* and *Plesiopliopithecus*. The buccal cingulid is very broad as in *Plesiopliopithecus*, and the distal fovea is not isolated from the talonid basin as in *Crouzelia*. In summary, *Pliobates* closely resembles other crouzeliines in dental morphology but displays a unique combination of features that supports its distinction at the genus rank.

The dental dimensions of *P. cataloniae* are compared with those of dendropithecids and pliopithecoids in Supplementary Figs. 4 and 5 (see Supplementary Table 2 for more information on the comparative taxa). The upper premolars of *Pliobates* most closely resemble in size and proportions those of *Simiolus* and the crouzeliine from Mörgen, whereas the upper molars approach the condition of *Barberapithecus*, *Dionysopithecus*, and the crouzeliine from Mörgen. In turn, the lower molars of *Pliobates* most closely resemble those of *Crouzelia*, *Barberapithecus*, and *Plesiopliopithecus*. Dental body mass (BM) estimates for *P. cataloniae* range from 4.4 to 5.8 kg, with an average estimated BM of 5.3 kg and an uncertainty degree (based on the combined 50% confidence intervals for each tooth locus) of 3.7 to 7.3 kg (Supplementary Table 3).

Cladistic analysis

Our phylogenetic analysis based on dental features (Supplementary Data 1 and 2) recovers 192 most parsimonious trees with equal length (tree length = 302). The strict consensus (Fig. 5) recovers pliopithecoids (including *Pliobates*) as a clade of stem catarrhines more basal than dendropithecids but less so than *Saadanius*. Our analysis further recovers the monophyly of dionysopithecids and crouzeliids, but not of pliopithecids, as *Pliopithecus antiquus* appears more closely related to crouzeliids than the remaining pliopithecids, whose relationships are not resolved. The analysis recovers two crouzeliid clades, here distinguished as subfamilies Crouzeliinae and Anapithecinae (Table 2). *Pliobates* is recovered as a crouzeliine, less basal than *Barberapithecus* but more so than *Plesiopliopithecus* and *Crouzelia*, which are recovered as sister taxa. In turn, *Fanchangia* is recovered as the basalmost anapithecine; *Krishnapithecus* and *Laccopithecus* are also recovered as anapithecines, constituting a clade sister to that including *Egarapithecus* and *Anapithecus*.

Based on our cladistic analysis, *Pliobates* possesses the following pliopithecoid synapomorphies (Supplementary Data 3): i2 mesiodistally waisted basally at cervix; female c1 with prominent mesiolingual cristid-lingual cingulid thickening located at about crown-midheight; M1–M2 with paracone not markedly buccally located relative to the metacone; and lower molars (m1–m2) with a distinct distal arm of a pliopithecine triangle. In turn, *Pliobates* displays several synapomorphies of crouzeliids (i2 with clearly inclined mesial margin; P3 with relatively narrow distal basin; p4 with moderately developed buccal cingulid; and very narrow m2) and crouzeliines (P3 longer than P4; molars with buccolingually compressed cusps; M1–M2 with relatively small hypocone; m1–m2 with a large, almost as long as broad, mesial fovea; and entoconid almost transversely aligned with hypoconid (even though this synapomorphy is ambiguous because it would have been reversed in *Plesiopliopithecus* and *Crouzelia*, which display an entoconid clearly more distal than the hypoconid). Finally, among crouzeliids, *Pliobates* most closely resembles *Plesiopliopithecus* and *Crouzelia* in the possession of multiple synapomorphies absent from *Barberapithecus* (female c1 relatively broad with a cuspulid-like mesiolingual cristid-lingual cingulid; molars with and markedly sharp crests; very narrow m1; hypoprotocristid originating distally from protoconid with inclined cristid oblique connecting to where the hypoprotocristid originates, at least in m1; and distal fovea not separated from the talonid basin, at least in m2), but differs from them in the lesser developed buccal cingulid in p4 and the m1 and m2 that show a more distinct distal arm of the pliopithecine triangle, a larger hypoconulid, and an entoconid almost transversely aligned with the hypoconid.

While the dental-only cladistic analysis reported above was devised to determine the closer phylogenetic relationships of *Pliobates* with pliopithecoids, a second cladistic analysis was performed to further investigate the relationships between *Pliobates*, other pliopithecoids,

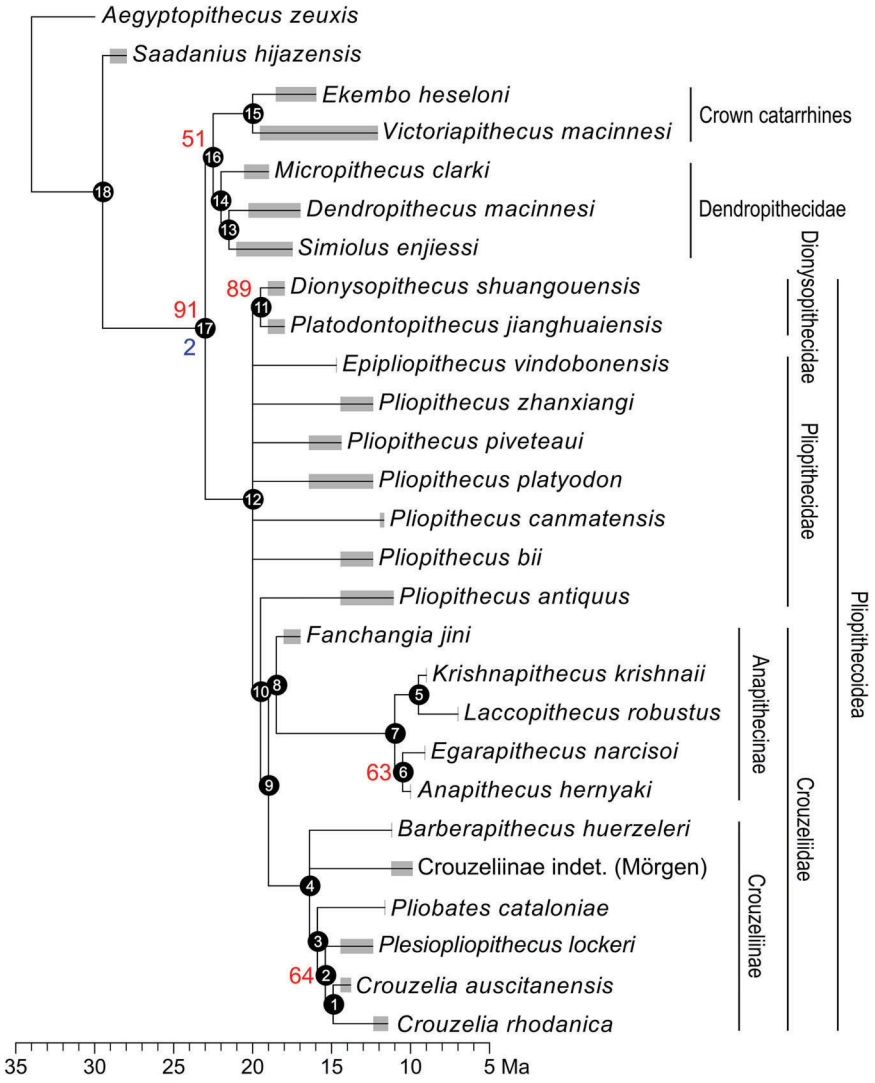


Fig. 5 | Time-calibrated strict consensus cladogram derived from the 192 most parsimonious trees based on a taxon-character data matrix for 27 taxa and 95 dental characters. Tree length = 302 steps; CI (excluding uninformative characters) = 0.374; RI = 0.505; RCI = 0.189. Bremer's indices (only shown when >1) and bootstrap percentages (only shown when ≥50%) are reported next to the nodes in blue and red, respectively. Gray semitransparent rectangles represent the chronostratigraphic ranges (including dating uncertainties) of the depicted taxa (Supplementary Table 5). Internal nodes have been depicted arbitrarily 0.5 Myr before the oldest record of the group or the next oldest node included within that clade. The list of characters and taxon-character matrix can be found in Supplementary Data 1 and 2, respectively. Node numbers within black dots refer to clades in the list of apomorphies reported in Supplementary Data 3.

and hominoids. This analysis, run at the genus level, included a more restricted sample of pliopithecoids but a wider array of hominoids and further considered cranial and postcranial characters. The results differ depending on whether postcranial characters are included (Supplementary Text 4). The iterations based on dental and craniodental characters (Supplementary Fig. 6a, b) yield similar results to the more detailed dental-only analysis of pliopithecoids at the species level reported above. In particular, pliopithecoids are recovered as a stem catarrhine clade and the monophyly of crouzeliids is supported, with *Pliobates* being a crouzeliid more derived than *Barberapithecus*. In contrast, the iteration exclusively based on postcranial features only adequately resolves the phylogeny of the crown hominoid clade and recovers *Pliobates* as a stem hominoid more derived than *Ekembo* (Supplementary Fig. 6c). Finally, the iteration based on both craniodental and postcranial evidence yields a relatively well-resolved but very heterodox topology (Supplementary Fig. 6d), in which *Pliobates* still branches among crouzeliids but the position of *Ekembo* remains unresolved and dendropithecids and pliopithecoids are recovered as successive paraphyletic assemblages of stem hominoids.

Discussion

The systematic position of *Pliobates* based on dental morphology

Pliobates was originally proposed as a stem hominoid[1] but subsequently recovered as a pliopithecoid[2,3] or even as a more basal stem catarrhine[8] by cladistic analyses including craniodental and postcranial features (Fig. 1; Supplementary Fig. 7). Dental morphology—which provides the main basis for the taxonomy of fossil primates and most other groups of mammals, and is highly diagnostic for pliopithecoids—offers the prospect to settle the debate on the systematic position of *Pliobates*. Its dental morphology did not play a central role in the original description because available remains were not particularly informative, merely noting dental similarities with dendropithecids[1], particularly to the upper molars of *Micropithecus*. However, some of these features (e.g., markedly convex lingual profile with a C-shaped lingual cingulum that does not surround the hypocone) are not exclusive to these taxa. In contrast, the newly reported molars (especially the lower ones) show much closer resemblances to crouzeliines. At the same time, *Pliobates* displays several differences relative to

Table 2 | Updated classification of pliopithecoids to the subfamily rank based on the published literature[8,20], and this study

Superfamily Pliopithecoidea
Family Dionysopithecidae
Genus *Dionysopithecus*
Dionysopithecus shuangouensis
Dionysopithecus orientalis
Genus *Platodontopithecus*
Platodontopithecus jianghuaiensis
Family Pliopithecidae*
Genus *Epipliopithecus*
Epipliopithecus vindobonensis
Genus *Pliopithecus*
Pliopithecus antiquus
Pliopithecus bii
Pliopithecus canmatensis
Pliopithecus piveteaui
Pliopithecus platyodon
Pliopithecus zhanxiangi
Family Crouzeliidae
Subfamily Anapithecinae
Genus *Anapithecus*
Anapithecus hernyaki
?Anapithecus priensis
Genus *Egarapithecus*
Egarapithecus narcisoi
Genus *Fanchangia*
Fanchangia jini
Genus *Krishnapithecus*
Krishnapithecus krishnaii
Genus *Laccopithecus*
Laccopithecus robustus
Subfamily Crouzeliinae
Genus *Barberapithecus*
Barberapithecus huerzeleri
Genus *Crouzelia*
Crouzelia auscitanensis
Crouzelia rhodanica
Genus *Plesiopliopithecus*
Plesiopliopithecus lockeri
Genus *Pliobates*
Pliobates cataloniae

Taxa denoted with an asterisk are likely paraphyletic. *Pliopithecus antiquus* is provisionally retained within the Pliopithecidae despite our cladistic results supporting a closer link with the Crouzeliidae (rendering the former paraphyletic). Based on our results, *Krishnapithecus* is included within the Anapithecinae (with Krishnapithecidae being a junior synonym of Crouzeliidae). *Kapi* might also belong to the Anapithecinae, given the similarities with *Krishnapithecus* noted by Ji et al.[8], but we prefer to leave it as incertae sedis at the superfamily rank given that it was not included in our cladistic analysis. The Mörgen material is left unassigned to genus given the lack of lower teeth.

previously known crouzeliine genera that warrant a genus distinction, while the generic ascription of the material from Mörgen[23,24] cannot be adequately determined because it cannot be directly compared with *Crouzelia* and *Plesiopliopithecus*.

The cladistic analysis of dental features at the species level reported here, including a wide representation of pliopithecoid taxa, further supports that *Pliobates* is a crouzeliid pliopithecoid most closely related to *Crouzelia* and *Plesiopliopithecus*. The recovery of pliopithecoids (including *Pliobates*) as a clade of stem catarrhines more basal than dendropithecids is consistent with some[2,3,8] but not all[1,8] previous results. Nevertheless, our results support that *Barberapithecus* is not a pliopithecid[18] but a crouzeliid[1,20,25] more closely related to crouzeliines[20] than to anapithecines[25]. *Krishnapithecus*, previously included in a distinct pliopithecoid family[8,20,26], appears more closely related to anapithecines—Krishnapithecidae thus being here considered a junior subjective synonym of Crouzeliidae. The nesting of *Pliobates* within the crouzeliine clade further implies that Pliobatidae must be also considered a junior subjective synonym of the Crouzeliidae.

A second cladistic analysis of (cranio)dental features at the genus level, including a wider representation of hominoids, further recovers *Pliobates* as a crouzeliid and supports pliopithecoids as a clade of stem catarrhines, but yields a somewhat different topology regarding *Anapithecus*. Postcranial features alone are not informative enough about the phylogeny of Miocene catarrhines (probably due to large amounts of missing data) but in contrast to craniodental evidence support a stem hominoid status for *Pliobates*. When postcranial features are combined with craniodental data, *Pliobates* branches again among crouzeliid genera but dendropithecids and pliopithecoids as a whole are recovered as successive paraphyletic assemblages of stem hominoids instead of stem catarrhines, strongly resembling the cladistic results accompanying the original description of *Pliobates*[1]. Given the paraphyletic status of pliopithecids in our dental-only analysis at the species level and the different topologies of *Anapithecus* in the first and second cladistic analyses, further research would be required to clarify the internal phylogeny of pliopithecoids and their relationships with other extinct and extant catarrhines. The contrasting results obtained by (cranio) dental vs. craniodental + postcranial evidence reported here parallel the contradictory results obtained by previous cladistic analyses including *Pliobates*[1–3,8]. In our opinion, these contradictions stem from the fact that *Pliobates* displays a mosaic of primitive (stem catarrhine-like) and derived (crown hominoid-like) features[1], particularly in the postcranium, so that different topologies may be favored depending on the emphasis put on these features. Although the results based on all available evidence should be preferred on cladistic epistemological grounds, the fact that postcranial features alone yield a completely different topology for *Pliobates* and that postcranial homoplasy has repeatedly been noted as misleading in hominoid phylogenetics[11–15] suggest otherwise. The cranial morphology of *Pliobates* is also ambiguous because some similarities with hylobatids (anteriorly situated orbits, broad interorbital distance, short face, low zygomatic roots) are also displayed by the pliopithecoid *Epipliopithecus*[27], stem hominoids such as nyanzapithecids[2], and small-bodied catarrhines from East Africa such as the dendropithecid *Micropithecus*[28]. It is thus likely that the hylobatid-like features of *Pliobates* are either symplesiomorphic for crown catarrhines and/or homoplastic among pliopithecoids, hylobatids, and some stem hominoids, maybe being related to small body size[29]. However, while the inclusion of cranial characters does not alter the topology recovered on the basis of teeth, the postcranial dataset has a major influence on the most parsimonious topology, suggesting that, due to rampant homoplasy, it is introducing more 'noise' than phylogenetic signal in the case of *Pliobates*.

Implications for pliopithecoid locomotor diversity

Part of the problem when it comes to include postcranial characters in phylogenetic analyses of pliopithecoids is undoubtedly attributable to the large amount of missing data for most species. Besides *Pliobates*, which is now the most complete crouzeliid individual known, it is only well known in the pliopithecid *Epipliopithecus*[23,30,31], generally interpreted as a generalized quadruped with limited climbing and suspensory abilities[32–34]. However, the meager available record suggests that the group as a whole displayed much more diverse postcranial adaptations[34–36]. This is most clearly evidenced by the postcranium of *Pliobates*, which reveals a mosaic of stem catarrhine-like features

https://doi.org/10.1038/s41467-024-47034-9

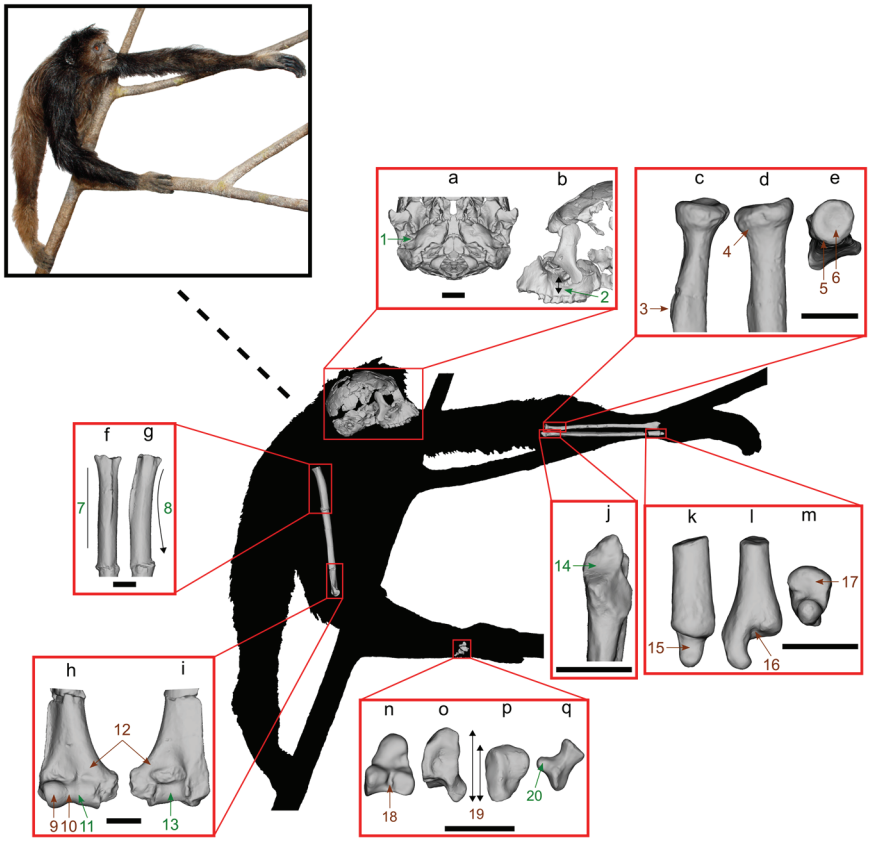


Fig. 6 | Life reconstruction of *Pliobates* in color and as a black silhouette indicating key morphological features that highlight its mosaic of primitive and derived features relative to crown hominoids. a, **b** cranium in inferior (**a**) and lateral (**b**) views; **c**–**e** left proximal radius in anterior (**c**), medial (**d**), and proximal (**e**) views; **f**–**g** left proximal humerus (mirrored) in anterior (**f**) and medial (**g**) views; **h**–**i** left distal humerus (mirrored) in anterior (**h**) and posterior (**i**) views; **j** left proximal ulna in anterior view; **k**–**m** left distal ulna in anterior (**k**), medial (**l**), and distal (**m**) views; **n** left capitate (mirrored) and **o** left hamate (mirrored) in radial views; **p** left triquetrum (mirrored) in proximal view; **q** right pisiform in radial view. Green numbers denote plesiomorphic (stem catarrhine-like) characters whereas brown numbers denote derived (crown hominoid-like) features, and are as follows: 1, short and incompletely ossified tubular ectotympanic; 2, low zygomatic root; 3, laterally facing bicipital tuberosity; 4, slightly tilted head with reduced lateral lip; 5, beveled surface for the zona conoidea; 6, almost circular head; 7, straight shaft; 8, somewhat retroflexed shaft proximally; 9, moderately globular capitulum; 10, well-developed zona conoidea; 11, poorly defined trochlear lateral keel; 12, lack of entepicondylar foramen; 13, lack of spool-shaped trochlea; 14, narrow trochlear notch without a median keel; 15, slender and hook-like styloid process; 16, more developed ulnar fovea; 17, expanded head with a two-faceted semilunar articulation; 18, facet for the second metacarpal divided by a deep groove for the carpometacarpal ligament; 19, small triquetrum relative to hamate size; 20, small facet for the styloid process. Scale = 1 cm.

combined with crown catarrhine and even crown hominoid synapomorphies absent in *Epipliopithecus*[1] (see Fig. 6 and Supplementary Table 4), such as modern hominoid-like humeroradial and diarthrodial distal radioulnar joints[1]. Previous inferences about the positional behavior of crouzeliid pliopithecoids were very restricted, based on a few isolated specimens available for each genus, suggesting (semi) arboreal quadrupedalism with strong climbing abilities and a varying degree of suspensory behaviors[18,34,35]. Based on the phalanges and femora of *Anapithecus*[18,37] and especially a phalanx of *Laccopithecus*[38], anapithecines may be inferred as more suspensory than *Epipliopithecus*. In turn, a talus and a calcaneus of *Crouzelia* indicate a strong quadrupedal component[35], whereas a proximal radius of the stem crouzeliine *Barberapithecus* indicates enhanced mobility at the elbow joint compared with *Epipliopithecus* but evinces no clear climbing or suspensory adaptations[34]. In contrast, the hominoid-like humeroradial articulation of *Pliobates*, characterized among others by a moderately globular capitulum, a well-developed zona conoidea, and an almost circular radial head with a reduced lateral lip, is clearly adapted for climbing, while its reduced ulnocarpal articulation (more derived than in *Ekembo*) indicates a decreased emphasis on quadrupedalism[1]. Overall, the mosaic postcranial morphology of *Pliobates* is compatible with a versatile arboreal positional repertoire combining significant amounts of eclectic and cautious climbing with above-branch quadrupedalism and some degree of below-branch suspensory behaviors[1].

Implications for ape evolution

Several decades ago, pliopithecoids were considered broadly ancestral to hylobatids (Supplementary Fig. 7) because of resemblances in cranial morphology as well as body size and proportions[27,31,39,40]. However, since the spread of cladistics in the 1980s, pliopithecoids have been generally regarded as stem catarrhines more derived than the Early Oligocene propliopithecoids from Afro-Arabia but less so than dendropithecids[19] (Supplementary Fig. 7). Our cladistic analyses support *Pliobates* as a crouzeliid pliopithecoid but yield different results regarding the systematic status of pliopithecoids depending on whether postcranial characters are considered. In that case, *Pliobates* and other pliopipthecoids are supported as members of the stem hominoid lineage, as in some[1,4] but not most[2,3,5,41] previous cladistic analyses, which support instead a stem catarrhine status. The latter is supported by the lack of crown catarrhine synapomorphies coupled with the retention of more plesiomorphic features including an incompletely ossified ectotympanic, the presence of entepicondylar foramen in the distal humerus, and the possession of a single hinge-like carpometacarpal thumb joint[16–19,42–46]. *Pliobates* is more derived than pliopithecoids by lacking the entepicondylar foramen and displaying

multiple hominoid-like elbow and wrist specializations[1], but its short tubular and incompletely ossified ectotympanic[1], less derived than hose of the stem cercopithecoid *Victoriapithecus*[47] and the stem hominoids *Ekembo*[48] and *Nyanzapithecus*[2], is more similar to that of *Epipliopithecus*[23] and thus more consistent with a stem catarrhine status.

Deciphering the phylogenetic relationships among pliopithecoids, crown catarrhines, and other Miocene catarrhines is not the main aim of this work but the results of our cladistic analyses support the view that pliopithecoids (including *Pliobates*) are stem catarrhines and that previous results indicating a stem hominoid status[1] are probably attributable to the independent acquisition in crouzeliids of postcranial ape-like features. This interpretation illustrates the confounding effect that postcranial convergences might also have when inferring the internal phylogeny of living and fossil hominoids[11–15], not only between extinct taxa such as *Oreopithecus* and crown hominids, but also between hylobatids and hominids. The spread of cladistics promoted the view that postcranial similarities between these clades are synapomorphic[45,49], but the discovery that the pongine *Sivapithecus* displayed a much more primitive postcranium than expected[50] reopened this debate during the 1990s[11]. Subsequent discoveries of *Sivapithecus*[51] and the stem hominid *Pierolapithecus*[52,53] further reinforced the previous contention[11,54] that such similarities may be largely homoplastic[12–15]. However, cladistic analyses performed during the last decades[14,55,56] have continued to support a close relationship between hylobatids and hominids to the exclusion of all Early and most Middle Miocene apes despite molecular evidence indicating that they diverged during the Early Miocene[57,58]. Hominoid phylogenetic inference might be affected by a problem of long-branch attraction between hylobatids and hominids due to the numerous postcranial similarities presumably evolved in parallel between these lineages[15]. Uncertainties surrounding the origin of hylobatids and the lack of associated postcrania for many Miocene apes precludes adequately testing this hypothesis, which is nevertheless supported by preliminary results of tip-dating Bayesian analyses (Fig. 4.3 in ref. 59) and the contradictory results provided by craniodental and postcranial evidence regarding the branching of hylobatids relative to many Miocene apes (Fig. 4 in ref. 14).

The existence of evolutionary convergences in multiple postcranial features among crown hominoids, *Pliobates*, and more distantly related primates such as atelids does not necessarily imply that these features cannot be truly synapomorphic between hylobatids and hominids. However, our cladistic analyses and the more plesiomorphic condition displayed by *Epipliopithecus* support that the crown hominoid-like features of the elbow and wrist joints in *Pliobates* were independently acquired. Given some similarities with *Ekembo*, which lacks suspensory adaptations but displays a rather modern humeroradial joint[11] and an incipient distal radioulnar diarthrosis[60], the condition of *Pliobates* for these joints may still represent a good analog (not homolog) for an ancestral morphotype from which crown hominoids evolved, supporting the view that the aforementioned features originally evolved as climbing adaptations that were later co-opted for suspensory behaviors[61,62] in crown hominoids. The presence of purported crown hominoid synapomorphies—functionally related to orthograde behaviors (i.e., those performed with the trunk held vertically, such as vertical climbing and suspension)—in a pliopithecoid stem catarrhine should not be surprising because climbing adaptations similar to those of apes are also present in lorisids[61,62], while suspensory adaptations have repeatedly evolved in distantly related taxa other than hominoids, such as atelid New World monkeys[11,63,64] and sloth lemurs[65]. Nevertheless, the possession of such features in *Pliobates* renders additional plausibility to the hypothesis that they could have also independently evolved between hylobatids and hominids, as argued in multiple studies[11–15], and as traditionally assumed before the advent of cladistics[11,48,66]. In particular, *Pliobates* illustrates how easily the inclusion of postcranial features prone to homoplasy may override phylogenetic signal—in the case of *Pliobates*, recovering all pliopithecoids as stem hominoids instead of stem catarrhines, as supported instead by (cranio)dental features. In summary, the pliopithecoid status of *Pliobates* supports that similar postcranial features have repeatedly evolved among various catarrhine lineages—likely owing to similar locomotor selection pressures related to orthograde behaviors—and highlights the dramatically misleading (and often underrated) effects that such convergences might have on most parsimonious cladograms in hominoid phylogenetics.

Methods

No relevant ethical regulations were required for the present study.

Age and geological background

The newly described remains come from locality ACM/C5-D1, which is located on meter 188 of the 300-m-thick composite stratigraphic sequence of ACM (els Hostalets de Pierola, Vallès-Penedès Basin, NE Iberian Peninsula), being correlated to chron C5r.2n with an interpolated age of 11.63 Ma[21,22], which roughly coincides with the Middle/Late Miocene boundary. This locality is thus only minimally older than the type locality of *P. cataloniae* (ACM/C8-A4), which is located stratigraphically 6 m above ACM/C5-D1 within the same chron, with an interpolated age of 11.62 Ma[21,22]. Both localities were located close to each other (Supplementary Figs. 8 and 9). On biostratigraphic grounds, they are correlated to the *Democricetodon crusafonti – Hippotherium* interval subzone of the Vallès-Penedès Basin[67], MN7 + 8, late Aragonian[22].

MicroCT scan acquisition and segmentation

IPS58443 was originally scanned at a resolution of 95 μm[1]. To explore dental structures, the specimen was scanned again by X-ray microtomography at the Centro Nacional de Investigación sobre la Evolución Humana (CENIEH; Burgos, Spain) using a GE Phoenix V|Tome|X s240 mCT scanner with the following parameters: 0.35 mA current, 170 kV voltage, 0.2 mm Cu filter, and a magnification of 9.52. The final reconstructed volume has an isometric voxel size of 33 μm. Nine specimens from ACM/C5-D1 were also scanned by X-ray microtomography at the CENIEH with the following parameters: 120 mA current and 115 kV voltage, 0.2 mm Cu filter, and a magnification of 16.67. The final reconstructed volumes have an isometric voxel size of 12 μm. The μCT scans were segmented using Avizo v.7.0 (Visualization Sciences Group, Mérignac) to digitally reconstruct the EDJ surface.

Dental measurements, dental nomenclature, and comparative sample

Dental size measurements of *P. cataloniae* consist of mesiodistal length (MD) and buccolingual breadth (BL), the latter measured separately at the mesial (BLm) and distal (BLd) lobes in the case of molars and dp4. These measurements were taken to the nearest 0.1 mm with a digital caliper in all specimens except for the P4 of IPS42977 and the m1 and m2 of IPS43936, which had to be digitally extracted from microCT scans and were thus measured using the 2D Length tool in Avizo v. 7.0. The breadth/length index (BLI, in %) was computed for cheek teeth as BLI = maximum BL/MD × 100 in Microsoft Excel 2023. Dental nomenclature follows Harrison and Gu[17]. Dental measurements for the comparative sample (including dendropithecids and pliopithecoids) were taken from published sources and/or measured from casts by D.M.A. (see Supplementary Table 2). Details on all taxa analyzed are provided in Supplementary Table 5.

Systematics

A modified classification is proposed here for pliopithecoids, which updates the previously available classification from Harrison et al.[20] based on recent results for *Kapi*[8] and the results of our cladistic analysis (Fig. 5; Table 2).

Body mass estimation

The body mass (BM, in kg) of *P. cataloniae* was estimated from dental measurements of upper and lower molars (M1–M3 and m1–m2) using anthropoid allometric equations based on occlusal tooth square area (A, in mm^2)[68], computed as A = MD × BL. For tooth positions represented by several specimens, average A was used to estimate BM. Logarithmic detransformation bias was corrected using the ratio estimator[68]. The 50% confidence interval (CI) was computed for each tooth locus using the standard error of estimate and an inverse Student's *t* distribution with the degrees of freedom determined by the effective sample size[68]. An average estimate was computed as the arithmetic mean of estimates for the various tooth loci, with the CI taken as the maximum and minimum ends of the 50% CIs of the included tooth loci. All computations were performed in Microsoft Excel 2023.

Cladistic analysis

The phylogenetic relationships of *P. cataloniae* were inferred by means of a cladistic analysis based on maximum parsimony using PAUP* v. 4.0a169[69]. A character-taxon matrix including all pliopithecoids, three dendropithecid species, and two crown catarrhine species, along with the stem catarrhines *Aegyptopithecus zeuxis* (used as outgroup) and *Saadanius hijanzensis*, was compiled, using and/or modifying dental characters from published sources[1,8,20] and defining new ones (see Supplementary Data 1 for character statements). All characters were treated as unordered, variable characters were scored as multistate, and continuous characters were discretized using the gap-weighted coding method[70]. 23 characters were continuous and discretized. 9 characters were parsimony uninformative. A heuristic search method was applied to search for most parsimonious trees and a strict consensus tree computed. The following metrics were computed: consistency index (CI) excluding uninformative characters, retention index (RI), and rescaled consistency index (RCI). Clade robusticity was assessed by means of bootstrap analysis (1000 replicates) and Bremer's support indices. The analyzed pliopithecoid taxa are the following (Supplementary Table 5): *Dionysopithecus shuangouensis* and *Platodontopithecus jianghuaiensis* from China; *Fanchangia jini* from China; *Pliopithecus* spp. from Europe and China; *Epipliopithecus vindobonensis* from Slovakia; *Crouzelia auscitanensis* and *Plesiopliopithecus lockeri* from France and Austria, respectively; *Crouzelia rhodanica* from France; *Barberapithecus huerzeleri* from Spain; *Anapithecus hernyaki* from Austria, Germany, and Hungary; the Mörgen crouzeliine from Germany; *Egarapithecus narcisoi* from Spain; *Krishnapithecus krishnaii* from India; and *Laccopithecus robustus* from China. Other analyzed taxa include the stem cercopithecoid *Victoriapithecus macinnesi* from Kenya and Uganda, the stem hominoid *Ekembo heseloni* from Kenya, the stem catarrhine *Saadanius hijazensis* from Saudi Arabia, and the dendropithecids *Dendropithecus macinnesi* from Kenya, *Micropithecus clarki* from Uganda, and *Simiolus enjiessi* from Kenya.

A second cladistic analysis at the genus level, essentially based on a modified version of the dental features used for the dental analysis at the species level but further including cranial and postcranial characters, and with a more restricted representation of pliopithecoids but a wider sample of both extant and extinct hominoids, was performed. The taxa included are those used in the analysis in ref. 1 with some improvements: *Proconsul* s.l. was replaced by *Ekembo* (i.e., excluding *Proconsul* s.s.), the dendropithecids *Simiolus* and *Dendropithecus* were kept separate, and the the crouzeliines *Crouzelia* and *Plesiopliopithecus* were analyzed separately as well. We further grouped all *Pliopithecus* species (as in ref. 1), implying that some dental characters were coded as multistate. Regarding the dental features, we added two additional characters, #96 and #97, corresponding to characters #4 and #40 in ref. 1 (Supplementary Data 4 and 5); furthermore, due to the addition of new taxa, we modified the definition and/or recoded the taxa for the following characters: #18, #24, #35, #38, #41, #43, #45, #47, #53–56, #58–59, #64–69, and #88 (Supplementary Data 4 and 5). We further updated the cranial and postcranial features based on recently published papers dealing with *Pliobates* and/or other pliopithecoids[9,10,34,46] (Supplementary Data 4 and 5): in the case of the cranium, we updated the characters related to the carotid canal based on ref. 9 (i.e., discarding characters #106 and #107 of ref. 1 and rather adding the two characters from ref. 9 corresponding to #167 and #168 here; Supplementary Data 4 and 5) and added those of the semicircular canals based on ref. 10 and the preliminary results reported so far for *Pliobates* in ref. 46 (characters #169–175; Supplementary Data 4 and 5). For the postcranial characters, we only modified some of the character states of *Barberapithecus* proximal radius following the results of ref. 34 (i.e., #143–145, #150–151, and #156–157 in ref. 1, corresponding to #205–207, #212–213, and #218–219 here; Supplementary Data 4 and 5). The rationale behind the use of the cranial and postcranial characters and taxa analyzed in ref. 1 as a base for this second cladistic analysis is that the analysis of ref. 1 is the only that thus far recovered *Pliobates* as a stem hominoid instead of a pliopithecoid. Similar parameters to those of the dental analysis were applied (i.e., character types and scoring, search methods, and metric computation). In total, 22 characters were parsimony uninformative. Given the suspicion that postcranial homoplasy might be distorting the most parsimonious topology recovered for hominoids by parsimony analyses[14,15], we decided to analyze dental, craniodental, and postcranial characters both jointly and separately, to evaluate the influence of each of these anatomical regions on the results. In the analysis based exclusively on postcranial characters, *Saadanius*, *Dionysopithecus*, *Plesiopliopithecus*, and *Crouzelia* were removed because of the excessive amount of missing data for the characters considered in ref. 1. Some dental measurements necessary to code some features in extant taxa were downloaded from PRIMO, the NYCEP PRImate Morphology Online database (http://primo.nycep.org).

Reporting summary

Further information on research design is available in the Nature Portfolio Reporting Summary linked to this article.

Data availability

All dentognathic remains of *P. cataloniae*, including those from ACM/C5-D1 and the holotype, are housed in the Institut Català de Paleontologia Miquel Crusafont (ICP), Sabadell, Spain, and available to study by other researchers. 3D models of the outer enamel surface (OES) are openly available from MorphoSource (Supplementary Table 6), whereas 3D models of the enamel-dentine junction (EDJ) have been uploaded to MorphoSource (Supplementary Table 6) but are embargoed until ongoing research of tooth endostructural morphology is published. MicroCT scans are curated at the ICP and have also been deposited in MorphoSource. They are accessible upon reasonable request by other researchers, as in the case of the physical fossils housed in the same institution. Most dental measurements for the comparative sample (including both extinct and extant taxa) are available from various published sources. Some dental measurements for extant taxa are available from PRIMO, the NYCEP PRImate Morphology Online database (http://primo.nycep.org). The authors declare that all other data supporting the findings of this study are available within the paper, its supplementary information files, and supplementary data files. Source data are provided as a Source Data file. Source data are provided with this paper.

References

1. Alba, D. M. et al. Miocene small-bodied ape from Eurasia sheds light on hominoid evolution. *Science* **350**, aab2625 (2015).
2. Nengo, I. et al. New infant cranium from the African Miocene sheds light on ape evolution. *Nature* **548**, 169–174 (2017).

3. Gilbert, C. C. et al. New Middle Miocene ape (Primates: Hylobatidae) from Ramnagar, India fills major gaps in the hominoid fossil record. *Proc. R. Soc. B Biol.* **287**, 20201655 (2020).
4. Zalmout, I. S. et al. New Oligocene primate from Saudi Arabia and the divergence of apes and Old World monkeys. *Nature* **466**, 360–365 (2017).
5. Rossie, J. B. & Hill, A. A new species of *Simiolus* from the middle Miocene of the Tugen Hills, Kenya. *J. Hum. Evol.* **125**, 50–58 (2018).
6. Benefit, B. & McCrossin, M. L. A window into ape evolution. *Science* **350**, 515–516 (2015).
7. Gilbert, C. C., Pugh, K. D. & Fleagle, J. G. Dispersal of Miocene hominoids (and pliopithecoids) from Africa to Eurasia in light of changing tectonics and climate. in *Biological Consequences of Plate Tectonics: New Perspectives on Post-Gondwana Break-up—A Tribute to Ashok Sahni* (eds. Prasad, G. V. R. & Patnaik, R.) 393–412 (Springer, 2020).
8. Ji, X. et al. The earliest hylobatid from the Late Miocene of China. *J. Hum. Evol.* **171**, 103251 (2022).
9. Bouchet, F. et al. Comparative anatomy of the carotid canal in the Miocene small-bodied catarrhine *Pliobates cataloniae*. *J. Hum. Evol.* **161**, 103073 (2021).
10. Urciuoli, A. et al. Semicircular canal morphology of the Miocene small-bodied catarrhine *Pliobates cataloniae*: Phylogenetic implications. *Am. J. Biol. Anthropol.* **177**, 187 (2022).
11. Larson, S. G. Parallel evolution in the hominoid trunk and forelimb. *Evol. Anthropol.* **6**, 87–99 (1998).
12. Alba, D. M. Fossil apes from the Vallès-Penedès Basin. *Evol. Anthropol.* **21**, 254–269 (2012).
13. Almécija, S. et al. Fossil apes and human evolution. *Science* **372**, eabb4363 (2021).
14. Pugh, K. D. Phylogenetic analysis of Middle-Late Miocene apes. *J. Hum. Evol.* **165**, 103140 (2022).
15. Urciuoli, A. & Alba, D. M. Systematics of Miocene apes: State of the art of a neverending controversy. *J. Hum. Evol.* **175**, 103309 (2023).
16. Andrews, P., Harrison, T., Delson, E., Bernor, R. & Martin, L. Distribution and biochronology of European and southwest Asian Miocene catarrhines. in *The Evolution of Western Eurasian Neogene Mammal Faunas* (eds. Bernor, R. L., Fahlbusch, V. & Mittmann H.-W) 168–207 (Columbia University Press, 1996).
17. Harrison, T. & Gu, Y. Taxonomy and phylogenetic relationships of Early Miocene catarrhines from Sihong. *China J. Hum. Evol.* **37**, 225–277 (1999).
18. Begun, D. R. The Pliopithecoidea. in *The Primate Fossil Record* (ed. Hartwig, W. C.) 221–240 (Cambridge University Press, 2002).
19. Harrison, T. Catarrhine origins. in *A Companion to Paleoanthropology* (ed. Begun, D. R.) 376–396 (Blackwell Publishing Ltd., 2013).
20. Harrison, T. et al. A new genus of pliopithecoid from the late Early Miocene of China and its implications for understanding the paleozoogeography of the Pliopithecoidea. *J. Hum. Evol.* **145**, 102838 (2020).
21. Alba, D. M., Casanovas-Vilar, I., Garcés, M. & Robles, J. M. Ten years in the dump: An updated review of the Miocene primate-bearing localities from Abocador de Can Mata (NE Iberian Peninsula). *J. Hum. Evol.* **102**, 12–20 (2017).
22. Alba, D. M. et al. A revised (earliest Vallesian) age for the hominoid-bearing locality of Can Mata 1 based on new magnetostratigraphic and biostratigraphic data from Abocador de Can Mata (Vallès-Penedès Basin, NE Iberian Peninsula). *J. Hum. Evol.* **170**, 103237 (2022).
23. Heißig, K. Ein Pliopithecide aus dem Vallesium (MN 9) der Oberen Süßwassermolasse Bayerns. *Ber. Naturwiss. Ver. Schwab.* **103**, 1–2 (1999).
24. Seehuber, U. Litho- und biostratigraphische Untersuchungen in der Oberen Süßwassermolasse in der Umgebung von Kirchheim in Schwaben. (Ludwig-Maximilians-Universität München, 2008).
25. Alba, D. M. & Moyà-Solà, S. A new pliopithecid genus (Primates, Pliopithecoidea) from Castell de Barberà (Vallès-Penedès Basin, Catalonia, Spain). *Am. J. Phys. Anthropol.* **147**, 88–112 (2012).
26. Sankhyan, A. R., Kelley, J. & Harrison, T. A highly derived pliopithecoid from the Late Miocene of Haritalyangar, India. *J. Hum. Evol.* **105**, 1–12 (2017).
27. Zapfe, H. Die Primatenfunde aus der miozänen Spaltenfüllung von Neudorf an der March (Děvinská Nová Ves), Tschechoslowakei. *Schweiz. Palaeontol. Abh.* **78**, 4–293 (1961).
28. Fleagle, J. G. & Simons, E. L. *Micropithecus clarki*, a small ape from the Miocene of Uganda. *Am. J. Phys. Anthropol.* **49**, 427–440 (1978).
29. Pugh, K. D. et al. The reconstructed cranium of *Pierolapithecus* and the evolution of the great ape face. *Proc. Natl Acad. Sci. USA* **120**, e2218778120 (2023).
30. Zapfe, H. & Hürzeler, J. Die Fauna der miozänen Spaltenfüllung von Neudorf an der March (ČSR). Primates. *Sitzungsber. Öst. Akad. Wiss. Math. Naturwiss. Kl.* **166**, 113–123 (1957).
31. Zapfe, H. The skeleton of *Pliopithecus* (*Epipliopithecus*) *vindobonensis* Zapfe and Hürzeler. *Am. J. Phys. Anthropol.* **16**, 441–457 (1958).
32. Rose, M. D. Quadrupedalism in some Miocene catarrhines. *J. Hum. Evol.* **26**, 387–411 (1994).
33. Arias-Martorell, J., Alba, D. M., Potau, J. M., Bello-Hellegouarch, G. & Pérez-Pérez, A. Morphological affinities of the proximal humerus of *Epipliopithecus vindobonensis* and *Pliopithecus antiquus*: Suspensory inferences based on a 3D geometric morphometrics approach. *J. Hum. Evol.* **80**, 83–95 (2015).
34. Arias-Martorell, J. et al. A proximal radius of *Barberapithecus huerzeleri* from Castell de Barberà: Implications for locomotor diversity among pliopithecoids. *J. Hum. Evol.* **157**, 103032 (2021).
35. Senut, B. Les restes post-crâniens des Pliopithecidae (Primates) de Sansan. *Mém. Mus. Natl Hist. Nat.* **203**, 535–558 (2012).
36. Alba, D. M. & Moyà-Solà, S. New fossil remains of *Pliopithecus canmatensis* from Abocador de Can Mata, and their implications for the taxonomic validity and phylogenetic position of *Epipliopithecus* (Primates, Pliopithecidae). *Am. J. Phys. Anthropol.* **153**, 64 (2014).
37. Kordos, L. & Begun, D. R. Femora of *Anapithecus* from Rudabànya. *Am. J. Phys. Anthropol.* **108**, 173 (1999).
38. Meldrum, D. J. & Pan, Y. Manual proximal phalanx of *Laccopithecus robustus* from the latest Miocene site of Lufeng. *J. Hum. Evol.* **17**, 719–731 (1988).
39. Hürzeler, J. Contribution à l'odontologie et à la phylogénèse du genre *Pliopithecus* Gervais. *Ann. Paleontol.* **40**, 5–63 (1954).
40. Simons, E. L. & Fleagle, J. G. The history of extinct gibbon-like primates. in *Gibbon and Siamang Vol. 2. Anatomy, Dentition, Taxonomy, Molecular Evolution and Behavior* (ed. Rumbaugh, D. M.) 121–148 (Karger, 1973).
41. Stevens, N. J. et al. Palaeontological evidence for an Oligocene divergence between Old World monkeys and apes. *Nature* **497**, 611–614 (2013).
42. Delson, E. Catarrhine phylogeny and clasification: Principles, methods and comments. *J. Hum. Evol.* **6**, 433–459 (1977).
43. Szalay, F. & Delson, E. *Evolutionary History of the Primates* (Academic Press, 1979).
44. Fleagle, J. G. Are there any fossil gibbons? in *The Lesser Apes: Evolutionary and Behavioral Biology* (eds. Preuschoft, H., Chivers, D. J., Brockelman, W. Y. & Creel, N.) 431–447 (Edinburgh University Press, 1984).

45. Harrison, T. The phylogenetic relationships of the early catarrhine primates: a review of the current evidence. *J. Hum. Evol.* **16**, 41–80 (1987).
46. Urciuoli, A. et al. A comparative analysis of the vestibular apparatus in *Epipliopithecus vindobonensis*: Phylogenetic implications. *J. Hum. Evol.* **151**, 102930 (2021).
47. Benefit, B. R. & McCrossin, M. L. Earliest known Old World monkey skull. *Nature* **388**, 368–371 (1997).
48. Napier, J. R. & Davis, P. R. The forelimb skeleton and associated remains of *Proconsul africanus*. *Foss. Mamm. Afr.* **16**, 1–69 (1959).
49. Pilbeam, D. Genetic and morphological record of the Hominoidea and hominid origins: A synthesis. *Mol. Phylogenet. Evol.* **5**, 155–168 (1996).
50. Pilbeam, D., Rose, M. D., Barry, J. C. & Shah, S. M. I. New *Sivapithecus* humeri from Pakistan and the relationship of *Sivapithecus* and *Pongo*. *Nature* **348**, 237–239 (1990).
51. Morgan, M. E. et al. A partial hominoid innominate from the Miocene of Pakistan: Description and preliminary analyses. *Proc. Natl Acad. Sci. USA* **112**, 82–87 (2015).
52. Moyà-Solà, S., Köhler, M., Alba, D. M., Casanovas-Vilar, I. & Galindo, J. *Pierolapithecus catalaunicus*, a new Middle Miocene great ape from Spain. *Science* **306**, 1339–1344 (2004).
53. Almécija, S., Alba, D. M. & Moyà-Solà, S. *Pierolapithecus* and the functional morphology of Miocene ape hand phalanges: paleobiological and evolutionary implications. *J. Hum. Evol.* **57**, 284–297 (2009).
54. Thenius, E. Zur systematischen Stellung der Gibbons oder Langarmaffen (Hylobatidae, Primates). *Sitz. Ber. K. Akad. Wiss. Math. Naturwiss. Kl.* **190**, 1–5 (1981).
55. Begun, D. R., Ward, C. V. & Rose, M. D. Events in hominoid evolution. in *Function, Phylogeny and Fossils: Miocene Hominoid Evolution and Adaptation* (eds. Begun, D. R., Ward, C. V. & Rose, M. D.) 389–415 (Plenum Press, 1997).
56. Finarelli, J. A. & Clyde, W. C. Reassessing hominoid phylogeny: evaluating congruence in the morphological and temporal data. *Paleobiology* **30**, 614–651 (2004).
57. Chatterjee, H. J., Ho, S. Y. W., Barnes, I. & Groves, C. Estimating the phylogeny and divergence times of primates using a supermatrix approach. *BMC Ecol. Evol.* **9**, 259 (2009).
58. Roos, C. & Zinner, D. Primate phylogeny. in *The International Encyclopedia of Primatology* (ed. Fuentes, A.) (John Wiley & Sons, 2017), https://doi.org/10.1002/9781119179313.wbprim0394.
59. Pugh, K. D. The phylogenetic relationships of middle-late Miocene apes: Implications for early human evolution. (City University of New York, 2020).
60. Daver, G. & Nakatsukasa, M. *Proconsul heseloni* distal radial and ulnar epiphyses from the Kaswanga Primate Site, Rusinga Island, Kenya. *J. Hum. Evol.* **80**, 17–33 (2015).
61. Cartmill, M. & Milton, C. The lorisiform wrist joint and the evolution of "brachiating" adaptations in the Hominoidea. *Am. J. Phys. Anthropol.* **47**, 249–272 (1977).
62. Sarmiento, E. E. Cautious climbing and folivory: a model of hominoid differentiation. *Hum. Evol.* **10**, 289–321 (1995).
63. Tuttle, R. Parallelism, brachiation, and hominoid phylogeny. In *Phylogeny of the Primates* (eds. Luckett, W. P. & Szalay, F. S.) 447–480 (Springer, 1975).
64. Hunt, K. D. Why are there apes? Evidence for the co-evolution of ape and monkey ecomorphology. *J. Anat.* **228**, 630–685 (2016).
65. Jungers, W. L., Godfrey, L. R., Simons, E. L. & Chatrath, P. S. Phalangeal curvature and positional behavior in extinct sloth lemurs (Primates, Palaeopropithecidae). *Proc. Natl Acad. Sci. USA* **94**, 11998–12001 (1997).
66. Le Gros Clark, W. & Thomas, D. P. Associated jaws and limb bones of *Limnopithecus macinnesi*. *Foss. Mamm. Afr.* **3**, 1–27 (1951).
67. Casanovas-Vilar, I. et al. The Miocene mammal record of the Vallès-Penedès Basin (Catalonia). *C. R. Palevol* **15**, 791–812 (2016).
68. Egi, N., Takai, M., Shigehara, N. & Tsubamoto, T. Body mass estimates for Eocene eosimiid and amphipithecid primates using prosimian and anthropoid scaling models. *Int. J. Primatol.* **25**, 211–236 (2004).
69. Swofford, D. *PAUP* 4.0* (Sinauer Associates, 2003).
70. Thiele, K. The holy grail of the perfect character: The cladistic treatment of morphometric data. *Cladistics* **9**, 275–304 (1993).
71. Almécija, S. et al. Early anthropoid femora reveal divergent adaptive trajectories in catarrhine hind-limb evolution. *Nat. Comm.* **10**, 4778 (2019).
72. Fleagle, J. G. *Primate Adaptation and Evolution*, 3rd ed. (Academic Press, 2013).

Acknowledgements

This publication is part of R + D + I projects PID2020-116908GB-I00 (to S.M.S. and J.M.R.), PID2020-117289GB-I00 (to D.M.A. and J.M.R.), and PID2020-117118GB-I00 (to J.F.), funded by the Agencia Estatal de Investigación of the Ministerio de Ciencia e Innovación from Spain (MCIN/AEI/10.13039/501100011033/). Research has also been funded by the Generalitat de Catalunya/CERCA Programme (to F.B., A.U., S.A., J.F., J.M.R., S.M.S. and D.M.A.); the Agència de Gestió d'Ajuts Universitaris i de Recerca of the Generalitat de Catalunya (Consolidated Research Groups 2022 SGR 00620 to D.M.A. and J.M.R., 2022 SGR 01184 to J.F., and 2022 SGR 01188 to S.M.S.); the Departament de Cultura of the Generalitat de Catalunya (CLT009/18/00071 to S.M.S. and CLT0009_22_000018 to D.M.A.); a predoctoral grant from the Ministerio de Ciencia e Innovación (PRE2018-083299 to F.B.); a Margarita Salas postdoctoral fellowship funded by the European Union NextGenerationEU to A.U.; and a Ramón y Cajal grant (RYC2021-032857-I) financed by the Agencia Estatal de Investigación of the Ministerio de Ciencia e Innovación from Spain (MCIN/AEI/10.13039/501100011033) and the European Union «NextGenerationEU» / PRTR to J.F. Fieldwork was defrayed by CESPA Gestión de Residuos and UTE Ampliació Can Mata. We further acknowledge the support of the Servei d'Arqueologia i Paleontologia of the Generalitat de Catalunya and the collaboration of the Centre d'Interpretació i Restauració Paleontològica (Ajuntaments dels Hostalets de Pierola). µCT scans of *Pliobates* were performed at the CENIEH facilities (Burgos, Spain) with the collaboration of the CENIEH staff. We thank M. Méndez and other ICP technicians for their efforts in screen-washing and concentrate sorting of sediments from ACM/C5-D1, Sergio Llácer for the segmentation of most of the dental specimens of *Pliobates*, E. Delson for granting us access to the PRIMO database and his collection of casts at the AMNH, J. Galindo for collection assistance, S.G. Arranz for assistance with photographs, the staff of the Preparation Area of the ICP for the excellent preparation of the described specimens, and all the field paleontologists that worked at ACM throughout the years for their endurance.

Author contributions

F.B., S.M.S. and D.M.A. designed research and assembled the cladistic data matrix; F.B., performed the phylogenetic analyses; F.B. and D.M.A. performed the descriptions and comparisons; J.F. supervised microCT-scanning and segmentation; C.Z. contributed to the segmentations and reconstructions of some of the virtual models; J.M.R. directed fieldwork and performed stratigraphic correlations; C.Z., A.U., S.A., J.F., A.B., S.M.S. and D.M.A. contributed to the interpretation of the results; S.A. contributed to the design of some of the figures; F.B., S.A, and D.M.A. wrote the paper with input from all other authors.

Competing interests

The authors declare no competing interest.

Additional information

Supplementary information The online version contains supplementary material available at https://doi.org/10.1038/s41467-024-47034-9.

Correspondence and requests for materials should be addressed to Florian Bouchet or David M. Alba.

Peer review information *Nature Communications* thanks the anonymous reviewer(s) for their contribution to the peer review of this work. A peer review file is available.

Reprints and permissions information is available at http://www.nature.com/reprints

Publisher's note Springer Nature remains neutral with regard to jurisdictional claims in published maps and institutional affiliations.

Open Access This article is licensed under a Creative Commons Attribution 4.0 International License, which permits use, sharing, adaptation, distribution and reproduction in any medium or format, as long as you give appropriate credit to the original author(s) and the source, provide a link to the Creative Commons licence, and indicate if changes were made. The images or other third party material in this article are included in the article's Creative Commons licence, unless indicated otherwise in a credit line to the material. If material is not included in the article's Creative Commons licence and your intended use is not permitted by statutory regulation or exceeds the permitted use, you will need to obtain permission directly from the copyright holder. To view a copy of this licence, visit http://creativecommons.org/licenses/by/4.0/.

© The Author(s) 2024

Supplementary Information

The Miocene primate *Pliobates* is a pliopithecoid

Florian Bouchet*, Clément Zanolli, Alessandro Urciuoli, Sergio Almécija, Josep Fortuny, Josep M. Robles, Amélie Beaudet, Salvador Moyà-Solà, David M. Alba*

*To whom correspondence may be addressed: florian.bouchet@icp.cat, david.alba@icp.cat

This file includes:

Supplementary Text 1 to 4
Supplementary Figure 1 to 9
Supplementary Table 1 to 6
Supplementary References

Supplementary Text 1. Differential diagnosis (Differential diagnosis relative to other pliopithecoids emended from the original description based on dental features; for cranial and postcranial features, see ref. 1). *Pliobates* differs from non-crouzeliid pliopithecoids in the relatively narrower P4 with a narrower distal basin; the more buccolingually compressed cusps and sharper crests in the molars; the M1 and M2 markedly longer buccally than lingually; the relatively narrower M2; the relatively broader and more trapezoidal M3, with a lingually located metacone and a lesser developed lingual cingulum; the more inclined i2; the relatively narrower m1 and m2, with a longer mesial fovea, a distal fovea continuous with the talonid basin (more clearly so in the m1), and the hypoprotocristid originating distally from the protoconid; and the lack of the mesial arm of the pliopithecine triangle in both m1 and m2 (although it is only variably present and poorly developed in *Epipliopithecus*). It also differs from dionysopithecids in the more asymmetrical I1 (unknown in *Platodontopithecus*); the more mesial paracone in the upper premolars; the upper molars with a more distally located protocone and a smaller hypocone; the less developed lingual cingulum distally to the hypocone in M1 and M2; the lesser developed buccal cingulum in M3; the relatively broader P3 with a less peripheral paracone (unknown in *Dionysopithecus*); and the less peripheralized cusps of the lower molars. *Pliobates* further differs from pliopithecids in the more asymmetrical I1; the more ovoid and relatively narrower P3 with a narrower distal basin and a more peripheral paracone; the relatively narrower M1 with a relatively longer trigon basin; the more distally located protocone and the smaller hypocone in M3; the female c1, with a more marked mesiolingual cuspulid-like enamel thickening (only known in *Pliopithecus platyodon*). Finally, *Pliobates* also differs from *Epipliopithecus* in the m1 and m2 with a more medial hypoconulid and a very distinct distal arm of the pliopithecine triangle.

In turn, *Pliobates* differs from other crouzeliid genera in the more suboval p4 with more mesial metaconid and protoconid (unknown in *Krishnapithecus*), and the m1 and m2 with entoconid almost transversely aligned with the hypoconid (except *Barberapithecus*) and lacking the mesial arm of the pliopithecine triangle (although it is variably present in *Anapithecus* and absent to only incipiently developed in *Laccopithecus* and *Krishnapithecus*). It also differs from anapithecines in the more ovoid P3 with a less peripheral paracone (unknown in *Krishnapithecus*); the relatively broader and more trapezoidal M3, with less peripheral metacone and smaller hypocone (unknown in *Egarapithecus*); and the relatively narrower m1 and m2. From anapithecines other than *Fanchangia*, in the smaller M2–M3 metacone; the lack of distinct p4 distal cuspids; and the presence of a distinct distal arm of the pliopithecine triangle in both m1 and m2 (variably present in *Anapithecus*). From anapithecines other than *Anapithecus*, in the better developed (more ledge-like) buccal cingulid in lower molars. From anapithecines other than *Krishnapithecus*, in the distal fovea of lower molars, continuous with the talonid basin (more clearly so in m1). From *Fanchangia*, *Krishnapithecus*, and *Laccopithecus*, in the more buccolingually compressed cusps and sharper crests in the molars; and

the m1 and m2 with a longer mesial fovea and hypoprotocristid originating distally from the protoconid. From *Fanchangia*, *Laccopithecus*, and *Anapithecus*, in the more asymmetrical I1, with narrower cingulum and slenderer crown base; the more suboval and relatively broader P4; the less buccolingually waisted M1 and M2; and the relatively broader female c1. From *Fanchangia* and *Laccopithecus*, in the presence of a rudimentary hypocone in the P4; and the broader lingual cingulum in M1 and M2. From *Laccopithecus* and *Anapithecus*, in the lesser developed lingual cingulum in M3. From *Anapithecus* and *Egarapithecus*, in the less inclined cristid obliqua in m1 and m2 (directed toward the protoconid instead of the hypoprotocristid-hypometacristid merging). From *Krishnapithecus*, in the lower, less peripheral, but more extensive cuspids in m1 and m2, including a larger hypoconulid with distinct postcristid and hypoentocristid. From *Anapithecus* in the mesiodistally waisted i2 towards cervix. And from *Egarapithecus*, in the more medial hypoconulid in m1 and m2.

Finally, *Pliobates* differs from other crouzeliine genera (*Barberapithecus*, *Plesiopliopithecus*, and *Crouzelia*) in a unique combination of dental features. From *Barberapithecus* and *Plesiopliopithecus*, in the distal fovea continuous with the talonid basin in the lower molars (especially m1). From *Barberapithecus* and *Crouzelia*, in the wider buccal cingulid in m1 and m2. From *Barberapithecus*, in the more asymmetrical I1; the upper molars with narrower buccal cingulum and more peripheral buccal cusps; the M1 and M2 with wider lingual cingulum and less buccolingual waisting; the relatively broader and more trapezoidal M3, with more lingually located metacone, smaller hypocone, and narrower lingual cingulum; the female c1 with a more marked mesiolingual cuspulid-like thickening; and the relatively narrower m1 and m2, with hypoprotocristid originating more distally from the protoconid. From *Plesiopliopithecus* and *Crouzelia*, in the lesser developed buccal cingulid in p4; and the m1 and m2 with larger hypoconulid, and a more distinct distal arm of the pliopithecine triangle. Finally, from *Crouzelia*, in the distinct postcristid and hypoentocristid in m1 and m2.

Supplementary Text 2. Preservation of the specimens The dental remains of the holotype are preserved in two different maxillary fragments (Fig. 1 in ref. 1): IPS58443.1 includes the right I1–C1 alveoli filled with sediment, the broken P3, and the complete P4–M3 series (Fig. 2m); in turn, IPS58443.2 (Fig. 2m) preserves the left M3, the broken M2 (the buccal moiety is broken away), and the apicalmost portion of the lingual and distobuccal roots of the M1. The molars of the holotype show an advanced (M1–M2) to moderately advanced (M3) degree of wear. In the M1, the four main cusps have been completely eroded by wear (the dentine exposures corresponding to the paracone and metacone being continuous with one another). The M2 shows a comparable degree of wear, except for the metacone, which is only worn at its tip, with its dentine exposed area not being continuous with that of the paracone. The M3 shows a more moderate degree of wear, with dentine exposure being limited to the protocone and the apex of the paracone.

IPS44014 (Figs. 2a–c) is a left maxillary fragment preserving the I1–I2 and C1 alveoli (the latter somewhat damaged distally) as well as the socketed P3–M1 series. The P3 and P4 crowns are well preserved and only show slight wear with minimal dentine exposure restricted to the paracone apex. The M1 is only slightly more worn than the premolars, with dentine exposure limited to the apices of its four main cusps.

The right maxillary fragment IPS43758 (Fig. 2d–e) preserves the M1–M2, which show an advanced degree of wear (even more marked in the M2 than in the M1). The M1 further has its mesiolingual portion slightly damaged (a fragment of the enamel cap is missing), and the M2 is more severely damaged on its distal portion, since a crown fragment is missing, although measurements can be readily taken. There is abundant dentine exposure in the four main cusps, with the exposed areas corresponding to the protocone and hypocone completely merged in the M2. The M1 also shows dentine exposure at the metacone. Owing to bone breakage, the roots are visible.

The left maxillary fragment IPS42977 (Figs. 2j–l) preserves an almost complete DP4 that is only missing a chip of enamel from the distolingual portion of the crown wall. It shows some dentine exposure along the crista obliqua and the apices of the three cusps.

The left I1 IPS43488 (Fig. 2z) is completely preserved except for the apical end of the root. The crown is very worn, both labially and, more markedly, lingually, so that dentine is abundantly exposed along the whole distolingual portion of the crown (from the incisal edge to close to the base) and its mesiolingual basal portion.

The left M2 germ IPS94888 (Figs. 2q and 4i) is very well preserved and further includes the basalmost portion of the forming roots.

The right M1 IPS100379 (Figs. 2p and 4g) preserves the crown, which is very corroded, as well as the complete lingual root. The occlusal surface is covered by a carbonaceous crust that extends onto the root. The cusp apices show a moderate degree of wear. In contrast, most of the lingual,

mesial, and distal parts of the crown completely expose the dentine exposure, probably because the enamel cap has been dissolved.

The left M2 germ IPS100384 (Figs. 2r and 4h) preserves the unworn occlusal morphology.

The mandibular fragment IPS43936 (Figs. 1g–I and 3) includes the symphysis and the left corpus. The alveoli of the left di1–dc1 and right di1 are preserved. The crown of the dp3 is only partially preserved (since its distalmost portion is missing) and shows very slight wear with no dentine exposure (Figs. 2x and 4o). The crown of the dp4 is well preserved, except for a small enamel chip missing from the mesial aspect of the metaconid, and only shows minimal wear on the cuspid apices (Figs. 2x and 4p). The occlusal morphology of the m1 is perfectly preserved because it is an unerupted germ, but it can only be partially ascertained because it is still inside its crypt. 3D models of the m1 and the m2 germs could nevertheless be digitally extracted from the CT scans (Figs. 3 h–i and 4k–l), that of the m2 lacking a larger portion of the crown base, although reliable estimates of BL and MD measurements could be taken. 3D models of tooth germs of the right i1 and left i1–p4 were similarly extracted from their crypts (Fig. 3c–g). While the i1 crowns are nearly completed down to the cervix and show a beginning of root formation, the i2 and c1 crowns are close to completion, but lack the basalmost portion of the crown. The crown germs of p3–p4 only show parts of the cusps. Due to the lack of completion of enamel formation, no measurements were taken.

The left i2 IPS44273 (Fig. 2a') preserves the whole crown and most of the root. The crown is moderately worn with some dentine exposure along the incisal edge.

The left c1 IPS43433 (Fig. 2b') is completely preserved. The crown displays a moderate degree of wear at its apex and more abundant dentine exposure on the distobuccal basal portion of the crown.

The right p4 IPS43820 (Fig. 2t) is very fragmentary, consisting of a very worn partial crown that is missing its mesiolingual portion and only preserves the basalmost portion of the roots. Most occlusal details have been worn away.

The right p4 IPS93524 (Figs. 2s and 4j) is only partially preserved, including the damaged crown and the basalmost portion of the roots. Most of the mesial end of the crown is broken away, and enamel is also missing from the distal end and the buccal margin of the talonid basin. The preserved occlusal portions display an advanced degree of wear, with dentine exposure at the metaconid apex.

The right m2 unworn germ IPS94886 (Figs. 2u and 4m) only preserves the mesial part of the crown, including the protoconid, the metaconid, and the trigonid basin.

The right DI1 IPS44393 (Fig. 2z) is an unworn germ.

The left DP3 germ IPS43013 (Fig. 2v) displays a moderate degree of wear, mainly restricted to the three main cusps, with minimal dentine exposure, and to the distal portion of the crown.

The left dp4 IPS106878 crown (Figs. 2m and 3q) is overall well preserved, showing minimal to slight wear on the apices of the five main cuspids. However, there is an oblique crack running from

the hypoconid to the mesiolingualmost corner of the crown, revealing some dentine along the cristid obliqua. The roots of this tooth seem to have been broken away.

Supplementary Text 3. Extended Descriptions

Upper incisors As preserved, the crown of the left I1 IPS43488 displays a subovoid occlusal contour that is tilted mesiolabially relative to its main mesiodistal axis (Fig. 2z). The crown is spatulate and waisted at the cervix, with an inclined incisal edge (the crown being higher mesially than distally). It is broader than long (although mesiodistal length is probably affected by wear) and moderately high (the preserved labial height of 4.7 mm is only slightly greater than occlusal dimensions). The cervix displays an inverted V-shape distolabially and especially mesiolabially. On the mesial aspect of the crown, there is an interproximal wear facet against the right I1 close to the incisal edge. Lingual morphology cannot be adequately ascertained due to wear, but the distal ridge appears shorter than the mesial, which displays a marked angulation at about midheight. The root is mesiodistally compressed (MD = 2.9 mm, BL = 4.4 mm) and somewhat curved distalward, with a marked constriction toward the cervix. The I1 alveoli of both the holotype (Fig. 1 in ref. 1) and IPS44014 (Fig. 2a–c) suggest that this tooth was slightly procumbent.

The I2 alveoli of the holotype (MD = 3.0 mm, BL = 4.0 mm) and of IPS44014 (MD = 2.2 mm, BL = 3.4 mm) suggest that this incisor displayed a somewhat mesiodistally compressed root and was more vertically and distally socketed than the I1 (Fig. 1 in ref. 1; Fig. 2a–c). The dimensions of their alveoli indicate some degree of incisor heteromorphy.

Upper canine No C1 is available, but its alveolus is preserved in two specimens (Fig. 1 in ref. 1; Fig. 2a–c), displaying an elliptical occlusal contour that is longer than broad, with its main mesiodistal axis being slightly exorotated. The C1 alveolus of the holotype (MD = 4.9, BL = 3.8 mm) is much smaller than that of IPS44014 (MD = 8.6 mm, BL = 5.6 mm), being respectively attributed to female and male individuals, and thus hinting at a marked degree of canine sexual dimorphism. In both specimens, the C1 and the I2 are separated by small diastema (1.8 mm in the holotype and 1.3 mm in IPS44014). The postcanine tooth row slightly diverges distalward from the sagittal plane.

Upper premolars The P3 occlusal morphology cannot be adequately ascertained from the holotype due to damage (Fig. 2m) but is well preserved in IPS44014 (Figs. 2n and 4c). The crown displays a suboval contour much broader than long (BLI = 145%) and slightly longer buccally than lingually, with a more markedly convex profile on the lingual side. The two main cusps are buccolingually compressed to some extent (particularly the paracone, which is taller and more extensive than the protocone). There is considerable buccal flare, with the crown base appearing inflated due to the non-peripheral position of the paracone, but the buccal cingulum is very narrow (barely distinguishable except at its mesial and distal ends). The protocone is more mesially and peripherally located than the paracone (close to the mesiolingual corner of the crown) and there is no lingual cingulum (except for a tiny remnant distolingually from the protocone). The two cusps are connected by a sinuous and fine hypoparacrista that extends from the preparacrista to the mesiobuccal aspect of the protocone.

Together with the long, steep, and straight preparacrista, as well as the shorter and mesiobuccally oriented preprotocrista, the hypoparacrista defines a restricted (broader than long) mesial fovea that is centrally located. The distal basin is trapezoidal (wider distally than mesially) and much more extensive and deeper than the mesial fovea, being delimited by the straight and short postparacrista buccally and by the curved and longer postprotocrista lingually. The latter crest becomes continuous with the distal marginal ridge, whereas the postparacrista shapes an abrupt angle with the latter. The occlusal surface shows some enamel wrinkling. A subtle longitudinal groove can be discerned on the deepest portion of the distal basin but it does not interrupt the hypoparacrista.

The P4 occlusal morphology cannot be adequately ascertained in the holotype due to wear (Fig. 2m) and is better preserved in the less worn specimen IPS44014 (Figs. 2n and 4d) as well as in the germ of IPS42977, which is still in crypt but was digitally reconstructed based on microCT scans (Fig. 4e). The P4 crown displays a slightly suboval occlusal contour that is broader than long (BLI = 128–166%; Table 1), and slightly longer buccally than lingually, where the crown displays a more marked convex profile (more tapering in IPS44014 and seemingly IPS42977 than it the holotype). The size of the P4 relative to the P3 cannot be adequately assessed in the holotype due to damage, but in IPS44014 the former is slightly smaller in all dimensions. As in the P3, the P4 protocone is slightly more mesially located than the paracone, and both cusps are buccolingually compressed (albeit the protocone is larger and more bulbous). In contrast, in the P4 the paracone is more peripheral and the protocone is less peripheral than in the P3. No distinct distal cuspules are present except for a rudimentary hypocone close to the distolingual corner of the crown. The mesial crests display a similar orientation as in the P3, but the P4 preparacrista is shorter than that of the P3 (subequal in length to the preprotocrista). The mesial fovea is similarly developed, being much wider than long and crescent-shaped (except in IPS42977), mostly located on the buccal half of the crown. The hypoparacrista similarly extends from the mesiolingual aspect of the paracone (close to the origin of the preparacrista) to the mesiobuccal aspect of the protocone base. Unlike in the P3, there is a longitudinal groove that extends from the mesial fovea to the distal basin, although it does not interrupt the hypoparacrista. As in the P3, the distal basin is spacious and quadrangular, only slightly longer than broad, much larger and deeper than the mesial fovea, and displays some enamel wrinkling. The postparacrista is longer than in the P3 (and thus more similar in length to the postprotocrista), but similarly forms an abrupt angle with the distal marginal ridge. The buccal cingulum is variably developed, being more marked in IPS42977, where it is nevertheless discontinuous. The lingual cingulum is restricted to the lingual and distolingual aspects of the protocone but much better developed than in the P3 in which it is merely a remnant.

Upper molars Several first and second upper molars are available, including the M1–M2 of the holotype (Figs. 2m and 4a) and IPS43758 (Fig. 2o), the M1 of IPS44014 (Figs. 2n and 4f), the isolated M1 IPS100379 (Figs. 2p and 4g), and the isolated M2s IPS94888 (Figs. 2q and 4i) and

IPS100384 (Figs. 2r and 4h). Their occlusal morphology can be better ascertained in IPS44014 and IPS100379 (M1), as well as IPS94888 and IPS100384 (M2). They display a similar subrectangular occlusal contour that is slightly wider than long (BLI = 117–122% in the M1 and BLI = 117–127% in the M2; Table 1), as well as more markedly convex and somewhat tapering lingually (with most specimens displaying a variably developed lingual constriction between the mesial and distal lobes). The M2 is larger and more lingually than the M1. Both molars are low-crowned and display four main pyramidal and buccolingually compressed cusps, the buccal ones being more peripheral and more mesially situated than the corresponding lingual ones. However, the hypocone is more peripheral than the protocone, being located close to the distolingual corner of the crown. The two buccal cusps are similar in size and shape in the M1, the paracone being slightly higher than the metacone, but the metacone is smaller in the M2. The protocone is larger but lower than the buccal cusps, whereas the hypocone is the smallest. There is some variability in the degree of cusp compression, crest sharpness, lingual cingulum development, and hypocone size and shape among the available sample of M1s and M2s. However, unworn and slightly worn specimens (IPS94888, IPS100379, and IPS100384) invariably display a degree of cusp compression and crest sharpness that, due to wear, was not evident from the holotype when it was first described. The preparacrista is very short and slightly obliquely oriented, whereas the preprotocrista is much longer and more inclined. A small paraconule (= protoconule) at the junction between the preprotocrista and the marginal ridge can barely be discerned. The hypoparacrista is somewhat sinuous and slightly oriented distolingually, extending from the mesiolingual aspect of the paracone base or the preparacrista to the mesiobuccal aspect of preprotocrista. The hypoparacrista distally encloses the small mesial fovea (which is broader than long and mostly located on the buccal half of the crown) from the much larger and deeper trigon basin. The latter is subtriangular in shape and approximately as broad as long, distally delimited by a continuous crista obliqua much longer than the hypoparacrista, and buccally delimited by the similarly long and continuous postparacrista and premetacrista. The distal fovea is wider, shorter, and more centrally located than the trigon basin. The short prehypocrista links the hypocone with the distal aspect of the protocone but there is also a similarly developed crest originating from the hypocone that joins the postprotocrista portion of the crista obliqua, in some specimens flanked by a secondary crest or cuspule-like developments visible at the enamel-dentine junction. The postmetacrista is short and rather mesiodistally aligned, whereas the posthypocrista is similarly short but curved and more continuous with the distal marginal ridge. The buccal cingulum is discontinuous and more developed between the two buccal cusps, whereas the lingual cingulum is much wider and ledge-like (especially in the M2), extending from the protoconule to the prehypocrista (i.e., not distally from the hypocone) and being frequently disrupted by one or more secondary crests that radiate from the base of the protocone. Both M1 and M2 display two buccal roots and a single lingual root with a biconvex lingual contour in cross section.

The M3 is only represented by the two antimeres of the holotype (Figs. 2m and 4b). It differs from the preceding molars in the shorter length (resulting in a relatively much broader proportions: BLI = 139–149%), the lesser development of the talon (with smaller metacone and rudimentary hypocone), and the trapezoidal occlusal contour (with a convex lingual side and an obliquely oriented buccal side). The mesial fovea, although similarly restricted, is slightly broader than in the preceding molars, whereas the trigon basin is more triangular and somewhat smaller due to the more median location of the metacone relative to the paracone. The metacone is comparatively smaller and less distinct, being located on the distobuccal corner of the crown without a distinct postmetacrista. The hypocone is rudimentary (much lesser developed than in the preceding molars). Some development of enamel wrinkling can still be discerned on the distal fovea in spite of wear. The development of the buccal cingulum is similar to that of the M2, being more developed around the paracone (although it is partially interrupted) and progressively narrowing until it reaches the metacone, where it fades away. The lingual cingulum is much broader, as in the preceding molars, constituting a curved shelf-like extension around the protocone that displays secondary enamel ridges that radiate from the base of this cusp.

Lower incisors The lower incisors are represented by the left i1 and i2 germs of IPS43936 (Fig. 3c–d) and the left i2 IPS44273 (Fig. 2a'). The i1 crown is quite symmetrical (only minimally higher mesially than distally) and displays three mamelons on the unworn incisal edge. It is mesiodistally longest close to the incisal edge, progressively tapering but becoming labiolabially wider toward the cervix. The mesial and distal ridges are not very marked and the lingual surface is concave and devoid of distinct structures, except for two subtle vertical grooves on the apicalmost portion of the crown.

The i2 morphology markedly differs from that of the i1, being characterized by a very asymmetrical crown that progressively becomes labiolingually wider toward the cervix but displays a similar mesiodistal length throughout its apical half. The crown is mesiodistally shorter than labiolingually broad (BLI = 127% in IPS44273) The mesial margin displays a moderately convex profile, whereas the distal margin displays a distinct distal prong that shapes a marked angulation at about crown midheight (the prong has been eroded by wear in IPS44273, but its position can be inferred based on the angulation of the distal margin). While IPS44273 appears moderately high-crowned based on maximum preserved labial height (4.5 mm), the i2 germ IPS43936 indicates that the crown would have originally been somewhat higher (based on the inferred position of the prong). Based on IPS44273, the i2 display a marked and ledge-like lingual cingulid above a bulbous basal swelling, whereas there is no basal swelling in the i1 germ. The lingual aspect of the i2 crown displays a marked mesial pillar, running from the crown apex to the lingual cingulid, that separates the mesial fovea from the distal one, the latter being more extensive than the former. In IPS44273 only a faint central crest runs vertically through the distal fovea. The root of the i2 is very mesiodistally

compressed and constricted toward the cervix, which shapes an inverted V-shape both mesially and distally.

Lower canine The lower canines are represented by the left c1 IPS43433 (Fig. 2b') and the c1 germ of IPS43936 (Fig. 3e). Both may be attributed to female individuals based on crown size and shape, whereas the male c1 remains unknown. The crown is low (preserved labial height = 5 mm in IPS43433) and displays an oval occlusal contour that is longer than broad (BLI 76% in IPS43433), with maximum breadth attained mesially from the crown midlength. The crown is much higher labially than on the lingual side, where the cervix shapes a shallow inverted V-shape. The occlusal contour is moderately convex lingually and otherwise more markedly convex. However, while the mesial crown wall is uniformly convex, both mesiolingual and distolabial crown walls are concave (in the latter case, being accentuated by wear against the C1), being separated from one another by three steep cristids that originate from the single main cuspid. The mesiolingual cristid is marked but short, ending at about crown midheight in a cuspulid-like enamel developed on the narrow but distinct lingual cingulid, which extends until the distal end of the crown but progressively fades out mesially. The distolingual cristid is fainter and longer, merging with the lingual near the distal end of the crown. The distobuccal cristid is the longest, being somewhat affected by wear. The root is long and labiolingually compressed, somewhat constricted basally below the cervix and progressively tapering along its apical two-thirds.

Lower premolars The p3 germ of IPS43936 is too incompletely formed to adequately ascertain occlusal morphology (Fig. 3f), although some details can be ascertained. There is a single main cuspid (the protoconid) probably located on the mesial half of the crown. Three steep and sharp cristids originate from its apex: the preprotocristid mesiolingually, the postprotocristid distally, and the hypoprotocristid distolingually. The two latter cusps define a steep distal fovea but, given that the crown is not completed, their length and the development of distal cuspulids cannot be ascertained.

The occlusal morphology of the p4 cannot be adequately ascertained because available specimens are quite worn and incompletely preserved (IPS43820 and IPS93524; Figs. 2s–t and 4j) or too incompletely formed (IPS43936; Fig. 3g), although the very partial crown germ of the latter enables a better assessment of the morphology of the mesial cuspids than the remaining specimens. The crown displays an elliptical to suboval contour (longer than broad), with its main mesiodistal axis apparently exorotated (as judged from the position of the distal contact facet against the m1 in IPS93524). Based on IPS93524 and IPS43936 the metaconid seems more buccolingually compressed and peripheral than the protoconid, which is higher and more extensive. The two cusps are connected by a well-defined transverse cristid formed by the hypoprotocristid and hypometacristid, which separates the mesial fovea from the larger and deeper talonid basin, which occupies most of the distal portion of the crown. The two available specimens display a secondary cristid on the mesial fovea,

extending from the base of the protoconid (IPS43936) or from the hypoprotocristid-hypometacristid junction (IPS93524) to the mesiolingual end of the crown. The premetacristid is poorly defined in both specimens. The postmetacristid and the longer postprotocristid are more distinct and distally oriented, terminating at the vestigial entoconid and hypoconid, respectively (only observable in IPS93524). There is no lingual cingulid, while a discontinuous buccal cingulid can be discerned at least distally from the protoconid at about crown midlength. In both IPS43820 and IPS93524 there are two roots (the distal one slightly larger than the mesial) which appear partially fused as one, each one displaying an elliptical cross-section and being somewhat obliquely oriented.

Lower molars The m3 is as yet unknown, whereas the m1 and m2 can be described based on the unerupted germs digitally extracted from IPS43936 (Figs. 3 h–i and 4k–l) as well as on the basis of the m2 germ mesial fragment IPS94886 (Figs. 2u and 4m). The m1 and m2 show very similar occlusal morphology except for the larger dimensions of the latter. Their occlusal contour is subrectangular (much longer than broad; BLI = 76–77%), slightly broader distally, with a somewhat convex mesial contour and very mildly constricted buccal and lingual sides between the mesial and distal lobes. They have five main cuspids of pyramidal shape, the buccal ones being less buccolingually compressed and peripherally located than the lingual ones, whereas the hypoconid and entoconid are more peripheral than the trigonid cuspids. The protoconid is clearly more mesially located than the metaconid, whereas the hypoconid and entoconid are transversely aligned. The hypoconulid is centrally located at the distal end of the crown in the m1 and slightly more buccally and less distally situated in the m2. The trigonid is higher than the talonid and displays an extensive mesial fovea that is only minimally broader than long. This fovea is delimited by the protoconid base and the short preprotocristid buccally, the longer and curved premetacristid (which becomes continuous with the mesial marginal ridge) lingually, and a continuous and slightly oblique cristid distally, formed by the merging of the hypoprotocristid (originated from the distolingual aspect of the protoconid) and the hypometacristid. There is also a secondary transverse cristid that originates from the mesiolingual aspect of the protoconid, terminating at the center of the mesial fovea (IPS43936) or completely dividing it into two distinct foveae (IPS94886). The talonid basin is very extensive and somewhat longer than broad, progressively broadening distalward. It is delimited lingually by a short postmetacristid and a much longer and curved pre-entocristid, while buccally it is closed by a cristid obliqua constituted by a short postprotocristid and a much longer prehypocristid. Both buccal cristids are continuous in the m1, shaping a straight but mesiolingually tilted cristid obliqua that terminates close to the origin of the hypoprotocristid, whereas in the m2 the prehypocristid is more mesiodistally aligned and angled relative to the postprotocristid, which originates more buccally than the hypoprotocristid. Both the m1 and the m2 display an incompletely developed pliopithecine triangle: the distal arm is as well developed as the prehypocristid and only minimally shorter, being obliquely oriented toward the center of the talonid basin and originating

from the prehypocristid (m1) or the mesiobuccal aspect of the hypoconid (m2); in contrast, there is no distinct mesial arm of the triangle, although a very short secondary crest originating from the hypometacristid (m1) or the merging of the hypometacristid and hypoprotocristid (m2) might be homologous to it. There is no cristid connecting the hypoconid with the entoconid. The posthypocristid and prehypoconulid cristid are short and directed to one another, whereas the hypoentocristid and postcristid are somewhat longer (particularly in the m2) but not completely aligned, thus not completely demarcating the relatively distal fovea located on the distolingual corner of the crown from the rest of the talonid basin. The postentocristid (shorter and more indistinct in the m1 than in the m2) curves to become continuous with the distal marginal ridge. The posthypoconulid cristid is very short in the m2 and lacking in the m1. The buccal cingulid (incompletely formed in the m2 germ) is continuous and moderately well developed, becoming shelf-like around the protoconid and the distal aspect of the hypoconid, but narrower and partly interrupted by secondary ridges along the hypoconid base. There is no lingual cingulid except for a small remnant at the junction between the postmetacristid and the pre-entocristid in the m1.

Deciduous upper incisors The right DI1 germ IPS44393 (Fig. 2c') shows a spatulate, waisted (i.e., constricted toward the cervix), asymmetrical, and low crown—with maximum labial height (2.9 mm) being lower than mesiodistal length (3.3 mm), although it should be taken into account that the germ is not completed. It displays an elliptical occlusal contour that is mesiodistally longer than labiolingually broad (BLI = 76%) and tapers mesially. The labial crown wall is markedly convex. In contrast, the lingual aspect of the crown is markedly concave except at its basalmost portion. The mesial ridge is slightly longer than the distal, and both are continuous with the moderately ledge-like lingual cingulum. Above the latter, the lingual aspect is rather smooth, only showing very subtle subvertical enamel grooves and folds and a very diffuse central swelling that separates the mesial from the somewhat larger distal fovea but does not constitute a distinct pillar. There is no DI2 available.

Deciduous upper premolars The left dP3 IPS43013 (Fig. 2v) is smaller than the permanent cheek teeth and displays a very asymmetrical, trapezoidal contour somewhat broader than long (BLI = 123%). The lingual side is markedly convex, whereas the buccal profile is almost straight but very obliquely oriented, so that the crown is broader mesially than distally. The mesial cusps are transversely aligned, buccolingually compressed, and much better developed than the distal ones. The paracone is higher and more extensive than the protocone, to which it is connected by a distinct and slightly oblique hypoparacrista that separates rectangular (much broader than long) mesial fovea (further bounded by the short preprotocrista and the somewhat longer preparacrista) from the deeper and much more extensive distal basin. A small hypocone is located on the distolingual corner of the crown, being linked to the distal aspect of the protocone by a short prehypocrista. In contrast, there is no distinct metacone, except for a rudimentary and largely worn ridge-like thickening of the enamel

at the distobuccal corner on the crown, where the long postparacrista reaches the distal marginal ridge. There are no traces of a crista obliqua, so that the distal basin is very extensive. No distinct posthypocrista can be distinguished from the distal marginal ridge. There are no well-developed cingula except for a small cingular development between the protocone and hypocone, which displays an oblique groove that slightly extends onto the lingual crown wall but does not interrupt the prehypocrista.

The left dP4 IPS42977 (Figs. 2w and 4n) displays a subtriangular occlusal contour that is only minimally broader than long (BLI = 104%) but much longer buccally than lingually. The crown base is much more convex lingually than buccally or distally, whereas the mesial profile is rather sinuous and very obliquely oriented. The trigon cusps are pyramidal and of similar size, although the paracone is more protruding and more buccolingually compressed than the others. The protocone is less peripheral than the buccal cusps, and located in an intermediate position between the latter along the mesiodistal crown axis. The hypocone is much smaller than the trigon cusps and more peripheral than the protocone, being situated close to the distolingual corner of the crown. A short and thick preparacrista extends from the paracone apex to the mesiobuccal corner of the crown. The preprotocrista is straight, sharper and longer than the preparacrista, and obliquely oriented in a mesiobuccal direction, merging with mesial marginal ridge at about crown midline. The sinuous and distinct hypoparacrista originates from the mesiolingual aspect of the paracone and merges with the preprotocrista at about its midlength, thus completely separating the slit-like mesial fovea (mostly located on the buccal half of the crown) from the more extensive and deeper trigon basin. The trigon basin is polygonal in shape, being approximately as long as broad, being buccally enclosed by the long postparacrista and the shorter premetacrista (which merge with one another forming an obtuse angle) and distally delimited by a fine and slightly curved crista obliqua. The latter separates the trigon basin from the similarly extensive but rectangular (broader than long) distal fovea, which is lingually delimited by the hypocone and its associated crests, including a fine and short prehypocrista (directed toward the distal aspect of the protocone) and an even shorter posthypocrista. In turn, a longer but blunt and indistinct postmetacrista further delimits the distal fovea on the buccal side. The distal marginal ridge is not very well defined. No enamel wrinkling can be discerned on the occlusal basins. The buccal cingulum is narrow and rather discontinuous (partly interrupted at the level the buccal cusps by secondary folds of the enamel), whereas the C-shaped lingual cingulum is much wider (shelf-like), extending around the protocone until the mesial aspect of the hypocone and the prehypocrista, being interrupted by a secondary enamel fold that radiates from the distolingual aspect of the protocone base. Based on the microCT scan data, there is a single lingual root of subquadrangular cross-section as well as two distinct and divergent buccal roots that are more triangular and buccodistally compressed.

Deciduous lower incisors No deciduous lower incisors are available, only their alveoli are preserved in IPS43936 (Figs. 1g–I and 3a). Those of the di1 (right: MD = 2.6 mm, BL = 2.7 mm; left: MD = 2.5 mm, BL = 2.7 mm) indicate that the root base was only slightly mesiodistally compressed, whereas the left di2 alveolus (MD = 1.7, BL = 2.4 mm) indicates that the lateral incisor was somewhat smaller than the central and displayed a more mesiodistally compressed root basally.

Deciduous lower canine As for the deciduous lower incisors, only the left dc1 alveolus is preserved in IPS43936 (Fig. 1g–I and 3a; MD = 3.2, BL = 2.5 mm), suggesting that this tooth was somewhat buccolingually compressed and that, despite being aligned with the postcanine deciduous dentition, its main mesiodistal axis was somewhat exorotated relative to the postcanine tooth row.

Deciduous lower premolars The crown of the single available dp3 IPS43936 (Figs. 2x and 4o) is distally broken but apparently displayed a suboval occlusal profile longer than broad and widest distally, with a markedly convex and tapering mesial outline. Only the two trigonid main cuspids are preserved. The protoconid is very buccolingually compressed and centrally located; a marked, straight and long preprotocristid descends from the protoconid apex until the mesial end of the crown. The metaconid is lower, smaller, more bulbous, and as peripheral as but more distal than the protoconid. No distinct postprotocristid originates from the protoconid. Instead, a short hypoprotocristid originates distally from the protoconid and curves until merging with the more transversely aligned hypometacristid, separating the longer than broad mesial fovea from the deeper and more extensive trigonid basin. This mesial fovea, located on the lingual half of the crown, is steeply inclined and lingually open, as there is no distinct premetacristid. No paraconid is present either at the mesial end of the crown. The preserved portion of the talonid basin indicates that it was originally longer than broad, and preferentially located on the lingual moiety of the crown, being buccally delimited by a very obliquely oriented cristid obliqua, apparently constituted exclusively by the prehypocristid, as it merges with the junction between the hypoprotocristid and the hypometacristid. The preserved portion of the seemingly postmetacristid progressively curves toward the distolingual portion of the crown, suggesting that the entoconid (like the hypoconid, given the inclination of the cristid obliqua) would have originally been much more peripheral than the trigonid cuspids. Cingulids are restricted to the mesiobuccal and especially the mesiolingual aspect of the crown, flanking the terminal portion of the preprotocristid. MicroCT scan data show that this tooth is biradiculate.

The two available dp4s (IPS43936 and IPS106878; Figs. 2x–y and 4p–q) display a subquadrangular to suboval occlusal contour that is much longer than broad (BLI 72.3–76%; Table 1) and, like in the dp3, wider distally, with mesially tapering convex outline. There are five main cuspids as well as a poorly-developed paraconid (unlike in the dp3). The protoconid and hypoconid are more buccolingually compressed, more mesially located, more protruding, and less peripheral than their lingual counterparts, with the entoconid being the most peripheral cusp. In IPS106878, the buccal

cuspids (especially the hypoconid) are slightly more median than in IPS43936. The hypoconulid has a bulbous shape and is the smallest cusp, being centrally located close to the distal marginal ridge. A thick and short preprotocristid (shorter than in the dp3) and a shaper and slightly longer premetacristid (indistinct in the dp3) extend in mesial to mesiobuccal direction from the protoconid and metaconid apices, respectively, to the mesial marginal ridge. A poorly-developed paraconid is present at the junction of premetacristid, the mesial marginal ridge, and a secondary oblique cristid (absent from the dp3) that originates from the protoconid and splits the mesial fovea. No postprotocristid distinct from the hypoprotocristid originates from the distal aspect of the protoconid; in contrast, a single short cristid (that we interpret as the hypoprotocristid) originates distolingually from the protoconid and curves until merging with the more transversely aligned hypometacristid. They conform a continuous cristid that separates the somewhat longer than broad mesial fovea from the deeper and more extensive talonid basin. The talonid basin is longer than broad, and more lingually located than the mesial fovea (especially in IPS106878). Lingually, the talonid basin is delimited by a slightly curved postmetacristid that is directed toward the straighter pre-entocristid. Buccally, the talonid basin is delimited by the very obliquely oriented cristid obliqua (more so in IPS43936 than in IPS106878) constituted by the prehypocristid and, according to our interpretation, the displaced postprotocristid, which reaches the junction between the hypoprotocristid and the hypometacristid. The hypoconid and hypoconulid are connected by the short but well-developed posthypocristid and the prehypoconulid cristid. In contrast, the postentocristid can barely be discerned, curving distobuccally to become continuous with the distal marginal ridge, whereas a posthypoconulid cristid is lacking. There is no hypoentocristid or postcristid, so that the distal fovea, located on the distolingual corner of the crown, is completely open to the talonid basin. As in m1–m2, in the dp4 there is no lingual cingulid except for a small remnant at the junction between the postmetacristid and the pre-entocristid (less marked in IPS106878). The buccal cingulid is moderately developed (slightly more so in IPS43936 than IPS106878) but discontinuous, being widest between the protoconid and the hypoconid, but interrupted at the buccal level of these cusps. In IPS43936 there are two (mesial and distal) roots of bilobed cross-section, each one corresponding to a pair of fused roots.

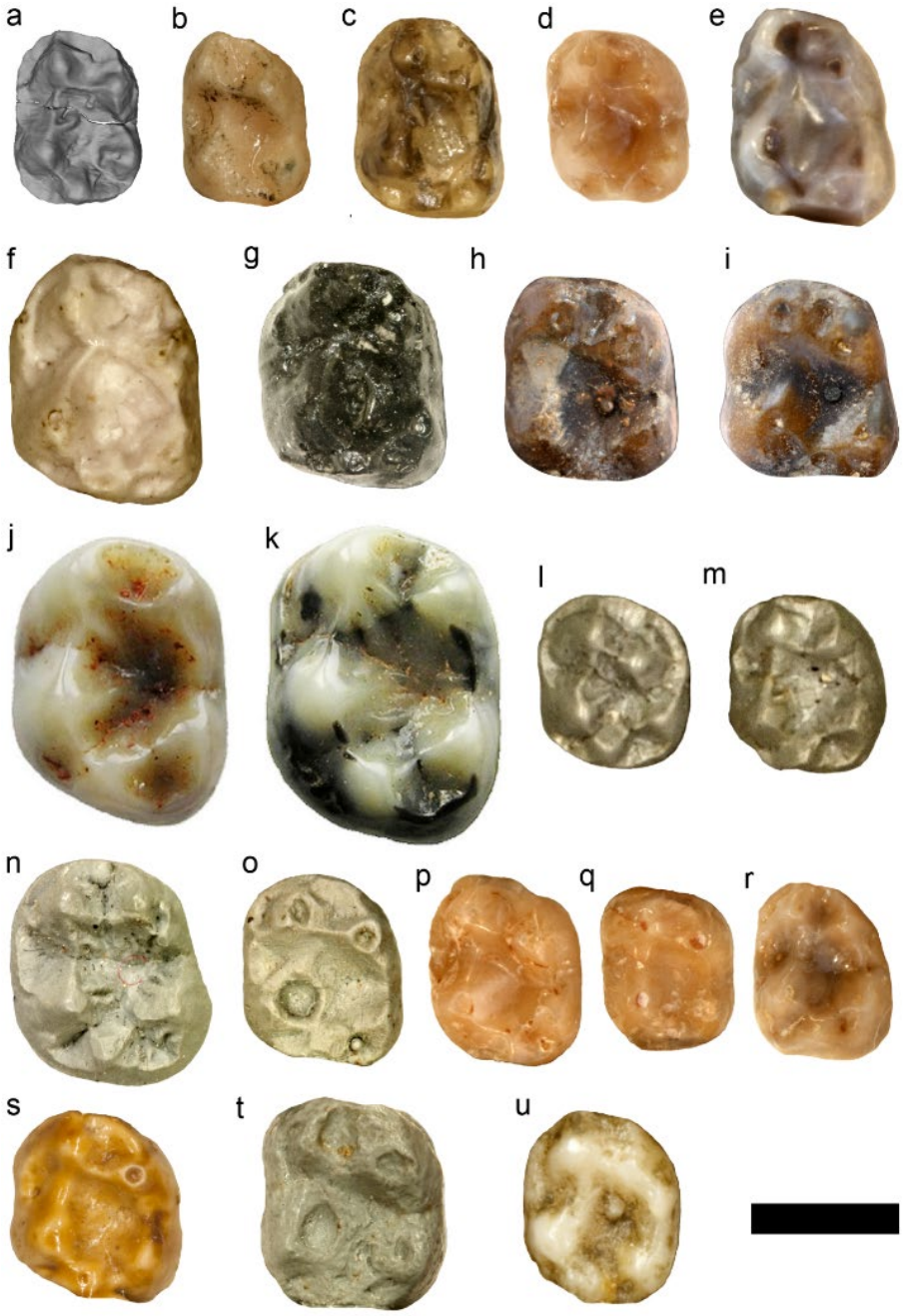
Supplementary Text 4. Results of the additional cladistic analysis

The dental-only analysis at the genus level based on a wider representation of taxa (Supplementary Fig.6a) also recovers pliopithecoids as a clade of stem catarrhines but displays some differences relative to the dental-only analysis at the species level reported in the main text (Fig. 6). In particular, dendropithecids are recovered as a paraphyletic assemblage of stem cercopithecoids instead of a stem-catarrhine clade more derived than pliopithecoids, which we consider an unreliable result based on current knowledge of catarrhine evolution and the results of multiple previous cladograms (see main text). In contrast, *Ekembo* is recovered as a stem hominoid and both *Pierolapithecus* and *Hispanopithecus* as crown hominoids, in agreement with previous results based on different matrices[1,2], although the molecular phylogeny of crown hominoids is not recovered. The most parsimonious topology of the dental-only analysis at the genus level further displays some differences from that reported in the main text regarding the internal topology of pliopithecoids, with *Anapithecus* being more derived than both *Barberapithecus* and *Pliobates* toward *Plesiopliopithecus* + *Crouzelia*. Nevertheless, both analyses recover the monophyly of crouzeliids and support the placing of *Pliobates* within this clade. The differences in the most parsimonious arrangement of pliopithecoids might simply result from the more restricted representation of pliopithecoid taxa in the genus-level analysis than in that reported in the main text, the latter being arguably more reliable because of this reason. The craniodental analysis (Supplementary Fig. 6b) yields very similar results (identical regarding *Pliobates* and other pliopithecoids), but recovers the monophyly of crown hominids (in agreement with molecular data), with *Hispanopithecus* being supported as a stem hominid and *Pierolapithecus* as a pongine.

Unlike the dental and craniodental analyses, the postcranial-only analysis is not well-resolved (Supplementary Fig. 6c), because most clades (including pliopithecoids, dendropithecids, and cercopithecoids) are collapsed except crown hominoids, hominids, and a hominoid clade that excludes *Ekembo* but includes *Pliobates* as the only stem hominoid. This cladogram indicates that postcranial characters are informative regarding the internal phylogeny of crown hominoids (recovering the molecular topology) but yield very contradictory results for *Pliobates* as compared with the (cranio)dental dataset. When the postcranial characters are analyzed simultaneously with the craniodental ones, the former play an important role in determining the topology of *Pliobates* (and, indirectly, of other pliopithecoids). Thus, a well-resolved consensus tree is obtained (Supplementary Fig. 6d), although displaying a different topology than that based on dental or craniodental characters (Supplementary Fig. 6a–b). In particular, the phylogenetic position of *Ekembo* is not resolved, and while the molecular phylogeny of crown hominoids is recovered and dryopithecines are supported as stem hominids (in agreement with refs. 1 and 2), the results for dendropithecids and pliopithecoids are very heterodox and reminiscent of those previously obtained by Alba et al.[1]. In particular, dendropithecids and pliopithecoids are supported as successive

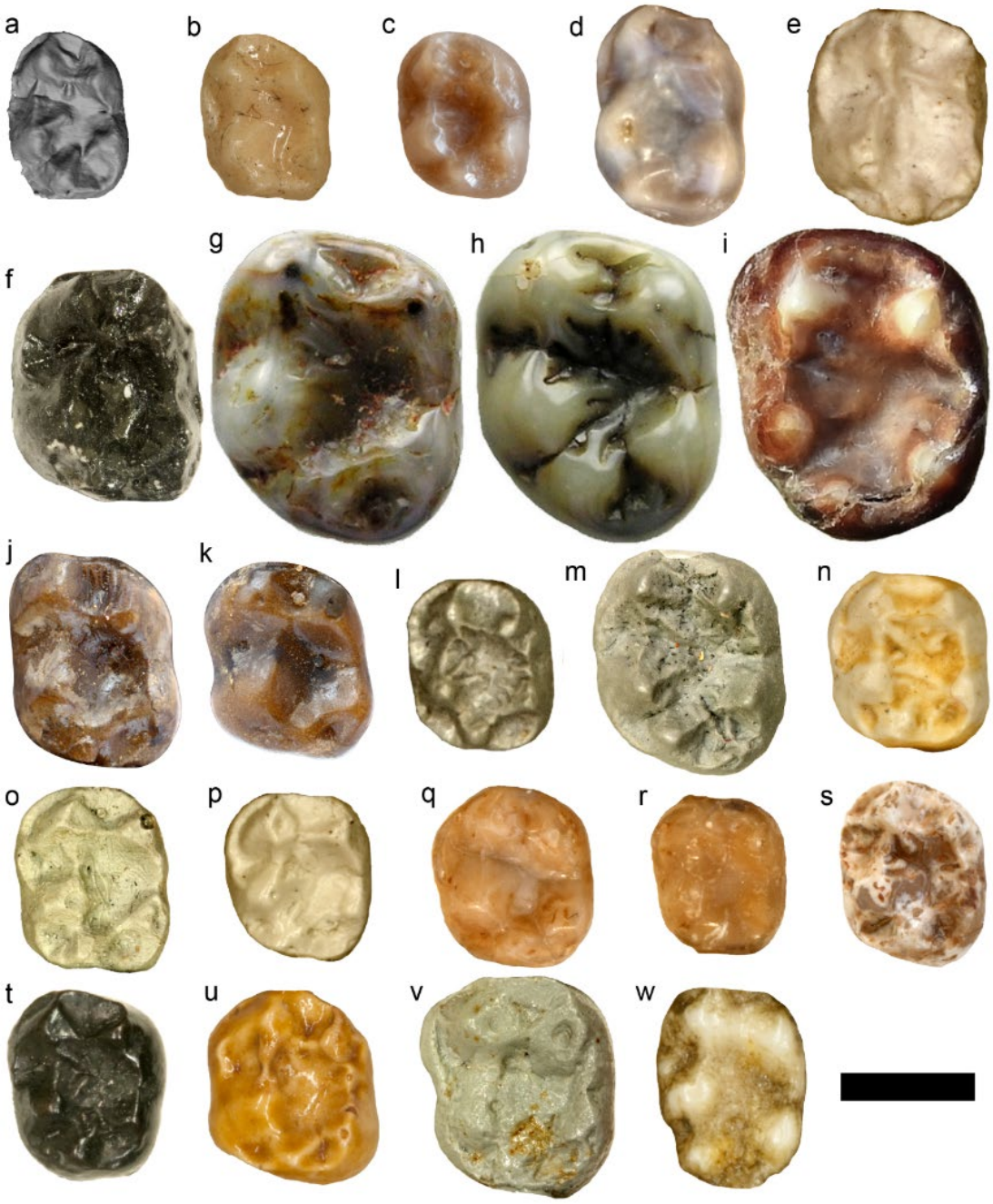
paraphyletic assemblages of stem hominoids, which is probably an artifact caused by several factors: first, the omission from the analysis of a wider representation of Early and Middle Miocene apes from Africa (such as afropithecids and nyanzapithecids) that are customarily considered stem hominoids; second, the large amount of missing data in most dendropithecids and pliopithecoids; and, third, the possession of multiple crown hominoid-like postcranial features in *Pliobates*. The fact that *Pliobates* shares both dental derived features with pliopithecoids and postcranial derived features with hominoids appears to be pulling the whole pliopithecoid clade toward crown hominoids. This is similar to what has previously been argued for *Oreopithecus*—a likely stem hominoid that clusters with crown hominoids in total evidence analyses presumably owing to postcranial convergences[2]—as well as hypothesized for hylobatids and hominids among crown hominoids[3].

Given the contradictory results obtained for (cranio)dental data vs. total evidence (i.e., further including the postcranial data), two alternative interpretations are possible. It might be argued on cladistic epistemological grounds that the results based on all the available evidence are always preferable. Such reasoning seems logical on theoretical grounds but in this particular case would imply supporting not only *Pliobates*, but all other pliopithecoids, as members of the hominoid stem lineage—which goes against other, independently derived cladograms as well as generally accepted knowledge about ape evolution. Alternatively, it may be argued that the total evidence results are biased by postcranial parallelisms between *Pliobates* and hominoids and, thus, less realiable than the most parsimonious topology based on (cranio)dental data. While the phylogenetic position of pliopithecoids from Eurasia relative to dendropithecids and putative stem hominoids from Africa certainly deserves further research, several lines of evidence favor the second interpretation that postcranial features are biasing the results and that pliopithecoids (including *Pliobates*) constitute a catarrhine clade that is not closely related to crown hominoids. This is directly supported by the fact that our postcranial-only analysis does not resolve the phylogenetic relationships of most Miocene catarrhines (with the exception of dryopithecines), so that postcranial evidence is introducing more 'noise' than true phylogenetic signal regarding these taxa (especially *Pliobates*). Also, more indirectly, the contention that postcranial characters are biasing the cladistic results for particular taxa is further supported by the fact that similar contradictory results between craniodental and postcranial data have been previously found among hominoids[2], being attributed to postcranial homoplasy between *Oreopithecus* and crown hominoids, as well as between hylobatids and hominids (for further discussion, see ref. 3). Incidentally, even the total evidence analysis recovers *Pliobates* as closely related to crouzeliid pliopithecoids (branching off, like *Plesiopliopithecus* + *Crouzelia*, between *Barberapithecus* and *Anapithecus*), thereby supporting our taxonomic assessment that the former taxon is a derived crouzeliid.



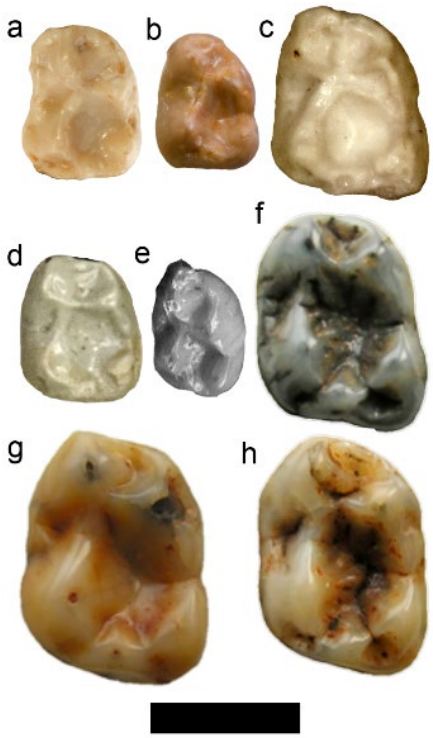
Supplementary Figure 1. Comparisons of the lower first molar occlusal morphology of *Pliobates* and other pliopithecoids. Specimens are depicted in occlusal view as if from the left side (indicated when reversed; mesial is on top). **a** *Pliobates cataloniae*, virtual model rendering of IPS43936; **b** *Crouzelia auscitanensis*, Sa 999 (holotype; cast); **c** *Plesiopliopithecus lockeri*, OLL 2010/6 (holotype; cast); **d** *Barberapithecus huerzeleri*, IPS1724m (holotype); **e** *Egarapithecus narcisoi*, IPS45757 (holotype); **f** *Anapithecus hernyaki*, RUD 9 (holotype; cast); **g** *Anapithecus hernyaki* RUD 98 (reversed; cast); **h** *Laccopithecus robustus*, PA 879 (paratype; reversed; cast); **i** *Laccopithecus robustus*, PA 881 (paratype; cast); **j** *Fanchangia jini*, V 18115.1 (paratype; reproduced from ref. 4); **k** *Fanchangia jini*, V 18115.17 (paratype; reproduced from ref. 4); **l** *Dionysopithecus shuangouensis*, PA 1249 (cast); **m** *Dionysopithecus shuangouensis*, PA 1251 (reversed; cast); **n** *Platodontopithecus jianghuaiensis*, PA 1225 (reversed; cast); **o** *Pliopithecus antiquus*, MNHN Sa 995 (holotype; cast); **p** *Pliopithecus canmatensis* IPS35036 (holotype); **q** *Pliopithecus canmatensis*, IPS41719 (paratype). **r** *Pliopithecus canmatensis*, IPS41955 (paratype); **s** *Pliopithecus platyodon*, Graz Joanneum 2100 (holotype; cast); **t**

Pliopithecus zhanxiangi, BGN mandible (paratype; reversed; cast); **u** *Epipliopithecus vindobonensis*, Individual II (cast). Scale = 5 mm.

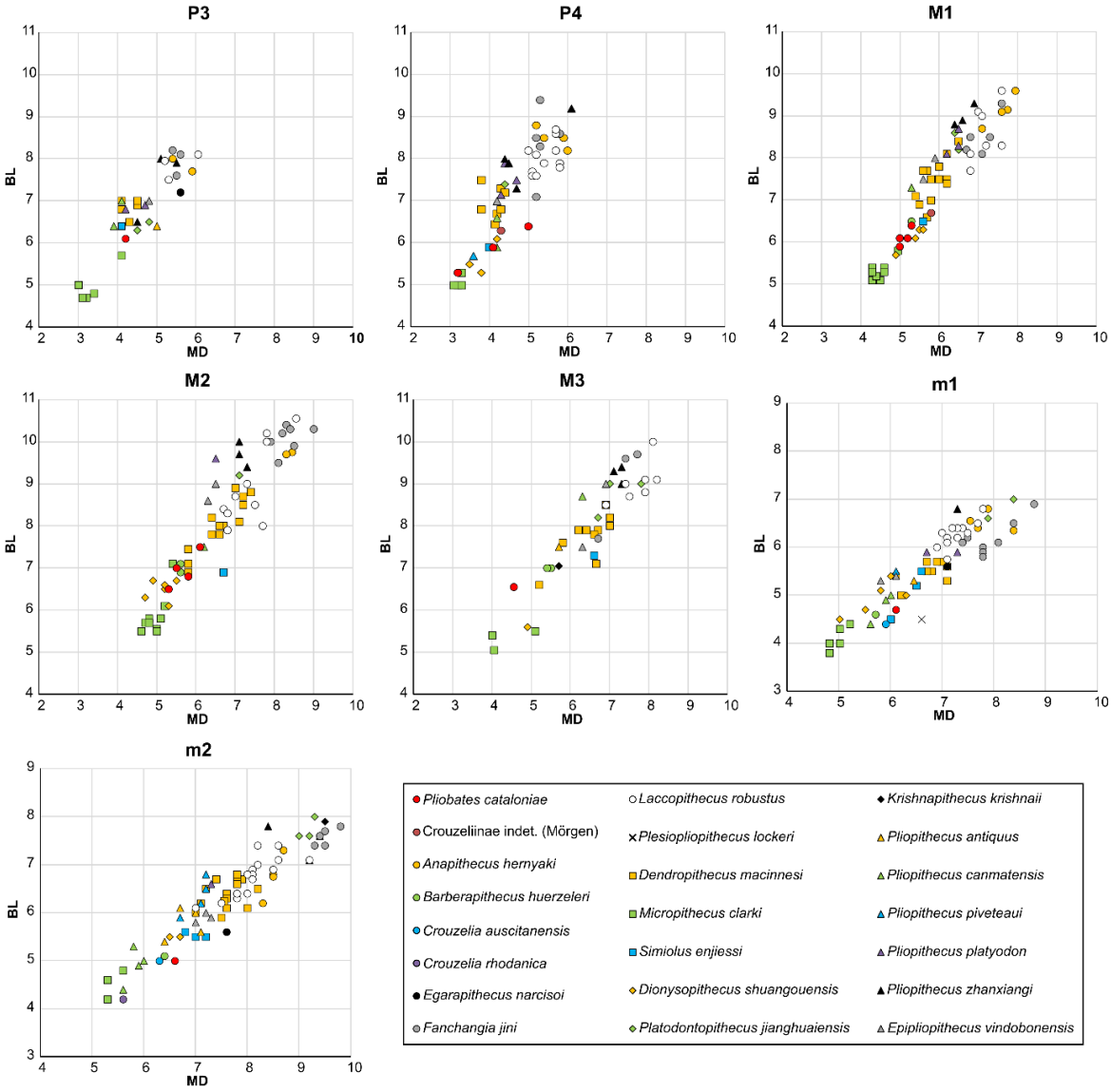


Supplementary Figure 2. Comparisons of the lower second molar occlusal morphology of *Pliobates* and other pliopithecoids. Specimens are depicted in occlusal view as if from the left side (indicated when reversed; mesial is on top). **a** *Pliobates cataloniae*, virtual model rendering of IPS43936; **b** *Crouzelia auscitanensis*, MNHN Sa 999 (holotype; cast); **c** *Barberapithecus huerzeleri*, IPS1724n (holotype; reversed); **d** *Egarapithecus narcisoi* IPS 2943 (holotype); **e** *Anapithecus hernyaki*, RUD 9 (holotype; cast); **f** *Anapithecus hernyaki*, RUD 98 (reversed; cast); **g** *Fanchangia jini* V 18115.2 (paratype; reproduced from ref. 4); **h** *Fanchangia jini* V 18114 (holotype; reversed; reproduced from ref. 4); **i** *Krishnapithecus krishnaii*, PRS04/12 (reproduced from ref. 5); **j** *Laccopithecus robustus* PA 879 (paratype; reversed; cast); **k** *Laccopithecus robustus* PA 881 (paratype; cast); **l** *Dionysopithecus shuangouensis*, PA 1252 (reversed; cast); **m** *Platodontopithecus jianghuaiensis*, PA 1220 (cast); **n** *Pliopithecus antiquus*, L. G. 109 (reversed; cast); **o** *Pliopithecus antiquus*, MNHN Sa 995 (holotype; cast); **p** *Pliopithecus antiquus* (reversed; cast); **q** *Pliopithecus canmatensis*, IPS35036 (holotype); **r** *Pliopithecus canmatensis*, IPS41719 (paratype). **s** *Pliopithecus canmatensis*, IPS41660 (paratype; reversed);

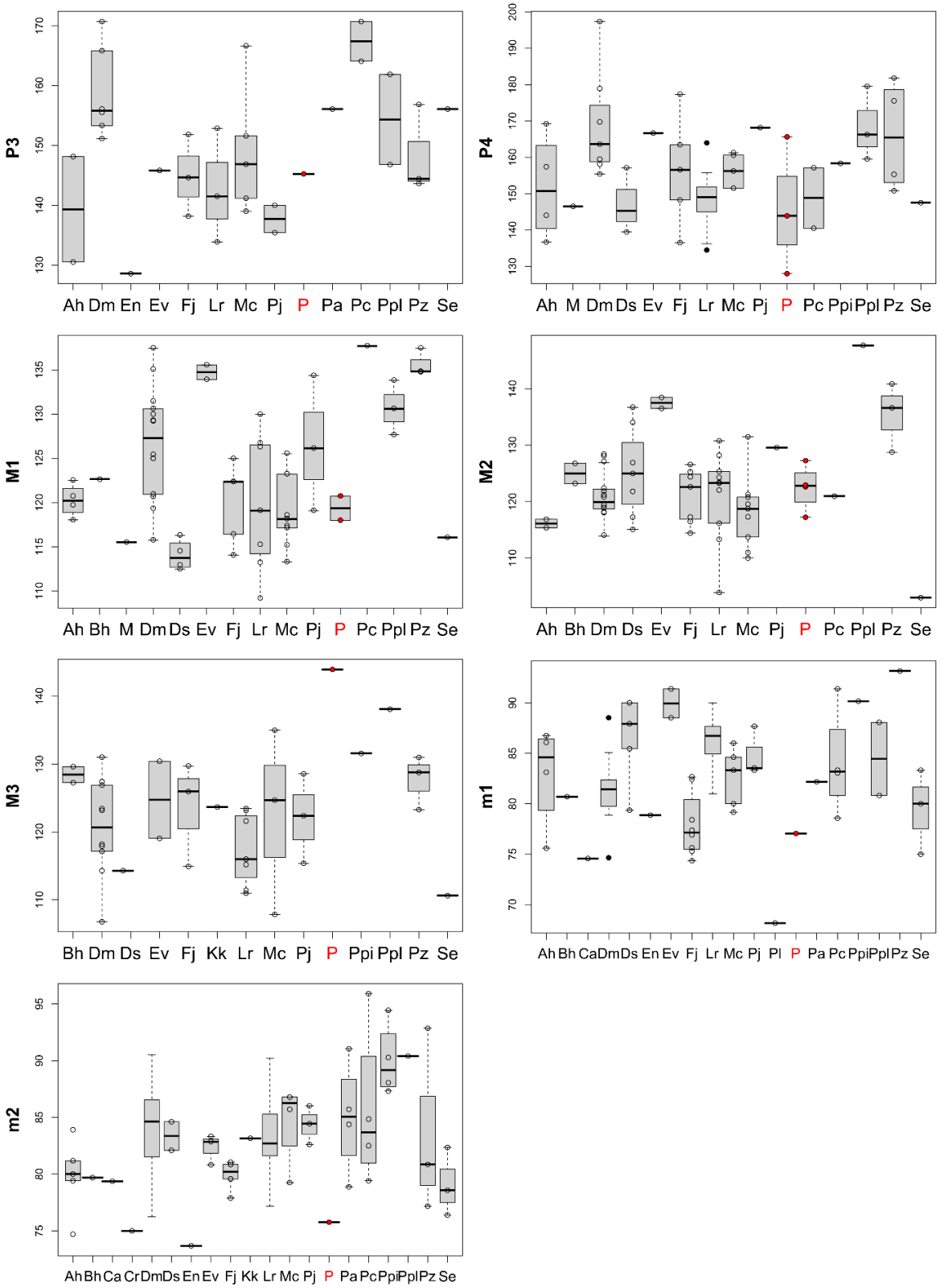
t *Pliopithecus piveteaui*, Collections Lecointre (holotype; cast); **u** *Pliopithecus platyodon*, Graz Joanneum 2100 (holotype; cast); **v** *Pliopithecus zhanxiangi*, BGN mandible (paratype; reversed; cast); **w** *Epipliopithecus vindobonensis*, Individual II (cast). Scale = 5 mm.



Supplementary Figure 3. Comparisons of the deciduous lower fourth premolar occlusal morphology of *Pliobates* and other pliopithecoids. Specimens are depicted in occlusal view as if from the left side (indicated when reversed; mesial is on top). **a** *Pliobates cataloniae*, IPS43936; **b** *Pliobates cataloniae*, IPS106878; **c** *Anapithecus hernyaki*, RUD 9 (holotype; cast); **d** *Dionysopithecus shuangouensis*, PA 1241 (reversed; cast); **e** *Pliopithecus piveteaui* (reproduced from ref. 6); **f** *Fanchangia jini*, V 18115.15 (paratype; reversed; reproduced from ref. 4); **g** *Fanchangia jini*, V 18115.20 (paratype; reversed; reproduced from ref. 4); **h** *Fanchangia jini*, V 18115.21 (paratype; reversed; reproduced from ref. 4). Scale = 5 mm.

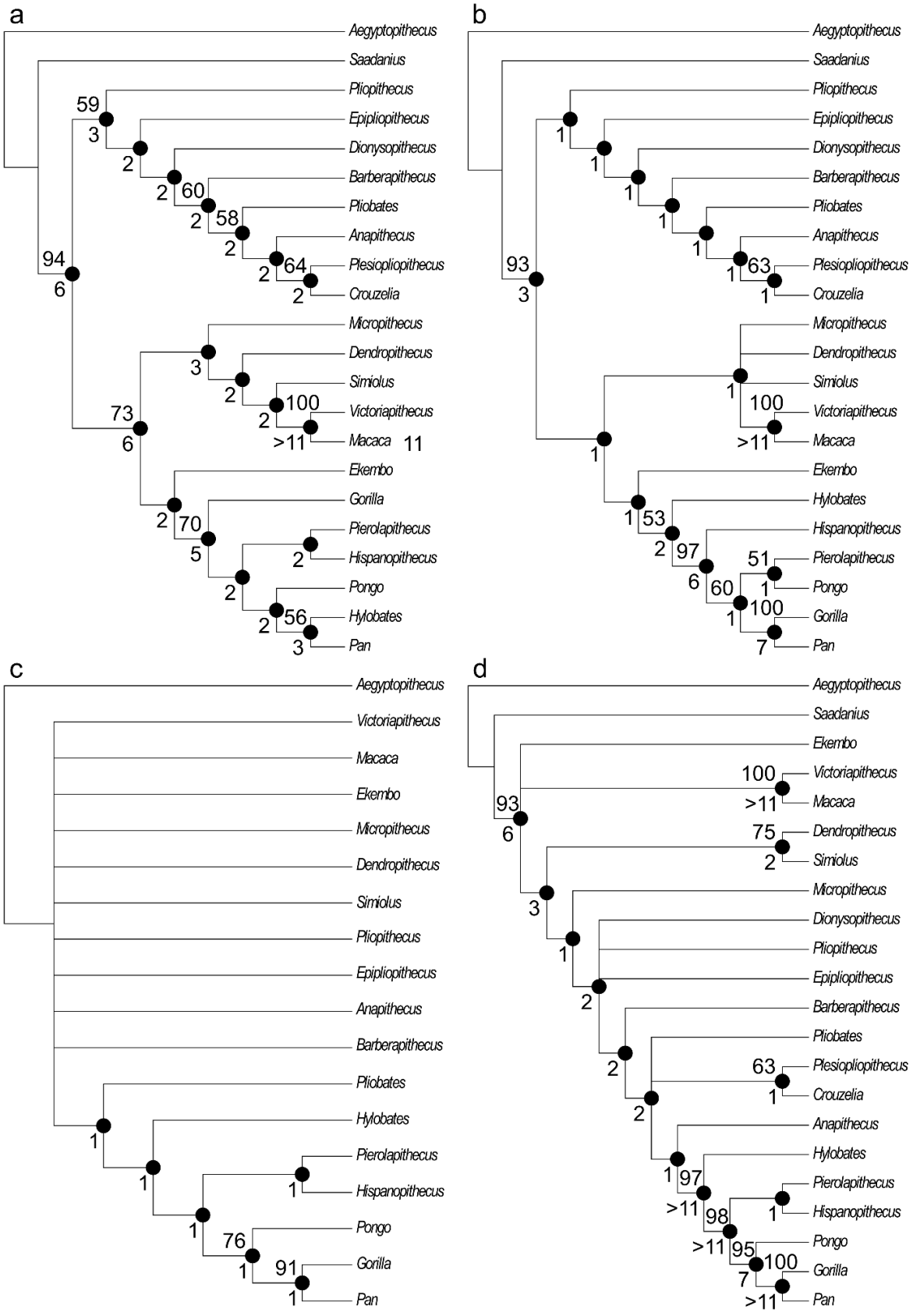


Supplementary Figure 4. Dental size and proportions. Bivariate plots of buccolingual breadth (BL; in mm) vs. mesiodistal length (MD; in mm) in upper and lower cheek teeth of *Pliobates cataloniae* compared with pliopithecoids and dendropithecids. Each species is defined by a unique color-coded symbol. See Supplementary Table 2 for data sources. Source data are provided as a Source Data file.



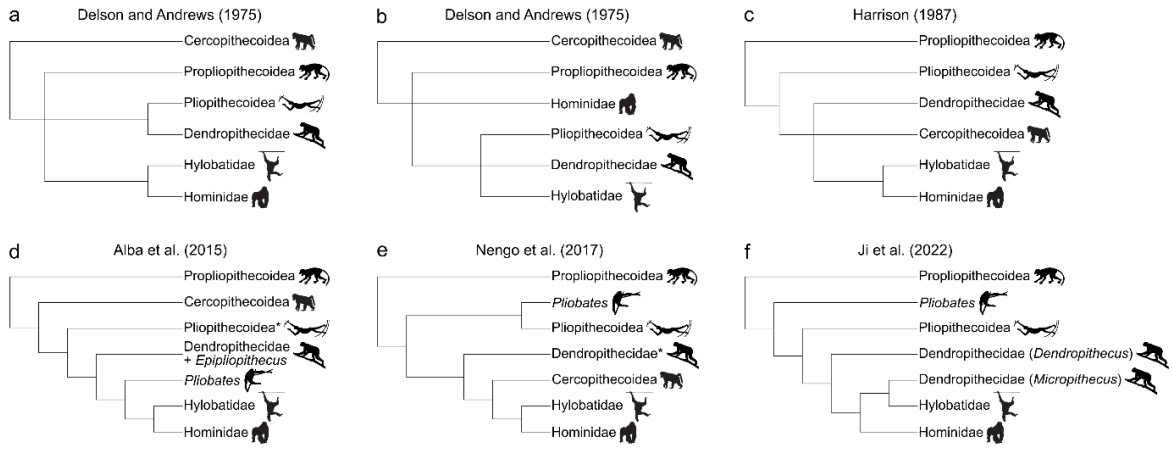
Supplementary Figure 5. Dental proportions. Box-and-whisker plots of breadth/length index (BLI; in %) in upper and lower cheek teeth of *Pliobates cataloniae* compared with pliopithecoids and dendropithecids. White dots (red dots in the case of *P. cataloniae*) represent single specimen values and are shown when $n \leq 10$. For box-and-whisker plots, horizontal lines denote medians, boxes depict the interquartile range, whiskers the minimum-maximum values excluding outliers, and black dots denote outliers (beyond 1.5 times above or below the interquartile range). Abbreviations: Ah = *Anapithecus*

hernyaki; Bh = *Barberapithecus huerzeleri*; Ca = *Crouzelia auscitanensis*; Cr = *Crouzelia rhodanica*; Dm = *Dendropithecus macinnesi*; Ds = *Dionysopithecus shuangouensis*; En = *Egarapithecus narcisoi*; Ev = *Epipliopithecus vindobonensis*; Fj = *Fanchangia jini*; Kk = *Krishnapithecus krishnaii*; Lr = *Laccopithecus robustus*; M = Crouzeliinae indet. from Mörgen; Mc = *Micropithecus clarki*; Pj = *Platodontopithecus jianghuaiensis*; Pl = *Plesiopliopithecus lockeri*; P = *Pliobates cataloniae*; Pa = *Pliopithecus antiquus*; Pc = *Pliopithecus canmatensis*; Ppi = *Pliopithecus piveteaui*; Ppl = *Pliopithecus platyodon*; Pz = *Pliopithecus zhanxiangi*; Se = *Simiolus enjiessi*. See Supplementary Table 2 for data sources. Source data are provided as a Source Data file.



Supplementary Figure 6. Results of the additional cladistic analyses considering a wider sample of catarrhines at the genus level. a cladogram derived from the single most parsimonious tree based on 97 dental characters for 22 taxa (tree length = 324 steps; CI = 0.451; RI = 0.613; RCI = 0.276); **b** strict consensus cladogram derived from the two most

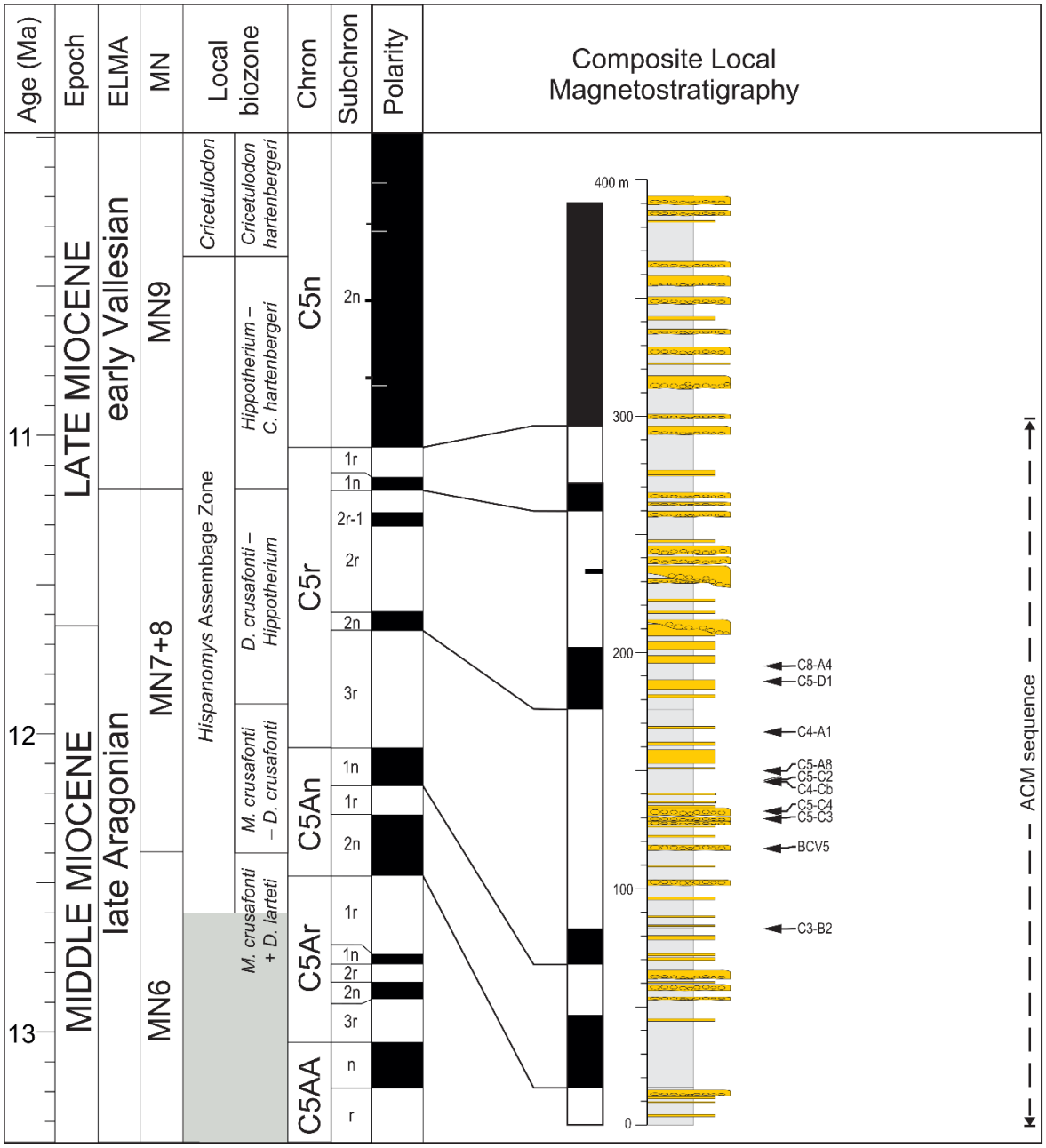
parsimonious trees based on 175 craniodental characters for 22 taxa (tree length = 543 steps; CI = 0.417; RI = 0.557; RCI = 0.232); **c** strict consensus cladogram derived from the 90 most parsimonious trees based on 206 postcranial characters for 18 taxa (tree length = 353 steps; CI = 0.333; RI = 0.254; RCI = 0.085); **d** strict consensus cladogram derived from the five most parsimonious trees based on 381 postcranial characters for 22 taxa (tree length = 920 steps; CI = 0.400; RI = 0.524; RCI = 0. 210). Bremer's indices and bootstrap percentages (only shown when ≥50%) are reported below and above nodes, respectively. The list of characters and taxon-character matrix can be found in Supplementary Data 4 and 5, respectively.



Supplementary Figure 7. Different views on the phylogenetic relationships between major extant and extinct catarrhine groups before and after 1980, including recent cladistic analyses that considered *Pliobates*. a–b alternative hypotheses of Delson and Andrews, 1975 (modified from Fig. 3 in ref. 7); **c** hypothesis of Harrison, 1987 (modified from Fig. 6 in ref. 8); **d-e** results of the cladistic analyses of Alba et al., 2015 (**d**; modified from Fig. 8 in ref. 1), Nengo et al., 2017 (**e**; modified from Fig. 5 in ref. 9), and Ji et al., 2022 (**f**; modified from Fig. 10 in ref. 10). Groups denoted with an asterisk were recovered as paraphyletic, with *Epipliopithecus* being recovered as a dendropithecid instead of a pliopithecoid in ref. 1 and *Simiolus* and *Micropithecus* being recovered as a clade more derived than an East African small-bodied catarrhine clade including *Dendropithecus* in ref. 9. Black silhouettes (not to scale) of Propliopithecoidea, Cercopithecoidea, Hylobatidae, and Hominidae were taken from the following sources: Propliopithecoidea from Fig. 3 in ref. 11; Cercopithecoidea, Hylobatidae, and Hominidae from Summary Figure in ref. 12. Reprinted with permission from AAAS. Black silhouettes (not to scale) of Dendropithecidae and Pliopithecoidea were redrawn from Fig. 15.8 and Fig. 15.12, respectively, in ref. 13. Reprinted with permission from Elsevier.



Supplementary Figure 8. Ortophotomaps of Abocador de Can Mata in 2008 and 2011, showing the location of the two localities that have yielded *Pliobates* remains (ACM/C5-D1 and ACM/C8-A4). The location of ACM/BCV1 (the type locality of *Pierolapithecus catalaunicus*) is provided for comparison. Fossil localities are denoted by yellow stars. The situation of the farmhouses of Can Mata de la Garriga (CMG) and Can Vila (CV) are also provided for reference. Base orthophotomaps: © Institut Cartogràfic i Geològic de Catalunya, downloaded from VISSIR v. 3.26 and reproduced with permission by means of a Creative Commons license CC BY 4.0 (ICGC, 2021).



Supplementary Figure 9. Correlation of the composite local magnetostratigraphy of ACM and nearby areas with the Geomagnetic Polarity Time Scale (GPTS). European Land Mammal Ages (ELMA), Mammal Neogene units, and local biozones of the Vallès-Penedès Basin (after 14) are shown on the left. For the local biozonation, a plus symbol denotes a concurrent range subzone, whereas an en dash denotes an interval subzone. The stratigraphic position of the pliopithecoid-bearing localities is shown to the right on the composite lithostratigraphic column (black arrows). *Pliobates cataloniae* is recorded from ACM/C8-A4 and ACM/C5-D1, the Pliopithecoidea indet. (oldest pliopithecoid occurrence in the Iberian Peninsula) from ACM/C3-B2[15], and *Pliopithecus canmatensis* from all remaining localities. Modified from Fig. 8 in ref. 16.

Supplementary Table 1. Dentognathic remains of *Pliobates cataloniae* from ACM/C5-D1.

Catalogue No.	Anatomical identification	Figure(s)
IPS42977	Left maxillary fragment with DP4	Fig. 2j–l
IPS43013	Left DP3 crown	Fig. 2v
IPS43433	Left c1 crown and nearly complete root; female	Fig. 2b’
IPS43488	Left I1 partial crown and nearly complete root	Fig. 2z
IPS43758	Right maxillary fragment with M1 and damaged M2	Fig. 2d–e
IPS43820	Right p4 broken crown and partial roots	Fig. 2t
IPS43936	Partial infant mandible with left dp3–dp4 and permanent tooth germs inside their crypts; female	Figs. 2g–I and 3
IPS44014	Left maxillary fragment with I1–C1 alveoli and P3–M1; male	Fig. 2a–c
IPS44273	Left i2 crown and nearly complete root	Fig. 2a’
IPS44393	Right DI1 germ	Fig. 2c’
IPS93524	Right p4 partial crown and basalmost portion of the roots	Figs. 2s and 4j
IPS94886	Right m2 germ mesial fragment	Figs. 2u and 4m
IPS94888	Left M2 germ with basalmost portion of the roots	Figs. 2q and 4i
IPS100379	Right M1 damaged crown and partial roots	Figs. 2p and 4g
IPS100384	Left M2 germ	Figs. 2r and 4h
IPS106878	Left dp4 crown	Figs. 2y and 4q

Supplementary Table 2. Comparative sample used in this study.

Taxon	Sources for dental measurements
Dionysopithecus shuangouensis	(17)
Platodontopithecus jianghuaiensis	(17)
Pliopithecus antiquus	(18, 19); authors' own data from casts
Pliopithecus bii	(20)
Pliopithecus canmatensis	(21)
Pliopithecus piveteaui	(19, 22)
Pliopithecus platyodon	authors' own data from casts
Pliopithecus zhanxiangi	(23)
Epipliopithecus vindobonensis	(19); authors' own data from casts
Krishnapithecus krishnaii	(5, 24)
Anapithecus hernyaki	authors' own data from casts
Barberapithecus huerzeleri	(25)
Crouzelia auscitanensis	(26); authors' own data from casts
Crouzelia rhodanica	(26)
Crouzeliinae indet. (Mörgen)	(27, 28)
Egarapithecus narcisoi	(29)
Fanchangia jini	(4)
Laccopithecus robustus	(30)
Plesiopliopithecus lockeri	authors' own data from casts
Dendropithecus macinnesi	(31); authors' own data from casts
Micropithecus clarki	(32, 33); authors' own data from casts
Simiolus enjiessi	(34–36); authors' own data from casts

Supplementary Table 3. Dental BM estimates of *Pliobates cataloniae.* When the two antimeres of the same tooth locus were available for a single individual, average of the R and L MD and BL measurements (in mm) were employed to compute A.

Specimen	Tooth	A (mm^2)	BM (kg)	50% CI	
IPS58443 (holotype)	M1	29.50	3.95	3.66	4.24
IPS43758	M1	30.50	4.19	3.90	4.48
IPS44014 (male)	M1	33.92	5.06	4.76	5.35
IPS100379	M1	31.72	4.49	4.20	4.78
M1 average		31.41	4.41	3.66	5.35
IPS58443 (holotype)	M2	34.45	4.84	4.56	5.13
IPS43758	M2	39.44	5.79	5.50	6.08
IPS94888	M2	38.50	5.61	5.32	5.89
IPS100384	M2	45.75	7.04	6.75	7.33
M2 average		39.54	5.81	4.56	7.33
IPS58443 (holotype)	M3	29.80	5.42	5.15	5.68
IPS43936	m1	28.67	5.46	5.25	5.67
IPS43936	m2	33.00	5.48	5.24	5.71
Average for all tooth loci			5.31	3.66	7.33

Abbreviations: A = occlusal tooth square area (in mm^2); BL = (maximum) buccolingual breadth (in mm); BM = body mass; CI = confidence interval; L = left; MD = mesiodistal length (in mm); R = right.

Supplementary Table 4. Main postcranial features of *Pliobates* based on Alba et al. (2015), distinguishing between primitive (plesiomorphic) and derived (purportedly synapomorphic) features compared with crown hominoids.

Plesiomorphic features	
Proximal humerus	Anteriorly straight and somewhat proximally retroflexed shaft
Distal humerus	Poorly defined trochlear lateral keel and lack of spool-shaped trochlea
Proximal ulna	Narrow trochlear notch without a median keel
Pisiform	Small facet for the styloid process
Derived features	
Distal humerus	Moderately globular capitulum; no entepicondylar foramen; well-developed zona conoidea
Proximal radius	Laterally facing bicipital tuberosity; slightly tilted and almost circular head with reduced lateral lip and beveled surface for the zona conoidea
Distal ulna	Expanded head with a two-faceted semilunar articulation; more developed ulnar fovea; slender and hook-like styloid process
Capitate	Facet for the second metacarpal divided by a deep ligamentary notch
Triquetrum	Small triquetrum relative to hamate size

Supplementary Table 5. Comparative taxa used in this study.

Superfamily	Family	Taxon	Chronostratigraphic range	Geographical distribution	Material	Main references
Pliopithecoidea	Dionysopithecidae	*Dionysopithecus shuangouensis*	~19–18 Ma	China	Dental	(17)
Pliopithecoidea	Dionysopithecidae	*Platodontopithecus jianghuaiensis*	~19–18 Ma	China	Dental, postcranial	(17)
Pliopithecoidea	Pliopithecidae	*Epipliopithecus vindobonensis*	~14.7 Ma	Slovakia	Cranial, dental, postcranial	(19, 37–38)
Pliopithecoidea	Pliopithecidae	*Pliopithecus antiquus*	14.4–11.2 Ma	France	Dental, postcranial	(18, 19, 39–40)
Pliopithecoidea	Pliopithecidae	*Pliopithecus bii*	14.4–12.4 Ma	China	Dental	(20)
Pliopithecoidea	Pliopithecidae	*Pliopithecus canmatensis*	~11.9–11.7 Ma	Spain	Cranial, dental, postcranial	(21, 41)
Pliopithecoidea	Pliopithecidae	*Pliopithecus piveteaui*	16.4–14.4 Ma	France	Dental	(19, 22, 39, 42)
Pliopithecoidea	Pliopithecidae	*Pliopithecus platyodon*	16.4–12.4 Ma	Switzerland and Austria	Dental	(39, 43–44)
Pliopithecoidea	Pliopithecidae	*Pliopithecus zhangxiangi*	14.4–12.4 Ma	China	Cranial, dental	(23)
Pliopithecoidea	Crouzeliidae	*Fanchangia jini*	~18–17 Ma	China	Dental	(4)
Pliopithecoidea	Crouzeliidae	*Krishnapithecus krishnai*	~9 Ma	India	Dental	(5, 24)
Pliopithecoidea	Crouzeliidae	*Laccopithecus robustus*	7 Ma	China	Cranial, dental, postcranial	(30, 45–47)
Pliopithecoidea	Crouzeliidae	*Egarapithecus narcisoi*	~9.1 Ma	Spain	Dental	(29)
Pliopithecoidea	Crouzeliidae	*Anapithecus hernyaki*	~10 Ma	Austria, Germany, and Hungary	Cranial, dental, postcranial	(39, 48–51)
Pliopithecoidea	Crouzeliidae	*Barberapithecus huerzeleri*	~11.2 Ma	Spain	Dental, postcranial	(25, 52)
Pliopithecoidea	Crouzeliidae	Crouzeliinae indet. (Mörgen)	11.2–9.9 Ma	Germany	Dental	(27–28)
Pliopithecoidea	Crouzeliidae	*Plesiopliopithecus lockeri*	14.4–12.4 Ma	Austria	Dental	(39, 53–55)

Pliopithecoidea	Crouzeliidae	*Crouzelia auscitanensis*	14.4–13.8 Ma	France	Dental, postcranial	(26, 39)
Pliopithecoidea	Crouzeliidae	*Crouzelia rhodanica*	12.4–11.9 Ma	France	Dental	(26, 39)
Incertae sedis	Dendropithecidae	*Dendropithecus macinnesi*	~20.3–17 Ma	Kenya	Cranial, dental, postcranial	(31, 56–58)
Incertae sedis	Dendropithecidae	*Micropithecus clarki*	~20.5–19 Ma	Uganda	Cranial, dental, postcranial	(32–33, 57–59)
Incertae sedis	Dendropithecidae	*Simiolus enjiessi*	~21–17.5 Ma	Kenya	Cranial, dental, postcranial	(34–36, 58, 60)
Cercopithecoidea	Victoriapithecidae	*Victoriapithecus macinnesi*	~19.5–12.1 Ma	Kenya and Uganda	Cranial, dental, postcranial	(61–66)
Hominoidea	Proconsulidae	*Ekembo heseloni*	~18.5–16 Ma	Kenya	Cranial, dental, postcranial	(58, 67–68)
Saadanioidea	Saadaniidae	*Saadanius hijazensis*	29–28 Ma	Saudi Arabia	Cranial, dental	(69)

Supplementary Table 6. Digital object identifiers (DOIs) for outer enamel surface 3D models of *Pliobates cataloniae* teeth available from MorphoSource after this work. 3D models of the enamel dentine junction have been uploaded to MorphoSource but are embargoed until ongoing research of tooth endostructural morphology is published.

Catalogue No.	Tooth	Digital objet identifier (DOI)	
		OES	EDJ
IPS58443.1	R M2	https://doi.org/10.17602/M2/M494194	https://doi.org/10.17602/M2/M494191
IPS58443.2	L M3	https://doi.org/10.17602/M2/M494200	https://doi.org/10.17602/M2/M494197
IPS42977	L DP4	https://doi.org/10.17602/M2/M493937	https://doi.org/10.17602/M2/M493934
IPS42977	L P4 germ	https://doi.org/10.17602/M2/M493943	https://doi.org/10.17602/M2/M493940
IPS43936	L i1 germ	https://doi.org/10.17602/M2/M494140	https://doi.org/10.17602/M2/M494137
IPS43936	L i2 germ	https://doi.org/10.17602/M2/M494143	https://doi.org/10.17602/M2/M494146
IPS43936	L c1 germ	https://doi.org/10.17602/M2/M494122	https://doi.org/10.17602/M2/M494119
IPS43936	L p3 germ	https://doi.org/10.17602/M2/M494164	https://doi.org/10.17602/M2/M494161
IPS43936	L p4 germ	https://doi.org/10.17602/M2/M494170	https://doi.org/10.17602/M2/M494684
IPS43936	L m1 germ	https://doi.org/10.17602/M2/M494152	https://doi.org/10.17602/M2/M494149
IPS43936	L m2 germ	https://doi.org/10.17602/M2/M494158	https://doi.org/10.17602/M2/M494155
IPS43936	L dp3	https://doi.org/10.17602/M2/M494128	https://doi.org/10.17602/M2/M494125
IPS43936	L dp4	https://doi.org/10.17602/M2/M494134	https://doi.org/10.17602/M2/M494131
IPS44014	L P3	https://doi.org/10.17602/M2/M494182	https://doi.org/10.17602/M2/M494179
IPS44014	L P4	https://doi.org/10.17602/M2/M494188	https://doi.org/10.17602/M2/M494185
IPS44014	L M1	https://doi.org/10.17602/M2/M494173	https://doi.org/10.17602/M2/M494176
IPS93524	R p4	https://doi.org/10.17602/M2/M494206	https://doi.org/10.17602/M2/M494203
IPS94886	R m2 germ	https://doi.org/10.17602/M2/M494212	https://doi.org/10.17602/M2/M494209
IPS94888	L M2 germ	https://doi.org/10.17602/M2/M494218	https://doi.org/10.17602/M2/M494215
IPS100379	R M1	https://doi.org/10.17602/M2/M494224	https://doi.org/10.17602/M2/M494221
IPS100384	L M2 germ	https://doi.org/10.17602/M2/M494230	https://doi.org/10.17602/M2/M494227
IPS106878	L dp4 crown	https://doi.org/10.17602/M2/M494236	https://doi.org/10.17602/M2/M494233

Abbreviations: L = left; R = right.

Supplementary References

1. Alba, D. M. et al. Miocene small-bodied ape from Eurasia sheds light on hominoid evolution. *Science* **350**, aab2625 (2015).
2. Pugh, K. D. Phylogenetic analysis of Middle-Late Miocene apes. *J. Hum. Evol.* **165**, 103140 (2022).
3. Urciuoli, A. & Alba, D. M. Systematics of Miocene apes: State of the art of a neverending controversy. *J. Hum. Evol.* **175**, 103309 (2023).
4. Harrison, T. et al. A new genus of pliopithecoid from the late Early Miocene of China and its implications for understanding the paleozoogeography of the Pliopithecoidea. *J. Hum. Evol.* **145**, 102838 (2020).
5. Sankhyan, A. R., Kelley, J. & Harrison, T. A highly derived pliopithecoid from the Late Miocene of Haritalyangar, India. *J. Hum. Evol.* **105**, 1–12 (2017).
6. Gagnaison, C., Castillo, L., Grugier, O. & Renou, J.-C. Une hémimandibule de *Pliopithecus piveteaui* dans le Miocène de Contres (41, France). *Symbioses* **16**, 26–29 (2006).
7. Delson, E. & Andrews, P. Evolution and interrelationships of the catarrhine primates. in *Phylogeny of the Primates: A Multidisciplinary Approach* (eds. Luckett, W. P. & Szalay, F. S.) 405–446 (Plenum Press, 1975).
8. Harrison, T. The phylogenetic relationships of the early catarrhine primates: a review of the current evidence. *J. Hum. Evol.* **16**, 41–80 (1987).
9. Nengo, I. et al. New infant cranium from the African Miocene sheds light on ape evolution. *Nature* **548**, 169–174 (2017).
10. Ji, X. et al. The earliest hylobatid from the Late Miocene of China. *J. Hum. Evol.* **171**, 103251 (2022).
11. Almécija, S., Tallman, N., Sallam, H. M., Fleagle, J. G., Hammond, A. S. & Seiffert, E. R. Early anthropoid femora reveal divergent adaptive trajectories in catarrhine hind-limb evolution. *Nat. Comm.* **10**, 4778 (2019).
12. Almécija, S., Hammond, A. S., Thompson, N. E., Pugh, K. D., Moyà-Solà, S. & Alba, D. M. Fossil apes and human evolution. *Science* **372** eabb4363 (2021). DOI: 10.1126/science.abb436
13. Fleagle, J. G. *Primate Adaptation and Evolution, Third Edition* (Academic Press, 2013). https://doi.org/10.1016/C2009-0-01979-5
14. Casanovas-Vilar, I. et al. The Miocene mammal record of the Vallès-Penedès Basin (Catalonia). *C. R. Palevol* **15**, 791–812 (2016).
15. Alba, D. M., Moyà-Solà, S., Robles, J. M. & Galindo, J. Brief communication: The oldest pliopithecid record in the Iberian Peninsula based on new material from the Vallès-Penedès Basin. *Am. J. Phys. Anthropol.* **147**, 135–140 (2012).

16. Alba, D. M. et al. A revised (earliest Vallesian) age for the hominoid-bearing locality of Can Mata 1 based on new magnetostratigraphic and biostratigraphic data from Abocador de Can Mata (Vallès-Penedès Basin, NE Iberian Peninsula). *J. Hum. Evol.* **170**, 103237 (2022).
17. Harrison, T. & Gu, Y. Taxonomy and phylogenetic relationships of Early Miocene catarrhines from Sihong, China. *J. Hum. Evol.* **37**, 225–277 (1999).
18. Hürzeler, J. Contribution à l'odontologie et à la phylogénèse du genre *Pliopithecus* Gervais. *Ann. Paleontol.* **40**, 5–63 (1954).
19. Z apfe, H. Die Primatenfunde aus der miozänen Spaltenfüllung von Neudorf an der March (Děvinská Nová Ves), Tschechoslowakei. *Schweizer. Palaeontol. Abh.* **78**, 4–293 (1961a).
20. Wu, W.-Y., Meng, J., & Ye, J. The discovery of *Pliopithecus* from northern Junggar Basin, Xinjiang. *Vert. PalAs.* **41**, 76–86. (2003).
21. Alba, D. M. et al. A new species of *Pliopithecus* Gervais, 1849 (Primates: Pliopithecidae) from the Middle Miocene (MN8) of Abocador de Can Mata (els Hostalets de Pierola, Catalonia, Spain). *Am. J. Phys. Anthropol.* **141**, 52–75 (2010).
22. Ginsburg, L. Le Pliopithèque des faluns Helvétiens de la Touraine et de l'Anjou. in *Problèmes Actuels de Paléontologie (Évolution des Vertébrés). Paris, 4-9 Juin, 1973.* 877–886 (CNRS, Paris, 1975).
23. Harrison, T., Delson, E. & Guan, J. A new species of *Pliopithecus* from the Middle Miocene of China and its implications for early catarrhine zoogeography. *J. Hum. Evol.* **21**, 329–361 (1991).
24. Chopra, S. R. K. & Kaul, S. A new species of *Pliopithecus* from the Indian Sivaliks. *J. Hum. Evol.* **8**, 475–477 (1979).
25. Alba, D. M. & Moyà-Solà, S. A new pliopithecid genus (Primates, Pliopithecoidea) from Castell de Barberà (Vallès-Penedès Basin, Catalonia, Spain). *Am. J. Phys. Anthropol.* **147**, 88–112 (2012).
26. Ginsburg, L & Mein, P. *Crouzelia rhodanica*, nouvelle espèce de primate catarhinien, et essai sur la position systématique des Pliopithecidae. *Bull. Mus. Natl. Hist. Nat.* **2**, 57–85 (1980).
27. Heißig, K. *Ein Pliopithecide aus dem Vallesium* (*MN 9) der Oberen* Süßwassermolasse Bayerns. *Ber. naturwiss. Ver. Schwaben* **103**, 1–2 (1999).
28. Seehuber, *U. Litho- und biostratigraphische Untersuchungen in der Oberen Süßwassermolasse in der Umgebung von Kirchheim in Schwaben* (Ludwig-Maximilians-Universität München, München, Germany. 2008).
29. Moyà-Solà, S., Köhler, M. & Alba, D. M. *Egarapithecus narcisoi*, a new genus of Pliopithecidae (Primates, Catarrhini) from the Late Miocene of Spain. *Am. J. Phys. Anthropol.* **114**, 312–324 (2001).
30. Pan, Y., Waddle, D. M. & Fleagle, J. G. Sexual dimorphism in *Laccopithecus robustus*, a Late Miocene hominoid from China. *Am. J. Phys. Anthropol.* **79**, 137–158 (1989).

31. Andrews, P. A revision of the Miocene Hominoidea of East Africa. *Bull. Br. Mus. Nat. Hist. Geol.* **30**, 85–224 (1978).
32. Pickford, M., Musalizi, S., Senut, B., Gommery, D. & Musiime, E. Small apes from the early Miocene of Napak, Uganda. *Geo-Pal Uganda* **3**, 1–111 (2010).
33. Pickford, M., Senut, B., Gommery, D., Musalizi, S. & Ssebuyungo, C. Revision of smaller-bodied anthropoids from Napak, early Miocene, Uganda: 2011-2020 collections. *Münchner Geowiss. Abh.* **51**, 1–135 (2021).
34. Leakey, R. E. F & Leakey, M. G. A. new Miocene small-bodied ape from Kenya. *J. Hum. Evol.* **16**, 369–387 (1987).
35. Harrison, T. A reassessment of the taxonomic and phylogenetic affinities of the fossil catarrhines from Fort Ternan, Kenya. *Primates* **33**, 501–522 (1992).
36. Pickford, M., Senut, B., Gommery, D., Musalizi, S. & Musiime, E. Revision of the Miocene Hominoidea from Moroto I and II, Uganda. *Geo-Pal Uganda* **10**, 1–32 (2017).
37. Zapfe, H. & Hürzeler, J. Die Fauna der miozänen Spaltenfüllung von Neudorf an der March (ČSR.). *Primates. Sitzungsber. Öst. Akad. Wiss. Math. Naturwiss. Kl.* **166**, 113–123 (1957).
38. Zapfe, H. The skeleton of *Pliopithecus* (*Epipliopithecus*) *vindobonensis* Zapfe and Hürzeler. *Am. J. Phys. Anthropol.* **16**, 441–457 (1958).
39. Begun, D. R. The Pliopithecoidea. in *The Primate Fossil Record* (ed. Hartwig, W. C.) 221–240 (Cambridge University Press, 2002).
40. Senut, B. Les restes post-crâniens des Pliopithecidae (Primates) de Sansan. *Mém. Mus. Natl. Hist. Nat.* **203**, 535–558 (2012).
41. Alba, D. M. & Moyà-Solà, S. New fossil remains of *Pliopithecus canmatensis* from Abocador de Can Mata, and their implications for the taxonomic validity and phylogenetic position of *Epipliopithecus* (Primates, Pliopithecidae). *Am. J. Phys. Anthropol.* **153**, 64 (2014).
42. Gagnaison, C., Castillo, L., Grugier, O. & Renou, J.-C. Une hémimandibule de *Pliopithecus piveteaui* dans le Miocène de Contres (41, France). *Symbioses* **16**, 26–29. (2006).
43. Ginsburg, L. Chronology of the European pliopithecids. in *Primate Evolution* (eds. Else, J. G. & Ice, P. C.) 47–57 (Cambridge University Press, 1986).
44. Steininger, F. Dating the Paratethys Miocene hominoid record. in *Primate Evolution* (eds. Else, J. G. & Ice, P. C.) 71–84 (Cambridge University Press, 1986).
45. Wu, R. & Pan, Y. A late Miocene gibbon-like primate from Lufeng, Yunnan Province. *Acta Anthropol. Sin.* **3**, 185–194. (1984).
46. Wu, R. & Pan, Y. Preliminary observation on the cranium of *Laccopithecus robustus* from Lufeng, Yunnan with reference to its phylogenetic relationship. *Acta Anthropol. Sin*. **4**, 7–12. (1985).

47. Meldrum, D. J. & Pan, Y. Manual proximal phalanx of *Laccopithecus robustus* from the latest Miocene site of Lufeng. *J. Hum. Evol.* **17**, 719–731 (1988).
48. Begun, D. R. Catarrhine phalanges from the Late Miocene (Vallesian) of Rudabánya, Hungary. *J. Hum. Evol.* **17**, 413–438 (1988).
49. Begun, D. R. New catarrhine phalanges from Rudabánya (Northeastern Hungary) and the problem of parallelism and convergence in hominoid postcranial morphology. *J. Hum. Evol.* **24**, 373–402 (1993).
50. Kordos, L. & Begun, D. R. Femora of *Anapithecus* from Rudabànya. *Am. J. Phys. Anthropol.* **108** (S28), 173 (1999).
51. Kordos, L. & Begun, D. R. Primates from Rudabánya: allocation of specimens to individuals, sex and age categories. *J. Hum. Evol.* **40**, 17–39 (2001).
52. Arias-Martorell, J., Almécija, S., Urciuoli, A., Nakatsukasa, M., Moyà-Solà, S. & Alba, D. M. A proximal radius of *Barberapithecus huerzeleri* from Castell de Barberà: Implications for locomotor diversity among pliopithecoids. *J. Hum. Evol.* **157**, 103032 (2021).
53. Zapfe, H. A new fossil anthropoid from the Miocene of Austria. *Curr. Anthropol*. **1**, 428–429. (1960).
54. Zapfe, H. Ein Primatenfund aus der miozänen Molasse von Oberösterreich. *Z. Morphol. Anthropol*. **51**, 247–267. (1961b).
55. Alba, D. M. & Berning, B. On the holotype and original description of the pliopithecid *Plesiopliopithecus lockeri* (Zapfe, 1960). *J. Hum. Evol*. **65**, 338–340. (2013).
56. Le Gros Clark, W. E. & Thomas, D. P. *Associated jaws and limb bones of* Limnopithecus macinnesi, *Fossil Mammals Afr. 3* (British Museum, 1951).
57. Harrison, T. *Small-bodied apes from the Miocene of East Africa* (University College London, London, 1982).
58. Harrison, T. Dendropithecoidea, Proconsuloidea and Hominoidea (Catarrhini, primates). in *Cenozoic Mammals of Africa* (eds. Werdelin, L. & Sanders, W. J.) 429–469 (California Press, 2010).
59. Fleagle, J. G. & Simons, E. L. *Micropithecus clarki*, a small ape from the Miocene of Uganda. *Am. J. Phys. Anthropol.* **49**, 427–440 (1978).
60. Rossie, J. B., Gutierrez, M. M. & Goble, E. Fossil forelimbs of *Simiolus* from Moruorot, Kenya. *Am. J. Phys. Anthropol.* **147** (S54), 252. (2012).
61. Benefit, B. R. The permanent dentition and phylogenetic position of *Victoriapithecus* from Maboko Island, Kenya. *J. Hum. Evol.* **25**, 83–172 (1993).
62. Benefit, B. R. *Victoriapithecus*: The key to Old World monkey and Catarrhine origins. *Evol. Anthropol*. **7**, 155–174 (1999).

63. Benefit, B. R. & McCrossin, M. L. Earliest known Old World monkey skull. *Nature*, **388**, 368–371 (1997).
64. Benefit, B. R. & McCrossin, M. L. The Victoriapithecidae, Cercopithecoidea. in *The Primate Fossil Record* (ed. Hartwig, W. C.) 241–253 (Cambridge University Press, 2002).
65. Jablonski, N. G. & Frost, S. Cercopithecoidea. in *Cenozoic Mammals of Africa* (eds. Werdelin, L. & Sanders, W. J.) 393–428 (California Press, 2010).
66. Pickford, M., Senut, B., Musalizi, S., Gommery, D. & Ssebuyungo, C. Early Miocene victoriapithecid monkey from Napak, Uganda. *Geo-Pal Uganda* **12**, 1–17 (2019).
67. Walker, A., Teaford, M. F., Martin, L. & Andrews, P. A new species of *Proconsul* from the Early Miocene of Rusinga/Mfangano Islands, Kenya. *J. Hum. Evol.* **25**, 43–56 (1993).
68. McNulty, K. P., Begun, D. R., Kelley, J., Manthi, F. K. & Mbua, E. N. A systematic revision of *Proconsul* with the description of a new genus of early Miocene hominoid. *J. Hum. Evol.* **84**, 42–61 (2015).
69. Zalmout, I. S. et al. New Oligocene primate from Saudi Arabia and the divergence of apes and Old World monkeys. *Nature* **466**, 360–365 (2017).

Supplementary Data

Supplementary Data 1. Dental character statements employed in the dental-only cladistic analysis. Character number (in bold type) is followed by character and character state definition. 23 characters were continuous and discretized.

#001: I1–I2 size heteromorphy: 0, low; 1, moderate; 2, marked.
#002: I1–I2 lingual morphology: 0, lingual features (other than lingual cingulum, if present) absent or poorly-developed; 1, lingual features (basal bulge, pillar and/or crenulations) well developed.
#003: Lingual cingulum and crown base of I1: 0, narrow cingulum with slender crown base; 1, broad cingulum with bulging crown base.
#004: I2 morphology: 0, peg-shaped; 1, spatulate.
#005: Apicobasal height of I1 relative to mesiodistal length: 0, low-crowned; 1, high-crowned.
#006: Apicobasal height of I2 relative to mesiodistal length: 0, low-crowned; 1, high-crowned.
#007: i2 mesiodistal waisting: 0, absent; 1, present.
#008: i2 mesial margin: 0, straight to slightly inclined; 1, clearly inclined mesialward.
#009: i2 distal margin: 0, markedly angled; 1, rather straight.
#010: i2 distal prong: 0, absent to slightly developed; 1, well developed.
#011: Apicobasal height of i1 relative to mesiodistal length: 0, high-crowned; 1, very high-crowned.
#012: Apicobasal height of i2 relative to mesiodistal length: 0, high-crowned; 1, very high-crowned.
#013: Male C1 crown shape: 0, moderately compressed but not very high and not markedly dagger-like; 1, male upper canine crown very compressed, high, and dagger-like; 2, male upper canine crown stouter and less compressed.
#014: Male C1 sulcus: 0, sulcus not extending onto root; 1, sulcus extending onto root.
#015: Female c1 length/breadth index: 0, broad; 1, narrow.
#016: Female c1 apicobasal height relative to mesiodistal length: 0, low-crowned; 1, high-crowned.
#017: Mesiolingual cristid-lingual cingulid thickening in the female c1: 0, restricted angle to rounded angle; 1, slightly prominent angle; 2, prominent angle, cuspulid-like.
#018: Position of the Mesiolingual cristid-lingual cingulid junction in the female c1: 0, at about crown-midheight; 1, higher.
#019: P3 breadth/length index: 0, very broad; 1, broad.
#020: P3 length relative to P4 length: 0, P3 shorter to subequal in length to P4; 1, P3 longer than P4.
#021: P3 length relative to M2 length: 0, P3 markedly shorter than M2; 1, P3 moderately shorter than M2.
#022: P3 cusp heteromorphy: 0, strong with tall paracone; 1, reduced with tall paracone; 2, reduced with low paracone.
#023: P3 central fovea shape: 0, broader than long; 1, relatively narrower.
#024: P3 buccal wall shape: 0, clearly triangular; 1, subtriangular to slightly rhomboid; 2, clearly rhomboid.
#025: P3 buccal wall height in buccal view: 0, low; 1, high.
#026: P3 lingual cingulum: 0, conspicuously present in most instances; 1, usually absent or poorly developed.
#027: P3 paracone position along the crown buccolingual axis: 0, very peripheral; 1, not very peripheral.
#028: P4 occlusal contour: 0, (sub)triangular; 1, (sub)oval to (sub)elliptical.
#029: P4 breadth/length index: 0, very broad; 1, broad.
#030: P4 length relative to M2 length: 0, P4 markedly shorter than M2; 1, P4 moderately shorter than M2.
#031: P4 lingual cingulum: 0, conspicuously present in most instances; 1, usually absent or poorly developed.

#032: P4 central fovea shape: 0, broader than long; 1, relatively narrower.

#033: P4 paracone position along the crown buccolingual axis: 0, very peripheral; 1, not very peripheral.

#034: p3 sectoriality: 0, non-sectorial to poorly sectorial; 1, moderately sectorial; 2, markedly to strongly sectorial.

#035: p3 mesiobuccal honing face length: 0, long; 1, short.

#036: p3 mesiobuccal honing face inclination: 0, inclined; 1, steep.

#037: Metaconid on p3: 0, absent; 1, small; 2, prominent.

#038: p4 crown shape: 0, (sub)rectangular to (sub)elliptical; 1, more clearly (sub)oval.

#039: p4 breadth/length index: 0, very to slightly narrow; 1, slightly broader than long.

#040: p4 length relative to m2 length: 0, p4 markedly shorter than m2; 1, p4 moderately shorter than m2.

#041: p4 buccal cingulid: 0, shelf-like from mesial to distal; 1, clearly disrupted or limited to some portions of the crown.

#042: Bilophodont molars: 0, absent; 1, present.

#043: Molar cusp morphology: 0, rounded cusps; 1, pyramidal cusps; 2, pyramidal but somewhat compressed cusps; 3, very compressed cusps.

#044: Upper molar cusp height: 0, low cusps; 1, high cusps.

#045: (Lower) molar cusp peripheralization: 0, cusps not peripheral; 1, cusps moderately peripheral; 2, cusps very peripheral.

#046: Molar crest morphology: 0, blunt crests; 1, moderately sharp crests; 2, markedly sharp crests.

#047: M1–M2 waisting: 0, absent to slight; 1, moderate to marked.

#048: M1 length/breadth index: 0, very broad; 1, moderately broad.

#049: M2 length/breadth index: 0, very broad; 1, moderately broad.

#050: M3 length/breadth index: 0, very broad; 1, moderately broad.

#051: M1/M2 length ratio: 0, M1 moderately shorter than M2; 1, M1 slightly shorter to subequal in length to M2.

#052: M3/M2 length ratio: 0, M3 moderately shorter than M2; 1, M3 slightly shorter to subequal in length to M2.

#053: M1–M3 protoconule: 0, present and large; 1, present and small; 2, usually absent or poorly distinct.

#054: M1–M2 buccal cingulum: 0, well-developed; 1, variously present or discontinuous/poorly developed.

#055: M3 buccal cingulum: 0, well-developed; 1, poorly developed.

#056: M1–M2 lingual cingulum breadth: 0, very to moderately broad; 1, narrow.

#057: M1–M2 lingual cingulum distal development: 0, not surrounding the hypocone; 1, surrounding the hypocone or showing clear distal style(s).

#058: M3 lingual cingulum: 0, well-developed; 1, moderately developed; 2, poorly developed.

#059: Crista obliqua in upper molars: 0, present in all instances; 1, variably present.

#060: M2–M3 metacone size: 0, large; 1, small (compared to the protocone and paracone).

#061: M1–M2 hypocone size (relative to metacone and paracone): 0, similarly sized to slightly smaller; 1, much smaller.

#062: M3 hypocone size (relative to metacone and paracone): 0, large; 1, small; 2, absent or rudimentary.

#063: M1–M2 paracone buccal position relative to the metacone (more marked in the M2): 0, markedly buccal; 1, buccal.

#064: M1–M2 protocone distal position relative to the paracone: 0, clearly distal; 1, distal; 2, aligned.

#065: M3 protocone distal position relative to the paracone: 0, clearly distal; 1, distal; 2, aligned.

#066: M1–M2 hypocone lingual position relative to the protocone: 0, clearly more lingual; 1, almost aligned or lingual.

#067: M3 hypocone lingual position relative to the protocone: 0, aligned; 1, clearly lingual.

#068: M1–M2 buccal profile length: 0, moderately longer than the lingual profile; 1, markedly longer than the lingual profile.

#069: M1–M3 hypocone-metacone crista: 0, absent; 1, disrupted; 2, complete.

#070: M1–M2 prehypocrista: 0, present and meets protocone; 1, variably present (meets protocone); 2, present and meets crista obliqua.

#071: M1–M2 trigon basin: 0, as long as broad; 1, broader than long.

#072: M1–M2 distal fovea: 0, shorter than trigon; 1, clearly longer than trigon, at least in some molars.

#073: m1–m3 cusps: 0, medium-sized to extensive; 1, more discrete.

#074: m1–m3 mesial arm of pliopithecine triangle: 0, always absent; 1, variably present and/or incipient; 2, present in some molar, constituting a pliopithecine triangle.

#075: m1–m3 distal arm of pliopithecine triangle: 0, always absent; 1, variably present and/or poorly constituted; 2, well constituted.

#076: m1–m3 buccal cingulid width: 0, Ledge-like; 1, moderately broad; 2, narrow to absent.

#077: m1–m3 buccal cingulid extent: 0, continuous at least in some molar; 1, usually discontinuous; 2, limited to some stylids.

#078: m1–m3 mesial fovea: 0, very large, about as long as broad; 1, small to restricted, clearly broader than long.

#079: m1 breadth/length index: 0, very narrow; 1, moderately narrow.

#080: m2 breadth/length index: 0, very narrow; 1, moderately narrow.

#081: m1/m2 length ratio: 0, m1 moderately shorter than m2; 1, m1 only slightly shorter than m2.

#082: m1–m2 hypoconulid size: 0, present and well developed in all instances; 1, present in all instances but clearly reduced in size; 2, almost indistinguishable or absent.

#083: m1–m2 protoconid mesial position relative to the metaconid: 0, clearly more mesial; 1, almost transversely aligned.

#084: m1–m2 entoconid distal position relative to the hypoconid: 0, clearly more distal; 1, almost transversely aligned.

#085: m1–m2 hypoconulid position if present: 0, median or slightly buccal; 1, clearly buccal.

#086: m1–m3 crest pattern: 0, hypoprotocristid originates lingually from protoconid, cristid obliqua (if present) joins the protoconid distally; 1, hypoprotocristid originates distally or distolingually from protoconid, from where the inclined cristid obliqua joins protoconid, at least in m1; 2, hypoprotocristid originates distally from protoconid, the inclined cristid obliqua joins the hypoprotocristid-hypometacristid (Y crest pattern) at least in m1; 3, only cristid obliquid is present so that the mesial fovea communicates with the talonid.

#087: m1–m3 postcristid-hypoentocristid: 0, present; 1, absent.

#088: m1–m3 talonid secondary wrinkling: 0, present; 1, absent.

#089: m1–m2 distal fovea: 0, opens on the talonid basin (at least in some molars); 1, large to medium-sized and separated from the talonid basin; 2, small and separated from the talonid basin.

#090: m3 breadth/length index: 0, very narrow; 1, moderately narrow.

#091: m3/m2 length ratio: 0, m1 moderately shorter than m2; 1, m1 only slightly shorter than m2.

#092: p4 distal tubercles: 0, small or indistinct; 1, prominent.

#093: m3 entoconid relative size: 0, small; 1, large.

#094: m3 hypoconulid size: 0, present and well developed in all instances; 1, present in all instances but clearly reduced in size; 2, almost indistinguishable or absent.

#095: m3 hypoconulid position if present: 0, median or slightly buccal; 1, clearly buccal.

Supplementary Data 2. Taxon-character matrix of 95 characters and 27 taxa used in the dental-only cladistic analysis. Missing data are denoted by a question mark. Variable character states are denoted by capital letters: A=(0,1), B=(0,2), C=(0,3), D=(1,2). Parsimony uninformative characters are italicized. See character statements in Supplementary Data 1.

	00000000000000000000000000000000000000000000000000000000000000000000000000000000000000000000000
	00000000011111111112222222222333333333344444444445555555555666666666677777777778888888888999999
Taxon/character	**12345678901234567890123456789012345678901234567890123456789012345678901234567890123456789012345**
Aegyptopithecus zeuxis	00?0??0001000000?1011010?01111011101011000000000001110101000000000100000000001111000000002110000
Saadanius hijazensis	???1?????????0?????10?1??????0?1?????????01??0100001101000000000000100?10??????????????????????
Pliobates cataloniae	0?0???1101????0?2011101101110101O????1??1021020110101110020112100001000000200000100101000??0???
Micropithecus clarki	00000101000100100110110101110100010001110000100111101110100102011010111100110111101100001010001
Dendropithecus macinnesi	100?110010?00011??1010021111110001000010001111001111111010010101110010D1100110111001110001100101
Simiolus enjiessi	10????0010110011011000021111010001000101001111011101111010010101100020010012110010101000111010 1
Pliopithecus platyodon	0000????????0010101010010111110011110111001101100111111101011110100000100220011110000100 1?10011
Pliopithecus antiquus	??????1001????????1??00??11???????1110111001101????????????????????????0??0220011110000000101 0011
Pliopithecus canmatensis	?0?1??10011???????10100??1110100011101110011010 01?0?11?10?010?10?0?0001002100111100001001110011
Pliopithecus zhanxiangi	?????????????00????10100101111100 1????????01101000011111101010110100000100220011100000000111001 1
Pliopithecus piveteaui	????????????????????????????0?????????11100110 1???0??????????????????????0??022001100000000011 00011
Pliopithecus bii	?00?????????????????????????????????????01101???????????????????????????022001?1?0000000110?011
Epipliopithecus vindobonensis	?000001001110 0????111001011111001111101100111110001101101001A1111A0010110110011000001000111001 1
Dionysopithecus shuangouensis	?00?0?1001?0????????????????1010001111?00?010010101111110010010111100010010220011000010100110001 1
Platodontopithecus jianghuaiensis	?????????????11????00101??10?11???1111?00?0100100011111100100101111000?0000220011100110100110001 1
Egarapithecus narcisoi	????????????????????0??011010??????01120011 02?01?????????????????????????????0??11?0010001200101101 1
Barberapithecus huerzeleri	?00??????????001110?????????????????1111001102101100011110101011110000100000221001010010000101001 1
Anapithecus hernyaki	0010??0101??0010200010110101010100112011103102111?1?110001000110000100000210101010000200201101 1
Laccopithecus robustus	0010??1101??10101000101??10101010111100110110111111111111010011100001000000102111010000000101101 1
Plesiopliopithecus lockeri	??????1101??????????????????????????111000?002?02?????????????????????????????021000 0??1000100 2??0???
Crouzelia auscitanensis	?????????????????????????????????????001002?02????????????????????????????021100001100011 00??0???
Crouzelia rhodanica	??2?02????????????????????????????021100?0?2000110 0??????
Crouzeliinae indet. (Mörgen)	????????????????????????????10?010?????????021?101????11?10?011?10?0?10000??????????????????????
Fanchangia jini	?01110????0???0???10101??10101010111101000100111100011110201 0?1000010000022211000000000002000011
Krishnapithecus krishnaii	???00?21???0??1?1??10??2??0???0???11 1211?011000311 0??????
Ekembo heseloni	0000100010112010001110011111110001000010001111011001011102000211110 00B000001111100100000111000 1
Victoriapithecus macinnesi	1000110011010101110001111110011112001101011111111110021110210010221 00A200000221110D1100111010001

Supplementary Data 3. List of apomorphies of the clades recovered in the consensus tree from the 192 most parsimonious trees. Double arrows '==>' denote unambiguous changes, whereas single arrows '-->' denote ambiguous changes (i.e., including reversals). See character statements in Supplementary Data 1 and node numbers in Fig. 5.

Branch	Character	Steps	CI	Change
node 18 <-> *Aegyptopithecus zeuxis*	11	1	0.250	1 <-> 0
	12	1	0.333	1 <-> 0
	15	1	0.250	1 <-> 0
	19	1	0.250	1 <-> 0
	24	1	1.000	1 <-> 0
	26	1	1.000	1 <-> 0
	29	1	0.143	0 <-> 1
	33	1	0.200	0 <-> 1
	40	1	0.200	1 <-> 0
	43	1	0.500	1 <=> 0
	44	1	0.250	1 <-> 0
	57	1	0.250	0 <=> 1
	71	1	0.200	1 <=> 0
	81	1	0.143	0 <-> 1
	89	1	0.333	1 <-> 2
	95	1	1.000	1 <-> 0
node 18 --> *Saadanius hijazensis*	4	1	0.333	0 ==> 1
	21	1	0.333	1 ==> 0
	30	1	1.000	1 ==> 0
	47	1	0.167	0 ==> 1
	51	1	0.200	1 ==> 0
node 18 --> node 17	20	1	0.250	1 ==> 0
	23	1	0.250	1 ==> 0
	32	1	0.333	1 ==> 0
	46	1	0.500	0 ==> 1
	54	1	1.000	0 ==> 1
	56	1	0.167	0 --> 1
	60	1	0.333	0 --> 1
	62	1	0.400	0 ==> 1
	65	1	0.667	0 ==> 1
	67	1	0.500	1 ==> 0
node 17 --> node 12	7	1	0.500	0 ==> 1
	17	1	0.500	0 --> 1
	18	1	0.500	1 ==> 0
	35	1	1.000	0 ==> 1
	58	1	0.333	0 --> 1
	63	1	0.500	0 ==> 1
	74	1	0.500	0 ==> 2
	75	1	0.286	0 ==> 2

	94	1	1.000	0 ==> 1
node 12 --> node 10	5	1	0.333	0 --> 1
	11	1	0.250	1 --> 0
	32	1	0.333	0 --> 1
	48	1	0.200	0 --> 1
	49	1	0.250	0 --> 1
	65	1	0.667	1 --> 0
	68	1	1.000	0 --> 1
	71	1	0.200	1 --> 0
	81	1	0.143	0 --> 1
	90	1	0.333	1 ==> 0
node 10 --> node 9	8	1	0.500	0 ==> 1
	23	1	0.250	0 ==> 1
	37	1	0.333	0 --> 1
	38	1	0.200	1 ==> 0
	39	1	0.167	1 --> 0
	41	1	0.333	0 --> 1
	80	1	0.200	1 ==> 0
node 9 --> node 4	16	1	0.333	0 --> 1
	20	1	0.250	0 --> 1
	43	1	0.500	1 ==> 2
	61	1	0.500	0 ==> 1
	78	1	0.500	1 ==> 0
	84	1	0.167	0 --> 1
node 4 --> node 3	15	1	0.250	1 --> 0
	17	1	0.500	1 --> 2
	37	1	0.333	1 --> 0
	46	1	0.500	1 ==> 2
	52	1	0.250	1 --> 0
	56	1	0.167	1 --> 0
	58	1	0.333	1 --> 2
	62	1	0.400	1 --> 2
	79	1	0.250	1 ==> 0
	86	1	0.500	0 ==> 1
	89	1	0.333	1 ==> 0
node 3 --> *Pliobates cataloniae*	38	1	0.200	0 ==> 1
	74	1	0.500	2 ==> 0
node 3 --> node 2	41	1	0.333	1 --> 0
	75	1	0.286	2 ==> 1
	82	1	0.600	0 ==> 1
	84	1	0.167	1 --> 0
node 2 --> *Plesiopliopithecus lockeri*	89	1	0.333	0 ==> 2
node 2 --> node 1	76	1	0.250	0 ==> 1
	87	1	0.333	0 ==> 1
node 1 --> *Crouzelia rhodanica*	82	1	0.600	1 ==> 2

node 4 --> *Barberapithecus huerzeleri*	47	1	0.167	0 ==> 1
	48	1	0.200	1 ==> 0
	49	1	0.250	1 --> 0
	55	1	0.500	1 ==> 0
	76	1	0.250	0 ==> 1
node 9 --> node 8	3	1	1.000	0 ==> 1
	27	1	0.500	1 ==> 0
	47	1	0.167	0 ==> 1
	76	1	0.250	0 --> 2
	77	1	0.500	0 ==> 1
node 8 --> *Fanchangia jini*	4	1	0.333	0 ==> 1
	15	1	0.250	1 ==> 0
	39	1	0.167	0 --> 1
	40	1	0.200	1 ==> 0
	41	1	0.333	1 --> 0
	44	1	0.200	1 ==> 0
	51	1	0.200	1 ==> 0
	52	1	0.250	1 ==> 0
	58	1	0.333	1 --> 2
	79	1	0.250	1 ==> 0
	81	1	0.143	1 ==> 0
	89	1	0.333	1 ==> 2
	91	1	0.200	1 ==> 0
node 8 --> node 7	19	1	0.250	1 ==> 0
	60	1	0.333	1 ==> 0
	75	1	0.286	2 ==> 1
	92	1	1.000	0 ==> 1
node 7 --> node 5	13	1	0.667	0 --> 1
	61	1	0.500	0 --> 1
	74	1	0.500	2 ==> 1
node 5 --> *Krishnapithecus krishnai*	43	1	0.500	1 ==> 0
	45	1	0.667	0 ==> 2
	62	1	0.400	1 ==> 2
	73	1	1.000	0 ==> 1
	82	1	0.600	0 ==> 1
	86	1	0.500	0 ==> 3
	87	1	0.333	0 ==> 1
	88	1	0.500	0 ==> 1
	89	1	0.333	1 ==> 0
node 5 --> *Laccopithecus robustus*	50	1	0.200	0 ==> 1
	75	1	0.286	1 ==> 0
node 7 --> node 6	7	1	0.500	1 --> 0
	17	1	0.500	1 --> 2
	34	1	1.000	1 ==> 0
	37	1	0.333	1 ==> 2

	43	1	0.429	1 --> 2
	55	1	0.333	1 --> 0
	56	1	0.167	1 --> 0
	76	1	0.250	2 --> 0
	78	1	0.500	1 --> 0
	86	1	0.500	0 ==> 2
node 6 --> *Egarapithecus narcisoi*	76	1	0.250	0 --> 1
	79	1	0.250	1 ==> 0
	85	1	0.333	0 ==> 1
node 6 --> *Anapithecus hernyaki*	39	1	0.167	0 --> 1
	43	1	0.429	2 --> 3
	46	1	0.500	1 ==> 2
	89	1	0.333	1 ==> 2
node 12 --> node 11	12	1	0.333	1 --> 0
	13	1	0.667	0 --> 1
	14	1	0.500	0 --> 1
	19	1	0.250	1 --> 0
	23	1	0.250	0 --> 1
	27	1	0.500	1 --> 0
	37	1	0.333	0 ==> 1
	39	1	0.167	1 ==> 0
	40	1	0.200	1 ==> 0
	44	1	0.250	1 ==> 0
	50	1	0.200	0 ==> 1
	55	1	0.333	1 ==> 0
	56	1	0.167	1 ==> 0
	57	1	0.250	0 ==> 1
	58	1	0.333	1 --> 0
	64	1	0.500	0 ==> 1
	69	1	0.600	0 --> 1
	71	1	0.200	1 ==> 0
	84	1	0.167	0 ==> 1
	86	1	0.500	0 ==> 1
	91	1	0.200	1 ==> 0
node 11 --> *Dionysopithecus shuangouensis*	48	1	0.200	0 ==> 1
	72	1	0.333	0 ==> 1
	80	1	0.200	1 ==> 0
node 11 --> *Platodonpithecus jianghuaiensis*	29	1	0.143	0 --> 1
	83	1	0.500	0 ==> 1
node 12 --> *Epipliopithecus vindobonensis*	20	1	0.250	0 ==> 1
	29	1	0.143	0 --> 1
	33	1	0.200	0 --> 1
	37	1	0.333	0 ==> 1
	38	1	0.200	1 ==> 0
	45	1	0.667	0 ==> 1

	47	1	0.167	0 ==> 1
	53	1	0.667	1 ==> 0
	56	1	0.167	1 ==> 0
	57	1	0.250	0 ==> 1
	58	1	0.333	1 --> 0
	61	1	0.500	0 --> A
	64	1	0.500	0 ==> 1
	66	1	0.667	0 --> A
	69	1	0.600	0 ==> 1
	72	1	0.333	0 ==> 1
	74	1	0.500	2 ==> 1
	75	1	0.286	2 ==> 1
	80	1	0.200	1 ==> 0
	85	1	0.333	0 ==> 1
node 12 --> *Pliopithecus bii*	91	1	0.200	1 ==> 0
node 12 --> *Pliopithecus zhanxiangi*	29	1	0.143	0 --> 1
	33	1	0.200	0 --> 1
	53	1	0.400	1 ==> 0
node 12 --> *Pliopithecus piveteaui*	80	1	0.200	1 ==> 0
	91	1	0.200	1 ==> 0
node 12 --> *Pliopithecus platyodon*	29	1	0.143	0 --> 1
	33	1	0.200	0 --> 1
	47	1	0.167	0 ==> 1
	50	1	0.200	0 ==> 1
	61	1	0.500	0 ==> 1
	81	1	0.143	0 --> 1
	86	1	0.500	0 ==> 1
node 12 --> *Pliopithecus canmatensis*	4	1	0.333	0 ==> 1
	49	1	0.250	0 ==> 1
	51	1	0.200	1 ==> 0
	75	1	0.286	2 ==> 1
	81	1	0.143	0 --> 1
	86	1	0.500	0 ==> 1
node 17 --> node 16	5	1	0.333	0 --> 1
	6	1	0.500	0 --> 1
	9	1	0.500	0 --> 1
	10	1	0.500	1 --> 0
	25	1	0.500	0 --> 1
	36	1	1.000	1 ==> 0
	45	1	0.667	0 ==> 1
	48	1	0.200	0 ==> 1
	49	1	0.250	0 ==> 1
	50	1	0.200	0 --> 1
	64	1	0.500	0 ==> 1
	70	1	0.800	0 --> 1

	76	1	0.250	0 ==> 1
	83	1	0.500	0 ==> 1
	84	1	0.167	0 --> 1
node 16 --> node 14	56	1	0.167	1 --> 0
	57	1	0.250	0 ==> 1
	69	1	0.600	0 ==> 1
	72	1	0.333	0 ==> 1
	75	1	0.286	0 ==> 1
	81	1	0.143	0 --> 1
node 14 --> *Micropithecus clarki*	5	1	0.333	1 --> 0
	8	1	0.500	0 ==> 1
	9	1	0.500	1 --> 0
	11	1	0.250	1 --> 0
	22	1	0.500	0 ==> 1
	25	1	0.500	1 --> 0
	43	1	0.429	1 ==> 0
	44	1	0.200	1 ==> 0
	46	1	0.500	1 ==> 0
	52	1	0.250	1 ==> 0
	62	1	0.400	1 ==> 2
	67	1	0.500	0 ==> 1
	90	1	0.333	1 ==> 0
node 14 --> node 13	1	1	0.500	0 ==> 1
	16	1	0.333	0 ==> 1
	24	1	1.000	1 ==> 2
	85	1	0.333	0 ==> 1
	93	1	1.000	0 ==> 1
node 13 --> *Dendropithecus macinnesi*	12	1	0.333	1 ==> 0
	29	1	0.143	0 --> 1
	38	1	0.200	1 ==> 0
	40	1	0.200	1 ==> 0
	48	1	0.200	1 ==> 0
	66	1	0.667	0 ==> 1
	70	1	0.800	1 --> D
	81	1	0.143	1 --> 0
	91	1	0.200	1 ==> 0
node 13 --> *Simiolus enjiessi*	21	1	0.333	1 ==> 0
	39	1	0.167	1 ==> 0
	51	1	0.200	1 ==> 0
	69	1	0.600	1 ==> 2
	70	1	0.800	1 --> 0
	71	1	0.200	1 ==> 0
	76	1	0.250	1 ==> 2
	77	1	0.500	0 ==> 1
	79	1	0.250	1 ==> 0

	80	1	0.200	1 ==> 0
	84	1	0.167	1 --> 0
node 16 --> node 15	51	1	0.200	1 ==> 0
	53	1	0.667	1 --> 0
	58	1	0.333	0 ==> 2
	60	1	0.333	1 --> 0
	66	1	0.667	0 ==> 1
	70	1	0.800	1 --> 2
	71	1	0.200	1 ==> 0
	77	1	0.500	0 --> 1
node 15 --> *Ekembo heseloni*	6	1	0.500	1 --> 0
	13	1	0.667	0 ==> 2
	18	1	0.500	1 ==> 0
	20	1	0.250	0 ==> 1
	29	1	0.143	0 --> 1
	38	1	0.200	1 ==> 0
	40	1	0.200	1 ==> 0
	50	1	0.200	1 --> 0
	62	1	0.400	1 ==> 2
	63	1	0.500	0 ==> 1
	70	1	0.800	2 --> B
	84	1	0.167	1 --> 0
node 15 --> *Victoriapithecus macinnesi*	1	1	0.500	0 ==> 1
	10	1	0.500	0 --> 1
	11	1	0.250	1 --> 0
	14	1	0.500	0 ==> 1
	15	1	0.250	1 ==> 0
	16	1	0.333	0 ==> 1
	17	1	0.500	0 --> 1
	19	1	0.250	1 ==> 0
	21	1	0.333	1 ==> 0
	22	1	0.500	0 ==> 1
	23	1	0.250	0 ==> 1
	28	1	1.000	1 ==> 0
	31	1	1.000	0 ==> 1
	32	1	0.333	0 ==> 1
	33	1	0.200	0 --> 1
	34	1	1.000	1 ==> 2
	37	1	0.333	0 ==> 1
	39	1	0.167	1 ==> 0
	42	1	1.000	0 ==> 1
	47	1	0.167	0 ==> 1
	52	1	0.250	1 ==> 0
	53	1	0.667	0 --> 2
	59	1	1.000	0 ==> 1

```
64              1   0.500  1 ==> 2
65              1   0.667  1 ==> 2
69              1   0.600  0 --> A
76              1   0.250  1 ==> 2
77              1   0.500  1 --> 2
82              1   0.600  0 ==> D
87              1   0.333  0 ==> 1
88              1   0.500  0 ==> 1
90              1   0.333  1 ==> 0
```

Supplementary Data 4. Character statements employed in the additional cladistic analysis. Character number (in bold type) is followed by character and character state definition. 23 characters were continuous and discretized.

Dental

#001 I1–I2 size heteromorphy: 0, low; 1, moderate; 2, marked.

#002 I1–I2 lingual morphology: 0, lingual features (other than lingual cingulum, if present) absent or poorly-developed; 1, lingual features (basal bulge, pillar and/or crenulations) well developed.

#003 Lingual cingulum and crown base of I1: 0, narrow cingulum with slender crown base; 1, broad cingulum with bulging crown base.

#004 I2 morphology: 0, peg-shaped; 1, spatulate.

#005 Apicobasal height of I1 relative to mesiodistal length: 0, low-crowned; 1, high-crowned.

#006 Apicobasal height of I2 relative to mesiodistal length: 0, low-crowned; 1, high-crowned.

#007 i2 mesiodistal waisting: 0, absent; 1, present.

#008 i2 mesial margin: 0, straight to slightly inclined; 1, clearly inclined mesialward.

#009 i2 distal margin: 0, markedly angled; 1, rather straight.

#010 i2 distal prong: 0, absent to slightly developed; 1, well developed.

#011 Apicobasal height of i1 relative to mesiodistal length: 0, high-crowned; 1, very high-crowned.

#012 Apicobasal height of i2 relative to mesiodistal length: 0, high-crowned; 1, very high-crowned.

#013 Male C1 crown shape: 0, moderatelyv compressed but not very high and not markedly dagger-like; 1, male upper canine crown very compressed, high, and dagger-like; 2, male upper canine crown stouter and less compressed.

#014 Male C1 sulcus: 0, sulcus not extending onto root; 1, sulcus extending onto root.

#015 Female c1 length/breadth index: 0, broad; 1, narrow.

#016 Female c1 apicobasal height relative to mesiodistal length: 0, low-crowned; 1, high-crowned.

#017 Mesiolingual cristid-lingual cingulid thickening in the female c1: 0, restricted angle to rounded angle; 1, slightly prominent angle; 2, prominent angle, cuspulid-like.

#018 Position of the Mesiolingual cristid-lingual cingulid junction in the female c1: 0, low; 1, at about crown-midheight; 2, higher.

#019 P3 breadth/length index: 0, very broad; 1, broad.

#020 P3 length relative to P4 length: 0, P3 shorter to subequal in length to P4; 1, P3 longer than P4.

#021 P3 length relative to M2 length: 0, P3 markedly shorter than M2; 1, P3 moderately shorter than M2.

#022 P3 cusp heteromorphy: 0, strong with tall paracone; 1, reduced with tall paracone; 2, reduced with low paracone.

#023 P3 central fovea shape: 0, broader than long; 1, relatively narrower.

#024 P3 buccal wall shape: 0, clearly triangular, without mesiobuccal expansion onto root; 1, subtriangular or somewhat rhomboid, with clear mesiobuccal expansion onto root; 2, slightly rhomboid, with no mesiobuccal expansion onto root; 3, clearly rhomboid.

#025 P3 buccal wall height in buccal view: 0, low; 1, high.

#026 P3 lingual cingulum: 0, conspicuously present in most instances; 1, usually absent or poorly developed.

#027 P3 paracone position along the crown buccolingual axis: 0, very peripheral; 1, not very peripheral.

#028 P4 occlusal contour: 0, (sub)triangular; 1, (sub)oval to (sub)elliptical.

#029 P4 breadth/length index: 0, very broad; 1, broad.

#030 P4 length relative to M2 length: 0, P4 markedly shorter than M2; 1, P4 moderately shorter than M2.

#031 P4 lingual cingulum: 0, conspicuously present in most instances; 1, usually absent or poorly developed.

#032 P4 central fovea shape: 0, broader than long; 1, relatively narrower.

#033 P4 paracone position along the crown buccolingual axis: 0, very peripheral; 1, not very peripheral.

#034 p3 sectoriality: 0, non-sectorial to poorly sectorial; 1, moderately sectorial; 2, markedly to strongly sectorial.

#035 p3 mesiobuccal honing face length: 0, long; 1, medium-size; 2, short.

#036 p3 mesiobuccal honing face inclination: 0, inclined; 1, steep.

#037 Metaconid on p3: 0, absent; 1, small; 2, prominent.

#038 p4 crown shape: 0, (sub)rectangular to (sub)elliptical; 1, more clearly (sub)oval.

#039 p4 breadth/length index: 0, very to slightly narrow; 1, slightly broader than long.

#040 p4 length relative to m2 length: 0, p4 markedly shorter than m2; 1, p4 moderately shorter than m2.

#041 p4 buccal cingulid: 0, shelf-like from mesial to distal; 1, clearly disrupted or limited to some portions of the crown.

#042 Bilophodont molars: 0, absent; 1, present.

#043 Molar cusp morphology: 0, rounded cusps; 1, pyramidal cusps; 2, pyramidal but somewhat compressed cusps; 3, very compressed cusps.

#044 Upper molar cusp height: 0, low cusps; 1, high cusps.

#045 (Lower) molar cusp peripheralization: 0, cusps not peripheral; 1, cusps moderately peripheral; 2, cusps very peripheral.

#046 Molar crest morphology: 0, blunt crests; 1, moderately sharp crests; 2, markedly sharp crests.

#047 M1–M2 waisting: 0, slight to moderate; 1, marked.

#048 M1 length/breadth index: 0, very broad; 1, moderately broad.

#049 M2 length/breadth index: 0, very broad; 1, moderately broad.

#050 M3 length/breadth index: 0, very broad; 1, moderately broad.

#051 M1/M2 length ratio: 0, M1 moderately shorter than M2; 1, M1 slightly shorter to subequal in length to M2.

#052 M3/M2 length ratio: 0, M3 moderately shorter than M2; 1, M3 slightly shorter to subequal in length to M2.

#053 M1–M3 protoconule: 0, present and large; 1, present and small; 2, usually absent or poorly distinct.

#054 M1–M2 buccal cingulum: 0, well-developed; 1, variously present or discontinuous/poorly developed; 2, absent.

#055 M3 buccal cingulum: 0, well-developed; 1, variously present or discontinuous/poorly developed; 2, absent.

#056 M1–M2 lingual cingulum breadth: 0, well-developed; 1, reduced or discontinuous; 2, absent.

#057 M1–M2 lingual cingulum distal development: 0, not surrounding the hypocone; 1, surrounding the hypocone or showing clear distal style(s).

#058 M3 lingual cingulum: 0, well-developed; 1, reduced or discontinuous; 2, absent.

#059 Crista obliqua in upper molars: 0, present in all instances; 1, variably present; 2, absent.

#060 M2–M3 metacone size: 0, large; 1, small (compared to the protocone and paracone).

#061 M1–M2 hypocone size (relative to metacone and paracone): 0, similarly sized to slightly smaller; 1, much smaller.

#062 M3 hypocone size (relative to metacone and paracone): 0, large; 1, small; 2, absent or rudimentary.

#063 M1–M2 paracone buccal position relative to the metacone (more marked in the M2): 0, markedly buccal; 1, buccal.

#064 M1–M2 protocone distal position relative to the paracone: 0, clearly distal; 1, distal; 2, aligned.

#065 M3 protocone distal position relative to the paracone: 0, clearly distal; 1, distal; 2, aligned.

#066 M1–M2 hypocone lingual position relative to the protocone: 0, more distal than metacone and/or lingual than protocone; 1, in line with metacone and paracone.

#067 M3 hypocone lingual position relative to the protocone: 0, in line with metacone and paracone; 1, more distal than metacone and/or lingual than protocone.

#068 M1–M2 buccal profile length: 0, equal in size to moderately longer than the lingual profile; 1, markedly longer than the lingual profile.

#069 M1–M3 hypocone-metacone crista: 0, discontinuous or absent; 1, variably present but without constituting a true hypoloph; 2, true hypoloph.

#070 M1–M2 prehypocrista: 0, present and meets protocone; 1, variably present (meets protocone); 2, present and meets crista obliqua.

#071 M1–M2 trigon basin: 0, as long as broad; 1, broader than long.

#072 M1–M2 distal fovea: 0, shorter than trigon; 1, clearly longer than trigon, at least in some molars.

#073 m1–m3 cusps: 0, medium-sized to extensive; 1, more discrete.

#074 m1–m3 mesial arm of pliopithecine triangle: 0, always absent; 1, variably present and/or incipient; 2, present in some molar, constituting a pliopithecine triangle.

#075 m1–m3 distal arm of pliopithecine triangle: 0, always absent; 1, variably present and/or poorly constituted; 2, well constituted.

#076 m1–m3 buccal cingulid width: 0, Ledge-like; 1, moderately broad; 2, narrow to absent.

#077 m1–m3 buccal cingulid extent: 0, continuous at least in some molar; 1, usually discontinuous; 2, limited to some stylids.

#078 m1–m3 mesial fovea: 0, very large, about as long as broad; 1, small to restricted, clearly broader than long.

#079 m1 breadth/length index: 0, very narrow; 1, moderately narrow.

#080 m2 breadth/length index: 0, very narrow; 1, moderately narrow.

#081 m1/m2 length ratio: 0, m1 moderately shorter than m2; 1, m1 only slightly shorter than m2.

#082 m1–m2 hypoconulid size: 0, present and well developed in all instances; 1, present in all instances but clearly reduced in size; 2, almost indistinguishable or absent.

#083 m1–m2 protoconid mesial position relative to the metaconid: 0, clearly more mesial; 1, almost transversely aligned.

#084 m1–m2 entoconid distal position relative to the hypoconid: 0, clearly more distal; 1, almost transversely aligned.

#085 m1–m2 hypoconulid position if present: 0, median or slightly buccal; 1, clearly buccal.

#086 m1–m3 crest pattern: 0, hypoprotocristid originates lingually from protoconid, cristid obliqua (if present) joins the protoconid distally; 1, hypoprotocristid originates distally or distolingually from protoconid, from where the inclined cristid obliqua joins protoconid, at least in m1; 2, hypoprotocristid originates distally from protoconid, the inclined cristid obliqua joins the hypoprotocristid-hypometacristid (Y crest pattern) at least in m1; 3, only cristid obliquid is present so that the mesial fovea communicates with the talonid.

#087 m1–m3 postcristid-hypoentocristid: 0, present; 1, absent.

#088 m1–m3 talonid secondary wrinkling: 0, absent to weak; 1, moderate; 2, marked.

#089 m1–m2 distal fovea: 0, opens on the talonid basin (at least in some molars); 1, large to medium-sized and separated from the talonid basin; 2, small and separated from the talonid basin.

#090 m3 breadth/length index: 0, very narrow; 1, moderately narrow.

#091 m3/m2 length ratio: 0, m1 moderately shorter than m2; 1, m1 only slightly shorter than m2.

#092 p4 distal tubercles: 0, small or indistinct; 1, prominent.

#093 m3 entoconid relative size: 0, small; 1, large.

#094 m3 hypoconulid size: 0, present and well developed in all instances; 1, present in all instances but clearly reduced in size; 2, almost indistinguishable or absent.

#095 m3 hypoconulid position if present: 0, median or slightly buccal; 1, clearly buccal.

#096 Lower incisor lingual enamel: 0, present; 1, absent.

#097 m3 hypoconid and entoconid linked by crest: 0, no; 1, yes; 2, true distal lophid.

Cranial

#098 Splanchnocranium orientation relative to cranial base: 0, slightly klinorhynch; 1, airorhynch; 2, strongly klinorhynch.

#099 Inion position relative to glabella (with the cranium oriented in the Frankfurt plane): 0, on the same plane; 1, inion below glabella.

#100 Rostrum length: 0, long rostrum, distance from orbitale to the anterior-most point of maxilla roughly equals C1–M1 tooth row length; 1, short rostrum, distance from orbitale to the anterior-most point of maxilla roughly equals P1–C1 tooth row length.

#101 Angle between interorbital plane/nasals and frontal squama in lateral view: 0, clearly obtuse angle (>90º); 1, roughly right angle (90º).

#102 Orbitale-rhinion distance relative to tooth row (with the cranium oriented in the Frankfurt plane): 0, long (C1–M2); 1, short (C1–P4); very short (M1–M2).

#103 Orbitale position relative to the tooth row (with the cranium oriented in the Frankfurt plane): 0, over the molars; 1, over the premolars.

#104 Rhinion position relative to the tooth row (with the cranium oriented in the Frankfurt plane): 0, over C1–P3; 1, over P4–M1.

#105 Glabella position relative to the tooth row (with the cranium oriented in the Frankfurt plane): 0, over the molars; 1, over the premolars/canine.

#106 Supraorbital region: 0, superciliary arches; 1, supraorbital costae, coalescent with temporal lines; 2, supraorbital torus with inflated glabella.

#107 Frontal sulcus: 0, absent; 1, depression of the mid-frontal region just above glabella; 1, well-developed frontal sulcus present.

#108 Orbital/nasal surface: 0, concave; 1, flat.

#109 Premaxillomaxillary suture: 0, contacts nasal near midpoint; 1, contacts nasal (or frontal) superiorly; 2, contacts nasal inferiorly.

#110 Interorbital pillar: 0, broad; 1, narrow.

#111 Orbital shape: 0, (sub)circular; 1, oval (higher than broad); 2, oval, rectangular or rhomboid (broader than high).

#112 Orbital convergence (relative to the sagittal plane): 1, slightly laterally-directed orbits; 2, frontalized orbits.

#113 Orbital frontation (relative to the Frankfurt plane): 0, orbits posteriorly inclined; 1, orbits close to vertical.

#114 anteriorly or slightly laterally; 1, thin, sharp and laterally-facing lateral orbital rim, with the the zygomaticomaxillary foramina facing laterally.

#115 Infraorbital plane: 0, curved; 1, flat.

#116 Position of the infraorbital foramen relative to the orbit: 0, low; 1, very close to the orbital rim.

#117 Position of the infraorbital foramen relative to tooth row (with the cranium oriented in the Frankfurt plane): 0, above molars; 1, above P3–P4; 2, anteriorly from the premolars.

#118 Zygomatic root pneumatization: 0, solid; 1, hollow.

#119 Zygomatic root height relative to the alveolar plane: 0, low (close to the alveolar plane); 1, moderately high; 2, very high.

#120 Zygomatic height: 0, high; 1, low.

#121 Zygomatic root position relative to the tooth row (with the cranium oriented in the Frankfurt plane): 0, over the M2; 1, over the M1.

#122 Zygomatic orientation in lateral view (relative to the alveolar plane): 0, vertical: 1, posteriorly inclined; 2, anteriorly inclined.

#123 Frontozygomatic suture: 0, vertical; 1, medially directed.

#124 Ethmosphenoid contact: 0, none or very restricted (0-39%); 1, moderately short contact (40-90%); long contact (91-100%).

#125 Pterygoid process: 0, robust; 1, compressed.

#126 Nasal bones at nasion: 0, broad; 1, narrow.

#127 Nasal bones length: 0, short; 1, moderately long; 2, very long.

#128 Nasal aperture position relative to the alveolar plane: 0, low; 1, high.

#129 Frontal sinus: 0, absent; 1, present.

#130 Maxillary sinus size: 0, absent; 1, small; 2, large; 3, very extensive.

#131 Maxillary sinus floor: 0, low; 1, high.

#132 Maxillary sinus position relative to the tooth row: 0, at the level of C1; 1, at the level of P3–P4; 2, behind the premolars.

#133 Atrioturbinal ridges: 0, present and well developed; 1, present but moderate to weak; 2, absent.

#134 Premaxillary suture: 0, does not contact nasals or contacts nasals below the superior-most level of nasal aperture; 1, contacts nasals near their mid-height and above the superior-most level of nasal aperture; 2, contacts nasals near their superior-most level.

#135 Alveolar prognathism of the premaxilla: 0, absent; 1, present.

#136 Premaxilla ascending wing: 0, broad; 1, narrow.

#137 Subnasal floor: 0, fenestrated; 1, stepped; 2, smooth.

#138 Incisive fossa position: 0, opposite to C1; 1, distal to C1; 2, distal to P3.

#139 Incisive canal caliber: 0, absent; 1, large; 2, small.

#140 Greater palatine foramen: 0, round; 1, elongate.

#141 Number of incisive foramina: 0, double (i.e., one on each side of the midline); 1, single (confluence of two foramina, at least close to the surface).

#142 Size of incisive foramina: 0, large; 1, small; 2, tiny.

#143 Palate: 0, shallow; 1, deep.

#144 Posterior palate: 0, shallow; 1, deep.

#145 Canine fossa: 0, shallow; 1, deep.

#146 Palate shape: 0, anteriorly narrower; 1, parallel tooth rows; 2, bowed laterally.

#147 Palatine process: 0, thin; 1, thick.

#148 Palatine crest: 0, strong; 1, weak.

#149 Glenoid fossa: 0, shallow; 1, deep.

#150 Entoglenoid process: 0, large and pronounced; 1, diminutive, indistinct or absent; 2, moderately developed.

#151 Articular portion (postglenoid process) and tympanic portion of temporal bone (ordered): 0, unfused; 1, fused.

#152 Postglenoid foramen (ordered): 0, present; 1, absent.

#153 Temporal fossa: 0, narrow; 1, broader.

#154 Length of the frontal in temporal fossa: 0, short; 1, long.

#155 Condylar canal: 0, absent; 1, present.

#156 Ectotympanic: 0, annular; 1, tubular.

#157 Ossification of the external auditory meatus (ordered): 0, not ossified (annular ectotympanic); 1, large portion of the meatus not ossified (semitubular ectotympanic); 2, almost completely ossified (only the lateral end is not ossified); 3, tubular ectotympanic, completely ossified.

#158 Length of the tubular ectotympanic (ordered): 0, short external auditory tube reaching only the postglenoid process; 1, auditory tube long surpassing the postglenoid process.

#159 Depth of the subarcuate fossa: 0, deep; 1, moderately deep to shallow; 2, very shallow to non-existent.

#160 Anteroposterior position of the carotid foramen on the bulla: 0, posterior (close to the occipital and far from the Eustachian aperture; posterior to line joining midpoints of tympanic bones); 1, more anterior (over the line joining midpoints of tympanic bones).

#161 Foramen ovale position : 0, posteriorly situated, just below the Eustachian aperture, between the glenoid eminence and the bulla; 1, placed well anterior to the Eustachian aperture and laterally displaced.

#162 Bulla tympanica inflation: 0, well inflated; 1, little inflated; 2, not inflated at all.

#163 Foramen spinosum (ordered): 0, present; 1, absent.

#164 Jugular foramen: 0, small and lateralized; 1, large and occlusally visible.

#165 Mandibular condyle height: 0, lower than coronoid; 1, equal or higher than coronoid.

#166 Most lateral position of the occipital crest relative to the anterior-most point of the occipital-temporal suture (in basioccipital view): 0, posterior; 1, anterior.

#167 Carotid canal orientation: 0, oblique; 1, vertical.

#168 Carotid canal direction: 0, anterior; 1, medial.

#169 Size of the vestibule relative to the semicircular canals: 0, small; 1, large.

#170 Robusticity of the semicircular canals: 0, slender; 1, stout.

#171 Shape of the anterior semicircular canal: 0, vertically compressed; 1, rounded; 2, elongated superiorly.

#172 Shape of the anterior portion of the anterior semicircular canal: 0, non-projecting anterosuperiorly; 1, anterosuperiorly projecting.

#173 Shape of the posterior semicircular canal: 0, vertically compressed; 1, rounded; 2, elongated superiorly.

#174 Shape of the lateral semicircular canal ampullary portion: 0, flat or only slightly bent superiorly; 1, markedly bent superiorly.

#175 Length of the common crus: 0, long; 1, intermediate; 2, short.

Postcranial

#176 Humeral head torsion 0, <15º; 1, >15º.

#177 Humeral head shape 0, oblong, extending between tuberosities; 1, less oblong; 2, spherical with tuberosities anterior.

#178 Humeral head height 0, lower than tuberosities; 1, as high or slightly higher than tuberosities; 2, much higher than tuberosities.

#179 Humeral tuberosities relative sizes 0, lesser tuberosity <60% of greater tuberosity; 1, lesser tuberosity 60-80% of greater tuberosity.

#180 Humeral intertuberosity angle 0, <90º; 1, >90º.

#181 Bicipital groove in humerus 0, broad; 1, intermediate; 2, narrow.

#182 Deltoid insertion in humerus 0, on proximal half of shaft; 1, on distal half.

#183 Deltopectoral plane in humerus 0, prominent; 1, reduced.

#184 Proximal humeral shaft shape 0, angular; 1, rounded.

#185 Humeral shaft curvature 0, retroflected; 1, straight; 2, strongly retroflected.

#186 Length of the humerus relative to body mass 0, short; 1, long.

#187 Entepicondylar foramen in humerus (ordered) 0, present; 1, absent.

#188 Olecranon fossa in humerus 0, shallow; 1, deep, sharp laterally.

#189 Olecranon fossa articular surface in humerus 0, no extension into fossa; 1, extends into fossa laterally.

#190 Coronoid/radial fossae size in humerus 0, radial > coronoid; 1, radial < coronoid.

#191 Coronoid fossa in humerus 0, shallow; 1, deep.

#192 Medial epicondyle/keel in humerus 0, distinct; 1, merged.

#193 Medial epicondyle orientation in humerus 0, very retroflexed; 1, slightly retroflexed; 2, medial.

#194 Humeral capitulum proportions 0, longer proximodistally; 1, similar proximodistal and anteroposterior dimensions.

#195 Humeral capitulum articular surface 0, no distal expansion of articular surface; 1, distal expansion of articular surface.

#196 Humeral trochlear shape 0, cylindrical with a weak medial keel; 1, trochleiform with a strong medial keel.

#197 Humeral trochlear breadth 0, < capitular breadth 1, > capitular breadth.

#198 Humeral trochlear proximal border 0, straight; 1, notched (V-shaped for coronoid beak).

#199 Humeral conoid facet 0, absent; 1, present.
#200 Lateral trochlear keel in humerus 0, weak; 1, moderate; 2, strong.
#201 Medial trochlear keel in humerus 0, anterior to epicondyle; 1, projects distally from epicondyle.
#202 Zona conoidea width in humerus 0, broad; 1, narrow.
#203 Zona conoidea depth in humerus 0, shallow; 1, deep.
#204 Distal radioulnar articulation on radius 0, proximodistally narrow; 1, proximodistally expanded.
#205 Radial head outline 0, oval with flat posterolateral area; 1, smaller flat area; 2, round.
#206 Radial head lateral lip 0, large; 1, present; 2, absent.
#207 Radial neck shape 0, oval; 1, circular.
#208 Humeral capitular tail 0, present; 1, absent.
#209 Sigmoid median keel in ulna 0, none; 1, strong keel.
#210 Humeral shaft 0, shaft concave in anterior view; 1, shaft straight.
#211 Radius length relative to body mass 0, short; 1, long 2, very long.
#212 Radial head fossa for capitulum 0, small; 1, relativelly large.
#213 Beveled surface in radius for humeral zona conoidea 0, absent or reduced; 1, present but not very developped; 2, extensive around the margin of radial head; 3, present all around the radial head.
#214 Radial lunate articular surface 0, anteroposteriorly narrow; 1, ventrally expanded.
#215 Ulnar olecranon process 0, not abbreviated; 1, abbreviated.
#216 Radial articulation with radial notch of the ulna 0, small; 1, extends along a great portion of the radial head; 2, extends all over the radial head.
#217 Radial shaft 0, small curvature; 1, very curved.
#218 Bicipital tuberosity in radius 0, facing anteriorly; 1, facing more laterally.
#219 Radial head tilt 0, marked; 1, low or absent.
#220 Ulnar shelf of radius 0, not excludes ulnar head from distal radiocarpal joint; 1, excludes ulnar head from joint:
#221 Radial notch shape in ulna 0, single oval facet; 1, two facets forming a right angle; 2, two distinct facets.
#222 Ulnar shaft cross-section 0, proximally flat; 1, proximally wider.
#223 Ulnar shaft bowing 0, convex dorsally; 1, concave or straight dorsally.
#224 Arm angle of ulna 0, inexistent or small; 1, large.
#225 Cubital angle in ulna 0, inexistent or low (<5º); 1, higher (>5º).
#226 Brachialis insertion in ulna 0, not buttressed medially; 1, buttressed medially.
#227 Laterally-facing ulnar articular area with lateral side of humeral trochlea 0, reduced; 1, extensive.
#228 Radial notch in ulna 0, anterolaterally oriented; 1, laterally oriented.
#229 Trochlear notch in ulna 0, mediolaterally narrow; 1, mediolaterally wide.
#230 Olecranon beak in ulna 0, relatively long; 1, relatively short.
#231 Radioulnar joint 0, non diarthrodial; 1, fully diarthrodial.
#232 Ulnar styloid process 0, massive; 1, with reduced girth.
#233 Ulnar styloid process length 0, long; 1, short.
#234 Ulnar styloid process articulation 0, articulates with pisiform; 1, does not articulate with pisiform.
#235 Ulnar head 0, small facet; 1, large semilunar articulation.
#236 Ulnar styloid process 0, distally straight or ulnarly horiented; 1, hook-like, radially facing.
#237 Ulnar head 0, widest transverse area placed close to styloid; 1, widest transverse area placed on radial articulation.
#238 Ulnar fovea (ordered) 0, not developed; 1, partially developed; 2, fully developed.

#239 Dorsal epitrochlear fossa 0, deep and large; 1, restricted and shallow; 2, absent.

#240 Position of the groove for the extensor pollicis longus tendon 0, dorsomedial; 1, dorsal over lunate facet.

#241 Groove for the m. extensor carpi ulnaris tendon 0, strong and laterally limited by a dorsally prominent ridge; 1, lateral ridge smooth or inexistent; 2, canal absent.

#242 Ulnar styloid articulation with triquetrum 0, present; 1, absent.

#243 Dorsal ridges on distal radius and scaphoid 0, absent; 1, present.

#244 Os centrale facet on scaphoid 0, not beaked; 1, beaked.

#245 Os centrale and scaphoid 0, separate; 1, fused.

#246 Os centrale articulation with trapezium 0, present; 1, absent.

#247 Scaphoid-radial facet in lunate 0, low angle; 1, high angle.

#248 Lunate mediolateral width 0, narrow; 1, broad.

#249 Trapezium-metacarpal I joint 0, sellar; 1, modified hinge; 2, non-sellar.

#250 Capitate head mediolaterally 0, broad; 1, narrow.

#251 Dorsal/palmar extension of the proximal articular facet of the capitate 0, < 1.4; 1, ≥ 1.4.

#252 Proximal capitate surface 0, hemispherical in lateral view; 1, oblong in lateral view.

#253 Hamate border of the capitate 0, ulnarly oriented; 1, radially oriented.

#254 Centrale facet on capitate 0, flat; 1, concavoconvex.

#255 Metacarpal II facet on capitate 0, continuous; 1, divided.

#256 Metacarpal III facet on capitate 0, flat; 1, irregular.

#257 Hamate hamulus 0, not projecting; 1, distally projecting.

#258 Hamate distolateral edge 0, uninterrupted; 1, interrupted by ligament pit.

#259 Metacarpal IV facet on hamate 0, deep; 1, shallow.

#260 Dorsal extension of metacarpal head articular surfaces 0, absent; 1, present.

#261 Dorsal transverse ridge on metacarpal heads 0, absent; 1, present.

#262 Metacarpal I proximal articulation 0, no lateral extension; 1, lateral extension.

#263 Metarcapal I head dorsal part 0, narrow; 1, browed.

#264 Metacarpal II medial facet 0, undivided; 1, divided by ligament pit.

#265 Distal metacarpal shape 0, widest palmarly; 1, quadrilateral.

#266 Proximal articulation surface of proximal phalanges 0, oval; 1, square.

#267 Proximal phalangeal palmar tubercles 0, large; 1, small.

#268 Phalangeal secondary shaft features 0, small; 1, large.

#269 Palmar gutters in metacarpals head 0, strong; 1, poorly-developed.

#270 Pollical distal phalanx's tendon insertion in palmar side 0, present; 1, poorly-developed or absent.

#271 Scaphoid tubercle length 0, similarly long or longer than body; 1, shorter.

#272 Triquetral surface on hamate is highly globular proximally 0, absent; 1, present.

#273 Triquetral surface on hamate is proximodistally long and narrow 0, absent; 1, present.

#274 Large pits for collateral ligaments on metacarpals converging dorsally 0, absent; 1, present.

#275 Proximal articular surface on proximal phalanges is dorsally canted 0, present; 1, absent.

#276 Trochlea in proximal phalanges is palmarly bent or "beaked" 0, absent; 1, present.

#277 Triquetrum size relative to hamate 0, large; 1, small.

#278 Lunate proximodistal length 0, long; 1, short.

#279 Trochleae in proximal phalanges are distally convergent (in palmar view) 0, present; 1, absent.

#280 Capitate and hamate proximally (heads) 0, capitate dominates; 1, hamate dominates.

#281 Reciprocal articular surfaces on capitate and metacarpal IV 0, present; 1, absent.

#282 Dorsal extension in proximal articular surface of metacarpal V 0, present; 1, absent.
#283 Pisiform position 0, not distally migrated; 1, distally migrated.
#284 Pisiform length 0, long; 1, short.
#285 Pisiform facet for ulnar styloid process 0, present; 1, absent.
#286 Pisiform orientation 0, palmar; 1, distal.
#287 Stylotriquetral facet relative size and presence 0, occupies mostly of the proximal surface; 1, occupies only half of the proximal surface; 2, smaller; 3, absent.
#288 Proximally protruding beak on the dorsoulnar side of the triquetrum 0, present; 1, absent.
#289 Triquetrum articular surface for hamate 0, relativelly small and flat; 1, large and concavo-convex.
#290 Triquetrum proximal and distal articular facets 0, paralell; 1, convergent.
#291 Articular surface for os centrale on the capitate 0, anteriorly oriented; 1, laterally oriented.
#292 Exposed metacarpal III facet on the lateral aspect of the capitate 0, not exposed; 1, well exposed.
#293 Size of trapezium facet on capitate 0, small; 1, large.
#294 Articular facet of the scafoid for lunate 0, narrow and small; 1, wide and large.
#295 Scapula shape 0, vertebral border smaller than caudal; 1, longer vertebral border.
#296 Scapula position relative to thorax 0, lateral; 1, dorsal.
#297 Scapular spine 0, oblique to axial border; 1, low angle relative to axial border.
#298 Spinous process root in scapula 0, robust; 1, gracile.
#299 Spinous process inclination in scapula 0, cranially inclined; 1, caudally inclined.
#300 Glenoid shape in scapula 0, elongate; 1, round.
#301 Glenoid curvature in scapula 0, more curved craniocaudally than dorsoventrally; 1, uniformly and moderately curved.
#302 Glenoid-axillary angle in scapula 0, large; 1, small.
#303 Infraglenoid tubercle in scapula 0, broad; 1, narrow.
#304 Teres minor attachment in scapula 0, axillary; 1, anterior.
#305 Coracoid deflection in scapula 0, less; 1, greatest.
#306 Acromial process in scapula 0, short; 1, elongate.
#307 Acromion root in scapula 0, inferior; 1, superior.
#308 Clavicle 0, short; 1, long.
#309 Torso shape 0, craniocaudally long and mediolaterally narrow; 1, craniocaudally short and mediolaterally broad.
#310 Sternum 0, long and narrow; 1, short and broad.
#311 Costal angle 0, low; 1, high.
#312 Ventral keeling of vertebral body 0, present; 1, absent or reduced.
#313 Vertebral body height 0, tall; 1, medium; 2, short.
#314 Spooling of lumbar centrum 0, present; 1, absent or reduced.
#315 Hollowing of lumbar centrum 0, present; 1, absent or reduced.
#316 Sternebrae 0, narrow; 1, intermediate; 2, broad.
#317 Accessory processes in vertebrae 0, large; 1, small; 2, absent.
#318 Transverse process position in lumbar vertebrae 0, ventral (on body); 1, intermediate (on body-pedicle junction); 2, dorsal (on pedicle).
#319 Transverse process inclination in lumbar vertebrae 0, ventrally inclined; 1, neutral (horizontally incline); 1, dorsally and caudally inclined.
#320 Modal number of lumbar vertebrae 0, ≥ 6; 1, ca. 5; 2, ≤ 4:
#321 Sacrum shape 0, broad; 1, narrow.
#322 Sacral number 0, 3 vertebrae; 1, 4 vertebrae; 2, 5 vertebrae; 3, 6 vertebrae.

#323 External tail 0, present; 1, absent.
#324 Iliac blade breadth 0, narrow; 1, intermediate; 2, wide.
#325 Lower iliac height 0, short; 1, long.
#326 Anterior inferior iliac spine 0, not knob-like; 1, knob-like.
#327 Anterior iliac spine 0, absent or separated; 1, near acetabulum.
#328 Acetabulum 0, expanded with raised lip; 1, cranially expanded lunate surface; 2, symmetrical lunate surface.
#329 Pubic length 0, short; 1, medium; 2, long.
#330 Ischial spine 0, distal to acetabulum; 1, same level as acetabulum.
#331 Femoral head height 0, below trochanter; 1, at or above trochanter.
#332 Size of femoral head relative to midshaft diameter 0, small; 1, expanded.
#333 Trochanteric fossa 0, open; 1, intermediate; 2, deep.
#334 Linea aspera ridge up to or above lesser trochanter 0, absent; 1, present.
#335 Femoral neck tubercle 0, present; 1, absent.
#336 Femoral shaft 0, vertical; 1, outwardly angled.
#337 Distal femur shaft shape 0, round; 1, anteroposteriorly flattened.
#338 Buttressing of intercondylar notch in femur 0, no buttressing; 1, buttressing.
#339 Patellar groove 0, narrow and deep; 1, broad and shallow; 2, wider than shaft.
#340 Femoral condyles 0, nearly symmetrical; 1, medial condyle larger.
#341 Femoral condyle depth 0, deep; 1, shallow.
#342 Popliteal groove in femur 0, shallow; 1, deep.
#343 Tibial condylar facets 0, symmetrical; 1, medial facet larger; 2, lateral facet larger.
#344 Lateral tibial facet 0, convex; 1, concave.
#345 Lateral proximal tibial facet 0, below the medial facet; 1, same level as medial facet.
#346 Distal tibial facet 0, square; 1, short.
#347 Lateral malleolus in tibia 0, small; 1, intermediate; 2, large.
#348 Fibular robusticity 0, thin; 1, robust.
#349 Distal fibula 0, robust and laterally flaring; 1, reduced, with less lateral flare.
#350 Talar trochlear depth 0, deep; 1, intermediate; 2, shallow.
#351 Talar trochlear wedging 0, strong; 1, weak.
#352 Talar trochlear rim asymmetry 0, subequal height; 1, lateral keel taller; 2, lateral keel much taller.
#353 Talar head 0, as wide as high; 1, wider than high.
#354 Fibular facet of talus 0, vertical; 1, laterally projecting.
#355 Curve of medial trochlear margin in talus 0, gently curved; 1, strongly curved.
#356 Anterior talar facet 0, curved; 1, intermediate; 2, flat.
#357 Talus height 0, tall; 1, short.
#358 Cotylar fossa in talus 0, distinct cup; 1, shallow.
#359 Plantar calcaneal tubercle 0, small; 1, large.
#360 Posterior calcaneoastragalar joint 0, faces medially; 1, faces dorsally.
#361 Calcaneocuboid joint 0, round facet with deep pit; 1, smaller pit.
#362 Sustentacular facet 0, undivided; 1, divided.
#363 Ectal facet curve in calcaneus 0, gently concave; 1, sharply concave.
#364 Ectal facet shape in calcaneus 0, broadest anterolaterally; 1, broadest proximomedially:
#365 Cuboid peg 0, small; 1, intermediate; 2, large.
#366 Cuboid wedging 0, slight; 1, stronger.

#367 Cuboid length 0, long; 1, short.

#368 Flexor hallucis longus groove 0, small; 1, intermediate; 2, large.

#369 Entocuneiform-metatarsal I joint 0, distal; 1, medial.

#370 Entocuneiform-metatarsal I facet 0, convex with medial extension; 1, less convex with slight extension.

#371 Cuneiform length 0, long; 1, short.

#372 Metartarsal I robusticity 0, gracile; 1, intermediate; 2, robust.

#373 Metartarsal I sesamoid grooves 0, small; 1, large.

#374 Metartarsal I head shape 0, symmetrical; 1, asymmetrical.

#375 Metartarsal I head position 0, aligned; 1, twisted.

#376 Metatarsal II lateral facet 0, divided; 1, single.

#377 Metatarsals II-V robusticity 0, gracile; 1, robust.

#378 Foot axis 0, runs through digit III; 1, runs through digit II.

#379 Phalangeal robusticity 0, gracile; 1, robust.

#380 Phalangeal curvature 0, straight; 1, curved.

#381 Phalangeal flexor ridges 0, weak; 1, intermediate; 2, strong.

Taxon/character	000000000000000000000000000000000000000000000000000000000000000000000000000000000000000000000000000011111111111111111111111 000000000111111111122222222223333333333444444444455555555556666666666777777777788888888889999999999000000000011111111112222 12345678901234567890123456789012345678901234567890123456789012345678901234567890123456789012345678901234567890123456789012
Aegyptopithecus	00?0??0001000000?2011010?0111101111101100010000000111000100000000010000000000111100000000211000000000000000010?010000000000
Saadanius	???1?????????0?????10?1??????0?1?????????01??000000110000000000000100?10?????????????????????????????000000000?0100000?0001
Pliobates	0?0???1101????0?21111012011101010????0??10210201101011100001121000110000002000001001010000??0?????1011110100000011101101102
Micropithecus	00000101000100100210110201110100010000110010100111101110100102011010111100110111101100011010001000??1??10?0???0?0???110010?
Dendropithecus	100?110010?00011??1010031111110001000011001111001111110100101011010 1D11001101110011100011001010 0??1?1?????????0???1?00?0?
Simiolus	10????00101100110210000311110100010000010011110111011110100101011010100100111100101010001110101 00??1?1?????????0???1?00?0?
Pliopithecus	0000??10011?001011101002011111100A1210011001101000011111000011A110001000100 2D0011100000A0011000110 1??0??0?????????0?0????0100
Epipliopithecus	?00000100111 00????11100201111100112110110011110000110110100 1A110001000110110011000001000101001101 1?10110100?00001001110100
Dionysopithecus	?00?0?1001?0???????????????101000121 1?01?0100101011111101001011000101001022001100001010011000110 0??????????????????????????
Barberapithecus	?00?????????001111???????????????12110011021010000111110000111100011000000221001010010000101001 1?1??????????????????0?????????
Anapithecus	0010??0101??001021001012010101010021201110310201 1?1?11100000001100011000002101010100002002011011 00?????????00???0??1???11?1?
Plesiopliopithecus	??????1101??????????????????????????121000?002?02??????????????????????????????0210000??1000100 2??0???0???????????????????????????
Crouzelia	??001002?02???????????????????????????????021100001D0001100??0?????????????????????????????????
Ekembo	00001000101120100011100211111100011001100001110110010110000002111 0100B000001111100100001111000100000000000000200000?0000001
Victoriapithecus	100011001101010112000111111001111200100101111111111002110001001022100120000022111 0B1100101010001020100000 0110?1100000000002
Macaca	100011000100111112000111111000111200000121111111110122210120001221002000000022011 0211-0101010001122100000000 1011001000001001
Pierolapithecus	?11?????????20????10120211111111 00????????000?00110100111010101111010101 0?????????????????????????0000101012011101?011011
Hispanopithecus	11101?0010??20????101203111101100 1??0111100010001111022101010101101010100002211100101001110000100000110101 00?011101?012000
Hylobates	0010000100001001100110120111011111220010120002001111002210100011110100000001221111010000021001100010111101000000 11101101102
Pongo	21100000010002001000012030111011001102111200010011111 0222-201011110100010000221111010 10A2A100001001000201010121111010012000
Gorilla	11110000100020000010020200110100011021101011210111110221010101111010001000011111001010011101101002001000122020211000012000
Pan	11110000100020010001120201110110011021112000200111101221010101111010001000022111110101 0A0A1001110020011011220202110000 12000

Taxon/character	1111111111111111111111111111111111111111111111111111111111111111111111111111111111112222222222222222222222222222222222222222222222222222222222222222333333333344444444455555555556666666666777777777888888888899999999900000000001111111112222222222233333333344444444 3456789012345678901234567890123456789012345678901234567890123456789012345678901234567890123456789012345678901234567890123456789012345678901234
Aegyptopithecus	0?00200201000000000000000?000000?00-?0?0?000??00202000011000?01000000100000000000???000?????????000???0000?????????0???0??
Saadanius	???0000112001000?000100??000????120?????????00202002???
Pliobates	0?0?10120110010001?001000?1011??0110111111?10000102010????10000110000011000010011111010111121?1111000011000?11011111101000
Micropithecus	????????201?1?0?0011000?1?????????????????0???0???
Dendropithecus	????????201?1?1?0000001?0???000001?1000001000000000000000001?000000000000000000000000000000?????
Simiolus	????????201?1?1?0000001?0?????????????????????????????????????000001?1000001000000000000000001?000000000000000000000000000000?????
Pliopithecus	??0?????????????????01110??0??10?00??
Epipliopithecus	?????012?????1??????0?10????0????11001?1??0?01001020001100001110000000100000000000000000100000000000000000000000000200?00
Dionysopithecus	??0??
Barberapithecus	??0???000????00????01??????????????????????????
Anapithecus	?????01201?????????????00?????????????????0??
Plesiopliopithecus	??
Crouzelia	??0??
Ekembo	??0000110?01010000??000000000?00?120?0????0?01100011201??000000011100011101011011011010001110100100010010000100011011200000
Victoriapithecus	1?012000--22110001000002000100000120??0??001000101010001000?02011000100000000100000???0?????0?????20????0000?????????000???
Macaca	10002000--21110000001102000100000131000010001000101010001010002010000100000000100000000000000000002000000000000000000200001
Pierolapithecus	1??11103121011?1????1101??100
Hispanopithecus	0??1110201?00?11????1?11??100??0?1212?????1???0010101??????1111?11?110?101?11??11?????????????1?????????111????????2???00
Hylobates	0000100101100100010001010000110001311111111100000111202101201111111110211101120111221111213112111101011011111101111221100 0
Pongo	120111031210112121121111100001000131200211100011 01A1212101211111111111021111112010122111111311211110101111111101110122121 00
Gorilla	011111131010111210111111111011111131201201100011 00A1B1210121111111111021111112011112111101311211100101011111101110122121 1-
Pan	011101131010111210111111111011111131201201100011 00B1B1210121111111111021111112011112111101311211100101011111101110122121 1-

Taxon/character	2222222222222222222222222222222222222222222222222222222333333333333333333333333333333333333333333333333333333333333333333 4444455555555555666666666677777777777888888888899999999999000000000000011111111112222222222223333333333444444444455555555556666666 5678901234567890123456789012345678901234567890123456789012345678901234567890123456789012345678901234567890123456789012345 6
Aegyptopithecus	????????????????0??????1??????10??1?????????????????0???????????????????????????0???????1?1??10?210????????1011111000?0000??
Saadanius	??
Pliobates	0????11100111011 0???01101?0111111?0100111010111101???12?0101?10111010???10
Micropithecus	???1??1??????????????????????????????
Dendropithecus	???0??1?1?????????????????1111111101000000??
Simiolus	???0??1?1?????????????????1111111101000000??
Pliopithecus	??????????????10???0??
Epipliopithecus	??101???????0001000000101?000111?00?0?000????????0???0000??0???10000100021001000 0????112000110111211111??21011011111111100??
Dionysopithecus	??
Barberapithecus	??
Anapithecus	???1??????????????????????????????????
Plesiopliopithecus	??
Crouzelia	??
Ekembo	0010000000000001010100011000010010010000000000000 1?0010??000????0?0010001000??1001020011 0?0000?110???0110111110 0?00001??20
Victoriapithecus	????0?????????100??00000????100??0??????????????????0?????????????????????????0?0??2?0002???1??????0101?11?100010?00?11???
Macaca	0110000000000001000000000010010001000000000000000000000001000100000200020000000000020000210110000101001011020001010111111 0
Pierolapithecus	000001000011010 10??1000110100100110 00???1?21110100?1????????????11?11211??12??????1??
Hispanopithecus	0?10011000110101 0??101011??01101?00000???????????????11?????????0?11?11211??221???????????1121101????????02????????????????????
Hylobates	01002111101011110011111111000101110010111112111110111101111110111101111111111 1D1110001111100010201000112002100111110000000010
Pongo	01010110001111100111111111100001111101011103111011111101111111111111121122222121210002111011001211110012102011111101 0000021
Gorilla	1000001001111111111111111111000101110111011311111101111111110000011011211222221B1210102111211001211110012102011111101 1000011
Pan	1000001001111101111111111111000111110111110311101101111111110000011011211222221B1210102111211001211110012102011111101 1000011

Taxon/character	333333333333333 666777777777788 789012345678901
Aegyptopithecus	?????1?011??112
Saadanius	????????????????
Pliobates	10100????1??0?1
Micropithecus	????????????????
Dendropithecus	?????1??????011
Simiolus	?????1??????011
Pliopithecus	????????????????
Epipliopithecus	??100011000?011
Dionysopithecus	????????????????
Barberapithecus	????????????????
Anapithecus	?????????????12
Plesiopliopithecus	????????????????
Crouzelia	????????????????
Ekembo	011001111100001
Victoriapithecus	??011??0????101
Macaca	101111000000001
Pierolapithecus	??????????0?000
Hispanopithecus	????????????????
Hylobates	111001011000012
Pongo	121002011011112
Gorilla	121012011011112
Pan	121012011011112

Source Data

Supplementary Figure 4. Dental size and proportions.

COLUMN	DESCRIPTION
Tooth	Tooth position considered (P3–M3 and m1–m2)
Taxon	Species to which the reported specimen data belong (in many cases there are several specimens per species)
Length	Mesiodistal length of the tooth (in mm)
Breadth	Buccolingual breadth of the tooth (in mm). For molars it is measured separately at the mesial and distal lobes but here only the maximum breadth is used.

Tooth	Taxon	Length	Breadth
P3/	*Pliobates cataloniae*	4.20	6.10
P3/	*Micropithecus clarki*	3.20	4.70
P3/	*Micropithecus clarki*	3.10	4.70
P3/	*Micropithecus clarki*	3.40	4.80
P3/	*Micropithecus clarki*	3.00	5.00
P3/	*Micropithecus clarki*	4.10	5.70
P3/	*Dendropithecus macinessi*	4.50	6.90
P3/	*Dendropithecus macinessi*	4.50	7.00
P3/	*Dendropithecus macinessi*	4.10	6.80
P3/	*Dendropithecus macinessi*	4.10	6.40
P3/	*Dendropithecus macinessi*	4.30	6.50
P3/	*Dendropithecus macinessi*	4.10	7.00
P3/	*Simiolus enjiessi*	4.10	6.40
P3/	*Pliopithecus canmatensis*	3.90	6.40
P3/	*Pliopithecus canmatensis*	4.10	7.00
P3/	*Pliopithecus antiquus*	4.10	6.40
P3/	*Pliopithecus platyodon*	4.20	6.80
P3/	*Pliopithecus platyodon*	4.70	6.90
P3/	*Pliopithecus zhanxiangi*	5.10	8.00
P3/	*Pliopithecus zhanxiangi*	5.50	7.90
P3/	*Pliopithecus zhanxiangi*	4.50	6.50
P3/	*Anapithecus hernyaki*	5.40	8.00
P3/	*Anapithecus hernyaki*	5.90	7.70
P3/	*Egarapithecus narcisoi*	5.60	7.20
P3/	*Epipliopithecus vindobonensis*	4.80	7.00
P3/	*Epipliopithecus vindobonensis*	4.80	7.00
P3/	*Fanchangia jini*	5.60	8.10
P3/	*Fanchangia jini*	5.50	7.60
P3/	*Fanchangia jini*	5.40	8.20
P3/	*Laccopithecus robustus*	5.20	7.95
P3/	*Laccopithecus robustus*	6.05	8.10
P3/	*Laccopithecus robustus*	5.30	7.50
P3/	*Platodontopithecus jianghuaiensis*	4.50	6.30
P3/	*Platodontopithecus jianghuaiensis*	4.80	6.50
P4/	*Pliobates cataloniae*	3.20	5.30
P4/	*Pliobates cataloniae*	4.10	5.90
P4/	*Pliobates cataloniae*	5.00	6.40
P4/	Crouzeliinae indet. (Mörgen)	4.30	6.30
P4/	*Dendropithecus macinessi*	4.20	6.70
P4/	*Dendropithecus macinessi*	4.30	6.80
P4/	*Dendropithecus macinessi*	4.30	7.30
P4/	*Dendropithecus macinessi*	3.80	6.80
P4/	*Dendropithecus macinessi*	4.40	7.20
P4/	*Dendropithecus macinessi*	3.80	7.50

P4/	*Dendropithecus macinessi*	4.15	6.45
P4/	*Micropithecus clarki*	3.30	5.00
P4/	*Micropithecus clarki*	3.30	5.30
P4/	*Micropithecus clarki*	3.20	5.00
P4/	*Micropithecus clarki*	3.10	5.00
P4/	*Micropithecus clarki*	3.30	5.00
P4/	*Simiolus enjiessi*	4.00	5.90
P4/	*Dionysopithecus shuangouensis*	4.20	6.10
P4/	*Dionysopithecus shuangouensis*	3.80	5.30
P4/	*Dionysopithecus shuangouensis*	3.50	5.50
P4/	*Platodontopithecus jianghuaiensis*	4.40	7.40
P4/	*Pliopithecus canmatensis*	4.20	5.90
P4/	*Pliopithecus canmatensis*	4.20	6.60
P4/	*Pliopithecus piveteaui*	3.60	5.70
P4/	*Pliopithecus platyodon*	4.30	7.15
P4/	*Pliopithecus platyodon*	4.70	7.50
P4/	*Pliopithecus platyodon*	4.40	7.90
P4/	*Pliopithecus zhanxiangi*	4.50	7.90
P4/	*Pliopithecus zhanxiangi*	4.40	8.00
P4/	*Pliopithecus zhanxiangi*	6.10	9.20
P4/	*Pliopithecus zhanxiangi*	4.70	7.30
P4/	*Epipliopithecus vindobonensis*	4.20	7.00
P4/	*Epipliopithecus vindobonensis*	4.20	7.00
P4/	*Anapithecus hernyaki*	5.20	8.80
P4/	*Anapithecus hernyaki*	5.40	8.50
P4/	*Anapithecus hernyaki*	5.90	8.50
P4/	*Anapithecus hernyaki*	6.00	8.20
P4/	*Fanchangia jini*	5.20	8.50
P4/	*Fanchangia jini*	5.30	8.30
P4/	*Fanchangia jini*	5.80	8.60
P4/	*Fanchangia jini*	5.30	9.40
P4/	*Fanchangia jini*	5.20	7.10
P4/	*Laccopithecus robustus*	5.80	7.90
P4/	*Laccopithecus robustus*	5.80	7.80
P4/	*Laccopithecus robustus*	5.10	7.70
P4/	*Laccopithecus robustus*	5.20	8.10
P4/	*Laccopithecus robustus*	5.10	7.60
P4/	*Laccopithecus robustus*	5.40	7.90
P4/	*Laccopithecus robustus*	5.20	7.60
P4/	*Laccopithecus robustus*	5.70	8.60
P4/	*Laccopithecus robustus*	5.00	8.20
P4/	*Laccopithecus robustus*	5.70	8.70
P4/	*Laccopithecus robustus*	5.70	8.20
M1/	*Pliobates cataloniae*	5.00	5.90
M1/	*Pliobates cataloniae*	5.00	6.10

M1/	*Pliobates cataloniae*	5.20	6.10
M1/	*Pliobates cataloniae*	5.30	6.40
M1/	Crouzeliinae indet. (Mörgen)	5.80	6.70
M1/	*Dendropithecus macinessi*	5.70	6.60
M1/	*Dendropithecus macinessi*	5.40	7.10
M1/	*Dendropithecus macinessi*	6.00	7.50
M1/	*Dendropithecus macinessi*	5.70	7.70
M1/	*Dendropithecus macinessi*	5.50	6.90
M1/	*Dendropithecus macinessi*	6.00	7.80
M1/	*Dendropithecus macinessi*	6.20	7.50
M1/	*Dendropithecus macinessi*	5.80	7.50
M1/	*Dendropithecus macinessi*	6.20	8.10
M1/	*Dendropithecus macinessi*	5.60	7.70
M1/	*Dendropithecus macinessi*	6.20	7.40
M1/	*Dendropithecus macinessi*	6.00	7.50
M1/	*Dendropithecus macinessi*	6.50	8.40
M1/	*Dendropithecus macinessi*	5.80	7.00
M1/	*Micropithecus clarki*	4.30	5.30
M1/	*Micropithecus clarki*	4.30	5.40
M1/	*Micropithecus clarki*	4.50	5.10
M1/	*Micropithecus clarki*	4.30	5.10
M1/	*Micropithecus clarki*	4.40	5.20
M1/	*Micropithecus clarki*	4.30	5.30
M1/	*Micropithecus clarki*	4.60	5.40
M1/	*Micropithecus clarki*	4.60	5.30
M1/	*Micropithecus clarki*	4.95	5.80
M1/	*Simiolus enjiessi*	5.60	6.50
M1/	*Dionysopithecus shuangouensis*	5.50	6.30
M1/	*Dionysopithecus shuangouensis*	5.40	6.10
M1/	*Dionysopithecus shuangouensis*	5.60	6.30
M1/	*Dionysopithecus shuangouensis*	4.90	5.70
M1/	*Platodontopithecus jianghuaiensis*	6.80	8.10
M1/	*Platodontopithecus jianghuaiensis*	6.50	8.20
M1/	*Platodontopithecus jianghuaiensis*	6.40	8.60
M1/	*Pliopithecus canmatensis*	5.30	7.30
M1/	*Pliopithecus platyodon*	6.20	8.10
M1/	*Pliopithecus platyodon*	6.50	8.30
M1/	*Pliopithecus platyodon*	6.50	8.70
M1/	*Pliopithecus zhanxiangi*	6.60	8.90
M1/	*Pliopithecus zhanxiangi*	6.90	9.30
M1/	*Pliopithecus zhanxiangi*	6.40	8.80
M1/	*Epipliopithecus vindobonensis*	5.60	7.50
M1/	*Epipliopithecus vindobonensis*	5.90	8.00
M1/	*Anapithecus hernyaki*	7.75	9.15
M1/	*Anapithecus hernyaki*	7.60	9.10

M1/	*Anapithecus hernyaki*	7.95	9.60
M1/	*Anapithecus hernyaki*	7.10	8.70
M1/	*Barberapithecus huerzeleri*	5.30	6.50
M1/	*Fanchangia jini*	7.60	9.30
M1/	*Fanchangia jini*	6.70	8.20
M1/	*Fanchangia jini*	7.10	8.10
M1/	*Fanchangia jini*	6.80	8.50
M1/	*Fanchangia jini*	7.30	8.50
M1/	*Laccopithecus robustus*	7.60	8.30
M1/	*Laccopithecus robustus*	6.80	8.10
M1/	*Laccopithecus robustus*	7.60	9.60
M1/	*Laccopithecus robustus*	7.00	9.10
M1/	*Laccopithecus robustus*	7.10	9.00
M1/	*Laccopithecus robustus*	6.80	7.70
M1/	*Laccopithecus robustus*	7.20	8.30
M2/	*Pliobates cataloniae*	5.30	6.50
M2/	*Pliobates cataloniae*	5.80	6.80
M2/	*Pliobates cataloniae*	5.50	7.00
M2/	*Pliobates cataloniae*	6.10	7.50
M2/	*Dendropithecus macinessi*	5.80	7.10
M2/	*Dendropithecus macinessi*	6.70	8.00
M2/	*Dendropithecus macinessi*	6.60	7.80
M2/	*Dendropithecus macinessi*	5.80	6.90
M2/	*Dendropithecus macinessi*	7.40	8.80
M2/	*Dendropithecus macinessi*	7.10	8.10
M2/	*Dendropithecus macinessi*	6.70	8.00
M2/	*Dendropithecus macinessi*	7.00	8.90
M2/	*Dendropithecus macinessi*	6.40	8.20
M2/	*Dendropithecus macinessi*	7.20	8.50
M2/	*Dendropithecus macinessi*	6.60	8.00
M2/	*Dendropithecus macinessi*	6.40	7.80
M2/	*Dendropithecus macinessi*	7.20	8.70
M2/	*Dendropithecus macinessi*	5.80	7.45
M2/	*Micropithecus clarki*	5.40	7.10
M2/	*Micropithecus clarki*	4.70	5.70
M2/	*Micropithecus clarki*	5.10	5.80
M2/	*Micropithecus clarki*	5.00	5.55
M2/	*Micropithecus clarki*	4.80	5.80
M2/	*Micropithecus clarki*	4.60	5.50
M2/	*Micropithecus clarki*	5.00	5.50
M2/	*Micropithecus clarki*	4.80	5.70
M2/	*Micropithecus clarki*	4.80	5.70
M2/	*Micropithecus clarki*	5.20	6.10
M2/	*Simiolus enjiessi*	6.70	6.90
M2/	*Dionysopithecus shuangouensis*	4.90	6.70

M2/	*Dionysopithecus shuangouensis*	5.20	6.50
M2/	*Dionysopithecus shuangouensis*	5.80	6.80
M2/	*Dionysopithecus shuangouensis*	4.70	6.30
M2/	*Dionysopithecus shuangouensis*	5.20	6.60
M2/	*Dionysopithecus shuangouensis*	5.50	6.70
M2/	*Dionysopithecus shuangouensis*	5.30	6.10
M2/	*Platodontopithecus jianghuaiensis*	7.10	9.20
M2/	*Pliopithecus canmatensis*	6.20	7.50
M2/	*Pliopithecus platyodon*	6.50	9.60
M2/	*Pliopithecus zhanxiangi*	7.10	9.70
M2/	*Pliopithecus zhanxiangi*	7.10	10.00
M2/	*Pliopithecus zhanxiangi*	7.30	9.40
M2/	*Epipliopithecus vindobonensis*	6.30	8.60
M2/	*Epipliopithecus vindobonensis*	6.50	9.00
M2/	*Anapithecus hernyaki*	8.45	9.75
M2/	*Anapithecus hernyaki*	8.30	9.70
M2/	*Barberapithecus huerzeleri*	5.60	6.90
M2/	*Barberapithecus huerzeleri*	5.60	7.10
M2/	*Fanchangia jini*	8.20	10.20
M2/	*Fanchangia jini*	9.00	10.30
M2/	*Fanchangia jini*	8.30	10.40
M2/	*Fanchangia jini*	8.40	10.30
M2/	*Fanchangia jini*	8.50	9.90
M2/	*Fanchangia jini*	7.90	10.00
M2/	*Fanchangia jini*	8.10	9.50
M2/	*Laccopithecus robustus*	6.70	8.40
M2/	*Laccopithecus robustus*	7.30	9.00
M2/	*Laccopithecus robustus*	7.00	8.70
M2/	*Laccopithecus robustus*	6.80	7.90
M2/	*Laccopithecus robustus*	7.50	8.50
M2/	*Laccopithecus robustus*	7.70	8.00
M2/	*Laccopithecus robustus*	8.55	10.55
M2/	*Laccopithecus robustus*	7.80	10.00
M2/	*Laccopithecus robustus*	7.80	10.20
M2/	*Laccopithecus robustus*	6.80	8.30
M3/	*Pliobates cataloniae*	4.55	6.55
M3/	*Dendropithecus macinessi*	7.00	8.00
M3/	*Dendropithecus macinessi*	6.20	7.90
M3/	*Dendropithecus macinessi*	5.20	6.60
M3/	*Dendropithecus macinessi*	6.70	7.90
M3/	*Dendropithecus macinessi*	6.40	7.90
M3/	*Dendropithecus macinessi*	6.60	7.80
M3/	*Dendropithecus macinessi*	6.90	8.50
M3/	*Dendropithecus macinessi*	5.80	7.60
M3/	*Dendropithecus macinessi*	7.00	8.20

M3/	*Dendropithecus macinessi*	6.65	7.10
M3/	*Micropithecus clarki*	4.00	5.40
M3/	*Micropithecus clarki*	4.05	5.05
M3/	*Micropithecus clarki*	5.10	5.50
M3/	*Simiolus enjiessi*	6.60	7.30
M3/	*Dionysopithecus shuangouensis*	4.90	5.60
M3/	*Platodontopithecus jianghuaiensis*	7.00	9.00
M3/	*Platodontopithecus jianghuaiensis*	6.70	8.20
M3/	*Platodontopithecus jianghuaiensis*	7.80	9.00
M3/	*Pliopithecus piveteaui*	5.70	7.50
M3/	*Pliopithecus platyodon*	6.30	8.70
M3/	*Pliopithecus zhanxiangi*	7.30	9.40
M3/	*Pliopithecus zhanxiangi*	7.10	9.30
M3/	*Pliopithecus zhanxiangi*	7.30	9.00
M3/	*Epipliopithecus vindobonensis*	6.30	7.50
M3/	*Epipliopithecus vindobonensis*	6.90	9.00
M3/	*Krishnapithecus krishnaii*	5.70	7.05
M3/	*Barberapithecus huerzeleri*	5.50	7.00
M3/	*Barberapithecus huerzeleri*	5.40	7.00
M3/	*Fanchangia jini*	7.40	9.60
M3/	*Fanchangia jini*	6.70	7.70
M3/	*Fanchangia jini*	7.70	9.70
M3/	*Laccopithecus robustus*	7.90	9.10
M3/	*Laccopithecus robustus*	7.90	8.80
M3/	*Laccopithecus robustus*	8.20	9.10
M3/	*Laccopithecus robustus*	7.50	8.70
M3/	*Laccopithecus robustus*	8.10	10.00
M3/	*Laccopithecus robustus*	7.40	9.00
M3/	*Laccopithecus robustus*	6.90	8.50
M/1	*Pliobates cataloniae*	6.10	4.70
M/1	*Dendropithecus macinessi*	6.20	5.00
M/1	*Dendropithecus macinessi*	7.10	5.60
M/1	*Dendropithecus macinessi*	7.10	5.60
M/1	*Dendropithecus macinessi*	6.70	5.50
M/1	*Dendropithecus macinessi*	6.10	5.40
M/1	*Dendropithecus macinessi*	6.80	5.50
M/1	*Dendropithecus macinessi*	6.70	5.70
M/1	*Dendropithecus macinessi*	7.00	5.70
M/1	*Dendropithecus macinessi*	6.90	5.70
M/1	*Dendropithecus macinessi*	6.70	5.50
M/1	*Dendropithecus macinessi*	7.10	5.30
M/1	*Micropithecus clarki*	5.00	4.30
M/1	*Micropithecus clarki*	5.00	4.00
M/1	*Micropithecus clarki*	4.80	3.80
M/1	*Micropithecus clarki*	4.80	4.00

M/1	*Micropithecus clarki*	5.20	4.40
M/1	*Simiolus enjiessi*	6.50	5.20
M/1	*Simiolus enjiessi*	6.60	5.50
M/1	*Simiolus enjiessi*	6.00	4.50
M/1	*Dionysopithecus shuangouensis*	5.50	4.70
M/1	*Dionysopithecus shuangouensis*	5.00	4.50
M/1	*Dionysopithecus shuangouensis*	5.80	5.10
M/1	*Dionysopithecus shuangouensis*	6.00	5.40
M/1	*Dionysopithecus shuangouensis*	6.30	5.00
M/1	*Platodontopithecus jianghuaiensis*	7.30	6.40
M/1	*Platodontopithecus jianghuaiensis*	7.90	6.60
M/1	*Platodontopithecus jianghuaiensis*	8.40	7.00
M/1	*Pliopithecus antiquus*	6.45	5.30
M/1	*Pliopithecus canmatensis*	5.90	4.90
M/1	*Pliopithecus canmatensis*	5.60	4.40
M/1	*Pliopithecus canmatensis*	6.00	5.00
M/1	*Pliopithecus canmatensis*	5.80	5.30
M/1	*Pliopithecus piveteaui*	6.10	5.50
M/1	*Pliopithecus platyodon*	6.70	5.90
M/1	*Pliopithecus platyodon*	7.30	5.90
M/1	*Pliopithecus zhanxiangi*	7.30	6.80
M/1	*Epipliopithecus vindobonensis*	5.80	5.30
M/1	*Epipliopithecus vindobonensis*	6.10	5.40
M/1	*Anapithecus hernyaki*	7.70	6.40
M/1	*Anapithecus hernyaki*	7.90	6.80
M/1	*Anapithecus hernyaki*	8.40	6.35
M/1	*Anapithecus hernyaki*	7.55	6.55
M/1	*Barberapithecus huerzeleri*	5.70	4.60
M/1	*Crouzelia auscitanensis*	5.90	4.40
M/1	*Egarapithecus narcisoi*	7.10	5.60
M/1	*Fanchangia jini*	7.80	6.00
M/1	*Fanchangia jini*	8.40	6.50
M/1	*Fanchangia jini*	7.80	5.90
M/1	*Fanchangia jini*	8.10	6.10
M/1	*Fanchangia jini*	7.50	6.20
M/1	*Fanchangia jini*	8.80	6.90
M/1	*Fanchangia jini*	7.40	6.10
M/1	*Fanchangia jini*	7.80	5.80
M/1	*Laccopithecus robustus*	6.90	6.00
M/1	*Laccopithecus robustus*	7.40	6.40
M/1	*Laccopithecus robustus*	7.20	6.40
M/1	*Laccopithecus robustus*	7.80	6.80
M/1	*Laccopithecus robustus*	7.30	6.20
M/1	*Laccopithecus robustus*	7.50	6.30
M/1	*Laccopithecus robustus*	7.70	6.50

M/1	*Laccopithecus robustus*	7.30	6.40
M/1	*Laccopithecus robustus*	7.00	6.30
M/1	*Laccopithecus robustus*	7.10	6.20
M/1	*Laccopithecus robustus*	7.10	5.75
M/1	*Laccopithecus robustus*	7.20	6.40
M/1	*Laccopithecus robustus*	7.30	6.20
M/1	*Laccopithecus robustus*	7.10	6.10
M/1	*Plesiopliopithecus lockeri*	6.60	4.50
M/2	*Pliobates cataloniae*	6.60	5.00
M/2	*Dendropithecus macinessi*	8.00	6.10
M/2	*Dendropithecus macinessi*	7.90	6.70
M/2	*Dendropithecus macinessi*	7.80	6.70
M/2	*Dendropithecus macinessi*	7.80	6.60
M/2	*Dendropithecus macinessi*	8.20	6.50
M/2	*Dendropithecus macinessi*	7.10	6.20
M/2	*Dendropithecus macinessi*	7.60	6.40
M/2	*Dendropithecus macinessi*	7.40	6.70
M/2	*Dendropithecus macinessi*	7.50	5.90
M/2	*Dendropithecus macinessi*	7.60	6.10
M/2	*Dendropithecus macinessi*	7.80	6.80
M/2	*Dendropithecus macinessi*	7.60	6.30
M/2	*Dendropithecus macinessi*	7.00	6.00
M/2	*Dendropithecus macinessi*	7.20	6.50
M/2	*Dendropithecus macinessi*	7.55	6.25
M/2	*Micropithecus clarki*	5.30	4.20
M/2	*Micropithecus clarki*	5.60	4.80
M/2	*Micropithecus clarki*	5.30	4.60
M/2	*Micropithecus clarki*	5.30	4.60
M/2	*Simiolus enjiessi*	7.00	5.50
M/2	*Simiolus enjiessi*	6.80	5.60
M/2	*Simiolus enjiessi*	7.20	5.50
M/2	*Dionysopithecus shuangouensis*	6.50	5.50
M/2	*Dionysopithecus shuangouensis*	6.70	5.50
M/2	*Platodontopithecus jianghuaiensis*	9.20	7.60
M/2	*Platodontopithecus jianghuaiensis*	9.00	7.60
M/2	*Platodontopithecus jianghuaiensis*	9.30	8.00
M/2	*Krishnapithecus krishnaii*	9.50	7.90
M/2	*Pliopithecus antiquus*	6.40	5.40
M/2	*Pliopithecus antiquus*	6.70	6.10
M/2	*Pliopithecus antiquus*	7.10	5.60
M/2	*Pliopithecus antiquus*	7.00	6.00
M/2	*Pliopithecus canmatensis*	6.60	5.60
M/2	*Pliopithecus canmatensis*	6.00	4.95
M/2	*Pliopithecus canmatensis*	6.80	5.40
M/2	*Pliopithecus canmatensis*	6.10	5.85

M/2	*Pliopithecus piveteaui*	7.10	6.20
M/2	*Pliopithecus piveteaui*	7.20	6.50
M/2	*Pliopithecus piveteaui*	7.20	6.80
M/2	*Pliopithecus piveteaui*	6.70	5.90
M/2	*Pliopithecus platyodon*	7.30	6.60
M/2	*Pliopithecus zhanxiangi*	8.40	7.80
M/2	*Pliopithecus zhanxiangi*	9.40	7.60
M/2	*Pliopithecus zhanxiangi*	9.20	7.10
M/2	*Epipliopithecus vindobonensis*	7.00	5.80
M/2	*Epipliopithecus vindobonensis*	7.30	5.90
M/2	*Epipliopithecus vindobonensis*	7.20	6.00
M/2	*Anapithecus hernyaki*	8.30	6.20
M/2	*Anapithecus hernyaki*	8.50	6.90
M/2	*Anapithecus hernyaki*	8.70	7.30
M/2	*Anapithecus hernyaki*	8.50	6.80
M/2	*Anapithecus hernyaki*	8.50	6.75
M/2	*Barberapithecus huerzeleri*	6.40	5.10
M/2	*Crouzelia auscitanensis*	6.30	5.00
M/2	*Crouzelia rhodanica*	5.60	4.20
M/2	*Egarapithecus narcisoi*	7.60	5.60
M/2	*Fanchangia jini*	9.50	7.40
M/2	*Fanchangia jini*	9.80	7.80
M/2	*Fanchangia jini*	9.40	7.60
M/2	*Fanchangia jini*	9.30	7.40
M/2	*Fanchangia jini*	9.40	7.60
M/2	*Fanchangia jini*	9.50	7.70
M/2	*Laccopithecus robustus*	7.00	6.10
M/2	*Laccopithecus robustus*	9.20	7.10
M/2	*Laccopithecus robustus*	8.50	6.90
M/2	*Laccopithecus robustus*	8.10	6.90
M/2	*Laccopithecus robustus*	8.10	6.80
M/2	*Laccopithecus robustus*	8.00	6.80
M/2	*Laccopithecus robustus*	8.20	7.00
M/2	*Laccopithecus robustus*	8.60	7.10
M/2	*Laccopithecus robustus*	8.60	7.40
M/2	*Laccopithecus robustus*	8.20	7.40
M/2	*Laccopithecus robustus*	7.80	6.30
M/2	*Laccopithecus robustus*	8.10	6.70
M/2	*Laccopithecus robustus*	7.80	6.40
M/2	*Laccopithecus robustus*	8.00	6.40
M/2	*Laccopithecus robustus*	7.80	6.40
M/2	*Laccopithecus robustus*	7.50	6.20

Supplementary Figure 5. Dental proportions.

COLUMN	DESCRIPTION
Tooth	Tooth position considered (P3–M3 and m1–m2)
Taxon	Species to which the reported specimen data belong (in many cases there are several specimens per species)
BLI	Breadth/length index (in %). It is computed as tooth maximum buccolingual breadth / tooth mesiodistal length x 100.

Tooth	Taxon	BLI
P3/	*Pliobates cataloniae*	145.24
P3/	*Micropithecus clarki*	146.88
P3/	*Micropithecus clarki*	151.61
P3/	*Micropithecus clarki*	141.18
P3/	*Micropithecus clarki*	166.67
P3/	*Micropithecus clarki*	139.02
P3/	*Dendropithecus macinessi*	153.33
P3/	*Dendropithecus macinessi*	155.56
P3/	*Dendropithecus macinessi*	165.85
P3/	*Dendropithecus macinessi*	156.10
P3/	*Dendropithecus macinessi*	151.16
P3/	*Dendropithecus macinessi*	170.73
P3/	*Simiolus enjiessi*	156.10
P3/	*Pliopithecus canmatensis*	164.10
P3/	*Pliopithecus canmatensis*	170.73
P3/	*Pliopithecus antiquus*	156.10
P3/	*Pliopithecus platyodon*	161.90
P3/	*Pliopithecus platyodon*	146.81
P3/	*Pliopithecus zhanxiangi*	156.86
P3/	*Pliopithecus zhanxiangi*	143.64
P3/	*Pliopithecus zhanxiangi*	144.44
P3/	*Anapithecus hernyaki*	148.15
P3/	*Anapithecus hernyaki*	130.51
P3/	*Egarapithecus narcisoi*	128.57
P3/	*Epipliopithecus vindobonensis*	145.83
P3/	*Epipliopithecus vindobonensis*	145.83
P3/	*Fanchangia jini*	144.64
P3/	*Fanchangia jini*	138.18
P3/	*Fanchangia jini*	151.85
P3/	*Laccopithecus robustus*	152.88
P3/	*Laccopithecus robustus*	133.88
P3/	*Laccopithecus robustus*	141.51
P3/	*Platodontopithecus jianghuaiensis*	140.00
P3/	*Platodontopithecus jianghuaiensis*	135.42
P4/	*Pliobates cataloniae*	165.63
P4/	*Pliobates cataloniae*	143.90
P4/	*Pliobates cataloniae*	128.00
P4/	Crouzeliinae indet. (Mörgen)	146.51
P4/	*Dendropithecus macinessi*	159.52
P4/	*Dendropithecus macinessi*	158.14
P4/	*Dendropithecus macinessi*	169.77
P4/	*Dendropithecus macinessi*	178.95
P4/	*Dendropithecus macinessi*	163.64

P4/	*Dendropithecus macinessi*	197.37
P4/	*Dendropithecus macinessi*	155.42
P4/	*Micropithecus clarki*	151.52
P4/	*Micropithecus clarki*	160.61
P4/	*Micropithecus clarki*	156.25
P4/	*Micropithecus clarki*	161.29
P4/	*Micropithecus clarki*	151.52
P4/	*Simiolus enjiessi*	147.50
P4/	*Dionysopithecus shuangouensis*	145.24
P4/	*Dionysopithecus shuangouensis*	139.47
P4/	*Dionysopithecus shuangouensis*	157.14
P4/	*Platodontopithecus jianghuaiensis*	168.18
P4/	*Pliopithecus canmatensis*	140.48
P4/	*Pliopithecus canmatensis*	157.14
P4/	*Pliopithecus piveteaui*	158.33
P4/	*Pliopithecus platyodon*	166.28
P4/	*Pliopithecus platyodon*	159.57
P4/	*Pliopithecus platyodon*	179.55
P4/	*Pliopithecus zhanxiangi*	175.56
P4/	*Pliopithecus zhanxiangi*	181.82
P4/	*Pliopithecus zhanxiangi*	150.82
P4/	*Pliopithecus zhanxiangi*	155.32
P4/	*Epipliopithecus vindobonensis*	166.67
P4/	*Epipliopithecus vindobonensis*	166.67
P4/	*Anapithecus hernyaki*	169.23
P4/	*Anapithecus hernyaki*	157.41
P4/	*Anapithecus hernyaki*	144.07
P4/	*Anapithecus hernyaki*	136.67
P4/	*Fanchangia jini*	163.46
P4/	*Fanchangia jini*	156.60
P4/	*Fanchangia jini*	148.28
P4/	*Fanchangia jini*	177.36
P4/	*Fanchangia jini*	136.54
P4/	*Laccopithecus robustus*	136.21
P4/	*Laccopithecus robustus*	134.48
P4/	*Laccopithecus robustus*	150.98
P4/	*Laccopithecus robustus*	155.77
P4/	*Laccopithecus robustus*	149.02
P4/	*Laccopithecus robustus*	146.30
P4/	*Laccopithecus robustus*	146.15
P4/	*Laccopithecus robustus*	150.88
P4/	*Laccopithecus robustus*	164.00
P4/	*Laccopithecus robustus*	152.63
P4/	*Laccopithecus robustus*	143.86
M1/	*Pliobates cataloniae*	118.00

M1/	*Pliobates cataloniae*	122.00
M1/	*Pliobates cataloniae*	117.31
M1/	*Pliobates cataloniae*	120.75
M1/	Crouzeliinae indet. (Mörgen)	115.52
M1/	*Dendropithecus macinessi*	115.79
M1/	*Dendropithecus macinessi*	131.48
M1/	*Dendropithecus macinessi*	125.00
M1/	*Dendropithecus macinessi*	135.09
M1/	*Dendropithecus macinessi*	125.45
M1/	*Dendropithecus macinessi*	130.00
M1/	*Dendropithecus macinessi*	120.97
M1/	*Dendropithecus macinessi*	129.31
M1/	*Dendropithecus macinessi*	130.65
M1/	*Dendropithecus macinessi*	137.50
M1/	*Dendropithecus macinessi*	119.35
M1/	*Dendropithecus macinessi*	125.00
M1/	*Dendropithecus macinessi*	129.23
M1/	*Dendropithecus macinessi*	120.69
M1/	*Micropithecus clarki*	123.26
M1/	*Micropithecus clarki*	125.58
M1/	*Micropithecus clarki*	113.33
M1/	*Micropithecus clarki*	118.60
M1/	*Micropithecus clarki*	118.18
M1/	*Micropithecus clarki*	123.26
M1/	*Micropithecus clarki*	117.39
M1/	*Micropithecus clarki*	115.22
M1/	*Micropithecus clarki*	117.17
M1/	*Simiolus enjiessi*	116.07
M1/	*Dionysopithecus shuangouensis*	114.55
M1/	*Dionysopithecus shuangouensis*	112.96
M1/	*Dionysopithecus shuangouensis*	112.50
M1/	*Dionysopithecus shuangouensis*	116.33
M1/	*Platodontopithecus jianghuaiensis*	119.12
M1/	*Platodontopithecus jianghuaiensis*	126.15
M1/	*Platodontopithecus jianghuaiensis*	134.38
M1/	*Pliopithecus canmatensis*	137.74
M1/	*Pliopithecus platyodon*	130.65
M1/	*Pliopithecus platyodon*	127.69
M1/	*Pliopithecus platyodon*	133.85
M1/	*Pliopithecus zhanxiangi*	134.85
M1/	*Pliopithecus zhanxiangi*	134.78
M1/	*Pliopithecus zhanxiangi*	137.50
M1/	*Epipliopithecus vindobonensis*	133.93

M1/	*Epipliopithecus vindobonensis*	135.59
M1/	*Anapithecus hernyaki*	118.06
M1/	*Anapithecus hernyaki*	119.74
M1/	*Anapithecus hernyaki*	120.75
M1/	*Anapithecus hernyaki*	122.54
M1/	*Barberapithecus huerzeleri*	122.64
M1/	*Fanchangia jini*	122.37
M1/	*Fanchangia jini*	122.39
M1/	*Fanchangia jini*	114.08
M1/	*Fanchangia jini*	125.00
M1/	*Fanchangia jini*	116.44
M1/	*Laccopithecus robustus*	109.21
M1/	*Laccopithecus robustus*	119.12
M1/	*Laccopithecus robustus*	126.32
M1/	*Laccopithecus robustus*	130.00
M1/	*Laccopithecus robustus*	126.76
M1/	*Laccopithecus robustus*	113.24
M1/	*Laccopithecus robustus*	115.28
M2/	*Pliobates cataloniae*	122.64
M2/	*Pliobates cataloniae*	117.24
M2/	*Pliobates cataloniae*	127.27
M2/	*Pliobates cataloniae*	122.95
M2/	*Dendropithecus macinessi*	122.41
M2/	*Dendropithecus macinessi*	119.40
M2/	*Dendropithecus macinessi*	118.18
M2/	*Dendropithecus macinessi*	118.97
M2/	*Dendropithecus macinessi*	118.92
M2/	*Dendropithecus macinessi*	114.08
M2/	*Dendropithecus macinessi*	119.40
M2/	*Dendropithecus macinessi*	127.14
M2/	*Dendropithecus macinessi*	128.13
M2/	*Dendropithecus macinessi*	118.06
M2/	*Dendropithecus macinessi*	121.21
M2/	*Dendropithecus macinessi*	121.88
M2/	*Dendropithecus macinessi*	120.83
M2/	*Dendropithecus macinessi*	128.45
M2/	*Micropithecus clarki*	131.48
M2/	*Micropithecus clarki*	121.28
M2/	*Micropithecus clarki*	113.73
M2/	*Micropithecus clarki*	111.00
M2/	*Micropithecus clarki*	120.83
M2/	*Micropithecus clarki*	119.57
M2/	*Micropithecus clarki*	110.00
M2/	*Micropithecus clarki*	118.75
M2/	*Micropithecus clarki*	118.75

M2/	*Micropithecus clarki*	117.31
M2/	*Simiolus enjiessi*	102.99
M2/	*Dionysopithecus shuangouensis*	136.73
M2/	*Dionysopithecus shuangouensis*	125.00
M2/	*Dionysopithecus shuangouensis*	117.24
M2/	*Dionysopithecus shuangouensis*	134.04
M2/	*Dionysopithecus shuangouensis*	126.92
M2/	*Dionysopithecus shuangouensis*	121.82
M2/	*Dionysopithecus shuangouensis*	115.09
M2/	*Platodontopithecus jianghuaiensis*	129.58
M2/	*Pliopithecus canmatensis*	120.97
M2/	*Pliopithecus platyodon*	147.69
M2/	*Pliopithecus zhanxiangi*	136.62
M2/	*Pliopithecus zhanxiangi*	140.85
M2/	*Pliopithecus zhanxiangi*	128.77
M2/	*Epipliopithecus vindobonensis*	136.51
M2/	*Epipliopithecus vindobonensis*	138.46
M2/	*Anapithecus hernyaki*	115.38
M2/	*Anapithecus hernyaki*	116.87
M2/	*Barberapithecus huerzeleri*	123.21
M2/	*Barberapithecus huerzeleri*	126.79
M2/	*Fanchangia jini*	124.39
M2/	*Fanchangia jini*	114.44
M2/	*Fanchangia jini*	125.30
M2/	*Fanchangia jini*	122.62
M2/	*Fanchangia jini*	116.47
M2/	*Fanchangia jini*	126.58
M2/	*Fanchangia jini*	117.28
M2/	*Laccopithecus robustus*	125.37
M2/	*Laccopithecus robustus*	123.29
M2/	*Laccopithecus robustus*	124.29
M2/	*Laccopithecus robustus*	116.18
M2/	*Laccopithecus robustus*	113.33
M2/	*Laccopithecus robustus*	103.90
M2/	*Laccopithecus robustus*	123.39
M2/	*Laccopithecus robustus*	128.21
M2/	*Laccopithecus robustus*	130.77
M2/	*Laccopithecus robustus*	122.06
M3/	*Pliobates cataloniae*	143.96
M3/	*Dendropithecus macinessi*	114.29
M3/	*Dendropithecus macinessi*	127.42
M3/	*Dendropithecus macinessi*	126.92
M3/	*Dendropithecus macinessi*	117.91
M3/	*Dendropithecus macinessi*	123.44
M3/	*Dendropithecus macinessi*	118.18

M3/	*Dendropithecus macinessi*	123.19
M3/	*Dendropithecus macinessi*	131.03
M3/	*Dendropithecus macinessi*	117.14
M3/	*Dendropithecus macinessi*	106.77
M3/	*Micropithecus clarki*	135.00
M3/	*Micropithecus clarki*	124.69
M3/	*Micropithecus clarki*	107.84
M3/	*Simiolus enjiessi*	110.61
M3/	*Dionysopithecus shuangouensis*	114.29
M3/	*Platodontopithecus jianghuaiensis*	128.57
M3/	*Platodontopithecus jianghuaiensis*	122.39
M3/	*Platodontopithecus jianghuaiensis*	115.38
M3/	*Pliopithecus piveteaui*	131.58
M3/	*Pliopithecus platyodon*	138.10
M3/	*Pliopithecus zhanxiangi*	128.77
M3/	*Pliopithecus zhanxiangi*	130.99
M3/	*Pliopithecus zhanxiangi*	123.29
M3/	*Epipliopithecus vindobonensis*	119.05
M3/	*Epipliopithecus vindobonensis*	130.43
M3/	*Krishnapithecus krishnaii*	123.68
M3/	*Barberapithecus huerzeleri*	127.27
M3/	*Barberapithecus huerzeleri*	129.63
M3/	*Fanchangia jini*	129.73
M3/	*Fanchangia jini*	114.93
M3/	*Fanchangia jini*	125.97
M3/	*Laccopithecus robustus*	115.19
M3/	*Laccopithecus robustus*	111.39
M3/	*Laccopithecus robustus*	110.98
M3/	*Laccopithecus robustus*	116.00
M3/	*Laccopithecus robustus*	123.46
M3/	*Laccopithecus robustus*	121.62
M3/	*Laccopithecus robustus*	123.19
M/1	*Pliobates cataloniae*	77.05
M/1	*Dendropithecus macinessi*	80.65
M/1	*Dendropithecus macinessi*	78.87
M/1	*Dendropithecus macinessi*	78.87
M/1	*Dendropithecus macinessi*	82.09
M/1	*Dendropithecus macinessi*	88.52
M/1	*Dendropithecus macinessi*	80.88
M/1	*Dendropithecus macinessi*	85.07
M/1	*Dendropithecus macinessi*	81.43
M/1	*Dendropithecus macinessi*	82.61
M/1	*Dendropithecus macinessi*	82.09

M/1	*Dendropithecus macinessi*	74.65
M/1	*Micropithecus clarki*	86.00
M/1	*Micropithecus clarki*	80.00
M/1	*Micropithecus clarki*	79.17
M/1	*Micropithecus clarki*	83.33
M/1	*Micropithecus clarki*	84.62
M/1	*Simiolus enjiessi*	80.00
M/1	*Simiolus enjiessi*	83.33
M/1	*Simiolus enjiessi*	75.00
M/1	*Dionysopithecus shuangouensis*	85.45
M/1	*Dionysopithecus shuangouensis*	90.00
M/1	*Dionysopithecus shuangouensis*	87.93
M/1	*Dionysopithecus shuangouensis*	90.00
M/1	*Dionysopithecus shuangouensis*	79.37
M/1	*Platodontopithecus jianghuaiensis*	87.67
M/1	*Platodontopithecus jianghuaiensis*	83.54
M/1	*Platodontopithecus jianghuaiensis*	83.33
M/1	*Pliopithecus antiquus*	82.17
M/1	*Pliopithecus canmatensis*	83.05
M/1	*Pliopithecus canmatensis*	78.57
M/1	*Pliopithecus canmatensis*	83.33
M/1	*Pliopithecus canmatensis*	91.38
M/1	*Pliopithecus piveteaui*	90.16
M/1	*Pliopithecus platyodon*	88.06
M/1	*Pliopithecus platyodon*	80.82
M/1	*Pliopithecus zhanxiangi*	93.15
M/1	*Epipliopithecus vindobonensis*	91.38
M/1	*Epipliopithecus vindobonensis*	88.52
M/1	*Anapithecus hernyaki*	83.12
M/1	*Anapithecus hernyaki*	86.08
M/1	*Anapithecus hernyaki*	75.60
M/1	*Anapithecus hernyaki*	86.75
M/1	*Barberapithecus huerzeleri*	80.70
M/1	*Crouzelia auscitanensis*	74.58
M/1	*Egarapithecus narcisoi*	78.87
M/1	*Fanchangia jini*	76.92
M/1	*Fanchangia jini*	77.38
M/1	*Fanchangia jini*	75.64
M/1	*Fanchangia jini*	75.31
M/1	*Fanchangia jini*	82.67
M/1	*Fanchangia jini*	78.41
M/1	*Fanchangia jini*	82.43
M/1	*Fanchangia jini*	74.36

M/1	*Laccopithecus robustus*	86.96
M/1	*Laccopithecus robustus*	86.49
M/1	*Laccopithecus robustus*	88.89
M/1	*Laccopithecus robustus*	87.18
M/1	*Laccopithecus robustus*	84.93
M/1	*Laccopithecus robustus*	84.00
M/1	*Laccopithecus robustus*	84.42
M/1	*Laccopithecus robustus*	87.67
M/1	*Laccopithecus robustus*	90.00
M/1	*Laccopithecus robustus*	87.32
M/1	*Laccopithecus robustus*	80.99
M/1	*Laccopithecus robustus*	88.89
M/1	*Laccopithecus robustus*	84.93
M/1	*Laccopithecus robustus*	85.92
M/1	*Plesiopliopithecus lockeri*	68.18
M/2	*Pliobates cataloniae*	75.76
M/2	*Dendropithecus macinessi*	76.25
M/2	*Dendropithecus macinessi*	84.81
M/2	*Dendropithecus macinessi*	85.90
M/2	*Dendropithecus macinessi*	84.62
M/2	*Dendropithecus macinessi*	79.27
M/2	*Dendropithecus macinessi*	87.32
M/2	*Dendropithecus macinessi*	84.21
M/2	*Dendropithecus macinessi*	90.54
M/2	*Dendropithecus macinessi*	78.67
M/2	*Dendropithecus macinessi*	80.26
M/2	*Dendropithecus macinessi*	87.18
M/2	*Dendropithecus macinessi*	82.89
M/2	*Dendropithecus macinessi*	85.71
M/2	*Dendropithecus macinessi*	90.28
M/2	*Dendropithecus macinessi*	82.78
M/2	*Micropithecus clarki*	79.25
M/2	*Micropithecus clarki*	85.71
M/2	*Micropithecus clarki*	86.79
M/2	*Micropithecus clarki*	86.79
M/2	*Simiolus enjiessi*	78.57
M/2	*Simiolus enjiessi*	82.35
M/2	*Simiolus enjiessi*	76.39
M/2	*Dionysopithecus shuangouensis*	84.62
M/2	*Dionysopithecus shuangouensis*	82.09
M/2	*Platodontopithecus jianghuaiensis*	82.61
M/2	*Platodontopithecus jianghuaiensis*	84.44
M/2	*Platodontopithecus jianghuaiensis*	86.02

M/2	*Krishnapithecus krishnaii*	83.16
M/2	*Pliopithecus antiquus*	84.38
M/2	*Pliopithecus antiquus*	91.04
M/2	*Pliopithecus antiquus*	78.87
M/2	*Pliopithecus antiquus*	85.71
M/2	*Pliopithecus canmatensis*	84.85
M/2	*Pliopithecus canmatensis*	82.50
M/2	*Pliopithecus canmatensis*	79.41
M/2	*Pliopithecus canmatensis*	95.90
M/2	*Pliopithecus piveteaui*	87.32
M/2	*Pliopithecus piveteaui*	90.28
M/2	*Pliopithecus piveteaui*	94.44
M/2	*Pliopithecus piveteaui*	88.06
M/2	*Pliopithecus platyodon*	90.41
M/2	*Pliopithecus zhanxiangi*	92.86
M/2	*Pliopithecus zhanxiangi*	80.85
M/2	*Pliopithecus zhanxiangi*	77.17
M/2	*Epipliopithecus vindobonensis*	82.86
M/2	*Epipliopithecus vindobonensis*	80.82
M/2	*Epipliopithecus vindobonensis*	83.33
M/2	*Anapithecus hernyaki*	74.70
M/2	*Anapithecus hernyaki*	81.18
M/2	*Anapithecus hernyaki*	83.91
M/2	*Anapithecus hernyaki*	80.00
M/2	*Anapithecus hernyaki*	79.41
M/2	*Barberapithecus huerzeleri*	79.69
M/2	*Crouzelia auscitanensis*	79.37
M/2	*Crouzelia rhodanica*	75.00
M/2	*Egarapithecus narcisoi*	73.68
M/2	*Fanchangia jini*	77.89
M/2	*Fanchangia jini*	79.59
M/2	*Fanchangia jini*	80.85
M/2	*Fanchangia jini*	79.57
M/2	*Fanchangia jini*	80.85
M/2	*Fanchangia jini*	81.05
M/2	*Laccopithecus robustus*	87.14
M/2	*Laccopithecus robustus*	77.17
M/2	*Laccopithecus robustus*	81.18
M/2	*Laccopithecus robustus*	85.19
M/2	*Laccopithecus robustus*	83.95
M/2	*Laccopithecus robustus*	85.00
M/2	*Laccopithecus robustus*	85.37
M/2	*Laccopithecus robustus*	82.56
M/2	*Laccopithecus robustus*	86.05
M/2	*Laccopithecus robustus*	90.24

M/2	*Laccopithecus robustus*	80.77
M/2	*Laccopithecus robustus*	82.72
M/2	*Laccopithecus robustus*	82.05
M/2	*Laccopithecus robustus*	80.00
M/2	*Laccopithecus robustus*	82.05
M/2	*Laccopithecus robustus*	82.67

Chapter 5:

Molar enamel-dentine junction shape of *Pliobates cataloniae* and other Iberian pliopithecoids

Reproduced from:
Bouchet, F., Zanolli, C., Skinner, M.M., Urciuoli, A., Fortuny, J., Almécija, S., Bernardini, F., Tuniz, C., Schillinger, B., Moyà-Solà, S., Alba, D.M. (under review). Molar enamel-dentine junction shape of *Pliobates cataloniae* and other Iberian pliopithecoids. J. Hum. Evol.

Molar enamel-dentine junction shape of *Pliobates cataloniae* and other Iberian pliopithecoids

Florian Bouchet[a,*], Clément Zanolli[b], Matthew M. Skinner[c,d,e], Alessandro Urciuoli[f,g,h,a], Josep Fortuny[a], Sergio Almécija[i,j,a], Federico Bernardini[k,l], Claudio Tuniz[l], Burkhard Schillinger[m], Salvador Moyà-Solà[a,n,o], David M. Alba[a,*]

[a] *Institut Català de Paleontologia Miquel Crusafont (ICP-CERCA), Universitat Autònoma de Barcelona, Edifici ICTA-ICP, c/ Columnes s/n, 08193 Cerdanyola del Vallès, Barcelona, Spain*

[b] *Univ. Bordeaux, CNRS, MCC, PACEA, UMR 5199, F-33600 Pessac, France*

[c] *Centre for the Exploration of the Deep Human Journey, University of the Witwatersrand, Private Bag 3, WITS 2050, South Africa*

[d] *School of Anthropology and Conservation, University of Kent, Marlowe Building, Canterbury CT2 7NR, UK*

[e] *Department of Human Evolution, Max Planck Institute for Evolutionary Anthropology, Deutscher Platz 6, 04103 Leipzig, Germany*

[f] *Universitat Autònoma de Barcelona, Campus de la UAB, 08193 Cerdanyola del Vallès, Barcelona, Spain*

[g] *Division of Palaeoanthropology, Senckenberg Research Institute and Natural History Museum Frankfurt, Senckenberganlage 25, 60325 Frankfurt am Main, Germany*

[h] *Universidad de Alcalá, Cátedra de Otoacústica Evolutiva y Paleoantropología (HM Hospitales-UAH), Departamento de Ciencias de la Vida, 28871 Alcalá de Henares, Madrid, Spain*

[i] *Division of Anthropology, American Museum of Natural History, Central Park West at 79th Street, New York, NY 10024, USA*

[j] *New York Consortium in Evolutionary Primatology, New York, NY 10024, USA*

[k] *Department of Humanistic Studies, Universit a Ca'Foscari, Venezia, Italy*

[l] *Multidisciplinary Laboratory, 'Abdus Salam' International Centre for Theoretical Physics, Via Beirut 31, 34151 Trieste, Italy*

[m] *Heinz Maier-Leibnitz Zentrum (FRM II), Technische Universität München, Lichtenbergstr.1, 85748 Garching, Germany*

[n] *Institució Catalana de Recerca i Estudis Avançats, Pg. Lluís Companys 23, 08010 Barcelona, Spain*

[o] *Unitat d'Antropologia Biològica (Departament de Biologia Animal, de Biologia Vegetal i d'Ecologia), Universitat Autònoma de Barcelona, 08193 Cerdanyola del Vallès, Barcelona, Spain*

***Corresponding authors.**

E-mail addresses: florian.bouchet@icp.cat (F. Bouchet), david.alba@icp.cat (D.M. Alba).

Abstract

The phylogenetic relationships of the small-bodied catarrhine *Pliobates cataloniae*, from the Miocene (~11.6 Ma) of the Vallès-Penedès Basin (NE Iberian Peninsula), have been controversial since its original description. However, the recent report of additional dentognathic remains has supported its crouzeliid pliopithecoid status. Based on the currently available hypodigm, we compare the molar enamel-dentine junction (EDJ) shape of *P. cataloniae* with that of other pliopithecoids from the same basin and both extinct and extant hominoids to further evaluate its pliopithecoid affinities. Besides qualitative comparisons of occlusal morphology at the EDJ level, we also quantitatively compare EDJ shape by means of landmark-based three-dimensional geometric morphometrics using both principal component analysis (PCA) and canonical variate analysis (CVA). Permutation tests are also performed to test whether the variation displayed by *Pliobates* exceeds that of extant hominoid genera. Our results indicate that the molar EDJ shape of *Pliobates* is very similar to that of the other pliopithecoids analyzed, particularly crouzeliids. The variation displayed by *Pliobates* upper molars is less marked at EDJ level than at the outer enamel surface, which is probably attributable to differential enamel wear and intraspecific differences in enamel thickness. Multivariate analyses of EDJ shape show that all pliopithecoids (including *Pliobates*) consistently cluster together in both PCAs and CVAs, occupying a different portion of the morphospaces than extinct and extant hominoids. Both posterior and typicality probabilities strongly support the classification of *Pliobates* as a pliopithecoid instead of a hominoid, while permutation tests fail to reject the possibility that the *P. cataloniae* hypodigm mixes remains of another genus. We, therefore, conclude that *P. cataloniae* is a crouzeliid pliopithecoid, as recently supported by cladistic analyses of craniodental characters, and that previous cladistic results that supported a stem hominoid status are attributable to postcranial convergences with crown hominoids.

Keywords: Tooth endostructure; Geometric morphometrics; Pliopithecoidea; Crouzeliidae; Miocene; Spain.

1. Introduction

The Miocene small-bodied catarrhine *Pliobates cataloniae* Alba et al., 2015 is known from two roughly coeval (~11.6 Ma; Alba et al., 2017, 2022) localities of the Abocador de Can Mata (ACM) sequence in the Vallès-Penedès Basin, NE Iberian Peninsula (Alba et al., 2015; Bouchet et al., in press). Since its original description, the systematic position of *Pliobates* has been subject to debate. Alba et al. (2015) interpreted *Pliobates* as a stem hominoid more derived than proconsulids based on a cladistic analysis combining craniodental and postcranial characters. Nevertheless, as already

pointed out by Alba et al. (2015), *Pliobates* displays a mosaic of primitive (stem catarrhine-like) and derived (crown hominoid-like) cranial and postcranial features that complicates its systematic placement, leading to the alternative suggestion that *Pliobates* might be a pliopithecoid that convergently acquired hominoid-like postcranial specializations (Benefit and McCrossin, 2015; Gilbert et al., 2020a). This would agree with the partly ossified ectotympanic of *Pliobates*, most similar to that of the pliopithecid pliopithecoid *Epipliopithecus* than that of crown catarrhines (Alba et al., 2015). Subsequent cladistic analyses, based on a different matrix of craniodental and postcranial characters, recovered *Pliobates* as a pliopithecoid most closely related to dionysopithecids (Nengo et al., 2017; Gilbert et al., 2020b) or even as a stem catarrhine more basal than pliopithecoids (Ji et al., 2022).

Detailed studies of the carotid canal morphology of *Pliobates* showed no particular resemblances to that of *Epipliopithecus* (Bouchet et al., 2021), contrasting with preliminary data on the inner ear semicircular canals, which did denote some similarities to *Epipliopithecus* (Urciuoli et al., 2022). Most recently, the description of additional dentognathic material more conclusively demonstrated the close phylogenetic affinities between *Pliobates* and other small-bodied crouzeliid pliopithecoids from Europe (Bouchet et al., in press). This was confirmed by cladistic analyses based on dental, craniodental and total (craniodental + postcranial data) evidence, although the inclusion of postcranial characters led to the questionable positioning of dendropithecids and all pliopithecoids (including *Pliobates*) as successive members of the hominoid stem lineage instead of stem catarrhine clades (Bouchet et al., in press). The diverging cladistic results obtained when postcranial data are included support the contention that the previous recovery of *Pliobates* as a stem hominoid by Alba et al.'s (2015) cladistic analysis was artifactually driven by the possession by *Pliobates* of multiple derived (crown hominoid-like) elbow and wrist features (e.g., well-developed zona conoidea on the distal humerus, a hook-like and slender styloid process of the distal ulna, or a small triquetrum relative to the size of the hamate; Alba et al., 2015; Bouchet et al., in press), whose detailed analysis is currently underway (see preliminary results in Figueroa-Torrejón et al., 2023; Raventós-Izard et al., 2023a, 2023b).

Until recently, the dental morphology of *Pliobates* was exclusively known on the basis of the rather worn upper cheek teeth of the holotype from locality ACM/C8-A4 (Alba et al., 2015). In the original description, dental similarities to dendropithecids such as *Micropithecus* were noted, including some differences from *Epipliopithecus* and other pliopithecoids (upper cheek teeth with markedly convex lingual profiles, moderately developed buccal cingula in the upper molars, and narrower M^1 and M^2). In contrast, the description of additional and better preserved upper and lower teeth of *Pliobates* from locality ACM/C5-D1 showed clear synapomorphies with crouzeliid pliopithecoids and supported a close phylogenetic link with the European crouzeliine genera *Crouzelia* and *Plesiopliopithecus* (Bouchet et al., in press), whose upper dental morphology is

unknown. While external dental morphology has proven to accurately distinguish pliopithecoids from other catarrhines (Andrews et al., 1996; Harrison and Gu, 1999; Begun, 2002; Harrison, 2013; Harrison et al., 2020; Ji et al., 2022; Bouchet et al., in press), few analyses have been devoted to the endostructural morphology of pliopithecoids (Zanolli et al., 2022a).

To further corroborate the pliopithecoid status of *Pliobates*, here we investigate its molar endostructure based on three-dimensional geometric morphometric (3DGM) analyses of the enamel-dentine junction (EDJ). The EDJ shape carries a strong phylogenetic signal (Zanolli et al., 2022b) and has proven useful to distinguish extinct and extant catarrhine groups (Olejniczak et al., 2004, 2007; Zanolli et al., 2022b, 2023) as well as to diagnose closely related genera and species (Olejniczak et al., 2004, 2007; Skinner et al., 2008, 2009; Macchiarelli et al., 2013; Beaudet et al., 2016; Pan et al., 2016; Zanolli et al., 2012, 2014, 2015, 2019a, 2019b, 2022b, 2023). We predict, based on previous qualitative comparisons of the outer enamel surface (OES; Bouchet et al., in press), that *Pliobates* will display closest morphometric affinities with other pliopithecoids than with either extant or extinct hominoids. Based on EDJ shape, we further evaluate the degree of EDJ shape variation in *Pliobates* as compared with extant hominoid genera using permutation tests (to account for the small sample sizes available for *Pliobates*) so as to test the null hypothesis that the upper molars (especially the M^2s) included in the hypodigm of *P. cataloniae* by Bouchet et al. (in press) belong to a single taxon. This null hypothesis would be considered to be falsified (thus favoring the presence of multiple genera) if variation was found to be greater than for extant genera.

2. Materials and methods

2.1. Studied and comparative samples

The sample of *P. cataloniae* comprises three molars of the holotype from ACM/C8-A4 as well as six molars corresponding to five individuals from ACM/C5-D1 (Bouchet et al., in press). Combined, they include all molar loci except the M_3, which is currently unknown for this taxon (Table 1; Supplementary Online Material [SOM] Table S1). Scanning parameters for *Pliobates* specimens were reported in Bouchet et al. (in press). Pliopithecoids included in the analyses comprise 16 molars belonging to 10 individuals from four species of different genera (Table 2): the crouzeliids *Barberapithecus huerzeleri* Alba and Moyà-Solà, 2012 and *Egarapithecus narcisoi* Moyà-Solà et al., 2001; the pliopithecid *Pliopithecus canmatensis* Alba et al., 2010; and an indeterminate pliopithecoid from Sant Quirze (Harrison et al., 2002). The latter is represented by a single M^2 originally attributed to *Pliopithecus* sp. by Harrison et al. (2002) but here left as family incertae sedis until an alternative attribution to the Crouzeliidae is evaluated in greater detail. The comparison with other stem catarrhines is restricted to pliopithecoids from the Vallès-Penedès Basin because no µCT data are yet available for other pliopithecoids or dendropithecids. Eight specimens were scanned using X-ray microtomography (Table 2; SOM Table S2), either at the Centro Nacional de

Investigación sobre la Evolución Humana (CENIEH) in Burgos (Spain) or at the Multidisciplinary Laboratory of the 'Abdus Salam' International Centre for Theoretical Physics (ICTP, Trieste; Italy). The two remaining specimens were scanned using neutron-based computed microtomography at the cold neutron radiography and tomography station (ANTARES) of the Heinz Maier-Leibnitz Zentrum (Garching bei München, Germany; Table 1; see Urciuoli et al., 2018 for details on scanning settings). The neutron scan was required because these specimens show no contrast at all between the enamel and dentine materials for X-rays or synchrotron radiation (Urciuoli et al., 2018). This seems to depend on the mineral exchange with the soil during fossilization; a study of the exact atomic composition of such samples using neutron prompt gamma activation analysis is already foreseen at the FRM II reactor, but is delayed by a current major overhaul of the reactor. The OES models of pliopithecoid molars investigated in this study (including *Pliobates*) are openly available from MorphoSource whereas the EDJ models are also uploaded to MorphoSource but remain embargoed until an ongoing study of the enamel thickness is published (SOM Tables S1 and S3). MicroCT scans are curated at the ICP and have also been deposited in MorphoSource. They are accessible upon reasonable request by other researchers, as in the case of the physical fossils housed in the same institution.

The extinct hominoid sample includes 27 dryopithecine (12 upper and 15 lower) molars of *Anoiapithecus brevirostris*, *Dryopithecus fontani*, *Hispanopithecus crusafonti*, *Hispanopithecus laietanus*, *Pierolapithecus catalaunicus*, and '*Sivapithecus*' *occidentalis* species inquirenda, for which the EDJ shape was previously analyzed (Alba et al., 2020; Fortuny et al., 2021; Zanolli et al., 2023: SOM Table S1). In turn, the extant hominoid comparative sample consists of 10 teeth for each molar position for each of the three living great ape genera (*Pan*, *Gorilla*, and *Pongo*; see Zanolli et al., 2023: SOM Table S2) as well as 11 upper molars and 29 lower molars of extant hylobatids (*Hylobates* and *Symphalangus*; SOM Table S4). Although M^1 and M^3 positions are represented in *P. cataloniae*, due to the scarcity of μCT data of pliopithecoid teeth that could be used for comparison, we restricted the 3DGM analyses to the EDJ of M^2s, M_1s and M_2s.

2.2. Methods

Segmentation Virtual surfaces of the extant hylobatid and pliopithecoid molars were obtained using the watershed segmentation tool and semiautomatic threshold-based segmentations, respectively, in Avizo v. 7.0 (Visualization Sciences Group, Hillsboro). In order to have as many available pliopithecoid (including *Pliobates*) specimens as possible for 3DGM analyses, dentine horns were reconstructed for five *Pliobates* and nine other Iberian pliopithecoid molars by some of us (F.B. and C.Z.). Following previous studies (e.g., Smith et al., 2012; Fortuny et al., 2021; Alba et al., 2024b), reconstructions of dentine horn tips were made for sections showing light to moderate wear, based

on the curvature and orientation of the EDJ preserved portion and/or, when possible, based on the profile of the antimere, or other teeth, if less worn.

Geometric morphometrics The 3DGM analyses of the EDJ virtual surfaces were performed using two different sets of landmarks and semilandmarks for the M^2, M_1 and M_2. The set for the M^2s is composed of five landmarks—four placed at the dentine horn apices of the four main cusps (paracone, protocone, metacone, and hypocone) and the fifth at the mesiobuccal end of the cervix—plus 75 semilandmarks positioned along the occlusal crests and the mesial and distal marginal ridges (10 on the prehypocrista, 10 on the postparacrista–premetacrista, 20 on the preprotocrista–mesial marginal ridge–preparacrista, 20 on the postmetacrista–distal marginal ridge–posthypocrista, and 15 on the crista obliqua) and 29 semilandmarks distributed along the cervical contour of the crown (Fig. 1a–d). We chose to include cervix landmarks to capture differences in crown proportion (due to differences in the development of the lingual cingulum as well as lingual flare) and crown height among catarrhine groups.

The lower molar set (Fig. 1e–f), in turn, is composed of five landmarks placed at the dentine horn apices of the main cusps (metaconid, protoconid, entoconid, hypoconid, and hypoconulid) plus 70 semilandmarks positioned along most of the occlusal crests (15 on the postmetacristid–pre-entocristid, 15 on the cristid obliqua, 15 on the preparacristid–mesial marginal ridge–preprotocristid, 15 on the postmetacristid–distal marginal ridge–posthypoconulid cristid, and 10 on the posthypocristid–prehypoconulid cristid)—except the hyprotocristid–hypometacristid, which is variably present in great apes. In *Pliobates*, only the M_1 preserves the cervix while the M_2 crown is not fully formed. So, to make the lower molar analyses comparable, we did not place semilandmarks along the cervix of the mandibular molars.

Landmark data were imported into R v. 4.1.1 (R Development Core Team, 2021) to perform Procrustes alignments using the 'ProcSym' function of the package 'Morpho' v. 2.9 (Schlager, 2021).

Multivariate analyses For each molar position (M^2, M_1, and M_2), multivariate analyses of the Procrustes-aligned landmark data (i.e., EDJ shape data) were used to compare *Pliobates* to other pliopithecoids, extinct and extant hominids, and extant hylobatids. Due to limited sample sizes for pliopithecoid M^2s (n = 3), we only computed a principal component analysis (PCAs). Given the somewhat larger samples of pliopithecoid M_1s and M_2s (n = 6), we also performed cross-validated canonical variate analyses (CVAs) based on the principal component (PC) scores of these lower molars, with three groups (pliopithecoids, extant hominids, and extant hylobatids) defined a priori, and with *Pliobates* and dryopithecines projected *a posteriori* into the morphospace. The CVAs were performed based on the minimum number of PCs that enabled the highest percentage of correct classification after cross-validation (following Zanolli et al., 2023). For M_1 and M_2, six and ten PCs were selected, representing 91 and 98% of the total variance, respectively. The PCAs and CVAs were computed using the R packages 'ade4' v. 1.7-18 (Dray and Dufour, 2007) and 'Morpho,'

respectively. To evaluate the closest morphometric affinities of the EDJ shape of *Pliobates* molars, we classified them into the a priori-defined groups based on their CV scores by computing both posterior probabilities (assuming equal prior probabilities) and typicality probabilities, using the R package 'Morpho.' Posterior probabilities represent the likelihood of belonging to each of the a priori-defined groups given the CV scores of a specimen. In contrast, typicality probabilities denote the probability of having such scores if the specimen belongs to a given group. Hence, unlike posterior probabilities, typicality probabilities do not assume that the specimen belongs to one of the groups defined a priori and, thus, they do not add up to unity.

Permutation tests To evaluate the degree of EDJ shape variation displayed by the upper molars of *Pliobates* as compared with extant taxa, we relied on permutation tests. These allowed us to test the null hypothesis that all the M^2s included in the hypodigm of *P. cataloniae* by Bouchet et al. (in press) belong to a single taxon—due to comparative sample restrictions, the analyses were carried out at the genus level. The variation of *Pliobates* and the extant hominoid genera was measured as the average of the Euclidean distances (EDs) between pairs of specimens of the same taxon based on all the PC scores. For *Pliobates*, EDs were computed between each possible pair of specimens. For each extant hominoid genus, all possible combinations (i.e., permutations) of specimens for subsamples of the same size as the *Pliobates* sample were generated, and the average ED for each permutation was calculated. The average ED of *Pliobates* was then compared with the distribution of the average EDs for the permutations of each extant hominoid genus. We computed the probability (interpreted as a *p*-value) that *Pliobates* displays a lower variation than a given extant hominoid genus by dividing the number of permutations with a higher or equal average ED than that of *Pliobates* by the total number of permutations. The null hypothesis that the *Pliobates* sample is not more variable than a given extant hominoid genus would be rejected when $p < 0.05$.

3. Results

3.1. Description of the enamel-dentine junction shape in Pliobates

The OES and EDJ molar morphology of *Pliobates* is compared with that of other pliopithecoids in Figures 2 and 3. The OES occlusal details are generally present at the EDJ, albeit some features can be better ascertained or show some slight differences in the latter.

Upper molars In *Pliobates*, the M^1 and M^2 EDJ occlusal contour is subquadrangular (broader than long; Fig. 2a–e), whereas the M^3 EDJ occlusal contour is trapezoidal (Fig. 2i–j). In all the upper molars, the buccal side is longer than the lingual (more markedly so in the M^3) and there is a slight to moderate buccolingual constriction at about crown midlength. The buccal dentine horns are more mesially located than the lingual ones and the protocone horn is also less peripheral, whereas that of the hypocone is more lingually located than the former in the M^1 and M^2. The paracone horn is much more peripheral than that of the metacone in the M^3. The protocone horn is the most extensive

(although only slightly larger than the paracone horn in the M^3), whereas the hypocone horn is the smallest, decreasing in size from M^1 to M^3. The paracone and metacone horns are similar in size in the M^1, whereas the metacone horn is smaller in the M^2 and especially in the M^3. The mesial fovea is mostly located on the buccal half of the crown and much broader than long. It is delimited by the short preparacrista, the longer preprotocrista, and an obliquely oriented hypoprotocrista that extends between the bases of the protocone and paracone dentine horns. The trigon basin is deep and extensive, being buccally delimited by the postparacrista and premetacrista (which are aligned and merged with one another) and distally enclosed by a continuous and diagonally oriented crista obliqua that is more distinct in the M^1 and M^2 than in the M^3. The distal fovea is wider and somewhat shorter than the trigon basin in the M^1 and M^2, but narrower and longer in the M^3. It is lingually delimited by the prehypocrista, which connects the apex of the hypocone horn with the protocone horn in all specimens except IPS44014 (Fig. 2a) and IPS10379 (Fig. 2b), where it joins the mesial portion of the postprotocrista (i.e., the mesial-most portion of the crista obliqua). A secondary crest, more buccally located than the prehypocrista, further originates from the apex of the hypocone and joins the crista obliqua in all specimens except IPS10379 (Fig. 2b); this secondary crest is more marked in some specimens than others, but still more visible at the EDJ than at the OES. A short postmetacrista buccally encloses the distal fovea, whereas in contrast there is no posthypocrista distinct from the distal marginal ridge. The buccal cingulum at the EDJ level appears more developed between the two buccal dentine horns but is much narrower than the shelf-like and C-shaped lingual cingulum, which does not surround the hypocone. The development of the lingual cingulum is comparable among all the studied molars at the EDJ level, whereas in contrast it appears broader in some M^2s at the OES. Additional secondary crests can be discerned at the distal fovea and/or lingual cingulum in some specimens, although they appear less marked than at the OES level.

Lower molars The M_1 and M_2 EDJ contour of *Pliobates* (Fig. 3a and h) is subrectangular (clearly longer than broad and slightly broader distally than mesially). It is also slightly more mesially protruding buccally than lingually and displays a mild buccolingual constriction at about crown midlength. The buccal dentine horns are less peripheral than the lingual ones. The hypoconid and entoconid dentine horns are also more peripheral than those of the mesial cuspids. The protoconid horn is much more mesially located than that of the metaconid and similar in size to that of the hypoconid. The metaconid and entoconid horns are similar in size but slightly smaller than their buccal counterparts. The hypoconulid horn is the smallest, being centrally located at the distal end of the crown in the M^1 and slightly more buccally and less distally situated in the M^2. The mesial fovea is extensive and broader than long (more clearly so than at the OES). The secondary transverse cristid that extends from the preprotocristid toward the center of the fovea at the OES is not visible at the EDJ. The mesial fovea is distally separated from the talonid basin by a continuous and somewhat obliquely oriented straight crest, formed by the hypoprotocristid (which originates from

the distal aspect of the protoconid horn) and the hypometacristid. The talonid basin is deep and very extensive, being buccally delimited by a continuous cristid obliqua that links the hypoconid horn apex with the buccalmost portion of the hypoprotocristid and is formed by the prehypocristid and the shorter postprotocristid. In the M_1, these two cristids are aligned, forming a straight but obliquely oriented cristid obliqua. In contrast, in the M_2 the prehypocrista is mesiodistally aligned, forming an angle with the obliquely oriented postprotocristid. The distal arm of the pliopithecine triangle is well distinct at the EDJ level, originating from the distal portion of the prehypocristid. In contrast, the short secondary crest that is visible at the OES distally from the hypoprotocristid–hypometacristid junction (and which might be homologous to the mesial arm of the pliopithecine triangle) is barely visible at the EDJ. The talonid basin is distobuccaly enclosed by a continuous crest formed by the merged posthypocristid and prehypoconulid cristid. The EDJ confirms that a posthypoconulid cristid is lacking in the M_1 but present, even if very short, in the M_2. Along the lingual side of the talonid basin, the postmetacristid and pre-entocristid are not mesiodistally aligned, forming a continuous but sinous crest. The talonid basin is only partly separated from the much smaller distal fovea, located on the lingual half of the crown, by the hypoentocristid and the postcristid, which are not complitely aligned with one another and only faintly developed at the EDJ. The buccal cingulid appears better developed and more shelf-like at the EDJ level.

3.2. *Comparisons*

Hominoids The EDJ morphology of *Pliobates* upper and lower molars clearly differs from that of extant hylobatids (Fig. S1c, e, i–j, n–o, and q–r), dryopithecines (Fortuny et al., 2021: Fig. 4), and extant great apes (Fig. S1a–b, d, f–h, k–m, and p). More specifically, the upper molars of *Pliobates* differ from those of the hominoids analyzed here in the following features: relatively broader occlusal contour, more trapezoidal in the M^3; more buccolingually compressed and less peripheral dentine horns; well-defined hypoparacrista and crista obliqua (they are sometimes interrupted, low, or absent in hominoids); more distally located protocone horn; less buccally directed preprotocrista; less extensive metacone and hypocone horns, the latter further being more lingually but less distally located; smaller trigon basin and distal fovea; consistent presence of a secondary crest connecting the hypocone horn with the crista obliqua; and better developed cingula. The upper molars of *Pliobates* further differ from those of hylobatids in the more buccolingually constricted occlusal contour at crown midlength, and from hominids in the less marked buccal and/or lingual flare, the lack of accessory cuspules, and the absence of a crest linking the hypocone to the metacone (in the M^1 and M^2).

In turn, the M_1–M_2 EDJ of *Pliobates* differs from that of hominoids (Fortuny et al., 2021: Fig. 4; SOM Fig. S1) in the more compressed and less peripheral dentine horns; the relatively narrower mesial and central foveae and the smaller talonid overall; the mesial fovea consistently separated

from the talonid basin (they are sometimes continuous in hominoids); the presence of a single cristid (constituted by the merged hypoprotocristid–hypometacristid) separating the mesial fovea from the talonid (more than two crests sometimes separate the two foveae in hominoids); the protoconid horn more mesially located than that of the metaconid; the entoconid horn aligned with (instead of more distally located than) the hypoconid horn; the more extensive distal fovea; the origin of the hypoprotocristid from the distal (instead of lingual) aspect of the protoconid horn; the shorter postprotocristid emerging from the hypoprotocristid (instead of the protoconid horn), so that the cristid obliqua is more obliquely oriented; the presence of a pliopithecine triangle (at least the distal arm); and the better developed buccal cingulid (which may be entirely absent in hominoids). The lower molars of *Pliobates* further differ from those of hylobatids in the less extensive hypoconid horn, which is nonetheless consistently present (it is sometimes lacking in hylobatids), and from those of hominids in the relatively narrower occlusal outline with no buccal flare (it is marked in hominids), the absence of accessory cuspulids, the less distally situated hypoconid horn, a more median hypoconulid horn, and the lack of secondary cristids connecting the protoconid and the metaconid horns.

Pliopithecoids The EDJ morphology of the *Pliobates* molars is similar to that of the other pliopithecoids analyzed (Figs. 2f–h, 2k, 3b–g, and 3i–n; see a summary in Tables 3 and 4). They share several features in their upper molars that distinguish them from hominoids: broader occlusal contour; buccolingually compressed dentine horns that are not particularly peripheral; the consistently well-defined hypoparacrista and crista obliqua; the more distally located protocone horn relative to that of the paracone; the mesiobuccally directed preprotocrista; the smaller hypocone horn, which is more lingually located relative to that of the protocone horn and less distally located relative to that of the paracone; the less extensive trigon basin and distal fovea; the better developed buccal and lingual cingula; and the lack of hypocone–metacone crest and accessory cuspules.

Based on the EDJ morphology of the lower molars, *Pliobates* further shares with the studied pliopithecoids additional distinctive features from hominoids: the less peripheral dentine horns; the mesial fovea consistently separated from the talonid basin (the trigonid and talonid basins are sometimes continuous in hominoids); the presence of a single hypoprotocristid–hypometacristid separating the mesial fovea from the talonid basin (more than two crests sometimes separate the two foveae in hominoids); the less extensive mesial and central foveae and the more extensive distal fovea; the more mesially located protoconid horn relative to that of the metaconid (instead of transversely aligned as in hominoids); the more obliquely oriented cristid obliqua (postprotocristid+prehypocristid); the presence of at least the distal arm of the pliopithecine triangle; the better developed buccal cingulid; and lack of accessory cuspulids. Overall, *Pliobates* most closely resembles *Barberapithecus* than any other pliopithecoid investigated here (Tables 3 and 4)—for a

detailed differential diagnosis of *P. cataloniae* relative to other pliopithecoids, see Bouchet et al. (in press).

3.3. Multivariate analyses of the enamel-dentine junction shape

Principal component analyses The PCA plots of the two first PCs (Fig. 4) show that pliopithecoids and extant hominoids occupy different positions in the M^2 and lower molar morphospaces, being discriminated along PC2 and PC1, respectively.

In the M^2 (Fig. 4a) analysis, PC1 discriminates extant hylobatids and African apes (positive scores) from *Pongo* plus dryopithecines (negative scores), with only minimal overlap between African apes and *Pongo* plus dryopithecines. The EDJ of specimens with positive scores displays a relatively narrower contour and higher relief, as well as more peripheral dentine horns, and a relatively larger distal fovea than specimens with negative scores. Pliopithecoids have overall moderately negative scores, being closer to orangutans for those features. PC2 mainly distinguishes pliopithecoids (markedly positive values) from all hominoids (moderately positive to negative values). The EDJ of specimens with positive values show a higher relief, a relatively narrower trigon basin and a relatively larger distal fovea, less peripheral mesial horns and more peripheral distal horns, a hypocone horn more peripheral than that of the protocone (instead of aligned with the latter), and a metacone horn aligned with that of the paracone (instead of less peripheral than the latter). Pliopithecoids display the most extreme PC2 scores and fall far from all hominoids (Fig. 4a). The M^2s of *Pliobates* (Fig. 4a) fall closer to those of pliopithecoids than to those of hominoids, although outside the variation recorded by the scanty comparative sample available for the former.

For the M_1 and M_2 (Fig. 4b–c), PC1 distinguishes pliopithecoids (very negative scores for M_1 and very positive scores for M_2) from hominoids (moderately negative to positive scores for M_1 and negative to positive scores for M_2). The only exception is an M_2 of *H. laietanus* (IPS1780) that falls farther towards pliopithecoids but is still closest to other dryopithecines along this axis, and likely represents an outlier (Fig. 4c). Compared to hominoids, the EDJ of pliopithecoids displays a relatively narrower contour, with less peripheral dentine horns and relatively narrower foveae, a protoconid horn more mesially located than that of the metaconid, a more distally and less peripherally situated hypoconulid horn, and a more inclined cristid obliqua. In the M_1 analysis, PC2 discriminates hominids (positive to moderately negative scores) from extant hylobatids (negative scores), with some overlap. In turn, in the M_2 analysis, this axis discriminates *Pongo* (highest positive scores) from most African apes (more negative scores), with extant hylobatids being somewhat intermediate but completely overlapping with the variation of extant great apes. For the M_1 (Fig. 4b), the EDJ of specimens with positive scores displays a relatively narrower contour with less peripheral dentine horns (except that of the entoconid), relatively narrower mesial fovea and talonid basin, lower metaconid and protoconid horns, a slenderer hypoconid horn, a more buccally located hypoconulid

horn, and a larger distal fovea. For the M_2 (Fig. 4c), specimens with positive scores display much lower dentine horns. In both analyses, *Pliobates* falls closest to pliopithecoids, especially *Barberapithecus*.

Canonical variate analyses The CVAs for the lower molars (Fig. 5) show better discrimination than PCAs and have a high accuracy of classification for the specimens included in the a priori-defined groups—91.1% for the M_1 and 97.8% for the M_2 after cross-validation (see SOM Table S5 for further details). The CVAs separate pliopithecoids (very negative values for M_1 and very positive ones for M_2) from hominoids (moderately negative to positive values for M_1 and negative to moderately positive ones for M_2) along the first canonical variate (CV1), based on the same features mentioned above for each molar position regarding the corresponding PC1s. In turn, the CV2 discriminates extant hominids and dryopithecines (moderately negative to positive scores) from extant hylobatids (negative scores), albeit with some overlap. Specimens with more positive CV2 scores for both the M_1 (Fig. 5a) and the M_2 (Fig. 5b) show slightly lower dentine horns, a stouter and more peripheral hypocone horn, and a hypoconulid horn situated more towards buccal, and a larger distal fovea. The two latter differences are more marked in the M^1, for which specimens with more positive CV2 scores further display a relatively narrower EDJ contour and a protoconid horn aligned with that of the metaconid (instead of less mesially located than it).

Posterior probabilities (SOM Table S6) calculated from the CVAs confirm the very close similarities between *Pliobates* and other pliopithecoids, as both lower molars classify *Pliobates* as a pliopithecoid with a posterior probability of 1 ($p = 0$ for extant hominids and hylobatids). This is further supported by typicality probabilities (SOM Table S6) of 0.58 for both the M_1 and the M_2 (and $p < 0.01$ for extant hominids and hylobatids in both instances), indicating that *Pliobates* (unlike extant apes) fits well with the pliopithecoid variation. In turn, the posterior and typicality probabilities for the classification of dryopithecine specimens as pliopithecoids are lower than 0.01, except for the outlier M_2 of *H. laietanus* (IPS1780), which is predicted as such with a posterior probability of 0.92 (but with a typicality probability lower than 0.01; SOM Table S6). In contrast, the other lower molars of *Hispanopithecus* and other dryopithecines are classified as either hominids (4 over 6) or hylobatids (2 over 6) for the M_1, and as hominids for the M_2 (except for the aforementioned outlier, IPS1780; SOM Table S6).

3.4. Enamel-dentine junction shape variation analyses

The permutations tests based on the M^2 PC scores indicates that the variation of *Pliobates* never exceeds that of extant hominoid genera (Table 5). Therefore, the permutation tests based on the upper molar EDJ shape do not allow us to reject the null hypothesis that the upper molars of *Pliobates*—especially the M^2s—belong to a single genus.

4. Discussion

Geometric morphometric analyses of EDJ shape have become widespread since the earliest attempts almost two decades ago (Olejniczak et al., 2004). Molar EDJ shape, particularly in 3D, has been shown to embed useful taxonomic and phylogenetic information in catarrhines (e.g., Skinner et al., 2008, 2009; Zanolli et al., 2012, 2023; Beaudet et al., 2016). However, while most of the literature has focused on hominins (e.g., Skinner 2008, 2016; Macchiarelli et al., 2013; Pan et al., 2016; Zanolli et al., 2012, 2014, 2015, 2019a), much less effort has been devoted to other catarrhines, including cercopithecoids (Beaudet et al., 2016), apes (Skinner et al., 2009; Fortuny et al., 2021; Zanolli et al., 2022b, 2023), and stem catarrhines such as pliopithecoids (Zanolli et al., 2022a). The present study constitutes the first report and analysis of extensive data of pliopithecoid upper and lower molar EDJ morphology and, to the best of our knowledge, it further includes the largest dataset of extant hylobatid EDJ shape in 3D, with the aim of testing between the two alternative (hominoid vs. pliopithecoid) hypotheses previously supported by cladistic analyses for the Miocene small-bodied catarrhine *Pliobates*.

Pliobates was originally recovered as a stem hominoid more derived than proconsulids (Alba et al., 2015) and, subsequently, as a pliopithecoid most closely related to dionysopithecids (Nengo et al., 2017; Gilbert et al., 2020b) or even as a stem catarrhine more basal than pliopithecoids (Ji et al., 2022). Most recently, Bouchet et al. (in press) supported the crouzeliid pliopithecoid affinities of *Pliobates* based on cladistic analyses of craniodental features. These authors concluded that the previous cladistic results by Alba et al. (2015), indicating a stem hominoid status for *Pliobates*, were misguided by postcranial convergences with crown hominoids—as previously suggested by some authors that modern ape-like features of *Pliobates* postcranium would have been acquired convergently (Benefit and McCrossin, 2015; Gilbert et al., 2020a) and in further agreement with the view that many purported postcranial synapomorphies of extant apes might have independently evolved along various lineages (for recent reviews, see Almécija et al., 2021; Urciuoli and Alba, 2023).

The results of this paper further confirm the conclusions of Bouchet et al. (in press) regarding the phylogenetic relationships of *Pliobates*. Thus, the visual inspection of occlusal morphology at the EDJ level confirms the similarities between *Pliobates* and other pliopithecoids previously noted at the OES level (Bouchet et al., in press). The EDJ shape of pliopithecoid molars (including *Pliobates*) clearly differs from that extant and extinct crown hominoids in multiple features, namely: more compressed and less peripheral dentine horns, and no accessory dentine horns; upper molars with a relatively broader occlusal contour, consistently well-defined hypoparacrista and crista obliqua, more distal protocone horn, less buccally directed preprotocrista, less extensive and more lingually (but less distally) located hypocone horn, relatively smaller trigon basin and distal fovea, and better developed cingula; and lower molars with a relatively narrower foveae, protoconid horn more

mesially located than that of the metaconid, presence of at least the distal arm of the pliopithecine triangle, and better developed buccal cingulid. Alhought not directly comparable, our results for dryopithecines concur with those of Zanolli et al. (2023) in that most specimens fall closest to extant great apes—generally, near *Pongo*—in the morphospaces, as further confirmed by posterior and typicality probabilities. As in Zanolli et al. (2023), the EDJ of *Hispanopithecus* M_2s also varies the most among dryopithecines. Overall, the comparison between our 3DGM landmark-based results for dryopithecines and those previously provided by Zanolli et al. (2023) based on diffeomorphisms confirm that the former are efficient enough to adequately discriminate among taxa.

The multivariate analyses of molar EDJ further show that pliopithecoids occupy different positions of the morphospace than dryopithecines and extant hominoids, which are closer to one another and overlap to some extant. *Pliobates* consistently clusters with other pliopithecoids (generally falling closer to *Barberapithecus*), which—coupled with probabilities of group membership—further confirms that *Pliobates* is phenetically close to pliopithecoids and much more distinct from hominoids. Although *Pliobates* can be readily distinguished from the other analyzed pliopithecoid species, based on both occlusal qualitative comparisons and quantitative multivariate analyses of EDJ shape, it more closely resembles crouzeliids (*Barberapithecus* and, to a lesser extent, *Egarapithecus*) and the indeterminate pliopithecoid from Sant Quirze (whose potential crouzeliid status deserves further scrutiny) than the pliopithecid *Pliopithecus*. Our 3DGM results based on molar EDJ shape thus lend additional support to recent cladistic analyses of craniodental data supporting *Pliobates* as a crouzeliid pliopithecoid (Bouchet et al., in press).

The variation previously observed at the OES level in the degree of cusp compression, crest sharpness, lingual cingulum development, and hypocone size and shape among *Pliobates* upper molars (especially the M^2s; Bouchet et al., in press) is not reflected at the EDJ. In fact, when both OES and EDJ morphology are considered simultaneously, it appears that differences in cusp compression and size, as well as cingulum development, are more marked at the OES, whereas crest development and pattern, as well as cusp location, can be more readily compared at the EDJ level. Thus, at the EDJ, all the upper molars of *Pliobates* display pyramidal and similarly compressed dentine horns, sharp crests, a broad and ledge-like lingual cingulum, and a smaller hypocone horn relative to those of the remaining main cusps, not showing substantial differences that might hint at the presence of two different taxa. This suggests that the apparent variation of some occlusal structures at the OES is simply attributable to differential tooth wear and/or intraspecific differences in relative enamel thickness. This is further confirmed by permutation tests based on M^2 EDJ shape, which indicate that *Pliobates* does not surpass the variability displayed by extant hominoid genera separately. Our results therefore support the inclusion of all the upper molars currently included in the hypodigm of *P. cataloniae* after Bouchet et al. (in press), from the roughly coeval localities of ACM/C4-A8 and ACM/C5-D1, into a single taxon.

5. Conclusions

The results of our 3DGM analyses of upper and lower molar EDJ shape in *Pliobates* not only confirm its crouzeliid pliopithecoid affinities—recently supported by cladistic analyses—but further reject the potential mixture of two different genera within its hypodigm. From a broader perspective, our results further illustrate that the usefulness of EDJ shape analysis for resolving taxonomic and phylogenetic issues is not restricted to hominins and apes but further applies to stem catarrhines such as pliopithecoids. This paper thus lays the foundation for future studies focused on other Miocene primates of debated affinities, such as dendropithecids and other small-bodied catarrhines from East Africa (e.g., Rossie and Hill, 2018; Gilbert et al., 2020b), putative stem hylobatids from Asia (Gilbert et al., 2020b; Ji et al., 2022), or the enigmatic ape *Oreopithecus* (Nengo et al., 2017; Rossie and Cote, 2022; Zanolli et al., 2022a; Urciuoli and Alba, 2023; Alba et al., 2024a).

Acknowledgements

This publication is part of R+D+I projects PID2020-117289GB-I00/AEI/10.13039/501100011033 and PID2020-117118GB-I00/AEI/10.13039/501100011033, funded by the Agencia Estatal de Investigación of the Ministerio de Ciencia e Innovación from Spain. Research has also been funded by the Generalitat de Catalunya/CERCA Programme; the Agència de Gestió d'Ajuts Universitaris i de Recerca of the Generalitat de Catalunya (Consolidated Research Groups 2022 SGR 00620, 2022 SGR 01184, and 2022 SGR 01188); the Departament de Cultura of the Generalitat de Catalunya (CLT009/18/00071 and CLT0009_22_000018); a predoctoral grant from the Ministerio de Ciencia e Innovación (PRE2018-083299 to F.B.); a Margarita Salas postdoctoral fellowship funded by the European Union NextGenerationEU to A.U.; and a Ramón y Cajal grant (RYC2021-032857-I) financed by the Agencia Estatal de Investigación of the Ministerio de Ciencia e Innovación from Spain (MCIN/AEI/10.13039/501100011033) and the European Union «NextGenerationEU» / PRTR to J.F. Fieldwork was defrayed by CESPA Gestión de Residuos and UTE Ampliació Can Mata. We further acknowledge the support of the Servei d'Arqueologia i Paleontologia of the Generalitat de Catalunya and the collaboration of the Centre d'Interpretació i Restauració Paleontològica (Ajuntaments dels Hostalets de Pierola). Most of the μCT scans of *Pliobates* and other Iberian pliopithecoids were performed at the CENIEH facilities (Burgos, Spain) with the collaboration of the CENIEH staff. Finally, we thank M. Imbrasas for the image preprocessing of extant hylobatid specimens; P. Bayle, D. Arbulla, M. Landreau, A. Mazurier, N. Mémoire, and R. Macchiarelli for access to hominoid comparative material; and M. Méndez, S. Llácer, A. Serrano-Martínez, J. Galindo, and the staff of the Preparation Area of the ICP for technical assistance.

References

Alba, D.M., Moyà-Solà, S., 2012. A new pliopithecid genus (Primates, Pliopithecoidea) from Castell de Barberà (Vallès-Penedès Basin, Catalonia, Spain). Am. J. Phys. Anthropol. 147, 88–112.

Alba, D.M., Moyà-Solà, S., Malgosa, A., Casanovas-Vilar, I., Robles, J.M., Almécija, S., Galindo, J., Rotgers, C., Mengual, J.V.B., 2010. A new species of *Pliopithecus* Gervais, 1849 (Primates: Pliopithecidae) from the Middle Miocene (MN8) of Abocador de Can Mata (els Hostalets de Pierola, Catalonia, Spain). Am. J. Phys. Anthropol. 141, 52–75.

Alba, D.M., Almécija, S., DeMiguel, D., Fortuny, J., Pérez de los Ríos, M., Pina, M., Robles, J.M., Moyà-Solà, S., 2015. Miocene small-bodied ape from Eurasia sheds light on hominoid evolution. Science 350, aab2625.

Alba, D.M., Casanovas-Vilar, I., Garcés, M., Robles, J.M., 2017. Ten years in the dump: An updated review of the Miocene primate-bearing localities from Abocador de Can Mata (NE Iberian Peninsula). J. Hum. Evol. 102, 12–20.

Alba, D.M., Fortuny, J., Robles, J.M., Bernardini, F., Pérez de los Rios, M., Tuniz, C., Moyà-Solà, S., Zanolli, C., 2020. A new dryopithecine mandibular fragment from the middle Miocene of Abocador de Can Mata and the taxonomic status of '*Sivapithecus occidentalis*' from Can Vila (Vallàs-Penedès Basin, NE Iberian Peninsula). J. Hum. Evol. 145, 102790.

Alba, D.M., Robles, J.M., Casanovas-Vilar, I., Beamud, E., Bernor, R.L., Cirilli, O., DeMiguel, D., Galindo, J., Llopart, I., Pons-Mojo, G., Sánchez, I.M., Vinuesa, V., Garcés, M., 2022. A revised (earliest Vallesian) age for the hominoid-bearing locality of Can Mata 1 based on new magnetostratigraphic and biostratigraphic data from Abocador de Can Mata (Vallès-Penedès Basin, NE Iberian Peninsula). J. Hum. Evol. 170, 103237.

Alba, D.M., Urciuoli, A., Hammond, A.S., Almécija, S., Rook, L., Zanolli, C., 2024a. Miocene ape evolution: Where does *Oreopithecus* fit in? Boll. Soc. Paleontol. It. 64, 1–30.

Alba, D.M., Bouchet, F., Fortuny, J., Robles, J.M., Galindo, J., Luján, À.H., Moyà-Solà, S., Zanolli, C., 2024b. New remains of the fossil Miocene great ape *Anoiapithecus brevirostris* from Abocador de Can Mata. J. Hum. Evol. 188, 103497.

Almécija, S., Hammond, A.S., Thompson, N.E., Pugh, K.D., Moyà-Solà, S., Alba, D.M. 2021. Fossil apes and human evolution. Science 372, eabb4363.

Andrews, P., Harrison, T., Delson, E., Bernor, R.L., Martin, L., 1996. Distribution and biochronology of European and Southwest Asian Miocene catarrhines. In: Bernor, R.L., Fahlbusch, V., Mittmann, H.-W. (Eds.), The Evolution of Western Eurasian Neogene Mammal Faunas. Columbia University Press, New York, pp. 168–207.

Beaudet, A., Dumoncel, J., Thackeray, J.F., Bruxelles, L., Duployer, B., Tenailleau, C., Bam, L., Hoffman, J., de Beer, F., Braga, J., 2016. Upper third molar internal structural organization and semicircular canal morphology in Plio-Pleistocene South African cercopithecoids. J. Hum. Evol. 95, 104–120.

Begun, D.R., 2002. The Pliopithecoidea. In: Hartwig, W.C. (Ed.), The Primate Fossil Record. Cambridge University Press, Cambridge, pp. 221–240.

Benefit, B.R., McCrossin, M.L., 2015. A window into ape evolution. Science 350, 515–516.

Bouchet, F., Urciuoli, A., Beaudet, A., Pina, M., Moyà-Solà, S., Alba, D.M., 2021. Comparative anatomy of the carotid canal in the Miocene small-bodied catarrhine *Pliobates cataloniae*. J. Hum. Evol. 161, 103073.

Bouchet, F., Zanolli, C., Urciuoli, A., Almécija, S., Fortuny, J., Robles, J.M., Beaudet, A., Moyà-Solà, S., Alba, D.M. (in press). The Miocene primate *Pliobates* is a pliopithecoid. Nat. Commun.

Dray, S., Dufour, A.-B., 2007. The ade4 package: Implementing the duality diagram for ecologists. J. Stat. Softw. 22, 1–20.

Figueroa-Torrejón, A., Almécija, S., Moyà-Solà, S., Alba, D.M., Arias-Martorell, J., 2023. Geometric morphometric analysis of the distal humerus of *Pliobates cataloniae*: Locomotor inferences and anthropoid elbow evolution. In: Alba, D.M., Marigó, J., Nacarino-Meneses, C, Villa, A. (Eds.), Book of Abstracts of the 20th Annual Conference of the European Association of Vertebrate Palaeontologists, 26th June – 1st July 2023. Palaeovertebrata Special Volume 1-2023, 86–87.

Fortuny, J., Zanolli, C., Bernardini, F., Tuniz, C., Alba, D.M., 2021. Dryopithecine palaeobiodiversity in the Iberian Miocene revisited on the basis of molar endostructural morphology. Palaeontology 64, 531–554.

Gilbert, C.C., Pugh, K.D., Fleagle, J.G., 2020a. Dispersal of Miocene hominoids (and pliopithecoids) from Africa to Eurasia in light of changing tectonics and climate. In: Prasad, G.V., Patnaik, R. (Eds.), Biological Consequences of Plate Tectonics. New Perspectives on post-Gondwana Break-up—A Tribute to Ashok Sahni. Springer, Cham, pp. 393-412.

Gilbert, C.C., Ortiz, A., Pugh, K.D., Campisano, C.J., Patel, B.A., Premjit, N., Fleagle, J.G., Patnaik, R., 2020b. New Middle Miocene ape (Primates: Hylobatidae) from Ramnagar, India fills major gaps in the hominoid fossil record. Proc. R. Soc. B. 287, 20201655.

Harrison, T., 2013. Catarrhine origins. In: Begun, D.R. (Ed.), A Companion to Paleoanthropology. Blackwell Publishing, Chichester, pp. 376–396.

Harrison, T., Gu, Y., 1999. Taxonomy and phylogenetic relationships of Early Miocene catarrhines from Sihong, China. J. Hum. Evol. 37, 225–277.

Harrison, T., van der Made, J., Ribot, F., 2002. A new middle Miocene pliopithecid from Sant Quirze, northern Spain. J. Hum. Evol. 42, 371–377.

Harrison, T., Zhang, Y., Wei, G., Sun, C., Wang, Y., Liu, J., Tong, H., Huang, B., Xu, F., 2020. A new genus of pliopithecoid from the late Early Miocene of China and its implications for understanding the paleozoogeography of the Pliopithecoidea. J. Hum. Evol. 145, 102838.

Ji, X., Harrison, T., Zhang, Y., Wu, Y., Zhang, C., Hu, J., Wu, D., Hou, Y., Li, S., Wang, G., Wang, Z., 2022. The earliest hylobatid from the Late Miocene of China. J. Hum. Evol. 171, 103251.

Macchiarelli, R., Bayle, P., Bondioli, L., Mazurier, A., Zanolli, C., 2013. From outer to inner structural morphology in dental anthropology. The integration of the third dimension in the visualization and quantitative analysis of fossil remains. In: Scott, R.G., Irish, J.D. (Eds.), Anthropological Perspectives on Tooth Morphology: Genetics, Evolution, Variation. Cambridge University Press, Cambridge, 250–277.

Moyà-Solà, S., Köhler, M., Alba, D.M., 2001. *Egarapithecus narcisoi*, a new genus of Pliopithecidae (Primates, Catarrhini) from the Late Miocene of Spain. Am. J. Phys. Anthropol. 114, 312–324.

Nengo, I., Tafforeau, P., Gilbert, C.C., Fleagle, J.G., Miller, E.R., Feibel, C., Fox, D.L., Feinberg, J., Pugh, K.D., Berruyer, C., Mana, S., Engle, Z., Spoor, F., 2017. New infant cranium from the African Miocene sheds light on ape evolution. Nature 548, 169–174.

Olejniczak, A.J., Martin, L.B., Ulhaas, L., 2004. Quantification of dentine shape in anthropoid primates. Ann. Anat. 186, 479–485.

Olejniczak, A.J., Gilbert, C.C., Martin, L.B., Smith, T.M., Ulhaas, L., Grine, F.E., 2007. Morphology of the enamel-dentine junction in sections of anthropoid primate maxillary molars. J. Hum. Evol. 53, 292–301.

Pan, L., Dumoncel, J., de Beer, F., Hoffman, J., Thackeray, J.F., Duployer, B., Tenailleau, C., Braga, J., 2016. Further morphological evidence on South African earliest *Homo* lower postcanine dentition: Enamel thickness and enamel-dentine junction. J. Hum. Evol. 96, 82–96.

Raventós-Izard, G., Almécija, S., Moyà-Solà, S., Alba, D.M., Arias-Martorell, J., 2023a. The proximal ulnar morphology of the Miocene small-bodied catarrhine *Pliobates cataloniae*. In: Alba, D.M., Marigó, J., Nacarino-Meneses, C, Villa, A. (Eds.), Book of Abstracts of the 20th Annual Conference of the European Association of Vertebrate Palaeontologists, 26th June – 1st July 2023. Palaeovertebrata Special Volume 1-2023, 220–221.

Raventós-Izard, G., Almécija, S., Moyà-Solà, S., Alba, D.M., Arias-Martorell, J., 2023b. Distal ulnar morphology of the Miocene small-bodied catarrhine *Pliobates cataloniae*. In: 13th Annual ESHE Conference. Aarhus, Denmark. ESHE Abstracts, 106.

R Core Team, 2021. R: A Language and Environment for Statistical Computing. R Foundation for Statistical Computing, Vienna.

Rossie, J.B., Hill, A., 2018. A new species of *Simiolus* from the middle Miocene of the Tugen hills, Kenya. J. Hum. Evol. 125, 50–58.

Rossie, J.B., Cote, S.M., 2022. Additional hominoid fossils from the early Miocene of the Lothidok Formation, Kenya. Am. J. Biol. Anthropol. 179, 261–275.

Schlager, S., 2021. Morpho: Calculations and visualizations related to geometric morphometrics. R package version 2.9. http://cran.r-project.org/web/packages/Morpho/index.html.

Skinner, M.M., Wood, B.A., Boesch, C., Olejniczak, A.J., Rosas, A., Smith, T., Hublin, J.-J., 2008. Dental trait expression at the enamel-dentine junction of lower molars in extant and fossil hominoids. J. Hum. Evol. 54, 173–186.

Skinner, M.M., Gunz, P., Wood, A., Boesch, C., Hublin, J.J., 2009. Discrimination of extant *Pan* species and subspecies using the enamel-dentine junction morphology of lower molars. Am. J. Phys. Anthropol. 140, 234–243.

Skinner, M.M., de Vries, D., Gunz, P., Kupczik, K., Klassen, R.P., Hublin, J.-J.c, Roksandic, M., 2016. A dental perspective on the taxonomic affinity of the Balanica mandible (BH-1). J. Hum. Evol. 93, 63–81.

Urciuoli, A., Alba, D.M., 2023. Systematics of Miocene apes: State of the art of a neverending controversy. J. Hum. Evol. 175, 103309.

Urciuoli, A., Zanolli, C., Bouchet, F., Almécija, S., Moyà-Solà, S., Alba, D.M., 2022. Semicircular canal morphology of the Miocene small-bodied catarrhine *Pliobates cataloniae*: Phylogenetic implications. Am. J. Biol. Anthropol. 177 (S73), 187.

Urciuoli, A., Zanolli, C., Fortuny, J., Almécija, S., Schillinger, B., Moyà-Solà, S., Alba, D.M. 2018. Neutron-based computed microtomography: *Pliobates cataloniae* and *Barberapithecus huerzeleri* as a test-case study. Am. J. Phys. Anthropol. 166, 1–7.

Zanolli, C., Bondioli, L., Mancini, L., Mazurier, A., Widianto, H., Macchiarelli, R., 2012. Brief Communications: Two human fossil deciduous molars from the Sangiran Dome (Java, Indonesia): Outer and inner morphology. Am. J. Phys. Anthropol. 147, 472–481.

Zanolli, C., Bondioli, L., Coppa, A., Dean, M.C., Bayle, P., Candilio, F., Capuani, S., Dreossi, D., Fiore, I., Frayer, D.W., Libsekal, Y., Mancini, L., Rook, L., Medin Tekle, T., Tuniz, C., Macchiarelli, R., 2014. The late Early Pleistocene human dental remains from Uadi Aalad and MulhuliAmo (Buia), Eritrean Danakil: Macromorphology and microstructure. J. Hum. Evol. 74, 96–113.

Zanolli, C., Grine, F.E., Kullmer, O., Schrenk, F., Macchiarelli, R., 2015. Brief communication: The Early Pleistocene deciduous hominid molar FS-72 from the Sangiran Dome of Java, Indonesia: A taxonomic reappraisal based on its comparative endostructural characterization. Am. J. Phys. Anthropol. 157, 666–674.

Zanolli, C., Biglari, F., Mashkour, M., Abdi, K., Monchot, H., Debue, K., Mazurier, A., Bayle, P., Le Luyer, M., Rougier, H., Trinkaus, E., Macchiarelli, R., 2019a. A Neanderthal from the Central Western Zagros, Iran. Structural reassessment of the Wezmeh 1 maxillary premolar. J. Hum. Evol. 135, 102643.

Zanolli, C., Kullmer, O., Kelley, J., Bacon, A.M., Demeter, F., Dumoncel, J., Fiorenza, L., Grine, F.E., Hublin, J.J., Anh Tuan, N., Thi Mai Huong, N., Pan, L., Schillinger, B., Schrenk, F., Skinner,

M.M., Ji, X., Macchiarelli, R., 2019b. Evidence for increased hominid diversity in the Early-Middle Pleistocene of Indonesia. Nat. Ecol. Evol. 3, 755–764.

Zanolli, C., Alba, D.M., Begun, D., Bouchet, F., Costeur, L., Dean, C.M., Fortuny, J., Kelley, J., Macchiarelli R, Morita W., Nakatsukasa, M., Rook, L., Urciuoli, A., 2022a. Tracking *Oreopithecus* evolutionary history: Evidence from the enamel-dentine junction morphology. In: Oreopithecus150 a Miocene Hominoid Enshrouded in a 150-years-long Mystery. International Conference. Abstract book.

Zanolli, C., Urciuoli, A., Delgado, M., Davies, T.W., Bouchet, F., Fortuny, J., Beaudet, A., Alba, D.M., Kullmer, O., Skinner, M.M. 2022b. The phylogenetic signal of the enamel-dentine junction of primate molars. Am. J. Phys. Anthropol. 177 (S73), 202.

Zanolli, C., Bouchet, F., Fortuny, J., Bernardini, F., Tuniz, C., Alba, D.M., 2023. A reassessment of the distinctiveness of dryopithecine genera from the Iberian Miocene based on enamel-dentine junction geometric morphometric analyses. J. Hum. Evol. 177, 103326.

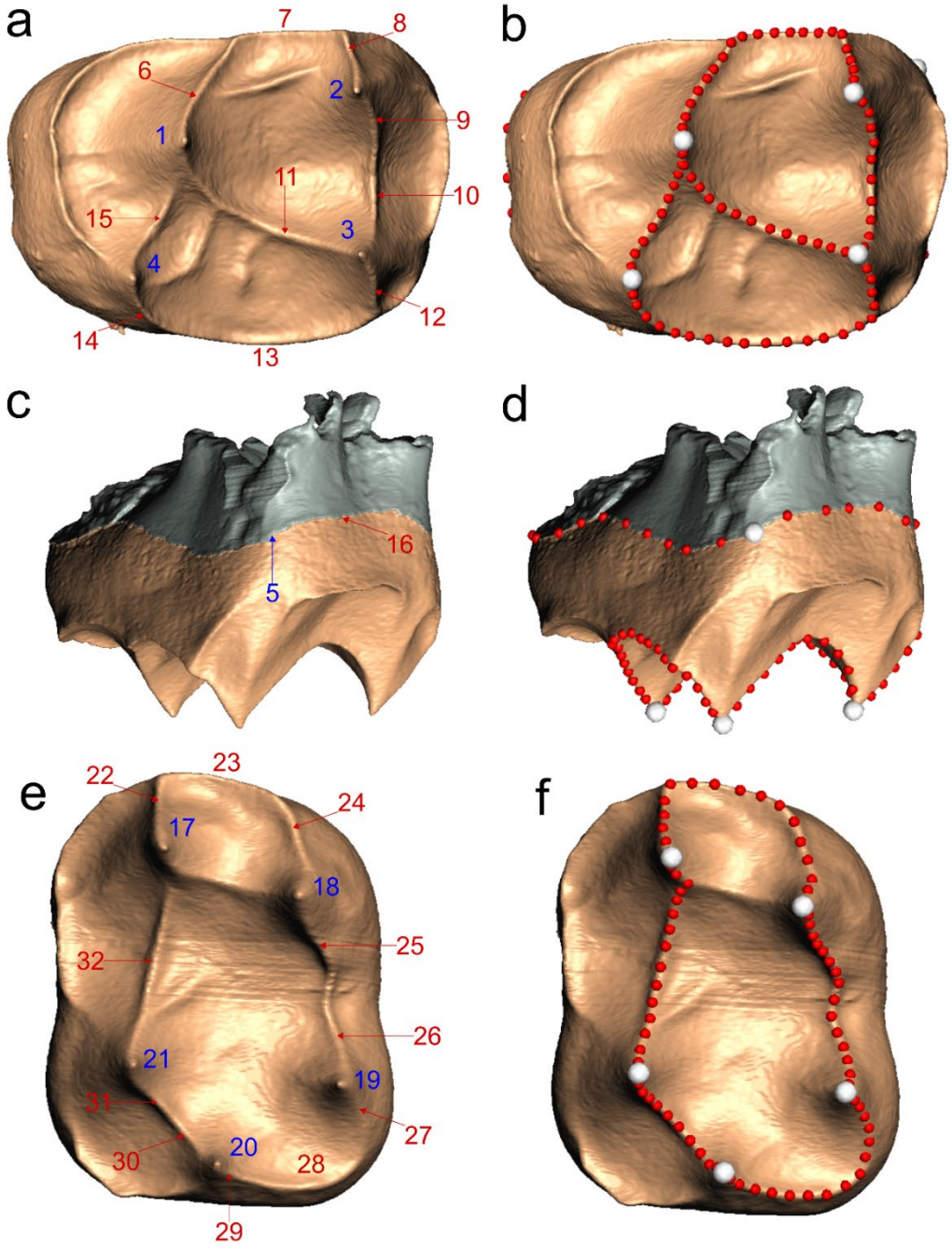


Figure 1. EDJ landmark protocol used for aligning the molar specimens as exemplified in two molars of *Pliobates cataloniae*: a–d) IPS94888, M^2 in occlusal (a–b) and mesiobuccal (c–d) views; e–f) IPS43936, M_1 in occlusal view. The EDJ molar terminology for the dentine horns/cervical landmarks (blue numbers) and crests/marginal ridges/cervical line landmarks (red numbers) used in this study is shown in panels a, c, and e, while the corresponding placement of landmarks (white points) and semilandmarks (red points) is depicted in panels b, d, and f. Legend: 1 = protocone; 2 = paracone; 3 = metacone; 4 = hypocone; 5 = mesiobuccal end of the cervix; 6 = preprotocrista; 7 = mesial marginal ridge; 8 = preparacrista; 9 = postparacrista; 10 = premetacrista; 11 = crista obliqua; 12 = postmetacrista; 13 = distal marginal ridge; 14 = posthypocrista; 15 = prehypocrista; 16 = cervical line; 17 = protoconid; 18 = metaconid; 19 = entoconid; 20 = hypoconulid; 21 = hypoconid; 22 = preprotocristid; 23 = mesial marginal ridge; 24 = premetacristid; 25 = postmetacristid; 26 = pre-entocristid; 27 = postentocristid; 28 = distal marginal ridge; 29 = posthypoconulid cristid (when present); 30 = prehypoconulid cristid; 31 = posthypocristid; 32 = cristid obliqua.

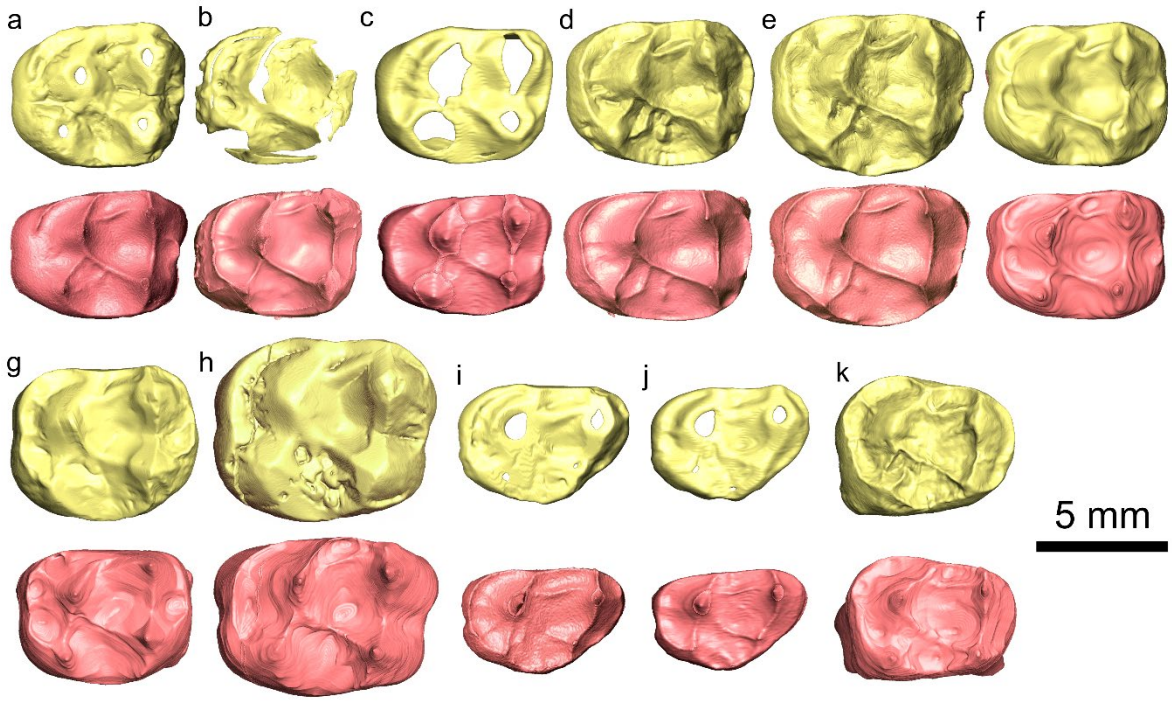


Figure 2. Three-dimensional virtual renderings of the upper molar outer enamel surface (OES) and enamel-dentine junction (EDJ) of *Pliobates cataloniae* and pliopithecoids from the Vallès-Penedès Basin in occlusal view. a–e) *Pliobates cataloniae*: left M^1 (IPS44014; a), right M^1 (IPS100379; reversed; b), right M^2 (IPS58443.1, holotype; reversed; c), left M^2 (IPS94888; d), left M^2 (IPS100384; e); f) *Barberapithecus huerzeleri*: left M^2 (IPS1724e); g) *Pliopithecus canmatensis*: right M^2 (IPS41718; reversed); h) Pliopithecoidea indet. from Sant Quirze: right M^2 (MGSB48874; reversed); i–j) *Pliobates cataloniae*: left M^3 (IPS584443.2, holotype; i), right M^3 (IPS584443.1, holotype; reversed; j); k) *Barberapithecus huerzeleri*: right M^3 (IPS1724f, holotype; reversed). Enamel of some cusps was reconstructed by F.B. for g–h. Dentine horns were reconstructed by F.B. and C.Z. for some specimens (a–c, g–j). The OES (in yellow) and EDJ (in rose) models are depicted in occlusal view as if from the left side (indicated when reversed). Mesial is on top.

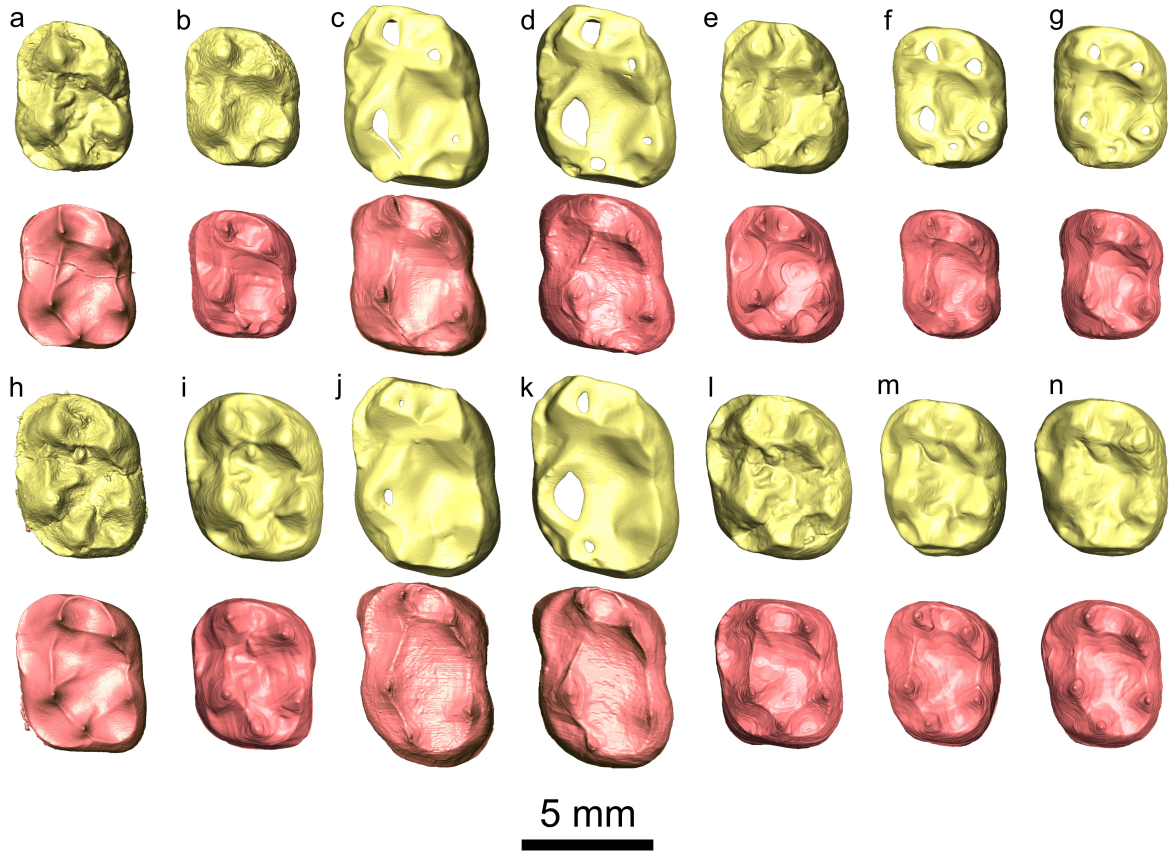


Figure 3. Three-dimensional virtual renderings of the lower molar outer enamel surface (OES) and enamel-dentine junction (EDJ) of *Pliobates cataloniae* and pliopithecoids from the Vallès-Penedès Basin in occlusal view. a) *Pliobates cataloniae*: left M_1 (IPS43936); b) *Barberapithecus huerzeleri*: left M_1 (IPS1724m, holotype); c–d) *Egarapithecus narcisoi*: left (c) and right (reversed; d) M_1 (IPS4575, holotype); e–g) *Pliopithecus canmatensis*: left M_1 (IPS41955; e), left (f) and right (reversed; g) M_1 (IPS41719); h) *Pliobates cataloniae*: left M_2 (IPS43936); i) *Barberapithecus huerzeleri*: right M_2 (IPS1724n, holotype; reversed); j–k) *Egarapithecus narcisoi*: left (j) and right (reversed; k) M_2 (IPS4575, holotype); l–n) *Pliopithecus canmatensis*: right M_2 (IPS41960; reversed; l), left (m) and right (reversed; n) M_2 (IPS41719). Enamel of some cusps was reconstructed by F.B. for e and m–n, and by C.Z. for l. Dentine horns were reconstructed by F.B. and C.Z. for some specimens (c–d, f–g, j–k and m–n). The OES (in yellow) and EDJ (in rose) models are depicted in occlusal view as if from the left side (indicated when reversed). Mesial is on top.

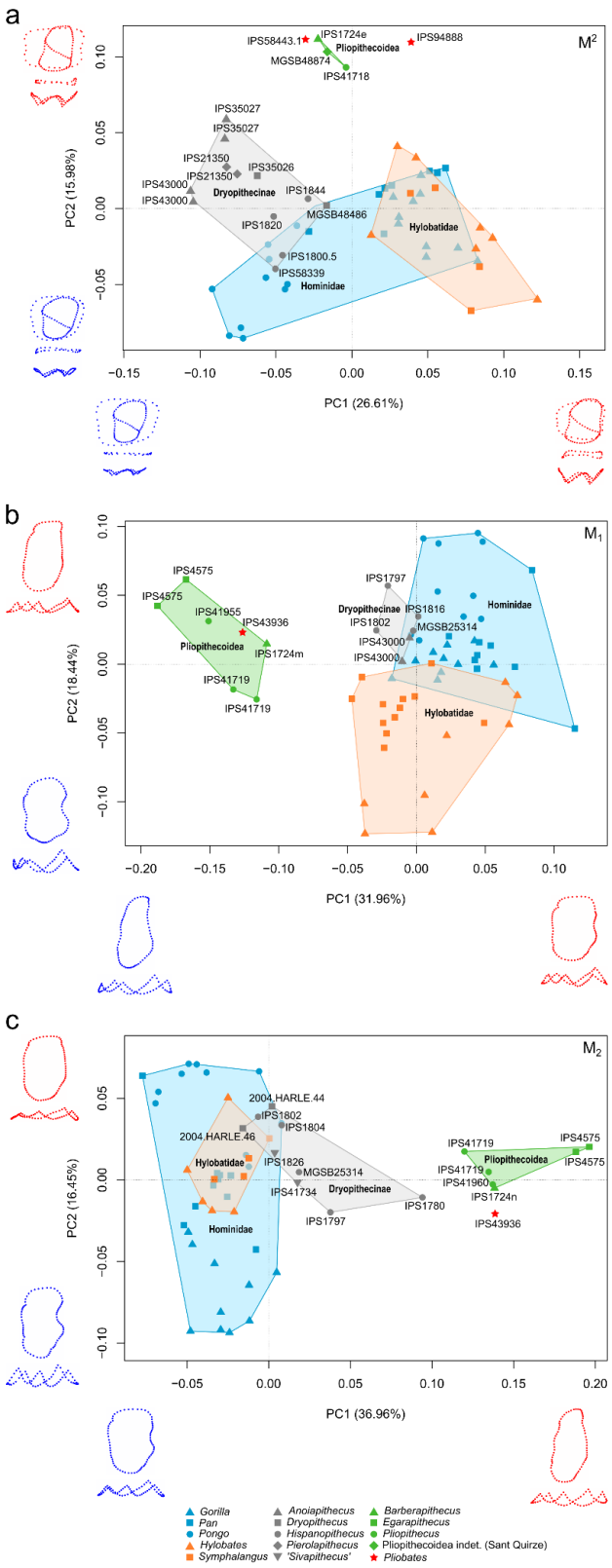


Figure 4. Results of principal component (PC) analyses of upper and lower molar enamel-dentine junction landmark configuration (after Procrustes alignment) for pliopithecoids and hominoids as depicted by bivariate plots of PC2 vs. PC1: a) M^2; b) M_1; c) M_2. The variance explained by each PC is denoted within parentheses. The minimum (blue) and maximum (red) landmark conformations for PC1 and PC2 are illustrated both in occlusal and buccal views along their corresponding axis for each molar position.

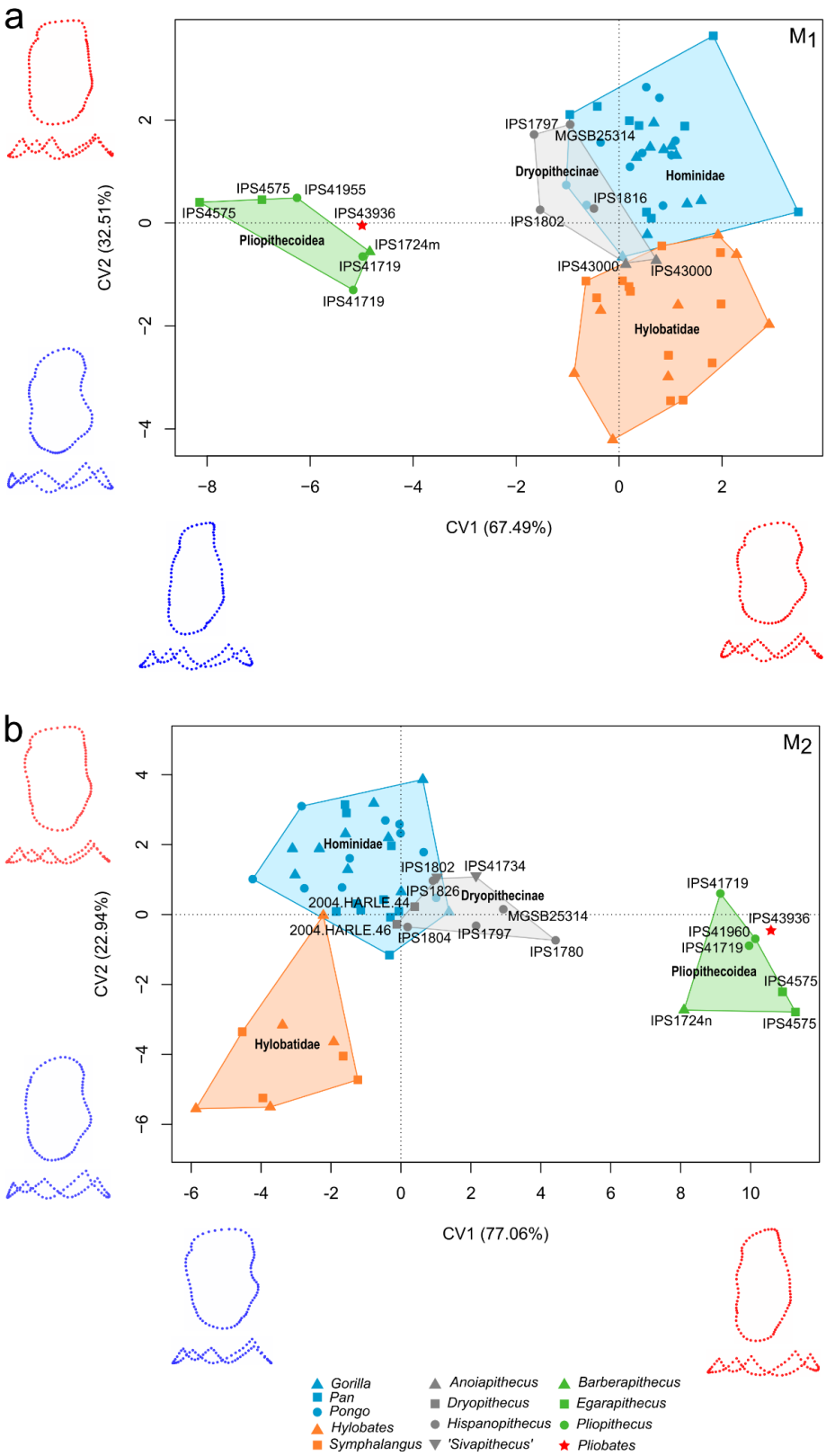


Figure 5. Results of canonical variate (CV) analyses of lower molar enamel-dentine junction landmark configuration (after Procrustes alignment) for pliopithecoids and hominoids as depicted by a bivariate plot of CV2 vs. CV1: a) M_1; b) M_2. The variance explained by each CV is denoted within parentheses. The minimum (blue) and maximum (red) landmark conformations for CV1 and CV2 are illustrated both in occlusal and buccal views along their corresponding axis for each molar position.

Table 1

Molars of *Pliobates cataloniae* analyzed in this study based on µCT data.

Catalog no.	Tooth	Locality[a]	Voxel size (µm)
IPS44014	L M^1	ACM/C5-D1	12
IPS100379	R M^1	ACM/C5-D1	12
IPS94888	L M^2 germ	ACM/C5-D1	12
IPS58443.1[b]	R M^2	ACM/C8-A4	33
IPS100384	L M^2 germ[c]	ACM/C5-D1	12
IPS58443.1[b]	R M^3	ACM/C8-A4	33
IPS58443.2[b]	L M^3	ACM/C8-A4	33
IPS43936	L M_1 germ	ACM/C5-D1	12
IPS43936	L M_2 germ[c]	ACM/C5-D1	12

Abbreviations: L = left; R = right; ACM = Abocador de Can Mata; C5 = Cell 5; C8 = Cell 8; IPS = acronym of the collections of the Institut Català de Paleontologia Miquel Crusafont (formerly Institut de Paleontologia de Sabadell).

[a] Alphanumeric combinations after ACM (separated by a dash) refer to ACM (sub)sectors and localities (see Alba et al., 2022, for further details).

[b] These molars are part of the holotype of the species.

[c] The crowns of these molar germs are not completely formed.

Table 2

Comparative sample of pliopithecoid molars used in this study.

Catalog no.	Tooth	Species	Locality[a]	Scanning source; year[b]	Voxel size (µm)	Reference
IPS1724e[c]	L M^2	*Barberapithecus huerzeleri*	Castell de Barberà	CENIEH; 2022	15.5	This study
IPS1724f[c]	R M^3	*Barberapithecus huerzeleri*	Castell de Barberà	CENIEH; 2022	15.5	This study
IPS1724m[c,d]	L M_1	*Barberapithecus huerzeleri*	Castell de Barberà	ANTARES[e]	7.6	This study
IPS1724n[c]	R M_2	*Barberapithecus huerzeleri*	Castell de Barberà	ANTARES[e]	7.6	Urciuoli et al. (2018)
IPS45757[c]	L M_1	*Egarapithecus narcisoi*	Torrent de les Febulines	CENIEH; 2018	12.0	This study
IPS45757[c]	L M_2	*Egarapithecus narcisoi*	Torrent de les Febulines	CENIEH; 2018	12.0	This study
IPS45757[c]	R M_1	*Egarapithecus narcisoi*	Torrent de les Febulines	CENIEH; 2018	12.0	This study
IPS45757[c]	R M_2	*Egarapithecus narcisoi*	Torrent de les Febulines	CENIEH; 2018	12.0	This study
IPS41718	R M^2	*Pliopithecus canmatensis*	ACM/C4-A1	CENIEH; 2022	12.5	This study
IPS41719	L M_1	*Pliopithecus canmatensis*	ACM/C4-Cb	CENIEH; 2014	19.6	This study
IPS41719	R M_1	*Pliopithecus canmatensis*	ACM/C4-Cb	CENIEH; 2014	19.6	This study
IPS41719	L M_2	*Pliopithecus canmatensis*	ACM/C4-Cb	CENIEH; 2014	19.6	This study
IPS41719	R M_2	*Pliopithecus canmatensis*	ACM/C4-Cb	CENIEH; 2014	19.6	This study
IPS41955	R M_1	*Pliopithecus canmatensis*	ACM/C5-A8	CENIEH; 2014	16.7	This study
IPS41960	L M_2	*Pliopithecus canmatensis*	ACM/C5-A8	ICTP	16.7	This study
MGSB48874	R M^2	Pliopithecoidea indet.	Sant Quirze	CENIEH; 2019	12.5	This study

Abbreviations: L = left; R = right; ACM = Abocador de Can Mata; C4 = Cell 4; C5 = Cell 5; MGSB = Museu de Geologia del Seminari de Barcelona, Spain; CENIEH = Centro Nacional de Investigación sobre la Evolución Humana, Burgos, Spain; IPS = acronym of the collections of the Institut Català de Paleontologia Miquel Crusafont (formerly Institut de Paleontologia de Sabadell), Sabadell, Spain; ANTARES = cold neutron beam port of the reactor of the Forschungs-Neutronenquelle Heinz Maier-Leibnitz (FRM II), Garching bei München, Germany; ICTP = Multidisciplinary Laboratory of the 'Abdus Salam' International Centre for Theoretical Physics, Trieste, Italy.

[a] Alphanumeric combinations after ACM (separated by a dash) refer to ACM (sub)sectors and localities (see Alba et al., 2022, for further details).

[b] Because some specimens were scanned independently over the years at the CENIEH, the acquisition date is specified for each of these specimens.

[c] These molars are part of the holotype of the species.

[d] IPS1724m was scanned along with IPS1724n, but only the latter is reported in Urciuoli et al. (2018). However, scanning parameters are the same for both specimens (detailed for IPS1724n in Urciuoli et al. 2018).

[e] These specimens were scanned using neutron-based computed microtomography instead of X-ray computed microtomography.

Table 3

Comparison of main upper molar features of *Pliobates cataloniae* and other studied pliopithecoids at the enamel-dentine junction.

Feature	*Pliobates cataloniae*	*Barberapithecus huerzeleri*	*Pliopithecus canmatensis*	Pliopithecoidea indet. (Sant Quirze)
M^1–M^2 occlusal proportions	Broader than long	Broader than long	Moderately broader than long	Broader than long
M^1–M^2 buccolingual constriction	Moderate to marked	Moderate to marked	Slight	Marked
M^1–M^2 buccal side length relative to lingual	Longer	Longer	Almost the same	Almost the same
Dentine horn shape	Very compressed	Very compressed	Moderately compressed	Moderately compressed
Metacone horn size relative to those of the protocone and paracone	Much smaller	Much smaller	Similar	Similar
Hypocone horn size relative to those of other cusps	Much smaller	Much smaller	Smaller	Smaller
Location of hypocone horn relative to that of the metacone	Moderately distal	Moderately distal	Markedly distal	Moderately distal
Secondary crest of the hypocone horn	Well developed	Variable	Poorly developed	Poorly developed
M^3 occlusal contour	Trapezoidal	Subrectangular	—	—

Table 4

Comparison of main lower molar features of *Pliobates cataloniae* and other studied pliopithecoids at the enamel-dentine junction.

Features	*Pliobates cataloniae*	*Barberapithecus huerzeleri*	*Egarapithecus narcisoi*	*Pliopithecus canmatensis*
Position of the trigonid dentine horns relative to the center of the crown mesiodistal axis	Mesial	Mesial	Markedly mesial	Markedly mesial
Position of the entoconid horn relative to that of the hypoconid	Transversely aligned	Transversely aligned	Distal	Distal
Hypoconulid horn size relative to those of the other cuspids	Smaller	Smaller	Much smaller	Smaller
M_1–M_2 hypoconulid horn position	Median	Median	Towards buccal	Median
Origin of hypoprotocristid from protoconid horn	Distolingual	Distolingual	Distolingual	Lingual
Length and origin of postprotocristid	Short, from hypoprotocristid	Short, from hypoprotocristid	Short, from hypoprotocristid	Long, from protoconid dentine horn
Cristid obliqua orientation	Oblique	Oblique	Very oblique	Mesiodistally aligned
Distal arm of the pliopithecine triangle in M_1	Marked	Poorly developed	Absent	Poorly developed
Mesial arm of the pliopithecine triangle in M_2	Absent	Present	Present	Present
Distal arm of the pliopithecine triangle in M_2	Marked	Marked	Poorly developed	Variable
Mesial fovea	Large	Large	Small	Small
Distal fovea of M_1	Large and semiopen	Small and closed	Large and closed	Small and variably open
Distal fovea of M_2	Large and semiopen	Small and closed	Large and semiopen	Large and variably open

Table 5

Results of permutation tests, given as both probabilities (interpreted as *p*-values) and frequencies (within parentheses)[a] based on a principal component analysis of enamel-dentine junction shape comparing the M^2s of *Pliobates* with those of extant hominoid genera.

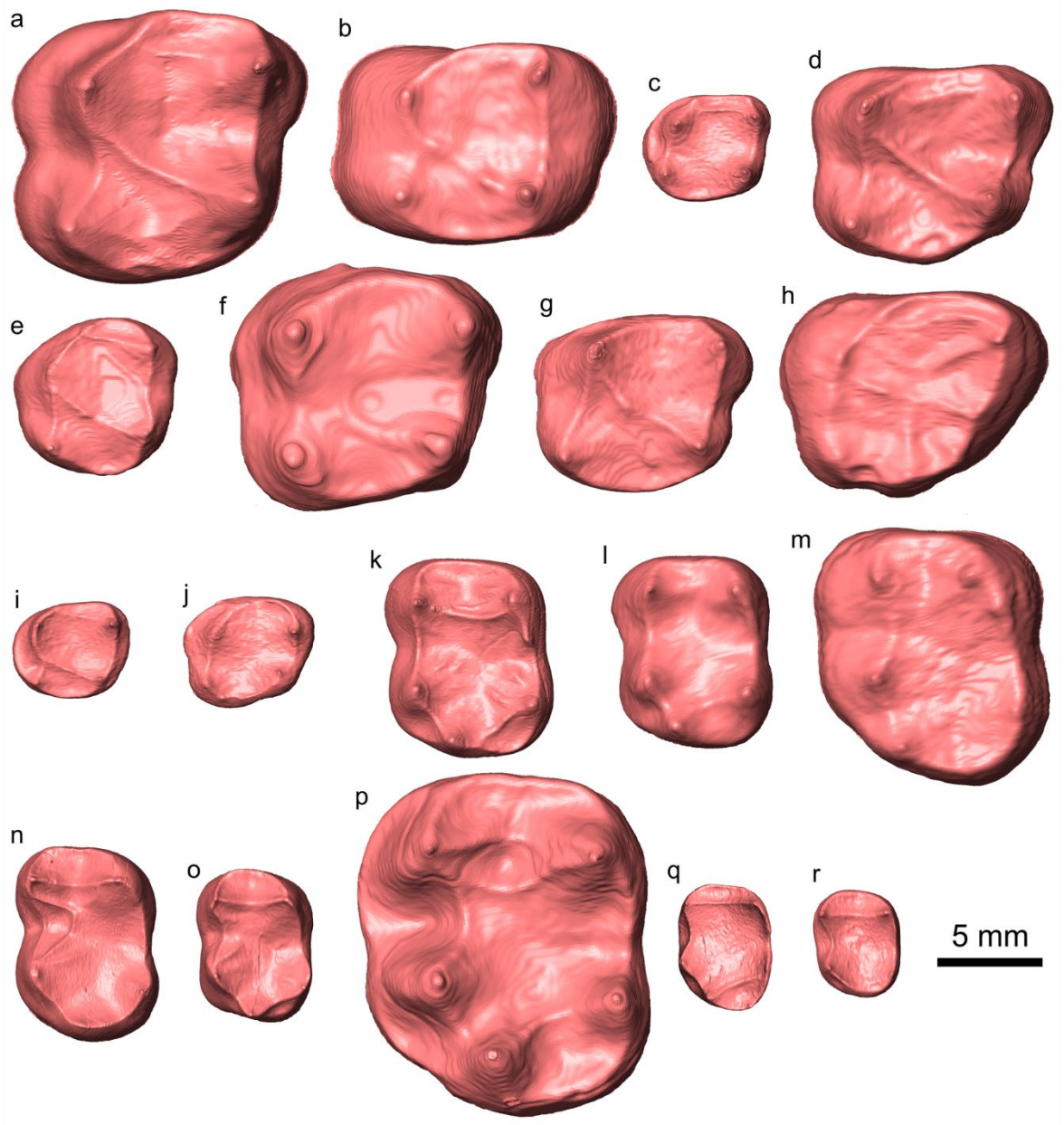
Tooth	M^2
n	2
Gorilla	0.533 (24/45)
Pan	0.400 (18/45)
Pongo	0.778 (35/45)
Hylobates	0.809 (17/21)
Symphalangus	0.500 (3/6)
Hylobatids[b]	0.836 (46/55)

[a] Cases in which *Pliobates* variation is smaller than that displayed by extant hominoid genera. The former therefore exceeds that of extant hominoid genera when $p < 0.05$.

[b] Given that the two analyzed hylobatid genera are represented by small sample sizes for each molar position ($n = 3–7$) only a few combinations are possible. Therefore, permutations were also run with a group including both genera to have more statistical power.

Supplementary Online Material (SOM):

Molar enamel-dentine junction shape of *Pliobates cataloniae* and other Iberian pliopithecoids



SOM Figure S1. Three-dimensional virtual renderings of the enamel-dentine junction (EDJ) of some comparative extant hominoid specimens in occlusal view. a) *Gorilla gorilla*: M^1 (CCEC-50001994); b) *Pongo sp.*: M^1 (IPS10647; reversed); c) *Hylobates sp.*: M^1 (ZMB 7826); d) *Pan troglodytes*: M^2 (AMNH M-167342; reversed); e) *Symphalangus syndactylus*: M^2 (AMNH M-106853); f) *Gorilla gorilla*: M^3 (MCZ 26850; reversed); g) *Pan troglodytes*: M^3 (AMNH M-51204); h) *Pongo sp.*: M^3 (IPS10647); i) *Hylobates muelleri*: M^3 (ZMB 7814; reversed); j) *Hylobates muelleri*: M^3 (ZMB 7826; reversed); k) *Pan troglodytes*: M_1 (CCEC-50002604; reversed); l) *Pan sp.*: M_1 (MHNB 2005.3234; reversed); m) *Pongo sp.*: M_1 (PACEA *Pongo*); n) *Symphalangus syndactylus*: M_1 (AMNH M-100048; reversed); o) *Symphalangus syndactylus*: M_1 (AMNH M-102722; reversed); p) *Gorilla gorilla*: M_2 (AMNH M-167338; reversed); q) *Hylobates funereus*: M_2 (AMNH M-103726); r) *Hylobates funereus*: M_2 (AMNH M-106328). Dentine horns were reconstructed by F.B. and C.Z. for some specimens (c–d, f–g). The EDJ models are depicted in occlusal view as if from the left side (indicated when reversed). Mesial is on top. See Zanolli et al. (2023: SOM Table S2) and SOM Table S4 for details on the extant hominoid specimens.

SOM Table S1.

Digital object identifiers (DOIs) for 3D models of the outer enamel surface (OES) and the enamel dentine junction (EDJ) of *Pliobates cataloniae* molars analyzed in this paper.[a]

Catalog no.	Tooth	Digital objet identifier (DOI)	
		OES	EDJ
IPS58443.1	R M^2	https://doi.org/10.17602/M2/M494194	https://doi.org/10.17602/M2/M494191
IPS58443.1	R M^3	ark:/87602/m4/572451	ark:/87602/m4/572457
IPS58443.2	L M^3	https://doi.org/10.17602/M2/M494200	https://doi.org/10.17602/M2/M494197
IPS43936	L M_1 germ	https://doi.org/10.17602/M2/M494152	https://doi.org/10.17602/M2/M494149
IPS43936	L M_2 germ	https://doi.org/10.17602/M2/M494158	https://doi.org/10.17602/M2/M494155
IPS44014	L M^1	https://doi.org/10.17602/M2/M494173	https://doi.org/10.17602/M2/M494176
IPS94888	L M^2 germ	https://doi.org/10.17602/M2/M494218	https://doi.org/10.17602/M2/M494215
IPS100379	R M^1	https://doi.org/10.17602/M2/M494224	https://doi.org/10.17602/M2/M494221
IPS100384	L M^2 germ	https://doi.org/10.17602/M2/M494230	https://doi.org/10.17602/M2/M494227

Abbreviations: L = left; R = right.

[a] The 3D models of the OES are available from MorphoSource after Bouchet et al. (in press) or after this work in the case of the R M^3 IPS58443.1. The 3D models of the EDJ remain embargoed until further study of the enamel thickness of pliopithecoids is published.

SOM Table S2

Parameters employed for µCT acquisitions of pliopithecoid specimens scanned by X-ray computed tomography in this study. Scanning parameters for all *Pliobates* specimens were reported in Bouchet et al. (in press).

Catalog no.	Species	Scanning source	Voltage (kV)	Current (µA)	Filter	Voxel size (µm)
IPS1724e	*Barberapithecus huerzeleri*	CENIEH	124	125	0.2 mm Cu	15.5
IPS1724f	*Barberapithecus huerzeleri*	CENIEH	124	125	0.2 mm Cu	15.5
IPS45757	*Egarapithecus narcisoi*	CENIEH	125	150	0.2 mm Cu	12.0
IPS41718	*Pliopithecus canmatensis*	CENIEH	124	125	0.2 mm Cu	12.5
IPS41719	*Pliopithecus canmatensis*	CENIEH	124	125	0.2 mm Cu	19.6
IPS41955	*Pliopithecus canmatensis*	CENIEH	124	125	0.2 mm Cu	16.7
IPS41960	*Pliopithecus canmatensis*	ICTP	120	80	1.0 mm Al	16.7
MGSB48874	Pliopithecoidea indet.	CENIEH	124	125	0.2 mm Cu	12.5

Abbreviations: MGSB = Museu de Geologia del Seminari de Barcelona, Spain; CENIEH = Centro Nacional de Investigación sobre la Evolución Humana, Burgos, Spain; IPS = acronym of the collections of the Institut Català de Paleontologia Miquel Crusafont (formerly Institut de Paleontologia de Sabadell), Sabadell, Spain; ICTP = Multidisciplinary Laboratory of the 'Abdus Salam' International Centre for Theoretical Physics, Trieste, Italy.

SOM TABLE S3

Digital object identifiers (DOIs) for 3D models of the outer enamel surface (OES) and the enamel dentine junction (EDJ) of the pliopithecoid molars included in the comparative sample.[a]

Catalog no.	Species	Tooth	DOI	
			OES	EDJ
IPS1724e[b]	*Barberapithecus huerzeleri*	L M^2	ark:/87602/m4/580638	ark:/87602/m4/580635
IPS1724f[b]	*Barberapithecus huerzeleri*	R M^3	ark:/87602/m4/580644	ark:/87602/m4/580641
IPS1724m[b]	*Barberapithecus huerzeleri*	L M_1	ark:/87602/m4/580650	ark:/87602/m4/580647
IPS1724n[b]	*Barberapithecus huerzeleri*	R M_2	ark:/87602/m4/580778	ark:/87602/m4/580775
IPS45757[b]	*Egarapithecus narcisoi*	L M_1	ark:/87602/m4/580784	ark:/87602/m4/580781
IPS45757[b]	*Egarapithecus narcisoi*	L M_2	ark:/87602/m4/580790	ark:/87602/m4/580787
IPS45757[b]	*Egarapithecus narcisoi*	R M_1	ark:/87602/m4/580796	ark:/87602/m4/580793
IPS45757[b]	*Egarapithecus narcisoi*	R M_2	ark:/87602/m4/580802	ark:/87602/m4/580799
IPS41718	*Pliopithecus canmatensis*	R M^2	ark:/87602/m4/580808	ark:/87602/m4/580805
IPS41719	*Pliopithecus canmatensis*	L M_1	ark:/87602/m4/580836	ark:/87602/m4/580833
IPS41719	*Pliopithecus canmatensis*	R M_1	ark:/87602/m4/580848	ark:/87602/m4/580845
IPS41719	*Pliopithecus canmatensis*	L M_2	ark:/87602/m4/580842	ark:/87602/m4/580839
IPS41719	*Pliopithecus canmatensis*	R M_2	ark:/87602/m4/580854	ark:/87602/m4/580851
IPS41955	*Pliopithecus canmatensis*	L M_1	ark:/87602/m4/580814	ark:/87602/m4/580811
IPS41960	*Pliopithecus canmatensis*	R M_2	ark:/87602/m4/580820	ark:/87602/m4/580817
MGSB48874	Pliopithecoidea indet.	R M^2	ark:/87602/m4/580826	ark:/87602/m4/580823

Abbreviations: L = left; R = right.

[a] The 3D models of the OES are available from MorphoSource after this work. The 3D models of the OES remain embargoed until further study of the enamel thickness of pliopithecoids is published.

[b] These molars belong to the holotype of the species.

SOM Table S4

Comparative sample of extant hylobatids.

Specimen	Tooth	Sex	Species	DOI or ARK	MorphoSource ID	Reference
MFN 7814	R M^2	F	*Hylobates muelleri*	—	—	MFN records
MFN 7828	L M^2	M	*Hylobates muelleri*	—	—	MFN records
MFN 46511	R M^2	?	*Hylobates* sp.	—	—	MFN records
MFN 7084	R M^2	?	*Hylobates muelleri*	—	—	MFN records
MFN 7826	L M^2	F	*Hylobates* sp.	—	—	MFN records
MFN 7826	R M^2	F	*Hylobates* sp.	—	—	MFN records
MFN 85396	R M^2	?	*Hylobates* sp.	—	—	MFN records
AMNH M-103725	R M_2	F	*Hylobates funereus*	—	—	MorphoSource
AMNH M-103726	L M_2	M	*Hylobates funereus*	—	—	MorphoSource
AMNH M-106328	L M_2	F	*Hylobates funereus*	—	—	MorphoSource
AMNH M-106781	R M_2	F	*Hylobates abbotti*	—	—	MorphoSource
CCEC 50001913	L M_1	F?	*Hylobates agilis*	—	—	ESRF Database
CCEC 50001913	R M_1	F?	*Hylobates agilis*	—	—	ESRF Database
CCEC 50001914	L M_1	F?	*Hylobates lar*	—	—	ESRF Database
CCEC 50001914	R M_1	F?	*Hylobates lar*	—	—	ESRF Database
MCZ 41411	L M_1	F	*Hylobates lar*	http://doi.org/10.17602/M2/M2959	S1004	MorphoSource
MCZ 41414	L M_1	F	*Hylobates lar*	http://doi.org/10.17602/M2/M2963	S1006	MorphoSource
MCZ 41414	R M_1	F	*Hylobates lar*	http://doi.org/10.17602/M2/M2963	S1006	MorphoSource
MCZ 41452	L M_1	F	*Hylobates lar*	http://doi.org/10.17602/M2/M3011	S1022	MorphoSource
MFN 7826	R M_2	F	*Hylobates* sp.	—	—	MFN records
AMNH M-102724	L M^2	F	*Symphalangus syndactylus*	ark:/87602/m4/M26158	S5810	MorphoSource
AMNH M-102724	R M^2	F	*Symphalangus syndactylus*	ark:/87602/m4/M26158	S5810	MorphoSource
AMNH M-106583	L M^2	F	*Symphalangus syndactylus*	—	S533	MorphoSource
AMNH M-106583	R M^2	F	*Symphalangus syndactylus*	—	S533	MorphoSource
AMNH M-100048	R M_1	M	*Symphalangus syndactylus*	—	S533	MorphoSource
AMNH M-102191	L M_2	F	*Symphalangus syndactylus*	—	—	MorphoSource
AMNH M-102193	L M_1	M	*Symphalangus syndactylus*	—	—	MorphoSource
AMNH M-106582	R M_2	F	*Symphalangus syndactylus*	—	S45457	MorphoSource
AMNH M-102722	R M_1	F	*Symphalangus syndactylus*	—	—	MorphoSource
AMNH M-102722	R M_2	F	*Symphalangus syndactylus*	—	—	MorphoSource
AMNH M-102724	L M_1	M	*Symphalangus syndactylus*	ark:/87602/m4/M26158	S5810	MorphoSource

AMNH M-102724	R M_1	M	*Symphalangus syndactylus*	ark:/87602/m4/M26158	S5810	MorphoSource
AMNH M-102729	R M_2	M	*Symphalangus syndactylus*	—	—	MorphoSource
EA 258	L M_1	?	*Symphalangus syndactylus*	http://doi.org/10.17602/M2/M58633	S15647	MorphoSource
EA 258	R M_1	?	*Symphalangus syndactylus*	http://doi.org/10.17602/M2/M58633	S15647	MorphoSource
Trieste	L M_1	?	*Symphalangus syndactylus*	—	—	TNHM
MCZ 36031	L M_1	M	*Symphalangus syndactylus*	http://doi.org/10.17602/M2/M4444	S1359	MorphoSource
MCZ 36031	R M_1	M	*Symphalangus syndactylus*	http://doi.org/10.17602/M2/M4444	S1359	MorphoSource
MCZ 36032	L M_1	F	*Symphalangus syndactylus*	http://doi.org/10.17602/M2/M4443	S1358	MorphoSource
MCZ 36032	R M_1	F	*Symphalangus syndactylus*	http://doi.org/10.17602/M2/M4443	S1358	MorphoSource

Abbreviations: L = left; R = right; F = female; M = male; ? = unknown sex; AMNH = American Museum of Natural History, New York, USA; AMNH-M = Mammal collection of the AMNH; CCEC = Centre de Conservation et d'Étude des Collections, Musée des Confluences, Lyon, France; EA = Evolutionary Anthropology, Duke University, Durham, USA; ESRF = European Synchrotron Radiation Facility (ESRF heritage database for palaeontology, evolutionary biology and archaeology; http://paleo.esrf.eu); MCZ = Museum of Comparative Zoology, Harvard University, Cambridge, USA; MFN = Museum für Naturkunde - Leibniz Institute for Evolution and Biodiversity Science; TNHM = Trieste Natural History Museum, Trieste, Italy.

SOM Table S5

Classification results of the canonical variate analysis for the specimens included in the a priori-defined groups (percentage results are provided within parentheses), both with and without cross validation.

Tooth	Without cross validation	Hominidae	Hylobatidae	Pliopithecoidea	Total correct[a]
M_1	Hominidae (*n* = 30)	29 (96.7%)	1 (3.3%)	0 (0.0%)	29 (96.7%)
	Hylobatidae (*n* = 20)	0 (0.0%)	20 (100.0%)	0 (0.0%)	20 (100.0%)
	Pliopithecoidea (*n* = 6)	0 (0.0%)	0 (0.0%)	6 (100.0%)	6 (100.0%)
	Total (*n* = 56)	29 (51.8%)	21 (37.5%)	6 (10.7%)	**55 (98.2%)**
M_2	Hominidae (*n* = 30)	30 (100.0%)	0 (0.0%)	0 (0.0%)	30 (100.0%)
	Hylobatidae (*n* = 9)	1 (11.1%)	8 (88.9%)	0 (0.0%)	8 (88.9%)
	Pliopithecoidea (*n* = 6)	0 (0.0%)	0 (0.0%)	6 (100.0%)	6 (100.0%)
	Total (*n* = 45)	31 (68.8%)	8 (17.8%)	6 (13.3%)	**45 (97.8)%**
Tooth	With cross validation	Hominidae	Hylobatidae	Pliopithecoidea	Total correct[a]
M_1	Hominidae (*n* = 30)	27 (90.0%)	3 (10.0%)	0 (0.0%)	27 (90.0%)
	Hylobatidae (*n* = 20)	2 (10.0%)	18 (90.0%)	0 (0.0%)	18 (90.0%)
	Pliopithecoidea (*n* = 6)	0 (0.0%)	0 (0.0%)	6 (100.0%)	6 (100.0%)
	Total (*n* = 56)	29 (51.8%)	21 (37.5%)	6 (10.7%)	**51 (91.1%)**
M_2	Hominidae (*n* = 30)	30 (100.0%)	0 (0.0%)	0 (0.0%)	30 (100.0%)
	Hylobatidae (*n* = 9)	1 (11.1%)	8 (88.9%)	0 (0.0%)	8 (88.9%)
	Pliopithecoidea (*n* = 6)	0 (0.0%)	0 (0.0%)	6 (100.0%)	6 (100.0%)
	Total (*n* = 45)	31 (68.9%)	8 (17.8%)	6 (13.3%)	**44 (97.8%)**

[a] The total of correctly classified specimens is bolded.

SOM Table S6

Classification results for *Pliobates* and dryopithecines from the Vallès-Penedès Basin based on the canonical variate analyses of the M^1 and M^2 enamel-dentine junction shape in the a priori-defined groups.[a]

Catalog no.	Species	M_1 posterior probabilities			M_1 typicality probabilities		
		Hominidae	Hylobatidae	Pliopithecoidea	Hominidae	Hylobatidae	Pliopithecoidea
IPS43936	*Pliobates cataloniae*	<0.01	<0.01	**1.00**	<0.01	<0.01	**0.58**
IPS43000 (L)	*Anoiapithecus brevirostris*	0.20	**0.80**	<0.01	0.16	**0.54**	<0.01
IPS43000 (R)	*Anoiapithecus brevirostris*	0.18	**0.82**	<0.01	0.13	**0.46**	<0.01
MGSB25314	*Hispanopithecus crusafonti*	**1.00**	<0.01	<0.01	**0.26**	<0.01	<0.01
IPS1816	*Hispanopithecus crusafonti*	**0.89**	0.11	<0.01	**0.35**	0.06	<0.01
IPS1797	*Hispanopithecus laietanus*	**1.00**	<0.01	<0.01	**0.09**	<0.01	<0.01
IPS1802	*Hispanopithecus laietanus*	**0.90**	0.10	<0.01	**0.08**	0.01	<0.01
Catalog no.	Species	M_2 posterior probabilities			M_2 typicality probabilities		
		Hominidae	Hylobatidae	Pliopithecoidea	Hominidae	Hylobatidae	Pliopithecoidea
IPS43936	*Pliobates cataloniae*	<0.01	<0.01	**1.00**	<0.01	<0.01	**0.58**
2004.HARLE.44	*Dryopithecus fontani*	**1.00**	<0.01	<0.01	**0.22**	<0.01	<0.01
2004.HARLE.46	*Dryopithecus fontani*	**1.00**	<0.01	<0.01	**0.20**	<0.01	<0.01
MGSB25314	*Hispanopithecus crusafonti*	**1.00**	<0.01	<0.01	<0.01	<0.01	<0.01
IPS1780	*Hispanopithecus laietanus*	0.08	<0.01	**0.92**	<0.01	<0.01	<0.01
IPS1797	*Hispanopithecus laietanus*	**1.00**	<0.01	<0.01	<0.01	<0.01	<0.01
IPS1802	*Hispanopithecus laietanus*	**1.00**	<0.01	<0.01	**0.18**	<0.01	<0.01
IPS1804	*Hispanopithecus laietanus*	**1.00**	<0.01	<0.01	**0.14**	<0.01	<0.01
IPS1826	*'Sivapithecus' occidentalis*	**1.00**	<0.01	<0.01	**0.15**	<0.01	<0.01
IPS41734	*'Sivapithecus' occidentalis*	**1.00**	<0.01	<0.01	0.02	<0.01	<0.01

Abbreviations: R = right; L = left.

[a] Both posterior and typicality probabilities are reported. The former, which add to unity, correspond to the likelihood of belonging to each of the groups defined a priori for a given specimen based on its scores (assuming the fossil specimens must belong to one of these groups). In contrast, typicality probabilities denote the probability of having the given score assuming the specimen belongs to that particular group, and hence indicate if a fossil specimen fits well with the variation of each extant group (rejected when $p < 0.05$). The highest probabilities for each specimen are bolded.

SOM references

Bouchet, F., Zanolli, C., Urciuoli, A., Almécija, S., Fortuny, J., Robles, J.M., Beaudet, A., Moyà-Solà, S., Alba, D.M. (in press). The Miocene primate *Pliobates* is a pliopithecoid. Nat. Commun.

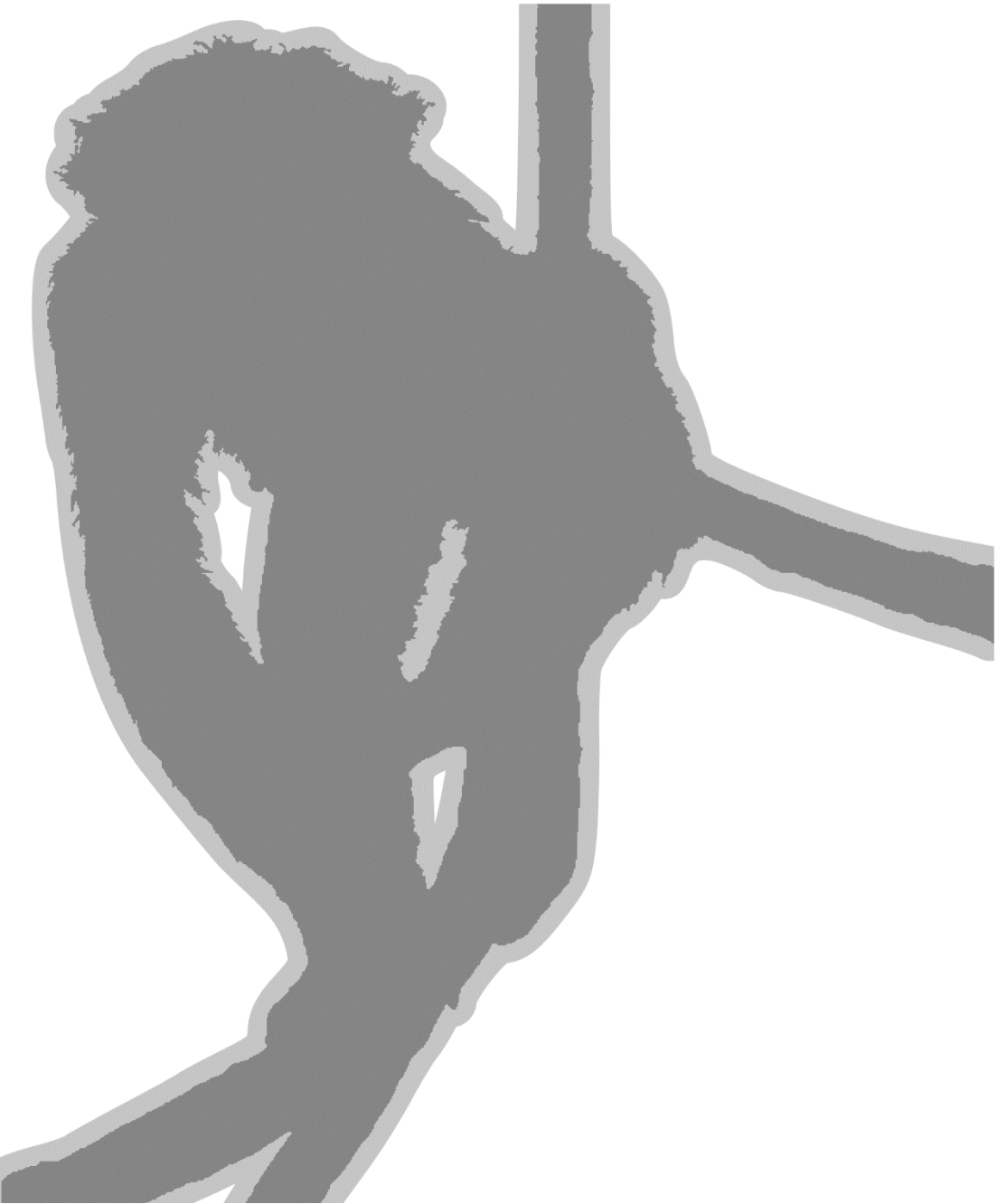
Zanolli, C., Bouchet, F., Fortuny, J., Bernardini, F., Tuniz, C., Alba, D.M., 2023. A reassessment of the distinctiveness of dryopithecine genera from the Iberian Miocene based on enamel-dentine junction geometric morphometric analyses. J. Hum. Evol. 177, 103326.

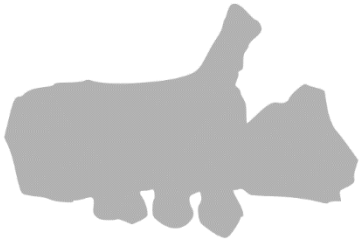


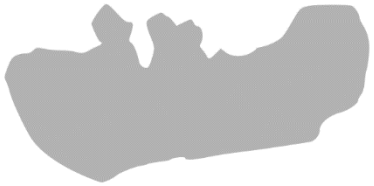


Chapter 6:

Discussion







Chapter 6. Discussion

6.1. Carotid canal morphology

6.1.1. Phylogenetic signal

The carotid canal of catarrhine primates is a bony tube that encloses the internal carotid artery, corresponding to a single and unique branch in adult individuals, the promontory artery (Bugge, 1974; Rosenberger and Szalay, 1980; MacPhee and Cartmill, 1986; Kay et al., 2008; Boyer et al., 2016). This major artery supplies the brain with blood, entering the auditory bulla through the posterior carotid foramen in the petrosal bone and going out into the endocranial space through an internal opening located anteriorly in the pyramidal part of the petrosal (Bugge, 1980; MacPhee and Cartmill, 1986; Kay et al., 2008; Boyer et al., 2016).

Despite its bony nature (Bugge, 1974; Cartmill et al., 1981; MacPhee and Cartmill, 1986; Boyer et al., 2016), the carotid canal is a vessel-related structure and may be thus considered a soft-tissue trait. Given that soft-tissue traits have been proven to be more efficient for primate phylogenetic inference than hard-tissue traits by some studies (Gibbs et al., 2000, 2002; Diogo and Wood, 2011), it is reasonable to expect that carotid canal may be less prone to homoplasy (false homology), and, hence, embed a strong phylogenetic signal. However, only a few previous studies found differences in carotid canal morphology among catarrhine taxa (Shoshani et al., 1996; Ross et al., 1998; Kay et al., 2008; Alba et al., 2015). In terms of carotid canal foramen position in the bulla, the propliopithecoid *Aegyptopithecus* and extant cercopithecoids have a more lateral foramen than *Hylobates* and the propliopithecoid *Catopithecus* (Ross et al., 1998; Kay et al., 2008). The foramen is also more anteriorly located in hylobatids and the pliopithecid *Epipliopithecus* than in other extinct and extant catarrhines (Alba et al., 2015). Regarding canal direction, hylobatids and *Epipliopithecus* have been characterized as having a more anteriorly (i.e., less laterally) directed canal than any other extinct or extant catarrhines (Shoshani et al., 1996; Alba et al., 2015). Alba et al. (2015) further coded *Saadanius* (stem catarrhine), cercopithecoids, and hominids as having a subvertically oriented canal, *Epipliopithecus* and the proconsulid (stem hominoid) *Ekembo* as having an obliquely oriented canal, and hylobatids as having a canal that is parallel to the basioccipital.

Chapter 3 represents the first study to quantitatively assess the orientation, direction, proportions, and course of the carotid canal in a large sample of extant anthropoids and some extinct catarrhines, including *Epipliopithecus*, the victoriapithecid (stem cercopithecoid) *Victoriapithecus*, *Ekembo*, and *Pliobates*. With this aim in mind, an innovative semiautomatic iterative protocol was specifically devised to cut the ends of the 3D canal models, in particular the anterior end, in a comparable manner.

It was necessary to develop a particular protocol because there is clear inter- and intraspecific variation in the ossification of the canal anterior opening. This protocol therefore compensates for such issues by allowing a comparable delimitation and subsequent cutting of the anterior end of the carotid canal in all specimens and all investigated taxa. The use of a simple landmark from which a plane can be computed to—at least—delimit an anatomical structure in a similar manner among specimens from distinct taxa, is an effective approach that could be extended to any morphological sample, when the anatomical structure considered cannot be investigated after a simple segmentation because it is an open structure or because it lacks anatomical boundaries. Simple visual inspections of the shape of the carotid canal (after being comparably cut in such a way) highlight remarkable variation among the different genera of the main extant anthropoid clades, although some patterns can be distinguished.

The quantitative assessment of the carotid canal orientation reported in Chapter 3 ("canal superior orientation") only discriminates extant cercopithecoids from apes (including *Ekembo*), while *Epipliopithecus* shows a hominoid-like condition, and *Victoriapithecus* matches the variation of all extant catarrhine clades. In turn, the canal direction (referred as "canal medial orientation") does not enable the distinction of the main extant catarrhine clades or extinct taxa, except *Ekembo* and *Epipliopithecus*, which only differ from cercopithecoids. Based on the results of this study, the data are not congruent with the qualitative coding and description provided by Alba et al. (2015): for canal orientation, cercopithecoids differ from hominids instead of sharing a similar condition and hylobatids are hominid-like instead of being distinguished from all other catarrhines; *Ekembo* and *Epipliopithecus* do not show a condition of their own but rather match the hominoid variation; and *Victoriapithecus* is not particularly close to extant cercopithecoids than to hominids or hylobatids for this feature. Regarding canal direction, while hylobatids were considered to differ from all other catarrhine taxa in Alba et al. (2015), the results reported in Chapter 3 show this is not the case. Furthermore, it clearly shows the discrimination efficiency of these canal features is very limited. In terms of canal volumetric proportions, the overlap among catarrhine lineages is total and no discrimination is possible. The carotid canal course variation also shows an almost complete overlap between extant catarrhine clades, only with minimal differentiation of great apes from other groups. Among the extinct taxa, all differ from both cercopithecoids and hylobatids, with *Epipliopithecus* differing also from great apes. The complete overlap between hylobatids and cercopithecoids does not support their differences of canal lateral position in the bulla noted in previous studies (Ross et al., 1998; Kay et al., 2008), as both groups cannot be distinguished based on the present results. In turn, the results reported in Chapter 3 lend some support to Alba et al. (2015) regarding foramen anteroposterior position: hylobatids and *Epipliopithecus* exhibit a more anteriorly located foramen—and canal as a whole—than hominids (but not than cercopithecoids).

The phylogenetic signal embedded in carotid canal course is quite strong for the variable that discriminates great apes from other catarrhine clades (canal anteroposterior position on the petrosal). However, since these variables explain an exceedingly small percentage of the total variation of the carotid canal course, it merely suggests that carotid canal course is minimally efficient in distinguishing great apes from other catarrhine primates. Despite of this fact, the results of Chapter 3 on carotid canal orientation and direction permitted adding two cranial characters to the total evidence character-taxon matrix coded at the genus-level in Chapter 4, this way updating (and correcting) the same carotid canal characters previously used in the matrix of Alba et al. (2015).

6.1.2. Phylogenetic implications for *Pliobates*

In its original description, *Pliobates* was coded as having an external carotid foramen anteriorly located as in hylobatids and *Epipliopithecus*, and a rather anteriorly directed canal coupled with a canal orientation parallel to the basioccipital as in hylobatids (Alba et al., 2015). The results of Chapter 3, however, do not concur with this original evaluation. For the foramen location, *Pliobates* rather resembles extant hominids. Most importantly, the canal orientation and direction of *Pliobates* are not uniquely like those of hylobatids and rather match the condition of all hominoids—and *Epipliopithecus*—for the first feature, or of all extant catarrhines for the second one. Finally, *Pliobates* does not have any specific affinities with any extant catarrhine clade in terms of canal volumetric proportions and overall canal course, and is somewhat more primitive (i.e., plesiomorphic for catarrhines) in its canal volumetric proportions. Its canal course condition is in fact most similar to that of the three other Miocene taxa, and *Pliobates* clusters most closely with *Epipliopithecus*. In addition, when ancestral carotid canal course morphotypes are reconstructed for the various catarrhine clades, *Pliobates* appears phenetically closer to the last common ancestor of all crown catarrhines—like the three other Miocene taxa—somewhat more so than *Epipliopithecus*, but less so than *Ekembo* and *Victoriapithecus*. Taken together, the results of Chapter 3 do not support specific affinities in carotid canal direction, orientation, foramen anteroposterior location, or any other canal feature between *Pliobates* and hylobatids, contrary to the original coding of Alba et al. (2015). The phylogenetic interpretation that can be drawn from carotid canal features is rather ambiguous for *Pliobates* but suggests a generalized catarrhine morphology, somewhat plesiomorphic for the canal volumetric proportions but also more derived toward great apes than the three other Miocene taxa (and, in particular, *Epipliopithecus*) in some aspects of the canal course. To sum up, the carotid canal morphology of *Pliobates* is consistent with this taxon being a derived species within a stem catarrhine clade. It should not be expected that a single anatomical structure that does not adequately discriminates among various catarrhine clades gives strong insights into the phylogenetic affinities of a particular taxon among catarrhine primates. Nonetheless, the results of Chapter 3 do not support

particularly close phylogenetic relationships of *Pliobates* with either hominoids (Alba et al., 2015) or pliopithecoids, at least *Epipliopithecus* (Nengo et al., 2017; Gilbert et al., 2020b). If *Pliobates* is interpreted as a pliopithecoid, its more derived canal course toward great apes adds to the plausibility of this Miocene species having evolved some aspects of its morphology convergently with hominoids (Benefit and McCrossin, 2015; Nengo et al., 2017; Gilbert et al., 2020b). In contrast, if interpreted as a hominoid, its more derived canal course condition compared with that of *Ekembo* would support a more derived stem hominoid status for the former (Alba et al., 2015).

6.2. Dental morphology of *Pliobates cataloniae*

6.2.1. Tooth external morphology

Dental morphology is a valuable source of information for primate systematics and is highly diagnostic in pliopithecoids (Andrews et al., 1996; Harrison and Gu, 1999; Harrison 2005, 2013; Begun, 2002, 2017; Harrison et al., 2020; Ji et al., 2022). Most pliopithecoids have been described based on dental material (Begun, 2002; Harrison, 2013; Sankhyan et al., 2017; Harrison et al., 2020), yet some molar positions are unknown for many species. Among those of the genus *Pliopithecus*, no upper molars are available for *Pliopithecus antiquus* or *Pliopithecus bii* (Hürzeler, 1954; Zapfe, 1961a; Wu et al., 2003), the latter being known only from the m2 and m3; the hypodigm of *Pl. canmatensis* does not include any M3 (Alba et al., 2010), whereas for *Pl. piveteaui* this molar locus is the only upper molar known (Ginsburg, 1975). In turn, *Krishnapithecus* was described on the basis of a M3 and two lower molars only (Chopra and Kaul, 1979; Sankhyan et al., 2017), and among the known crouzeliids *Egarapithecus* is known on the basis of the lower molars, *Crouzelia* based on one m1 and two m2s (Ginsburg and Mein, 1980), and *Plesiopliopithecus* on a single m1 (Zapfe, 1960, 1961b; Ginsburg, 1975; Alba and Berning, 2013), but the upper molars are unknown for them all. The fact that no upper molar of *Crouzelia* or *Plesiopliopithecus* have been yet described renders the Mörgen crouzeliine particularly interesting (Heißig, 1999; Seehuber, 2008). This specimen was described as most closely resembling the only crouzeliids known at that time (*Anapithecus* and *Laccopithecus*)—*Barberapithecus* and *Fanchangia* had not been published yet—perhaps representing *Plesiopliopithecus* or *Crouzelia* (Heißig, 1999; Seehuber, 2008). This is not unlikely based on chronostratigraphic and geographic data, as the Mörgen crouzeliine dates to MN9 and comes from Germany, whereas *Plesiopliopithecus lockeri* is from the MN6 of Austria (Trimmelkam; Zapfe, 1960, 1961b; Ginsburg, 1975; Alba and Berning, 2013), and the latest occurrence of *Crouzelia* is dated to MN7+8 in France (Ginsburg and Mein, 1980; Ginsburg, 1986). Unfortunately, the Mörgen crouzeliine has not been included in more recent studies of crouzeliid pliopithecoids (e.g., Alba and Moyà-Solà, 2012; Harrison et al., 2020). As described in Chapter 1, some other isolated pliopithecoid

molars of uncertain taxonomic attribution would also deserve further attention, including the isolated M2 from Sant Quirze (Spain; Harrison, 2002), the M3 from Abocador de Can Mata locality ACM/C3-B2 (Spain; Alba et al., 2012), and the M1 (or M2) from Damiao 01 (China; Zhang and Harrison, 2008).

In the original description of the upper molars of *P. cataloniae*, resemblances with dendropithecids (especially *Micropithecus*) were noted (Alba et al., 2015). These included a markedly convex lingual profile, a moderately developed buccal cingulum, a C-shaped lingual cingulum that does not surround the hypocone, a well-developed and lingually located hypocone, and relatively narrow M1–M2. Differences with *Micropithecus* were also pointed out, including a more developed buccal cingulum, the absence of a hypocone-metacone crest, and a relatively shorter and more trapezoidal M3 (Alba et al., 2015). According to Alba et al. (2015), the upper molars of the holotype of *P. cataloniae* also differ from those of pliopithecoids in having a more convex lingual profile, more peripheral buccal cusps, less developed cingula, narrower proportions in the M1–M2, and a distinct M3 occlusal contour. Gilbert et al. (2020b) supported the view that the broad cheek teeth and quite extensive molar cingula of the holotype are primitive features characteristic of stem catarrhines, particularly pliopithecoids and dendropithecids. These qualitative comparisons are somewhat subjective and dependent on the taxa being compared. For instance, Alba et al. (2015) considered the moderately developed buccal cingulum of the *Pliobates* upper molars to show closest resemblances to *Micropithecus* (to the exclusion of pliopithecoids), whereas Gilbert et al. (2020b) considered a fairly developed buccal cingulum in the upper molars to be a catarrhine symplesiomorphy, generally resembling both pliopithecoids and dendropithecids. Both considerations are not mutually exclusive but illustrate that a more detailed assessment of *Pliobates* dental morphology was necessary.

From the viewpoint of dental morphology, the problem with the original description of *Pliobates* is that only the teeth from the holotype individual, restricted to moderately to very worn upper cheek teeth, were available (Alba et al., 2015). The new dental specimens of *P. cataloniae* from ACM/C5-D1, described in Chapter 4, include less worn maxillary fragments and isolated upper molars that enable a more refined assessment of the dental morphology of *P. cataloniae*, including several tooth loci previously unknown for the species. A female infantile mandible is particularly diagnostic, as it shows the morphology of the deciduous lower premolars and permanent first and second lower molars. In Chapter 4, the teeth of *Pliobates* are compared with those of hominoids, dendropithecids, pliopithecoids, and Oligocene stem catarrhines, including quantitative comparisons with other Miocene stem taxa (dendropithecids and pliopithecoids) and a differential diagnosis relative to pliopithecoids. Indeed, the dental material of *Pliobates* shows most of the dental synapomorphies of the Pliopithecoidea (Andrews et al., 1996; Harrison and Gu, 1999; Harrison, 2013; Harrison et al., 2020; Ji et al., 2022): I1 slightly mesiodistally waisted toward the cervix, M2 considerably larger

than the M1, lower incisors relatively high-crowned, slender, and waisted toward the cervix, and lower molars relatively long and bearing a pliopithecine triangle.

Following the dental descriptions and comparisons provided in Chapter 4, *Pliobates* is considered here to be a stem catarrhine. However, contrary to some previous assertions (Alba et al., 2015; Gilbert et al., 2020b), it is considered a pliopithecoid. Regarding the similarities with dendropithecids (in particular, *Micropithecus clarki*) and the differences with pliopithecoids previously noted by Alba et al. (2015), a more detailed evaluation can be made based on the comparisons performed in Chapter 4 and literature published after 2015 (Pickford et al., 2017a, 2017b, 2021; Sankhyan et al., 2017; Harrison et al., 2020). The possession of a C-shaped lingual cingulum that does not surround the hypocone and a relatively narrow (i.e., moderately broad) M1–M2 occlusal contour is not exclusive to *Pliobates* and *M. clarki* and can be found in some other pliopithecoids and dendropithecids. In particular, the former feature is present in *Anapithecus*, *Barberapithecus*, *Fanchangia, Laccopithecus*, *Pl. canmatensis*, *Pl. platyodon*, *Pl. zhanxiangi*, Pliopithecoidea indet. from Sant Quirze, Anapithecinae indet. from Damiao 01, and Crouzeliinae indet. from Mörgen. In turn, the latter feature is present in *Dendropithecus macinnesi* (M2), *Simiolus enjiessi*, *Anapithecus*, *Dionysopithecus* (here *Dionysopithecus shuangouensis*) (M1), *Fanchangia*, *Laccopithecus*, *Pl. canmatensis* (M2), Pliopithecoidea indet. from Sant Quirze, Anapithecinae indet. from Damiao 01, and Crouzeliinae indet. from Mörgen. Regarding the markedly convex lingual profile, some specimens of *M.* clarki show such a convex profile (e.g.., NAP IV UMP 64-02 [holotype], NAP V 103’06, KNM-ZP 01670) but others are less convex, even showing some degree of buccolingual waisting at crown midlength (e.g., NAP IV 59’14, NAP IV 71’19, NAP V 21’20). The upper molars from the holotype *P. cataloniae* holotype show a markedly convex lingual profile but exhibit some degree of buccolingual waisting, more marked lingually than buccally, whereas most of the specimens from ACM/C5-D1 show a less convex lingual profile (IPS43758, IPS100379, IPS100384) and/or a somewhat more pronounced buccolingual waisting (IPS44014, M2 of IPS43758, IPS100384). Compared with other dendropithecids and pliopithecoids, a number of M1s and M2s of *M. clarki* and *Pliobates* (especially the molars of IPS58443, IPS44014, IPS100384) show a more markedly convex lingual profile than those of *D. macinnessi*, *S. enjiessi*, pliopithecids, Pliopithecoidea indet. from Sant Quirze, and most dionysopithecids (but see PA 1045, PA 1046), but not than those of *Anapithecus*, *Barberapithecus*, most specimens of *Fanchangia*, Anapithecinae indet. from Damiao 01, and Crouzeliinae indet. from Mörgen. The comparisons with crouzeliids are less evident as they generally have a more pronounced buccolingual waisting lingually. However, *Anapithecus, Barberapithecus* (M1), some specimens of *Fanchangia* (V18115.31, V18115.48, V 18115.51), Anapithecinae indet. from Damiao 01, and Crouzeliinae indet. from Mörgen are at least comparable to, or have more markedly convex lingual profiles than, *Pliobates*. In turn, regarding the M3, a lingual cingulum that does not surround the hypocone is a feature common to all

dendropithecids and pliopithecoids, except *Epipliopithecus*, dinoysopithecids, and Pliopithecidae indet. from ACM/C3-B2. The M3 of *Pliobates* is actually relatively broad, differing from that of *M. clarki* in this regard and, in terms of occlusal proportions, most closely approaches those of pliopithecids, *Barberapithecus*, *Fanchangia*, and *Krishnapithecus*. The convexity of the M3 lingual profile in *Pliobates* M3 is neither particularly similar to that of *M. clarki* and, while it is more marked than in *Anapithecus*, *Barberapithecus*, *Epipliopithecus*, *Laccopithecus, Pl. platyodon*, and Pliopithecidae indet. from ACM/C3-B2, it is rather similar to that of some *D. macinnesi* specimens, dinoysopithecids, *Fanchangia,* and *Pl. zhanxiangi*.

Pliobates M3 is most distinctive as a result of its trapezoidal occlusal outline, which can be found in the holotype of *M. clarki* (NAP IV UMP 64-02), but not in other M3 specimens of the species (e.g., KNM-ZP 01670, NAP IV 221'08, NAP V 130'15). Overall, the trapezoidal outline of *Pliobates* M3 differs from that of pliopithecoids and dendropithecids except *D. macinnesi*, and particularly *Fanchangia*. In the M1–M2, the hypocone is very lingually located in *Pliobates* and *M. clarki*, more so than in *D. macinnesi*, *S. enjiessi*, dionysopithecids, pliopithecids, *Barberapithecus*, *Laccopithecus*, and *Fanchangia*, but similarly than in *Anapithecus*, Pliopithecoidea indet. from Sant Quirze, Anapithecinae indet. from Damiao 01, and Crouzeliinae indet. from Mörgen. The buccal cingulum is actually better developed in *M. clarki* than in *Pliobates*, which is more similar in this regard to *Anapithecus*, *Fanchangia*, Anapithecinae indet. from Damiao 01, and Crouzeliinae indet. from Mörgen. In the M3, the hypocone is rather aligned with the protocone in all pliopithecoids (except Pliopithecidae indet. from ACM/C3-B2), including *Pliobates*, as well as in *D. macinnesi* and *S. enjiessi*, but not in *M. clarki* and Pliopithecidae indet. from ACM/C3-B2 in which it is located more lingually. In turn, the buccal cingulum of *Pliobates* M3 is as developed as in *M. clarki*, but also *D. macinnesi*, *S. enjiessi*, pliopithecids, *Laccopithecus*, *Fanchangia*, and *Krishnapithecus*. Alba et al. (2015) further described the hypocone of *Pliobates* M1–M2 as being well developed but taking into account the material from ACM/C5-D1 the hypocone appears smaller than the other cusps in the least worn molars. For that reason, in Chapter 4 the hypocone size of *Pliobates* M1–M2 is described as small, and the apparent variation in this regard is attributed to differential enamel wear and/or differences in enamel thickness (see below). Regarding M1–M2 proportions, *Pliobates* molars are relatively narrower than those of *D. shuangouensis* (M1), *Platodontopithecus*, *Epipliopithecus*, *Pl. canmatensis* (M1), *Pl. platyodon*, *Pl. zhanxiangi*, and *Barberapithecus* (but not than those of *Anapithecus*, *D. shuangouensis* M2, *Fanchangia*, *Laccopithecus*, *Pl. canmatensis* M2 those of other pliopithecoids). Finally, Alba et al. (2015) noted the more peripheral buccal cusps and less developed cingula of *Pliobates* upper molars compared to pliopithecoids. Both features are somewhat dependant, as narrower cingula result in cusps that are closer to the crown edges, at least in taxa without marked crown flare, as is generally the case of pliopithecoids. The buccal cingulum in the M1–M2 of *Pliobates* is indeed less developed (and the cusps are more peripheral) than in

dionysopithecids, pliopithecids, *Barberapithecus* and *Laccopithecus*, but not than in *Anapithecus*, *Fanchangia*, Pliopithecoidea indet. from Sant Quirze, Anapithecinae indet. from Damiao 01, and Crouzeliinae indet. from Mörgen. In turn, the buccal cingulum of the M3 is less developed than in dionysopithecids, *Anapithecus*, *Barberapithecus*, *Laccopithecus*, and Pliopithecidae indet. from ACM/C3-B2, but not than in pliopithecids and *Fanchangia*. The development of the lingual cingulum in the upper molars (especially M1 and M2) of *Pliobates* is as variable as the development of the hypocone (see above), so that in the most worn molars the cusps appear less compressed and the lingual cingulum somewhat narrower (which might also reflect differences of enamel thickness, as discussed in Chapters 4 and 5). In Chapter 4, the lingual cingulum of *Pliobates* M1–M2 is described as broad, similarly to that of dionysopithecids, *Epipliopithecus*, and *Anapithecus*; in the M3, in contrast, the cingulum is narrower than in all pliopithecoids, except *Fanchangia* (which was not published when *Pliobates* was described).

The results of the quantitative and qualitative comparisons in Chapter 4 show that the dental morphology of *Pliobates* most closely resembles that of the crouzeliine pliopithecoids, particularly the crouzeliine from Mörgen as well as *Plesiopliopithecus* and *Crouzelia*, while displaying a unique combination of features supporting its distinction at the genus rank. The *Pliobates* P4 and M1 are remarkably similar to those of the Mörgen crouzeliine, whereas the m1 and m2 more closely resemble those of *Plesiopliopithecus* and *Crouzelia*. More detailed descriptions focusing on the Mörgen crouzeliine and comparisons with other pliopithecoids would be required to give it a precise taxonomic attribution. However, the fact that *Pliobates* most closely resembles the Mörgen crouzeliine, as well as *Crouzelia* and *Plesiopliopithecus*, has implications for the systematics of crouzeliines as a whole: if the Mörgen crouzeliine was conspecific with *P. cataloniae*, it would extend both the chronostratigraphic range and geographical distribution of the species. However, if enough differences with *Pliobates* were found, it could still represent a species of *Crouzelia* or *Plesiopliopithecus*. More material from this locality, ideally lower molars, would be required to provide an attribution to genus and species rank for the Mörgen crouzeliine.

Traditionally, the most cited synapomorphy of the Pliopithecoidea is the presence of a pliopithecine triangle. Its occurrence and development generally increase from m1 to m3, but both parameters are variable among taxa. In dionysopithecids, the mesial arm is present—but variably-developed—in almost all (*Dionysopithecus*) or all (*Platodontopithecus*) m1s, while the distal arm is present in all (*Dionysopithecus*) or almost all (*Platodontopithecus*) m1s; the triangle is better defined (i.e., both arms more well-developed) in m2 and m3 (Harrison and Gu, 1999). In *Pliopithecus* the triangle is well-developed in m2 and m3 whereas in m1 both arms are generally not distinct, i.e., rudimentary (Begun, 2002; Alba et al., 2010). In *Epipliopithecus* there is no triangle in m1; in only one m2 a mesial arm is present, and a distal arm is vestigial; in m3 only the distal arm is distinct (Zapfe, 1961a). In *Anapithecus*, the presence of both arms is variable in m1 and m2 while in m3 the

triangle is generally well-developed (Begun, 2002; Nargolwalla et al., 2005). In *Barberapithecus*, the distal arm is distinct in all three molars and the mesial arm is vestigial in m1, reduced to a tubercle in m2 and distinct in m3 (Alba and Moyà-Solà, 2012). In *Crouzelia*, the distal arm is absent from the m1, and the mesial arm is present in *C. rhodanica* only, while in the m2 (*C. auscitanensis*) both arms are distinct (Ginsburg and Mein, 1980). In *Egarapithecus* molars, tooth wear prevents a proper evaluation of the occurrence and development of the pliopithecine triangle (Moyà-Solà et al., 2001). However, an inspection at the enamel-dentine junction (EDJ) level reveals that the triangle is sometimes present (see below). In *Fanchangia*, the triangle is always well-defined in all three molars (Harrison et al., 2020). In *Krishnapithecus*, the triangle is absent in m1 and only incipient (i.e., both arms poorly developed) in m2 (Sankhyan et al., 2017). In *Laccopithecus* the triangle only occurs rarely, especially on m3, being constituted by a poorly developed mesial arm whereas the distal arm is absent or vestigial (Ji et al., 2022). In *Plesiopliopithecus* (m1 only), only the mesial arm is present (Zapfe, 1961b). Following the descriptions provided in Chapter 4, *Pliobates* shows a very marked distal arm of the pliopithecine triangle in both m1 and m2, but completely lacks the mesial arm. Considering the details about the pliopithecine triangle given above, *Pliobates* most closely approximates the condition of *Barberapithecus* in this regard and further adds to the variation of this structure known in pliopithecoids.

6.2.2. Molar enamel-dentine junction

Chapter 5 reports for the first-time extensive data on pliopithecoid upper and lower molar 3D EDJ morphology, as compared with that of hominoids and *Pliobates*. Molar EDJ shape has been proven to embed strong phylogenetic information in various catarrhine lineages including extant apes, hominins, cercopithecoids, or fossil catarrhines such as *Oreopithecus* (e.g., Skinner et al., 2009, 2016; Macchiarelli et al., 2013; Beaudet et al., 2016; Pan et al., 2016; Fortuny et al., 2021; Zanolli et al., 2012, 2014, 2019, 2022a, 2022b, 2023). The results of Chapter 5 lend support to the usefulness of this structure and of geometric morphometric analyses for resolving taxonomical and phylogenetic questions, further showing that this kind of analyses are perfectly applicable to other extinct catarrhines. Based on the EDJ, pliopithecoids are clearly discriminated from hominoids as a whole, while among the latter, extant hylobatids can also be distinguished from extant hominids, although to a lesser extent (dryopithecines overlap with extant great apes).

Chapter 5 aims to test among three competing phylogenetic hypotheses regarding *Pliobates*, namely being a pliopithecoid, a hominoid, or a hylobatid. Unfortunately, no µCT scans are yet available for dendropithecids, and the pliopithecoid sample used in Chapter 5 is limited to those Iberian taxa for which the same molar loci as the ones available for *Pliobates* (M1–M3 and m1–m2) are preserved (*Barberapithecus*, *Egarapithecus*, *Pl. canmatensis*, Pliopithecoidea indet. from Sant

Quirze). The descriptions and comparisons of *Pliobates* molar EDJ—including multivariate analyses and group membership probabilities—concur with the evaluation of its dental morphology at the outer enamel surface (OES), showing that is shows closest affinities to pliopithecoids. Among the investigated pliopithecoids, *Pliobates* more closely resembles crouzeliids and particularly *Barberapithecus* in the occlusal morphology of its molar EDJ. An important result is that the visual inspection of the pliopithecoid molar OES and EDJ allows refining the evaluation of the pliopithecine triangle development in *Egarapithecus*. In the m1, a distal arm is incipient, nearly indistinguishable, at the OES, but is indistinct at the EDJ; in the m2, the distal arm is somewhat more distinct (than in the m1) at the OES, whereas at the EDJ both the mesial and distal arms can be distinguished, more clearly in the right antimere. The m3 was not included in Chapter 5 since it is not preserved in *Pliobates*. However, based on personal observations, both arms are well-defined at both the OES and EDJ, though very worn at the former level. This shows that μCT scans, through the segmentation of the OES, can be helpful for better visualizing particular occlusal features in specimens affected by wear, and that coupled with the EDJ, allow more detailed descriptions of the overall occlusal morphology.

Some degree of variation observed at the OES of *Pliobates* upper molars (especially the M2) was noted in Chapter 4, including differences in cusps compression and crest sharpness, lingual cingulum development, and hypocone size and shape. This apparent variation is not reflected at the EDJ, supporting the view that it is most probably attributable to differential enamel wear and/or intraspecific differences in enamel thickness. In any case, results of Chapter 5 fail to reject the hypothesis that the hypodigm of *P. cataloniae* might include more than one taxon. All specimens attributed to *P. cataloniae* from both localities ACM/C8-A4 and ACM/C5-D1 are thus considered to represent a single genus and species.

6.3. Cladistic analyses

6.3.1. Dental and cranial analyses

Chapter 4 presents a first cladistic analysis based on a newly compiled taxon-character matrix of dental data, which is the most comprehensive dental matrix published for pliopithecoids so far. It includes *P. cataloniae*, most pliopithecoid species (see above), three species representing each of the three genera included in the family Dendropithecidae (sensu Harrison, 2002)—namely, *D. macinnesi*, *M. clarki*, and *S. enjiessi*—the stem cercopithecoid *Victoriapithecus macinnesi*, the stem hominoid *Ekembo heseloni*, and the Oligocene stem catarrhines *Saadanius hijazensis* and *Aegyptopithecus zeuxis*, with the latter used as outgroup. The objective of this analysis at the species level was to decipher the precise phylogenetic relationships of *Pliobates* among pliopithecoids on

the basis of dental characters, as dental descriptions and comparisons support a crouzeliid status for this taxon. While the sole consideration of pliopithecoids would have been sufficient to clarify this point, the inclusion of some dendropithecids, stem catarrhines, and crown catarrhines makes the results more reliable since the topology recovered for this analysis is in agreement with the general consensus on the systematic status of these taxa: *S. hijazensis* is recovered as a stem catarrhine (Zalmout et al., 2010; Stevens et al., 2013; Alba et al., 2015), pliopithecoids as a clade of stem catarrhines less derived than dendropithecids (Delson, 1977; Szalay and Delson 1979; Fleagle, 1984; Harrison 1987, 2005, 2013; Andrews et al., 1996; Harrison and Gu 1999; Begun 2002, 2017; Stevens et al., 2013; Nengo et al., 2017; Rossie and Hill, 2018; Gilbert et al., 2020a; Urciuoli et al., 2021a; Ji et al., 2022), dendropithecids as a clade of stem catarrhines (more derived than pliopithecoids; Delson and Andrews, 1975; Fleagle and Simons, 1978; Szalay and Delson 1979; Harrison, 1982, 1987, 2002, 2005, 2010, 2013, 2017; Andrews, 1985; Fleagle, 1986; Nengo et al., 2017; Gilbert et al., 2020a), and *V. macinnesi* and *E. heseloni* as crown catarrhines (e.g., Harrison, 1987; Stevens et al., 2013; Alba et al., 2015; Nengo et al., 2017; Rossie and Hill, 2018; Gilbert et al., 2020a).

The analysis recovers the monophyly of both dionysopithecids and crouzeliids and resolves rather well the internal phylogeny of those latter. As supported by a qualitative assessment of its dental morphology, *Pliobates* is recovered by the cladistic analysis as a pliopithecoid nested within a crouzeliine clade including *Crouzelia* and *Plesiopliopithecus* (Fig. 6.1). Accordingly, the family Pliobatidae erected by Alba et al. (2015) is considered in Chapter 4 a junior synonym of the Crouzeliidae. A new classification for pliopithecoids, based on the results of this cladistic analysis of dental features (Fig. 6.1) and updating the one recently published by Harrison et al. (2020; see also Ji et al., 2022) is provided. Since the original description of *Barberapithecus* by Alba and Moyà-Solà (2012), crouzeliids are generally subdivided into two clades, currently distinguished at the subfamily rank (Harrison et al., 2020): Crouzeliinae Ginsburg and Mein, 1980 including *Crouzelia*, *Plesiopliopithecus*, and *Fanchangia* (Alba et al., 2012; Harrison et al., 2020); and Anapithecinae Alba and Moyà-Solà, 2012, including *Anapithecus*, *Egarapithecus*, and *Laccopithecus* (Alba and Moyà-Solà, 2012; Harrison et al., 2020). *Barberapithecus* was described as an anapithecine by Alba and Moyà-Solà (2012) but reassigned to crouzeliines by Harrison et al. (2020). In Chapter 4, *Fanchangia* is considered an anapithecine instead of a crouzeliine because it is more closely related to *Anapithecus* than *Crouzelia*, being recovered as the most basal anapithecine. *Krishnapithecus*, which was not included in the cladistic analysis of Harrison et al. (2020), branches off as the sister taxon of *Laccopithecus* (i.e., it is also recovered as an anapithecine). Until recently, *Krishnapithecus* was included in the monotypic family Krishnapithecidae (Sankhyan et al., 2017; Harrison et al., 2020; Ji et al., 2022), until Ji et al. (2022) provisionally placed the genus *Kapi*—formerly described by Gilbert et al. (2020a)—as the sister taxon of *Krishnapithecus* within the same family. *Kapi* was originally described by Gilbert et al. (2020a) as a stem hylobatid more derived than

Yuanmoupithecus. However, owing to the suite of similar occlusal features to *Krishnapithecus* and the incipient development of the mesial arm of the pliopithecine triangle, it was reinterpreted as a specialized pliopithecoid (Ji et al., 2022). The latter authors, however, only analyzed three other genera customarily recognized as pliopithecoids (*Epipliopithecus*, *Krishnapithecus*, and *Laccopithecus*). *Krishnapithecus* was recovered as the sister taxon of *Laccopithecus* within pliopithecoids in four out of the six most parsimonious trees obtained (Ji et al., 2022). The systematic placement of *Krishnapithecus* in Chapter 4 as an anapithecine is therefore not at odds with the results of Ji et al. (2022), but it implies that Krishnapithecidae must be considered a junior synonym of Crouzeliidae. Further analyses are required to clarify the exact phylogenetic position of *Kapi*, but some features—such as the presence of a mesial arm of the pliopithecine triangle (albeit only incipiently developed, which is not uncommon in pliopithecoids), the broad buccal cingulid, the relatively long mesial fovea, and the small hypoconulid—are characteristic of all or some pliopithecoid taxa, so that this taxon is likely a derived pliopithecoid. In turn, the indeterminate species from Mörgen is recovered as a crouzeliine, but its precise phylogenetic relationships remain unresolved. As mentioned before, further descriptions and comparisons, and ideally the recovery of lower molars, would be required to provide an attribution to genus and species rank for this material.

The Pliopithecidae are not recovered as a monophyletic group and their internal phylogeny is not resolved (most species are recovered in a polytomy with dionysopithecids and crouzeliids). In fact, pliopithecids appear paraphyletic because *Pl. antiquus* branches off as a stem crouzeliid (i.e., it is more closely related to crouzeliids than other pliopithecids are). However, given abundant morphological evidence that *Pl. antiquus* is most closely related to other *Pliopithecus* species (Hürzeler, 1954; Zapfe, 1961a; Harrison et al., 1991; Begun, 2002; Alba et al., 2010; Harrison, 2013; personal observations), this species is provisionally retained within pliopithecids in the systematic classification favored in Chapter 4. Interestingly, pliopithecids have been recovered as paraphyletic in other cladistic analyses, with *Epipliopithecus* forming a clade with *Laccopithecus* instead of *Pliopithecus* (Stevens et al., 2013; Nengo et al., 2017; Gilbert et al., 2020a), and it has been previously suggested that they might constitute a paraphyletic assemblage (Begun, 2002).

A second taxon-character matrix at the genus level is presented in Chapter 4. It comprises less pliopithecoid taxa but a wider representation of stem catarrhines, especially hominoids, to better test the original phylogenetic hypothesis that *Pliobates* is a stem hominoid. Apart from the dental features, which were adapted from the first taxon-character matrix, both cranial and postcranial features were also considered. This most comprehensive matrix builds primarily on the taxa investigated in Alba et al. (2015)—with some minor improvements—as well as the cranial and postcranial characters coded by these authors, since their cladistic analysis is the only that recovered *Pliobates* as a stem hominoid.

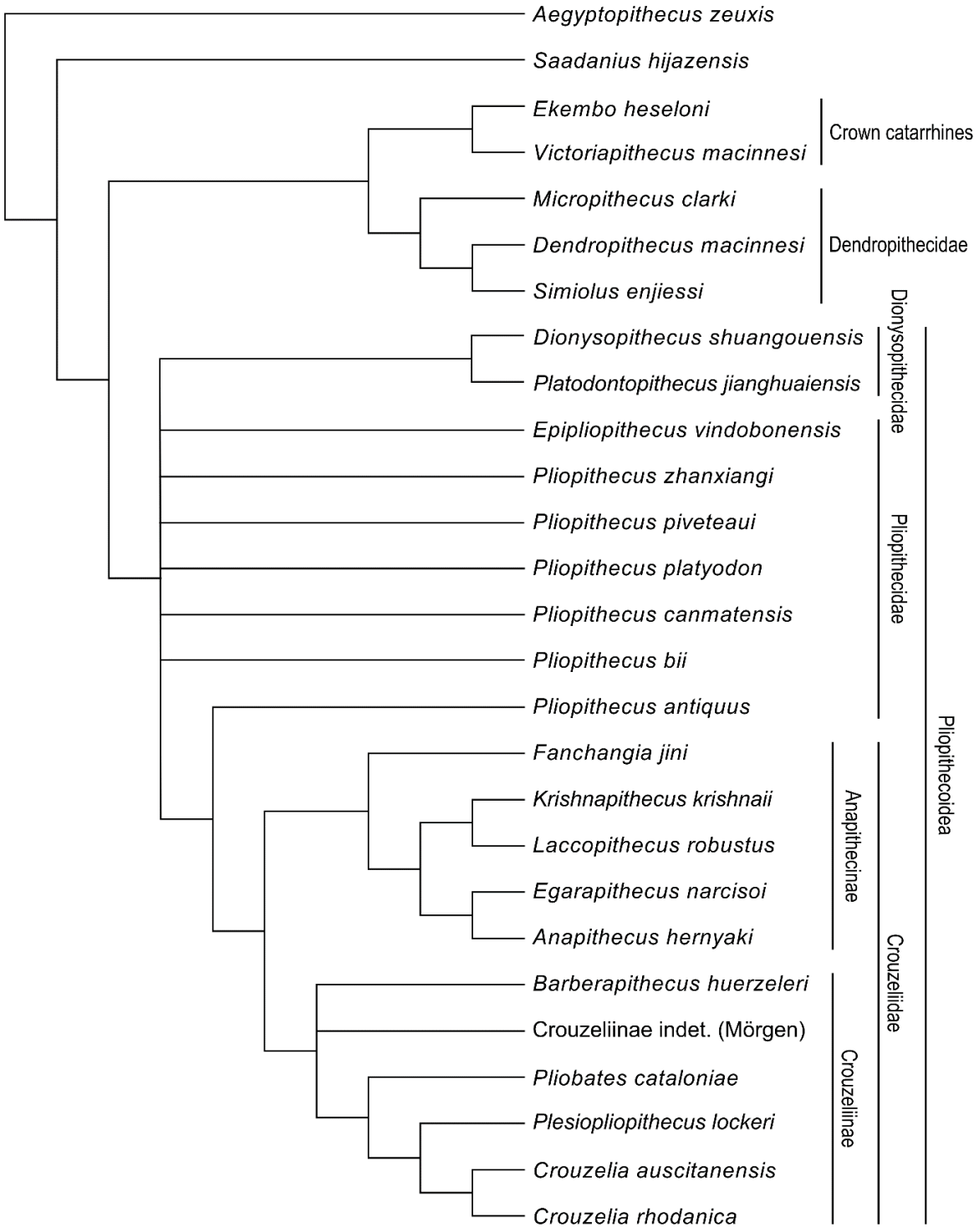


Figure 6.1. Phylogenetic relationships of pliopithecoids including *Pliobates*. Strict consensus cladogram derived from the most parsimonious trees based on a taxon-character data matrix of dental characters (see Chapter 4 for further details).

Both the dental and craniodental analyses at the genus level generally agree with the dental analysis at the species level. In particular, pliopithecoids are recovered as a clade of stem catarrhines less derived than dendropithecids, pliopithecids as a paraphyletic assemblage more basal than dionysopithecids (congruent with the results of Harrison et al., 2020), *Pliobates* as a crouzeliid more

derived than *Barberapithecus* but less so than *Plesiopliopithecus* + *Crouzelia*, nested within a monophyletic Crouzeliidae, and *Victoriapithecus* and *Ekembo* as crown catarrhines (stem cercopithecoid and hominoid, respectively). *Epipliopithecus* is more derived than *Pliopithecus* in both analyses, contra Alba and Moyà-Solà (2014), who rather suggested the opposite due to the retention of an entepicondylar foramen on the distal humerus of *Epipliopithecus*. Both analyses further recover the monophyly of cercopithecoids and hominoids, although in the dental one *Gorilla* and *Hylobates* are incorrectly placed, and only in the craniodental analysis the crown hominoid clade is correctly resolved. The results of the dental analysis at the genus level differ from those of the species-level analysis in the placement of *Anapithecus*, which branches off between *Pliobates* and *Plesiopliopithecus* + *Crouzelia*, and the recovery of dendropithecids as a paraphyletic assemblage of stem cercopithecoids. While this placement of *Anapithecus* can be simply attributed to the absence of any other anapithecine taxon in the analysis and the general small number of pliopithecoid taxa compared to the original dental analysis at the species level, the recovery of dendropithecids as cercopithecoids is considered unlikely because it stems from some purported synapomorphies recovered by the analyses (a high-crowned I2, a P3 shorter to subequal in length to P4, a M1–M2 with a lingual cingulum surrounding the hypocone or showing clear distal style(s), and a long mesiobuccal honing face on p3) that have most probably evolved convergently in both groups. It is nonetheless worth noting that the recovery of dendropithecids as paraphyletic is not uncommon in phylogenetic studies (Rae, 1999; Rossie and MacLatchy, 2006; Zalmout et al., 2010; Nengo et al., 2017; Rossie and Hill, 2018; Rasmussen et al., 2019; Gilbert et al., 2020a; Ji et al., 2022) and that some authors further note that cercopithecoids more basal than *Victoriapithecus* would be difficult to discriminate from (African) stem catarrhines (Rossie and MacLatchy, 2006).

6.3.2. Postcranial analyses

The postcranial analysis at the genus level reported in Chapter 4 excludes *Saadanius* as well as *Dionysopithecus*, *Plesiopliopithecus*, and *Crouzelia*, because of the large amount of missing data in these taxa. Still, it does not resolve the phylogeny of pliopithecoids, dendropithecids, or cercopithecoids. Only the monophyly of crown hominoids is recovered, and *Pliobates* branches off as a stem hominoid, but not *Ekembo*, supporting the suspicion that crown hominoid-like postcranial features were acquired independently in *Pliobates*. In any case, based on these results, postcranial features alone are not informative enough about the phylogeny of catarrhines, and appear useful only for resolving the monophyly of crown hominoids.

The combination of postcranial + craniodental features (total evidence) results in a well-resolved topology with only a few exceptions. The molecular phylogeny of crown hominoids is recovered, with the two Iberian dryopithecines branching off as stem hominids (as in Alba et al., 2015 and Pugh,

2022). The phylogenetic relationships between *Ekembo* and cercopithecoids are not resolved; however, since they are recovered as more basal than dendropithecids, pliopithecoids, and crown hominoids, it implies that dendropithecids and pliopithecoids are recovered as stem hominoid taxa in this analysis. As in the dental analysis at the species level, *Pliobates* appears closely related to crouzeliids (it is more derived than *Barberapithecus* and branches off before *Plesiopliopithecus* + *Crouzelia*). However, dendropithecids and pliopithecoids are recovered as successive paraphyletic assemblages of stem hominoids, as in Alba et al. (2015). This is probably attributable to the large amount of missing data in both groups and, in the case of pliopithecoids, to the fact that ape-like postcranial features of *Pliobates* artifactually pull the whole pliopithecoid clade toward crown hominoids.

6.3.3. Evolutionary implications

It is argued in Chapter 4 that the total evidence analysis is less reliable for inferring the phylogenetic relationships of *Pliobates* among catarrhines than the dental and craniodental analyses because of multiple postcranial homoplasies between *Pliobates* and hominoids. This is mainly illustrated by the fact that the postcranial-only analysis does not resolve the phylogeny of any clade except crown hominoids, whereas *Pliobates* is recovered as a stem hominoid, so that the hominoid-like postcranial features of *Pliobates* alone are pulling it toward the crown hominoid clade. All cladistic analyses except that including postcranial features recover *Pliobates* as nested within crouzeliids, with pliopithecoids constituting a clade of stem catarrhines. This indicates that the inclusion of postcranial features in the analyses, as a result of multiple convergences between hominoids and *Pliobates*, not only artifactually pulls *Pliobates* but other pliopithecoids (because of their craniodental similarities) toward crown hominoids. Other previous studies have reported contradictory results between cladistic analyses based on craniodental vs. postcranial features in hominoids (Pugh, 2022), with implications for the stem hominoid vs. stem hominid status of multiple Middle to Late Miocene taxa (see discussion in Urciuoli and Alba, 2023). This discrepancy is attributable to the presence of postcranial derived specializations (for suspensory and other orthograde behaviors) acquired independently in hylobatids and hominids (Thenius, 1981; Larson, 1998; Pugh, 2022; Urciuoli and Alba, 2023). Something similar probably applies to the Late Miocene ape *Oreopithecus*, which appears much more derived toward crown hominids postcranially than craniodentally (Pugh, 2022; Alba et al., 2024a). The hypothesis that hylobatids and hominids appear too closely related in previous cladistic analysis, due to postcranial convergences (Urciuoli and Alba, 2023) is further reinforced by the fact that the pongine *Sivapithecus* and the dryopithecine *Pierolapithecus* have a more primitive postcranium than expected based on the condition of extant hominids (Pilbeam et al., 1990; Moyà-Solà et al., 2004; Almécija et al., 2009; Morgan et al., 2015).

This is in line with the view that the numerous crown hominoid-like specializations for orthograde behaviors (including suspensory ones) possessed by *Pliobates* evolved convergently in this taxon, explaining the divergent results obtained by different analyses, depending on their emphasis on various anatomical regions. Finally, the possibility that postcranial features related to orthograde behaviors are homoplastic not only among various hominoid lineages, but also in some stem catarrhines such as *Pl. canmatensis* (Alba and Moyà-Solà, 2014) and especially *Pliobates* is further supported by the fact that some of these features are also present in more distantly related primate taxa (Erikson, 1963; Tuttle, 1975; Cartmill and Milton, 1977; Jungers, 1980; Sarmiento, 1995; Jungers et al., 1997; Larson, 1998; Hunt, 2016).

Based on the results presented in Chapter 3 and, especially, Chapters 4 and 5, it is concluded that *P. cataloniae* is a derived member of the Pliopithecoidea, most closely related to the small-bodied crouzeliids *Plesiopliopithecus* and *Crouzelia* from Europe. This conclusion is in agreement with previous suggestions (Benefit and McCrossin, 2015; Gilbert et al., 2020b) that *Pliobates* is a pliopithecoid convergent with apes, and further agrees with the recovery of this species as such in some cladistic analyses that put lesser emphasis on the derived postcranial features of *Pliobates* (Nengo et al., 2017; Gilbert et al., 2020a). It is noteworthy to remark that the results of Chapter 3 indicate that the carotid canal morphology of *Pliobates* agrees with the general catarrhine morphotype and shows no particular resemblances with that of hylobatids (contra Alba et al., 2015). Rather the contrary, in some specific features *Pliobates* appears more derived than *Epipliopithecus* toward the condition of great apes, which in all probability reflects an independent development. Similar conclusions have been reached based on the preliminary study of the semicircular canals of the inner ear (Urciuoli et al., 2022). The results reported in Chapter 3 and Urciuoli et al., (2022) do not specifically support a close phylogenetic relationship between *Pliobates* and *Epipliopithecus*, but this is probably because the latter is the sole pliopithecoid included in these studies. These anatomical areas are unknown for other pliopithecoids such as crouzeliids, which would probably show closest similarities in both carotid canal and inner ear morphology. As noted above, similarities in carotid canal morphology between *Pliobates* and hominids were likely acquired convergently, like some previously noted basicranial similarities (lack of a postglenoid foramen, fusion of the postglenoid process with the tympanic portion of temporal bone, large and occlusally visible jugular foramen, foramen ovale located laterally and well anteriorly to the Eustachian aperture, and moderately long common crus of the inner ear; Alba et al., 2015; Urciuoli et al., 2022).

Even more relevant for our current understanding of catarrhine evolution is the ectotympanic morphology of *Pliobates*. This taxon displays a short tubular and incompletely ossified ectotympanic that is most similar to that of *Epipliopithecus*, despite being slightly longer and more ossified. This supports a more derived status for *Pliobates* as compared with *Epipliopithecus* within pliopithecoids. The same applies to the propliopithecoid *Aegyptopithecus*, for which some specimens suggest an

incipient development of a tube, as compared to the more plesiomorphic condition (completely annular ectotympanic) of the older *Catopithecus* (Simons et al., 2007). Both configurations, however, are more primitive than that of crown catarrhines (cercopithecoids and hominoids), consistent with a stem catarrhine status for both pliopithecoids and propliopithecoids (Harrison, 1987; Rasmussen, 2002). Another stem catarrhine, *Saadanius*, is customarily regarded as the sister taxon to dendropithecids + crown catarrhines mainly because of its tubular ectotympanic—i.e., more derived than that of propliopithecoids and pliopithecoids (although the condition of dendropithecids in this regard is unknown)—and also because of its relatively broad molars (intermediate between those of propliopithecoids + pliopithecoids and those of dendropithecids + proconsulids; Zalmout et al., 2010; Harrison, 2013). However, in Chapter 4 *Saadanius* is recovered as a very basal stem catarrhine (except *Aegyptopithecus*, which is used as outgroup)—i.e., less derived than both pliopithecoids and dendropithecids—in all analyses where it is included. Interestingly, this systematic position recovered for *Saadanius* is the same as in all four cladograms of Zalmout et al. (2010), in three of the four cladograms of Stevens et al. (2013), and in the cladistic analysis of Alba et al. (2015). If the results reported in Chapter 4 for *Saadanius* are correct, this would imply that its tubular ectotympanic would have independently evolved from that of crown catarrhines. This interpretation is in line with the more recent results of Urciuoli et al. (2022) showing that the semicircular canal morphology of *Saadanius* inner ear is as plesiomorphic as that of *Aegyptopithecus*, and hence less derived than that of *Epipliopithecus* and *Pliobates*. Indeed, both stem cercopithecoids (*Victoriapithecus*) and stem hominoids (*Ekembo*) display an ectotympanic somewhat more plesiomorphic than that of extant representatives of both clades, suggesting some independent evolution of the tubular ectotympanic between these groups as well (Alba et al., 2015).

Some hylobatid-like features of the *Pliobates* face (i.e., broad interorbital distance, short face, low zygomatic roots; Alba et al., 2015) are also found in *Epipliopithecus* (Zapfe, 1961a), nyanzapithecids (stem hominoids; Nengo et al., 2017; Alba et al., 2024a), the small-bodied catarrhines from East Africa *Micropithecus* (Fleagle and Simons, 1978) and *Lomorupithecus* (Rossie and MacLatchy, 2006), and even *Oreopithecus* (Nengo et al., 2017; Alba et al., 2024a). In fact, an interorbital distance similar to that of hylobatids can also be found in some *Aegyptopithecus*, *Afropithecus*, *Anoiapithecus*, and *Ouranopithecus* specimens (Pugh et al., 2023), while the nyanzapithecid *Turkanapithecus* show the highest value for this trait (Pugh et al., 2023). In turn, *Pliobates* zygomatic root height is most similar to that of hylobatids, *Anapithecus*, and macaques, and is greater than that of Oligocene stem catarrhines, pliopithecids, and dendropithecids (Alba et al., 2015). In any case these hylobatid-like features are likely homoplastic among the above-mentioned taxa (Nengo et al., 2017; Pugh et al., 2023), since both the stem and crown hominoid last common ancestors might have had a more great ape-like face (Pugh et al., 2023). Similarly, the horizontal and moderately long nasals and frontalized orbits of *Pliobates* are traits shared with crown hominoids (Alba et al., 2015), and most probably

evolved convergently in both lineages. The fact that the nasals are more horizontal and the orbits more frontalized in *Pliobates* than in *Epipliopithecus* (Alba et al., 2015) is however consistent with a more derived status of *Pliobates* within pliopithecoids. Finally, the almost vertical orbits (relative to the Frankfurt plane) of *Pliobates* are shared with macaques, crown hominoids, and *Epipliopithecus* (Alba et al., 2015), so that this particular trait is also homoplastic among some catarrhine lineages.

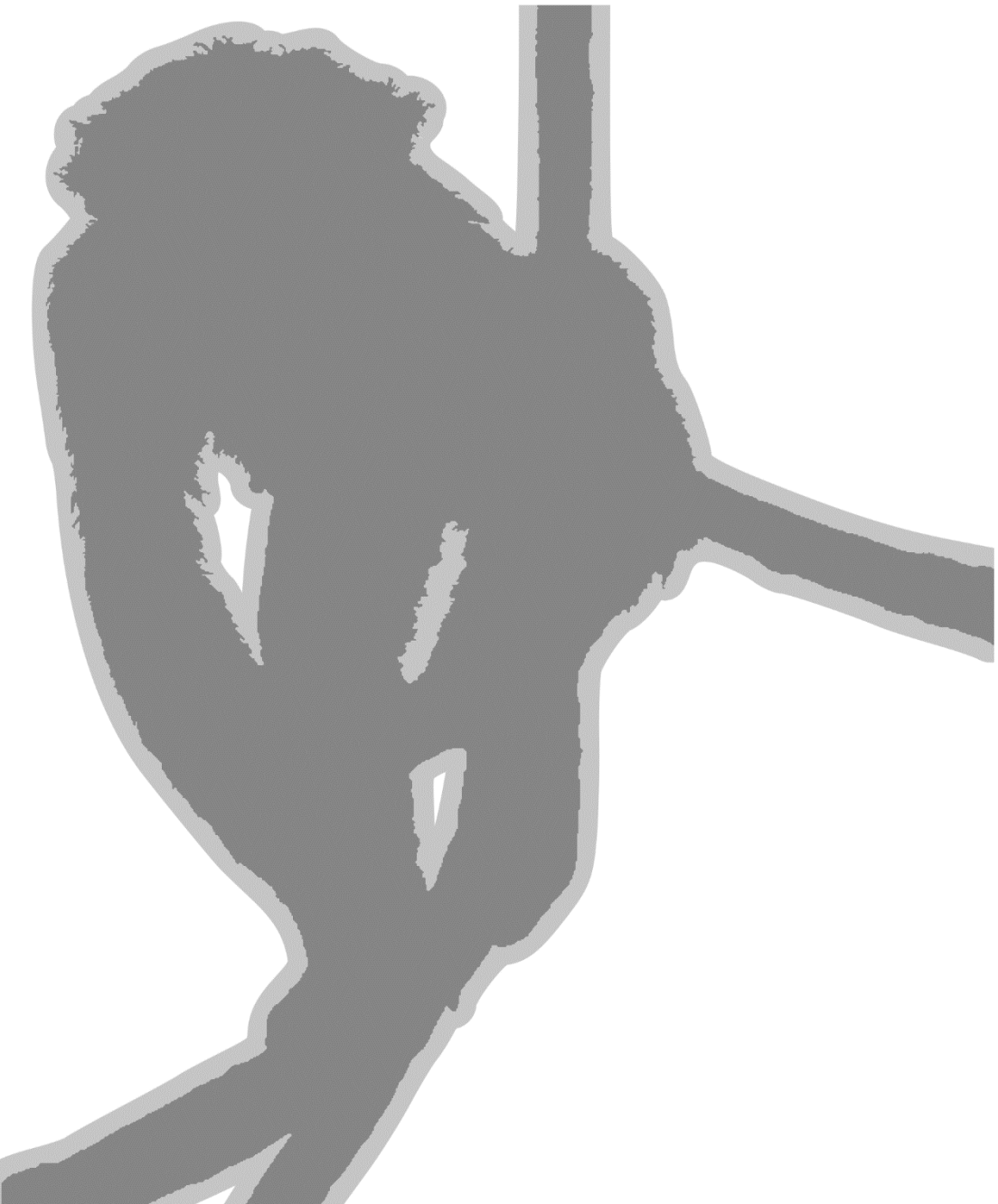
Pliobates represents the most completely known crouzeliid and, as such, it will play a key role in the future for understanding the evolution of pliopithecoids and stem catarrhines as a whole. Locomotor inferences based on the available postcranial remains expands the diversity of positional behaviors previously inferred for members this superfamily (Meldrum and Pan, 1988; Begun, 1993; Rose, 1994; Kordos and Begun, 1999; Harrison and Gu 1999; Senut, 2012; Rein et al., 2011, 2015; Arias-Martorell et al., 2015, 2021). This is not surprising because, with the exception of the partial skeletons of *Epipliopithecus* (Zapfe and Hürzeler, 1957; Zapfe, 1958; Zapfe, 1961a), the postcranial evidence available for other pliopithecoids is very meager, mostly consisting of isolated specimens (Begun, 1988, 1993; Meldrum and Pan, 1988; Harrison and Gu 1999; Kordos and Begun, 1999; Senut, 2012; Alba et al., 2014; Arias-Martorell et al., 2021). Dionysopithecids have been interpreted as likely arboreal quadrupeds (Harrison and Gu 1999), and pliopithecids as arboreal or semiterrestrial quadrupeds with limited climbing and suspensory abilities (Rose, 1994; Rein et al., 2011, 2015; Senut, 2012; Arias-Martorell et al., 2015, 2021). Among crouzeliids (as conceived in Chapter 4), anapithecines have been inferred to have strong grasping and suspensory abilities (Begun, 1988, 1993; Meldrum and Pan, 1988; Kordos and Begun, 1999), whereas crouzeliines were previously inferred to be agile arboreal or semiterrestrial quadrupeds with some degree of climbing, but no suspensory abilities (Senut, 2012; Arias-Martorell et al., 2021). The postcranial morphology of *Pliobates* indicates a more diverse arboreal locomotor repertoire, combining eclectic and cautious climbing with above-branch quadrupedalism and some degree of below-branch suspension. The postcranial morphology of *Pliobates* (Alba et al., 2015) further highlights that the lack of an entepicondylar foramen in the distal humerus evolved convergently between some pliopithecoids and crown catarrhines, as previously noted by Alba and Moyà-Solà (2014) regarding *Pl. canmatensis*. *Pliobates* thus illustrates that similar postcranial features have evolved convergently among multiple extinct and extant catarrhines, supporting the contention that such characters might have a confounding effect when reconstructing the phylogenetic relationships between fossil and living catarrhine taxa (Urciuoli and Alba, 2023).

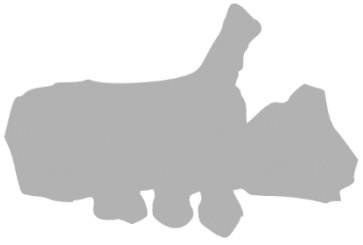


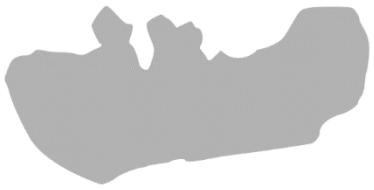


Chapter 7:

Conclusions







Chapter 7. Conclusions

The main conclusions of the present PhD dissertation are the following:

1. For the first time, the orientation, direction, proportions, and course of the carotid canal are quantitatively assessed in a large sample of extant anthropoids and some extinct catarrhines. A novel morphometric approach, including the first application of geometric morphometrics (GM) to the carotid canal, is devised specifically for that purpose. The results indicate that the carotid canal morphology is of limited utility for discriminating among catarrhine groups or inferring the closest phylogenetic affinities of extinct taxa.

2. Contrary to its original description, the carotid canal of *Pliobates cataloniae* does not closely resemble that of hylobatids in either orientation or direction. Instead, it variably resembles other catarrhine clades in these regards, including hominoids, the pliopithecoid *Epipliopithecus*, and cercopithecoids. The carotid canal volumetric proportions of *Pliobates* are plesiomorphic for catarrhines. In turn, the course of the canal in *Pliobates* is most similar to that of other investigated Miocene catarrhines, although the anteroposterior location of the former is derived toward the great ape condition.

3. New dentognathic material from ACM/C5-D1, attributed to *P. cataloniae*, is described. The material enables a more detailed description of the upper cheek tooth occlusal morphology than the holotype and first reveals the lower cheek tooth morphology of this taxon. On this basis, *Pliobates* shows pliopithecoid synapomorphies (distal arm of the pliopithecine triangle on lower molars, lower second incisor mesiodistally waisted at cervix, paracone only moderately more buccal than metacone on upper molars) and closest dental similarities with small-bodied crouzeliid pliopithecoids from the Middle and Late Miocene of Europe (*Crouzelia*, *Plesiopliopithecus*, and Crouzeliinae indet. from Mörgen). Several differences in occlusal morphology justify the distinction of *Pliobates* at the genus rank. In contrast, it is concluded that the family Pliobatidae is a junior subjective synonym of Crouzeliidae.

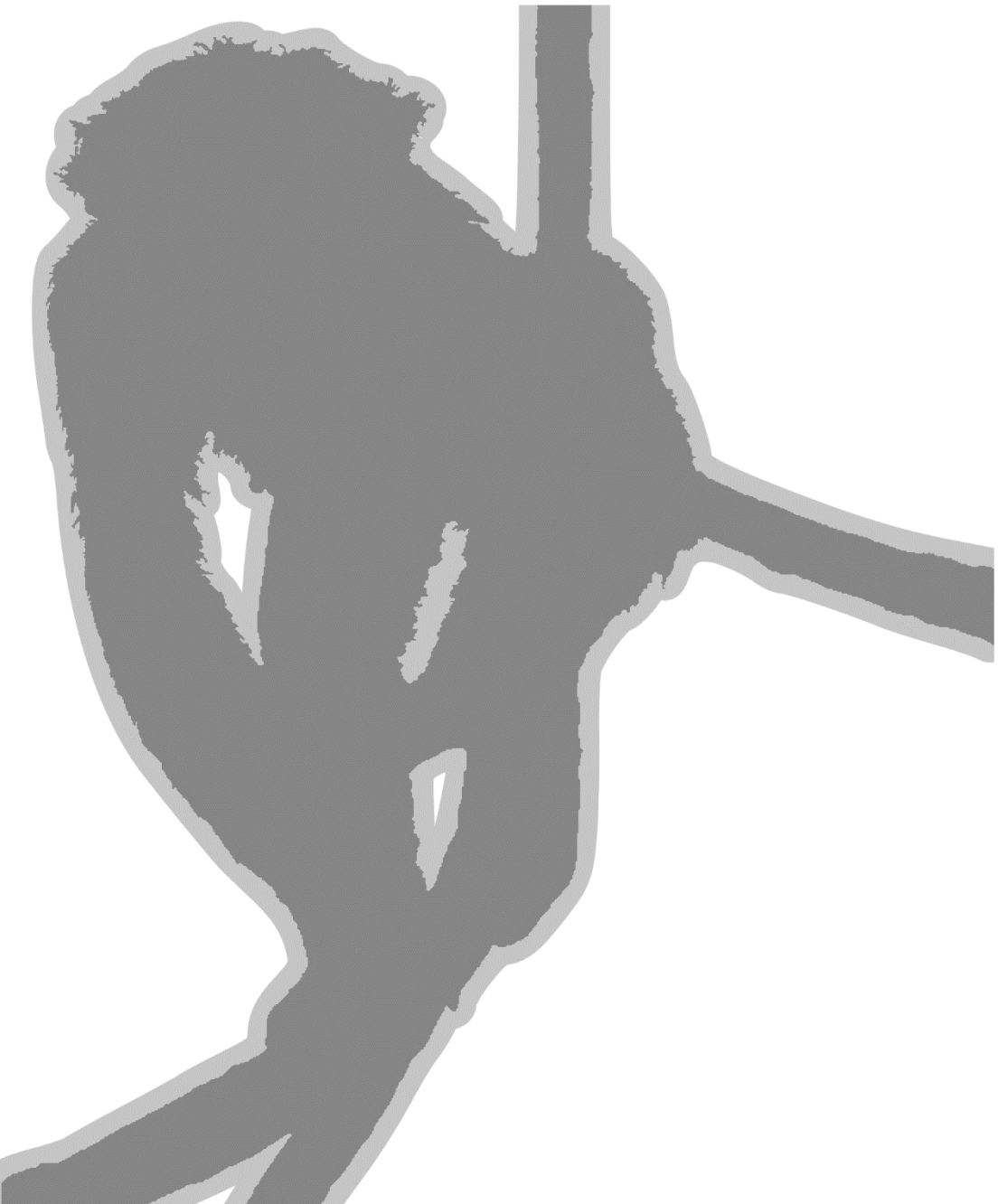
4. Extensive data of pliopithecoid molar enamel-dentine junction (EDJ) are reported for the first time and compared with those of *Pliobates* and hominoids. Three-dimensional geometric morphometric (3DGM) analyses of molar EDJ shape discriminate well between pliopithecoids and hominoids, and confirm that *Pliobates* is most similar to other pliopithecoids (particularly crouzeliids) in terms of EDJ shape. These phenetic results further support the pliopithecoid status of *Pliobates* and further indicate that 3DGM analyses properly capture the 3D shape variation of molar EDJ in non-hominoid catarrhines, supporting the usefulness of this anatomical structure for providing taxonomical and phylogenetic insights for extinct primates.

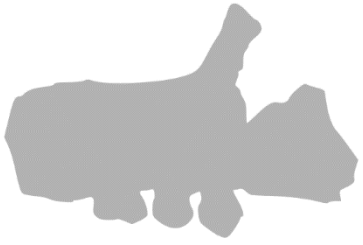
5. A new taxon-character matrix for cladistic analysis, based on dental characters and including *P. cataloniae* and other extinct catarrhine species is compiled, being by far the most comprehensive dental matrix devised so far for pliopithecoids. The cladistic analysis based on this matrix unambiguously supports *Pliobates* as a crouzeliid pliopithecoid most closely related to *Crouzelia* and *Plesiopliopithecus*. The analysis recovers the monophyly of the Pliopithecoidea and the Crouzeliidae, with the latter including two subclades distinguished at the subfamily rank (Anapithecinae and Crouzeliinae). Several previously known pliopithecoid genera are recovered as anapithecines (*Krishnapithecus* and *Fanchangia*) or crouzeliines (*Barberapithecus* and the indeterminate genus from Mörgen). An updated classification of the Pliopithecoidea at the subfamily level is therefore proposed.
6. Further cladistic analyses are also performed at the genus level for *Pliobates* and a wider sample of extinct and extant catarrhines, using a modified taxon-character matrix including dental, cranial, and postcranial features. These analyses yield contradictory results depending on whether cranial and postcranial characters are considered. Dental and craniodental analyses yield similar results to the dental-only analysis at the species level and recover *Pliobates* as a crouzeliid pliopithecoid stem catarrhine. In contrast, when postcranial characters are included, pliopithecoids (including *Pliobates*) are recovered as a paraphyletic assemblage of stem hominoids. These results support the interpretation that *Pliobates* is a derived pliopithecoid that was previously interpreted as a stem hominoid due to the possession of multiple convergences with extant apes, particularly in the elbow and wrist joints.
7. The contradictory results between cladistic analyses based on craniodental vs. postcranial features strengthen previous findings that hominid-like postcranial specializations related to orthograde behaviors were independently acquired not only in hylobatids, but also in some fossil hominoids, stem catarrhines, and even more distantly related primates. The pliopithecoid status of *Pliobates* further indicates the presence of homoplasy in some cranial structures among various catarrhine lineages.





References







References

Adams, D.C., Collyer, M.L., Kaliontzopoulou, A., 2019. Geomorph: Software for geometric morphometric analyses. R Package Version 3.3.1. https://cran.rproject.org/web/packages/geomorph/index.html.

Agustí, J., Sanz de Siria, A., Garcés, M., 2003. Explaining the end of the hominoid experiment in Europe. J. Hum. Evol. 45, 145–153.

Agustí, J., Cabrera, L., Garcés, M., Parés, J.M., 1997. The Vallesian mammal succession in the Vallés-Penedés basin (northeast Spain): Paleomagnetic calibration and correlation with global events. Paleogeogr. Paleoclim. Paleoecol. 133, 149–180.

Alba, D.M., 2012. Fossil apes from the Vallès-Penedès Basin. Evol. Anthropol. 21, 254–269.

Alba, D.M., Berning, B., 2013. On the holotype and original description of the pliopithecid *Plesiopliopithecus lockeri* (Zapfe, 1960). J. Hum. Evol. 65, 338–340.

Alba, D.M., Moyà-Solà, S., 2012. A new pliopithecid genus (Primates, Pliopithecoidea) from Castell de Barberà (Vallès-Penedès Basin, Catalonia, Spain). Am. J. Phys. Anthropol. 147, 88–112.

Alba, D.M., Moyà-Solà, S., 2014. New fossil remains of *Pliopithecus canmatensis* from Abocador de Can Mata, and their implications for the taxonomic validity and phylogenetic position of *Epipliopithecus* (Primates, Pliopithecidae). Am. J. Phys. Anthropol. 153, 64.

Alba, D.M., Moyà-Solà, S., Robles, J.M., Galindo, J., 2012. Brief Communication: The oldest pliopithecid record in the Iberian Peninsula based on new material from the Vallès-Penedès Basin. Am. J. Phys. Anthropol. 147, 135–140.

Alba, D.M., Casanovas-Vilar, I., Garcés, M., Robles, J.M., 2017. Ten years in the dump: An updated review of the Miocene primate-bearing localities from Abocador de Can Mata (NE Iberian Peninsula). J. Hum. Evol. 102, 12–20.

Alba, D.M., Almécija, S., DeMiguel, D., Fortuny, J., Pérez de los Ríos, M., Pina, M., Robles, J.M., Moyà-Solà, S., 2015. Miocene small-bodied ape from Eurasia sheds light on hominoid evolution. Science 350, aab2625.

Alba, D.M., Moyà-Solà, S., Malgosa, A., Casanovas-Vilar, I., Robles, J.M., Almécija, S., Galindo, J., Rotgers, C., Mengual, J.V.B., 2010. A new species of *Pliopithecus* Gervais, 1849 (Primates: Pliopithecidae) from the Middle Miocene (MN8) of Abocador de Can Mata (els Hostalets de Pierola, Catalonia, Spain). Am. J. Phys. Anthropol. 141, 52–75.

Alba, D.M., Fortuny, J., Robles, J.M., Bernardini, F., Perez de los Rios, M., Tuniz, C., Moyà-Solà, S., Zanolli, C., 2020. A new dryopithecine mandibular fragment from the middle Miocene of Abocador de Can Mata and the taxonomic status of '*Sivapithecus*' occidentalis from Can Vila (Vallès-Penedès Basin, NE Iberian Peninsula). J. Hum. Evol. 145, 102790.

Alba, D.M., Robles, J.M., Casanovas-Vilar, I., Beamud, E., Bernor, R.L., Cirilli, O., DeMiguel, D., Galindo, J., Llopart, I., Pons-Mojo, G., Sánchez, I.M., Vinuesa, V., Garcés, M., 2022. A revised (earliest Vallesian) age for the hominoid-bearing locality of Can Mata 1 based on new magnetostratigraphic and biostratigraphic data from Abocador de Can Mata (Vallès-Penedès Basin, NE Iberian Peninsula). J. Hum. Evol. 170, 103237.

Alba, D.M., Urciuoli, A., Hammond, A.S., Almécija, S., Rook, L., Zanolli, C., 2024a. Miocene ape evolution: Where does *Oreopithecus* fit in? Boll. Soc. Paleontol. It. 64, 1–30.

Alba, D.M., Bouchet, F., Fortuny, J., Robles, J.M., Galindo, J., Luján, À.H., Moyà-Solà, S., Zanolli, C., 2024b. New remains of the fossil Miocene great ape *Anoiapithecus brevirostris* from Abocador de Can Mata. J. Hum. Evol. 188, 103497.

Albrecht, G.H., 1992. Assessing the affinities of fossils using canonical variates and generalized distances. Hum. Evol. 4, 49–69.

Almécija, S., Alba, D.M., Moyà-Solà, S., 2009. *Pierolapithecus* and the functional morphology of Miocene ape hand phalanges: Paleobiological and evolutionary implications. J. Hum. Evol. 57, 284–297.

Almécija, S., Hammond, A.S., Thompson, N.E., Pugh, K.D., Moyà-Solà, S., Alba, D.M., 2021. Fossil apes and human evolution. Science 372, eabb4363.

Andrews, P., 1978. A revision of the Miocene Hominoidea of East Africa. Bulletin of the British Museum (Natural History), Geology Series 30, 85–224.

Andrews, P., 1985. Family group systematics and evolution among catarrhine Primates. In: Delson, E. (Ed.), Ancestors: The Hard Evidence. Alan R. Liss, New York, pp. 14–22.

Andrews, P., Simons, E.L., 1977. A new African Miocene gibbon-like genus, *Dendropithecus* (Hominoidea, Primates) with distinctive postcranial adaptations: its significance to origin of Hylobatidae. Folia Primatol. 28, 161–169.

Andrews, P., Harrison, T., Delson, E., Bernor, R.L., Martin, L., 1996. Distribution and biochronology of European and Southwest Asian Miocene catarrhines. In: Bernor, R.L., Fahlbusch, V., Mittmann, H.-W. (Eds.), The Evolution of Western Eurasian Neogene Mammal Faunas. Columbia University Press, New York, pp. 168–207.

Ankel, F., 1965. Der Canalis Sacralis als Indikator für die Länge der Caudalregion der Primaten. Folia Primatol. 3, 263–276.

Arias-Martorell, J., Alba, D.M., Potau, J.M., Bello-Hellegouarch, G., Pérez-Pérez, A., 2015. Morphological affinities of the proximal humerus of *Epipliopithecus vindobonensis* and *Pliopithecus antiquus*: Suspensory inferences based on a 3D geometric morphometrics approach. J. Hum. Evol. 80, 83–95.

Arias-Martorell, J., Almécija, S., Urciuoli, A., Nakatsukasa, M., Moyà-Solà, S., Alba, D.M., 2021. A proximal radius of *Barberapithecus huerzeleri* from Castell de Barberà: Implications for locomotor diversity among pliopithecoids. J. Hum. Evol. 157, 103032.

Arnold, C., Matthews, L.J., Nunn, C.L., 2010. The 10kTrees website: A new online resource for primate phylogeny. Evol. Anthropol. 19, 114–118.

Barry, J.C., Jacobs, L.L., Kelley, J., 1986. An early middle Miocene catarrhine from Pakistan with comments on the dispersal of catarrhines into Eurasia. J. hum. Evol. 15, 501–508.

Beaudet, A., Dumoncel, J., Thackeray, J.F., Bruxelles, L., Duployer, B., Tenailleau, C., Bam, L., Hoffman, J., de Beer, F., Braga, J., 2016a. Upper third molar internal structural organization and semicircular canal morphology in Plio-Pleistocene South African cercopithecoids. J. Hum. Evol. 95, 104–120.

Beaudet, A., Dumoncel, J., de Beer, F., Duployer, B., Durrleman, S., Gilissen, E., Hoffman, J., Tenailleau, C., Thackeray, J.F., Braga, J., 2016b. Morphoarchitectural variation in South African fossil cercopithecoid endocasts. J. Hum. Evol. 101, 65–78.

Begun, D.R., 1988. Catarrhine phalanges from the late Miocene (Vallesian) or Rudabánya, Hungary. J. Hum. Evol. 17, 413–438.

Begun, D.R., 1989. A large pliopithecine molar from germany and some notes on the pliopithecinae. Folia Primatol. 52, 156–166.

Begun, D.R., 1992. Phyletic diversity and locomotion in primitive European hominids. Am. J. Phys. Anthropol. 87, 311–340.

Begun, D.R., 1993. New catarrhine phalanges from Rudabánya (Northeastern Hungary) and the problem of parallelism and convergence in hominoid postcranial morphology. J. Hum. Evol. 24, 373–402.

Begun, D.R., 2002. The Pliopithecoidea. In: Hartwig, W.C. (Ed.), The Primate Fossil Record. Cambridge University Press, Cambridge, pp. 221–240.

Begun, D.R., 2015. Fossil record of Miocene hominoids. In: Henke, W., Tattersall, I. (Eds.), Handbook of paleoanthropology. Springer, Berlin, pp. 1261–1332.

Begun, D.R., 2017. Evolution of the Pliopithecoidea. In: Fuentes, A. (Ed.), The International Encyclopedia of Primatology. John Wiley & Sons. https://doi.org/10.1002/9781119179313.wbprim0165.

Benefit, B.R., 2000. Middle Miocene hominoid origins. Science 287, 2375.

Benefit, B.R., McCrossin, M.L., 2015. A window into ape evolution. Science 350, 515–516.

Bergounioux, F.-M., Crouzel, F., 1965. Les pliopithèques de France. Ann. Paléontol. (Vertébrés) 51(1), 45–65.

Bernor, R., Flynn, L., Harrison, T., Hussain, S.T., Kelley, J., 1988. Dionysopithecus from southern Pakistan and the biochronology and biogeography of early Eurasian catarrhines. J. Hum. Evol. 17, 339–358.

Blomberg, S.P., Garland, T.Jr., Ives, A.R., 2003. Testing for phylogenetic signal in comparative data: behavioral traits are more labile. Evolution 57, 717–745.

Bookstein, F.L., 1991. Morphometric Tools for Landmark Data: Geometry and Biology. Cambridge University Press, Cambridge.

Boyer, D.M., Lipman, Y., St Clair, E., Puente, J., Patel, B.A., Funkhouser, T., Jernvall, J., Daubechies, I., 2011. Algorithms to automatically quantify the geometric similarity of anatomical surface. Proc. Natl. Acad. Sci. USA 108, 18221–18226.

Boyer, D.M., Kirk, E.C., Silcox, M.T., Gunnell, G.F., Gilbert, C.C., Yapuncich, G.S., Allen, K.L., Welch, E., Bloch, J.I., Gonzales, L.A., Kay, R.F., Seiffert, E.R., 2016. Internal carotid arterial canal size and scaling in Euarchonta: Re-assessing implications for arterial patency and phylogenetic relationships in early fossil primates. J. Hum. Evol. 97, 123–144.

Bremer, K., 1988. 8 The limits of amino acid sequence data in angiosperm phylogenetic reconstruction. Evolution 42, 795–803.

Bugge, J., 1974. The cephalic arterial system in insectivores, primates, rodents, and lagomorphs, with special reference to the systematic classification. Acta Anat. 87, 1–160.

Campbell, N.A., Atchley, W.R., 1981. The geometry of canonical variate analysis. Syst. Zool. 30, 268–280.

Cardini, A., O'Higgins, P., Rohlf, F.J., 2019. Seeing distinct groups where there are none: Spurious patterns from between-group PCA. Evol. Biol. 46, 303–316.

Cardini, A., Polly, P.D., 2020. Cross-validated between group PCA scatterplots: A solution to spurious group separation? Evol. Biol. 47, 85–95.

Cartmill, M., 2018. A sort of revolution: Systematics and physical anthropology in the 20th century. Am. J. Phys. Anthropol. 165, 677–687.

Cartmill, M., Milton, K., 1977. The lorisiform wrist joint and the evolution of "brachiating" adaptations in the Hominoidea. Am. J. Phys. Anthropol. 47, 249–272.

Cartmill, M., MacPhee, R.D.E., Simons, E.L., 1981. Anatomy of the temporal bone in early anthropoids, with remarks on the problem of anthropoid origins. Am. J. Phys. Anthropol. 56, 1–21.

Casanovas-Vilar, I., Alba, D.M., Garcés, M., Robles, J.M., Moyà-Solà, S., 2011. Updated chronology for the Miocene hominoid radiation in Western Eurasia. Proc. Natl. Acad. Sci. USA 108, 5554–5559.

Casanovas-Vilar, I., Madern, A., Alba, D.M., Cabrera, L., García-Paredes, I., Van den Hoek Ostende, L.W., DeMiguel, D., Robles, J.M., Furió, M., Van Dam, J., Garcés, M., Angelone, C., Moyà-

Solà, S., 2016a. The Miocene mammal record of the Vallés-Penedés Basin (Catalonia). C. R. Palevol 15, 791–812.

Casanovas-Vilar, I., Garcés, M., Van Dam, J., García-Paredes, I., Robles, J.M., Alba, D.M., 2016b. An updated biostratigraphy for the late Aragonian and the Vallesian of the Vallès-Penedès Basin (Catalonia). Geol. Acta 14, 195–217.

Chaimanee, Y., Lazzari, V., Benammi, M., Euriat, A., Jaeger, J.-J., 2015. A new small pliopithecoid primate from the Middle Miocene of Thailand. J. Hum. Evol. 88, 15–24.

Chatterjee, H.J., Ho, S.Y.W., Barnes, I., Groves, C., 2009. Estimating the phylogeny and divergence times of primates using a supermatrix approach. BMC Evol. Biol.13, 259.

Chopra, S.R.K., Kaul, S., 1979. A new species of *Pliopithecus* from the Indian Sivaliks. J. Hum. Evol. 8, 475–477.

Collyer, M.L., Adams, D.C., 2018. RRPP: An R package for fitting linear models to high-dimensional data using residual randomization. Methods Ecol. Evol. 9, 1772–1779.

Cote, S., McNulty, K.P., Steven, N.J., Nengo, I.O., 2016. A detailed assessment of the maxillary morphology of *Limnopithecus evansi* with implications for the taxonomy of the genus. J. Hum. Evol. 94, 83–91.

Crusafont-Pairó, M., Golpe-Posse, J.M., 1981. Estudio de la dentición inferior del primer pliopitécido hallado en España (Vindoboniense terminal de Castell de Barberà, Cataluña, España. Butll. Inf. Inst. Paleontol. Sabadell 13, 25–38.

Davis, P.R., Napier, J.R., 1963. A reconstruction of the skull of *Proconsul africanus* (R.S.51). Folia Primatol. 1, 20–28.

Delson, E., 1977. Catarrhine phylogeny and clasification: Principles, methods and comments. J. Hum. Evol. 6, 433e459.

Delson, E., Terranova, C.J., Sargis, E.J., Jungers, W.L., Jablonski, N.G.C., Dechow, P., 2000. Body mass in Cercopithecidae (Primates, Mammalia): Estimation and scaling in extinct and extant taxa. Anthropol. Pap. Am. Mus. Nat. Hist. 83, 1–159.

Delson, E., Andrews, P.J., 1975. Evolution and interrelationships of the catarrhine primates. In: Luckett, W.P., Szalay, F.S. (Eds.), Phylogeny of the Primates: A Multidisciplinary Approach. Plenum Press, New York, pp. 405–446.

DeMiguel, D., Alba, D.M., Moyà-Solà, S., 2013. European pliopithecid diets revised in the light of dental microwear in *Pliopithecus canmatensis* and *Barberapithecus huerzeleri*. Am. J. Phys. Anthropol. 151, 573–582.

DeMiguel, D., Domingo, L., Sánchez, I.M., Casanovas-Vilar, I., Robles, J.M., Alba, D.M., 2021. Palaeoecological differences underlie rare co-occurrence of Miocene European primates. BMC Biol. 19, 6.

Diogo, R., Wood, B., 2011. Soft-tissue anatomy of the primates: Phylogenetic analyses based on the muscles of the head, neck, pectoral region and upper limb, with notes on the evolution of these muscles. J. Anat. 219, 272–359.

Dray, S., Dufour, A., 2007. The ade4 package: Implementing the duality diagram for ecologists. J. Stat. Softw. 22, 1–20.

Durrleman, S., Pennec, X., Trouvé, A., Ayache, N., Braga, J., 2012a. Comparison of the endocranial ontogenies between chimpanzees and bonobos via temporal regression and spatiotemporal registration. J. Hum. Evol. 62, 74–88.

Durrleman, S., Prastawa, M., Korenberg, J.R., Joshi, S., Trouvé, A., Gerig, G., 2012b. Topology preserving atlas construction from shape data without correspondence using sparse parameters. In: Ayache, N., Delingette, H., Golland, P., Mori, K. (Eds.), Proceedings of Medical Image Computing and Computer Aided Intervention. Nice, France, pp. 223–230.

Erikson, G.E., 1963. Brachiation in New World monkeys and in anthropoid apes. *Symp. Zool. Soc. London* 10, 135–163.

Egi, N., Takai, M., Shigehara, N., Tsubamoto, T., 2004. Body mass estimates for Eocene eosimiid and amphipithecid primates using prosimian and anthropoid scaling models. Int. J. Primatol. 25, 211–236.

Farris, J.S., 1983. The logical basis of phylogenetic analysis. In: Platnick, N.I., Funk, V.A. (Eds.), Advances in Cladistics. Vol. 2, Proceedings of the Second Meeting of the Willi Hennig Society. Columbia University Press, New York, pp. 7–36.

Farris, J.S., 1989a. The retention index and homoplasy excess. Syst. Zool. 38, 406–407.

Farris, J.S., 1989b. The retention index and the rescaled consistency index. Cladistics 5, 417–419.

Felsenstein, J., 1985. Confidence limits on phylogenies: An approach using the bootstrap. Evolution 39:783–791.

Felsenstein, J., 1988. Phylogenies and quantitative characters. Annu. Rev. Ecol. Syst. 19, 445–471.

Finarelli, J.A., Clyde, W.C., 2004. Reassessing hominoid phylogeny: Evaluating congruence in the morphological and temporal data. Paleobiology 30, 614–651.

Finstermeier, K., Zinner, D., Brameier, M., Meyer, M., Kreuz, E., Hofreiter, M., Roos, C., 2013. A mitogenomic phylogeny of living primates. PLoS One 8, e69504.

Fisher, D.C., 2008. Stratocladistics: Integrating temporal data and character data in phylogenetic inference. Annu. Rev. Ecol. Evol. Syst. 39, 365–385.

Fleagle, J.G., 1983. Locomotor adaptations of Oligocene and Miocene hominoids and their phyletic implications. In: Ciochon, R.L., Corruccini, R.S. (Eds.), New Interpretations of Ape and Human Ancestry. Plenum Press, New York, pp. 301–324.

Fleagle, J.G., 1984. Are there any fossil gibbons? In: Preuschoft, H., Chivers, D.J., Brockelman, W.Y., Creel, N. (Eds.), The Lesser Apes: Evolutionary and Behavioral Biology. Edinburgh University Press, Edinburgh, pp. 4431–447.

Fleagle, J.G., 1986. The fossil record of early catarrhine evolution. In: Wood, B.A., Martin L., Andrews, P. (Eds.), Major Topics in Primate and Human Evolution. Cambridge University Press, Cambridge, pp. 130–149.

Fleagle, J.G., Simons, E.L., 1978. *Micropithecus clarki*, a small ape from the Miocene of Uganda. Am. J. Phys. Anthropol. 49, 427–440.

Flynn, L.J., Lindsay, E.H., Pilbeam, D., Raza, M., Morgan, M.E., Barry, J.C., Badgley, C.E., Behrensmeyer, A.K., Cheema, I.U., Rajpar, A.R., Opdyke, N.D., 2013. The Siwalik and Neogene evolutionary biology in South Asia. In: Wang, X., Flynn, L.J., Fortelius, M. (Eds.), Fossil Mammals of Asia: Neogene Biostratigraphy and Chronology. Columbia University Press, New York, pp. 353–372.

Fortuny, J., Zanolli, C., Bernardini, F., Tuniz, C., Alba, D.M., 2021. Dryopithecine palaeobiodiversity in the Iberian Miocene revisited on the basis of molar endostructural morphology. Palaeontology 64, 531–554.

Freckleton, R.P., Harvey, P.H., Pagel, M., 2002. Phylogenetic analysis and comparative data:
a test and review of evidence. Am. Nat. 160, 712–726.

Gibbs, S., Collard, M., Wood, B., 2000. Soft-tissue characters in higher primate phylogenetics. Proc. Natl. Acad. Sci. USA 97, 11130–11132.

Gibbs, S., Collard, M., Wood, B., 2002. Soft-tissue anatomy of the extant hominoids: a review and phylogenetic analysis. J. Anat. 200, 3–49.

Gilbert, C.C., 2013. Cladistic analysis of extant and fossil African papionins using craniodental data. J. Hum. Evol. 64, 399–433.

Gilbert, C.C., Ortiz, A., Pugh, K.D., Campisano, C.J., Patel, B.A., Singh, N.P., Fleage, J.G., Patnaik, R., 2020a. New middle Miocene ape (Primates: Hylobatidae) from Ramnagar, India fills major gaps in the hominoid fossil record. Proc. R. Soc. B 287, 20201655.

Gilbert, C.C., Pugh, K.D., Fleagle, J.G., 2020b. Dispersal of Miocene hominoids (and pliopithecoids) from Africa to Eurasia in light of changing tectonics and climate. In: Prasad, G.V., Patnaik, R. (Eds.), Biological Consequences of Plate Tectonics. New Perspectives on Post-Gondwana Break-Up–A Tribute to Ashok Sahni. Springer, Cham, pp. 393–412.

Gingerich, P.D., Smith, B.H., Rosenberg, K., 1982. Allometric scaling in the dentition of primates and prediction of body weight from tooth size in fossils. Am. J. Phys. Anthropol. 58, 81–100.

Ginsburg, L., 1975. Le Pliopithèque des faluns Helvétiens de la Touraine et de l'Anjou. Coll. Int. CNRS 218, 877–886.

Ginsburg, L., 1986. Chronology of the European pliopithecids. In: Else, J.G., Ice, P.C. (Eds.), Primate Evolution. Cambridge University Press, Cambridge, pp. 47–57.

Ginsburg, L., Mein, P., 1980. *Crouzelia rhodanica*, nouvelle espèce de primate catarhinien, et essai sur la position systématique des Pliopithecidae. Bull. Mus. Natl. Hist. Nat. 2, 57–85.

Glaunès, J., Joshi, S., 2006. Template estimation from unlabelled point set data and surfaces for computational anatomy. In: Pennec, X., Joshi, S. (Eds.), Proceedings of the International Workshop on the Mathematical Foundations of Computational Anatomy. LNCS Springer, Copenhagen, pp. 29–39.

Goloboff, P.A., 2018. Weighted parsimony outperforms other methods of phylogenetic inference under models appropriate for morphology. Cladistics 34, 407–437.

Gu, Y., Lin, Y., 1983. First discovery of *Dryopithecus* in East China. Acta Anthropol. Sin. 2, 305–314.

Gunz, P., Mitteroecker, P., 2013. Semilandmarks: a method for quantifying curves and surfaces. HYSTRIX 24, 103–109.

Harrison, T., 1981. New Finds of Small Fossil Apes from the Miocene Locality at Koru in Kenya. J. Hum. Evol. 10, 129–137.

Harrison, T., 1982. Small-bodied Apes from the Miocene of East Africa. Ph.D. Dissertation, University College London.

Harrison, T., 1987. The phylogenetic relationships of the early catarrhine primates: a review of the current evidence. J. Hum. Evol. 16, 41–80.

Harrison, T., 1988. A taxonomic revision of the small catarrhine Primates from the Early Miocene of East Africa. Folia Primatol. 50, 59–108.

Harrison, T., 1989. A new species of *Micropithecus* from the middle Miocene of Kenya. J. Hum. Evol. 18, 537–557.

Harrison, T., 1992. A reassessment of the taxonomic and phylogenetic affinities of the fossil catarrhines from Fort Ternan, Kenya. Primates 33, 501–522.

Harrison, T., 2002. Late Oligocene to Middle Miocene catarrhines from Afro-Arabia. In: Hartwig, W.C. (Ed.), The Primate Fossil Record. Cambridge University Press, Cambridge, pp. 311–338.

Harrison, T., 2005. The zoogeographic and phylogenetic relationships of early catarrhine primates in Asia. Anthropol. Sci. 113, 43–51.

Harrison, T., 2010. Dendropithecoidea, Proconsuloidea and Hominoidea (Catarrhini, primates). In: Werdelin, L., Sanders, W.J. (Eds.), Cenozoic Mammals of Africa. University of California Press, Berkeley, pp. 429–469.

Harrison, T., 2013. Catarrhine origins. In: Begun, D.R. (Ed.), A Companion to Paleoanthropology. Blackwell Publishing, Chichester, pp. 376–396.

Harrison, T., 2017. Miocene primates. In: Fuentes, A. (Ed.), The International Encyclopedia of Primatology. John Wiley & Sons, Hoboken. https://doi.org/10.1002/9781119179313.wbprim0227.

Harrison, T., Gu, Y., 1999. Taxonomy and phylogenetic relationships of Early Miocene catarrhines from Sihong, China. J. Hum. Evol. 37, 225–277.

Harrison, T., Delson, E., Guan, J., 1991. A new species of *Pliopithecus* from the Middle Miocene of China and its implications for early catarrhine zoogeography. J. Hum. Evol. 21, 329–361.

Harrison, T., van der Made, J., Ribot, F., 2002. A new middle Miocene pliopithecid from Sant Quirze, northern Spain. J. Hum. Evol. 42, 371–377.

Harrison, T., Zhang, Y., Wei, G., Sun, C., Wang, Y., Liu, J., Tong, H., Huang, B., Xu, F., 2020. A new genus of pliopithecoid from the late Early Miocene of China and its implications for understanding the paleozoogeography of the Pliopithecoidea. J. Hum. Evol. 145, 102838.

Harzhauser, M., Kroh, A., Mandic, O., Piller, W.E., Göhlich, U., Reuter, M., Berning, B., 2007. Biogeographic responses to geodynamics: A key study all around the Oligo–Miocene Tethyan Seaway. Zool. Anz. 246, 241–256.

Heißig, K., 1999. *Ein Pliopithecide aus dem Vallesium (MN 9) der Oberen* Süßwassermolasse Bayerns. Ber. naturwiss. Ver. Schwaben 103, 1–2.

Hennig, W., 1966. Phylogenetic Systematics. University of Illinois Press, Urbana.

Hilgen, F.J., Lourens, L.J., Van Dam, J.A., 2012. The Neogen Period. In: Gradstein, F.M., Ogg, J.G., Schmitz, M., Ogg, G. (Eds.), The Geological Time Scale. Elsevier, Amsterdam, pp. 923–978.

Hopwood, A.T., 1933. Miocene primates from British East Africa. Ann. Mag. Nat. Hist. 11, 96–98.

Hunt, K.D., 2016. Why are there apes? Evidence for the co-evolution of ape and monkey ecomorphology. J. Anat. 228, 630–685.

Hürzeler, J., 1954. Contribution à l'odontologie et à la phylogénèse du genre *Pliopithecus* Gervais. Ann. Paleontol. 40, 5–63.

Ji, X., Harrison, T., Zhang, Y., Wu, Y., Zhang, C., Hu, J., Wu, D., Hou, Y., Li, S., Wang, G., Wang, Z., 2022. The earliest hylobatid from the Late Miocene of China. J. Hum. Evol. 171, 103251.

Jungers, W.L., 1980. Adaptive diversity in subfossil Malagasy prosimians. *Z. Morphol. Anthropol.* 71, 177–186.

Jungers, W.L., Godfrey, L.R., Simons, E.L., Chatrath, P.S., 1997. Phalangeal curvature and positional behavior in extinct sloth lemurs (Primates, Palaeopropithecidae*)*. Proc. Natl. Acad. Sci. U.S.A. 94, 11998–12001.

Kaup, J.J., 1861. Beitrage zur näheren Kenntniss der urweltlichen Säugethiere, vol. 5. Darmstadt and Leipzig.

Kay, R.F., 1977. Diets of Early Miocene African hominoids. Nature 268, 628–630.

Kay, R.S., Ungar, P.S., 1997. Dental evidence for diet in some Miocene catarrhines with comments on the effects of phylogeny on the interpretation of adaptation. In: Begun, D.R., Ward, C.V., Rose, M.D. (Eds.), Function, Phylogeny, and Fossils: Miocene Hominoid Evolution and Adaptations. Springer, New York, pp. 131–151.

Kay, R.F., Simons, E., Ross, J.L., 2008. The basicranial anatomy of African Eocene/Oligocene anthropoids. Are there any clues for platyrrhine origins? In: Fleagle, J.G., Gilbert, C.C. (Eds.), Elwyn Simons: A Search for Origins. Springer, New York, pp. 125–158.

Kendall, D.G., 1984. Shape manifolds, Procrustean metrics, and complex projective spaces. Bull. London Math. Soc.16, 81–121.

Klingenberg, C.P., 2020. Walking on Kendall's shape space: Understanding shape spaces and their coordinate systems. Evol. Biol. 47, 334–354.

Kluge, A.G., Farris, J.F., 1969. A simulation comparison of phylogeny algorithms under equal and unequal evolutionary rates. Mol. Biol. Evol. 18, 1–32.

Köhler, M., Alba, D.M., Moyà-Solà, S., MacLatchy, L., 2003. Taxonomic affinities of the Eppelsheim femur. Am. J. Phys. Anthropol. 119, 297–304.

Kordos, L., Begun, D.R., 1999. Femora of *Anapithecus* from Rudabànya. Am. J. Phys. Anthropol. 108 (S28), 173.

Kordos, L., Begun, D.R., 2001. Primates from Rudabánya: allocation of specimens to individuals, sex and age categories. J. Hum. Evol. 40, 17–39.

Kretzoi, M., 1975. New ramapithecines and *Pliopithecus* from the lower Pliocene of Rudabànya in northeastern Hungary. Nature 257, 578–581.

Larson, S.G., 1998. Parallel evolution in the hominoid trunk and forelimb. Evol. Anthropol. 6, 87–99.

Leakey, L.S.B., 1947. Fossil finds in Kenya. Ape or primitive Man? Antiquity 20, 201–205.

Leakey, R.E.F., Leakey, M.G., 1987. A new Miocene small-bodied ape from Kenya. J. Hum. Evol. 16, 369–387.

Le Cabec, A., Dean, M.C., Begun, D.R., 2017. Dental development and age at death of the holotype of *Anapithecus hernyaki* (RUD 9) using synchrotron virtual histology. J. Hum. Evol. 108, 161–175.

Le Gros Clark, W.E., 1949. New palaeontological evidence bearing on the evolution of the Hominoidea. Quart. J. Geol. Soc. London 105, 225–264.

Le Gros Clark, W., Thomas, D.P., 1951. Associated jaws and limb bones of *Limnopithecus macinessi*. Fossil Mammals of Africa 3, 1–27.

Le Gros Clark, W., Leakey, L.S.B., 1951. The Miocene Hominoidea of East Africa. Fossil Mammals of Africa 1, 1–117.

Li, C., 1978. A Miocene gibbon-like primate from Shihhung, Kiangsu Province. Vert. PalAs. 16, 187–192.

Liedigk, R., Roos, C., Brameier, M., Zinner, D., 2014. Mitogenomics of the Old World monkey tribe Papionini. BMC Evol. Biol.14, 176.

Macchiarelli, R., Bayle, P., Bondioli, L., Mazurier, A., Zanolli, C., 2013. From outer to inner structural morphology in dental anthropology. The integration of the third dimension in the visualization and quantitative analysis of fossil remains. In: Scott, R.G., Irish, J.D. (Eds.), Anthropological Perspectives on Tooth Morphology: Genetics, Evolution, Variation. Cambridge University Press, Cambridge, 250–277.

MacInnes, D.G., 1943. Notes on the East African Miocene primates. J. East Afr. Nat. Hist. Soc. 17:141–181.

MacPhee, R.D.E., Cartmill, M., 1986. Basicranial structures and primate systematics. In: Swisher, D.R., Erwin, J. (Eds.), Comparative Primate Biology: Systematics, Evolution, and Anatomy. Alan R. Liss, New York, pp. 219–275.

Marigó, J., Susanna, I., Minwer-Barakat, R., Madurell-Malapeira, J., Moyá-Solá, S., Casanovas-Vilar, I., Robles, J.M., Alba, D.M., 2014. The primate fossil record in the Iberian Peninsula. J. Iber. Geol. 40, 179–211.

Marmi, J.M., Casanovas-Vilar, I., Robles, J.M., Moyà-Solà, S., Alba, D.M.,2012. The paleoenvironment of *Hispanopithecus laietanus* as revealed by paleobotanical evidence from the Late Miocene of Can Llobateres 1 (Catalonia, Spain). J. Hum. Evol. 62, 412–423.

McKenzie, S., Casanovas-Vilar, I., Alba, D.M., 2022. Tetraconodont dental remains (Suidae, Tetraconodontinae) from the Middle Miocene site of Ca l'Almirall (Vallès-Penedès Basin, NE Iberian Peninsula). Hist. Biol. 35, 597–609.

McNulty, K.P., Begun, D.R., Kelley, J., Manthi, F.K., Mbua, E.N., 2015. A systematic revision of *Proconsul* with the description of a new genus of early Miocene hominoid. J. Hum. Evol. 84, 42–61.

Meldrum, D.J., Pan, Y., 1988. Manual proximal phalanx of *Laccopithecus robustus* from the latest Miocene site of Lufeng. J. Hum. Evol. 17, 719–731.

Merceron, G., Kaiser, T.M., Kostopoulos, D.S., Schulz, E. 2010. Ruminant diets and the Miocene extinction of European great apes. Proc. R. Soc. B 277, 3105–3112.

Meyer, D., Rinaldi, IrD., Ramlee, H., Perwitasari-Farajallah, D., Hodges, J.K., Roos, C., 2011. Mitochondrial phylogeny of leaf monkeys (genus *Presbytis*, Eschscholtz, 1821) with implications for taxonomy and conservation. Mol. Phylogenet. Evol. 59, 311–319.

Mitteroecker, P., Gunz, P., 2009. Advances in Geometric Morphometrics. Evol. Biol. 36, 235–247.

Mongiardino Koch, N., Garwood, R.J., Parry, L.A., 2021. Fossils improve phylogenetic analyses of morphological characters. Proc. R. Soc. B 288, 20210044.

Moyà-Solà, S., Pons-Moyà, J., Köhler, M., 1990. Primates catarrinos (Mammalia) del Neógeno de la península Ibérica. Paleontol. Evol. 23, 41–45.

Moyà-Solà, S., Köhler, M., Alba, D.M., 2001. *Egarapithecus narcisoi*, a new genus of Pliopithecidae (Primates, Catarrhini) from the Late Miocene of Spain. Am. J. Phys. Anthropol. 114, 312–324.

Moyà-Solà, S., Köhler, M., Alba, D.M., Casanovas-Vilar, I., Galindo, J., 2004. *Pierolapithecus catalaunicus*, a new Middle Miocene great ape from Spain. Science 306, 1339–1344.

Morgan, M.E., Lewton, K.L., Kelley, J., Otárola-Castillo, E., Barry, J.C., Flynn, L.J., Pilbeam, D., 2015. A partial hominoid innominate from the Miocene of Pakistan: Description and preliminary analyses. Proc. Natl. Acad. Sci. USA 112, 82–87.

Nargolwalla, M.C., Begun, D.R., Dean, M.C., Reid, D.J., Kordos, L., 2005. Dental development and life history in *Anapithecus hernyaki*. J. Hum. Evol. 49, 99–121.

Nengo, I., Tafforeau, P., Gilbert, C.C., Fleagle, J.G., Miller, E.R., Feibel, C., Fox, D.L., Feinberg, J., Pugh, K.D., Berruyer, C., Mana, S., Engle, Z., Spoor, F., 2017. New infant cranium from the African Miocene sheds light on ape evolution. Nature 548, 169–174.

Nylander, J.A.A., Ronquist, F., Huelsenbeck, J.P., Nieves-Aldrey, J.L., 2004. Bayesian phylogenetic analysis of combined data. Syst. Biol. 53, 46–67.

Olejniczak, A.J., Martin, L.B., Ulhaas, L., 2004. Quantification of dentine shape in anthropoid primates. Ann. Anat. 186, 479–485.

Olejniczak, A.J., Gilbert, C.C., Martin, L.B., Smith, T.M., Ulhaas, L., Grine, F.E., 2007. Morphology of the enamel-dentine junction in sections of anthropoid primate maxillary molars. J. Hum. Evol. 53, 292–301.

O'Reilly, J.E., Puttick, M.N., Parry, L., Tanner, A.R., Tarver, J.E., Fleming, J., Pisani, D., Donoghue, P.C.J., 2016. Bayesian methods outperform parsimony but at the expense of precision in the estimation of phylogeny from discrete morphological data. Biol. Lett. 12, 20160081.

Pagel, M., 1999. Inferring the historical patterns of biological evolution. Nature 401, 877–884.

Pan, L., Dumoncel, J., de Beer, F., Hoffman, J., Thackeray, J.F., Duployer, B., Tenailleau, C., Braga, J., 2016. Further morphological evidence on South African earliest *Homo* lower postcanine dentition: Enamel thickness and enamel-dentine junction. J. Hum. Evol. 96, 82–96.

Pan, Y., 1988. Small fossil primates from Lufeng, a latest Miocene site in Yunnan Province, China. J. Hum. Evol. 17, 359–366.

Pan, Y., Waddle, D.M., Fleagle, J.G., 1989. Sexual dimorphism in *Laccopithecus robustus*, a Late Miocene hominoid from China. Am. J. Phys. Anthropol. 79, 137–158.

Perelman, P., Johnson, W.E., Roos, C., Seuanez, H.N., Horvath, J.E., Moreira, M.A.M., Kessing, B., Pontius, J., Roelke, M., Rumpler, Y., Schneider, M.P.C., Silva, A., O'Brien, S.J., Pecon-Slattery, J., 2011. A molecular phylogeny of living primates. PLoS Genet. 7, e1001342.

Pickford, M., Kunimatsu, Y., 2005. Catarrhines from the Middle Miocene (ca. 14.5 Ma) of Kipsaraman, Tugen Hills, Kenya. Anthropol. Sci. 113, 189–224.

Pickford, M., Senut, B., Gommery, D., Musiime, E., 2003. New catarrhine fossils from Moroto II, early Middle Miocene (ca. 17.5 Ma) Uganda. C. R. Palevol 2, 649–662.

Pickford, M., Musalizi, S., Senut, B., Gommery, D., Musiime, E., 2010. Small apes from the Early Miocene of Napak, Uganda. Geo-Pal Uganda 3, 1–111.

Pickford, M., Senut, B., Gommery, D., Musalizi, S., Musiime, E., 2017a. Revision of the Miocene Hominoidea from Moroto I and II, Uganda. Geo-Pal Uganda 10, 1–32.

Pickford, M., Musiime, E., Musalizi, S., Gommery, D., Senut, B., 2017b. Bukwa II Hominoidea. Geo-Pal Uganda 11, 54–65.

Pickford, M., Senut, B., Gommery, D., Musalizi, S., Ssebuyungo, C., 2021. Revision of the smaller-bodied anthropoids from Napak, early Miocene, Uganda: 2011–2020 collections. Münch. Geowiss. Abh. A 51, 1–135.

Pilbeam, D., Walker, A., 1968. Fossil monkeys from the Miocene of Napak, North-East Uganda. Nature 220, 657–660.

Pilbeam, D.R., Rose, M.D., Barry, J.C., Shah, S.M.I., 1990. New *Sivapithecus* humeri from Pakistan and the relationship of *Sivapithecus* and *Pongo*. Nature 348, 237–239.

Pohlig, H., 1895. *Paidopithex rhenanus*, n.g.n.s., le singe anthropomorphe du Pliocène rhénan. Bull. Soc. Geol. Belge 9, 149–151.

Pozzi, L., Penna, A., 2022. Rocks and clocks revised: New promises and challenges in dating the primate tree of life. Evol. Anthropol. 31, 138–153.

Pozzi, L., Hodgson, J.A., Burrell, A.S., Sterner, K.N., Raaum, R.L., Disotell, T.R., 2014. Primate phylogenetic relationships and divergence dates inferred from complete mitochondrial genomes. Mol. Phylogenet. Evol. 75, 165–183.

Pugh, K.D., 2020. The phylogenetic relationships of Middle-Late Miocene apes: Implications for early human evolution. Ph.D. Dissertation, City University of New York.

Pugh, K.D., 2022. Phylogenetic analysis of Middle-Late Miocene apes. J. Hum. Evol. 165, 103140.

Pugh, K.D., Catalano, S.A., Pérez de los Ríos, M., Fortuny, J., Shearer, B.M., Vecino Gazabón, A., Hammond, A.S., Moyà-Solà, S., Alba, D.M., Almécija, S., 2023 The reconstructed cranium of *Pierolapithecus* and the evolution of the great ape face. Proc. Natl. Acad. Sci. USA 120, e2218778120.

Qiu, Z., Guan, J., 1986. A lower molar of *Pliopithecus* from Tongxin, Ningxia Hui Autonomous Region. Acta Anthropol. Sin. 5, 201–207.

R Core Team, 2020. R: A language and environment for statistical computing. R Foundation for Statistical Computing, Vienna.

Rae, T.C., 1999. Mosaic evolution in the origin of the Hominoidea. Folia Primatol. 70, 125–135.

Raffi, I., Wade, B.S., Pälike, H., Beu, A.G., Cooper, R., Crundwell, M.P., Krijgsman, W., Moore, T., Raine, I., Sardella, R., Vernyhorova, Y.V., 2020. The Neogene period. In: Gradstein, F.M., Ogg, J.G., Schmitz, M.D., Ogg, G.M. (Eds.), Geologic Time Scale 2020. Elsevier, Amsterdam, pp. 1141–1215.

Rasmussen, D.T., 2010. Early catarrhines of the African Eocene and Oligocene. In: Werdelin, L., Sanders, W.J. (Eds.), Cenozoic Mammals of Africa. University of California Press, Berkeley, pp. 203–220.

Rasmussen, D.T., Friscia, A.R., Gutierrez, M., Kappelman, J., Miller, E.R., Muteti, S., Reynoso, D., Rossie, J.B., Spell, T.L., Tabor, N.J., Gierlowski-Kordesch, E., Jacobs, B.F., Kyongo, B., Macharwas, M., Muchemi, F., 2019. Primitive Old World monkey from the earliest Miocene of Kenya and the evolution of cercopithecoid bilophodonty. Proc. Natl. Acad. Sci. USA 116, 6051–6056.

Rein, T.R., Harrison, T., Zollikofer, C.P.E., 2011. Skeletal correlates of quadrupedalism and climbing in the anthropoid forelimb: Implications for inferring locomotion in Miocene catarrhines. J. Hum. Evol. 61, 564–574.

Rein, T.R., Harvati, K., Harrison, T., 2015. Inferring use of forelimb suspensory locomotion by extinct primate species via shape exploration of the ulna. J. Hum. Evol. 78, 70–79.

Revell, L.J., 2012. Phytools: An R package for phylogenetic comparative biology (and other things). Methods Ecol. Evol. 3, 217–223.

Rögl, F., 1998. Palaeogeographic considerations for Mediterranean and Paratethys seaways (Oligocene to Miocene). Ann. Naturhistor. Mus. Wien 99, 279–310.

Rögl, F., 1999. Circum-Mediterranean Miocene paleogeography. In: Rössner, G., Heissig, K. (Eds.), The Miocene Land Mammals of Europe. Dr. Fritz Pfeil Verlag, Munich, pp. 39–48.

Rögl, V.F., Zapfe, H., Bernor, R.L., Brzobohaty, R.L., Daxner-Höck, G., Draxler, I., Fejfar, O., Gaudant, J., Herrmann, P., Rabeder, G., Schultz, O., Zetter, R., 1993. Die Primatenfundstelle Götzendorf an der Leitha (Obermiozän des Wiener Beckens, Niederösterreich). Jahrb. Geol. B.-A. 136, 503–526.

Rohlf, F.J., 2001. Comparative methods for the analysis of continuous variables: geometric interpretations. Evolution 55, 2143–2160.

Rohlf, F.J., Slice, D.E., 1990. Extensions of the Procrustes method for the optimal superimposition of landmarks. Syst. Zool. 39, 40–59.

Rohlf, F.J., Marcus, L.F., 1993. A revolution in morphometrics. Tree, 8, 129–132.

Ronquist, F., Lartillot, N., Phillips, M.J., 2016. Closing the gap between rocks and clocks using total-evidence dating. Philos. Trans. R. Soc. B 371, 20150136.

Roos, C, Zinner, D., 2017. Primate Phylogeny. In: Fuentes, A. (Ed.), The International Encyclopedia of Primatology. John Wiley & Sons. https://doi.org/10.1002/9781119179313.wbprim0394.

Rose, M.D., 1988. Another look at the anthropoid elbow. J. Hum. Evol. 17, 193–224.

Rose, M.D., 1993. Locomotor anatomy of Miocene hominoids. In: Gebo, D.L. (Ed.), Postcranial Adaptation in Nonhuman Primates. Northern Illinois University Press, DeKalb, pp. 252–272.

Rose, M.D., 1994. Quadrupedalism in some Miocene catarrhines. J. Hum. Evol. 26, 387–411.

Rose, M.D., 1997. Functional and phylogenetic features of the forelimb in Miocene hominoids. In: Begun, D.R., Ward, C.V., Rose, M.D. (Eds.), Function, Phylogeny and Fossils: Miocene Hominoid Evolution and Adaptation. Plenum Press, New York, pp. 79–100.

Rose, M.D., Leakey, M.G., Leakey, R.E.F., Walker, A., 1992. Postcranial specimens of *Simiolus enjiessi* and other primitive catarrhines from the early Miocene of Lake Turkana, Kenya. J. Hum. Evol. 22, 171–237.

Rosenberger, A.L., Szalay, F., 1980. On the tarsiiform origins of the Anthropoidea. In: Ciochon, R.L., Chiarelli, A.B. (Eds.), Evolutionary Biology of the New World Monkeys and Continental Drift. Plenum Press, New York, pp. 139–157.

Ross, C., Williams, B., Kay, R.F., 1998. Phylogenetic analysis of anthropoid relationships. J. Hum. Evol. 35, 221–307.

Rossie, J.B., MacLatchy, L., 2006. A new pliopithecoid genus from the early Miocene of Uganda. J. Hum. Evol. 50, 568–586.

Rossie, J.B., Hill, A., 2018. A new species of *Simiolus* from the middle Miocene of the Tugen Hills, Kenya. J. Hum. Evol. 125, 50–58.

Rossie, J.B., Gutierrez, M.M., Goble, E., 2012. Fossil forelimbs of *Simiolus* from Moruorot, Kenya. Am. J. Phys. Anthropol. 147(S54), 252.

Russo, G.A., 2016. Comparative sacral morphology and the reconstructed tail lengths of five extinct primates: *Proconsul heseloni*, *Epipliopithecus vindobonensis*, *Archaeolemur edwardsi*, *Megaladapis grandidieri*, and *Palaeopropithecus kelyus*. J. Hum. Evol. 90, 135–162.

Sabol, M., Joniak, P., Bilgin, M., Bonilla-Salomön, I., Cailleux, F., Čerňanský, A., Malíková, V., Šedivá, M., Tóth, C., 2021. Updated Miocene mammal biochronology of Slovakia. Geol. Carpath. 72, 425–443.

Saitou, N., Nei, M., 1987. The neighbor-joining method: a new method for reconstructing phylogenetic trees. Mol. Biol. Evol. 4, 406–425.

Sankhyan, A.R., Kelley, J., Harrison, T., 2017. A highly derived pliopithecoid from the Late Miocene of Haritalyangar, India. J. Hum. Evol. 105, 1–12.

Sarmiento, E.E., 1995. Cautious climbing and folivory: a model of hominoid differentiation. Hum. Evol. 10, 289–321.

Schlager, S., 2017. Morpho and Rvcg - shape analysis in R: R-packages for geometric morphometrics, shape analysis and surface manipulations. In: Zheng, G., Li, S., Székely, G.

(Eds.), Statistical Shape and Deformation Analysis. Methods, Implementation and Applications. Academic Press, London, pp. 217–256.

Schliep, K.P., 2011. phangorn: Phylogenetic analysis in R. Bioinformatics 27, 592–593.

Schluter, D., Price, T., Mooers, A.Ø., Ludwig, D., 1997. Likelihood of ancestor states in adaptive radiation. Evolution 51, 1699–1711.

Seehuber, U., 2008. Litho- und biostratigraphische Untersuchungen in der Oberen Süßwassermolasse in der Umgebung von Kirchheim in Schwaben. Ph.D. Dissertation, Ludwig-Maximilians-Universität München.

Senut, B., 2012. Les restes post-crâniens des Pliopithecidae (Primates) de Sansan. Mém. Mus. Natl. Hist. Nat. 203, 535–558.

Shearer, B.M., Ungar, P.S., McNulty, K.P., Harcourt-Smith, W.E.H., Dunsworth, H.M., Teaford, M.F., 2014. Dental microwear profilometry of African non-cercopithecoid catarrhines of the Early Miocene. J. Hum. Evol. 78, 33–43.

Shoshani, J., Groves, C.P., Simons, E.L., Gunnell, G.F., 1996. Primate phylogeny: Morphological vs molecular results. Mol. Phylogenet. Evol. 5, 102–154.

Sidlauskas, B., 2008. Continuous and arrested morphological diversification in sister clades of characiform fishes: a phylomorphospace approach. Evolution 62, 3135–3156.

Simons, E.L., Fleagle, J., 1973. The history of extinct gibbon-like primates. Gibbon Siamang 2, 121–148.

Simons, E.L., Pilbeam, D.R. 1965. Preliminary revision of the Dryopithecinae (Pongidae, Anthropoidea). Folia Primatol. 3, 81–152.

Simons, E.L., Seiffert, E.R., Ryan, T.M., Attia, Y., 2007. A remarkable female cranium of the early Oligocene anthropoid *Aegyptopithecus zeuxis* (Catarrhini, Propliopithecidae). Proc. Natl. Acad. Sci. USA. 104, 8731–8736.

Skinner, M.M., Gunz, P., Wood, A., Boesch, C., Hublin, J.J., 2009. Discrimination of extant *Pan* species and subspecies using the enamel-dentine junction morphology of lower molars. Am. J. Phys. Anthropol. 140, 234–243.

Skinner, M.M., de Vries, D., Gunz, P., Kupczik, K., Klassen, R.P., Hublin, J.-J.c, Roksandic, M., 2016. A dental perspective on the taxonomic affinity of the Balanica mandible (BH-1). J. Hum. Evol. 93, 63–81.

Smith, A.B., 2000. Stratigraphy in phylogeny reconstruction. J. Paleontol. 74, 763–766.

Smith, R.J., 1993. Bias in equations used to estimate fossil primate body mass. J. Hum. Evol. 25, 31–41.

Smith, R.J., 1994. Degrees of freedom in interspecific allometry: an adjustment for the effects of phylogenetic constraint. Am. J. Phys. Anthropol. 93, 95–107.

Smith, R.J., Jungers, W.L., 1997. Body mass in comparative primatology. J. Hum. Evol. 32, 523–559.

Springer, M.S., Meredith, R.W., Gatesy, J., Emerling, C.A., Park, J., Rabosky, D.L., Stadler, T., Steiner, C., Ryder, O.A., Janečka, J.E., Fisher, C.A., Murphy, W.J., 2012. Macroevolutionary dynamics and historical biogeography of primate diversification inferred from a species supermatrix. PLoS One 7, e49521.

Steininger, F., 1986. Dating the Paratethys Miocene hominoid record. In: Else, J.G., Lee, P.C. Lee (Eds.), Primate Evolution. Cambridge University Press, Cambridge, pp. 71–84.

Steinthorsdottir, M., Coxall, H.K., de Boer, A.M., Huber, M., Barbolini, N., Bradshaw, C.D., Burls, N.J., Feakins, S.J., Gasson, E., Henderiks, J., Holbourn, A.E., Kiel, S., Kohn, M.J., Knorr, G., Kürschner, W.M., Lear, C.H., Liebrand, D., Lunt, D.J., Mörs, T., Pearson, P.N., Pound, M.J., Stoll, H., Strömberg, C.A.E., 2021. The Miocene: the future of the past. Paleoceanogr. Paleoclimatol. 36, e2020PA004037.

Stevens, N.J., Seiffert, E.R., O'Connor, P.M., Roberts, E.M., Schmitz, M.D., Krause, C., Gorscak, E., Ngasala, S., Hieronymus, T.L., Temu, J., 2013. Palaeontological evidence for an Oligocene divergence between Old World monkeys and apes. Nature 497, 611–614.

Strait, D.S., Grine, F.E., 2004. Inferring hominoid and early hominid phylogeny using craniodental characters: the role of fossil taxa. J. Hum. Evol. 47, 399–452.

Swofford, D.L., Bell, C.D., 2017. PAUP Manual. https://paup.phylosolutions.com/documentation/

Symonds, M.R.E., Blomberg, S.P., 2014. A primer on phylogenetic generalised least squares. In: Garamszegi, L.Z. (Ed.), Modern Phylogenetic Comparative Methods and Their Application in Evolutionary Biology. Springer, Berlin, pp. 105–130.

Szalay, F., Delson, E., 1979. Evolutionary History of the Primates. Academic Press, New York.

Thenius, E., 1981. Bemerkungen zur taxonomischen und stammesgeschichtlichen Position des Gibbons (Hylobatidae, Primates). Z. Säugetierkd. 46, 232–242.

Thiele, K., 1993. The holy grail of the perfect character: The cladistic treatment of morphometric data. Cladistics 9, 275–304.

Turner, T.R., Schmitt, C.A., Cramer, J.D., Lorenz, J., Grobler, J.P., Jolly, C.J., Freimer, N.B., 2018. Morphological variation in the genus *Chlorocebus*: Ecogeographic and anthropogenically mediated variation in body mass, postcranial morphology, and growth. Am. J. Phys. Anthropol. 166, 682–707.

Tuttle, R., 2016. Parallelism, brachiation, and hominoid phylogeny. In: Luckett, W.P., Szalay, F.S. (Eds.), Phylogeny of the Primates. Springer, New York, pp. 447–480.

Ungar, P.S., 1996. Dental microwear of European Miocene catarrhines: evidence for diets and tooth use. J. Hum. Evo.l 31, 335–366.

Ungar, P.S., Kay, R.S., 1995. The dietary adaptations of European Miocene catarrhines. Proc. Natl. Acad. Sci. USA. 92, 5479–5481.

Ungar, P.S., Teaford, M.F., Kay, R.F., 2004. Molar microwear and shearing crest development in Miocene catarrhines. Anthropologie 42, 21–35.

Urciuoli, A., Alba, D.M., 2023. Systematics of Miocene apes: State of the art of a neverending controversy. J. Hum. Evol. 175, 103309.

Urciuoli, A., Zanolli, C., Bouchet, F., Almécija, S., Moyà-Solà, S., Alba, D.M., 2022. Semicircular canal morphology of the Miocene small-bodied catarrhine *Pliobates cataloniae*: Phylogenetic implications. Am. J. Biol. Anthropol. 177, 187 (2022).

Urciuoli, A., Zanolli, C., Beaudet, A., Dumoncel, J., Santos, F., Moyà-Solà, S., Alba, D.M., 2020. The evolution of the vestibular apparatus in apes and humans. eLife 9, e51261.

Urciuoli, A., Zanolli, C., Beaudet, A., Pina, M., Almécija, S., Moyà-Solà, S., Alba, D.M., 2021a. A comparative analysis of the vestibular apparatus in *Epipliopithecus vindobonensis*: Phylogenetic implications. J. Hum. Evol. 151, 102930.

Urciuoli, A., Zanolli, C., Almécija, S., Beaudet, A., Dumoncel, J., Morimoto, N., Nakatsukasa, M., Moyà-Solà, S., Begun, D.R., Alba, D.M., 2021b. Reassessment of the phylogenetic relationships of the late Miocene apes *Hispanopithecus* and *Rudapithecus* based on vestibular morphology. Proc. Natl. Acad. Sci. USA 118, e2015215118.

Van Couvering, J., Delson, E., 2020. African land mammal ages. J. Vertebr. Paleontol. 40, e1803340.

Walker, A., Teaford, M.F.,Martin, L., Andrews, P., 1993. A new species of *Proconsul* from the early Miocene of Rusinga/Mfangano Islands, Kenya. J. Hum. Evol. 25, 43–53.

Weber, G.W., Bookstein, F.L., 2011. Virtual anthropology: A Guide to a New Interdisciplinary Field. Springer, Wien.

Welcomme, J.L., Aguelar, J.P., Ginsburg, L., 1991. Découverte d'un nouveau pliopithèque (Primates, Mammalia) associé à des rongeurs dans les sables du Miocène supérieur de Priay (Ain, France) et remarques sur la paléogéographie de la Bresse au Vallésien. C. R. Acad. Sci. Paris 313, 723–729.

Wu, R., Pan, Y., 1984. A late Miocene gibbon-like primate from Lufeng, Yunnan Province. Acta Anthropol. Sin. 3, 185–194.

Wu, R., Pan, Y., 1985. Preliminary observation on the cranium of *Laccopithecus robustus* from Lufeng, Yunnan with reference to its phylogenetic relationship. Acta Anthropol. Sin. 4, 7–12.

Wu,W.-Y., Meng, J., Ye, J., 2003. The discovery of *Pliopithecus* from northern Junggar Basin, Xinjiang. Vert. PalAs. 41, 76–86.

Ye, J., Wu, W.-Y., Meng, J., 2001. The age of Tertiary Strata and Mammal Faunas in Ulungur River area of Xinjiang. J. Stratigr. 25(4), 283–287.

Zalmout, I.S., Sanders, W.J., MacLatchy, L., Gunnell, G., Al-Mufarreh, Y.A., Ali, M.A., Nasser, A.-A.H., Al-Masary, A.M., Al-Sobhi, S.A., Nadhra, A.O., Matari, A.H., Wilson, J.A., Gingerich, P.D., 2010. New Oligocene primate from Saudi Arabia and the divergence of apes and old World monkeys. Nature 466, 360–365.

Zanolli, C., Bondioli, L., Mancini, L., Mazurier, A., Widianto, H., Macchiarelli, R., 2012. Brief Communications: Two human fossil deciduous molars from the Sangiran Dome (Java, Indonesia): Outer and inner morphology. Am. J. Phys. Anthropol. 147, 472–481.

Zanolli, C., Bondioli, L., Coppa, A., Dean, M.C., Bayle, P., Candilio, F., Capuani, S., Dreossi, D., Fiore, I., Frayer, D.W., Libsekal, Y., Mancini, L., Rook, L., Medin Tekle, T., Tuniz, C., Macchiarelli, R., 2014. The late Early Pleistocene human dental remains from Uadi Aalad and MulhuliAmo (Buia), Eritrean Danakil: Macromorphology and microstructure. J. Hum. Evol. 74, 96–113.

Zanolli, C., Biglari, F., Mashkour, M., Abdi, K., Monchot, H., Debue, K., Mazurier, A., Bayle, P., Le Luyer, M., Rougier, H., Trinkaus, E., Macchiarelli, R., 2019. A Neanderthal from the Central Western Zagros, Iran. Structural reassessment of the Wezmeh 1 maxillary premolar. J. Hum. Evol. 135, 102643.

Zanolli, C., Urciuoli, A., Delgado, M., Davies, T.W., Bouchet, F., Fortuny, J., Beaudet, A., Alba, D.M., Kullmer, O., Skinner, M.M. 2022a. The phylogenetic signal of the enamel-dentine junction of primate molars. Am. J. Phys. Anthropol. 177 (S73), 202.

Zanolli, C., Alba, D.M., Begun, D., Bouchet, F., Costeur, L., Dean, C.M., Fortuny, J., Kelley, J., Macchiarelli R, Morita W., Nakatsukasa, M., Rook, L., Urciuoli, A., 2022b. Tracking *Oreopithecus* evolutionary history: Evidence from the enamel-dentine junction morphology. In: Oreopithecus150 a Miocene Hominoid Enshrouded in a 150-years-long Mystery. International Conference. Abstract book.

Zanolli, C., Bouchet, F., Fortuny, J., Bernardini, F., Tuniz, C., Alba, D.M., 2023. A reassessment of the distinctiveness of dryopithecine genera from the Iberian Miocene based on enamel-dentine junction geometric morphometric analyses. J. Hum. Evol. 177, 103326.

Zapfe, H., Hürzeler, J., 1957. Die Fauna der miozänen Spaltenfüllung von Neudorf an der March (ČSR.). Primates. Sitzungsber. Öst. Akad. Wiss. Math. Naturwiss. Kl. 166, 113–123.

Zapfe, H., 1958. The skeleton of *Pliopithecus* (*Epipliopithecus*) *vindobonensis* Zapfe and Hürzeler. Am. J. Phys. Anthropol. 16, 441–457.

Zapfe, H., 1960. A new fossil anthropoid from the Miocene of Austria. Curr. Anthropol. 1, 428–429.

Zapfe, H., 1961a. Die Primatenfunde aus der miozänen Spaltenfüllung von Neudorf an der March (Děvinská Nová Ves), Tschechoslowakei. Schweizer. Palaeontol. Abh. 78, 4–293.

Zapfe, H., 1961b. Ein Primatenfund aus der miozänen Molasse von Oberösterreich. Z. Morphol. Anthropol. 51, 247–267.

Zelditch, M.L., Swiderski, D.L., Sheets, H.D., 2012. Geometric Morphometrics for Biologists: A Primer (Second Edition). Academic Press, Cambridge (USA).

Zhang, Z., Harrison, T., 2008. A new Middle Miocene pliopithecoid from Inner Mongolia, China. J. Hum. Evol. 54, 444–447.

Zhisheng, A., Kutzbach, J.E., Prell, W., Porter, S.C., 2001. Evolution of Asian moonsoons and phased uplift of the Himalaya–Tibetan plateau since Late Miocene times. Nature 411, 62–66.

